Studies of VHMS-related alteration: geochemical and mineralogical vectors to ore

Regional Studies and Volcanic Facies Controls

AMIRA/ARC project P439

Volume 3, Final Report
May 1998

CODES SRC

Centre for Ore Deposit Research,
School of Earth Sciences,
University of Tasmania,
GPO Box 252-79,
Hobart, Tasmania,
Australia 7001

http://www.geol.utas.edu.au/codes

another Pongratz & Hlaing Production 1998

Contents

Use of immobile elements and chemostratigraphy to determine precursor volcanics

Walter Herrmann
Centre for Ore Deposit Research

Summary

A number of elements, including the high field strength elements Ti, Zr, Nb, Y, Th; the heavy rare earths Lu & Yb and to a lesser degree the light rare earths; Al, Hf, Ta; and in some cases Sc, V and Cr, tend to be conserved in alteration zones associated with VHMS deposits. Although nett mass gains or losses of mobile components associated with hydrothermal alteration can result in changes of concentration of immobile elements, the inter element ratios of immobile elements will be invariable.

Immobility of element pairs should be tested, rather than assumed, by plotting data from a single precursor unit (which had primary compositional uniformity) on X–Y scatterplots. Immobile element pairs should define highly correlated linear trends which regress to the origin of the plot. (e.g. Fig. 1)

In practice, Ti and Zr have been found to be the most reliable immobile elements in VHMS systems. They can be inexpensively and accurately analysed by XRF on pressed powder pellets and they exist at easily detectable levels in most volcanics.

Some immobile elements are also incompatible* (e.g. Y and Zr), and can be interpreted to infer regional magmatic affinities, melt sources and tectonic settings.

Pairs of compatible–incompatible immobile elements (e.g. Ti and Zr) are most useful in prospect scale exploration, to identify unrecognisably altered rocks, map individual emplacement units through alteration zones, subdivide sequences by "chemostratigraphy" and infer petrogenetic relationships. Individual units from different magmatic sources or fractionated magmas may have distinctive immobile element ratios which enable their discrimination even in intensely altered or weathered zones. This is particularly so for coherent volcanic units of uniform primary composition, but is also applicable to some massive volcaniclastic units (e.g. rhyolitic pumice breccias).

Recognition of immobile elements is a prerequisite for calculating estimates of mobile component mass changes in altered rocks, relative to their least altered precursors, using the Isocon, Reconstituted Composition or Pearce Element Ratio methods.

Introduction

Immobile elements are useful for:

- Identifying the magmatic affinities of otherwise unrecognisable altered volcanic rocks in which the concentrations of mobile components may have been substantially modified.
- Quantitative estimation of mobile component mass changes due to alteration.

The concentrations of immobile elements in altered rocks may vary due to losses and gains of the mobile components but, if they are immobile, their variation will be proportional. In other words, the ratios between immobile elements will remain constant despite major mass transfers of mobile components in the alteration system.

This offers a means of recognising and mapping of individual volcanic units within zones of intense

* Incompatible elements are partitioned into the melt fraction during crystallisation of magmas; compatible elements are readily incorporated into early crystal phases.

pervasive alteration around VHMS deposits, where primary mineralogy and texture may be completely obscured by hydrothermal or metamorphic assemblages.

Immobile element lithogeochemical techniques have applications in VHMS exploration at the regional scale in interpreting the tectonic setting in which volcanic suites were emplaced and identifying favourable horizons, and at the prospect scale in discriminating and mapping volcanic units within zones of pervasive alteration.

Tectono-magmatic discrimination diagrams developed in the 1970s (Pearce & Cann, 1973; Floyd & Winchester, 1978) were based on the high field strength elements Ti, Zr, Nb, Y which are considered to be relatively immobile in hydrothermal, diagenetic, weathering and metamorphic alteration systems upto about mid amphibolite facies. In addition, it has been shown that Al, P* and the rare earth elements (REE) are also substantially immobile in alteration zones around a number of Canadian VHMS deposits (MacLean & Barrett, 1993).

Testing for immobility

A large number of studies of VHMS deposits (e.g. MacLean & Kranidiotis, 1987; Skirrow & Franklin, 1994; Barrett and MacLean, 1994) have shown that Al, Ti, Zr, Nb, Y, heavy REE (Lu, Yb), Hf, Ta and Th (and in some cases Sc, V and Cr) remained essentially immobile in alteration processes, even in the most intense feeder zones beneath deposits.

Nevertheless, MacLean & Barrett (1993) recommended that element immobility should be tested, rather than assumed, in each study area. If possible, the test should be carried out on a single volcanic unit which originally had compositional uniformity, such as a sill or coherent flow, and can be sampled laterally from the least altered rock in to the hydrothermally altered zone.

Scatter plots of analyses of pairs of immobile elements, including altered and least altered samples from such single precursor systems, should show linear trends — "alteration lines" — due to mass gains and losses of the mobile components in the altered zones of the rock unit. Calculated linear regressions of such alteration lines ideally pass through the origin of the scatterplot, representing infinite mass gain. Datapoints between the origin and the (unaltered) precursor concentrations represent net mass gains and those at values higher than the precursor concentrations represent net mass losses.

MacLean & Barrett (op cit.) indicated that pairs of immobile element in single precursor systems, should produce linear regressions with correlation coefficients of $r \geq 0.9$. Slight mobility of Y and the light REE in some alteration systems may produce lower correlation factors.

In cases where homogenous single precursor units are not recognisable, it may still be possible to test for immobility by plotting (reasonably large) datasets including least altered and altered samples and inspecting for linear trends which may be selected and tested for correlation.

Elements which can be reasonably shown to be immobile, can be used as the immobile monitors for estimates of mobile component mass changes in altered rocks, relative to the least altered precursors, using the Isocon, Reconstituted Composition or PER methods (Huston, 1993; MacLean & Barrett, 1993; Stanley & Madeisky, 1996; respectively).

Regional scale applications

The recognition that most VHMS deposits formed in a variety of extensional tectonic settings in association with volcanics of characteristic composition has encouraged the use of lithogeochemistry, particularly of immobile elements, in identification of prospective areas (Galley, 1995).

In the Australian context, Crawford et al. (1992) used Ti, Zr, Y, Nb, P and REE in conjunction with Si, Fe and Mg to discriminate three calcalkaline and two tholeiitic suites in the Mt Read Volcanics, to improve volcano-stratigraphic correlation within the belt, indicate prospective volcanic associations and develop an interpretation that the volcanics were erupted in a post collisional tectonic setting.

Similarly, petrogenetic studies of the Benambra area, Victoria, and Mt Windsor Volcanics, North

* Phosphorus may be a metasomatic addition to some alteration systems linked with fluids of magmatic origin; eg: Mt Lyell, (Large et al., 1996)

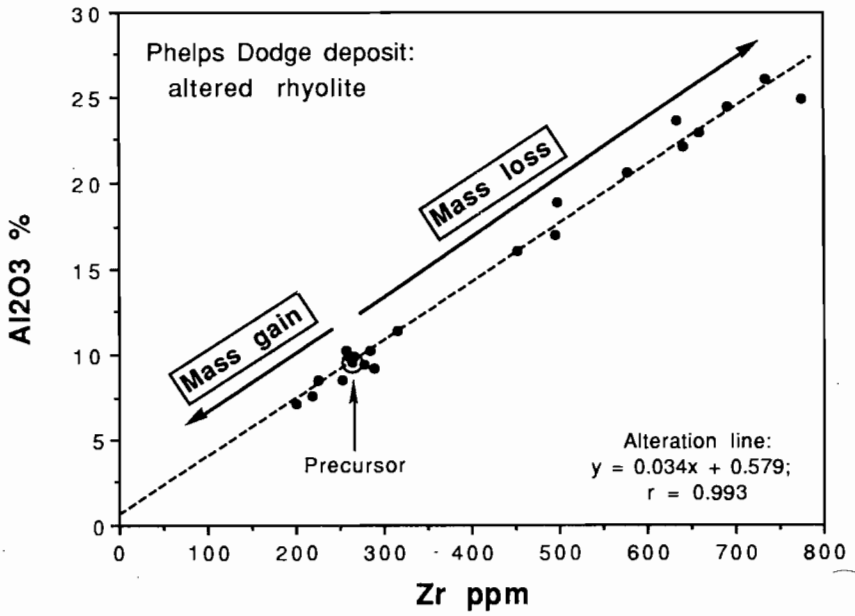

Figure 1. Effects of mobile mass gain and loss on immobile Al and Zr during alteration of an initially homogenous rhyolite unit (single precursor system) at the Phelps Dodge VMS deposit. (from MacLean and Barrett, 1993)

Queensland, by Stolz et al., (1995) and Stolz, (1995) were largely based on immobile elements Ti, Zr, Y, Nb, Th, P, REE and Nd isotopic data. In both of these regions, VHMS mineralisation was linked to the onset of mantle derived fractionated basalt–dacite volcanism following the accumulation of thick sequences of crustally derived rhyolitic volcanics, in probable back arc settings. Differing immobile element signatures enable discrimination of the less prospective footwall from the favourable host volcanic sequences, and can be applied in exploration to assess the mineral potential of volcanic terranes and map favourable stratigraphic levels.

Incompatible–Incompatible pairs

Once the immobility of elements is reasonably established, scatter plots of immobile incompatible–incompatible element pairs such as Zr–Y and Zr–Nb can distinguish rocks of different magmatic fractionation series (e.g. tholeiitic, calcalkaline etc.) within a volcanic sample set.

Incompatible elements are partitioned into the melt phase of fractionating magmas and hence they will exist at highest concentrations in the most evolved eruptive or intrusive units, and will retain similar inter element ratios throughout the fractionation series (if their partition co-efficients are similar). Samples from ***different*** magmatic suites thus produce separate linear trends of magmatic enrichment which regress to the origin. Subsequent hydrothermal alteration processes involving nett mass gain or loss could impose further changes in concentration but, because the elements were immobile and their primary ratios were preserved, the alteration trends will coincide with the fractionation trends (Fig. 2)

This approach could identify petrogenetic relationships between eruptive and intrusive units, favourable horizons and hydrothermal events.

Prospect scale applications

Compatible–incompatible pairs

Plots of immobile compatible–incompatible pairs (eg. TiO_2–Zr) and compatible–compatible pairs (eg. Al_2O_3–TiO_2) are generally the most useful in prospect scale mapping and interpretation.

As the compatible element is taken up in the crystal phases and the incompatible element remains in the melt, their relative concentrations in the

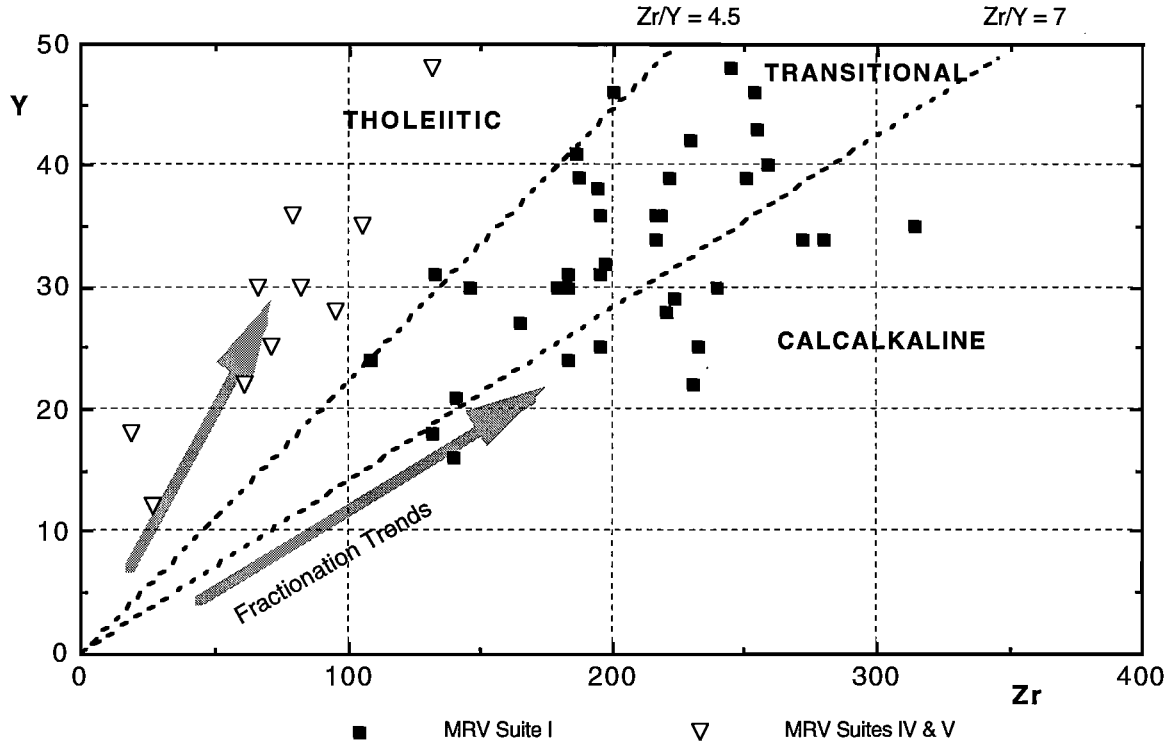

Figure 2. Incompatible and immobile element Y-Zr plot showing data for Suite I (calcalkaline) and Suites IV and V (tholeiitic) of the Mt Read Volcanics, from Crawford et al. (1992). Boundaries for tholeiitic, transitional and calcalkaline fields are from Barrett & MacLean (1994).

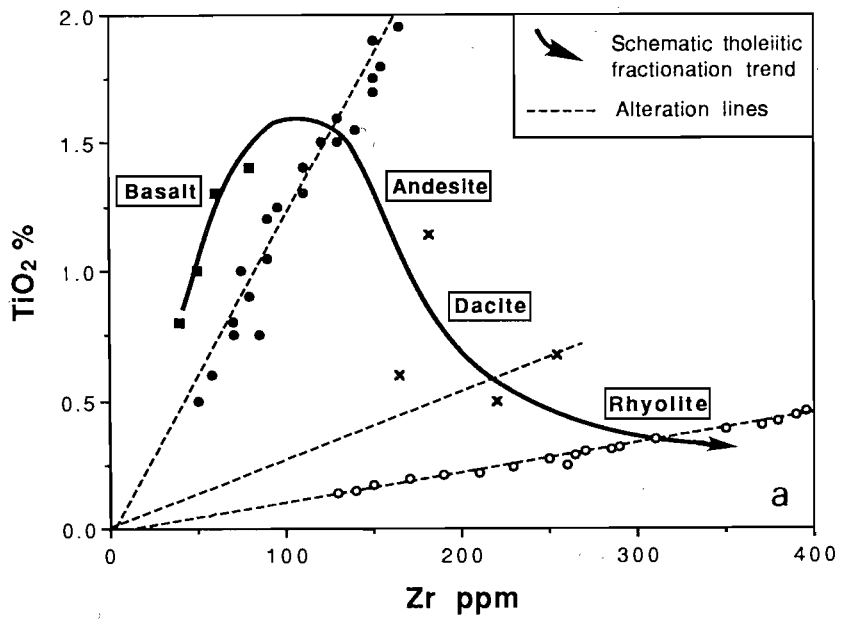

Figure 3. Idealized fractionation curve for immobile elements in a tholeiitic volcanic suite, with superposed chemical data for altered rocks. The two well defined alteration lines represent homogenous units within the stratigraphy. Their intersections with the fractionation curve identify the units as an andesite and a rhyolite. Other altered samples on these plots each have a distinct alteration line emanating from the origin. The fractionation curve exhibits strong Ti enrichment in t he basalts (paralleling typical iron enrichment in tholeiites) followed by strong Ti depletion from Andesite to rhyolite. (from MacLean and Barrett, 1993)

residual melts will change as fractionation proceeds. And successive batches of magma tapped off and emplaced as an eruptive or intrusive units, will have different (successively smaller) compatible/incompatible element ratios. Subsequent alteration mass gains and losses will produce (on a compatible/incompatible immobile element plot) separate alteration lines for each chemically distinct rock unit. This property enables discrimination and correlation of individual homogenous volcanic units within and through alteration zones at the prospect mapping scale (Fig. 3).

Chemostratigraphy

Figure 4 depicts TiO_2 and Zr data for 220 samples of volcanics from around the Thalanga deposit (data from Herrmann, 1994). The 134 rhyolite samples include variably altered coherent and volcaniclastic facies from a strike length of 6.5 km and stratigraphic thickness of ~400 m beneath the sulphide deposit. They plot as a tight linear array trending towards the origin. This group could reasonably be selected, by inspection, as a lithostratigraphic unit (or units), even without prior knowledge of the stratigraphic level of the samples. The high correlation coefficient is consistent with the immobility of Ti and Zr in this VHMS footwall alteration system.

Systematic immobile element analyses along drill holes or traverses across stratigraphy can be effectively used to distinguish volcanic emplacement units which may be difficult to recognise because of megascopic similarities or intense alteration. The same approach has also been successful in mapping bedrock geology from residual soil samples in areas of poor outcrop.

Figure 6 shows an example of Ti/Zr data for two Thalanga drill holes that intersect the favourable horizon from opposite sides, through the stratigraphic hangingwall and footwall. The rhyolites in the footwall are clearly distinguished, by Ti/Zr ratios of <5, from hangingwall dacites which have Ti/Zr ratios between 12 and 20. Alteration intensity in the footwall sequence intersected by TH270, grades from weak near the beginning of the hole, through broad zones of mottled chlorite+sericite±pyrite to semiconformable zones of intense chlorite+pyrite alteration near the favourable horizon, (Paulick, 1998). The Ti/Zr ratio remains constant.

Furthermore, dacites of two petrogenetic groups with different Ti/Zr ratios, of 10–12 (types 1&2) and 18–20 (type 3), have been recognised in the hangingwall sequence. These can also be distinguished by consistent differences in feldspar phenocryst contents, (Paulick, 1998).

The recognition of individual volcanic units, from immobile compatible–incompatible scatterplots, may be obscured where the sequence includes significant volcaniclastics of mixed derivation and variable composition (e.g. the Thalanga hangingwall fragmental unit and dacitic volcaniclastics in Figure 4).

In such cases, immobile element plots could show a radial fan of datapoints (Stanley and Madeisky, 1996). Sharp upper or lower boundaries of the fans, representing the compositional end members or sources of volcaniclastic materials, can be taken as evidence of element immobility. Stanley and Madeisky (op cit.) suggested that where the boundaries of such fans on immobile plots are well defined, the end member samples can be selected and treated as cogenetic in mass change calculation methods.

In the Thalanga example, the lower edge of the fan of data points in the rhyolite to dacite range, is more clearly defined because it includes many samples of intensely altered footwall rocks whereas the hangingwall units are much less altered and hence do not show a distinct radial linear trend, such as would be produced by significant mobile component mass changes.

Immobile element ratios of volcaniclastic units can also be used to infer provenance or relationships with other volcanic units in a sequence. For instance: in the Thalanga data the intermediate Ti/Zr values (6–11) of the "Hangingwall Fragmental Unit" indicate it is a mixture of rhyolitic and dacitic volcaniclastic materials — which is consistent with its stratigraphic location, immediately below the hangingwall dacite. In (reasonably fine grained) volcaniclastic units where the Ti/Zr ratio is variable in a definable range, it could be used to estimate the relative contributions from different volcanic provenances.

In another example: the high Ti/Zr ratios of the hangingwall volcaniclastic sandstone and associated black shales overlying sulphide lenses at the north

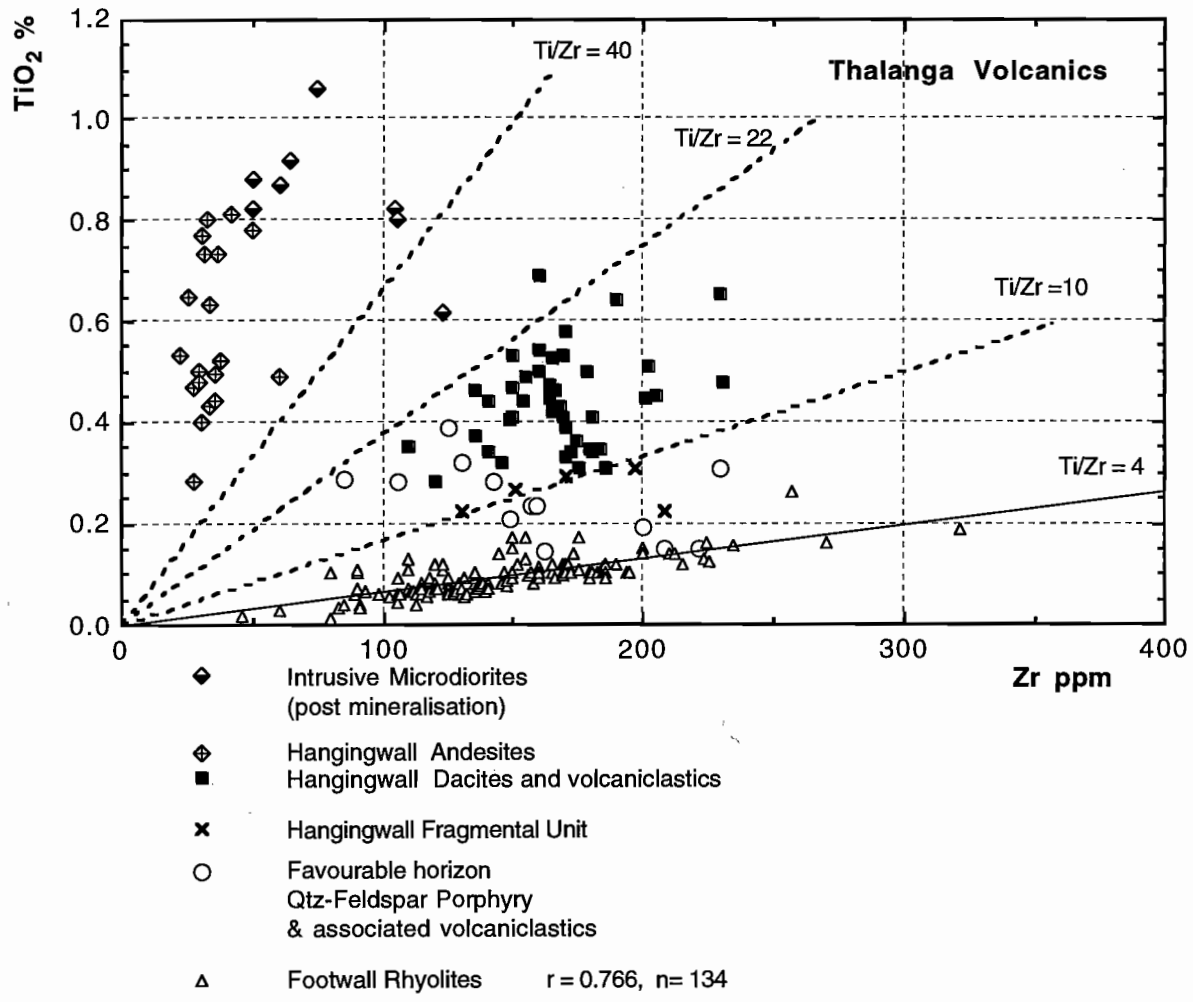

Figure 4. Zr-TiO_2 scatterplot of 220 Thalanga volcanic samples showing separation of lithostratigraphic units and strongly correlated linear array of 134 samples of footwall rhyolite.

end of the Rosebery deposit, suggest they contain some mafic volcaniclastic materials not derived from the Rosebery footwall sequence, (Large et al, 1998)

Relative mobility of elements

In practice, Ti and Zr have been found to be the most reliable immobile elements in VHMS systems. They can be inexpensively and accurately analysed by XRF on pressed powder pellets and they exist at easily detectable levels in most volcanics, unlike the heavy REE, Hf, Th, Ta & Sc which generally exist at <20 ppm levels. Barrett & MacLean (1994) noted some mobility of light REE within the most intensely chloritised proximal alteration zones beneath some VHMS deposits (where they may in fact provide exploration vectors). Y and Nb show considerable scatter in the Thalanga data (Herrmann, 1994) and may have been slightly mobile.

These degrees of immobility are exemplified in data from the footwall and host rocks at the north end of Rosebery, reported by Large & Allen (1997) and represented as scatterplots in Figure 5.

The linear arrays representing different volcanic units, on the plots involving Ti, Al and Zr, have high correlation coefficients (r = >0.8) and project close to the origin whereas those of Y, Nb, Sc and Th generally have lower correlation coefficients (as low as r = 0.2) and in some groups do not project towards the origin.

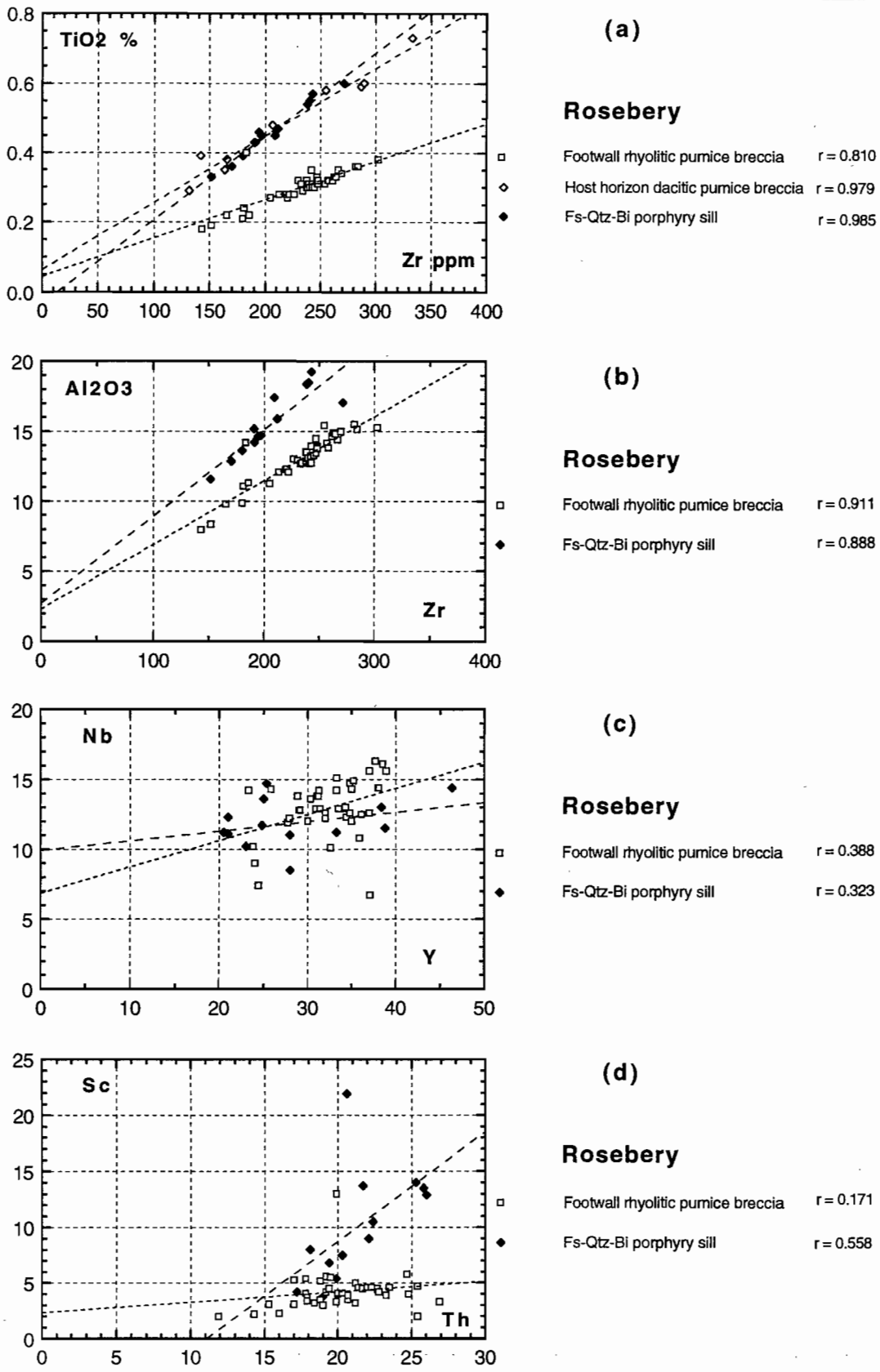

Figure 5. Scatterplots of potentially immobile element data for volcanic units at the north end of the Rosebery deposit.

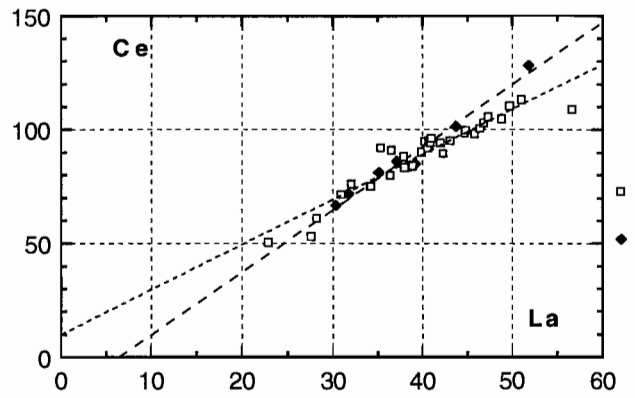

(e)

Rosebery

Footwall rhyolitic pumice breccia r = 0.947

Fs-Qtz-Bi porphyry sill r = 0.986

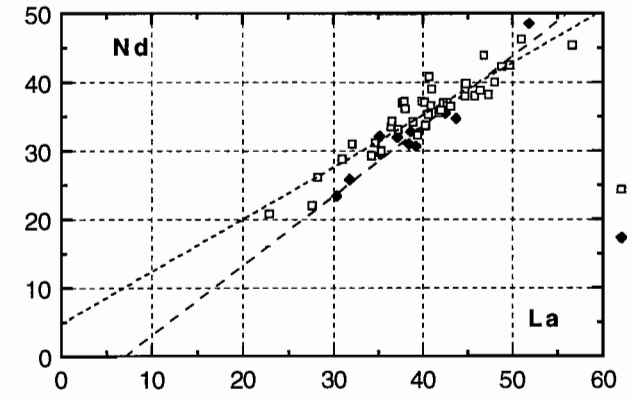

(f)

Rosebery

Footwall rhyolitic pumice breccia r = 0.934

Fs-Qtz-Bi porphyry sill r = 0.955

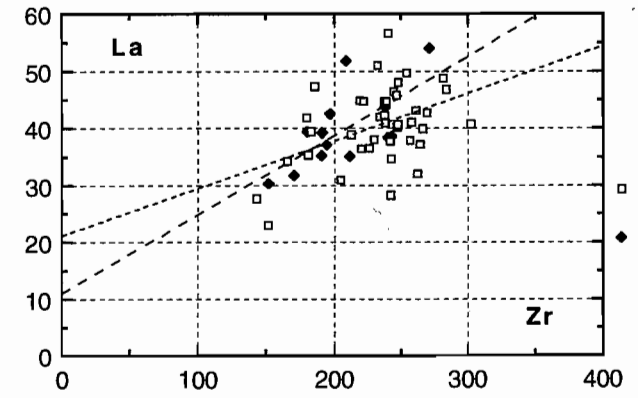

(g)

Rosebery

Footwall rhyolitic pumice breccia r = 0.439

Fs-Qtz-Bi porphyry sill r = 0.672

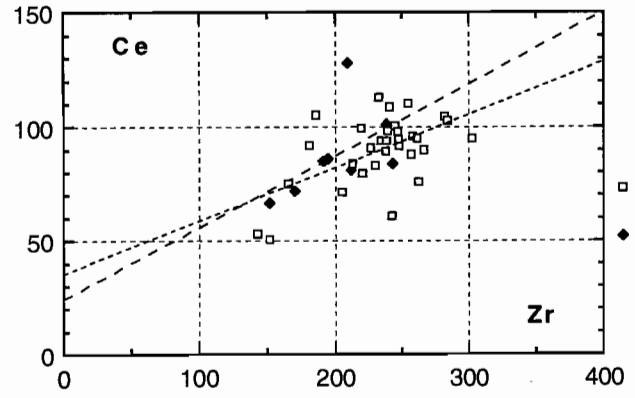

(h)

Rosebery

Footwall rhyolitic pumice breccia r = 0.562

Fs-Qtz-Bi porphyry sill r = 0.516

Figure 5. cont.

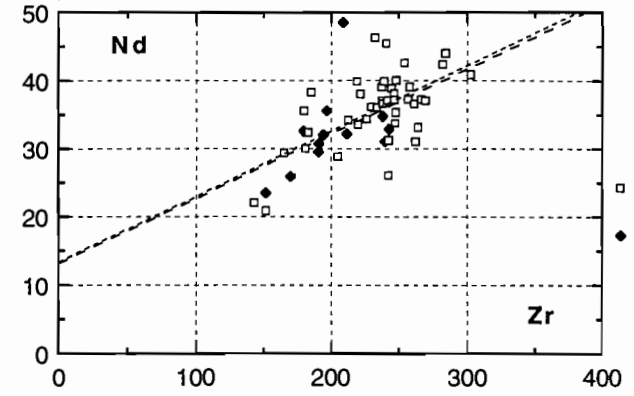

(i)

Rosebery

Footwall rhyolitic pumice breccia r = 0.621

Fs-Qtz-Bi porphyry sill r = 0.445

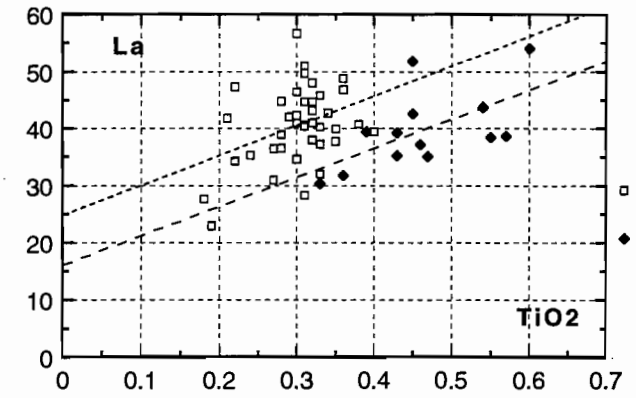

(j)

Rosebery

Footwall rhyolitic pumice breccia r = 0.375

Fs-Qtz-Bi porphyry sill r = 0.600

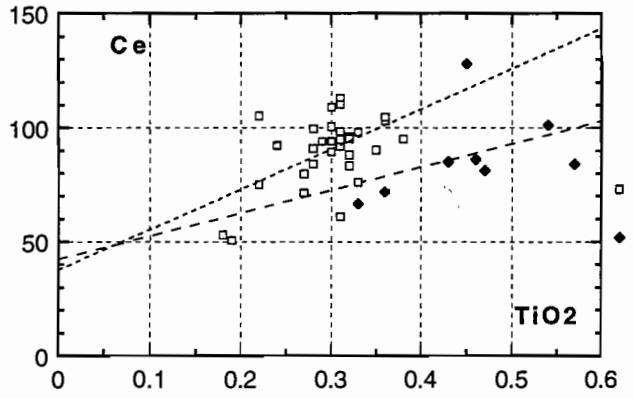

(k)

Rosebery

Footwall rhyolitic pumice breccia r = 0.535

Fs-Qtz-Bi porphyry sill r = 0.427

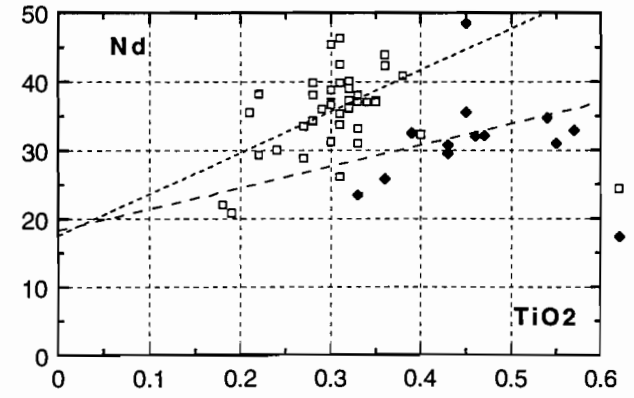

(l)

Rosebery

Footwall rhyolitic pumice breccia r = 0.531

Fs-Qtz-Bi porphyry sill r = 0.376

Figure 5. cont.

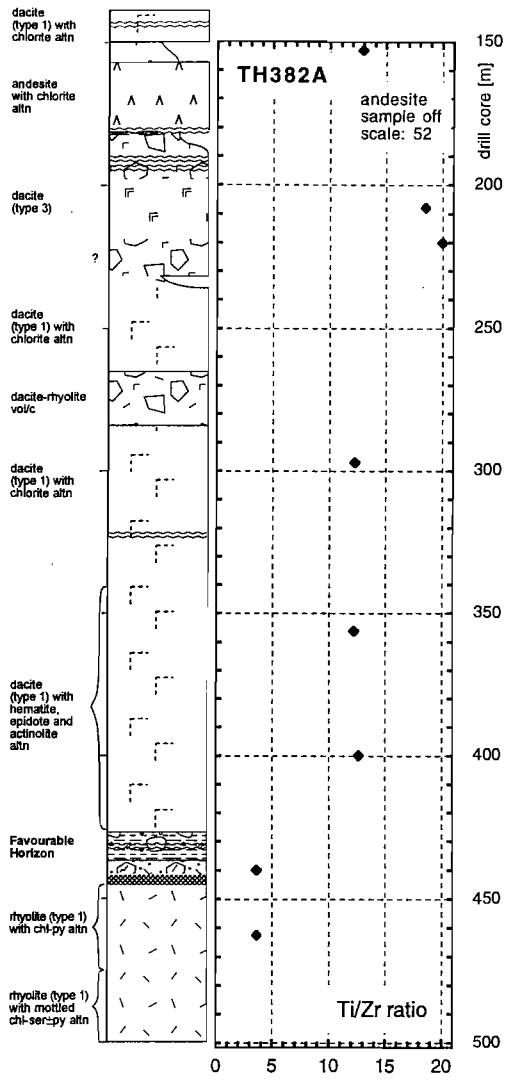

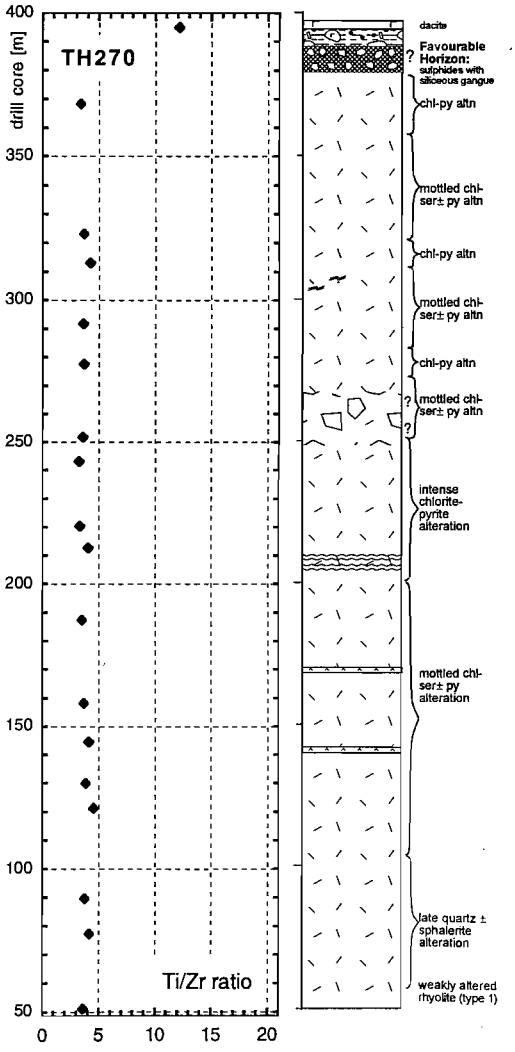

Figure 6. Lithofacies logs and downhole Ti/Zr plots for TH270 and TH382A, East Thalanga (cf. Fig. 4 in Paulick, 1998).

The available LREE analyses (La, Ce, Nd) plotted in Figure 5 (e & f) show strong linear correlations to each other but much lower correlation coefficients when plotted against Zr and TiO_2, (g to j). This infers that the LREE were partly mobile (assuming immobility of Zr and Ti) and also that the LREE were proportionally affected by hydrothermal changes, as might be expected from their similar chemical and physical properties (Rollinson, 1993). The second inference is contrary to the expectation of Finlow-Bates & Stumpfl (1981) that if an element has been mobile then it is usually readily identifiable as having moved, by its erratic distribution. The slight progressive increases in correlation coefficients, from La to Nd in both groups of pumice breccia data, are consistent with the observations of MacLean & Barrett (1993) that La is the most mobile of the trivalent REE with the others decreasing uniformly in mobility towards the heavier REE, Yb and Lu, which are consistently immobile during hydrothermal alteration. Surprisingly, the data for the feldspar–quartz–biotite porphyry sill show the reverse trend.

The Rosebery data also illustrate the utility of the immobile compatible–incompatible TiO_2–Zr scatterplot in discriminating different volcanic units and suggesting compositional relationships; in this case between pumice breccia closely associated with the ore horizon and a feldspar–quartz–biotite sill overlying it, (Figure 5a).

Large & Allen (op cit.) noted that the Hercules host rock has a similar "dacitic" Ti/Zr signature (~12–14) and recent analyses from sampling traverses (Herrmann, 1997) suggest that it (or a similar) unit exists immediately below the base of the White Spur Formation as far south as the Dobson Creek area. There is scope for immobile element lithogeochemistry to be applied in chemostratigraphic mapping of these otherwise massive and indistinguishable pumice breccia units and in tracing the lateral extent of the Rosebery–Hercules favourable horizon.

It is notable that although the Rosebery footwall and host rock pumiceous breccias are volcaniclastics, they retain uniform Ti/Zr and Al/Zr ratios suggesting that they were emplaced as essentially homogenous units and could therefore be examined for alteration mass transfers using the Isocon, Reconstituted Composition or PER methods.

References

Barrett, T.. and MacLean, W.H. 1994. Chemostratigraphy and hydrothermal alteration in exploration for VHMS deposits in greenstones and younger volcanic rocks. In Lentz, D.R., ed., Alteration and alteration processes associated with ore forming systems: Geological Society of Canada, Short course notes, V11, 433–467.

Crawford, A.J., Corbett, K.D. and Everard, J.L. 1992. Geochemistry of the Cambrian volcanic hosted massive sulphide rich Mount Read Volcanics, Tasmania, and some tectonic implications. Economic Geology, V87, 597–619.

Finlow-Bates, T. and Stumpfl, E.F., 1981. The behaviour of so-called immobile elements in hydrothermally altered rocks associated with volcanogenic submarine-exhalative ore deposits. Mineralium Deposita, V16, 319–328.

Floyd, P.A. and Winchester, J.A. 1978. Identification and discrimination of altered and metamorphosed volcanic rocks using immobile elements. Chemical Geology, V21, 291–306.

Galley, A.G. 1995. Target vectoring using lithogeochemistry: Applications to the exploration for volcanic hosted massive sulphide deposits. CIM Bulletin. V88(990):15–27.

Herrmann, W. 1994. Immobile element geochemistry of altered volcanics and exhalites at the Thalanga deposit, North Queensland. M.Econ.Geol. thesis, CODES, University of Tasmania.

Herrmann, W. 1997. Preliminary geochemical data from the Dobson Creek–White Spur traverses. AMIRA/ARC Project P439, Report 4, May 1997, 193–199.

Huston, D.L. 1993 The effect of alteration and metamorphism on wall rocks to the Balcooma and Dry River South volcanic hosted massive sulfide deposits, Queensland, Australia. Journal of Geochemical Exploration V48, p. 513–527.

Large, R.R., Allen, R.L., Blake, M. and Herrmann, W. 1998. Alteration halo model for the Rosebery VHMS deposit, Western Tasmania . AMIRA/ARC Project P439, Report 6 (in prep.)

Large, R.R. and Allen, R.L., 1997. Preliminary report on the Rosebery lithochemical halo study. AMIRA/ARC Project P439, Report 4, May 1997, 259–330.

Large, R.R., Doyle, M., Raymond, O., Cooke, D., Jones, A. and Heasman, L. 1996 Evaluation of the role of Cambrian granites in the genesis of world class VHMS deposits in Tasmania. Ore Geology Reviews, 10, p.215–230.

MacLean, W.H. and Kranidiotis, P., 1987. Immobile elements as monitors of mass transfer in hydrothermal alteration: Phelps Dodge massive sulfide deposit, Matagami, Quebec. Economic Geology, V82, 951–962.

MacLean, W.H. and Barrett, T.J., 1993. Lithogeochemical techniques using immobile elements. Journal of Geochemical Exploration, V48, 109–133.

Paulick, H. 1998 Alteration model for the Thalanga massive sulphide deposit, North Queensland. AMIRA/ARC Project P439, Report 6 (in prep.)

Paulick, H. 1997 Volcanic facies analysis, alteration and geochemistry of the host rock sequence to VHMS style mineralisation at Thalanga, North Queensland. AMIRA/ARC Project P439, Report 4, p.185–221.

Pearce, J.A. and Cann, J.R. 1973. Tectonic setting of basic volcanic rocks determined using trace element analyses. Earth and Planetary Science Letters, V19, 290–300.

Rollinson, H.R. 1993. Using geochemical data: evaluation, presentation, interpretation. Longman Scientific & Technical.

Skirrow, R.G. and Franklin, J.M., 1994. Silicification and metal leaching in semiconformable alteration beneath the Chisel

Lake massive sulfide deposit, Snow Lake, Manitoba. Economic Geology, V89, 31–50.

Stanley, C.R. & Madeisky, H.E. 1996 Lithogeochemical exploration for metasomatic zones associated with hydrothermal mineral deposits using Pearce Element Ratio Analysis. Short Course Notes on PER analysis; Mineral Deposit Research Unit, University of British Columbia, January 1996.

Stolz, A.J. 1995. Geochemistry of the Mount Windsor Volcanics: implications for the tectonic setting of Cambro-Ordovician volcanic hosted massive sulfide mineralisation in northeastern Australia. Economic Geology, V90, 1080–1097.

Stolz, A.J., Davies, G.R. and Allen, R.A. 1995. Geochemistry of the host volcanics to the Benambra massive sulfide deposits, Victoria, Australia, and the importance of silicic magmatism in VHMS mineralisation. AMIRA/ARC Project P439, Report 1, November 1995, 63–91.

Application of PIMA and FTIR spectrometry to VHMS alteration studies

Walter Herrmann, Michael Blake, Mark Doyle, David Huston and Julianne Kamprad

Centre for Ore Deposit Research and AGSO, Canberra

Summary

PIMA is a portable spectrometer that measures reflectance in the short wavelength infrared range. The PIMA's field portability and versatility in being able to rapidly and inexpensively spectrally analyse dry rock, core, drill cutting and soil samples, discriminate otherwise obscure clays, fine grained micas etc. and detect subtle compositional changes in some minerals (such as muscovite) opens up apparently wonderful opportunities to map and quantify hydrothermal alteration systems. Mapping the zonation of phyllosilicates, other silicates and carbonate phases, which are common products of alteration, is rarely easy, even by the practised eye, but could reveal important exploration vectors.

This study was designed to investigate the potential applications for PIMA spectrometry in interpreting hydrothermal alteration zones associated with Australian VHMS deposits.

Since most of these are deformed and metamorphosed to at least greenschist facies, the focus has been primarily on muscovite and chlorite; the early experience having shown that carbonates in alteration assemblages are not easily analysed by PIMA.

The study is based on a large number of PIMA spectra for samples from the alteration systems around the Rosebery, Western Tharsis and Highway–Reward deposits which represent contrasting styles of sulphide mineralisation hosted by felsic volcanics, in addition to spectra for background least altered rocks of the Mt Read Volcanics.

Rosebery and MRV regional traverses

Part of this study investigated the relationships between PIMA spectral characteristics, wholerock geochemistry and muscovite and chlorite compositions, in several hundred samples from regional traverses in the Mt Read Volcanics and drill holes around the northern end of the Rosebery massive sulphide deposit.

The results confirm that the wavelength of the PIMA spectral absorption feature attributed to AlOH bonds, is systematically related to the composition of muscovite. Sodic muscovites (with partial substitution of Na for K or muscovite-paragonite mixtures?) have wavelengths below 2200 nm and phengitic muscovites (with >0.5 Fe+Mg cations substituting for octahedral Al) generally have wavelengths between 2210 and 2220 nm.

However, the composition of muscovites is not linked to alteration intensity. Phengitic muscovite from the Rosebery footwall alteration zone has a similar range of composition, and AlOH wavelength, to muscovite in essentially unaltered rocks from elsewhere in the Mt Read Volcanics. Muscovite composition appears related to bulk rock composition in that the least phengitic, most sodic muscovites (with lowest wavelengths) exist in intermediate-mafic rocks with >10% chlorite and Ti/Zr 10–30. The hangingwall volcaniclastic sandstone unit at Rosebery contains muscovites of this type, in which the sodium content appears to be highest in proximity to sulphide lenses. Although there is probably no direct relationship to the VHMS forming hydrothermal system, this feature may have applications at the mine scale, as an exploration vector to ore lenses and to identify the favourable horizon. It requires more detailed PIMA observations on

additional drill cores to establish its value as a vector.

Chlorites in the samples analysed, have considerable compositional variations that are not systematically related to the Rosebery footwall alteration zone, or alteration intensity elsewhere. In any case, PIMA spectral characteristics show no systematic relationship to chlorite compositions in these Mt Read Volcanics and Rosebery samples.

Attempts at using PIMA spectral characteristics to estimate amounts, or relative amounts, of muscovite and chlorite in Mt Read Volcanics have met with very limited success. The results are probably inferior to ordinary megascopic visual estimates. The method may produce better results in sets of samples that have compositional and spectral uniformity.

Western Tharsis

In contrast to Rosebery, muscovite compositions at Western Tharsis show a clear and symmetrical compositional relationship to the ore lens and alteration system in bothe the stratigraphic footwall and hangingwall. The composition grades from moderately phengitic (~0.5 Fe+Mg) in the outer quartz+chlorite+sericite±carbonate zones to non phengitic (<0.1 Fe+Mg) in the proximal pyrophyllite±quartz±sericite zone.

This compositional change is very closely correlated to the AlOH absorption wavelength and constitutes a mine scale exploration vector which can be rapidly and effectively determined by PIMA analyses.

PIMA was instrumental in the recognition of several minor minerals — of major genetic importance — in the Western Tharsis alteration assemblage; they include pyrophyllite, topaz and zunyite.

Chlorites existing in the outer parts of the Western Tharsis alteration system show a weak trend of iron enrichment inwards towards the ore lens; (Mg numbers decreasing from ~45 to ~30). This compositional change is not measurable by PIMA analysis and the restriction of chlorite to the outer alteration zones limits its usefulness as an exploration vector.

Highway–Reward

PIMA AlOH feature wavelengths grade from intermediate to high (2202–2222 nm) in the outer zones of sericite+chlorite±feldspar alteration to significantly lower wavelengths (2195–2204 nm) in the proximal quartz+sericite±pyrite zones associated with pipe like pyrite bodies. Although as yet unsupported by microprobe analyses, there is a strong inference that white micas in the proximal zones are non phengitic, and possibly contain some Na substitution for K. The similarity to the pattern at Western Tharsis suggests a link between Cu–Au systems and low phengite contents of muscovites in proximal alteration zones. The muscovite composition is presumably determined by physico-chemical factors, perhaps related to the source of mineralising fluids.

Comparison of FTIR and PIMA spectrometry

FTIR and PIMA both provide qualitative information on white mica chemistry relating to the relative phengite (Fe+Mg) and paragonite (Na) composition. FTIR shows potential for measuring the Mg number variations in chlorite composition, in samples where the chlorite absorbance feature is not overshadowed by muscovite. In contrast, PIMA appears to be oblivious to chlorite chemistry, at least in mixed samples. Neither instrument has been proved to give information on carbonate chemistry in mixed assemblages, although FTIR has potential for investigation of other carbonate absorbance peaks in the low wavenumber region.

FTIR and PIMA use fundamentally different detection methods in that FTIR provides a measurement of sample transmission, whilst PIMA measures reflectivity. Because of this each may display different subtleties in particular wavelength regions, which may be complimentary.

Introduction

PIMA is a portable spectrometer that measures reflectance in the short wavelength infrared range between 1300 and 2500 nanometres. This (SWIR) range includes harmonics of fundamental absorption features attributed to OH, H_2O, CO_3, NH_4, AlOH, FeOH and MgOH molecular bonds and is thus useful for determination of a wide range of mineral groups including phyllosilicates, hydroxylated silicates and sulphates, carbonates and ammonium bearing minerals (Pontual et al., 1997)

Species in these groups produce characteristic SWIR spectra that enable identification of individual minerals and mineral mixtures in dry rock, soil and geochemical pulp samples. The magnitudes of various absorption features in spectra of mineral mixtures theoretically should allow estimation of quantities or relative abundances of the identifiable minerals in mixed samples. Compositional variations in some minerals are systematically related to the wavelengths of certain PIMA spectral absorption features. This property could enable the use of PIMA in mapping the zonation of mineral chemistry.

PIMA spectrometry thus offers a rapid, in-field technique of identifying and estimating quantities and compositions of the minerals in hydrothermally altered rocks. PIMA has potential applications in VHMS exploration for determination of white mica, chlorite and carbonates in metamorphosed settings, and clays in undeformed systems. These can be difficult to recognise and quantify by megascopic inspection but may have zonal and compositional variations that could reveal alteration vectors and allow discrimination of favourable horizons.

Preliminary investigations of the Hellyer alteration system (Yang et al., 1996a & 1996b) indicated that PIMA spectral characteristics vary through the alteration zones (at least in some drill holes) and could be used in determining alteration vectors. It was apparent that muscovite is most phengitic (with higher AlOH feature wavelengths) in proximal alteration zones but there is no systematic relationship between chlorite composition and alteration. Subsequent muscovite and chlorite microprobe analyses of doubtful quality, did not substantiate the spectral interpretations (Yang et al., 1997).

However, initial results from a single drill hole at Rosebery (120R) indicated good correlation between PIMA wavelengths of the AlOH absorption feature at ~2200 nm and muscovite microprobe analyses (Large et al., 1997).

They showed that:

- white micas in the altered footwall and ore host rocks at Rosebery are phengitic (and slightly barian) with upto 0.8 Fe+Mg atoms in Al octahedral sites, near zero Na/Na+K, and AlOH absorption wavelengths in the range 2208–2217 nm.
- white micas in the relatively unaltered hangingwall volcaniclastics, upto ~200m (stratigraphically?) above the favourable horizon, are slightly paragonitic and non phengitic, with upto 0.35 ionic proportion of Na/Na+K, ≤0.1 Fe+Mg atoms in Al octahedral sites, and lower AlOH absorption wavelengths between 2195–2200 nm.
- white micas in felsic volcaniclastic mass flow units ~200–300m above the favourable horizon are increasingly phengitic upwards towards the Mt Black Fault and contain 0.2 to 0.8 Fe+Mg atoms in Al octahedral sites, near zero Na/Na+K, with AlOH absorption wavelengths in the range 2208–2212 nm; ie: similar to the footwall characteristics.

These results collectively suggested that muscovite composition could be a useful indicator of proximity to VHMS deposits and associated footwall hydrothermal alteration zones, and that it is measurable by PIMA spectrometry.

This report presents the results of subsequent more extensive PIMA and microprobe analyses undertaken particularly to determine the regional background characteristics of **muscovite** and test its application as a vector at Rosebery, Western Tharsis and Highway–Reward deposits. It also summarises results of some spectral and microprobe analyses for **chlorites** (from Rosebery, Western Tharsis, Jukes prospect and Mt Read Volcanics (MRV) regional traverses, and **carbonates** from Western Tharsis.

Background notes on muscovite and chlorite composition and PIMA spectral analysis

Muscovite

Muscovite has the ideal formula of:

$K_2Al_4[Si_6Al_2O_{20}](OH,F)_4$ (Deer et al., 1966)

The principal substitutions are:

- Na,Rb,Cs,Ca,Ba for K in octahedral coordination. Na substitution can be upto ~20% just below the solidus but reduces markedly at lower temperatures with a complete absence of solid solution between K (muscovite) and Na (paragonite) at surface temperature. It is quantified by the ionic ratio Na/(Na+K).
- Fe^{+2},Mg,Mn,Li,Cr,Ti,V for Al in octahedral coordination and Si for Al in tetrahedral sites; the latter substitution balances the divalent ions substituting for Al in octahedral sites. Phengite is

the term used for muscovite of such composition (tetrahedral Si/Al of >3). The amount of phengite substitution can be quantified by either of the ionic ratios: tetrahedral Al / tetrahedral Al+Fe+Mg (=Al#) or octahedral Si/Al, or simply: Fe+Mg.

For this report, cationic proportions for muscovite have been calculated on the basis of 22 oxygens.

Chlorite

The basic formula is:

$(Mg,Fe,Al)_{12}[(Si,Al)_8O_{20}](OH)_{16}$

The principal substitutions are similar to phengitic muscovites:

- Al for Si; in the range Si_7Al_1 to Si_4Al_4
- Fe^{+2} and Mg by Al ($\pm Fe^{+3}$); in the range $(Fe,Mg)_{11}Al_1$ to $(Fe,Mg)_8Al_4$
- Fe^{+2} for Mg; in the complete range of $Mg/(Mg+Fe^{+2})$ from zero to one.

Unoxidised chlorites (with <4% Fe_2O_3) are thus classified on the basis of their ionic proportions of Si (or Si/Al) and Mg number (Mg/(Mg+Fe); (Deer et al., 1966).

In this investigation, chlorite cationic proportions were calculated on the basis of 28 oxygens from microprobe analyses in which total Fe is expressed as FeO (Fe_2O_3 not determined).

PIMA absorption features

The PIMA SWIR spectrum, from 1300 to 2500 nm, has diagnostic absorption features attributed to particular molecular bonds in the following ranges (Pontual et al., 1997) (see Fig. 1):

H_2O & OH	1350–1550 nm
OH	1700–1860 nm
H_2O	1880–2040 nm
AlOH	2160–2228 nm
FeOH	2230–2295 nm
MgOH	2300–2365 nm
CO_3	~1870, ~1990, ~2155 and 2300–2350 nm (coincident with MgOH)
secondary AlOH features	~2350 and ~2450 nm

Carbonate absorption features are difficult to interpret in spectra from mixed phyllosilicate + carbonate samples because of the coincidence of the CO_3, MgOH and secondary AlOH features at ~2350 and also the relatively weak absorption by CO_3 which is swamped by absorptions from smaller amounts of other minerals.

The PIMA ***muscovite*** spectrum (Fig. 2) is characterised by sharp, deep, single absorption features at ~2200 and 1400 (AlOH & H_2O-OH) moderate secondary AlOH features at ~2340 and 2440 and a weak H_2O feature at ~1900 (which distinguishes it from the deeper H_2O feature of illite).

The wavelength of the AlOH feature reportedly shifts according to composition as follows:

- paragonite <2200
- K muscovite 2200–2210
- increasing phengite 2210–2228

Chlorite spectra are dominated by strong FeOH and MgOH features of variable depth and wavelength according to Mg number, typically complex W shaped H_2O features at ~1900–2000, quite variable shapes and depths of H_2O features at ~1400 and ***no*** AlOH feature.

Fe rich chlorite spectra have significant positive gradients at low wavelengths (due to Fe^{+2} absorption off scale at ~1000 nm) and may have higher wavelengths in both the FeOH and MgOH absorption bands (Pontual et al., 1997, p1–85).

Mixed muscovite + chlorite spectra

Spectra for mixed muscovite+chlorite samples, therefore, typically have absorption features in all three of the AlOH, FeOH and MgOH bands (Fig. 2). The AlOH feature has less depth for muscovite + chlorite mixtures, whilst the MgOH feature (overlapping with a secondary AlOH feature) tends to be deeper. The FeOH feature is of variable depth according to the Mg# of the chlorite and the amount of chlorite present. Samples dominated by muscovite with small amounts of chlorite would show only a slight inflection at the FeOH band whereas the converse case would show a deeper FeOH feature and only a weak feature or inflection at the AlOH band.

This property, which is recognisable in subjective inspection of spectra, opens the possibility that spectral data can be used to quantitatively estimate the amounts, or relative amounts, of muscovite and chlorite in samples.

This study has tried several approaches, with limited success.

They include:

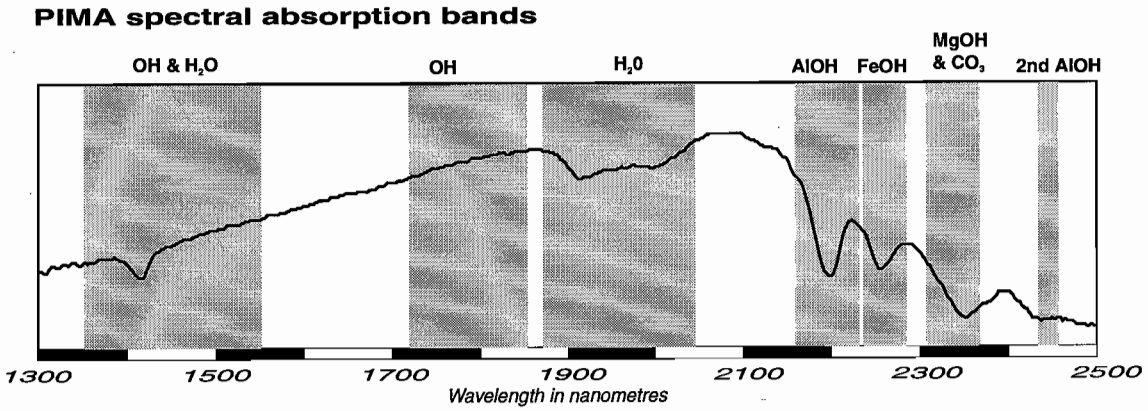

Figure 1. Major spectral absorption bands in the SWIR (after Pontual et al., 1997)

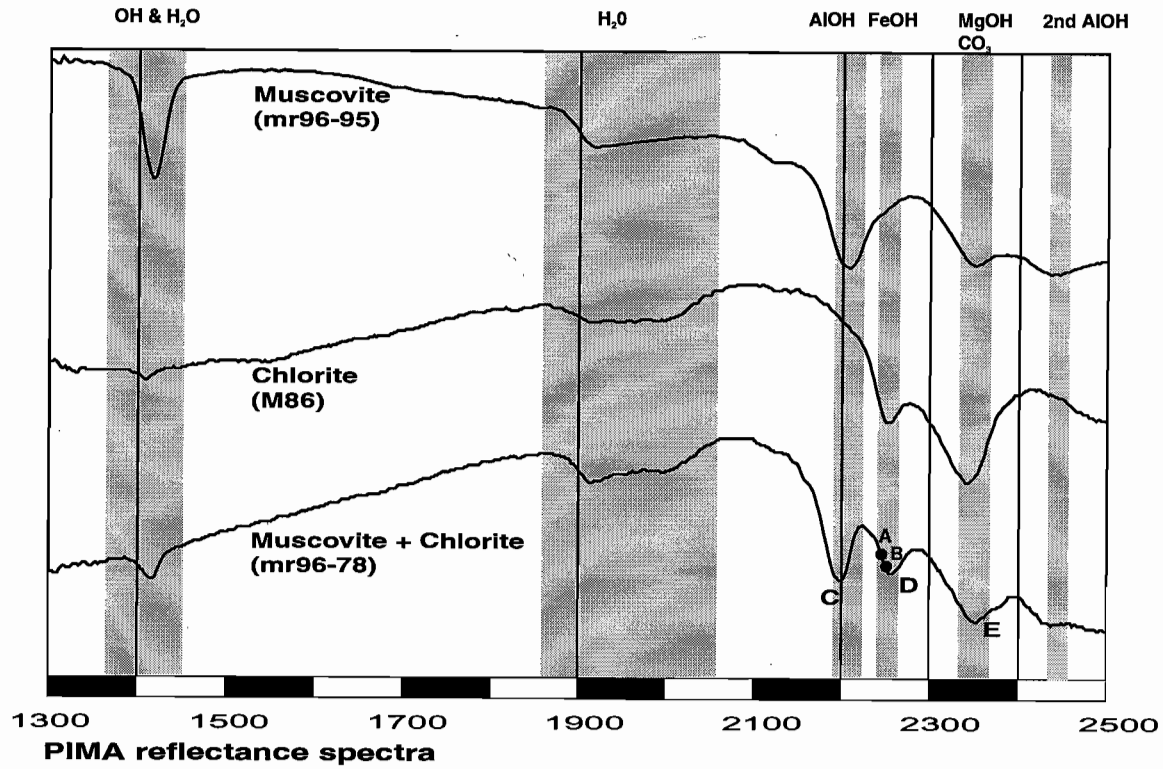

Figure 2. Typical PIMA spectra for muscovite, chlorite and mixtures of muscovite+chlorite

- Estimating the slope of the low wavelength side of the range occupied by the FeOH absorption feature. In muscovite samples this slope will be steep and positive, in mixed muscovite-chlorite samples it may be less steep, approach zero or become negative and in chlorite samples should be negative. The approach here has been to calculate ratios of raw reflectance values at 2236 and 2246 nm (denoted A & B in Fig. 2) and apply a normalising function: 100*((A/B)-1) to produce a negative value for muscovite dominant samples and a positive value for chloritic samples. Values around zero would equate to a slope of zero. The 2236–2246 nm segment of the spectrum was selected (after inspection of the PIMA data for MRV samples from the Hercules–Red Hills traverse) to ensure that it is not affected by shifts of the FeOH feature wavelength, remaining always on the low wavelength side of that feature.
- Calculating complex ratios of the depths of AlOH, MgOH and 2nd AlOH absorption features (C, E, F in Fig. 2). This approach is based on the assumption that the ratios of the depths of the 2200 nm AlOH feature (C) and secondary AlOH features at 2340 and 2440 nm (E, F), in relatively pure muscovite spectra, will remain proportional irrespective of reflectance level; ie: C/E and C/F remain constant, and (C/F)/(C/E) is ~1. Progressively more chlorite in mixed samples would reduce the depth of C and F and ***increase*** the depth of E, which coincides with the MgOH absorption feature in chlorite. Thus, in muscovite + chlorite mixtures, the ratio (C/F)/(C/E) would be >1 and positively correlated with chlorite content.

  A major shortcoming of this ratio as a measure of muscovite and chlorite content, is the absence of a secondary AlOH feature at ~2340 nm (F) in spectra dominated by chlorite, which effectively limits calculation of the ratio to muscovite dominated spectra.
- Calculating simple ratios (C/D and C/E) or differences (C–D and C–E) of the depths of AlOH and FeOH, MgOH absorption features. This approach reduces the problem of the absence of some absorption features in some spectra (eg: absence of FeOH or 2nd AlOH features in chlorite or muscovite poor samples).

  The ***ratio*** of the depths of absorption features (C/D and C/E) should be small (<<1) in chloritic samples and increase to ~2 in muscovite rich samples.

  The ***difference*** between the depths of the absorption features (C–D and C–E) should be positive in muscovite rich samples and negative in chloritic samples.

Reflectance and Hull Quotient Spectra

PIMA reflectance spectra commonly have a background convex curve, known as the reflectance hull, due to strong absorption features beyond the SWIR range attributed to Fe^{+2} at ~1000 nm and H_2O & CO_3 at ~2700 nm. The hull curve can be "straightened" for spectral analysis by two methods:

- subtracting observed reflectance from the hull curve to produce a Hull Difference spectrum; Hull Difference = 100–(hull reflectance–obs. reflectance)
- dividing the hull curve by observed reflectance to produce a Hull Quotient spectrum (HQ); Hull Quotient = 100 * (obs. reflectance ÷ hull reflectance)

In this report, the spectral interpretation of Rosebery and MRV background regional samples is based on raw Reflectance Spectra. This is mainly due to WH's preference for "observed" data and concerns that attempts to estimate mineral proportions could yield spurious correlations by ratioing ratios of the depths of certain absorption features.*

Spectral interpretations, by DH and JK on West Tharsis, and MD on Highway–Reward, etc. have been based mainly on hull quotient spectra.

Application of the hull quotient "correction" causes shifts in wavelengths of absorption features where the hull gradient is steep. Figure 3 shows; for comparisons, reflectance and HQ data for the AlOH, FeOH and MgOH absorption features of 268 Rosebery PIMA spectra. Evidently HQ wavelengths are

* In raw reflectance spectra the depths of absorption features are calculated by subtracting reflectances from the hull curve value. In hull quotient (HQ) spectra the depths of features are distorted by the ratioing of observed reflectances and hull and their position in the spectrum; eg: an absorption of 5% near the middle of the spectrum where background reflectance may be (say) 30% would produce a HQ depth of 16.6 whereas a 5% absorption near 2400nm where the reflectance may be (say) 10% would produce a HQ depth of 50.

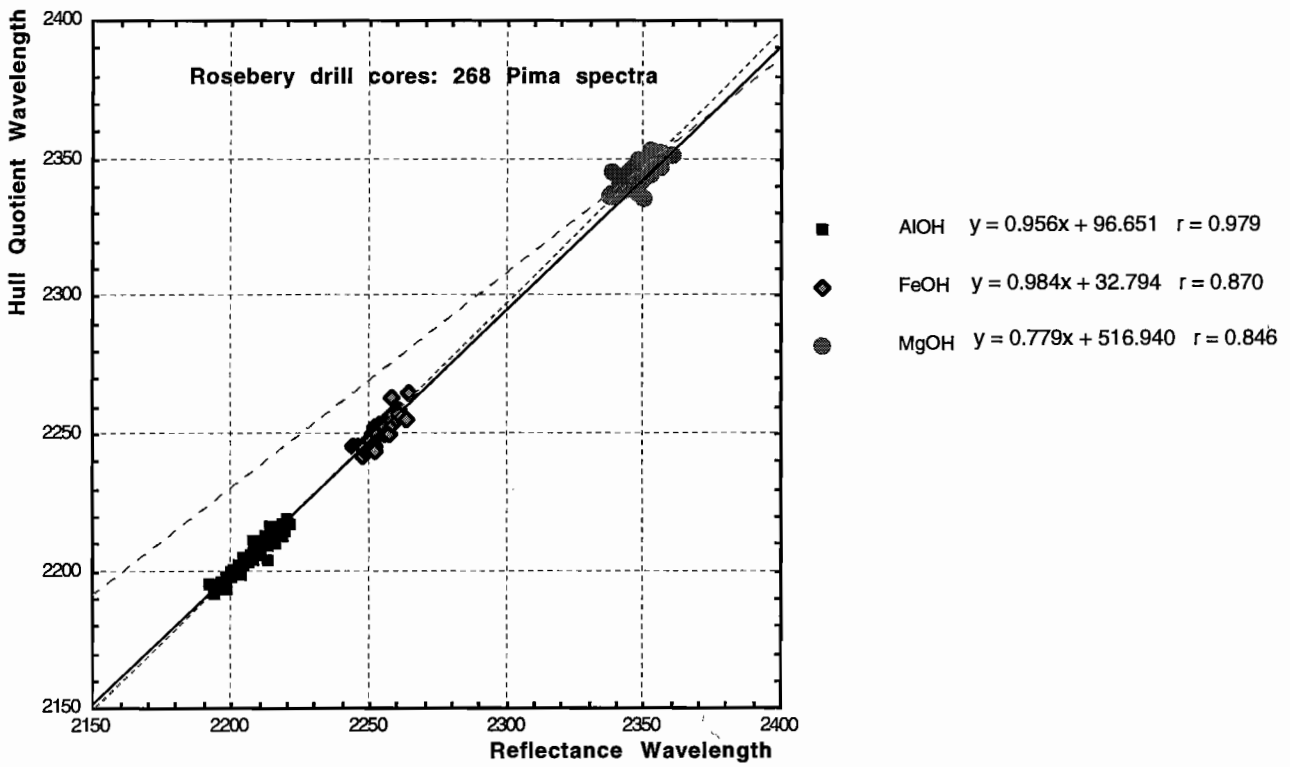

Figure 3. Comparison of wavelengths for AlOH, FeOH and MgOH absorption features in PIMA reflectance and hull quotient spectra of 268 Rosebery samples.

generally lower than reflectance wavelengths (by about 3 nm in FeOH and MgOH) and the correlation decreases as wavelength increases.

Precision of PIMA measurements

PIMA-II measures reflectances at 2 nm steps across the spectrum between 1300 and 2500 nm. However, the spectral analysis software (Pimacalc) estimates wavelengths of absorption features to an apparent precision of 0.01 nm, indicating that it applies some process of curve fitting.

In an informal test of the real precision of the instrument, eight spectra were recorded, consecutively over a period of eight minutes and without moving the sample, on a sawn core specimen from Rosebery 120R, 1403.4m. The resultant wavelength estimates for absorption features in the AlOH, FeOH and MgOH bands, tabulated below, suggest that the precision is only about the same as the reading interval (ie: about 2 nm) and decreases with increasing wavelength.

Wavelength	AlOH	FeOH	MgOH
Mean	2215.18	2241.21	2349.40
StdDev	1.09	2.10	3.72
Maximum	2216.50	2243.63	2354.14
Minimum	2213.16	2240.00	2342.00

PIMA spectral characteristics of Mt Read Volcanics

We used PIMA to analyse approximately 160 samples from regional traverses at Hercules–Red Hills, Mt.Black–Sterling Valley and White Spur, in order to obtain "background" spectral data on least altered Mt Read Volcanics (MRV).

CODES obtained a loan of CSIRO's PIMA instrument #2, during December 1997. The instrument measured spectra in the normal mode (not enhanced) on dry, flat, sawn surfaces of rock samples. Most of the samples are felsic, of adequate reflectance and of sufficiently fine grainsize to present a representative area to the measuring window. The advantage of being able to measure spectra on

different sericitic and chloritic domains in some rock samples outweighed the slightly higher reflectances that might be obtainable from powdered samples. The internal calibration standard was measured at start ups, shut downs and at about 2 hour intervals during sessions; no significant drifts were noted and no systematic corrections have been applied to the observations.

The MS-DOS programme "Pimacalc" was used (courtesy of Ausspec) to determine spectral characteristics, such as wavelengths and depths of absorption features, and produce stacked profiles for export to other spreadsheet and graphic applications.

Figures 4 to 10 present reflectance spectra as stacked profiles.

There are basically three types represented:

- Spectra with moderate to high amplitude and background reflectance and prominent AlOH and H_2O absorption features indicating dominance of muscovite (and/or illite due to surface weathering of muscovite and feldspar). Some of these have weak to moderate FeOH features indicating the presence of chlorite.
- Flatter, darker spectra (of lower reflectance) with more prominent FeOH and MgOH features and subtle or absent AlOH features indicating that chlorite is the dominant phyllosilicate.
- Flat, rather "noisy" spectra of low reflectance without recognisable absorption features indicating a low phyllosilicate content (as in fresh quartzo-feldspathic or siliceous samples) or high sulphide, carbon or magnetite contents (which dramatically lower the background reflectance).

The Mt Black spectra (Figs 6–8) have consistent characteristics related to bulk rock composition (as measured by Ti/Zr ratio) so that in rhyolites the dominant phyllosilicate appears to be muscovite with traces of chlorite; the dacites and andesites contain mixtures of chlorite ± minor to moderate muscovite; and mafic rocks are vastly dominated by chlorite ± traces of muscovite. This pattern is not evident in the Hercules–Red Hills and White Spur samples as they do not span a broad compositional range (are mostly felsic) and include some chloritic altered rhyolitic pumice breccias from the footwall alteration zone at Hercules.

Wavelength of AlOH absorption features

Absorption features in the AlOH band in MRV spectra, have wavelengths ranging from 2198 to 2225 nm, (Fig. 11). The great majority lie between 2205 and 2218 nm suggesting that the white micas have normal muscovite to phengitic compositions. Only one sample has a wavelength of <2200 nm; it is MR96-78, a possibly intrusive, chloritic andesitic rock from ~1km east of Mt Read.

There are no consistent relationships between wavelength and alteration intensity as measured by AI and CCPI, with wholerock composition as measured by Ti/Zr ratio, nor with stratigraphic level. Mafic rocks with Ti/Zr >20, amongst the Hercules and Mt Black samples, and very chloritic samples from the Hercules footwall zone, tend to have wavelengths in the lower half of the range. This suggests that muscovite is less phengitic in the presence of abundant chlorite.

These findings invalidate earlier implications (Large et al., 1997) that PIMA spectrometry is useful (to estimate muscovite chemistry) as a VHMS exploration vector at the deposit or district scales. High AlOH feature wavelengths, similar to those associated with phengitic muscovites in the footwall of the Rosebery deposit, have been measured in virtually all rock types across the entire spectrum from least altered to intensely hydrothermally altered.

The low wavelengths found in the immediate hangingwall units at Rosebery appear to be anomalous. It is notable that low wavelength muscovites do not exist in samples from the White Spur Formation (WSF) a few kilometres south of Hercules. It suggests that either the basal WSF is not equivalent to the Rosebery hangingwall sequence or that low wavelength micas exist only in the proximity of Rosebery.

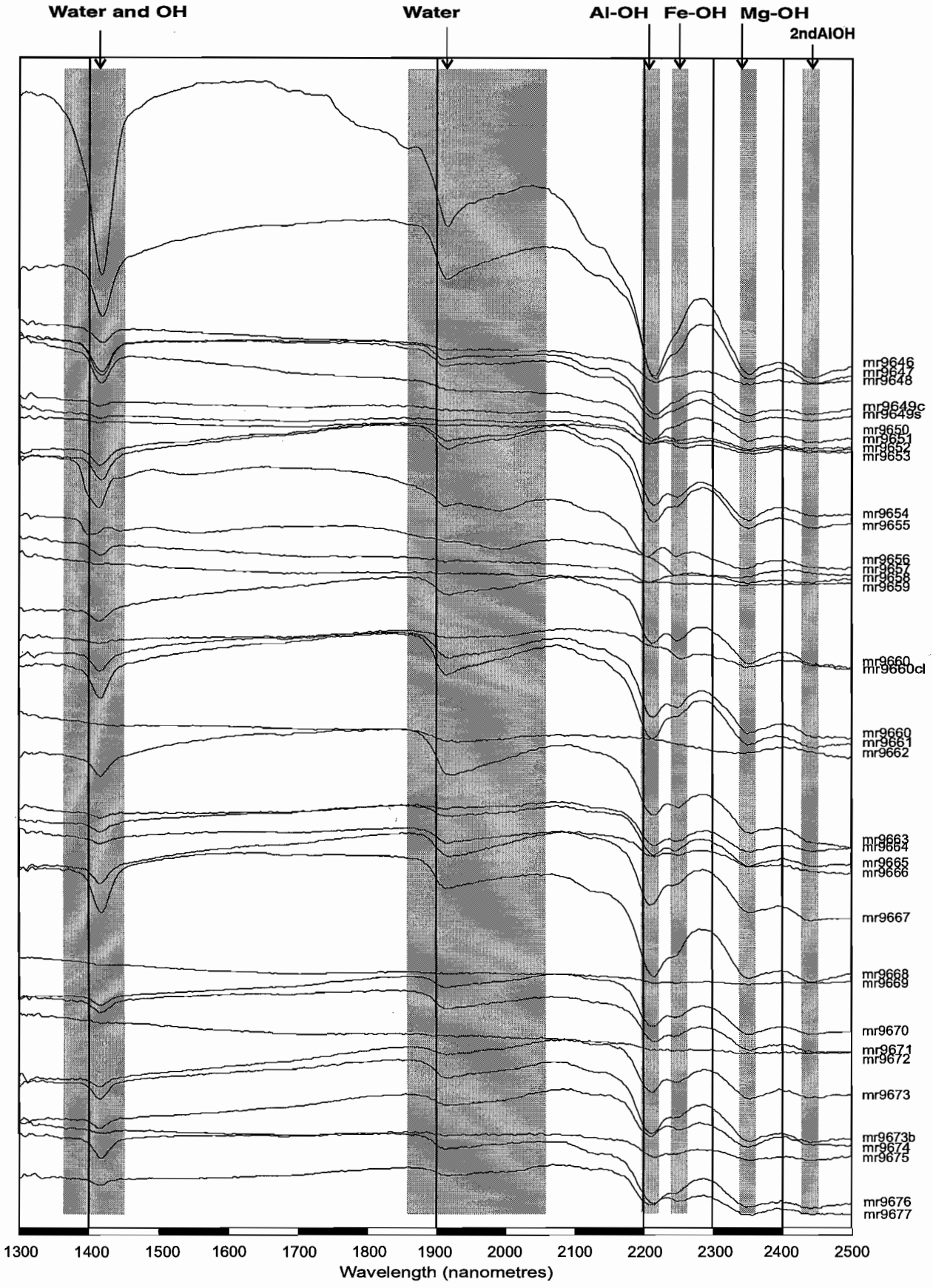

PIMA Reflectance Spectra **Hercules - Mt Read: MR96-46 to 96-77** **Figure 4**

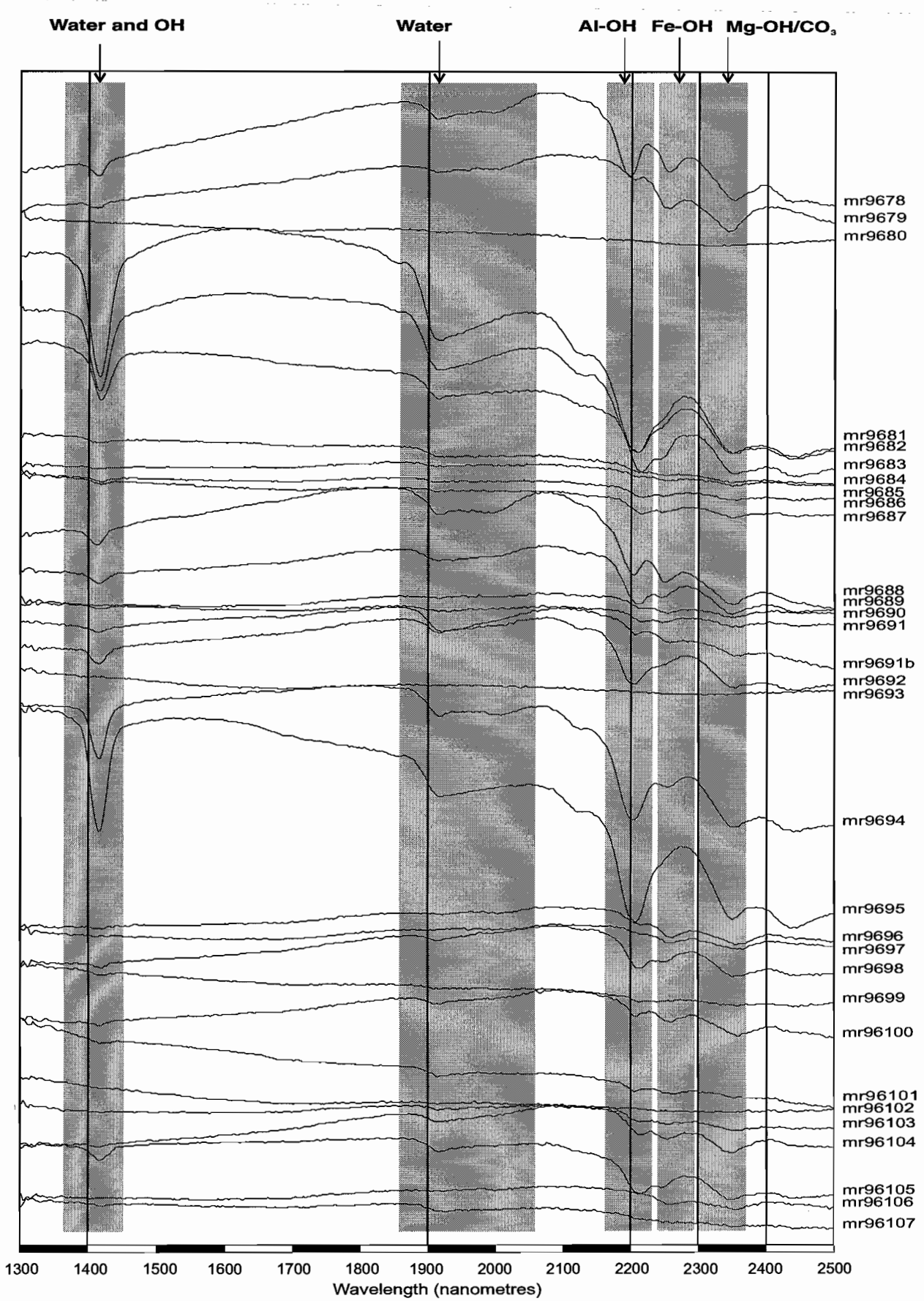

PIMA Reflectance Spectra **Mt Read - Red Hills MR96-78 to 96-107** **Figure 5**

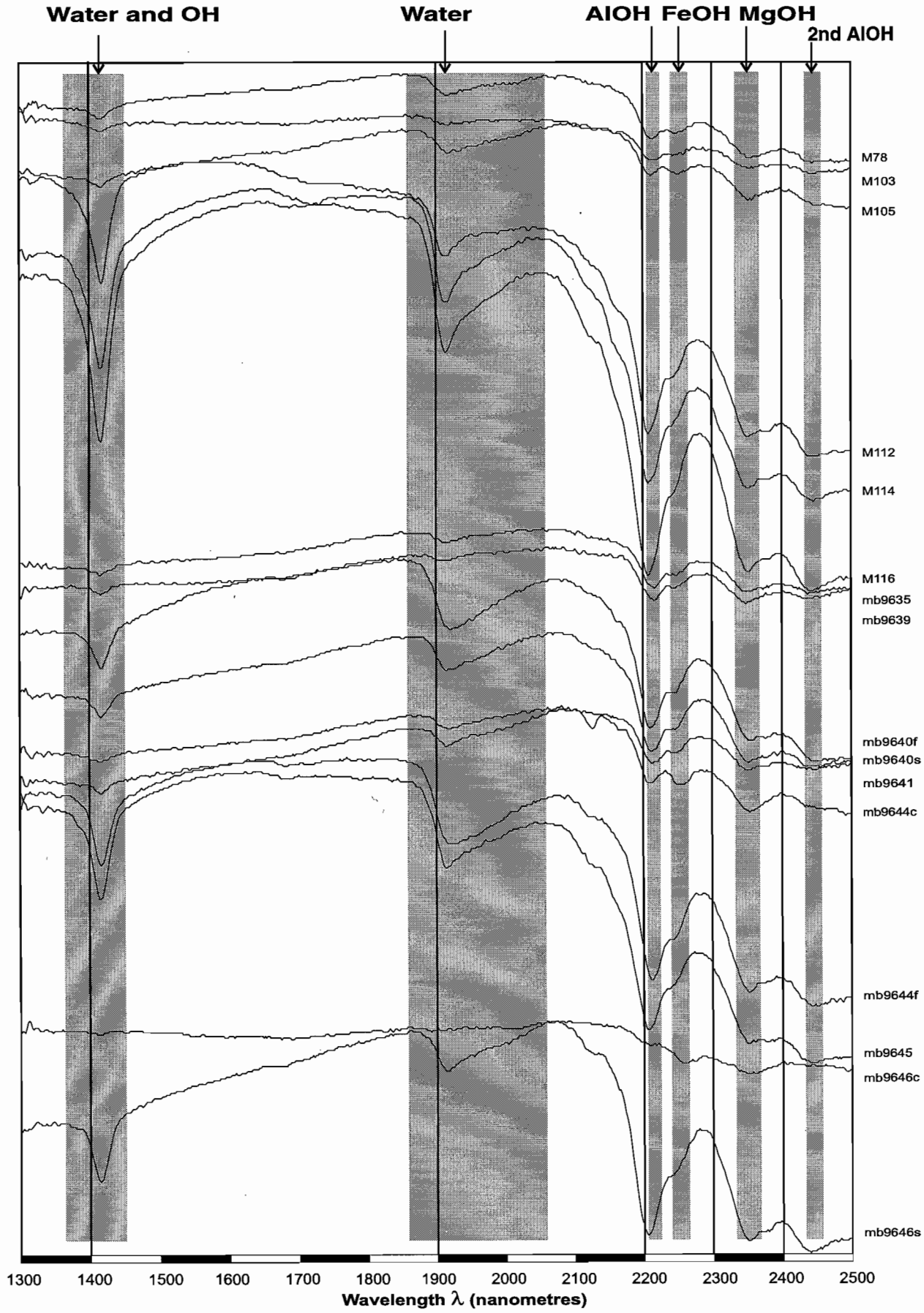

PIMA Reflectance Spectra **Mt Black & Sterling Valley Volcanics - Rhyolites** **Figure 6**

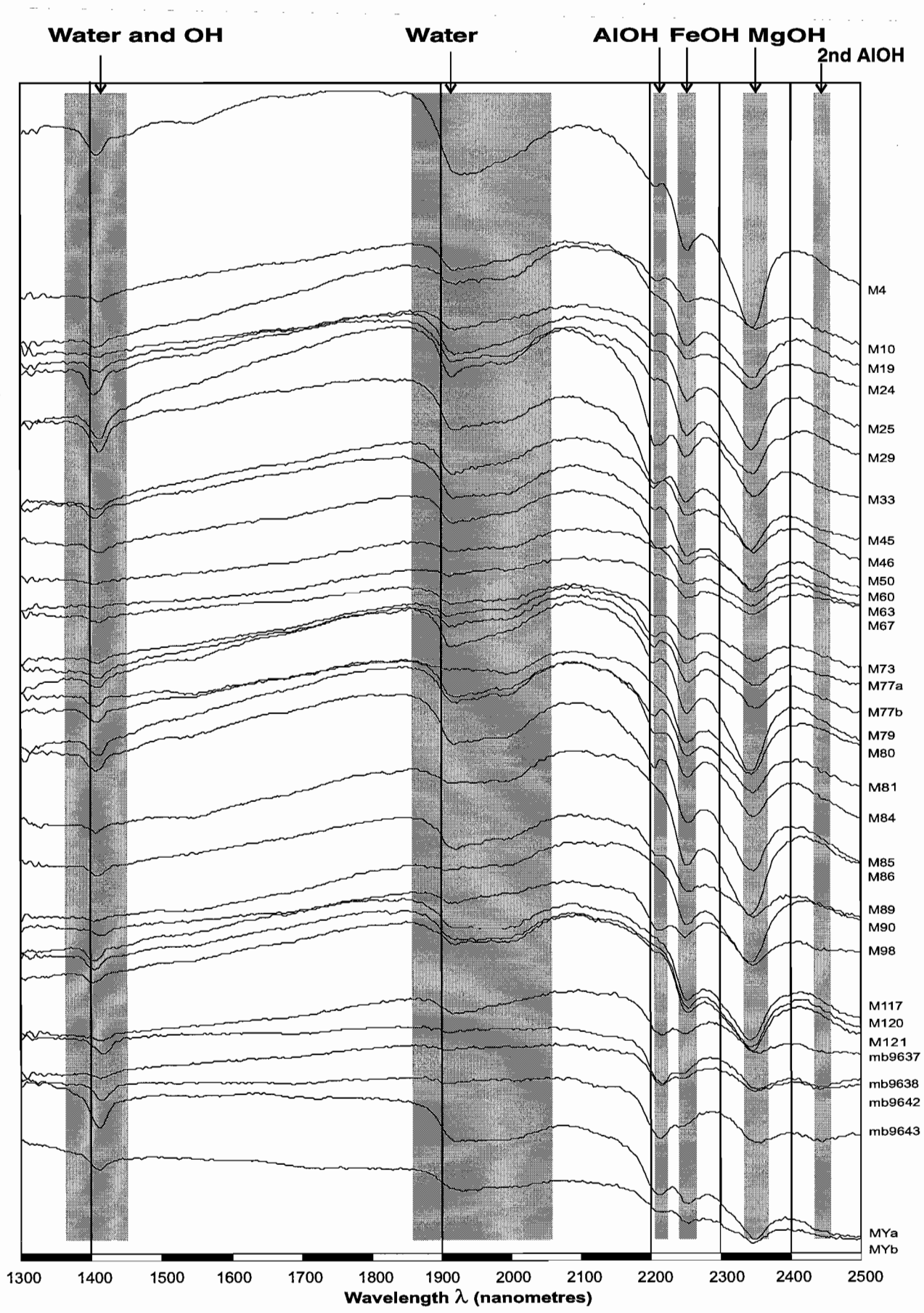

PIMA Reflectance Spectra **Mt Black & Sterling Valley Volcanics** **Dacites and Andesites** **Figure 7**

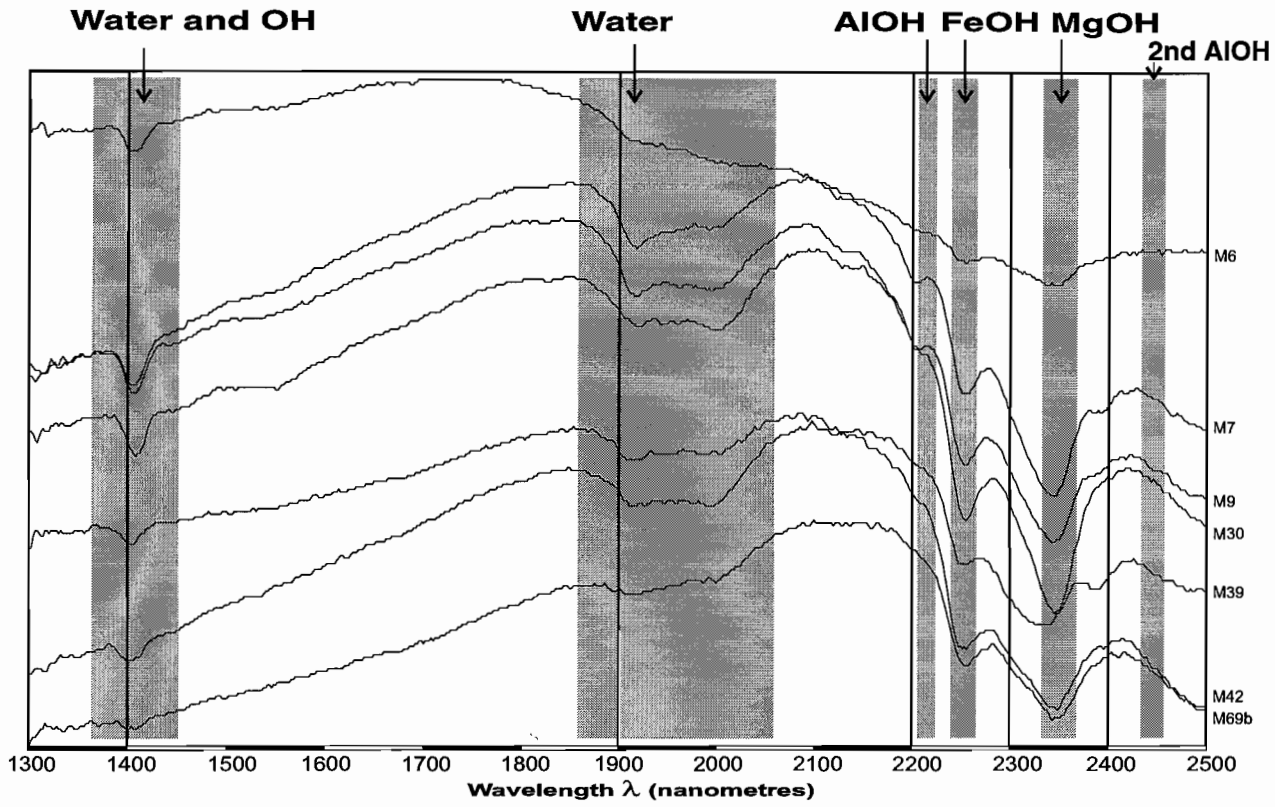

PIMA Reflectance Spectra

Mt Black & Sterling Valley Volcanics - Mafic Rocks **Figure 8**

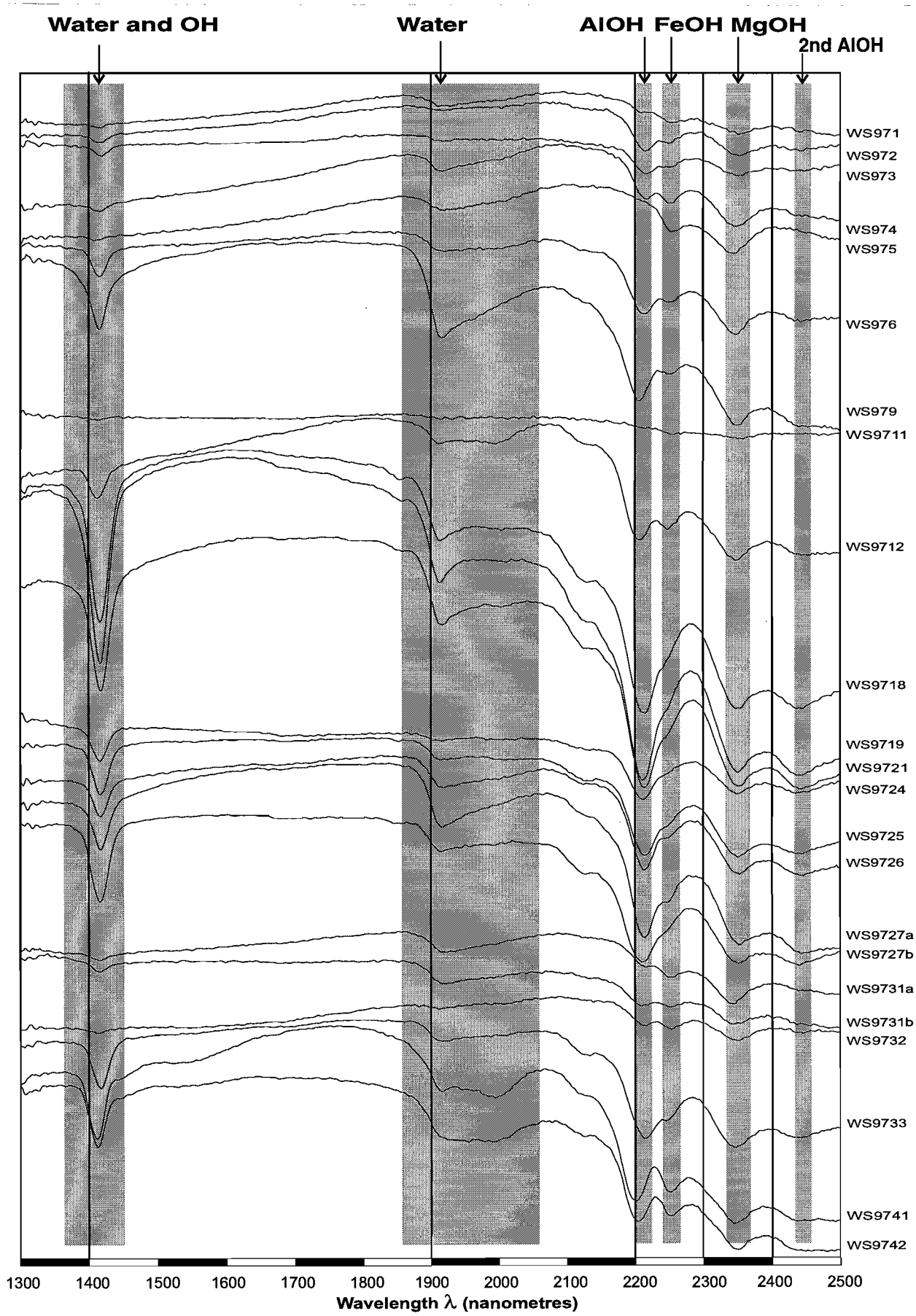

PIMA Reflectance Spectra **WHITE SPUR TRAVERSES Central volcanic Complex** **Figure 9**

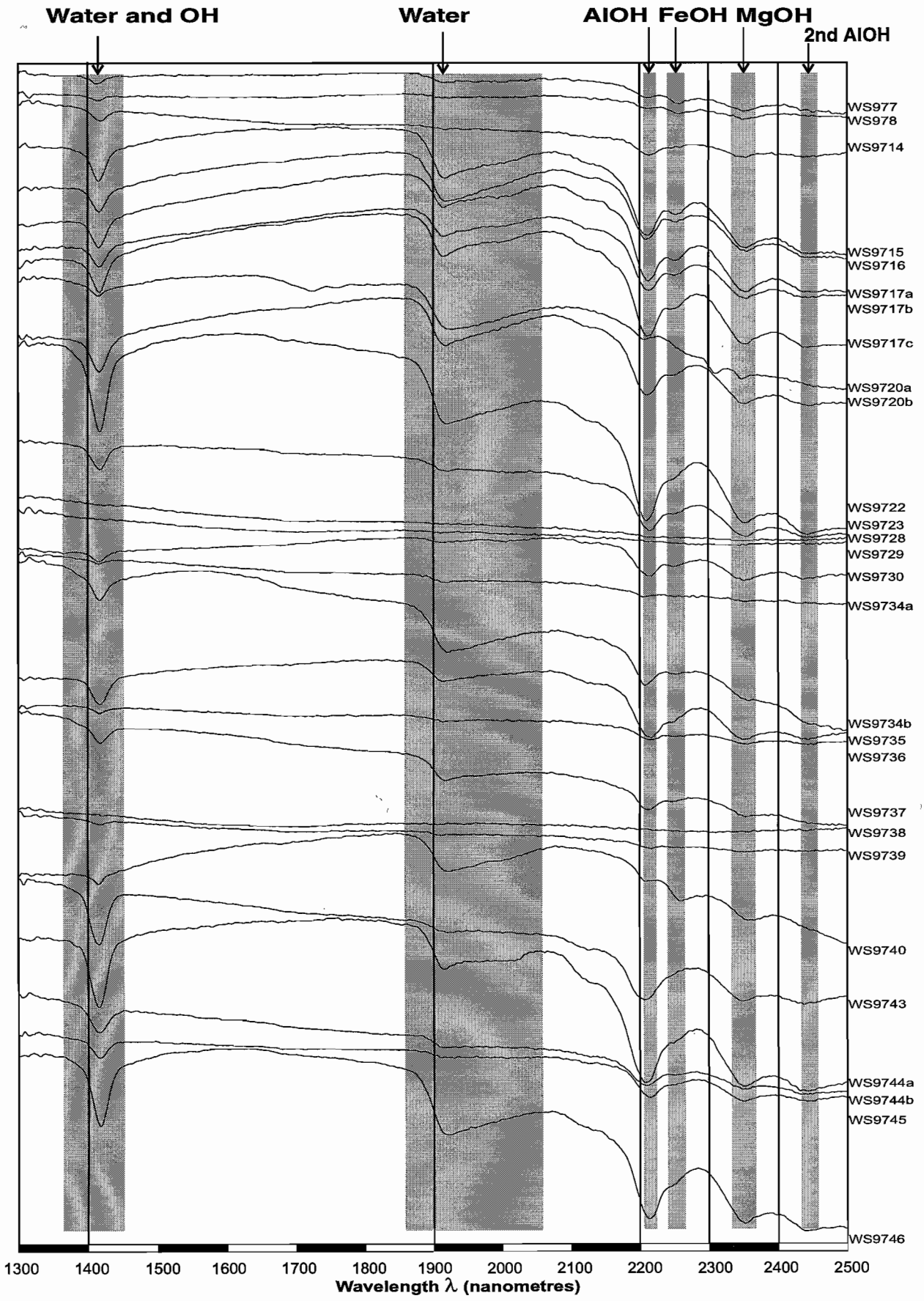

PIMA Reflectance Spectra **WHITE SPUR TRAVERSES White Spur Formation** **Figure 10**

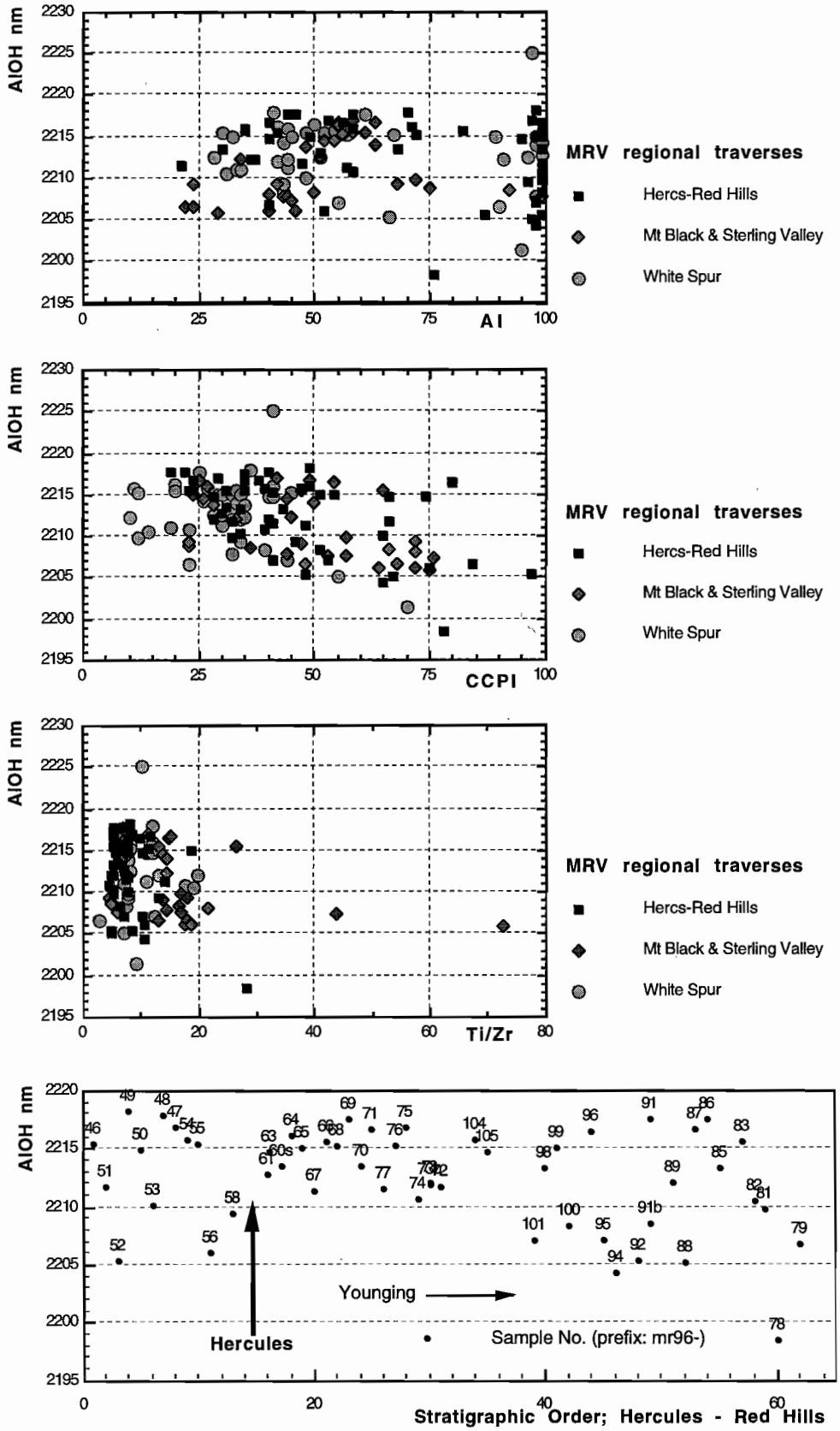

Figure 11. Scatterplot showing lack of relationships between the wavelengths of PIMA AlOH absorption features and Al, CCPI, Ti/Zr and stratigraphic level for MRV regional samples.

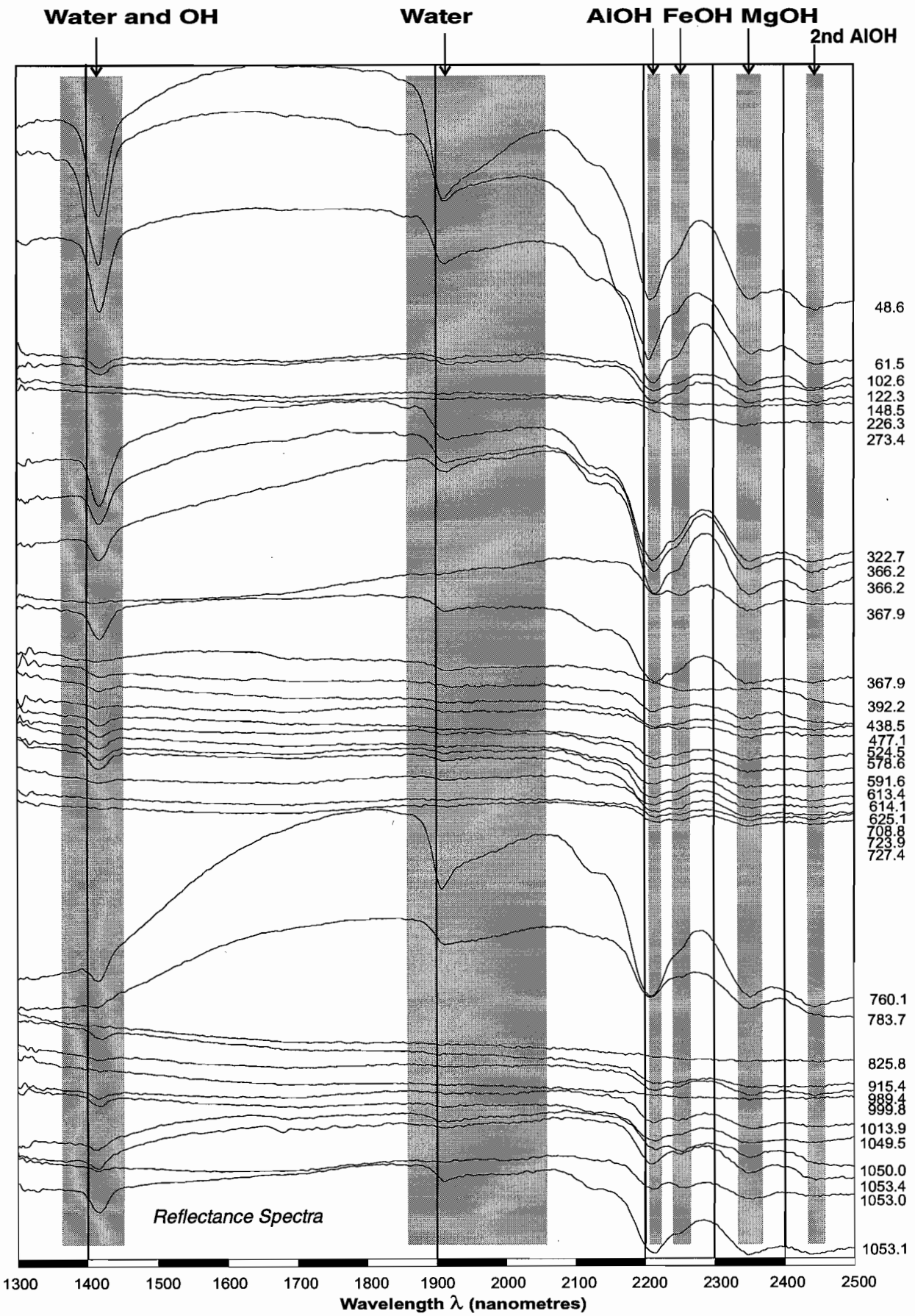

Rosebery 120R
Mt Black Volcanics above Mt Black Fault

Figure 12

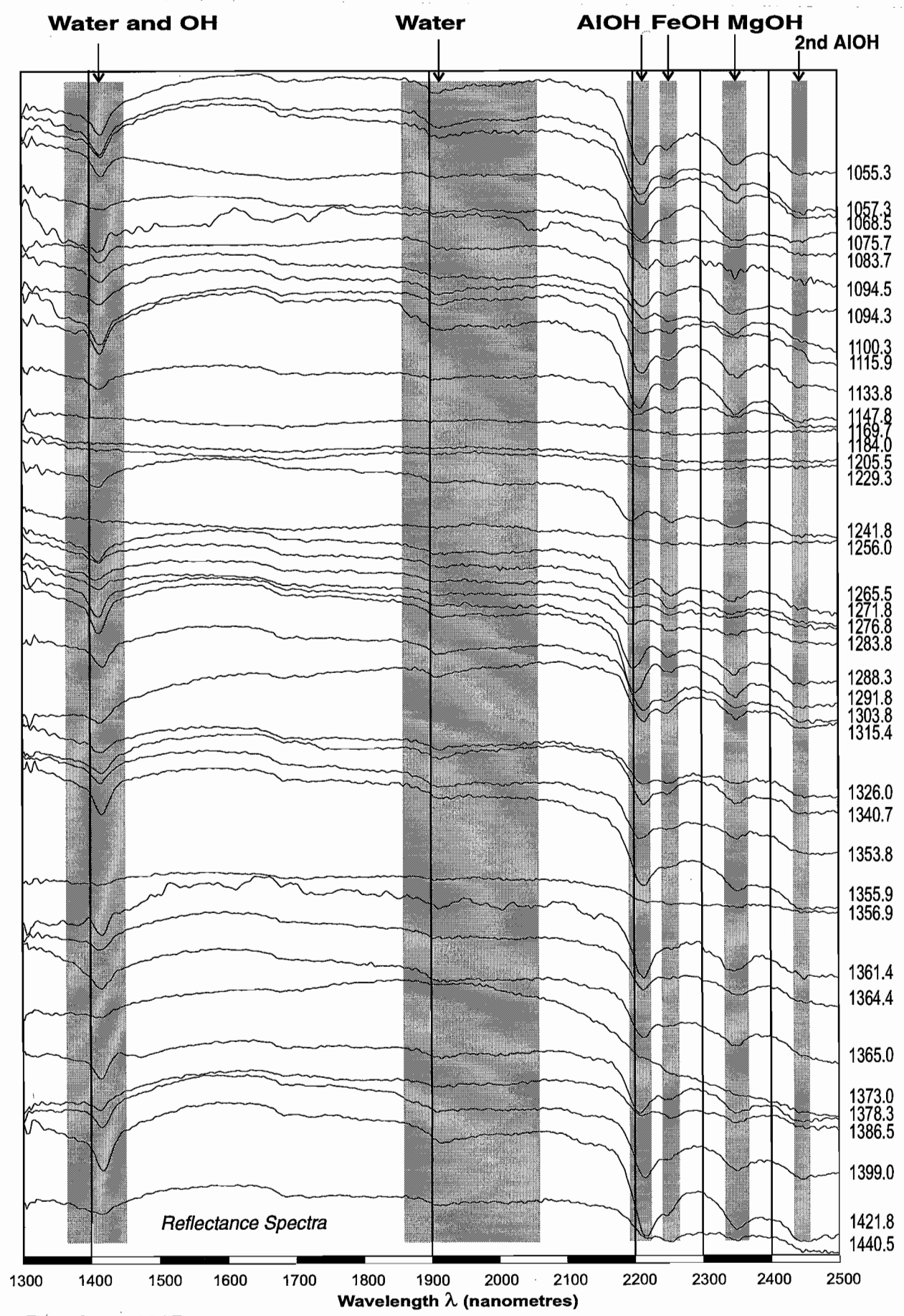

Rosebery 120R
FW, ore horizon and HW units below Mt Black Fault

Figure 13

PIMA spectral characteristics of Rosebery drill core samples

PIMA spectra have been measured on ~300 samples of core from eight drill holes intersecting the Rosebery host units at the north end of the deposit.* About 35 of the samples are of Mt Black Volcanics above the Mt Black Fault? contact, mainly from 120R (kindly supplied by C.Gifkins).

A representative group, from the full length of the deepest hole (120R) is shown as stacked profiles, with consistent vertical scales, in Figures 12 and 13.

The spectra have similar characteristics to those for samples from the MRV regional traverses. In most Rosebery spectra, the dominant absorption features are attributable to muscovite (±illite); many have subordinate features attributable to chlorite, and chlorite appears to be the most abundant phyllosilicate in a minority. Spectra for black siltstone samples are dark, flat and devoid of absorption features (eg: 120R: 1184.0, 1205.5, 1229.3, 1256.0 m). Several spectra from the top of the hole have deep H_2O features at ~1900 nm indicating presence of illite, due to weathering. Some spectra from mafic dykes in the MBV show steep gradients at low wavelengths, attributable to high Fe^{2+} absorption (eg: 760.1 and 783.7 m).

AlOH absorption features

Downhole plots of the wavelengths of absorption features in the AlOH band for eight Rosebery drill holes are shown in Figure 14.

The first of these, 120R from surface to 1440m, clearly illustrates that wavelengths of 2205–2220 (mostly 2210–2218) which are typical of the altered footwall pumice breccia unit are also characteristic of the weakly altered hanging wall volcaniclastic mass flows and the thick sequence of pumiceous breccias and coherent units of the MBV above the Mt Black Fault. This is entirely consistent with AlOH wavelengths from the regional traverse samples that suggest that the "background" muscovites are more or less phengitic. The lowest wavelengths for the MBV in 120R (2207.5–2210 nm) are associated with mafic dykes near 760m (reinforcing the inference from regional data that muscovite tends to be least phengitic where chlorite is abundant) and the illite bearing near surface samples (suggesting that weathering processes may strip some Fe+Mg from phengitic muscovite.

The low wavelengths associated with the hanging-wall volcaniclastic sandstone unit (immediately overlying the footwall pumice breccia, dacite sill or sulphide lenses in various cases) are anomalous in this context.

The remaining eight down hole plots in Figure 14 illustrate the PIMA AlOH wavelengths for scaled up sections of the Rosebery sequence, arranged in order of increasing lateral distance from massive sulphide lenses. In every case, low wavelengths are associated with the HW volcaniclastic sandstone unit (or its stratigraphic equivalent in 113RD1).[4] Furthermore, the lowest wavelengths (<2195) were observed in holes that intersected or passed close to sulphide lenses. The only exception is in 46R in which the sandstone unit is thin and only one spectrum was measured.

This distribution suggests that the low wavelength effect is spatially related to ore and could be used as an exploration method at the mine scale, at Rosebery, to infer near misses and vectors to ore. It could also be argued that this distribution is a sampling artefact controlled by the thickness of the sandstone unit — it is notable that the wavelengths of <2195 were observed only in holes where the sandstone unit is >20m thick and several samples were available for measurement. It requires closer spaced PIMA analyses to test the spatial variation in wavelengths.

PIMA feature wavelengths and muscovite and chlorite compositions of MRV and Rosebery

Microprobe analyses have been determined for muscovites and chlorites in selected samples to examine the relationships between PIMA spectral characteristics and mineral compositions.

The samples included representatives of the Rosebery host sequence from drill holes 109R and 120R and a suite of eleven MRV "background"

* Rosebery drill holes: 46R, 65R, 84R, 109R, 113RD1, 120R, 128R, 131R; see Figure 1 of Large et al. (1998) for locations in long projection.

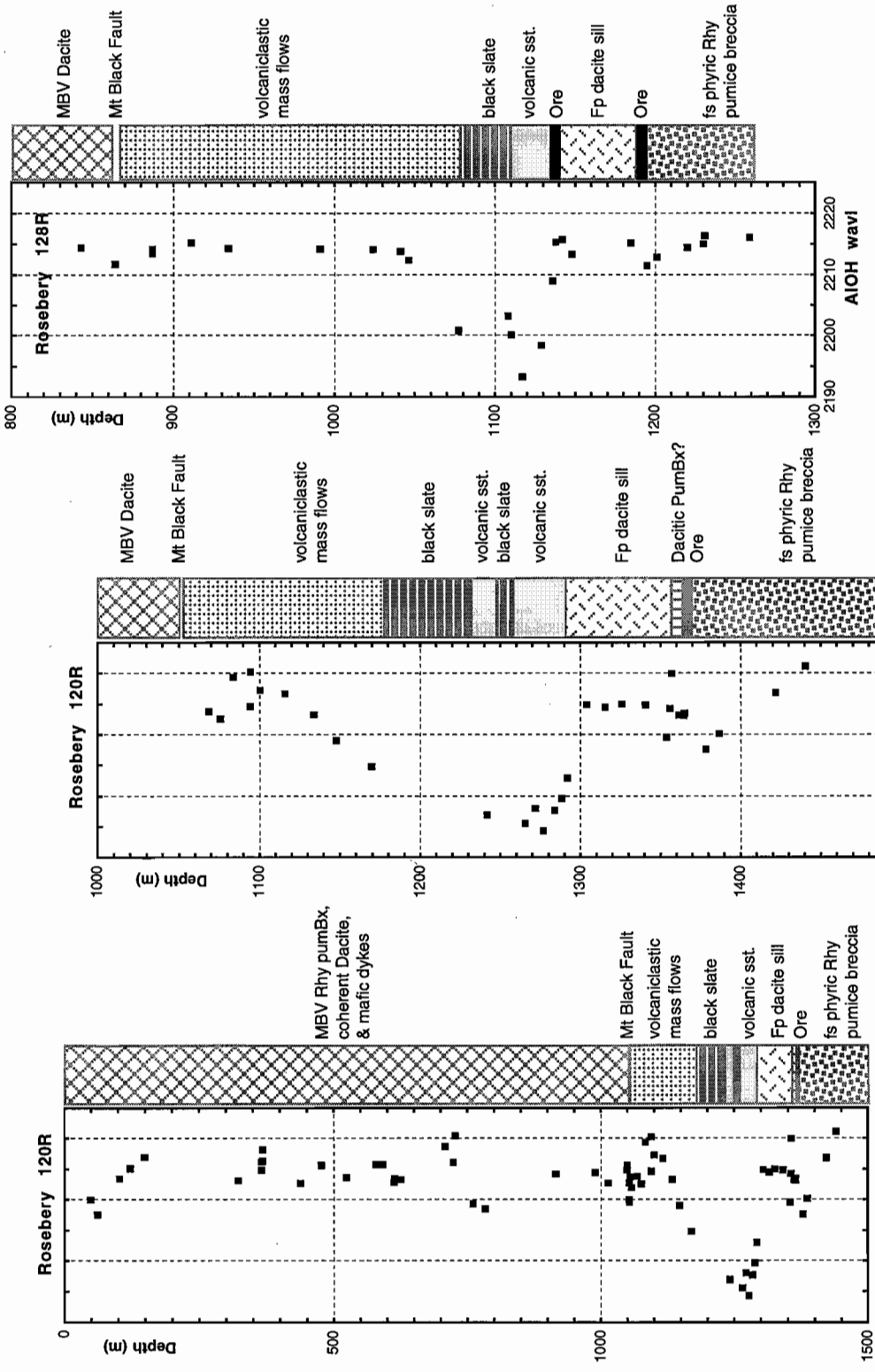

Figure 14. Down hole plots of Rosebery drill holes showing PIMA AlOH wavelengths related to lithological sequence.

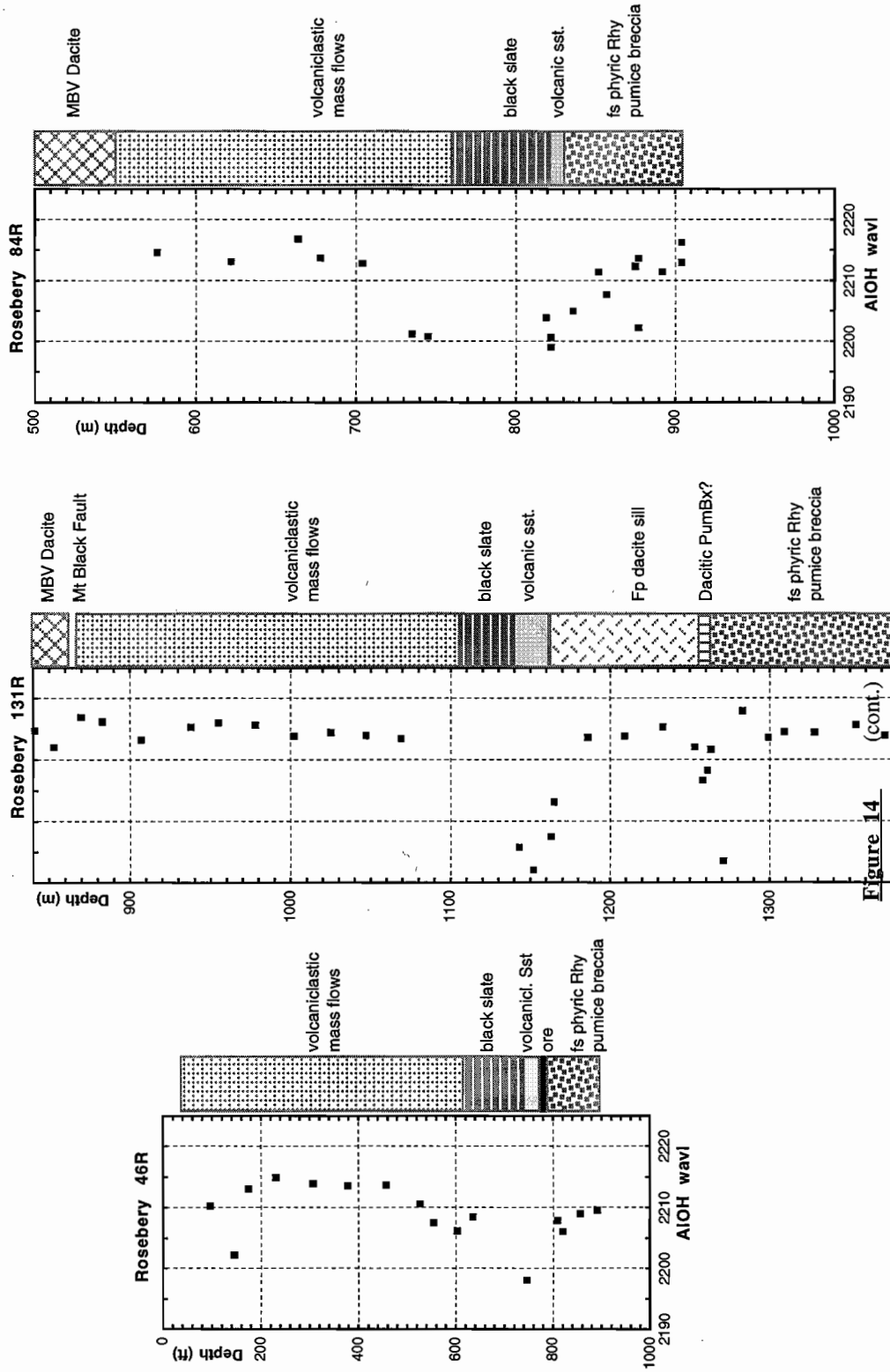

Figure 14 (cont.)

Figure 14 (cont.)

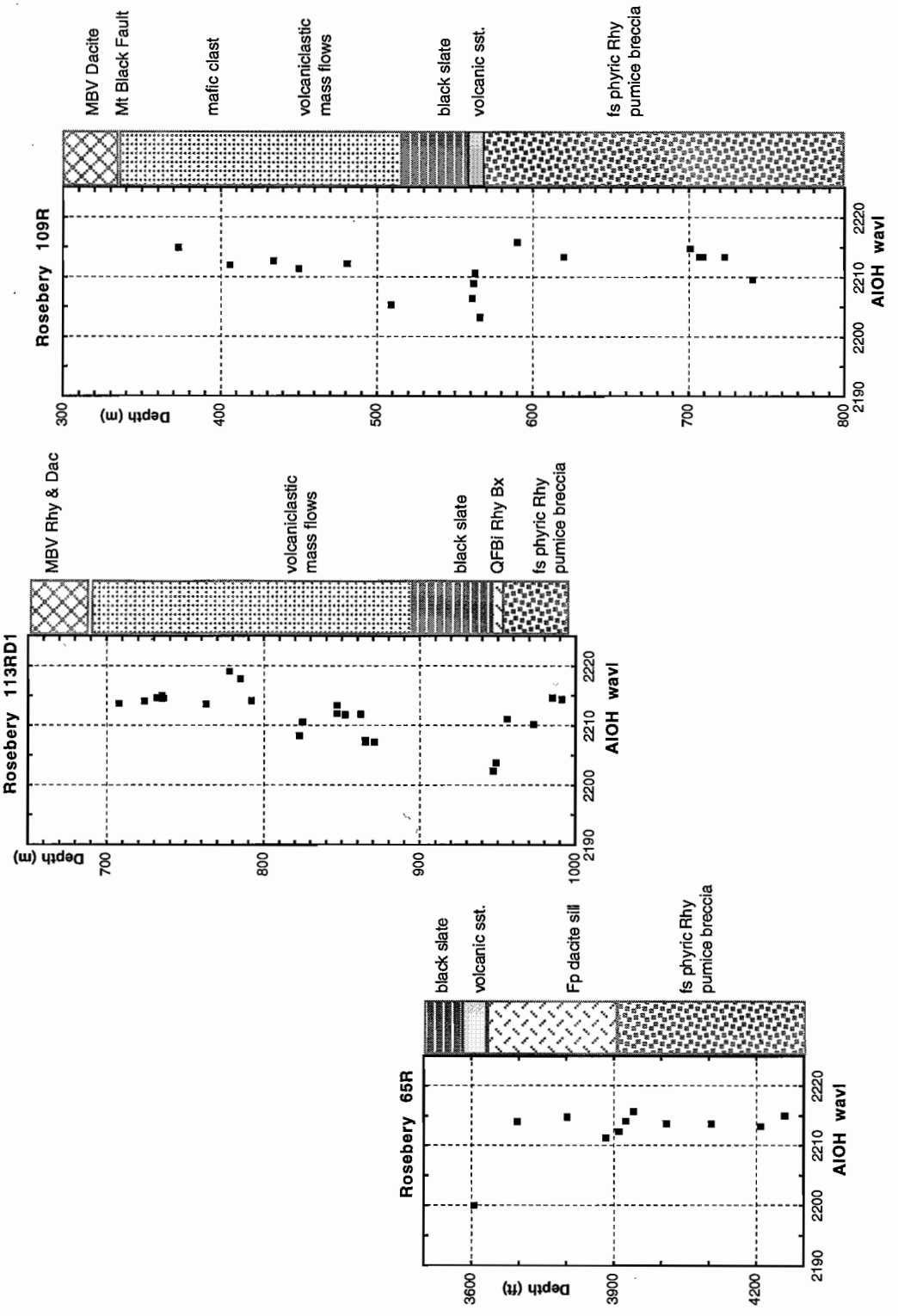

Figure 14 (cont.)

samples, covering the compositional range rhyolite to basalt, from the Hercules–Mt Read and Mt Black–Sterling Valley traverses.

After culling out the obvious mixtures and unreliable analyses, analyses were available for 162 muscovites and 120 chlorites, according to the breakdown:

Location	Mineral analyses	Sections probed
109R	51 muscovites	14
120R	78 muscovites	21
MRV regional traverses	33 muscovites	10
Totals	162 muscovites	35 sections
109R	53 chlorites	14
120R	30 chlorites	8
MRV regional traverses	37 chlorites	10
Totals	120 chlorites	32 sections

Microprobe analytical data were recalculated to ionic proportions by the MINTAB programme (Rock & Carroll, 1990) on the basis of 22 oxygens for muscovite and 28 oxygens for chlorite and all iron expressed as Fe^{2+}. The enclosed data disks include tabulated analyses and ionic proportions as Excel files.

Muscovite

Figure 15a shows 162 muscovites in a plot of ionic Al against Na/(Na+K). The majority lie in a cluster of muscovite-phengite composition (Na/Na+K <0.05) with two groups diverging towards the compositions of paragonite and albite. The latter group of 14 analyses, appears to represent fine intergrowths of muscovite and albite; these analyses have been excluded from subsequent interpretation. Muscovites in the group trending towards paragonite have Na/Na+K ratios upto 0.35 representing either solid solution Na substitution for K or mixtures of muscovite and paragonite. The former is least likely as the solid solution of paragonite in muscovite (and vice versa) is limited to ~20% at temperatures just below the solidus, and decreases dramatically at lower temperatures (Deer et al., 1966).

Various ionic proportions and ratios for ***averaged* muscovite compositions*** are illustrated in Figure 15b, with ionic Fe+Mg plotted on the horizontal axis and others on a logarithmic vertical axis. Linear curves are fitted to the data sets and associated correlation co-efficients [r] are shown in the legend. Apparently all of the ionic parameters involving Si and Al are reasonably well correlated to Fe+Mg and are effective measures of the "phengicity" of the muscovite compositions. It shows that the total amount of Fe+Mg ranges upto about one octahedrally co-ordinated cation (out of four) and even the least phengitic contain about 0.1 Fe+Mg cations per unit. The most sodic (paragonitic?) muscovites have the lowest phengite contents.

Figure 15c illustrates that phengicity of muscovites, as measured by ionic Fe+Mg, is generally unrelated to the wholerock geochemical parameters: Ti/Zr, AI, CCPI and Mg#.** There is a slight negative correlation (r= –0.37) between phengite content and Ti/Zr which is consistent with the inference, from PIMA AlOH wavelengths, that muscovites tend to be least phengitic in (mafic) rocks containing abundant chlorite ***or*** it may be a sampling artefact caused by too few muscovite analyses from mafic rocks.

Figure 15d shows the Mg# of muscovites (a measure of the relative amounts of Mg and Fe substituting for Al in octahedral sites) plotted against the wholerock geochemical parameters. In these data there is no discernible relationship between muscovite Mg# and Ti/Zr, AI or CCPI. However, there is a moderate positive correlation (r= 0.63) between muscovite Mg# and wholerock Mg#, suggesting that the latter is the principal controlling factor. Muscovite Mg# tends to be higher than the corresponding wholerock Mg#.

The relationships between (averaged) muscovite compositions and PIMA wavelengths are illustrated by three plots in Figure 16. The first shows moderate-high positive correlations (r ~0.7) between AlOH

* The mean of all muscovite probe analyses measured in an individual sample. All data plotted in Figures 15b,c,d and 16 are for *average* muscovite compositions.

** Mg# in wholerock geochem = 100 * MgO / ($MgO+Fe_2O_3$). Mg# in mineral analyses is calculated from ionic proportions: 100 * Mg / (Mg+Fe)

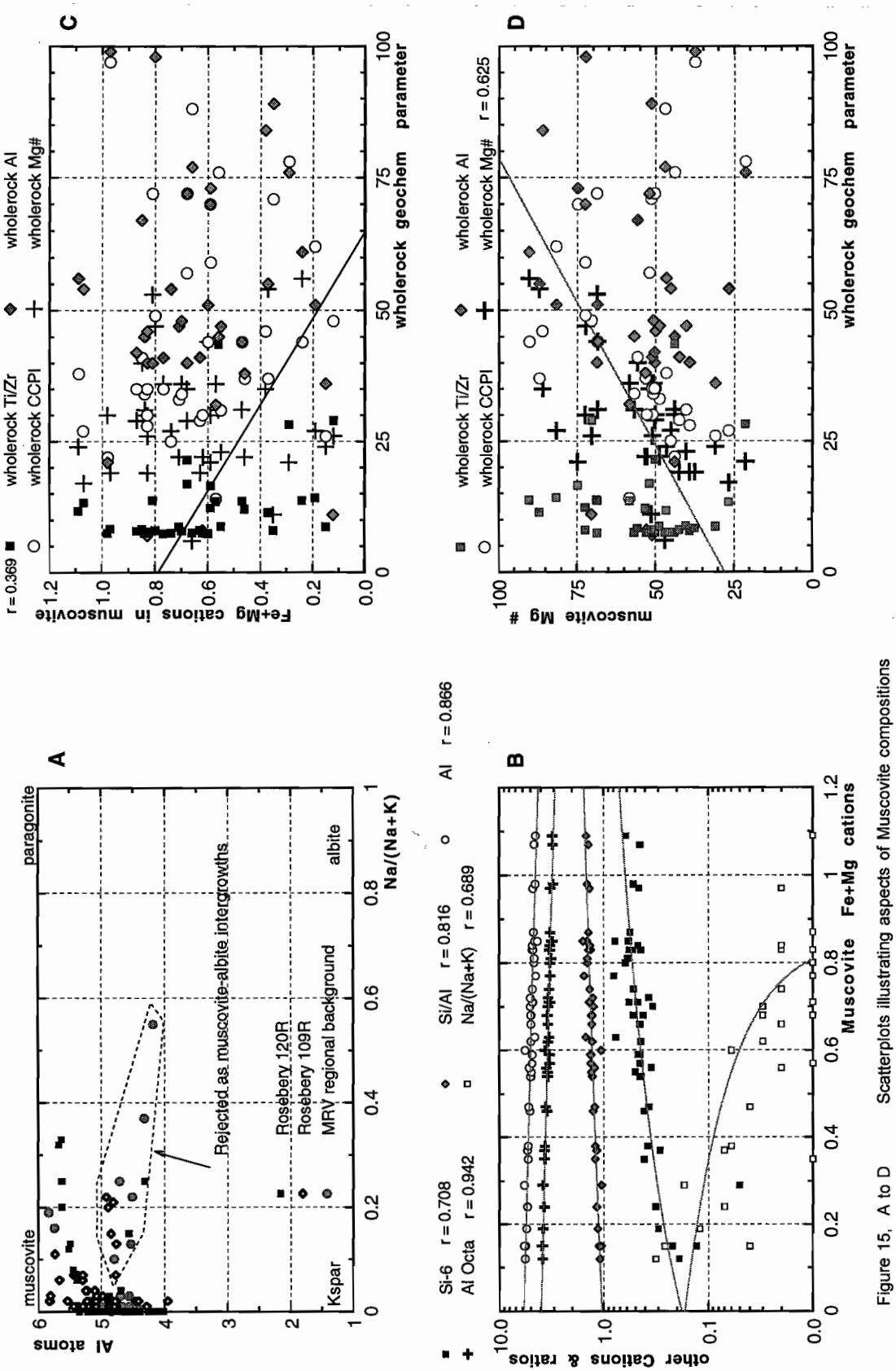

Figure 15, A to D Scatterplots illustrating aspects of Muscovite compositions

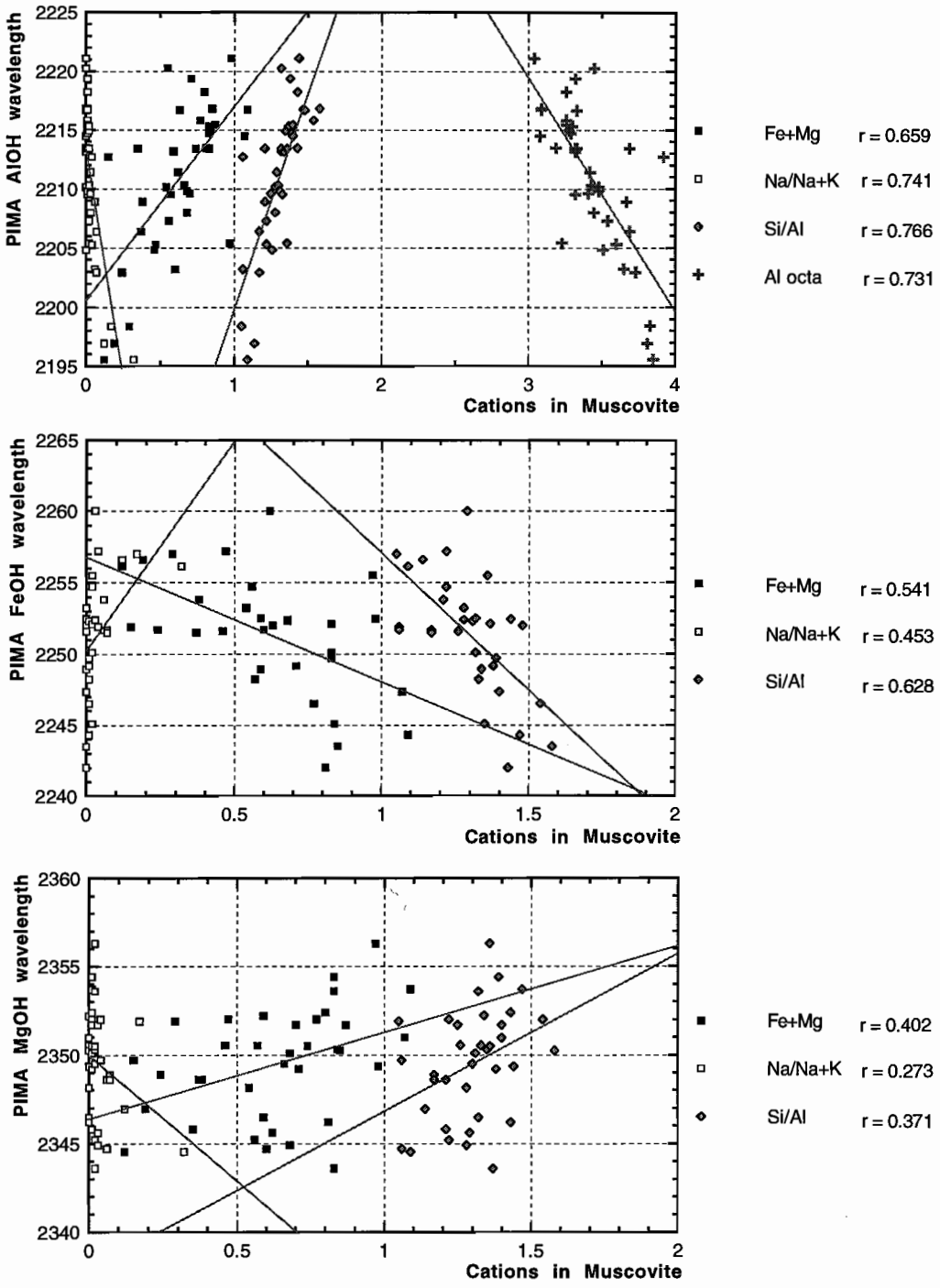

Figure 16 Ionic indicators of "phengicity" of Muscovite composition plotted against wavelengths of PIMA AlOH, FeOH and MgOH absorption features.

feature wavelengths and indicators of phengite content and a negative correlation of similar order, between wavelength and Na/Na+K. This confirms the preliminary indications from Rosebery 120R (Large et al., 1997) and is consistent with the conventional wisdom of PIMA spectral interpretation. However, most of the muscovites in the 2200–2210 nm range are moderately phengitic, with about 0.3 to 0.7 ions of Fe+Mg, whereas the aforementioned wisdom considers white micas in this range to be normal K muscovites. Nevertheless, the calculated linear regression line for Fe+Mg intersects the Y axis at 2200 nm in weak support of the notion that lower wavelengths, in general, are not merely due to absence of phengite but are pulled down by Na substitution or presence of paragonite mixtures. All samples with average muscovite of >0.1 Na/Na+K have wavelengths of <2200 nm.

Somewhat surprisingly, there are also moderate correlations (r= upto ~0.6), of reverse signs, between phengite contents of muscovite and wavelengths of the FeOH absorption band. Since the FeOH absorption is attributed to chlorite, it suggests some compositional relationship between muscovite and co-existing chlorite.

The various downhole plots in Figures 17 and 18 (for Rosebery holes 120R and 109R, respectively) depict the inter relationships of the amounts of phengite and paragonite in muscovite, and the PIMA wavelengths. The muscovite probe analyses support the inference from PIMA data (referred to above) that there may be a zonal relationship between muscovite composition (in the hangingwall sandstone unit) and sulphide lenses. The most sodic muscovites analysed in the most distal hole, 109R, contain less than one third of the amount of sodium found in muscovites in the same unit in 120R, which intersected sulphides.

It is uncertain whether this apparent zonation is due to:

- hangingwall alteration associated with mineralisation — either syn or post sulphides,
- stratigraphic or sediment provenance influences on deposition of the sandstone unit/s,
- an artefact of sampling imposed by apparent thinning of the sandstone unit up dip and away from the sulphide lenses.

Figure 17a shows that the hangingwall volcaniclastic sandstone unit (containing sodic, least phengitic muscovite) also contains anomalous amounts of chlorite; in the range 10–20 wt% compared to <10% in the footwall and other hangingwall units.* This coincidence is consistent with previous inferences that low wavelength, least phengitic, ± paragonitic muscovites in the MRV tend to exist in chlorite rich rocks; notably chloritic mafic rocks.

The relatively high Ti/Zr ratios (15–30; Figs 17a, 18a) of the anomalous volcaniclastic sandstone unit, suggests its provenance was at least partly mafic and that its high chlorite content is a relic of primary composition — rather than hydrothermal alteration (Large et al., 1998). This line of interpretation supports the last two possibilities — that the most sodic muscovites are spatially related to sulphide lenses because of depositional controls and/or sampling effects — and diminishes the hydrothermal connection with sulphide deposition. Nevertheless, the apparent zonation may still have some de facto or empirical value as an exploration vector. It may be postulated that the spatial association could be accounted for by sub basinal topography and structure which controlled the depositional thickness and extent of the hangingwall volcaniclastic sandstone ***and*** influenced footwall hydrothermal circulation and sulphide deposition.

Chlorite

Chlorite composition was not meant to be a major aspect of this study but 120 microprobe analyses were obtained from MRV and Rosebery 109R & 120R samples "while the sections were on the stage" as a by product of muscovite analyses.

These chlorites have mid range compositions with Mg numbers of 20–70 and 5.2 to 6 Si cations (Fig. 19a, after Deer et al., 1966). Figure 19b indicates that there are no strong associations between chlorite Mg# and alteration intensity as measured by AI and CCPI, or

* Chlorite and muscovite percentages shown in Figures 17a and 18a were calculated from wholerock analyses using a least squares method (nicknamed MINSQ) suggested by Ron Berry and based on a program developed by R.W. LeMaitre, 1981. Explanatory notes on MINSQ are provided in Appendix II.

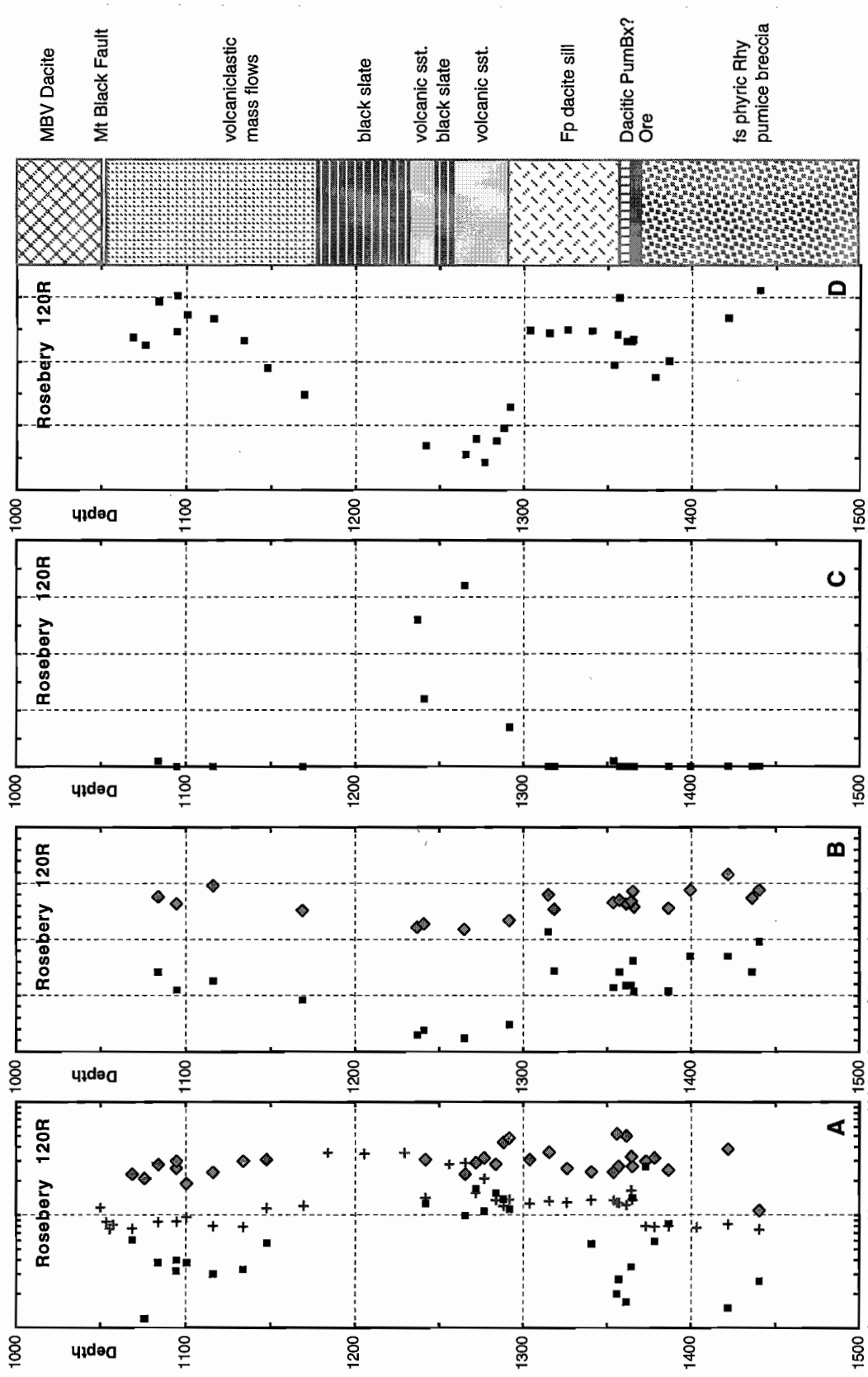

Figure 17 Downhole plots of muscovite and chlorite compositions and PIMA wavelengths, for Rosebery 120R.

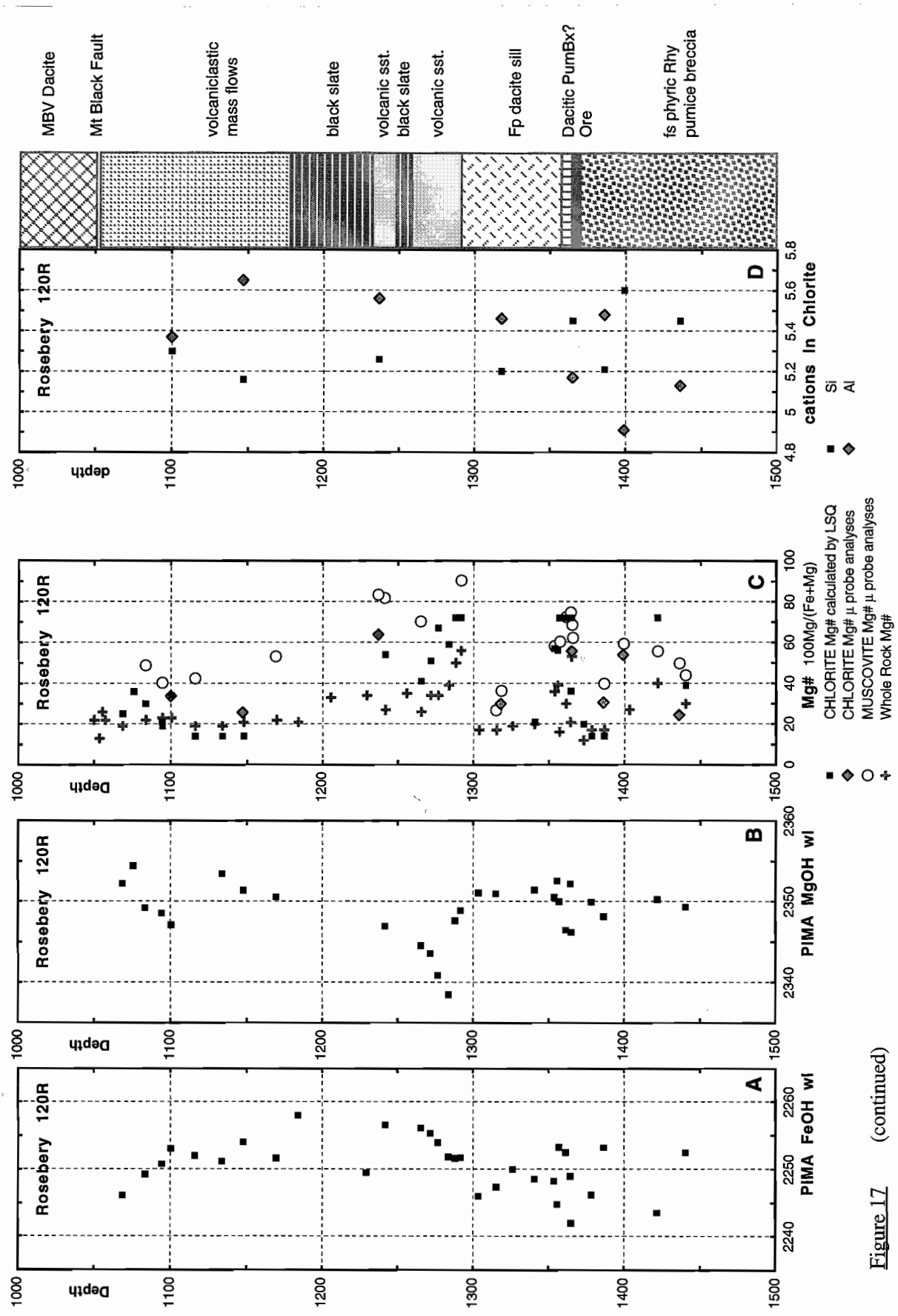

Figure 17 (continued)

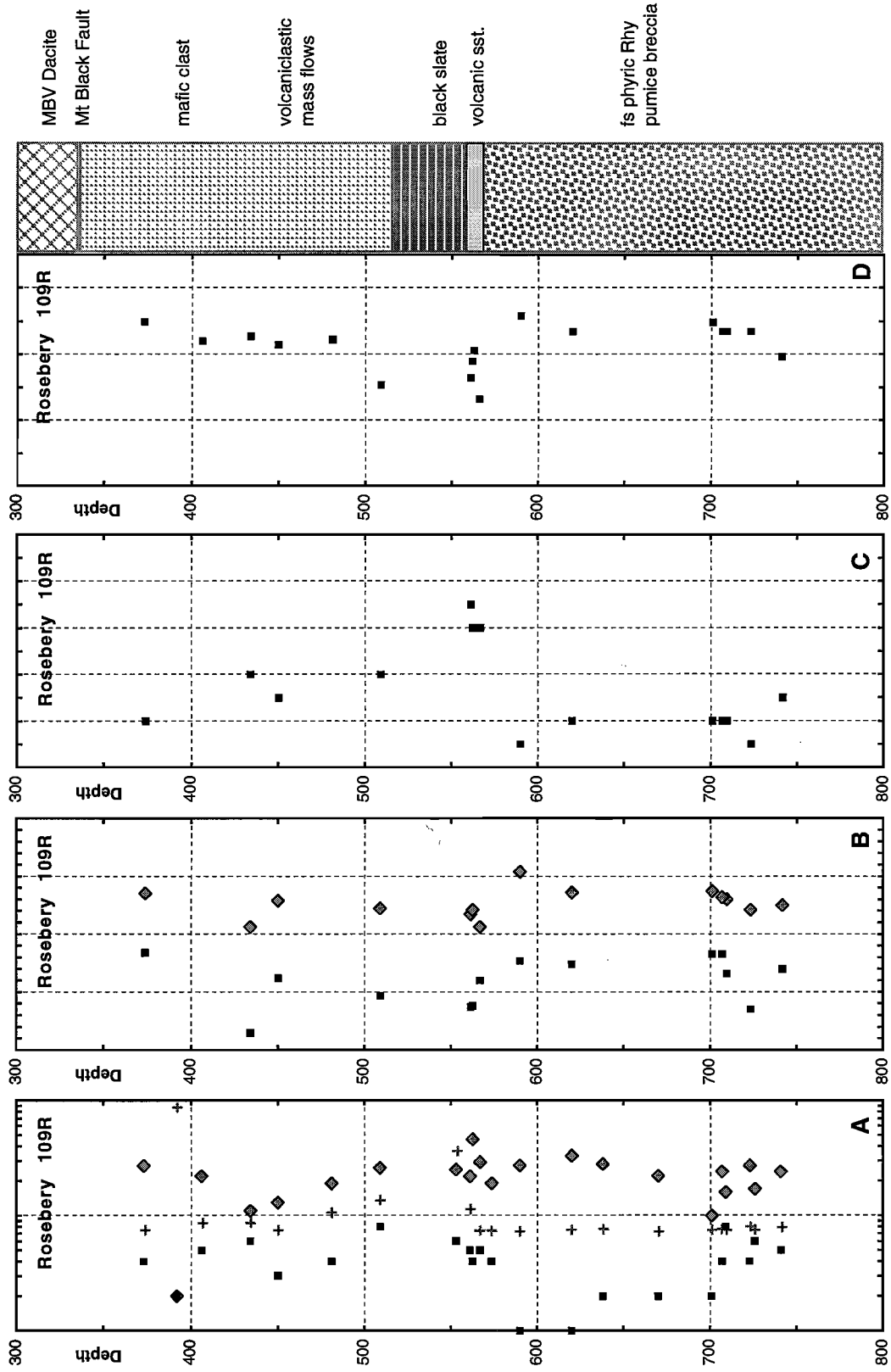

Figure 18 Downhole plots of muscovite and chlorite compositions and PIMA wavelengths, for Rosebery 109R.

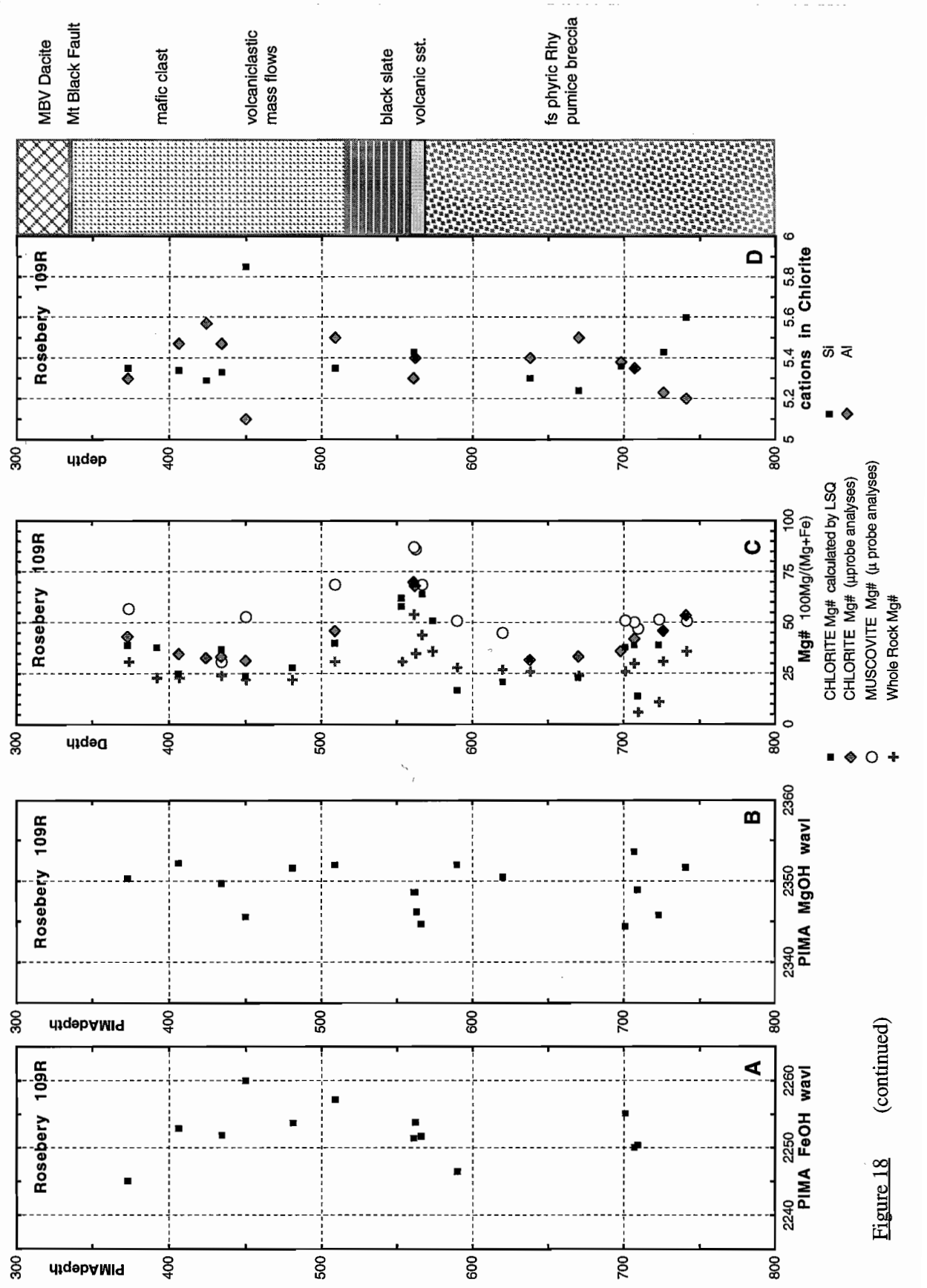

Figure 18 (continued)

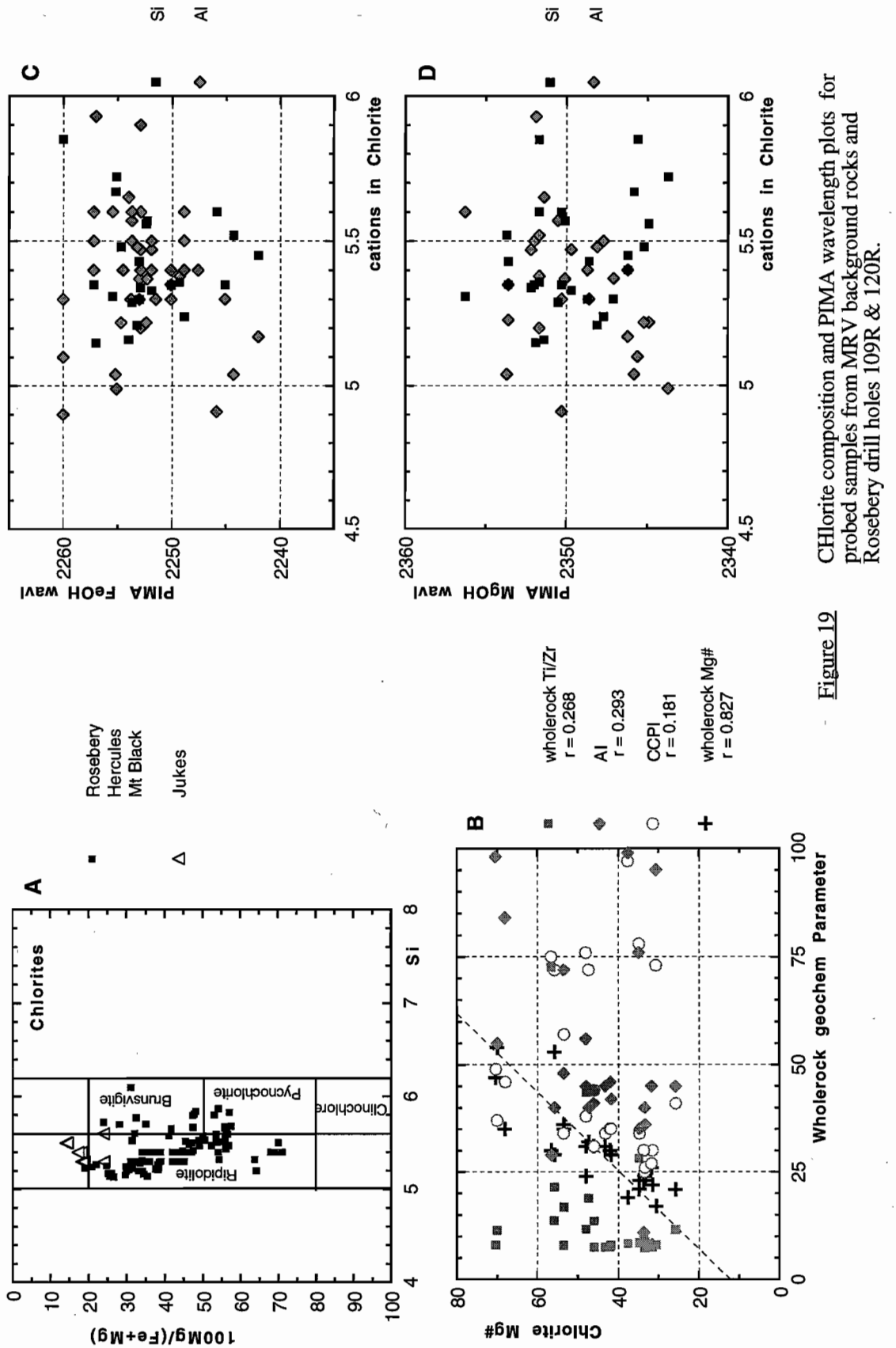

Figure 19 CHlorite composition and PIMA wavelength plots for probed samples from MRV background rocks and Rosebery drill holes 109R & 120R.

with bulk rock composition measured by Ti/Zr. There is, however, strong correlation (r = 0.8) between chlorite and wholerock Mg numbers which suggests (as for phengitic muscovites) that the wholerock Fe-Mg balance controls chlorite composition. In other words: the main Fe & Mg bearing phases are chlorite and muscovite.

Averaged chlorite Mg#, and Si and Al cations (from microprobe analyses) for Rosebery drill holes (plotted in Figs 17g, h, 18g, h) do not appear to have a consistent spatial relationship to sulphide lenses and the favourable horizon. However, the data are sparse in the footwall pumice breccia and it must be recognised that chlorites associated with sulphides in 120R have Mg# near the high end of the range: ~60.

Additional "chlorite Mg#" data was obtained from available wholerock analyses via the least squares estimates of Fe & Mg chlorite contents*; the calculated values are plotted as black squares in Figures 17g and 18g. They show a pretty fair agreement with the existing probe data and a likewise spiky variation down hole.

From this, we conclude that chlorite composition and Mg# does not constitute a useful exploration or alteration vector, in this setting.

The conventional wisdom amongst PIMA spectral interpreters is that chlorite Mg# is systematically related to wavelengths of absorption features in the FeOH and MgOH bands. Pontual et al.(1997, p.1–85), illustrated these relationships with scatterplots showing highly correlated (r >0.9) linear regressions of negative slope, such that wavelengths of both features decrease with increasing Mg# of chlorite.

The (averaged) data from Hercules, Mt Black and Rosebery chlorites and PIMA spectra plotted in Figure 20 does not substantiate those relationships. Additional analyses of iron rich chlorites from Jukes do not enhance them. At best, there is a very weak negative correlation between FeOH wavelength and chlorite Mg#, (Fig. 20a). An attempt at testing the relationships with additional data points (calculated from wholerock analyses as in Footnote 7) is shown in Figures 20 c, d. These data add little support.

Figures 19 c, d show that there is no relationship between PIMA wavelengths and the (averaged) Si or Al content of probed chlorites.

The general conclusions from this data are:

- PIMA is not able to measure compositional variations in chlorite.
- There is no systematic variation in chlorite composition around the Rosebery VHMS deposit. There is complete compositional overlap for chlorites in weakly altered background samples and intensely altered footwall samples.

Use of PIMA spectral parameters to quantitatively estimate muscovite and chlorite contents.

As outlined in the background notes on spectral analysis (above), there are several possible approaches to estimating quantities or relative quantities of muscovite and chlorite, based on the variations in depths of the AlOH, FeOH and MgOH absorption features associated with these phyllosilicates. A reliable and field portable method of quantification would be advantageous in mapping and drill core logging in hydrothermal alteration zones where the visual estimation of sericite and chlorite content is often difficult.

This section summarises a considerable effort which has been put into investigating this potential, subsequent to the realisation that phyllosilicate composition is not closely linked to syn VHMS hydrothermal alteration, in the MRV.

The principal difficulty in testing PIMA's capability is that it requires an independent and accurate estimate of the actual amounts of muscovite and chlorite in the samples.

Rod Allen's microscopic estimates of sericite and chlorite in thin section descriptions of Rosebery core samples are an obvious, but limited, source. In order

* Due to the variability of chlorite compositions and the relatively few chlorite microprobe analyses available, the least squares mineral calculations were run with two fairly extreme chlorites in the "theoretical" assemblage of: Qtz, Kspar, Ab, Musc, FeChl, MgChl, Cc, Ank, Rhodcr, Barite, Py, Cpy, Gn & Sp. The two chlorite compositions used are Fe and Mg rich varieties from Rosebery, with Mg numbers of 13.2 and 72.6 respectively, (from Green et al., 1981, Table 4, sample Nos:105174/1 & 105180/1a). This enabled estimation of the "true" chlorite Mg# by calculating the weighted average of the Mg#s of the theoretical chlorites. Further explanation is provided in Appendix II.

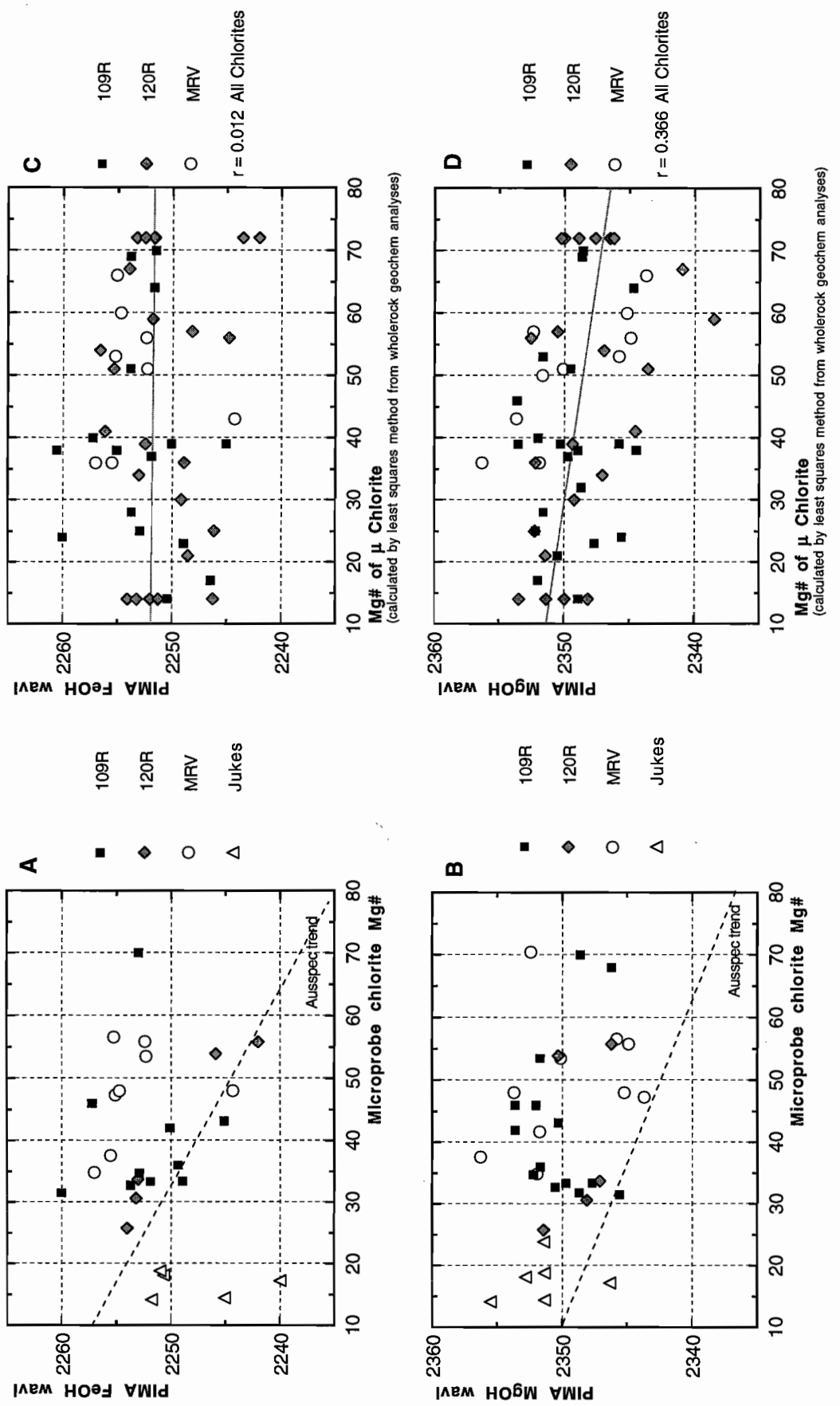

Figure 20 Comparisons of PIMA FeOH & MgOH wavelengths with chlorite Mg#; as determined by microprobe analyses and estimated from wholerock geochem by least squares method.

to extend the test over a broader range of samples and spectra, existing wholerock geochemical analyses were recalculated using a least sum of residual squares method suggested by Ron Berry to produce weight % estimates of the main mineral phases known to be present in the rocks (Appendix II). Comparisons of the recalculated mineral percentages with R. Allen's microscopic (visual — not point counted) estimates are favourable, especially for carbonates (Fig. 21).

The least squares method of recalculation has been shown to be internally consistent and we have considerable faith in its results; especially where the phase assemblages are well known and real (microprobe) analyses of the compositionally variable phyllosilicates are available to be plugged into it.

The scatterplots in Figures 22 and 23 show various functions and ratios of the (raw reflectance) PIMA absorption features plotted against the calculated chlorite and muscovite contents and muscovite/chlorite ratios.

100((A/B)-1)

This function measures the slope on the low wavelength side of the FeOH absorption band; A and B are reflectances at 2236 and 2246 nm, respectively (ref: Fig. 2). The function should produce a negative value for muscovite dominant samples and a positive value for chloritic samples. The general negative gradient in Figure 22a, for muscovite/chlorite, suggests that the function is responding as expected but there is a terrible amount of scatter and it is not a precise quantifier of phyllosilicate contents. For instance: a value of 2 could indicate anything between 5–40% chlorite and muscovite, and Muscovite/chlorite ratio of 0–4! In other words, this function is not very good at discriminating a little chlorite from a lot.

C/D

This is the ratio between depths of the AlOH and FeOH absorption features (Fig. 2). It is expected to be small (<<1) in chloritic samples and increase to ~2 in muscovite rich samples. Figures 22b and 23c, d show that the trends have the appropriate gradients but there is, again, a great deal of scatter indicating it does not offer any precision. At best, a value of <0.5 can be taken to indicate a low muscovite/chlorite ratio (<2) but does not constrain the amounts; upto 50% chlorite and 20% muscovite are possible. At the other extreme, a very high value of >2 indicates ≤15% chlorite and ≥15% muscovite but does not constrain their ratio.

C/E

This is the ratio between the depths of absorption features in the AlOH and MgOH bands. Although complicated by the possible existence of carbonate and secondary AlOH absorptions in this band, the presence of the latter will always permit the C/E ratio to be calculated for samples containing muscovite.* Similarly to C/D, the C/E ratio should be small (<<1) in chloritic samples and increase to ~2 in muscovite rich samples.

The data plotted in Figures 22c and 23e, f point to similar conclusions as for C/D; ie: it seems to work in a rough way but could not be used with any quantitative accuracy.

C–E

This parameter represents the difference between the depths of absorption features in the AlOH and MgOH bands. It is expected to be positive in muscovite rich samples and negative in chloritic samples.

Figure 23h shows reasonably linear trends relating C–E and muscovite content for the Rosebery and Hercules–Red Hills data, but of unfortunately low gradients. The near horizontal trend of the Hercules–Red Hills and Rosebery data is not useful for estimating muscovite or chlorite contents. The low gradients of these data trends are attributable to the low reflectance, flattish spectra in which absorption features of shallow depth produce small C–E values. The Mt Black and Sterling Valley data show a greater scatter in Figure 23h, and a predominance of negative values, consistent with their generally higher chlorite contents. This leads to their reasonably linear trend (but also of shallow gradient) on the chlorite plot (Fig. 23g).

* The absence of an FeOH feature in samples without chlorite precludes the use of the ratio C/D or the difference C-D. Obviously, neither C/D, C/E, C-D or C-E could be used for samples without muscovite.

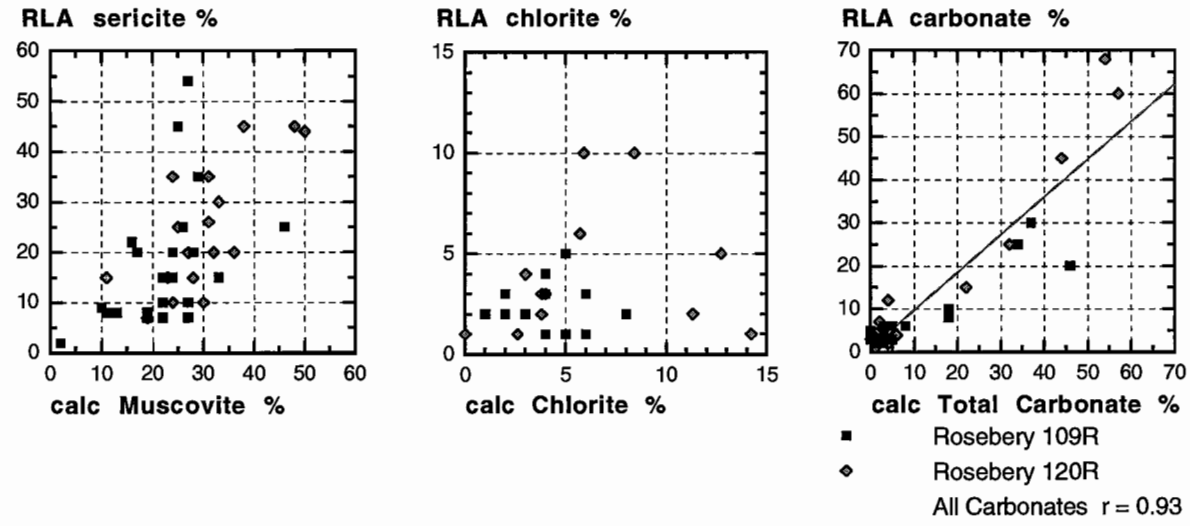

Figure 21 Comparisons between Rod Allen's microscopic estimates of muscovite, chlorite and carbonate abundances (on vertical axes) and theoretical estimates calculated from whole rock geochemical analyses (on horizontal axes) for Rosebery 109R & 120R samples.

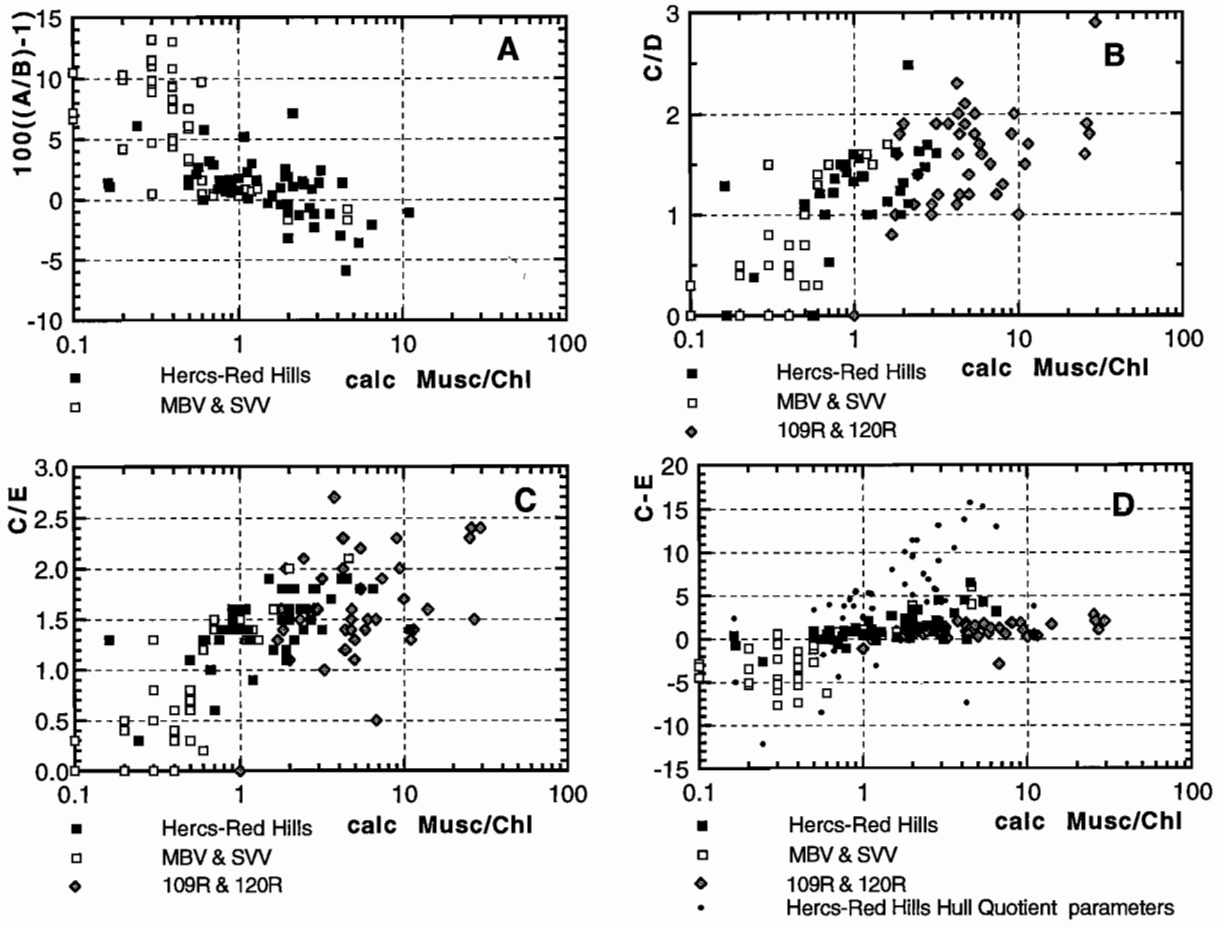

Figure 22 Calculated Muscovite/Chlorite ratios plotted against various PIMA spectral parameter ratios. (NB: log scale on x-axis)

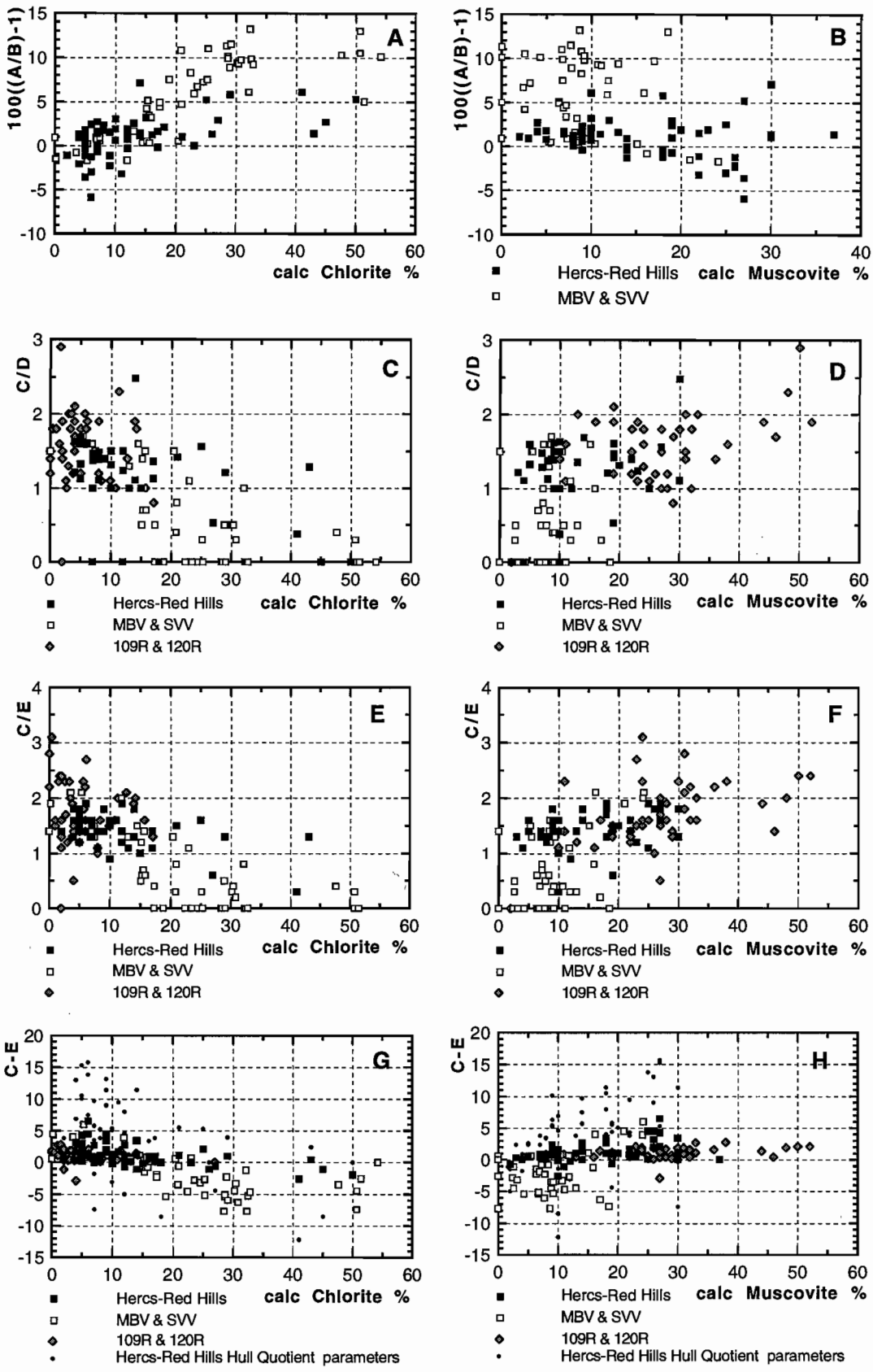

Figure 23 Calculated (wt%) amounts of chlorite and muscovite for MRV samples plotted against various PIMA spectral parameter ratios.

An attempt at increasing the gradients by calculating C–E values for ***hull quotient*** spectra (in which the depths of absorption features are amplified) for the Hercules–Red Hills samples was not successful. This significantly increases the scatter and renders it imprecise at values of <10.

The (reflectance) C–E parameter is imprecise in estimating muscovite/chlorite ratios (Fig. 22d). It could, however, be applied to very rough estimations, insofar as large negative values (< –5) appear to indicate ≥20% chlorite, ≤20% muscovite and muscovite/chlorite ratios of <1. Positive values indicate more muscovite than chlorite but the amounts are poorly constrained. A C–E value of >5 can be taken to indicate <10% chlorite, >20% muscovite and muscovite/chlorite ratios of >5, but there are many data points of lower C–E value with mica contents in these ranges.

It can be concluded that these PIMA parameters (and several others tested but not worth discussion here) can ***not*** be used to reliably estimate muscovite and chlorite contents, or relative amounts across a broad range of rock types and alteration intensity.

The fact that they show the appropriate trends but are rather broadly scattered in this data set, suggests that simple PIMA depth ratios or differences may have greater accuracy in estimating mica contents in sample sets of more restricted compositional range. Within, say, a particular alteration system or zone, or restricted to identifiable rock formations. For an example: it might work in a case like Thalanga, where the rhyolitic footwall rocks had uniform primary compositions and simple mineralogy and now exhibit extensive alteration to muscovite±chlorite±biotite assemblages.

David Huston (pers. comm., 1998) has indicated that a simple ratio of the depths of PIMA AlOH and FeOH features (C/D) shows a high correlation with chlorite content in altered rocks associated with the Panorama sulphide deposit in the Pilbara, W.A.

Yang et al. (1997) used the ratio of the second derivative functions of absorption features in the AlOH and FeOH bands to (unconvincingly) estimate muscovite/chlorite ratios in altered mafic volcanics from Hellyer. The second derivative is essentially a measure of the rate of change of slope of the PIMA spectrum and therefore would return high values at the wavelengths of an absorption feature, in magnitude proportional to the "sharpness" of the feature.

It is accepted wisdom in PIMA interpretation that mixtures of minerals have the effect of broadening absorption features, (Pontual & Merry, 1995). It is probable that this broadening is the effect being measured by the second derivative method. The conceptual basis of dividing the sharpness of the AlOH feature by the sharpness of the FeOH feature is unclear. The results of Yang et al. (op cit..) are subjective insofar as they were compared to mapped alteration zone boundaries — "sericitic", "chloritic" & etc. — but were not related to quantitative estimates of the actual amounts of muscovite and chlorite in the samples.

We made an attempt at testing the method of Yang et al. (op cit.) on quantitative muscovite and chlorite data from Hercules–Red Hills and Mt Black–Sterling Valley. However, it was inconclusive because the Pimacalc programme seemed unable to extract second derivative values for the nominated features.

PIMA spectral characteristics of the Western Tharsis alteration zones

(David Huston and Julianne Kamprad)

PIMA analyses were carried out on systematically spaced samples from drill holes on three cross sections at Western Tharsis (Huston, 1997a). The majority of samples (~203) were from 9 drill holes on Section 8850N which passes through the centre of the deposit and alteration zones. Additional samples from holes on cross sections to the north and south provided background information.

The alteration system is more or less symmetrically zoned around a steeply dipping stratiform lens of disseminated pyrite+chalcopyrite with localised pyrite+bornite+chalcopyrite ± chalcocite + mawsonite + enargite, (Huston and Kamprad, 1998).

It basically consists of:

- An inner quartz+chlorite+sericite zone associated with the deeper part of the ore lens.
- Enveloping zones of quartz + sericite ± pyrophyllite with >1% disseminated pyrite, enclosing the upper part of the ore lens and extending about 100–150 m out from the ore zone, into both the stratigraphic footwall and hangingwall (west and

east, respectively). Pyrophyllite appears to be localised near the inner parts of this zone, adjacent to the ore lens.

- Outer zones of quartz + chlorite + sericite with ankeritic-sideritic carbonate and <0.5% pyrite between about 100m to 250m out from the ore lens.

The PIMA spectral data shows that the local background for AlOH feature wavelengths, peripheral to the alteration zones, is ~2200–2210 nm.

Figure 24 shows the AlOH wavelength distribution on cross section 8850N.

The pyritic quartz+sericite±pyrophyllite alteration envelope corresponds to a zone with AlOH wavelengths of <2200 nm. The ore zone and parts of the flanking pyrophyllite zones are associated with AlOH wavelengths in the range 2194–2198 nm. These values are anomalously low in comparison to the 2205–2218 nm range typical for zones of intense sericite±chlorite alteration in the footwall of the Rosebery sulphide lens.

Figure 25a illustrates the AlOH wavelength profile down hole WT0050 in relation to the alteration zones and ore lens. The profile is remarkably smooth except for a 6 nm spike at ~360m (which shows up as a stratiform layer adjacent to the ore lens in Fig. 24) and a narrow low associated with an upper pyrophyllite zone near the end of the hole. There appears to be close correlation between AlOH wavelength and alteration intensity; particularly the presence of pyrophyllite. This is in marked contrast to the lack of correlation with footwall alteration intensity at Rosebery and Hercules.

No systematic variations in wavelength of the FeOH absorption feature, or the relative depths of AlOH and FeOH features, are apparent.

Apart from highlighting the alteration zonation, PIMA was effective at defining the zones containing pyrophyllite, which is otherwise difficult to distinguish from sericite — either megascopically or microscopically. Pyrophyllite has a distinctive absorption feature at 2167 nm in PIMA spectra (Fig. 29). PIMA also led to the initial recognition in the alteration assemblage, of topaz and zunyite which have diagnostic absorption features at 2083 and 2137 nm, respectively. Zunyite has particular genetic significance (Huston & Kamprad, op cit.) and appears to be easily detectable by PIMA at levels below 1% in rocks.

Western Tharsis: muscovite, chlorite and carbonate compositions

(David Huston and Julianne Kamprad)

Electron microprobe analysis was carried out on 25 samples from drill hole WT0050 to confirm the PIMA identifications of pyrophyllite, zunyite and topaz (which was shown to be flourine rich) and to obtain compositional data for muscovite, chlorite and carbonates.

The following interpretations are based on averaged microprobe analyses of 3–5 mineral grains in each sample.

Muscovite

Figure 25b illustrates that muscovites in the outer parts of the alteration system are more or less phengitic with about 0.3 to 0.5 Fe+Mg cations substituting for octahedral Al. They are comparable to the mid to low end of the range of phengite contents in (fresh and altered) rocks from Rosebery and the Hercules and Mt Black traverses.

The inner pyrophyllitic zone contains muscovite of very low phengicity with <0.1 Fe+Mg, and muscovites in the pyritic-sericitic envelope zone are of intermediate composition.

The sodium content of muscovites is fairly low, in the range 0 to 0.15 Na/Na+K (mostly <0.07), and there is no clear relationship to alteration zonation, (Fig. 25c). This compositional range is similar to the Rosebery muscovites at equivalent phengite concentrations.

Figure 26 shows the relationships between muscovite compositions and PIMA AlOH feature wavelengths. There is high correlation between wavelength and Fe+Mg ($r = 0.97$) confirming that the wavelength shift is due to the phengite content of muscovite. This relationship is far more pronounced in the Western Tharsis data than in those from Rosebery and etc. ($r = 0.66$, Fig. 16). The correlation between AlOH wavelength and Na/Na+K is considerably weaker ($r = 0.49$) but is consistent with the usual trend, that the most sodic muscovites have lowest wavelengths.

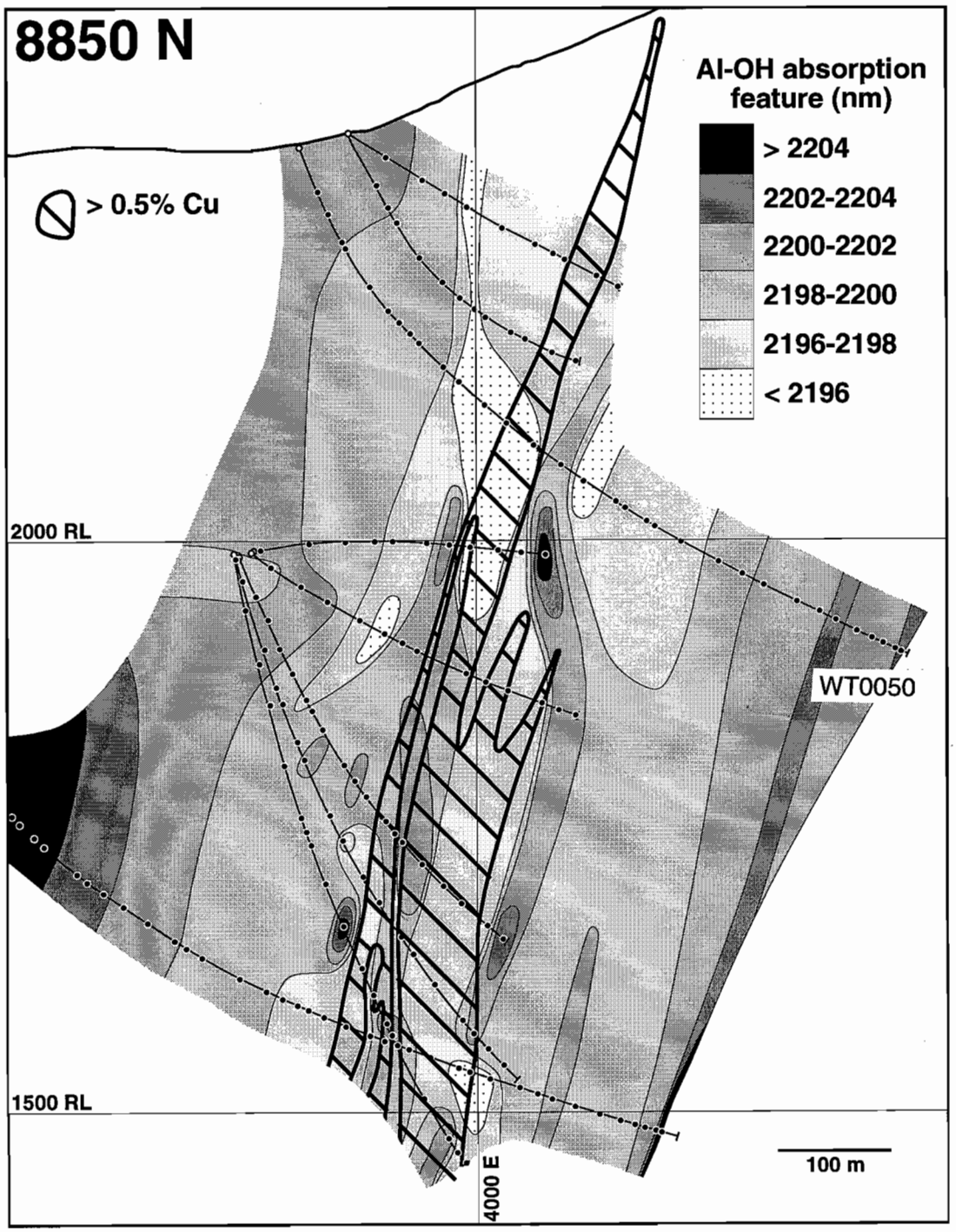

Figure 24. Cross section 8850N, Western Tharsis, showing the relationship between PIMA AlOH feature wavelength and the ore lens.

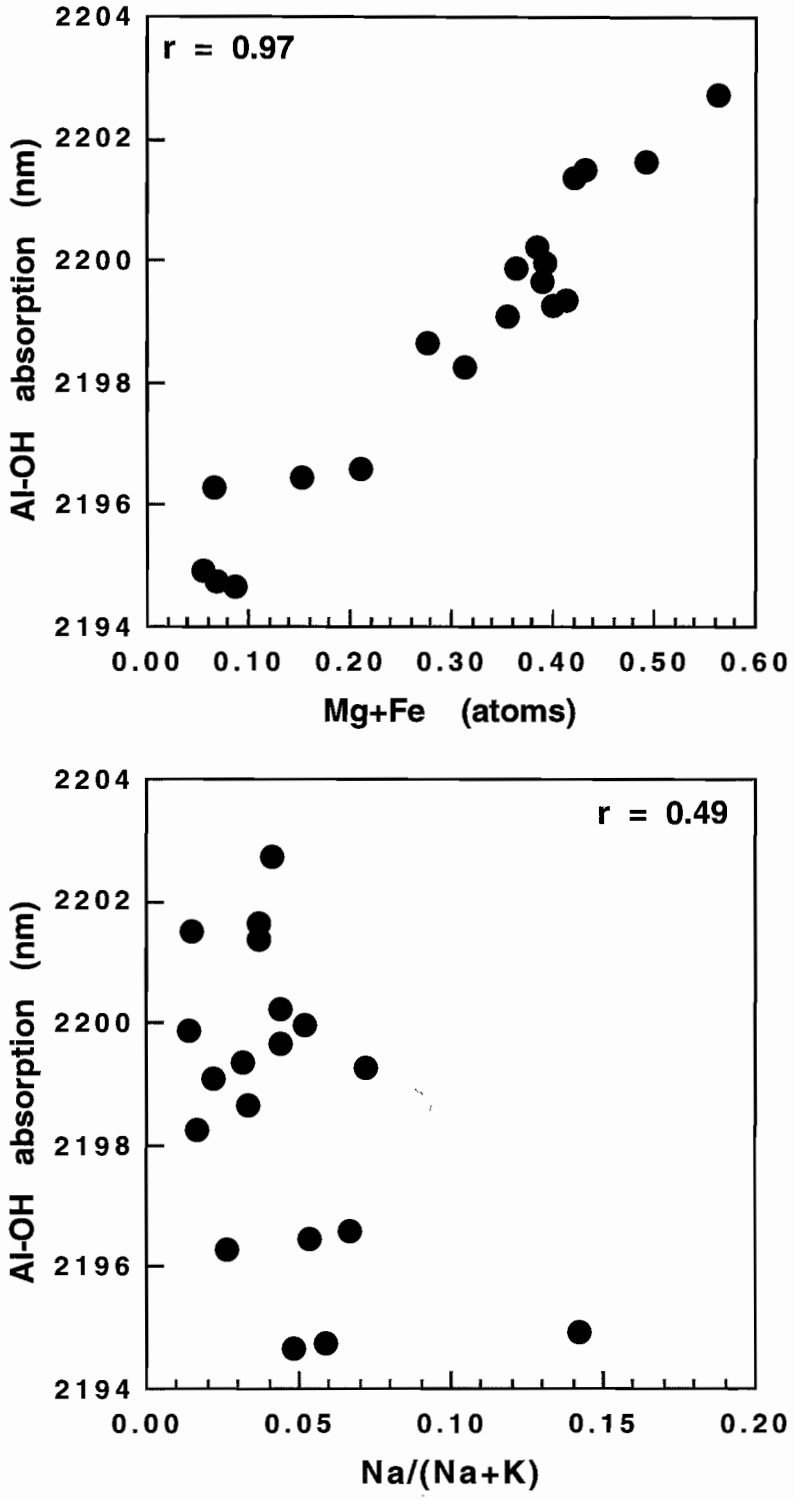

Figure 25. Scatterplots illustrating the correlation between phengite and sodium content of muscovites and PIMA AlOH wavelength in the Western Tharsis alteration system.

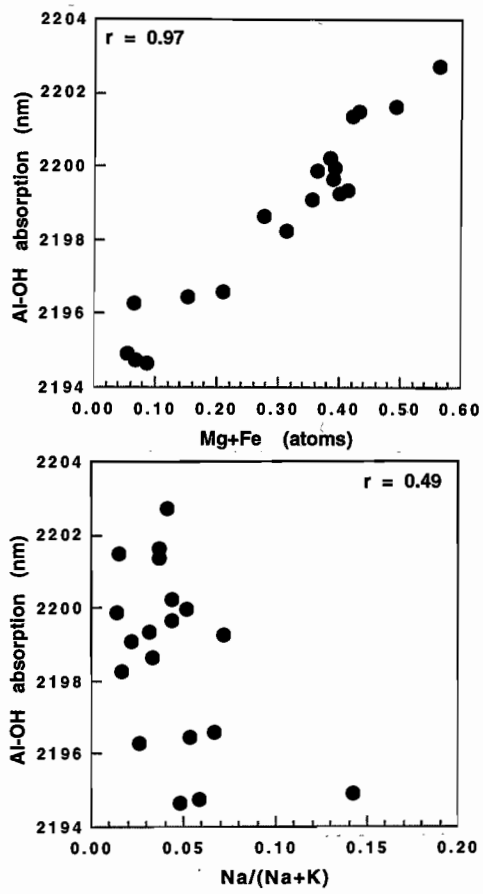

Figure 26. Downhole plots of WT0050 illustrating the zonal variations in muscovite composition and PIMA AlOH wavelength.

Chlorite

The microprobe data for chlorites is limited to the outer alteration zones in WT0050 (because no chlorite exists in the proximal sericitic and pyrophyllitic zones). Figure 27 shows that chlorite Mg number decreases toward the ore zone, from both the stratigraphic footwall and hangingwall sides. In other words, the chlorite compositions are more iron rich in proximity to the ore. The compositional range is, however, fairly small (0.27 to 0.48 Mg/Mg+Fe) and the chlorites in the stratigraphic hangingwall are slightly more magnesian. This range overlaps the low end of the range for fresh and altered volcanics from Rosebery and the Hercules and Mt Black traverses.

No relationship between chlorite composition and FeOH wavelength has been observed for these samples and it is unlikely that PIMA is applicable to mapping this dubious compositional vector to ore.

Carbonates

Microprobe analyses for WT0050 indicate that ankerite and siderite are dominant alteration related carbonates. Minor calcite exists in late stage veins that cut across tectonic foliation.

Carbonate in the outer, footwall, alteration zone associated with quartz + chlorite + sericite, is consistently ankeritic with ~0.2 Fe cations*. However, carbonate in the more proximal zone, overlapping the outer part of the pyritic quartz+sericite zone, is distinctly sideritic with ~0.8 Fe cations. Both types have low manganese contents ~0.05 cations per molecule. (Fig. 28).

Carbonate composition in the hangingwall is more erratic; alternating between about 0.2 and 0.6 Fe cations and ranging up to 0.2 Mn cations.

There are no consistent patterns for Ca and Mg composition of alteration related carbonates.

PIMA spectral characteristics of the Highway–Reward alteration zones
(Mark Doyle)

PIMA spectral analyses (Appendix 1) were undertaken on a suite of variably altered lavas, intrusions and volcaniclastic rocks sampled from drill core for whole rock geochemical studies of the host succession to the Highway–Reward deposit (Doyle, 1997b&c). The majority of the samples (125) are coherent rhyolite, rhyodacite and dacite; a few analyses of post mineralisation andesite dykes were also obtained. Analyses of volcaniclastic rocks were limited to samples of in situ hyaloclastite and pumice-crystal-lithic breccia and sandstone.

These PIMA spectra have had a hull quotient correction applied to enhance the spectral signatures of minerals present.

The Highway and Reward Cu–Au-rich pyrite pipes are enclosed within a discordant hydrothermal alteration envelope with spatial mineralogical zonation defined by various proportions of sericite, chlorite, anhydrite, quartz, pyrite, hematite and

* Carbonate mineral formulae were calculated on the basis of one metallic cation per molecule.

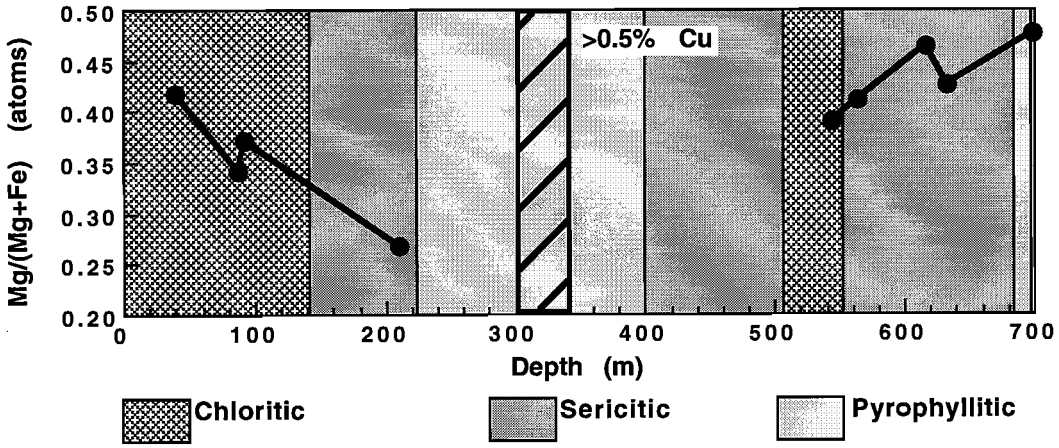

Figure 27. Downhole plots of WT0050 showing the proximal trend to iron-rich chlorite, in the outer zone of quartz + chlorite + sericite ± carbonate alteration, at Western Tharsis.

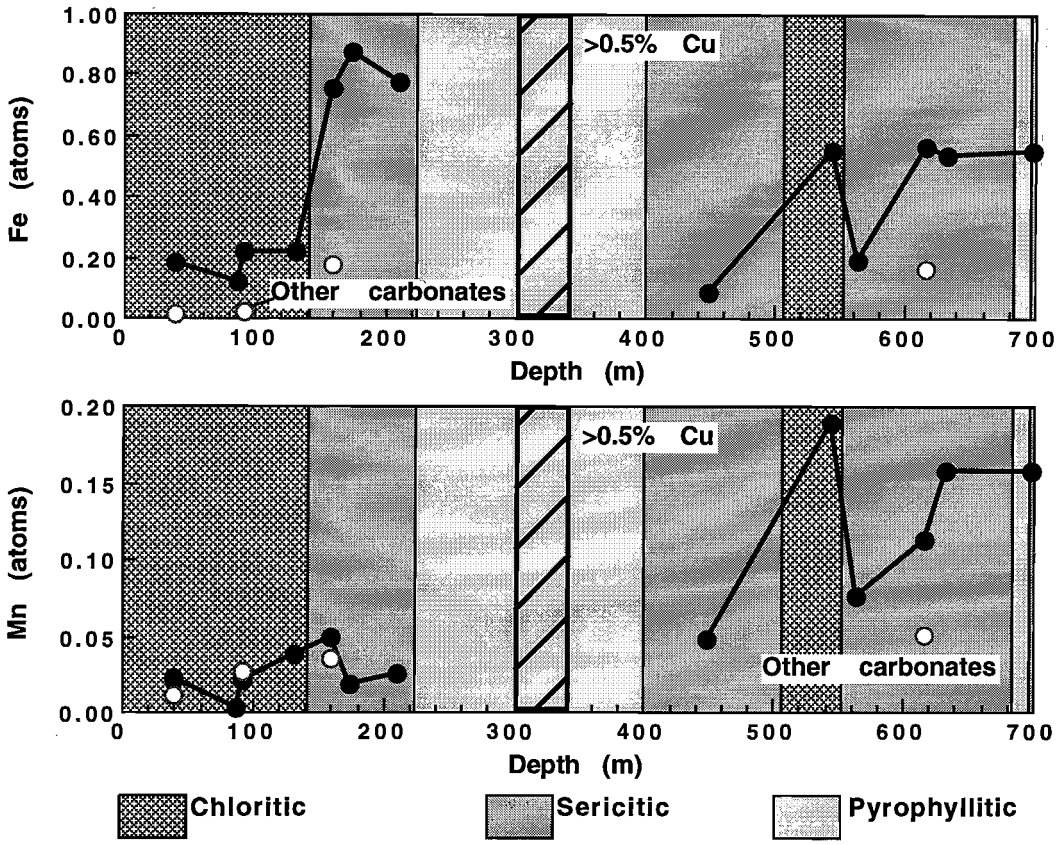

Figure 28. Downhole plots showing variations in iron and manganese content of carbonates in the outer zone of quartz + chlorite + sericite ± carbonate alteration, in WT0050, Western Tharsis.

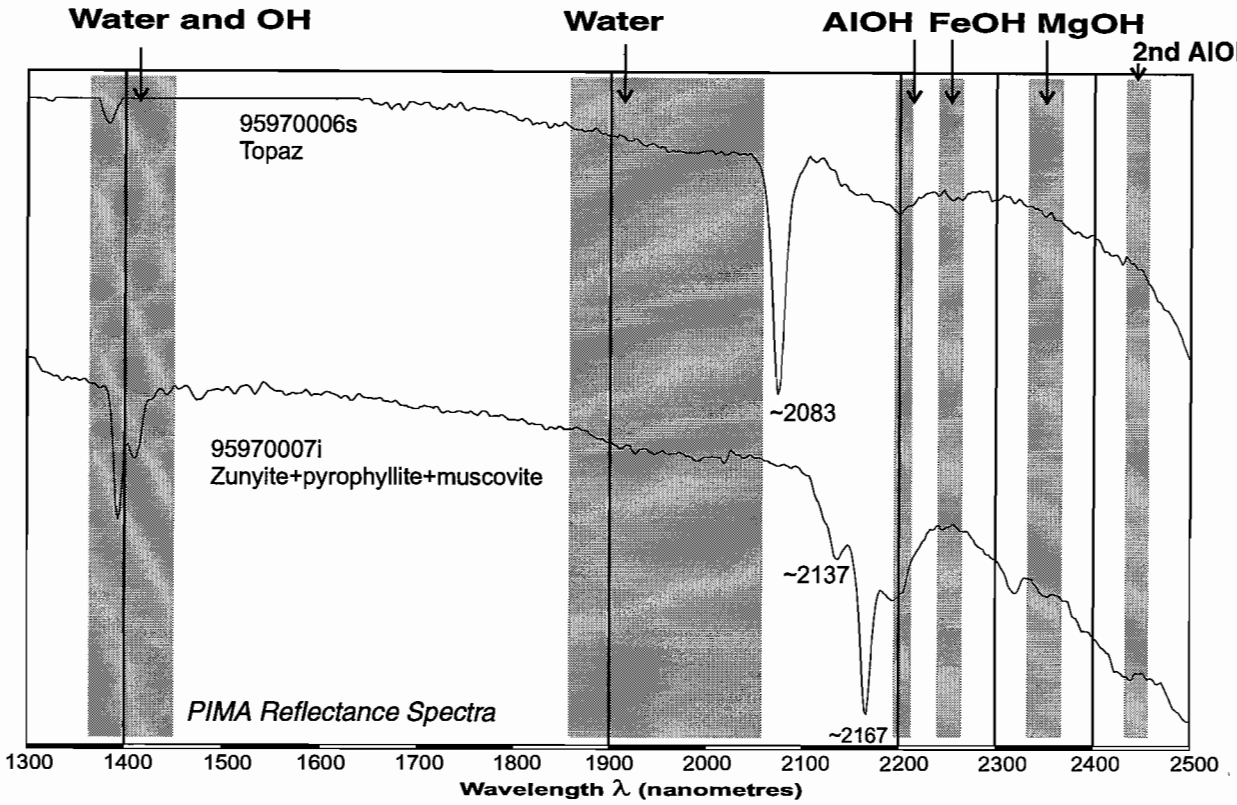

Figure 29
Spectra characteristic of topaz and zunyite+pyrophyllite bearing assemblages, Western Tharsis

barite. Minor and trace minerals include talc, carbonate and rutile (Doyle 1997a,b).

The new PIMA data suggests that alteration zones mapped as sericite comprise muscovite and phengitic muscovite (Fig. 30). In diamond drill holes HMO 47 and HMO 52 near surface samples have weathered to form montmorillonite (Fig. 30). The PIMA spectra support the visual estimates (Doyle, 1997a,b) of the relative proportions of sericite and chlorite in the different alteration zones.

Outside the hydrothermal alteration envelope, rhyolitic to dacitic lithofacies have altered to sericite-chlorite±feldspar±hematite±quartz. The PIMA AlOH wavelength data for muscovite in these samples is generally in the moderate to high range 2202–2222 (average = 2211; Fig. 31). This implies that the white micas within lithofacies greater than 50 to 200 m from the ore bodies have compositions in the muscovite to phengite range.

Within the Highway–Reward zones of hydrothermal alteration, AlOH wavelengths lie in the range 2195–2212 (average 2200, Fig. 31), characteristic of muscovites with low phengite content and possibly significant Na substitution for K. The alteration envelope has a mineralogical zoning, which is reflected in plots of Ishikawa Alteration Index versus AlOH wavelength (Fig. 31).

A quartz-sericite±pyrite zone is centred beneath the pyrite-chalcopyrite pipes and extends more than 60 m into the hanging wall on some sections. This zone is characterised by low AlOH wavelengths in the range 2195–2204 (av. 2199) and AI values >90.

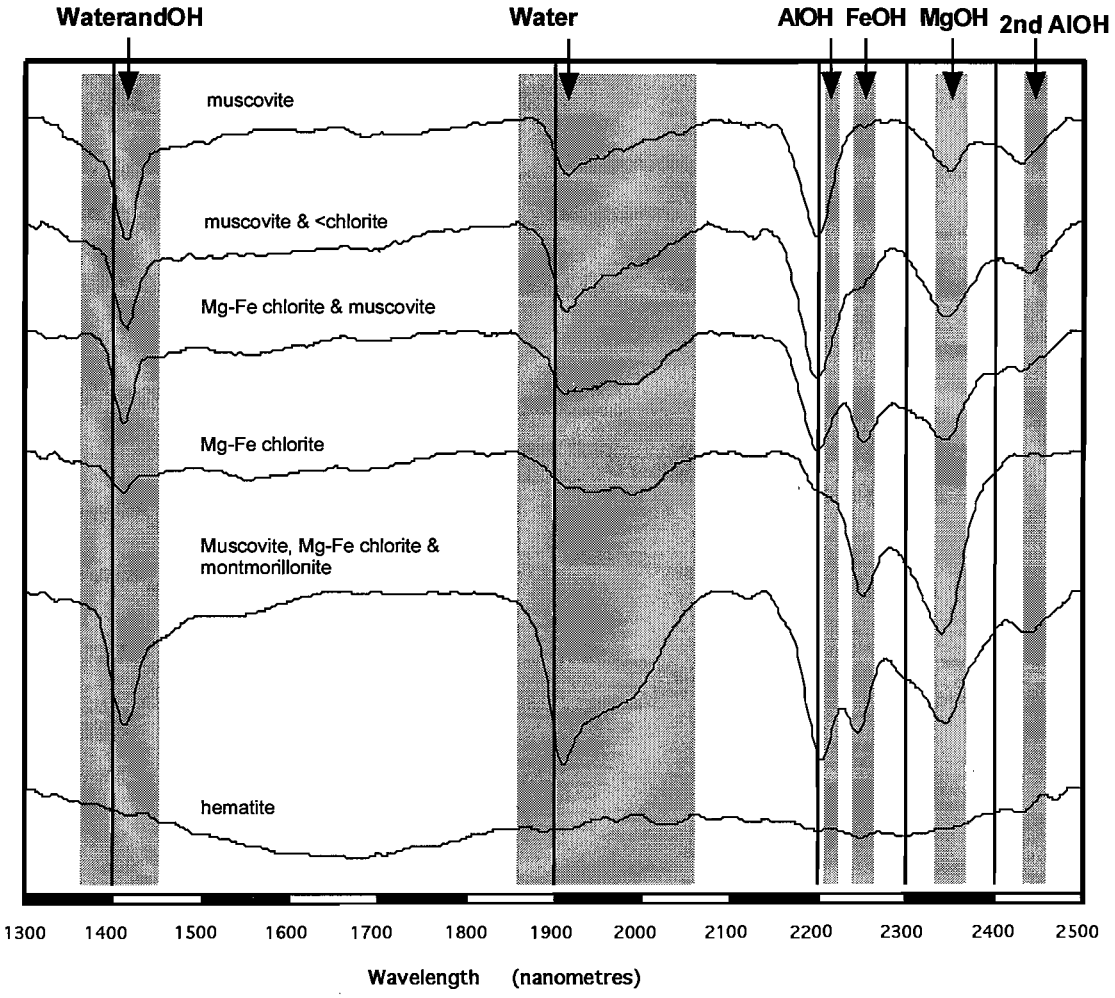

Figure 30. Representative PIMA spectra for altered lithofacies from the host succession to the Highway-Reward deposit.

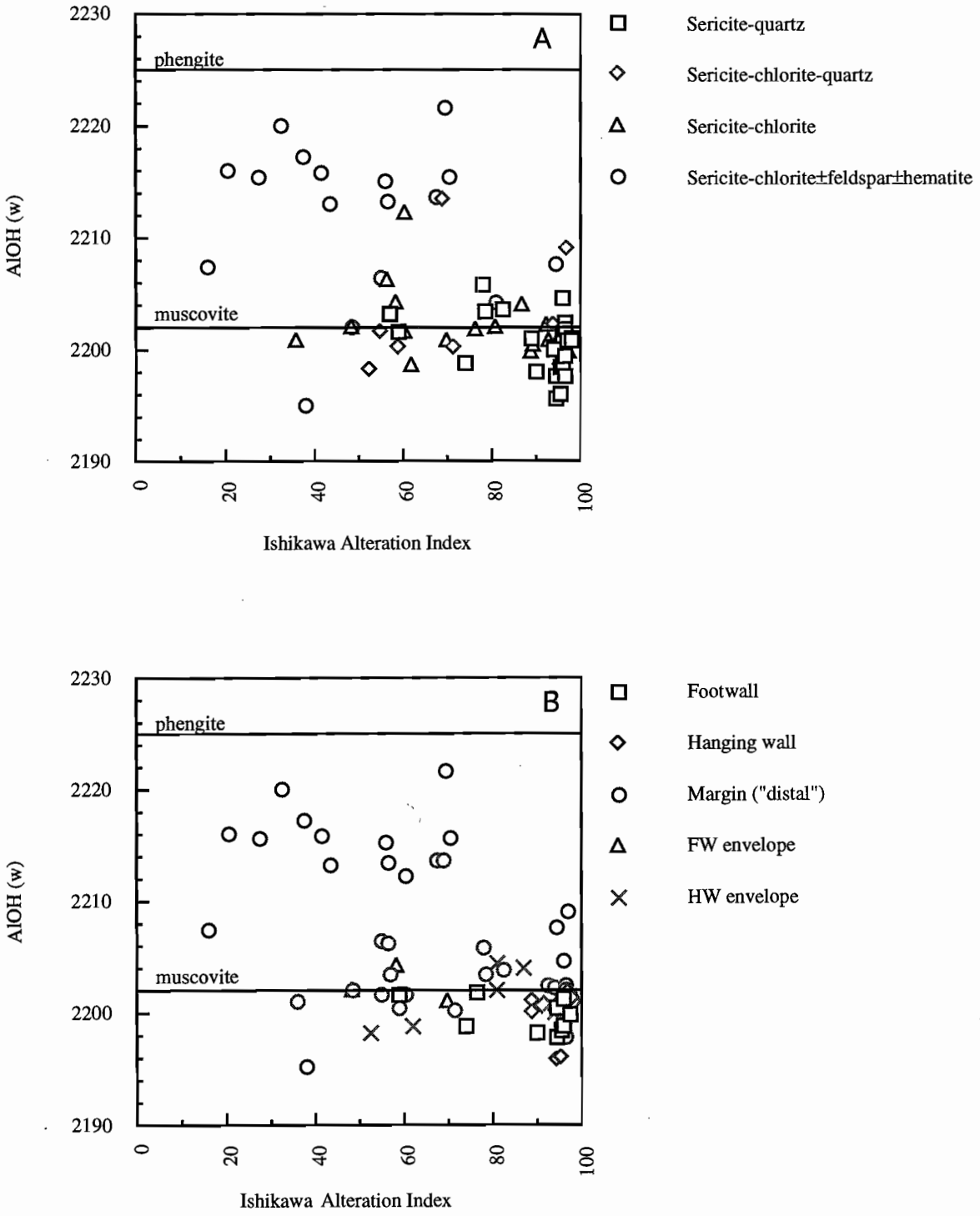

Figure 31. Variation in AlOH wavelength and Ishikawa Alteration Index as a function of alteration mineralogy and distribution.

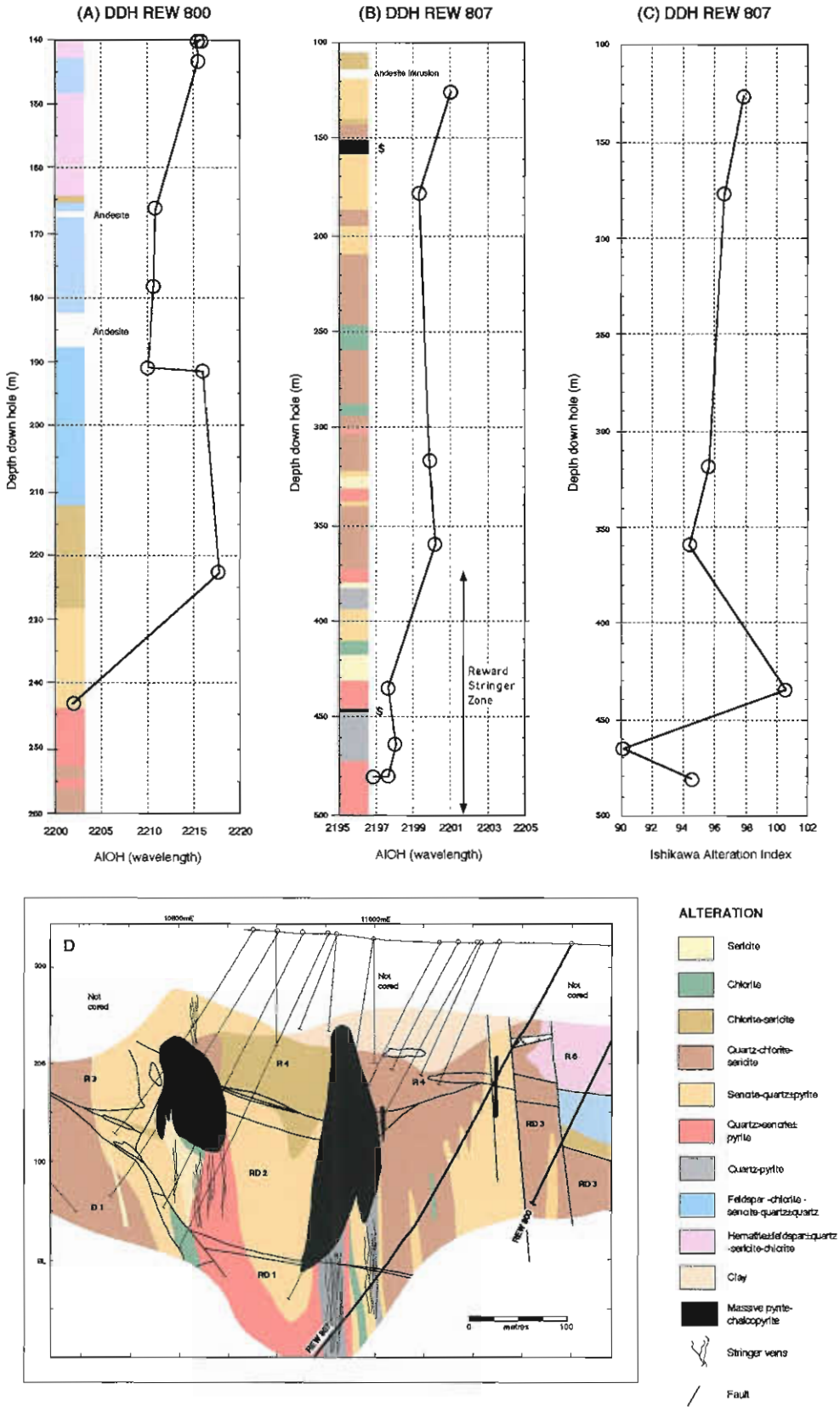

Figure 32. (A-B) Down hole AlOH wavelength variations in muscovite-bearing samples from DDH REW 800 and DDH REW 807. The distribution of alteration assemblages is also illustrated. (C) Down hole variation in Ishikawa Alteration Index values in DDH REW 807. (D) Simplified cross section showing the positions of DDH REW 800 and DDH REW 807 on section 10150N. Dacite D1, rhyodacites RD1-RD3 and rhyolites R2-4 and R6 are intersected on section 10150N.

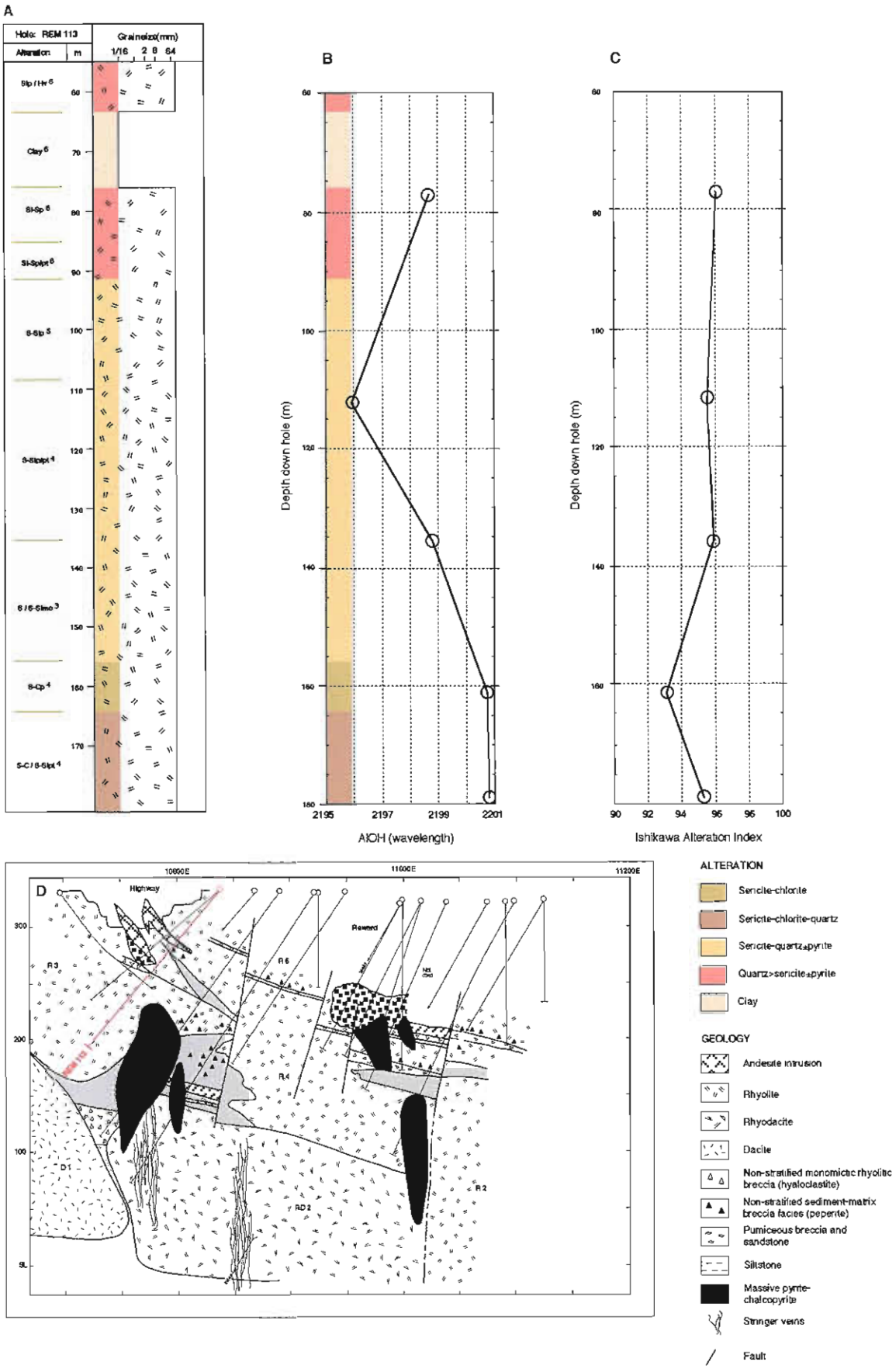

Figure 33. (A) Simplified graphic log for DDH REM 113 showing lithofacies variations, alteration assemblages and contact relationships (after Doyle, 1997b). (B) Down hole AlOH wavelength variation in muscovite-bearing samples from DDH REM 113 (Highway hanging wall). (C) Down hole variation in Ishikawa Alteration Index values for DDH REM 113. (D) Simplified cross section showing the position of DDH REM 113 on section 10075N. Dacite D1, rhyodacite RD2 and rhyolites R2-R6 are intersected on section 10075N.

Samples from the footwall and hanging wall lithofacies within this zone display similar AlOH wavelength and AI values (Fig. 31B). Marginal zones of less intense quartz-sericite±pyrite alteration peripheral to the Highway and Reward ore bodies, are characterised by AI values <90. Small zones of intense chlorite±anhydrite alteration occur within the quartz-sericite±pyrite zone, but contain little muscovite (eg. REM 154/335m, Appendix 1.).

Quartz-sericite±pyrite alteration grades laterally and vertically to enveloping zones of sericite-chlorite±quartz and sericite-chlorite alteration. These flanking zones are associated with AlOH wavelengths in the intermediate range 2198–2212 (av. 2201) and variable AI values of 27 to 98.

The alteration zones intersected in diamond drill holes REW 800 and REW 807 provide an example of the change in muscovite AlOH wavelength values passing into the Highway–Reward alteration envelope (Fig. 32).

In the eastern most hole (REW 800), values decrease from 2210–2217 in background sericite-chlorite±feldspar ±hematite±quartz-altered lithofacies (140–229.8m) to 2201 in the sericite-quartz ± pyrite zone.

In the more proximal drill hole REW 807 (100m grid west of REW 800), there is a relatively smooth trend of decreasing AlOH wavelength values (2201–2196) passing into the footwall stringer and sericite-quartz-pyrite alteration zone beneath the Reward pyrite-chalcopyrite pipe. The profile of AI values for the same hole is significantly more erratic and the lowest value (AI=90) occurs within quartz>sericite-pyrite-altered rhyodacite immediately beneath the Reward orebody (Fig. 32C).

Figure 33 illustrates the AlOH wavelength profile of drill hole REM 113. Although the number of samples is small, there appears to be a trend of increasing AlOH wavelength values passing through the Highway hanging wall sericite-quartz-pyrite zone down into the flanking sericite-chlorite and sericite-chlorite-quartz zones. Down hole variations in the Ishikawa Alteration Index do not appear to be as sensitive to the mineralogical variations within the different alteration zones.

These initial results from Highway–Reward indicate a good correlation between muscovite AlOH wavelength values, alteration mineralogy and alteration intensity. Muscovite composition may therefore, represent a useful indicator of proximity to Highway–Reward-type pyrite-chalcopyrite pipes. The absence of similar AlOH wavelength trends in the Rosebery footwall alteration system suggests that the vector may only be applicable to exploring for Cu–Au-rich mineralisation deposited from high temperature hydrothermal fluids.

More detailed PIMA spectral analyses of drill core from several cross sections (eg. 10200, 10150N, 10100N, 10025N, 9850) are required at Highway–Reward to test the robustness of the AlOH wavelength vector. Determination of the chemistry of background muscovite in samples from other parts of the will be important. Electron microprobe analyses of muscovites, from the alteration zones and elsewhere in the Trooper Creek Formation, are also required to confirm the implied compositional variations and determine the background composition.

Comparison of FTIR and PIMA spectral analysis

(Mike Blake)

Background

The FTIR spectrometer (Fourier Transform Infared) is an infared spectrometer which measures the absorbance of infared wavelengths in the test sample. The wavelength region in which the FTIR operates is variable depending on the source filament used, and can be in the range 66–25000 nm. An FTIR instrument manufactured by Bruker is housed in the University of Tasmania's Central Science Laboratory, and is dominantly used for compound fingerprint work. The usual wavelength region which this machine operates is 400–5000 wavenumbers, where wavenumber is equivalent to 10^7 divided by wavelength in nanometres. For comparison with PIMA , the equivalent wavelength range is 2000 to 25000 nm, or 2–25 microns. PIMA operates from 1300–2500 nm, only slightly overlapping with the high wavenumber end of the FTIR spectrum used for this study.

The FTIR differs from the PIMA spectrometer principally in that it measures transmittance of the sample medium, whereas PIMA measurements are based on reflectance from the sample surface. The

PIMA is a portable instrument whilst the FTIR is a laboratory based high precision instrument.

Samples measured by the absorbance method are prepared by mixing a small amount of sample powder in Potassium Bromide (KBr) powder, and pressing into a translucent disk under 2000 psi. KBr crystals liquefy and flow under pressure to produce a translucent disk with the sample powder disseminated throughout. A source beam from an infared laser in the instrument is passed through the sample, the transmitted beam is measured and the absorbance by the sample is calculated over the wavelength interval.

Initial work by Large et al 1997, showed that there was some correlation between FTIR and PIMA results in a limited dataset. This report follows on to extend that work , noting that the FTIR has considerable potential for further investigation.

The FTIR sampling for P439 has concentrated on the 120R drill hole from the Rosebery study in order to make a comparison between PIMA and FTIR, and to determine advantages and disadvantages of using these instruments.

The conversion from wavenumber to nanometres is :

wavenumber = 10^7/wavelength in nanometres

wavenumber = 10^4/ wavelength in micrometres

Minerals investigated with FTIR in this study are muscovite, chlorite, carbonate and quartz These produce characteristic peaks in from the FTIR spectrum as indicated on Figure 34.

Muscovite

White micas have a distinctive absorbance feature in the 3600 to 3640 wavenumber region, (Fig. 34) with muscovite having a feature at 3630 and paragonite at 3640, (Gadsen, 1975). This feature is distinctive in the FTIR spectrum and has no interferences from the other minerals present in the Rosebery sample suite. The position of this feature varies with Fe and Mg substitution for octahedral Al, in the same way as for the PIMA AlOH absorbtion feature, moving to lower wavenumbers (=higher wavelength) with increasing Fe and Mg.

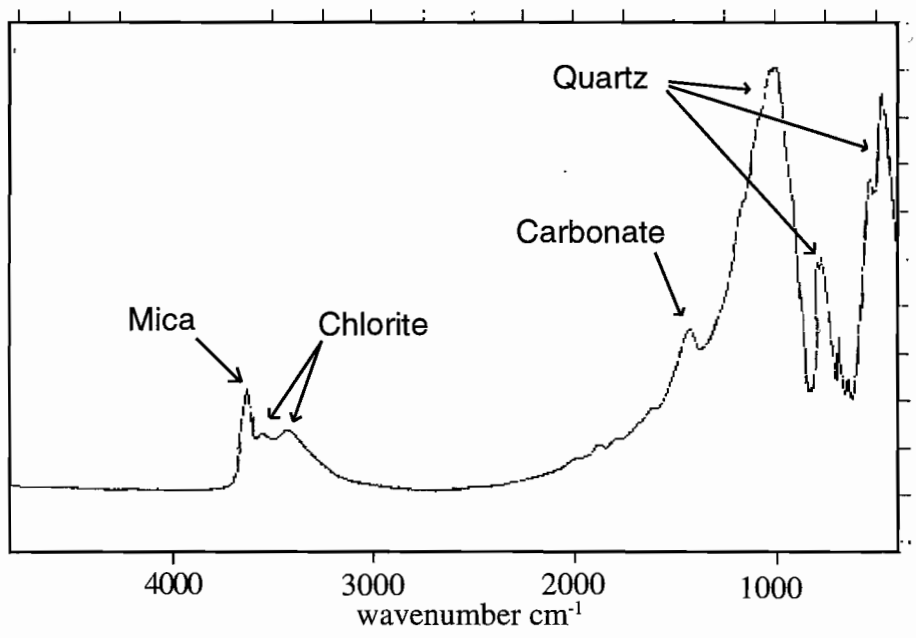

Figure 34. FTIR features from the Rosebery study

Gadsen (opcit.) reported a broad doublet feature at 535 and 480, which is masked by strong quartz interference, and therefore was not useful for identification, in the Rosebery samples.

A comparison of FTIR mica absorbtions with PIMA ALOH feature shown in Figure 35a shows that there is a good correlation between both instruments. FTIR muscovite wavenumbers plotted against of average muscovite atomic Fe+Mg content (microprobe data) in Figure 35b shows a highly correlated linear trend. All datapoints plot within about two wavenumbers of the trend line, which is comparable to the accepted precision of PIMA.

FTIR wavenumber shows the same pattern as PIMA in the downhole plots comparing spectral data to atomic Fe+Mg in muscovite (Fig. 36).

Chlorite

Chlorite has a characteristic doublet feature with peak absorbances observed around 3560 and 3430 in the Rosebery sample suite. Wilson, (1987) reported that the position of these features varies with composition, shifting to lower frequency with increasing aluminium and iron content. The chlorite feature is less intense than the muscovite and quartz features, as can be seen from Figure 1, and can be masked by the shoulder of the 3620 muscovite feature and a broad water feature from 3300 to 3500 wavenumbers. Spectral additions comparing pure chlorite with a wholerock spectra showed that a 20% weighting applied to pure chlorite spectra was needed to give chlorite an appreciable effect in the wholerock spectrum.. The result of these interferences mean that small amounts of chlorite are difficult to resolve from the water feature, and the shoulder of the muscovite feature.

Despite these interference problems, use of the FTIR chlorite spectrum shows promise. The comparison of calculated* chlorite Mg# with chlorite feature wavenumbers (from those spectra in which the chlorite feature could be confidently identified) shows a strong correlation, (Fig. 35c). The same samples are shown in the downhole plot in Figure 37.

* Chlorite Mg numbers calculated from wholerock analyses using the MINSQ least squares method (Appendix II).

Carbonate identification

In the FTIR wavelength region investigated, carbonate has its strongest absorbtion feature at around 1400 wavenumbers, (Fig. 34). Work has concentrated on this feature because of its sharp strong character, thus making it easy to identify. Other features occur at 2520 –2530, 1600–1700, 1000–950, 850–800 and 720–650, (Gadsen, 1975). Most of these are difficult to work with because of the proximity of dominant quartz absorbance features. Of these features, the 650–720 absorbance warrants further investigation, as it occurs in a quartz 'window'. The feature at 2520 is in a clear part of the spectrum, but is only a weak feature even in carbonate rich samples.

A comparison of downhole carbonate wavenumber with average carbonate probe data for MnO and FeO Mol% is shown in Figure 38. Wavenumber of the 1400 carbonate peak shows no obvious correlation with carbonate chemistry, and may be controlled by amount of CO_3 in the sample.

Comparison of applicability of FTIR and PIMA in alteration studies

The following comments about the applications of either instrument must be taken in the context that the FTIR work was a limited study looking only at a relatively simple alteration assemblage of micas, chlorites and carbonates in one Rosebery drill hole.

Advantages of FTIR

- FTIR can be used to investigate a much broader spectrum than PIMA, from 66 to 25000 nm, which includes the PIMA's operating range, 1300–2500 nm.
- Loss of spectra due to complete absorption, as in dark or carbonaceous samples, is not a problem, as sample transmission is a function of dilution. We have found that because PIMA measures reflectance, samples which are dark or contain strongly absorbing minerals such as sulphides, produce poor spectra. The presence of carbon in the sample can be a dominant feature, masking the effect of other minerals in PIMA spectra.
- FTIR has the possibility of mineral grain identification with an infared transmission microscope

connected to the spectrometer.
- Carbonate presents no interference to other minerals, and is visible as distinct peaks.

Advantages of PIMA

- PIMA has the advantage of being a portable instrument. However, some difficulties have been reported in field use in hot or humid conditions, as it is prone to overheating. FTIR spectrometer is a laboratory based instrument, and needs to be maintained by a specialist, in contrast to PIMA which is designed to be user maintained.
- The development of PIMA for the mining industry has produced extensive diagnostic libraries which are readily accessible and simplify spectral interpretation.
- When used with a PC, a large amount of data can be collected quickly, in the order of 30 per hour with each analysis taking only about one minute.
- Spectral interpretation software is due to be updated, and an improved model PIMA will be released. Currently available programs are Pimaspec and Pimacalc-MS DOS based programs which are not particularly robust or flexible, and run with difficulty on some PC's.
- PIMA has no quartz interferences in the operating band width 1300–2500 nm. A disadvantage in the FTIR 25000–2000 nm range, is the strong quartz features in the 400–1250 wavenumber region (see Fig. 34).
- To produce KBr disks for transmission measurements the rock sample first needs to be crushed and milled to a fine powder. PIMA can measure (dry) rock surfaces, drill core, cuttings, sediment and soil samples in the field, virtually eliminating the need for sample preparation.

Conclusions

- PIMA spectral wavelength data can be used to infer the composition of muscovite in terms of the amounts of phengite and Na substitution.
- The composition of muscovite in Rosebery footwall hydrothermal alteration zones is not dissimilar to that of essentially unaltered felsic rocks elsewhere in the Mt Read Volcanics. Muscovites in these volcanics are typically more or less phengitic (with 0.2 to 1.0 Fe+Mg octahedrally coordinated cations) but the variation is unrelated to hydrothermal alteration intensity.
- Muscovites in the hangingwall volcaniclastic sandstone unit immediately overlying the Rosebery deposit, are distinctively sodic (Na/Na+K upto 0.35) and non-phengitic. The amount of Na substitution in muscovite, in this unit, appears to be spatially related to sulphide lenses and may have application as a mine scale exploration vector, measurable by PIMA. It is likely that the muscovite composition is associated with unusually high chlorite content in the hangingwall volcaniclastic sandstone and its probable mafic provenance, but not directly related to the massive sulphide forming hydrothermal system.
- Muscovites at Western Tharsis show a clear and symmetrical compositional relationship to the ore lens and alteration system. The composition grades from moderately phengitic (~0.5 Fe+Mg) in the outer quartz+chlorite+sericite±carbonate zones to non phengitic (<0.1 Fe+Mg) in the proximal pyrophyllite ± quartz ± sericite zone. This compositional change is very closely correlated to the AlOH absorption wavelength and constitutes a mine scale exploration vector which can be rapidly and effectively determined by PIMA analyses.
- A similar association of low AlOH wavelengths and proximal zones of intense quartz + sericite + pyrite alteration is also evident in preliminary spectral data from Highway–Reward in the Mt Windsor Volcanics. (Although as yet unsupported by microprobe analyses) It suggests that low phengite contents of muscovites in proximal alteration zones may be linked to Cu–Au hydrothermal systems.
- Chlorite composition is considerably variable in the Mt Read Volcanics but there is no consistent relationship to alteration intensity, or systematic zonation in the Rosebery alteration system.
- Chlorites in the outer parts of the Western Tharsis alteration system show a weak trend of iron enrichment inwards towards the ore lens; (Mg numbers decreasing from ~45 to ~30). This compositional change is not measurable by PIMA analysis and the restriction of chlorite to the outer

alteration zones limits its usefulness as an exploration vector.

- PIMA spectrometry is not applicable to measurement of compositional variations in chlorites from the Hercules, Mt Black, Rosebery and Western Tharsis areas.
- PIMA spectral parameters can provide a rough measure of the quantities of muscovite and chlorite, and which of them is dominant, in altered volcanics. However, the precision of such estimates, across a broad range of volcanic rocks, is extremely poor and probably less reliable than visual estimates by ordinary megascopic or hand lens methods. The precision of PIMA mineral estimates may be acceptable within groups of samples with similar spectral characteristics.
- The PIMA and FTIR spectrometers can both be used for estimating the phengite content of muscovite in mixed phyllosilicate rock samples.
- FTIR shows potential for determinations of chlorite Mg number, at least in samples which are not dominated by muscovite.

Acknowledgments

Sincere thanks to:

Cathryn Gifkins for the loan of Mt Black–Sterling Valley samples and Bill Wyman for contributing analyses of chlorites from Jukes.

Ron Berry (CODES) for useful discussion of mica chemistry and introducing us to the least squares method of calculating quantitative mineral assemblages from geochemical numbers.

Nick Merry (Ausspec) and Andrew Davies (CODES) for illuminating the dark mysteries of PIMA spectral analysis.

Kai Yang and Jon Huntington (CSIRO) for the loan of a PIMA.

References

Deer, W.A., Howie, R.A. and Zussman, J., 1966. An introduction to the rock forming minerals. Longman, London.

Doyle M.G., 1997a. Alteration associated with sub-seafloor replacement style massive sulfide deposits: evidence from the Cambro-Ordovician Highway-Reward deposit, Mount Windsor Subprovince. AMIRA - P439, Studies of VHMS-related alteration: geochemical and mineralogical vectors to ore. Report 4: 231–257.

Doyle M.G., 1997b. A Cambro-Ordovician volcanic succession hosting massive sulfide mineralisation: Mount Windsor Subprovince, Queensland. [unpub. Ph.D thesis]. University of Tasmania, 264 pp.

Doyle M.G., 1997c. Alteration geochemistry of the sub-seafloor replacement style Highway-Reward deposit, Mount Windsor Subprovince. AMIRA - P439, Studies of VHMS-related alteration: geochemical and mineralogical vectors to ore. Report 5: 201–219.

Gadsen, J. A., 1975. Infared spectra of Minerals and Related Inorganic Compounds, Butterworth, England.

Green, G.R., Solomon, M. and Walshe, J.L., 1981. The formation of the volcanic hosted massive sulfide ore deposit at Rosebery, Tasmania. Economic Geology, V76, p.304–338.

Huston, D. L., 1997a. Research program and preliminary results of alteration studies at the Western Tharsis deposit, Mt Lyell field: AMIRA/ARC Project P439 Report 4, p331–335.

Huston, D. L., 1997b. Geochemical variations in the alteration zone surrounding the Western Tharsis deposit and their utility in exploration: AMIRA/ARC Project P439 Report 5, p. 1–34.

Huston, D. L. and Kamprad, J., 1998. Alteration zonation and geochemical dispersion at the Western Tharsis deposit, Mt Lyell, Tasmania: a summary. Unpub. CODES P439 AMIRA Report 6, (in prep.)

Large, R.R., Allen, R.L. and Blake, M., 1997. Carbonate and muscovite mineral chemistry, Rosebery VHMS deposit, Tasmania. AMIRA/ARC Project P439, Report 5, Oct 1997, p147–173.

Large, R.R., Allen, R.L., Blake, M. and Herrmann, W., 1998. Alteration halo model for the Rosebery VHMS deposit, western Tasmania. AMIRA/ARC Project P439, Report 6, May 1998, (in prep.).

LeMaitre, R.W., 1981 GENMIX: a generalised petrological mixing model program. Computers and Geosciences, V7,3 p229–247.

McLeod, R.L., Gabell, A.R., Green, A.A and Gardavsky, V., 1987. Chlorite infra red spectral data as proximity indicators of volcanogenic massive sulphide mineralisation. Proceedings of the Pacific rim Congress. p321–324.

Pontual, S., Merry, N and Gamson, P., 1997. Spectral Interpretation Field Manual. Ausspec International Pty. Ltd.

Pontual, S. and Merry, N., 1995. PIMA Workshop 2 - Practical implementation of the PIMA in exploration and mining. Workshop Notes for training sessions. Ausspec International P/L

Rock, N.M.S. and Carroll, G.W.,1990. MINTAB: a general purpose mineral recalculation and tabulation program for Macintosh microcomputers. American Mineralogist, V75, p.424–430.

Wilson, M. J., 1987, A Handbook of Determinative Methods in Clay Mineralogy, Blackie, Glasgow.

Yang, K., Gemmell, J.B. and Fulton, R., 1996a. PIMA-II Spectral analysis of alteration associated with the Hellyer VHMS deposit: Preliminary results. AMIRA/ARC Project P439, Report 2, May 1996, 171–177. CODES, University of Tasmania

Yang, K., Huntington, J.F., Gemmell, J.B. and Fulton, R., 1996b PIMA-II Spectral analysis of alteration associated with the Hellyer VHMS deposit: Progress report. AMIRA/ARC Project P439, Report 3, Oct 1996, 307–320. CODES, University of Tasmania

Yang, K., Huntington, J.F., Gemmell, J.B. and Fulton, R., 1997 PIMA-II Spectral analysis of alteration associated with the Hellyer VHMS deposit: New results. AMIRA/ARC Project P439, Report 5, Oct 1997, 175–192. CODES, University of Tasmania

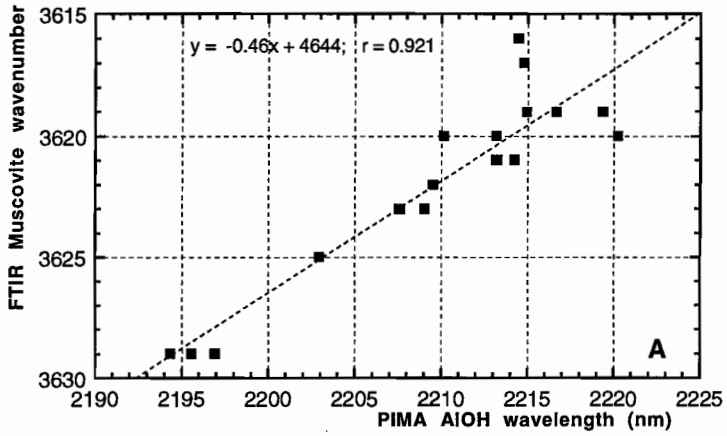

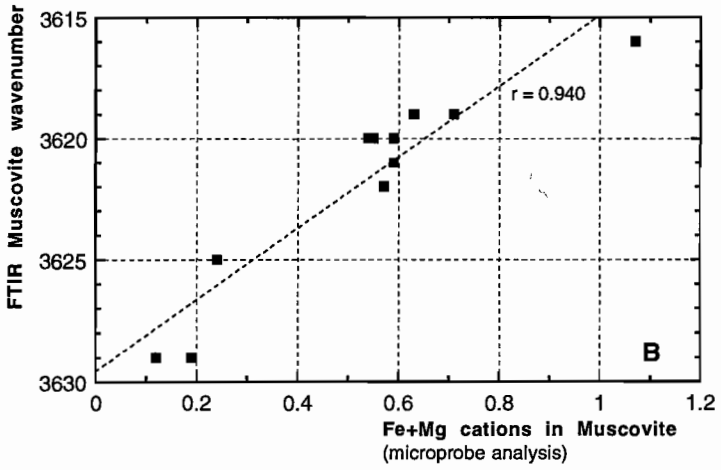

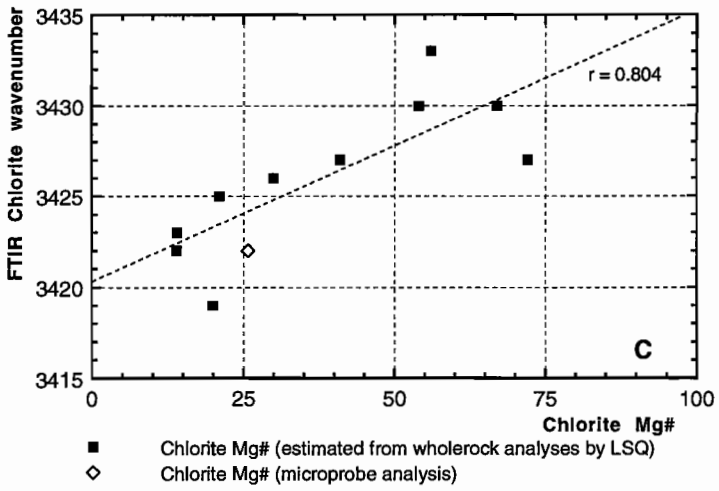

Figure 35 Plots of FTIR feature wavenumbers compared to:
A: PIMA AlOH wavelength
B: Muscovite Fe+Mg content
C: Chlorite Mg number

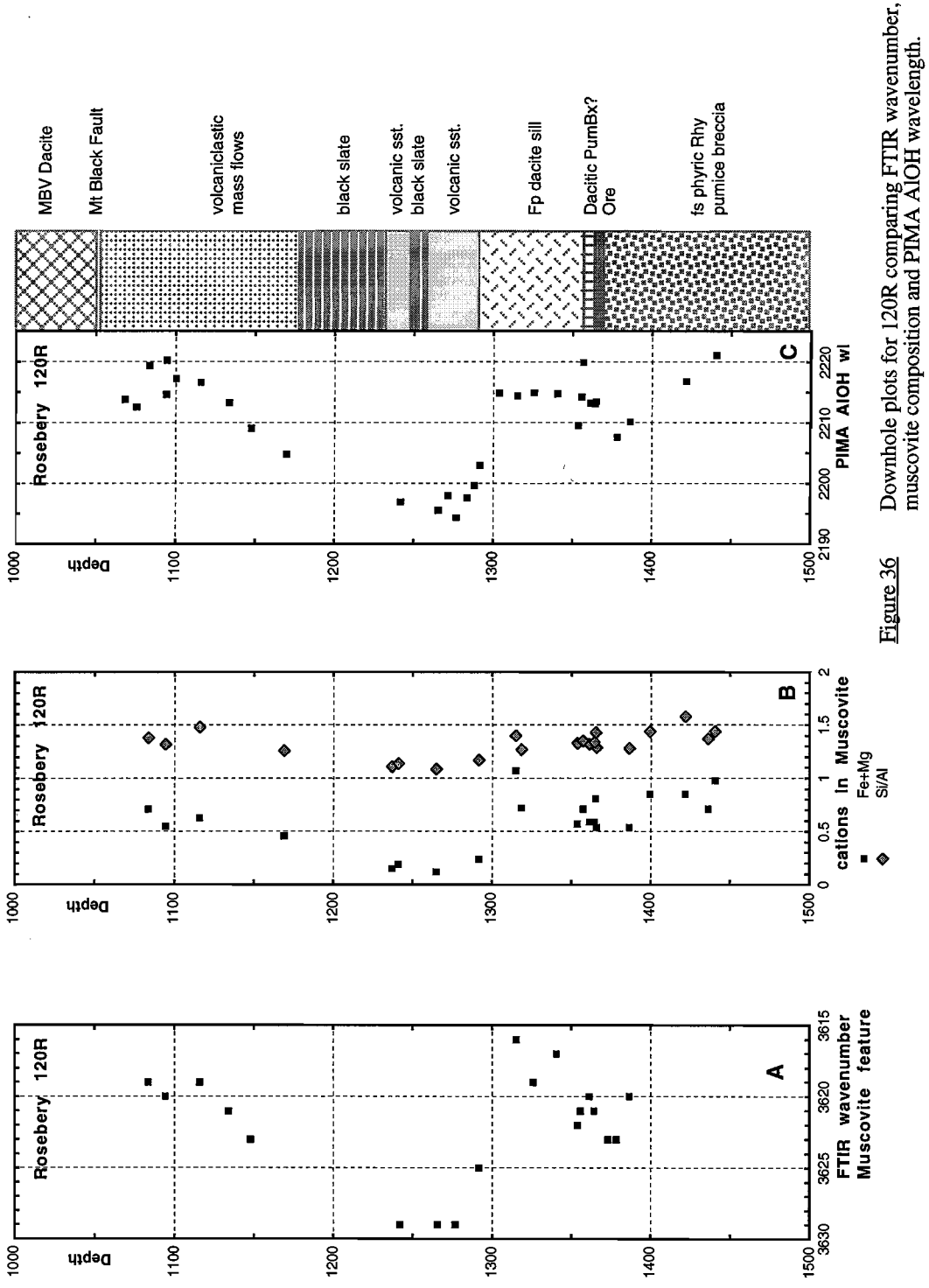

Figure 36 Downhole plots for 120R comparing FTIR wavenumber, muscovite composition and PIMA AlOH wavelength.

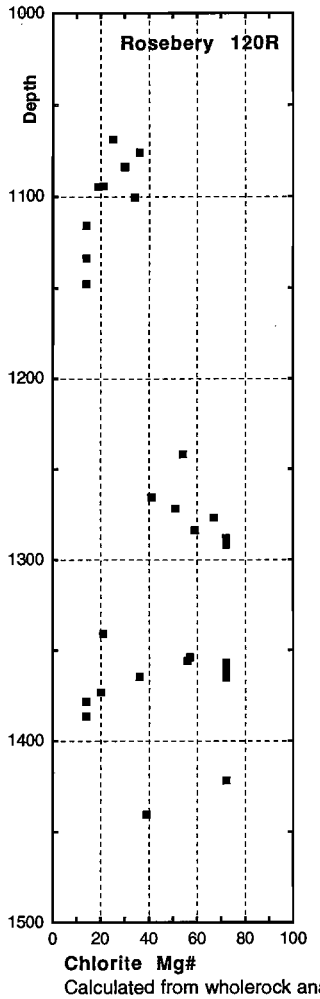

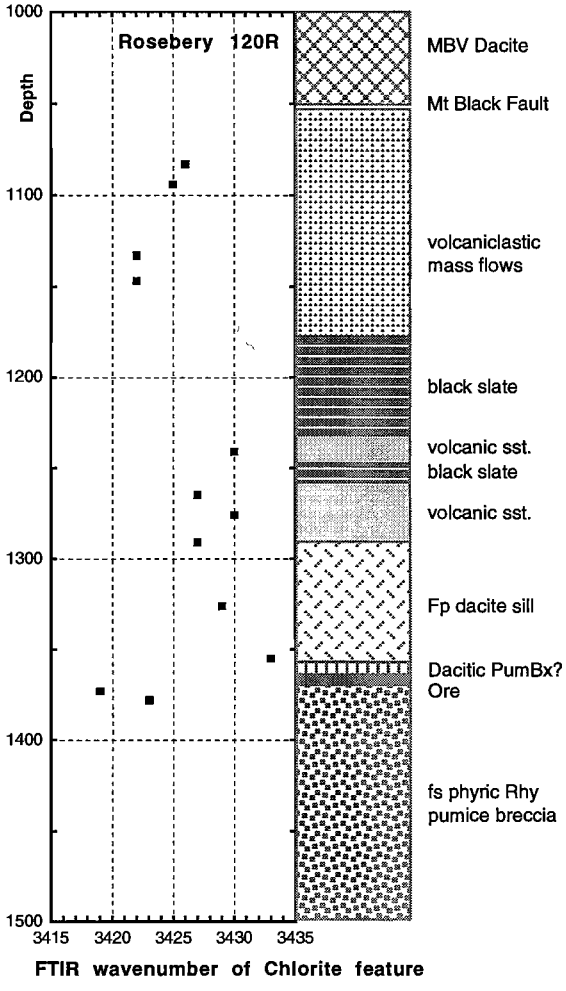

Figure 37 Downhole plots for 120R comparing FTIR wavenumber of chlorite feature with chlorite Mg number.

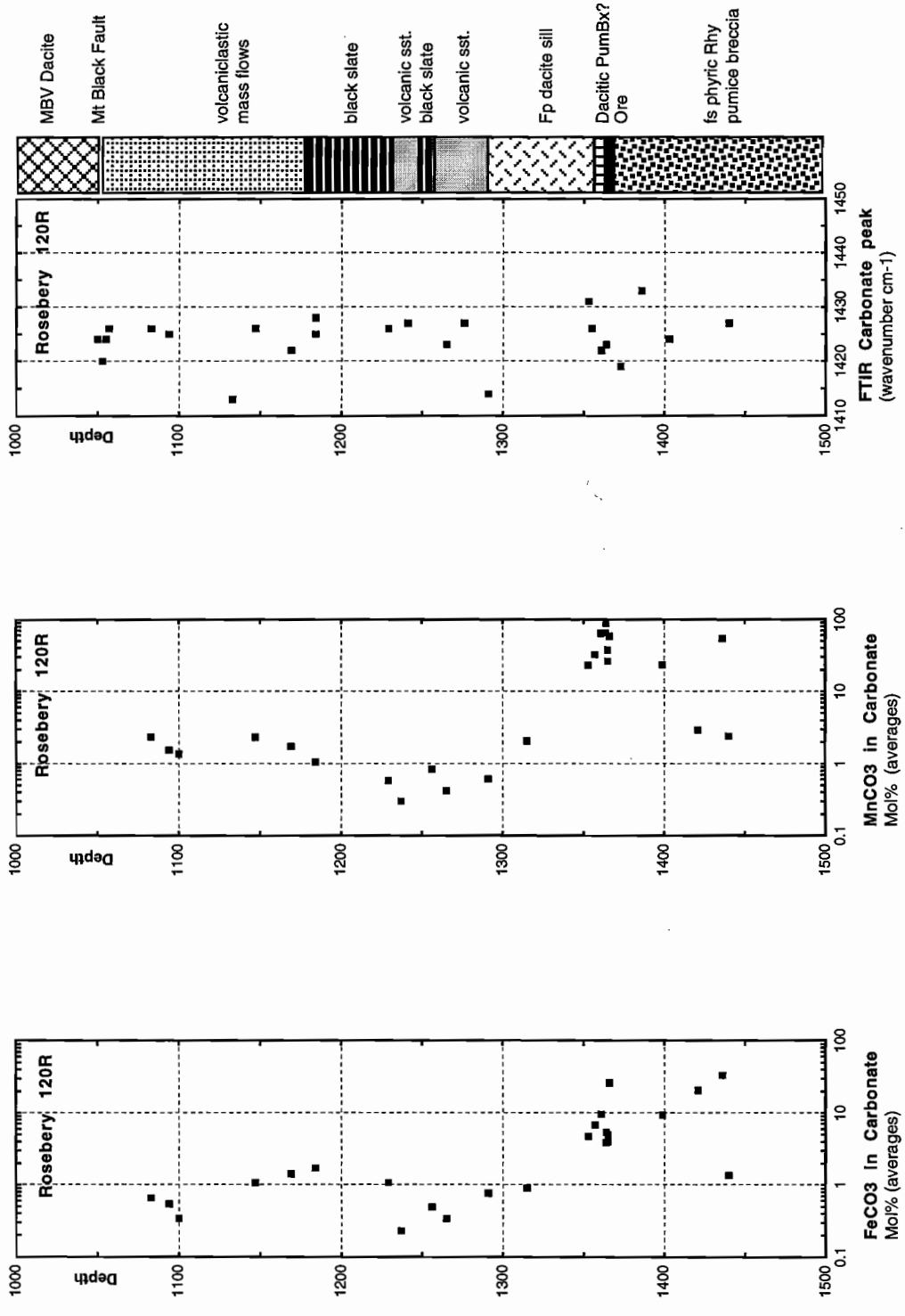

Figure 38 Iron and manganese content of carbonates compared to wavenumber of FTIR carbonate feature

Appendix I
Hull quotient spectra from Highway-Reward drill holes

Highway-Reward, MWV
HMO36, 39, 40, 47, 52: Rhyolite & dacite
Hull quotient reflectance spectra

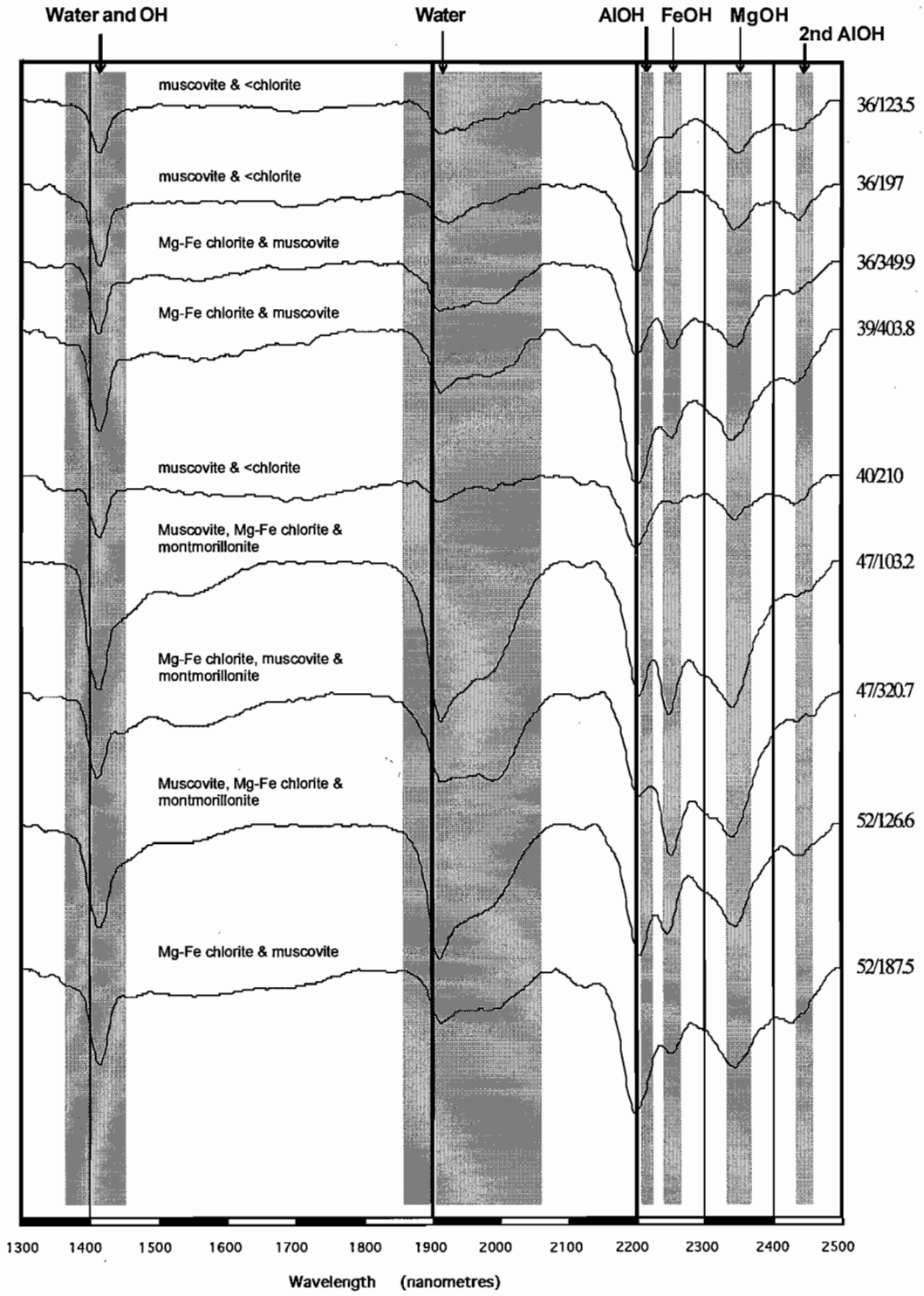

Appendix 1.1

Highway-Reward, MWV
REM113, 116, 118: Rhyolite
Hull quotient reflectance spectra

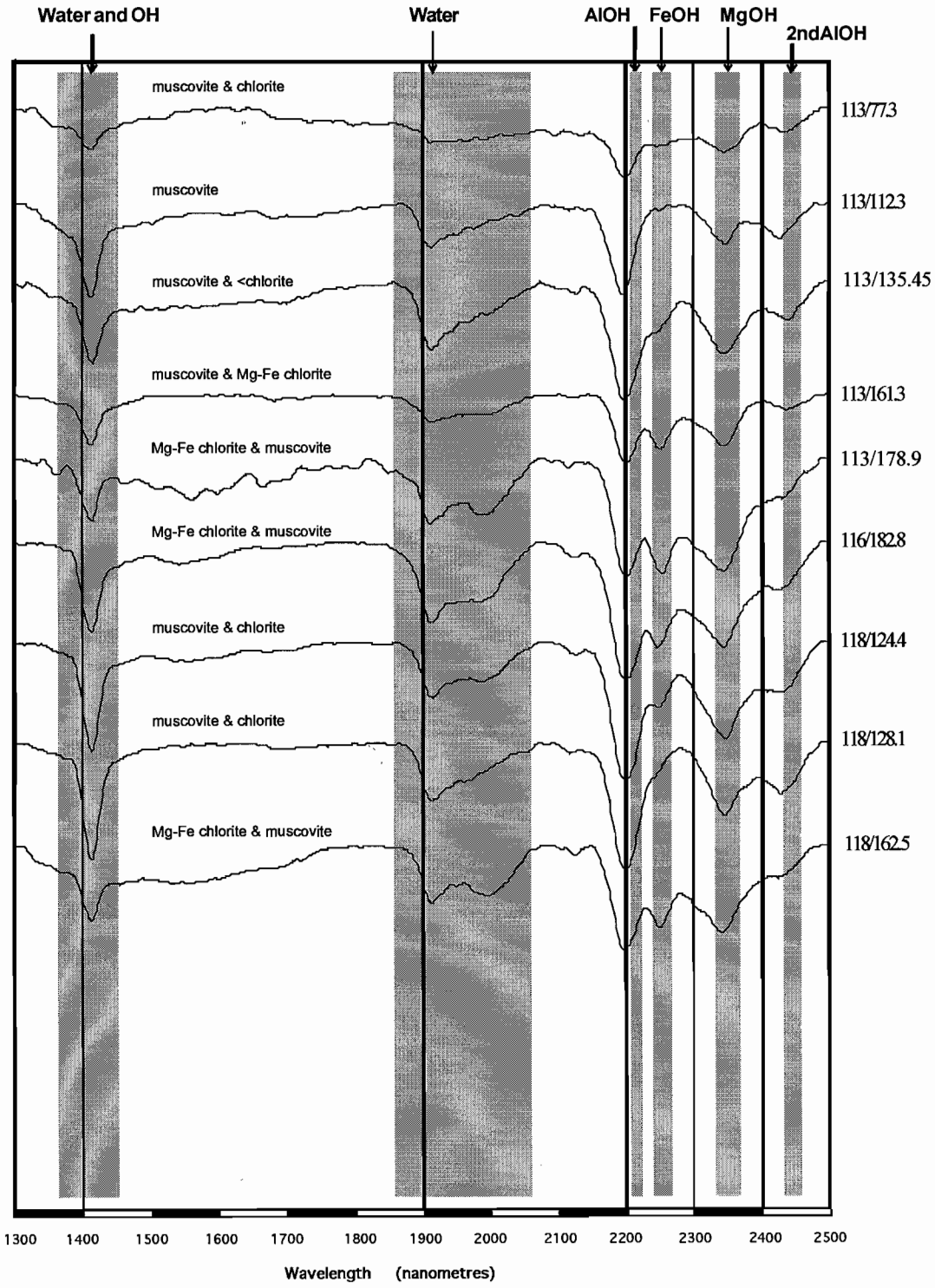

Appendix 1.2

Highway-Reward, MWV
REM132, 140, 144: Rhyolite & dacite
Hull quotient reflectance Spectra

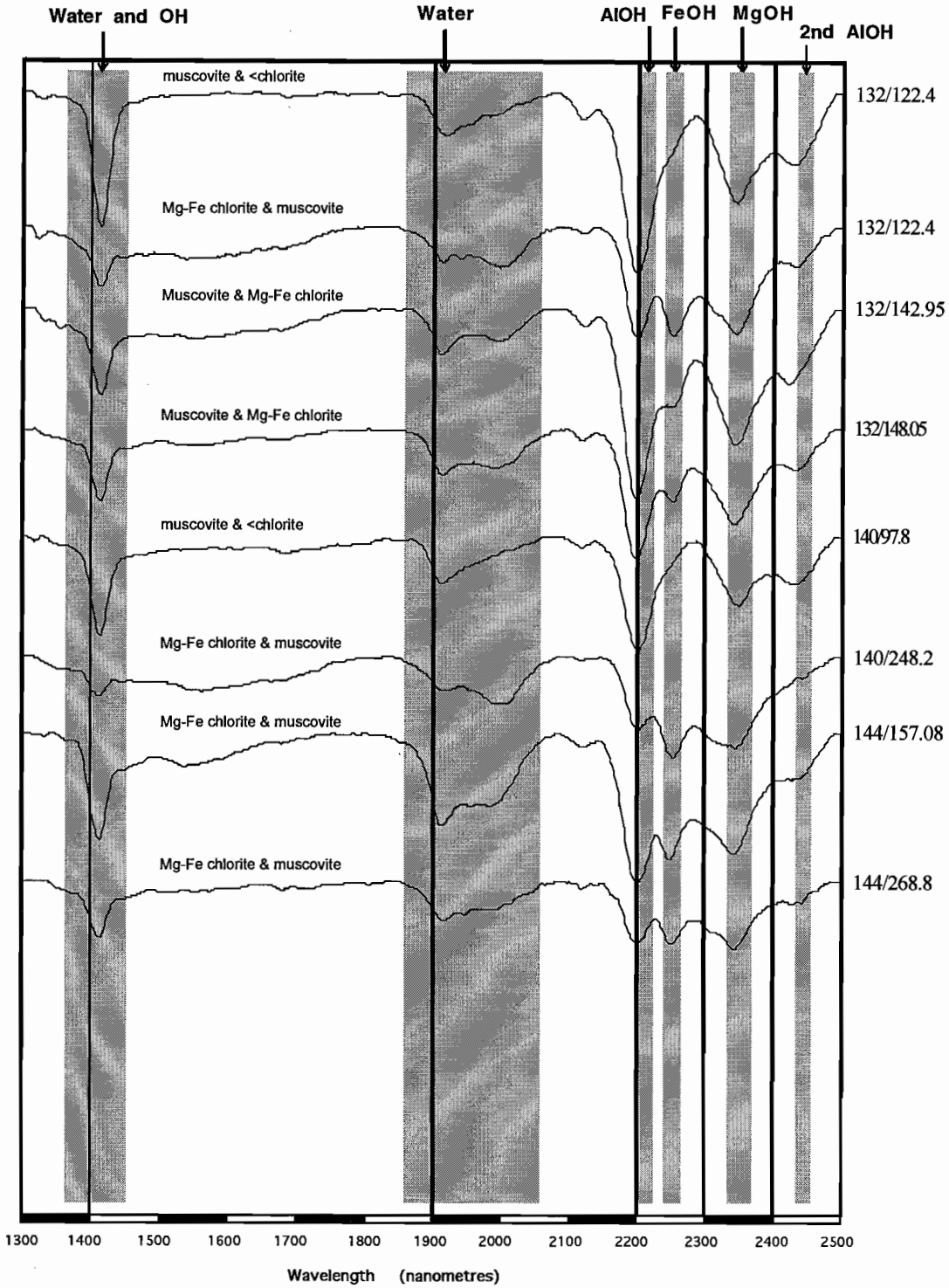

Appendix 1.3

Highway-Reward, MWV
REM151, 154: Rhyolite & dacite
Hull quotient reflectance spectra

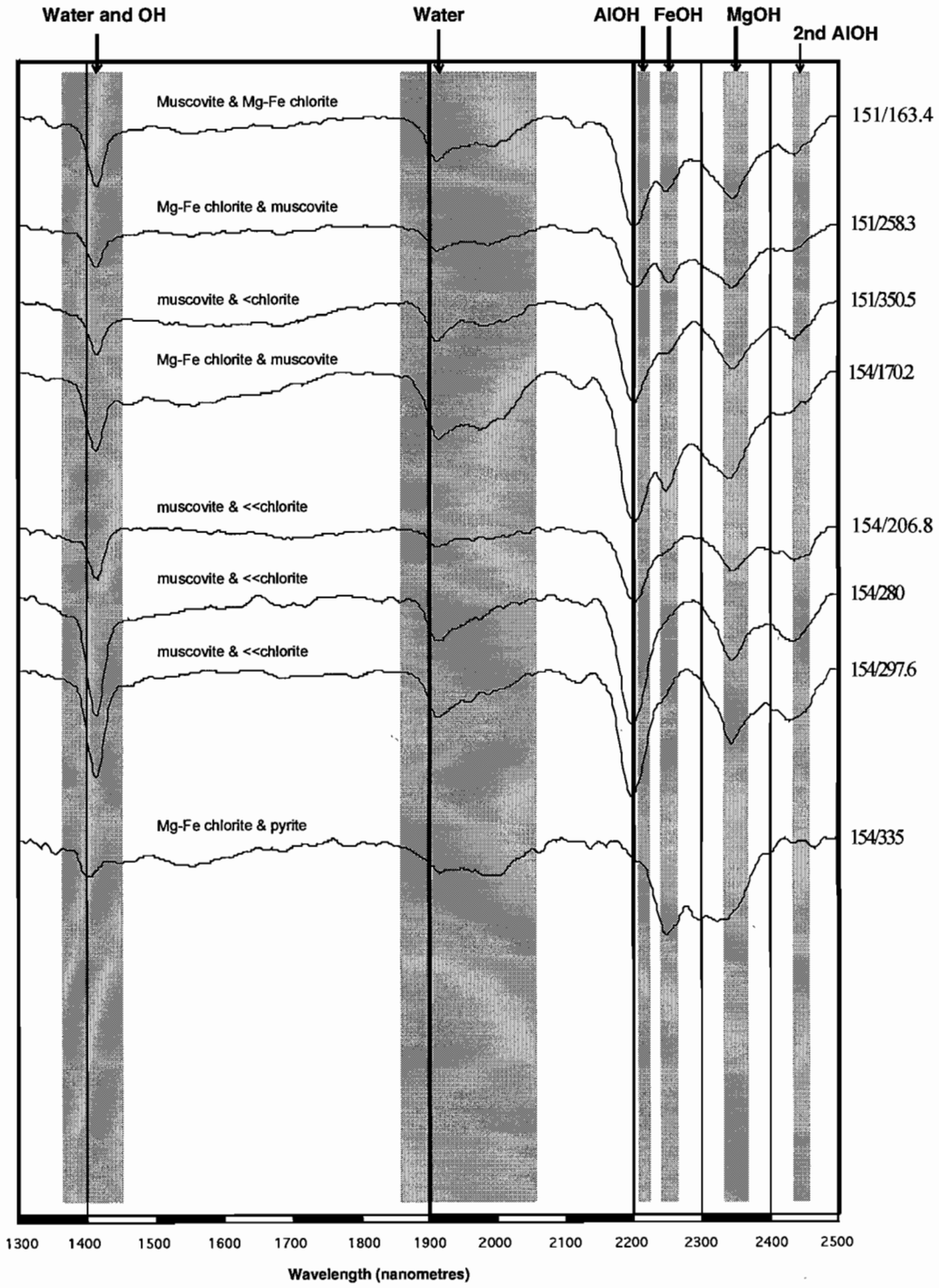

Appendix 1.4

Highway-Reward, MWV
REM155, 506, 515: Rhyolite & rhyodacite

Hull quotient reflectance spectra

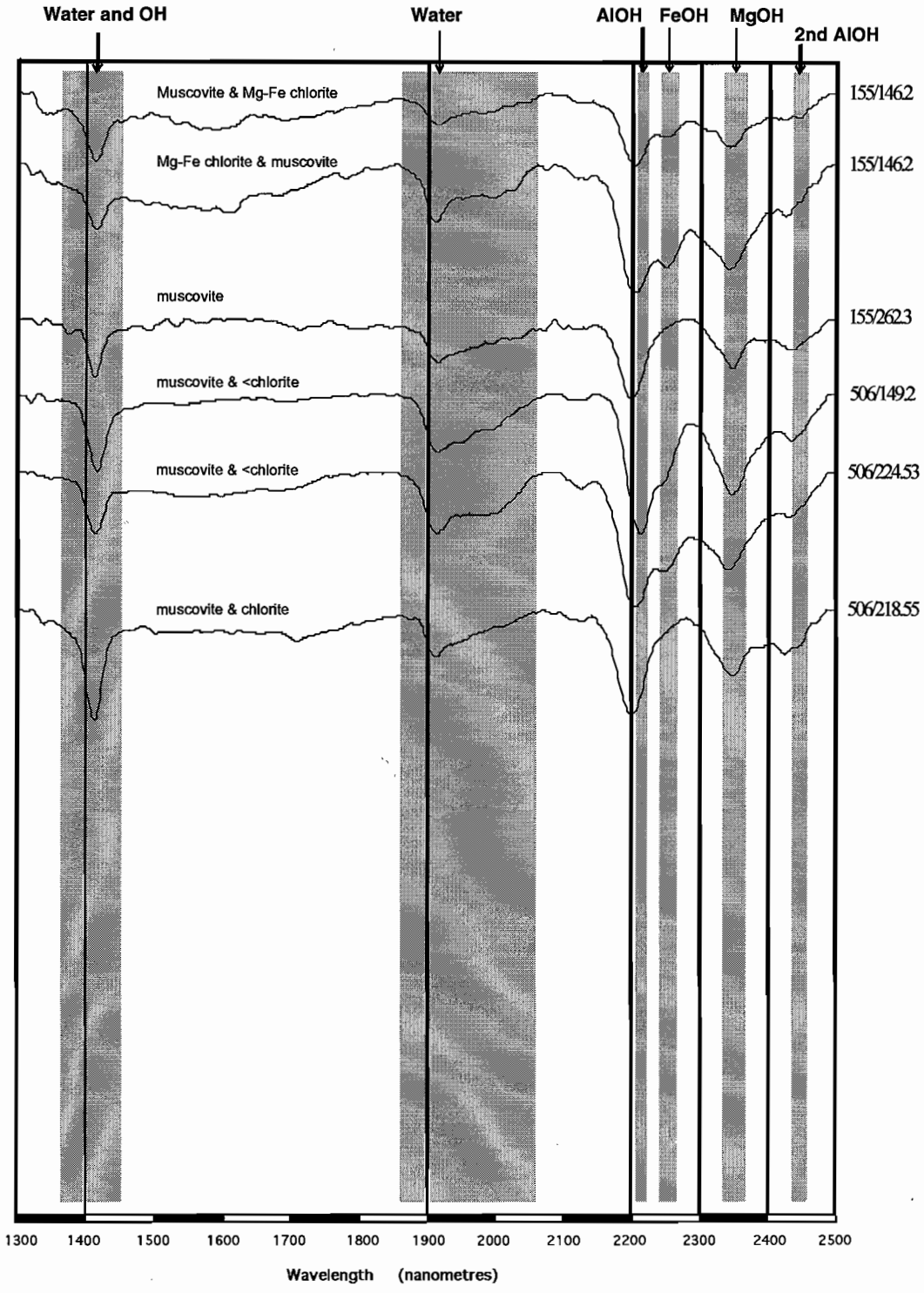

Appendix 1.5

Highway-Reward, MWV
REM551, 558, 560: Rhyolite & dacite

Hull quotient reflectance spectra

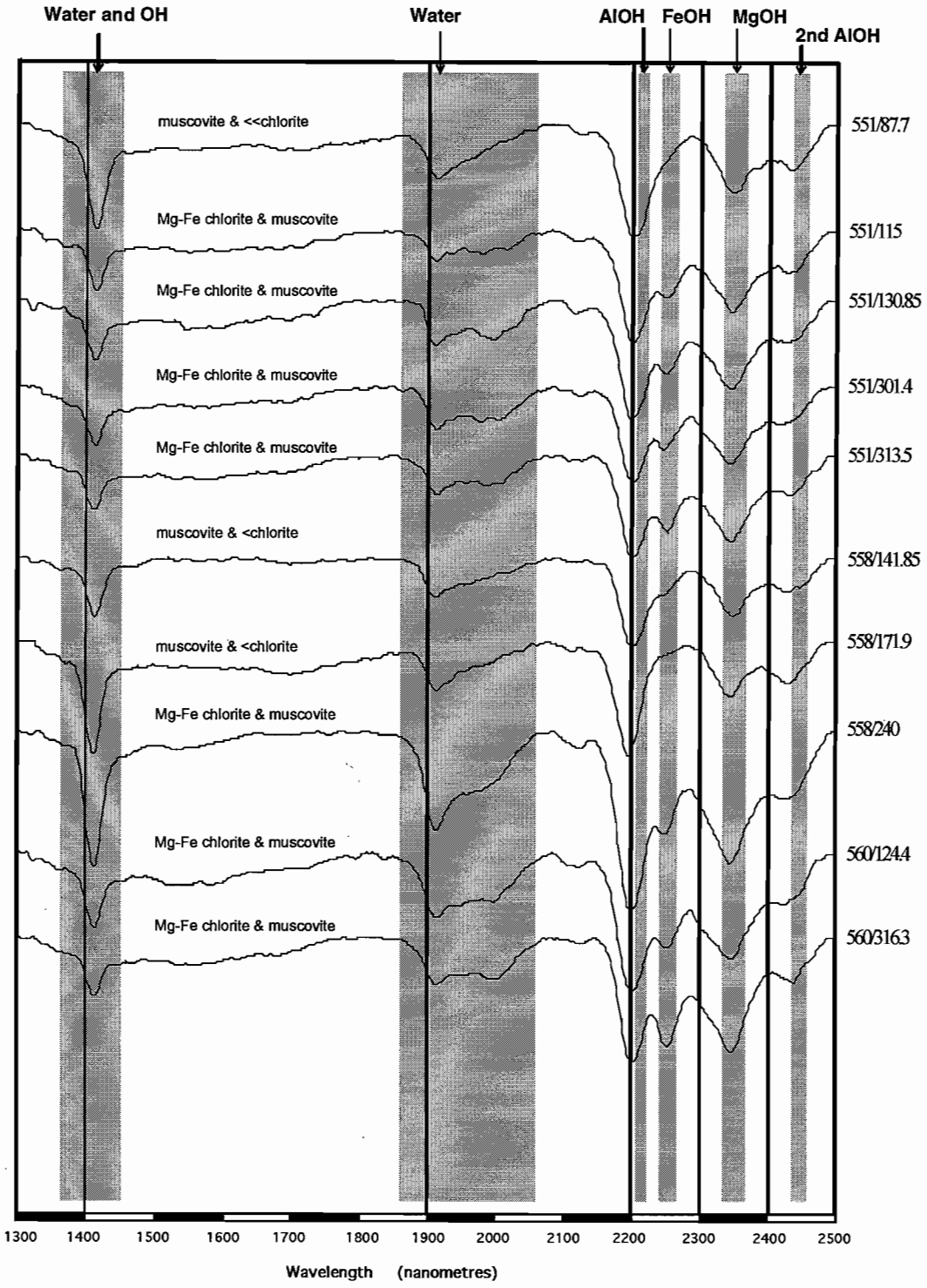

Appendix 1.6

Highway-Reward, MWV
REM600: Rhyolite

Hull quotient reflectance spectra

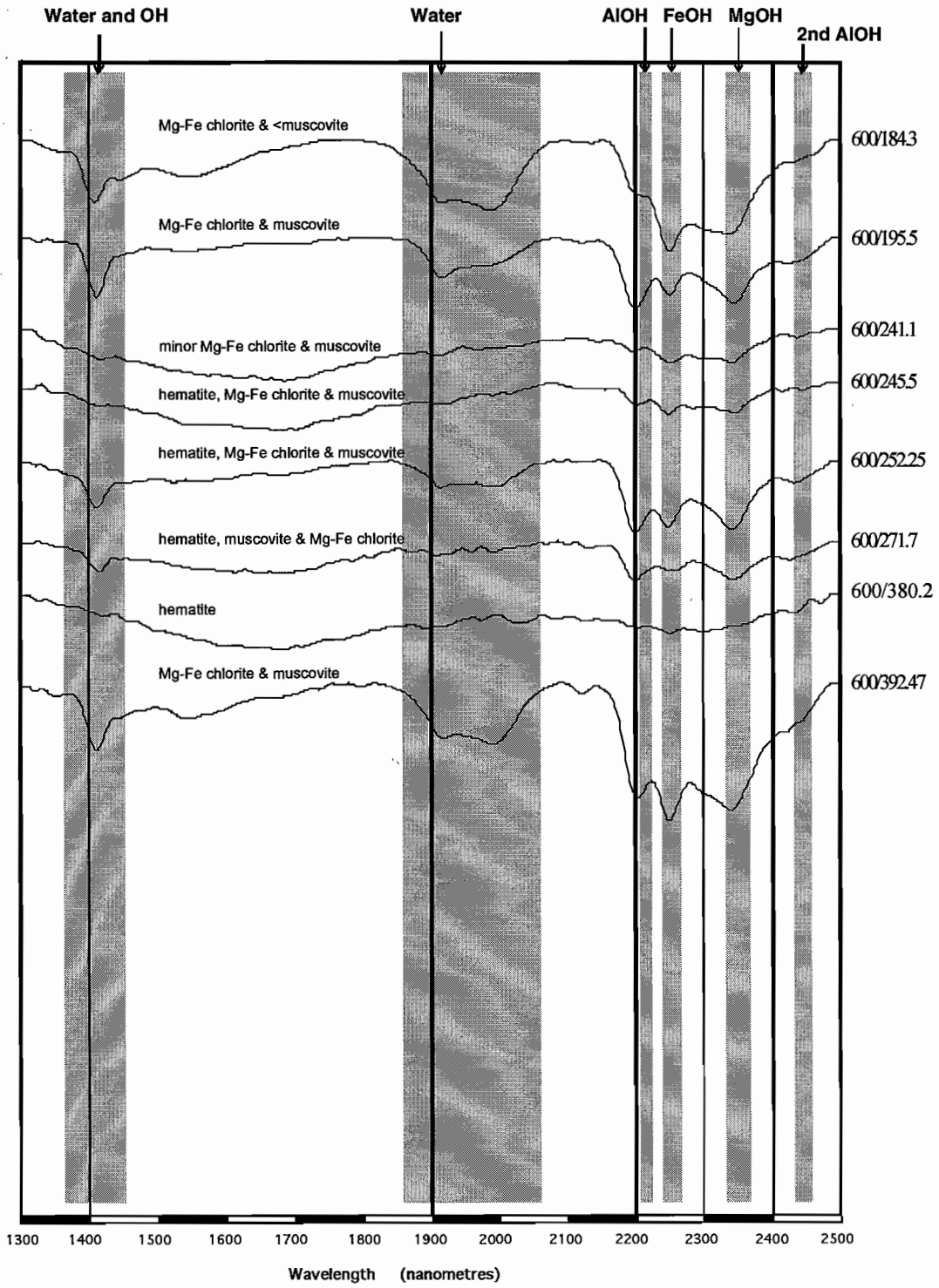

Appendix 1.7

Highway-Reward, MWV
REW800: Rhyolite, dacite, andesite and pumice breccia

Hull quotient reflectance spectra

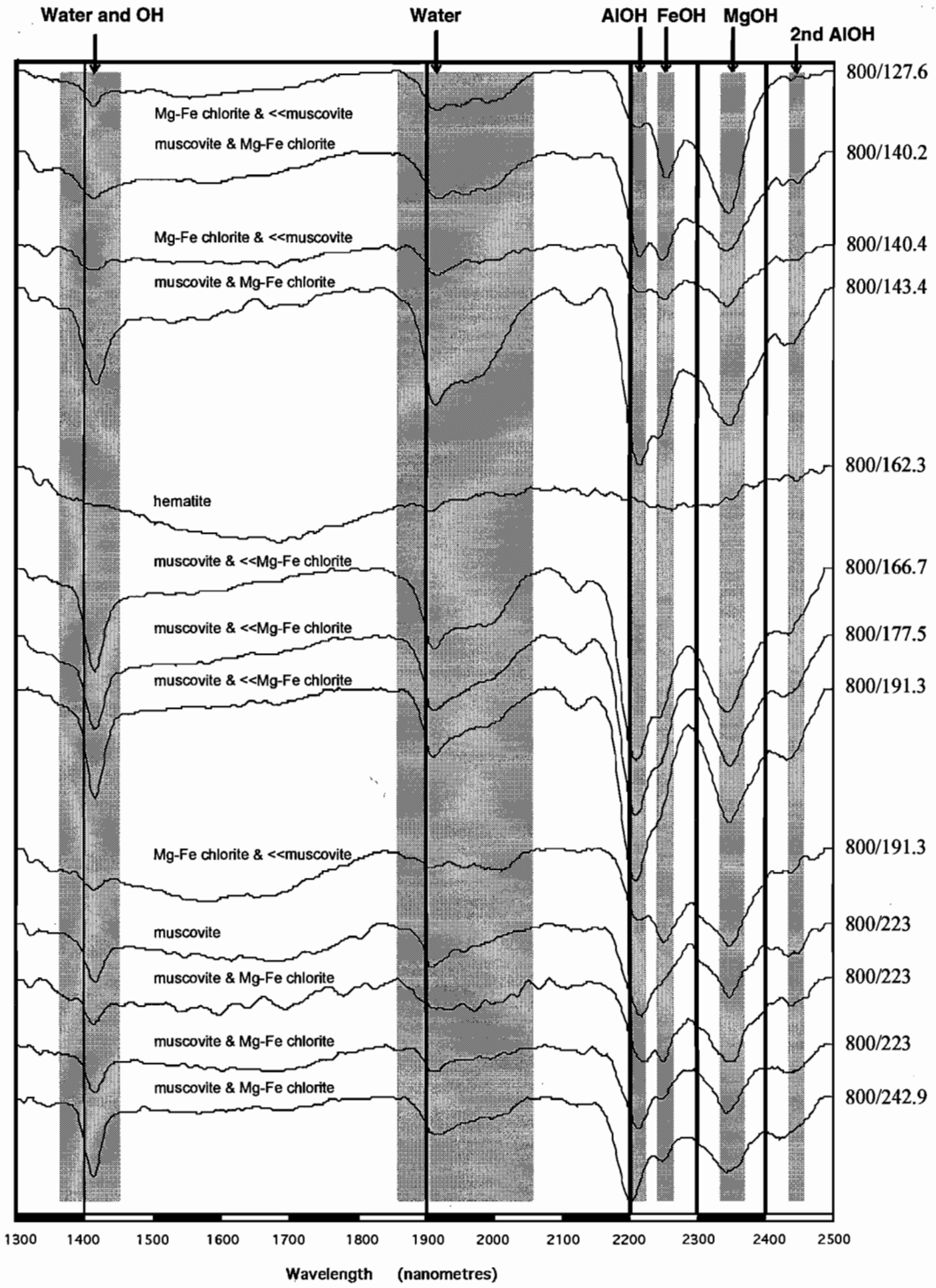

Appendix 1.8

Highway-Reward, MWV
REW801, 803, 804: Rhyolite & dacite

Hull quotient reflectance spectra

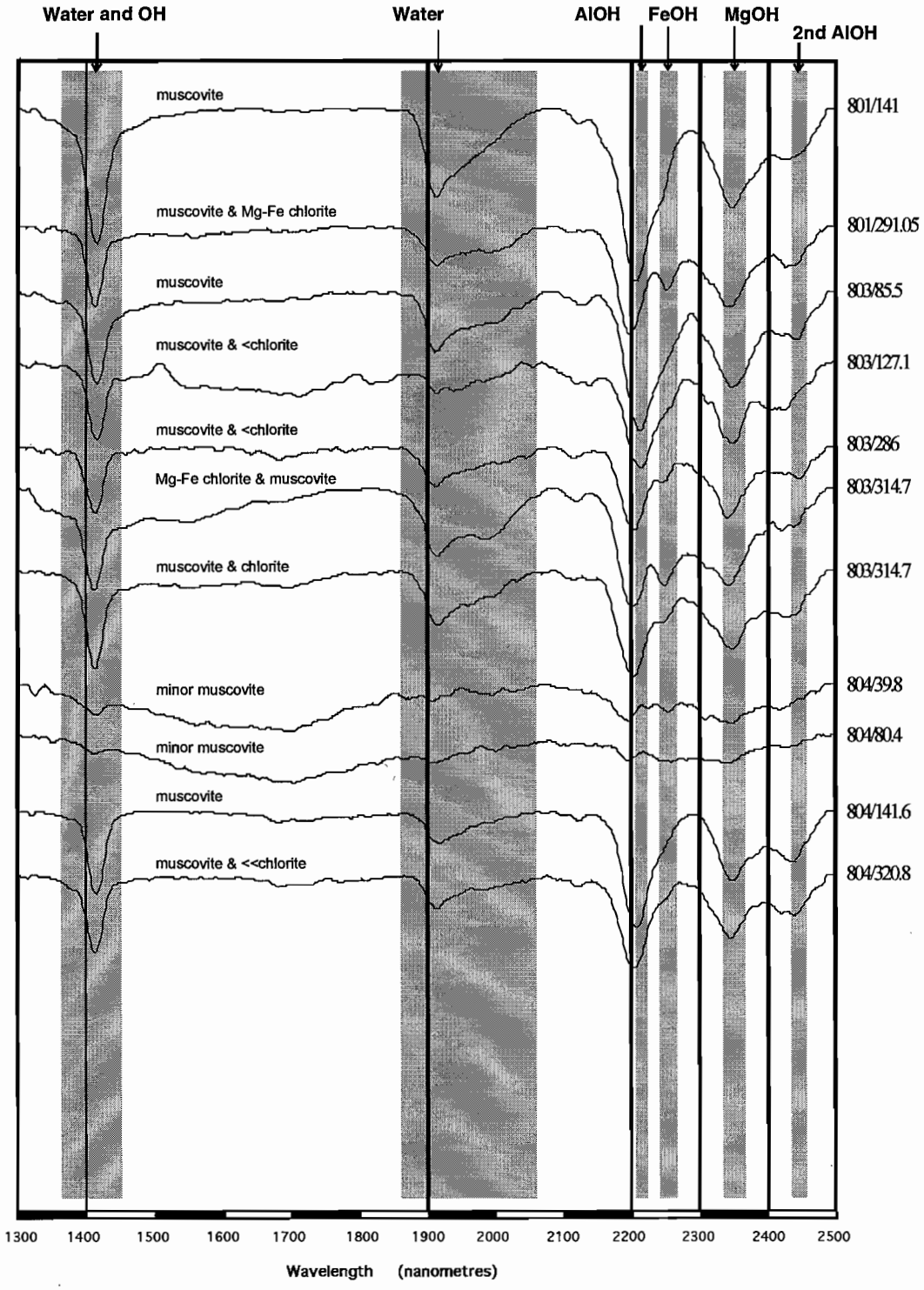

Appendix 1.9

Highway-Reward, MWV

REW805, 807: Rhyolite-rhyodacite, pumice breccia

Hull quotient reflectance spectra

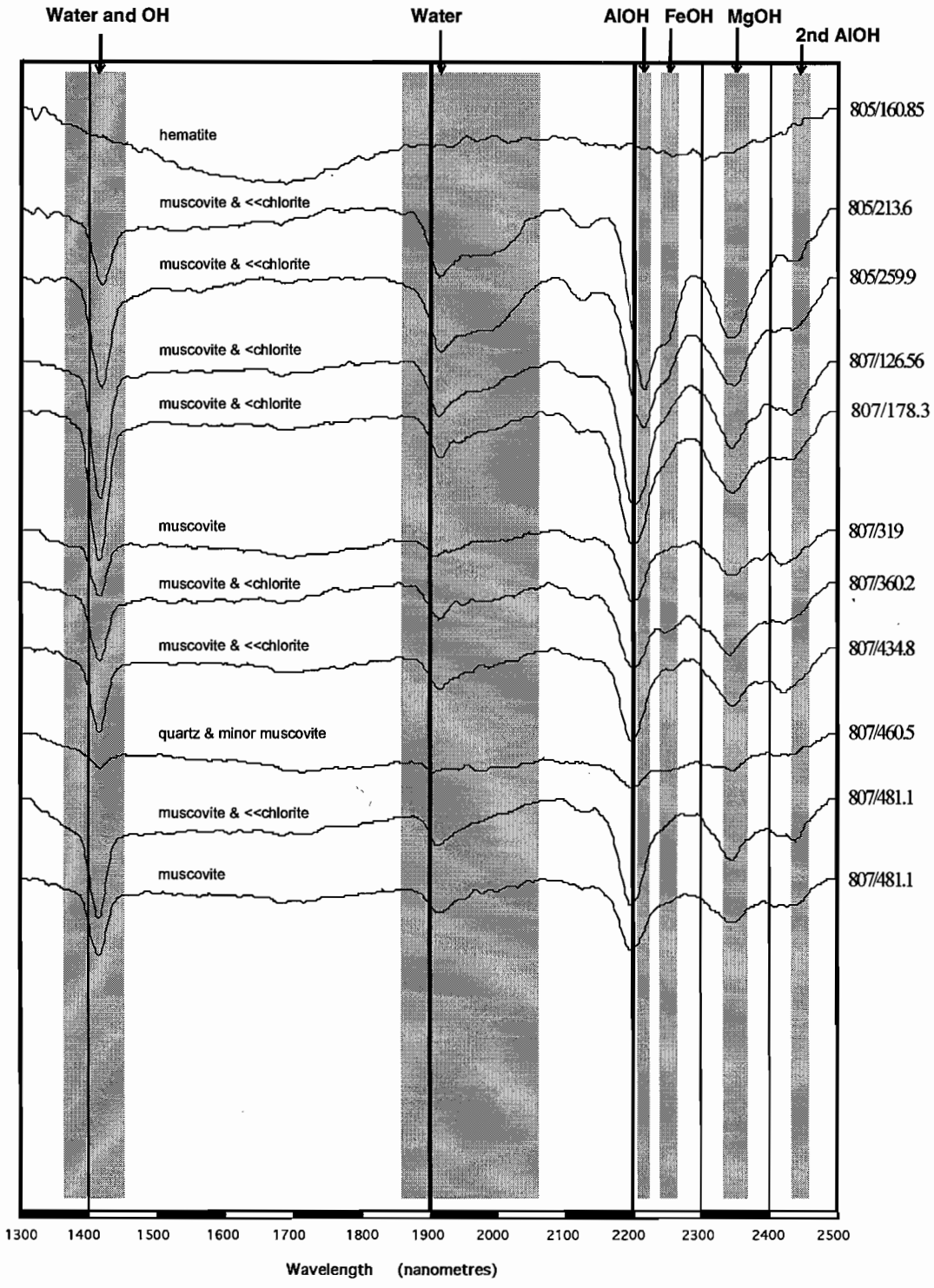

Appendix 1.10

Highway-Reward, MWV
REW808, 809: Rhyolite & rhyodacite

Hull quotient reflectance spectra

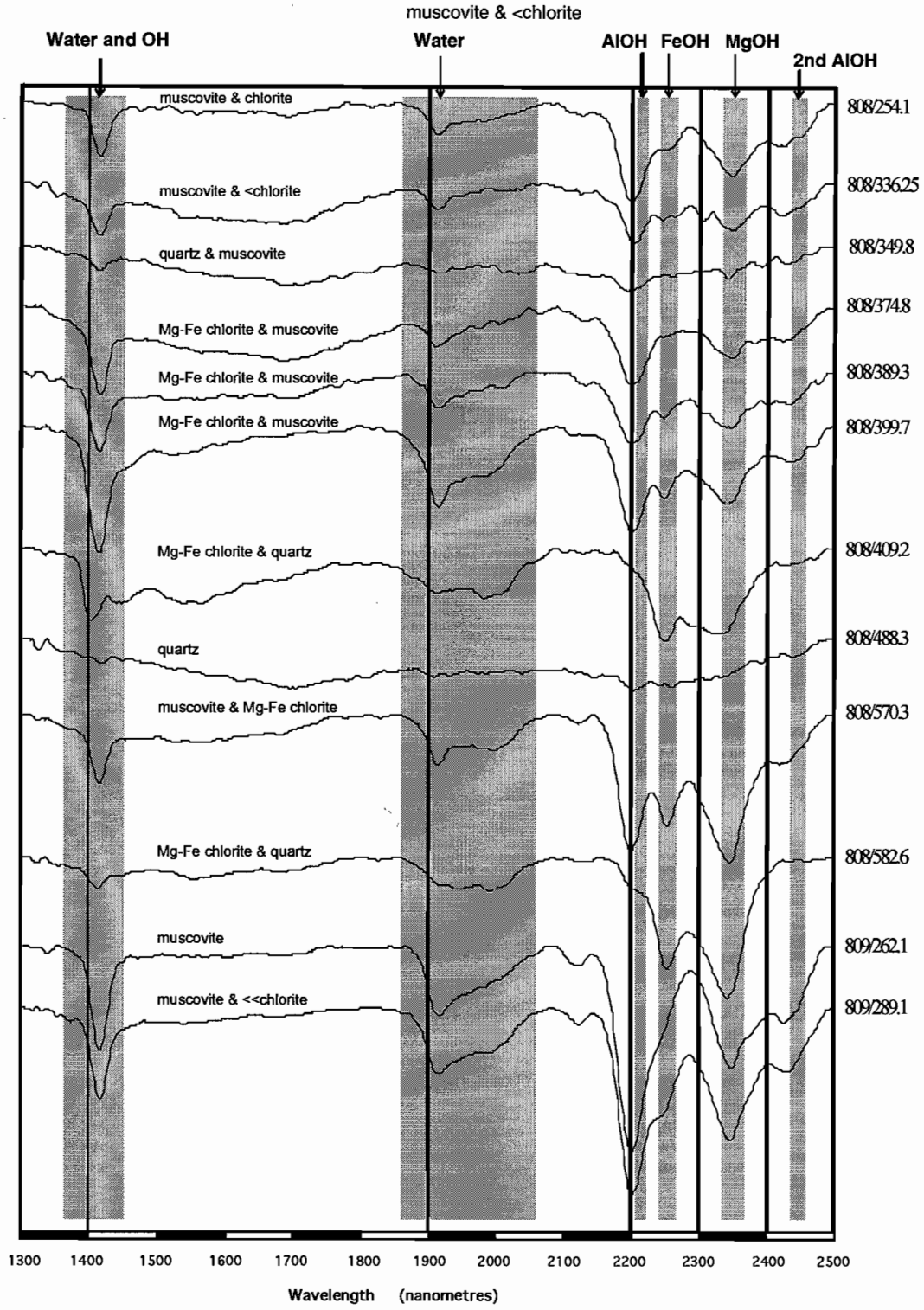

Appendix 1.11

Highway-Reward, MWV

REW814: Rhyolite, rhyodacite, andesite and pumice breccia

Hull quotient reflectance spectra

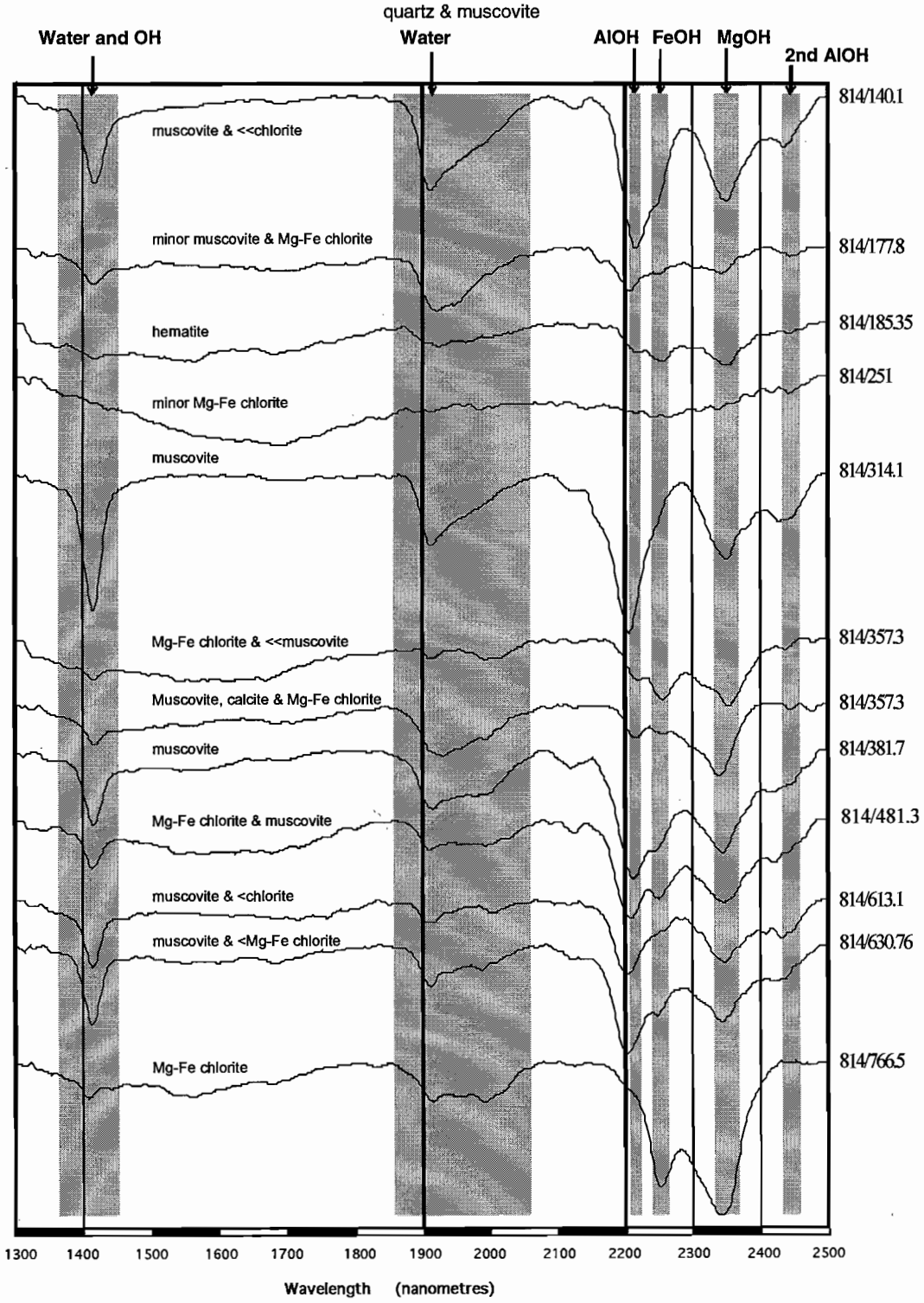

Appendix 1.12

Appendix II
MINSQ: an EXCEL version of the least squares method of calculating mineral proportions from wholerock major element analyses

Walter Herrmann, with guidance from Ron Berry

Introduction

This note provides an explanatory background to a PC spreadsheet method for calculating the amounts of minerals, of specified compositions, in observed or theoretical assemblages, from wholerock major element analyses. Considerable effort is expended in geological research and exploration, in "turning rocks into numbers' by geochemical analysis. This is a method for those who have completely lost touch with the real rocks, to turn their geochemical numbers into mineralogical numbers — almost (but not quite) turning the numbers back into rocks. Sadly, I have to admit that the real motivation behind its development was not turning numbers back into rocks, but rather to test the accuracy of PIMA spectral estimates of phyllosilicate contents — with the objective of eliminating the need for costly geochemical numbers altogether!

A program of this type — called GENMIX — was published by R.W. Le Maitre in 1981, and introduced to me in early 1998, by Ron Berry in a tea room discussion about the capability of PIMA to estimate amounts, or relative proportions, of sericite and chlorite in altered volcanics. To put PIMA to the test, I needed reliable quantitative sericite and chlorite data to compare with the estimates calculated from various spectral parameters.

Wholerock analyses were available for several hundred Mt Read Volcanics samples, for which we also had PIMA spectra. I was considering an incremental approach to calculating phyllosilicates from rock analyses (similar to that used in petrological norms but with different minerals) in order to avoid making microscopic estimates or (desperation) point counting.

Ron suggested a least squares solution would be preferable to the artificial and inflexible incremental process, and fired up his copy of GENMIX for a demo. And it worked well for the relatively simple alteration and relict primary mineral assemblages in a batch of rocks from Hercules.

However, GENMIX runs on MS-DOS and requires the analytical data to be in a very specific format of rows, tabs and etc. which makes it fairly difficult to use, and understand what is going on. The response from Ron was: "These days, you'd probably do it with 'Solver' in Excel" and in a few key strokes, the prototype of what follows was invented.

Background notes on the method of least squares

The least squares method is a well known mathematical approach to determining the best estimate of the value of a parameter. It is used in estimating parameters from data populations (eg: Figure 2.28 from Swan & Sandilands, 1995, p93) and fitting regression curves to paired data.

In this adaptation of the least squares method, there are about a dozen or more variables representing major element components in a wholerock analysis. It is based on taking a number of guesses at the amounts of specified minerals thought to be in the rock, and deriving from them "synthetic" estimated compositions of the rock. The values of the components in the estimated composition are subtracted from those of the actual analysis to obtain residuals, which are then individually squared and the squares summed. The guess which results in the minimum sum of squared residuals, represents the

closest comparison between the measured and estimated rock compositions and provides a fair estimate of the mineralogical composition of the rock.

Solver in Excel

Excel is a widely used spreadsheet application for desktop computers. According to the Microsoft Excel (V 5) help directory, the Solver tool in Excel is a powerful optimisation and resource allocation tool which answers questions such as "what product price or promotion mix will maximise profit?"

It does this by:

- Minimising, maximising or setting to a certain value, the value in a specified target cell in a spreadsheet.
- Iteratively changing the values in upto 200 other specified cells.
- Subject to upto 500 specified numerical constraints.

Solver resides in the TOOLS menu of Excel, (at least in version 5.0). Apparently it is a selectable option when installing Excel, so if it doesn't appear in the menu it may need to be reinstalled.

In this geochemical application we ask Solver to minimise the sum of the squared residuals by changing the spreadsheet cells containing the estimated amounts of specified minerals in the rock. The residuals are derived by subtracting the calculated wt% concentration of each major component (effectively an artificial analysis of a rock that has the mineralogical composition guessed at in the changing cells) from the actual analysed wt% concentration of that component.

In this procedure, Solver is constrained to keep the values of the changing cells (the estimates of amounts of specified minerals) between 0 and 100 (%) to avoid it offering solutions involving negative amounts of minerals.

This is, hopefully, better understood by referring to the type example, nicknamed MINSQ, in Worksheet 1.

MINSQ

In the accompanying example (Worksheet 1) the Rows 4 to 17 are occupied by compositions of the minerals which may exist in the rocks to be recalculated The components of the analysis are listed left to right in Columns B to Q (or more if required) in the usual order starting with SiO_2 but the order is not critical, provided it is consistent for both rock and mineral analyses.

The mineral compositions can be theoretical: calculated from ideal stoichiometric mineral formulas, or real: derived from microprobe analyses etc. of minerals existing in the rocks being treated or similar rocks. Concentrations of trace elements are converted to wt%.

The list of minerals can include as many as required but the calculation of the amounts of each mineral phase in the rock is limited to at least one less than the number of components in the analyses.

Since this is a least squares approach, the number of minerals must be less than the number of components analysed. Where the number of minerals is equal to the number of analysed components, there is only one exact solution. If the minerals are not independent "end members", the solution may fail, (eg: albite, anorthite, oligoclase: the method cannot distinguish albite + anorthite mixtures from oligoclase + anorthite mixtures).

The names of the minerals also appear in Row 25 as headers for the *changing cells* in Row 26 which Solver will iterate until it finds a good solution. The minerals lie along Row 25 in the same order as they appear down the column in cells B4 to B17, (to simplify entering the formulas in Row 21; see below). Again, this list of minerals can be as long as required. It could include more mineral phases than the number of analysed components but, to get a good result, a maximum of one less than the number of components must be selected for Solver to work on. The *changing cells* can be left blank at the start of a run of samples.

The actual analysis *(Sample Composition)* of the rock being recalculated is pasted into Row 20 *with the components in the same order as in the mineral analyses.* This line can be copied in from another worksheet or from a list of rock analyses as in Rows 41–50 in this example.

Row 21 contains formulas which calculate the concentration of each component *(Estimated Composition)* in the hypothetical rock made up of the amounts of specified minerals which Solver thinks best approximates the actual rock.

These formulas have the form:

Formula in cell B21 is:
=B4*$B$26/100+B5*$C$26/100+B6*$D$26/100+B7*$E$26/100+B8*$F$26/100+B9*$G$26/100+B10*$H$26/100+B11*$I$26/100+B12*$J$26/100+B13*$K$26/100+B14*$L$26/100+B15*$M$26/100+B16*$N$26/100+B17*$O$26/100

Formula in cell C21 is:
=C4*$B$26/100+C5*$C$26/100+C6*$D$26/100+C7*$E$26/100+C8*$F$26/100+C9*$G$26/100+C10*$H$26/100+C11*$I$26/100+C12*$J$26/100+C13*$K$26/100+C14*$L$26/100+C15*$M$26/100+C16*$N$26/100+C17*$O$26/100
and so on, across to cell Q21.

In other words: the estimated concentration of SiO_2 in the hypothetical rock (Cell B21) is calculated as the *sum* of the concentration of SiO_2 of the mineral in Row 4 (Qtz) multiplied by its proportional amount in the hypothetical rock (Cell $B$26 — the first of the changing cells) plus the concentration of SiO_2 of the mineral in Row 5 (Kspar) multiplied by its proportional amount in the hypothetical rock (Cell $C$26 — the second changing cell) ..... and so on.

(NB: the $s in the addresses of the changing cells; these enable the formula to be written once in Cell B21 and "filled right" through the other components.

The *Residuals* in Row 22 are simply calculated by formulas which subtract the component concentrations of the *Estimated Composition* from the actual *Sample Composition*.

(eg: cell B22: =B20–B21, cell C22: =C20–C21, etc.)

The sum of the residuals squared *(Residual SSQ)* is calculated by the formula in Cell Q26 which is the *target cell* to be *minimised* by Solver.

It has the formula:
=B22^2+C22^2+D22^2+E22^2+F22^2+G22^2+H22^2+I22^2+J22^2+K22^2+L22^2+M22^2+N22^2+O22^2+P22^2+Q22^2

Cell P26 contains a formula to sum all the values in the changing cells; ie: P26: =sum(B26:O26).

Cell A26 holds a formula repeating the value in cell A20 (the sample identifier pasted in with the sample composition) to expedite copying of the solution; ie: cell A26: =A20.

Once the lines of mineral analyses, sample wholerock analysis and formulas are in place, it is simply a matter of calling Solver into action (from the TOOLS menu), and in its dialogue window:

- selecting the target cell and opting for it to be minimised,
- selecting the cells to be changed
- writing the constraints that all the changing cells should be positive values between zero and 100 %; (ie: $B$26>=0, $B$26<=100, $C$26>=0, $C$26<=100, etc.).

It has also been found that Solver produces smaller values for *Residual SSQ* if the Total (cell P26) is constrained to equal 100 (%). This is probably analogous to the "constrained simple mixing model" of Le Maitre, (1979).

There are several other adjustable Options in the Solver dialogue window; it seems to work well enough with maximum time: 100 seconds, maximum iterations: 100, precision: 0.000001 and tolerance: 0.001%. Selecting "automatic scaling" will ensure that all components of the analysis will be treated fairly and not dominated by those of highest concentration, eg: SiO_2.

Click the SOLVE button and Solver sets to work; the number of iterations and value of the target cell are displayed in the bottom left corner of the worksheet window as it proceeds.

When an acceptable solution has been found, it is simply a matter of copying the mineral estimates in Row 26 and using "Paste Special - Values" to paste it into another part of the worksheet (eg: Rows 30 to 38 in this example) or another worksheet.

Since the analyses are expressed in wt%, the mineral estimates are also in wt%; corrections for relative density and normalisation to 100% can be applied if modal percentages are required.

Values for *Residual SSQ* of <1 are usually attained in under 50 trial solutions (taking a few seconds) and values of <0.5 seem to be pretty good. If the *Residual SSQ* is rather higher, then the offending components can be identified by inspecting the residuals in Row 22. This may give clues as to the appropriateness of the assemblage being calculated. For instance, if the residual for CO_2 is high and no carbonates had been selected in the *changing cells* then a re run of Solver with one or more carbonates selected should give an improved result. In the examples shown in this worksheet, the greater part of the *Residual SSQs* is attributable to TiO_2 (because apart from small

amounts in the micas) no TiO_2 phase has been included in the possible minerals.

It has been found that in cases where some residuals are high (say BaO) and appropriate minerals (eg: Barite) report at zero, then "priming" of the relevant *changing cell* with a small arbitrary value (say 0.1) will sometimes stimulate Solver to come up with a better solution, with lower *Residual SSQ*. This may have something to do with precision and sensitivity settings.

The method has been shown to be internally consistent. If a mineral analysis (say K-feldspar) is pasted into *Sample Composition* (Row 20), Solver will provide a solution with 100% of that mineral (K-feldspar), zero other minerals and zero *Residual SSQ* . Similarly, an arithmetic mean of two *mineral* analyses will return a solution with 50% of each.

We are confident that if the selected mineral assemblage and mineral compositions are appropriate to the rock, then the method will provide reliable estimates of the mineral proportions, to within ~1%.

In cases where the whole rock analysis is incomplete (say CO_2 is missing) it would be preferable to ***not*** select the *changing cells* of any phases involving the missing components (in this example: carbonates) and accept that the resultant MINSQ solution expresses the mineralogical proportions effectively normalised (to 100%) free of the excluded phases. It would also require acceptance of higher residuals for the other components in the affected phases and higher *Residual SSQ*, (eg: if CO_2 is missing and carbonates are excluded and there is actually significant calcite in the rock, the excess CaO may have no other phases to go to and will produce a large magnitude residual). If the selection of *changing cells* varies from sample to sample through a batch, take care to put zeros in the *changing cells* of the minerals which are to be eliminated from the calculation. Otherwise the value of that cell from the previous run will remain *unchanged*, and spoil the solution.

In cases where the composition of certain phases may vary (eg: muscovite in the Rosebery host sequence) the layout of MINSQ enables real mineral analyses to be pasted in as required, instead of being restricted to some ideal or average composition.

This possibility can be extended, in cases where the actual mineral compositions are not known, by putting in two extreme end member compositions. This is the rationale behind the Fe chlorite and Mg chlorite in the MINSQ example. These are respectively iron and magnesium rich chlorite compositions (from Green et al., 1981, Table 4, sample Nos:105174/1 & 105180/1a) with Mg numbers of 13.2 and 72.6. In the example, MINSQ calculated a percent proportion of both of these chlorites. An estimate of the composition and Mg number etc. of the chlorite actually in the rock can be obtained by calculating the average composition, weighted by the amounts of the two end members from the MINSQ estimate.

This was done for chlorite Mg numbers in Rosebery drill holes 109R and 120R and the several MRV traverse rocks for which chlorite microprobe analyses were available (Herrmann et al., 1998). The results are shown in Figure 1.

References

Green, G.R., Solomon, M. and Walshe, J.L., 1981. The formation of the volcanic hosted massive sulfide ore deposit at Rosebery, Tasmania. Economic Geology, V76, p.304–338.

Herrmann, W., Blake, M., Doyle, M., Huston, D. and Kamprad, J., 1998. Application of PIMA and FTIR to VHMS alteration studies. AMIRA/ARC Project P439, Final Report, May 1998, CODES, University of Tasmania (in prep.)

Le Maitre, R.W., 1979. A new generalised petrological mixing model. Contributions to mineralogy and petrology, V71, p133–137.

Le Maitre, R.W., 1981. GENMIX — A generalised petrological mixing model program. Computers and Geosciences, V7, p229–247.

Rollinson, H., 1993. Using geochemical data: evaluation, presentation, interpretation. Longman, London.

Swan, A.R.H. and Sandilands, M., 1995. Introduction to geological data analysis. Blackwell Science.

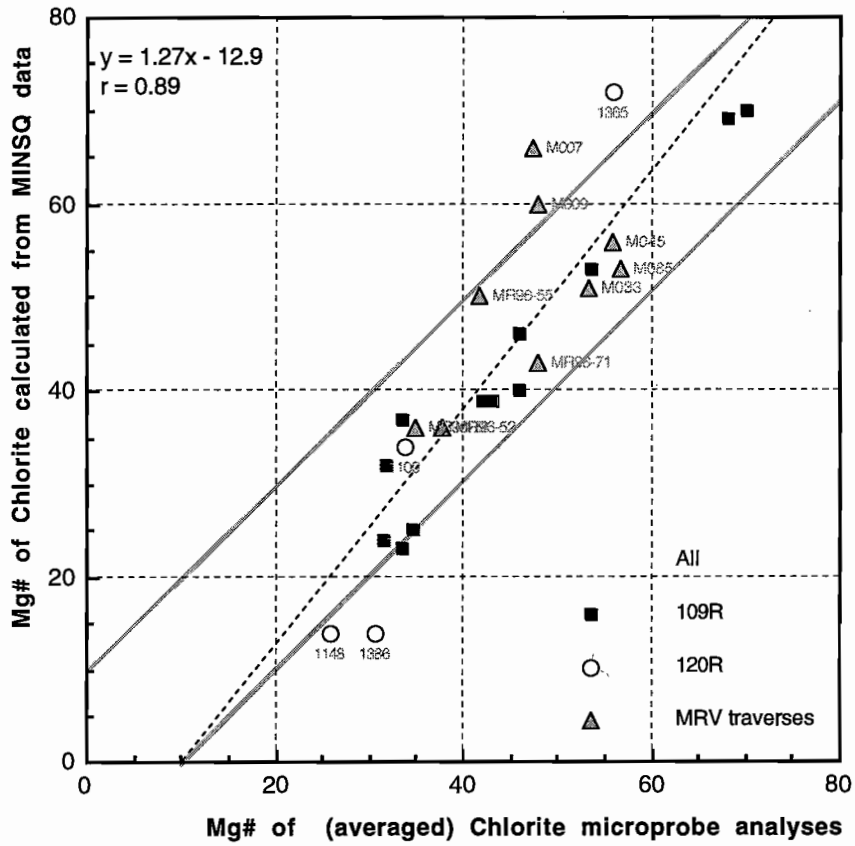

Figure 1. Comparison of chlorite Mg numbers calculated from MINSQ data and microprobe analyses for samples from Rosebery 109R, 120R and selected MRV traverse samples. Most of the MINSQ derived Mg#s lie within ±10 of the probe result, except at the high and low extremes. Most of the outliers (120R: 1147, 1386m & M007) are samples for which microprobe muscovite analyses were not available and hence the assumed muscovite composition may have been inappropriate. Sample 1365m in 120R is in the ore zone associated with carbonates of extremely variable Fe-Mn-Mg-Ca composition for which it is difficult to estimate a mean for MINSQ's input. It is also worth noting that the MINSQ estimate is based on the composition of the wholerock whereas the microprobe values are averages of a very few analyses (usually 2–5) from only a few mineral grains, which may not accurately represent the overall chlorite compositions in the rock.

MINERAL COMPOSITION

Minerals	SiO2 %	TiO2 %	Al2O3 %	Fe2O3 %	MnO %	MgO %	CaO %	Na2O %	K2O %	P2O5 %	CO2 %	S %	Ba %	Cu %	Pb %	Zn %
Qtz	100.0	0.0	0.0	0.0	0.0	0.0	0.0	0.0	0.0	0.0	0.0	0.0	0.0	0.0	0.00	0.00
Kspar	64.8	0.0	18.3	0.0	0.0	0.0	0.0	0.0	16.9	0.0	0.0	0.0	0.0	0.0	0.00	0.00
Ab	68.8	0.0	19.4	0.0	0.0	0.0	0.0	11.8	0.0	0.0	0.0	0.0	0.0	0.0	0.00	0.00
Muscovite	48.00	0.04	29.00	3.50	0.00	2.00	0.00	0.00	11.40	0.00	0.00	0.00	0.80	0.00	0.00	0.00
Fe Ch	22.9	0.1	19.4	46.9	1.2	3.7	0.1	0.0	0.0	0.0	0.0	0.0	0.0	0.0	0.00	0.00
Mg Chl	26.0	0.1	21.9	16.2	1.2	21.4	0.1	0.0	0.0	0.0	0.0	0.0	0.0	0.0	0.00	0.00
Calcite	0.0	0.0	0.0	0.0	0.0	0.0	56.0	0.0	0.0	0.0	43.0	0.0	0.0	0.0	0.00	0.00
Ankerite	0.0	0.0	0.0	19.9	0.0	10.1	28.0	0.0	0.0	0.0	43.0	0.0	0.0	0.0	0.00	0.00
Rhodochr	0.0	0.0	0.0	0.0	61.7	0.0	0.0	0.0	0.0	0.0	38.3	0.0	0.0	0.0	0.00	0.00
Barite	0.0	0.0	0.0	0.0	0.0	0.0	0.0	0.0	0.0	0.0	0.0	13.7	58.8	0.0	0.00	0.00
Pyrite	0.0	0.0	0.0	66.6	0.0	0.0	0.0	0.0	0.0	0.0	0.0	53.4	0.0	0.0	0.00	0.00
Cpy	0.0	0.0	0.0	43.6	0.0	0.0	0.0	0.0	0.0	0.0	0.0	35.0	0.0	34.5	0.00	0.00
Gn	0.0	0.0	0.0	0.0	0.0	0.0	0.0	0.0	0.0	0.0	0.0	13.4	0.0	0.0	86.60	0.00
Sp	0.0	0.0	0.0	0.0	0.0	0.0	0.0	0.0	0.0	0.0	0.0	33.0	0.0	0.0	0.00	67.00

Sample Composition

Sample No.	SiO2	TiO2	Al2O3	Fe2O3	MnO	MgO	CaO	Na2O	K2O	P2O5	CO2	S	Ba	Cu	Pb	Zn
1440.5	73.84	0.30	12.70	1.44	0.10	0.63	1.69	5.58	1.35	0.05	1.47	0.01	0.05	0.00	0.00	0.00
Estimated Comp:	73.90	0.01	12.78	1.50	0.05	0.71	1.83	5.61	1.39	0.00	1.43	0.00	0.06	0.00	0.00	0.00
Residuals:	-0.06	0.29	-0.08	-0.06	0.05	-0.08	-0.14	-0.03	-0.04	0.05	0.04	0.01	-0.00	0.00	0.00	0.00

Mineral Estimate wt%

Sample No.	Qtz	Kspar	Ab	Musc	Fe Chl	Mg Chl	Calcite	Ankerite	Rhodochr	Barite	Pyrite	Cpy	Gn	Sp	TOTAL	Residual SSQ
1440.5	34	4	48	7	2	2	3	0	0	0	0	0	0	0	99.00	0.13

SOLVER RESULTS (minerals in wt%)

Depth	Qtz	Kspar	Ab	Musc	Fe Chl	Mg Chl	Calcite	Ankerite	Rhodochr	Barite	Pyrite	Cpy	Gn	Sp	TOTAL	Residual SSQ
1356.9	3	0	0	30	0	1	19	14	16	0	13	0	2	2	99.00	0.21
1361.4	0	0	2	50	0	1	0	11	32	0	3	0	0	0	100.00	0.93
1364.4	0	0	0	33	1	3	0	9	48	0	6	0	0	0	100.00	0.60
1365.0	0	2	0	28	0	15	20	14	19	1	0	0	0	1	99.00	3.75
1373.0	22	0	2	31	22	4	0	0	2	0	7	0	0	10	100.00	0.28
1378.3	57	0	2	33	4	1	0	0	0	0	2	0	0	0	100.00	0.29
1386.5	61	0	0	26	8	0	0	4	1	0	1	0	0	0	99.00	4.30
1421.8	46	0	11	36	0	2	0	5	0	0	0	0	0	0	99.00	0.26
1440.5	34	4	48	7	2	2	3	0	0	0	0	0	0	0	99.00	0.13

WHOLEROCK ANALYSES

Depth	SiO2	TiO2	Al2O3	Fe2O3	MnO	MgO	CaO	Na2O	K2O	P2O5	CO2	S	Ba	Cu	Pb	Zn
1356.9	17.98	0.35	9.31	12.91	9.96	2.44	14.33	0.05	3.46	0.10	20.52	8.06	0.34	0.07	1.38	1.09
1361.4	25.60	0.59	15.57	5.70	20.02	2.48	3.22	0.05	5.31	0.08	17.59	1.85	0.53	0.00	0.02	0.03
1364.4	16.79	0.39	10.73	7.50	29.36	1.97	2.04	0.05	3.64	0.13	22.35	3.24	0.43	0.00	0.07	0.10
1365.0	18.44	0.38	11.86	5.14	11.84	5.91	14.98	0.05	4.04	0.14	23.08	1.29	0.42	0.00	0.01	0.07
1373.0	44.22	0.33	14.48	16.58	1.49	2.22	0.10	0.05	3.37	0.06	1.10	7.18	0.0:	0.17	0.06	6.82
1378.3	75.76	0.27	11.26	4.37	0.28	0.90	0.06	0.07	3.47	0.04	0.37	0.89	0.09	0.00	0.00	0.01
1386.5	75.46	0.22	9.79	6.50	0.38	1.29	0.11	0.09	2.58	0.04	3.30	1.09	0.06	0.03	0.00	0.04
1421.8	71.46	0.32	12.93	2.44	0.11	1.65	1.49	1.36	4.16	0.06	1.83	0.06	0.10	0.00	0.00	0.00
1440.5	73.84	0.30	12.70	1.44	0.10	0.63	1.69	5.58	1.35	0.05	1.47	0.01	0.05	0.00	0.00	0.00

P439 wholerock geochemistry and mineral chemistry database

Michael D. Blake
Centre for Ore Deposit Research

The analytical data colleced during P439 has been collated and is provided on a PC format CD-ROM with this concluding report. Data is provided as Excel '95 files, each workbook containing spreadsheets with geochemistry, probe data and isotope data where available. Studies of alteration systems have been placed in a heirachical file structure (visually represented in Fig1.), divided into two main categories — Mt Read Volcanics and Mt Windsor studies, with the Gossan Hill study independant.

The Mt Read Geochemical Database , MRCHEM is a separate, relational database modelled on the Mineral Resources Tasmania (MRT) 'Rockchem' database. It contains data collected from the Tasmanian case studies, regional traverses, geochemistry donated by Pasminco, and Data collated from University of Tasmania research Theses. Data provided by ISM at the beginning of the project is not included, but may be purchased from MRT with 25000 sheet GIS packages. MRCHEM is an ACCESS database, which has also been broken down and included as CSV files for easy importation into any relational database or GIS package. The structure of MRCHEM is documented in the file definitions.doc, included on the CD

Analytical suite

Standard major element analyses (SiO_2, TiO_2, Al_2O_3, Fe_2O_3, MnO, MgO, CaO, Na_2O, K_2O, P_2O_5, LOI, S) , and trace elements Ba, Ce, Cr, Cu, La, Nb, Nd, Ni, Pb, Rb, Sc, Sr, V, Y, Zn, Zr were obtained by XRF for all samples at the University of Tasmania Geology department facility under the direction of Mr Phil Robinson.

Trace element analyses for Ag, As, Bi, Mo, Cd, Sb, Cs Tl, Th and U were measured by ICPMS and total C by Leco at ANALABS facility in Perth .

Major element analyses are reported as wt % oxides with total Iron as Fe_2O_3. Trace elements are reported in ppm. Detection limits are reported in the file detections.doc on the CD.

A note on relational databases

The data generated by studies such as P439 is a valuable asset, and its integrity and documentation is an important issue. When dealing with a large dataset it becomes critical to have an efficient structure with which to store and retreive data, whilst protecting the data itself from corruption.

In a simple sense a relational database can be visualised as a collection of tables or spreadsheets which are interconnected by a unique identifier, such as sample fieldnumber. The reason for storing information in several tables is to reduce unnecessary data duplication and to organise and simplify complex collections of data.

Relational Database packages have features which can place security restrictions on access to data , allow multiuser access, show up to date information and enforce restrictions on the type of data which is stored to maintain consistency. Relational databases can allow compex searches and calculations , which may otherwise be too cumbersome to perform in a simple spreadsheet.

All data from the Mt Read study could be manipulated in an organised spreadsheet, however as the amount of information obtained in this database has increased, it has been safer and more convenient to store in an (relational) MS. ACCESS database.

Database structure

For convenience, all geochemical data has been includ ed on the provided CD ROM in a file structure shown in fig 1. This figure represents a set of computer folders and subfolders, with folders for an individual deposit study containing seperate Excel 4.0 spreadsheets of wholerock geochemistry, mineral chemistry and isotope data where available.

The Mt Read Geochemical Database MRCHEM has been broken down into its constituent tables, as CSV files, which importantly can be imported directly into any GIS package, database or spreadsheet.

The tables are :

MRCHEM.SAM
- contains lithological and other descriptive information
MRCHEM.MAJ
- contains major element geochemistry
MRCHEM.TRC
- contains trace element geochemistry

Definitions of fields contained in each table are documented in the file definitions.doc on the CD ROM

Using the database

Samples contained in the database have descriptive fields in which simple one to three letter codes are used for classifications. Using codes simplifies data searching and eliminates problems with mis - spelled words and variations of names.

For example, the Mount Read Volcanic Belt is defined in the database as region 'MR'

This code is unambiguous, whilst in a non coded example the Mt Read Volcanic Belt may be recorded as:

Mt Read Volcanics
Mount Read Volcanics
Mt Reed volcanics

A lithological classificaion system similar to the AGSO and MRT databases has been used to allow searching of lithological types which would be extremely difficult with simple text lithological descriptions.

For example, a rhyolitic pumice breccia has been coded in the following way :

CLASS = I Igneous
GROUP = L Volcaniclastic
COMPOSITION = A Acid
Lithology = BR Breccia

Searching the database for this combination will return all samples which have been classified as volcaniclastic breccias with an acid composition. Full descriptions of codes are listed in definitions.doc on the CD-ROM with MRCHEM.

Acknowledgements

Sincere thanks must go to Nilar Hlaing, Katie McGoldrick and Phil Robinson for their tireless work in preparation af all samples for geochemical analysis, and to Dr David Steele for his expert guidance with Probe analysis.

References

Blake, M.D., MRV geochemical database update, AMIRA project P439, Report 4, May 1997, 27-91

Date, C., An Introduction to Database Systems, 5th Ed., Addison Wesley, U.S.A., 1990

Date, C., Database : A Primer, Addison Wesley, U.S.A., 1983

Large, R.R., Stolz, J., and Duhig, N., Preliminary assessment of MRV geochemical database in terms of possible vectors to ore, AMIRA project P439, Report 2, May 1996, 197-209

Large, R.R., and Blake, M.D., Surface lithochemical responses of known VHMS deposits based on the MRV geochemical database, AMIRA project P439, Report 4, May 1997, 93-95

McClenaghan, M.P., Bottrill, R.S. and Bird, K.G., Structure of GIS Databases (Revision 1), Mineral Resources Tasmania - Tasmanian Geological Survey, Record 1996/06

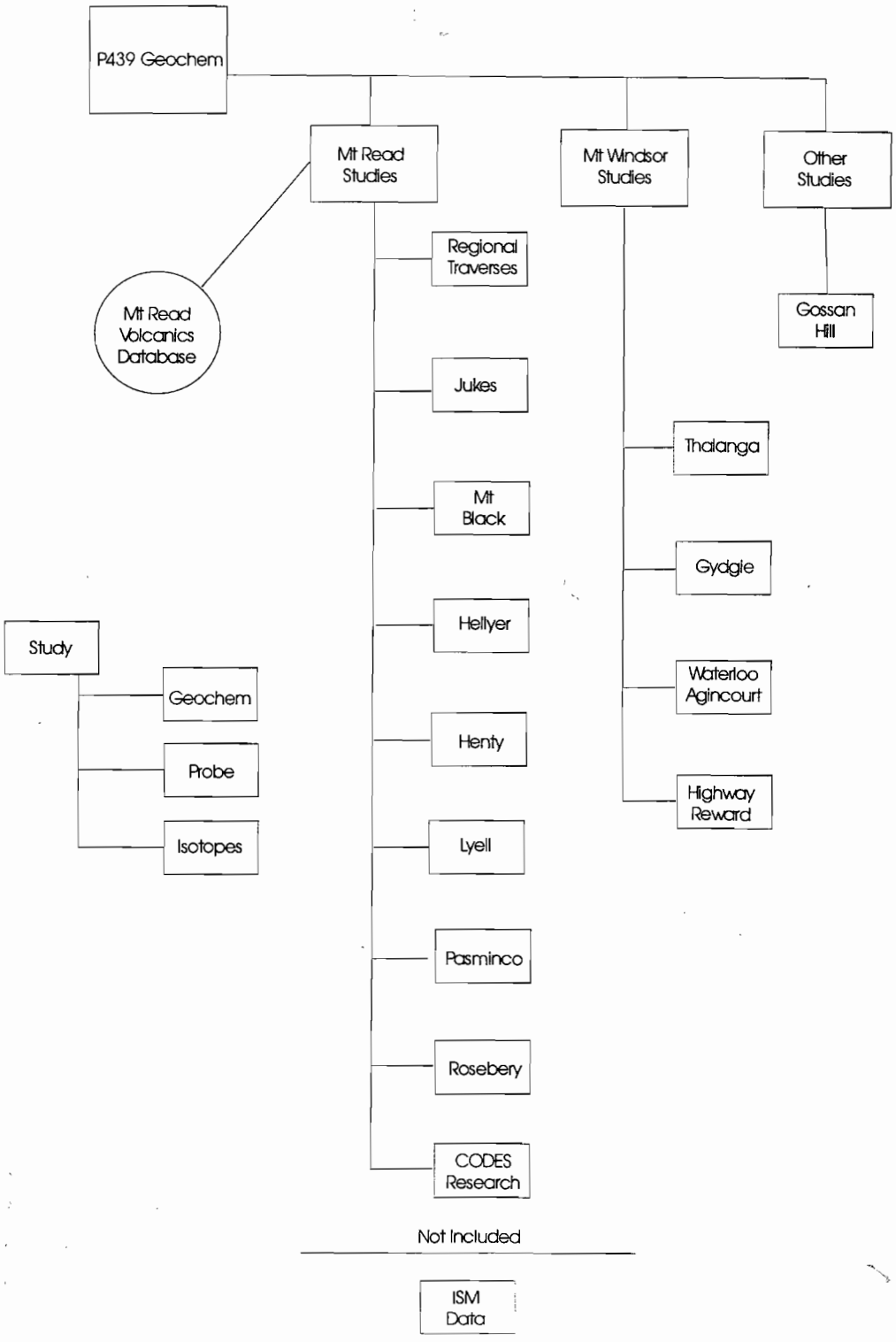

Figure 1. File structure of P439 geochemical dataset.

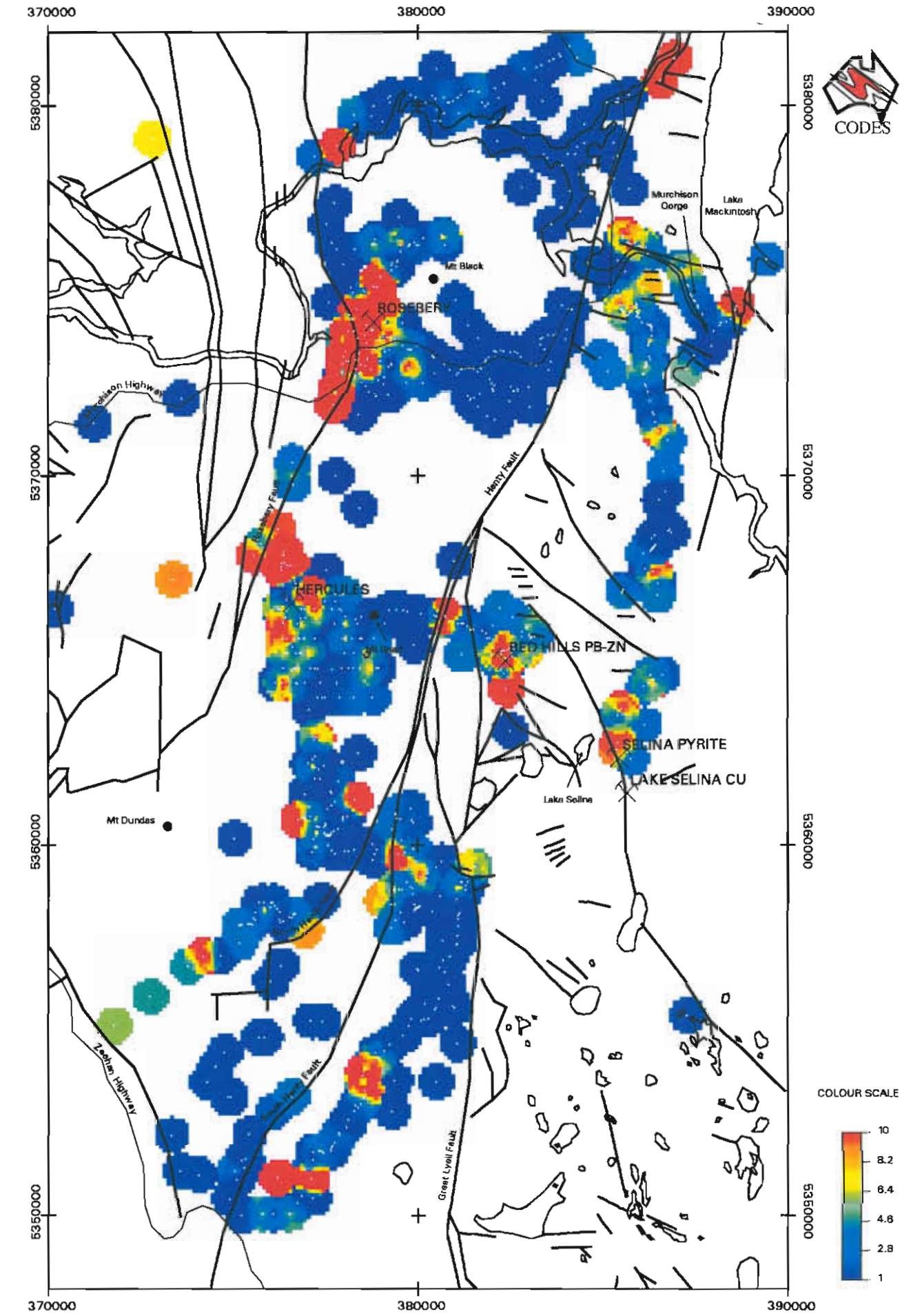
370000
380000
390000
5380000
5370000
5360000
5350000
CODES
Murchison Gorge
Lake Mackintosh
Mt Black
ROSEBERY
Henty Fault
HERCULES
RED HILLS PB-ZN
SELINA PYRITE
LAKE SELINA CU
Lake Selina
Mt Dundas
Zeehan Highway
Great Lyell Fault
COLOUR SCALE
10
8.2
6.4
4.6
2.8
1
0 1000 2000 3000 4000 5000
metres
WESTERN TASMANIA
Rb/Sr Ratios : Mt Read Volcanics
All Data

Discrimination of diagenetic, hydrothermal and metamorphic alteration

Rodney L. Allen, Cathryn C. Gifkins, Ross Large and Walter Herrmann
Centre for Ore Deposit Research

Introduction

Many mineralised terranes have evolved through a long and complex geological history that includes mineralisation, diagenesis, metamorphism and tectonic deformation. Each of these processes can result in alteration of the ore deposits and host rocks. Consequently, a fundamental requirement for the effective use of alteration studies in mineral exploration for hydrothermal ores, is that the alteration associated with the mineralising system can be distinguished from diagenetic, metamorphic and tectonic alterations. In this contribution we outline methods and criteria for discriminating between these alteration types.

Previous AMIRA reports

The petrography and geochemistry of hydrothermal, diagenetic and metamorphic alteration along regional traverses across the Mount Read Volcanics were described by Stolz et al. (1996). Using data from previous studies and new data from the AMIRA project, Allen (1997) described the evolution and zonation of diagenetic alteration in the Rosebery–Hercules area of the Mount Read Volcanics, and the relationship between this diagenetic alteration and hydrothermal alteration at the ore deposits.

PART 1: Rock textures, petrography and mineralogy

C. Gifkins and R. Allen

Diagenesis, hydrothermal alteration and metamorphism in VHMS settings

Volcanic-hosted massive sulphide deposits (VHMS) are generally interpreted to have formed at the discharge site of a high temperature (300°C) submarine hydrothermal system. The discharge of such a hydrothermal system produces a local set of alteration shells or zones that reflect alteration at successively lower temperatures outward from the ore deposit. Water to rock ratios that facilitate the hydrothermal alteration and mineralisation are typically relatively high. In contrast, diagenetic alteration is related to the regional geothermal gradient in the depositional basin. Temperatures range from near 0°C at the seafloor to 250°C at 2–10 km depth, the precise depths of particular isotherms depending on the geothermal gradient. The resulting diagenetic alteration pattern is generally a sequence of flat–lying zones (layers), each characterised by a particular mineral assemblage that formed within a particular temperature range. Although diagenetic alteration occurs on the basin scale and may involve much larger absolute volumes of water than the more localised hydrothermal alteration systems, the water to rock ratios are normally lower. It is generally inferred that the high temperature hydrothermal ore-related alteration either grades outward into synchronous, low temperature, diagenetic alteration, or is subsequently

enveloped by diagenetic alteration after the ore deposit and host rocks are buried deeper beneath younger strata in the depositional basin.

With increases in temperature and pressure, as consequences of deeper burial, diagenetic alteration grades into sub-greenschist and greenschist facies metamorphism. The boundary between diagenesis and low grade metamorphism is indistinct, but is commonly taken as the boundary between an albite + zeolite high grade diagenetic facies and a prehnite-pumpellyite or equivalent low grade metamorphic facies. The presence of zeolite in diagenetic mineral assemblages and the absence of zeolite from metamorphic assemblages is commonly the most distinct difference. Like diagenetic alteration, metamorphism is regional in extent, and for a particular rock composition is strongly influenced by the changing stabilities of minerals with increasing temperatures. Water to rock ratios are likewise relatively low. However, load pressure becomes increasingly important in influencing mineral stabilities and the dynamics of the alteration system.

Principles for discrimination of diagenetic, hydrothermal and metamorphic alteration

The textural and mineralogical aspects of the discrimination between diagenetic, hydrothermal and metamorphic alteration are conceptually simple, but require very strong observational skills and a thorough and systematic approach. The reason for this is that rocks evolve along a long path of hydrothermal alteration, diagenetic alteration, deformation and metamorphic alteration (although the order may vary). Each stage overprints and modifies the modifications (i.e. alterations) of the previous stage. Consequently, textural and mineralogical (and at least in part the chemical and isotopic) discrimination between the different stages or types of alteration is an exercise in backstripping and unravelling the chain of modifications. The difficulty is compounded because in many cases one alteration stage leaves only local relics of the former stage, and so on, and by the time the rock has experienced metamorphism, no primary relics of former diagenetic zeolites, clays and other minerals remain, only pseudomorphs. Despite the difficulty, such backstripping can be done, and the contribution in AMIRA P439 Report 5 (Allen, 1997) shows the extent to which such work can be carried out in strongly altered and deformed regions.

Discrimination between diagenetic, hydrothermal and metamorphic alteration requires:

1 A basic knowledge of the primary rock type, and the general textural evolution of volcanic rocks.
2 Visible overprinting relationships at hand specimen and microscopic scale between alteration assemblages, secondary rock fabrics (such as compaction foliation and tectonic cleavage), and primary rock textures.
3 Knowledge of the regional distribution and zonation of the alteration assemblages. Are they local or regional, and what is the zonation pattern?
4 Knowledge of the temperature, pressure, and chemical environment under which key diagenetic, hydrothermal and metamorphic minerals are stable and unstable.
5 Knowledge of the mineral transformations that occur during diagenesis, metamorphism and deformation that have been documented in geologically young, well preserved regions.

Point 1 can be partly learned from published literature, but also requires a moderate level of hands-on experience with rocks from various stages and types of alteration. Points 3 and 4 are readily gleaned from the literature. Points 2 and 3 are the ones that generally involve the most work: careful mapping and documentation of overprinting relationships in the rocks. Table 1 provides a list of some important overprinting relationships and resulting interpretations that can be routinely considered in each field area.

Diagnostic features of diagenetic alteration

- Widespread, regional scale distribution.
- Early in paragenetic sequence and always precedes metamorphic alteration.
- Complex pattern of overlapping alteration

Table 1. Determination of overprinting or timing relationships and their use in discriminating between hydrothermal, diagenetic and metamorphic alteration in volcanic rocks.

	Aspects of alteration to be investigated	Alternative relationships	Implications for timing of alteration
1.	Relationship to primary textures	Truncated by clast margins	Pre-fragmentation
		Clasts of different alteration types	Pre-fragmentation
		Infills primary porosity	Pre-lithification
		Crosscuts primary porosity or clast margins	Post-lithification
		Rock has relict devitrification textures	Post-devitrification
2.	Relationship to successive volcanic or intrusive units	Cut by younger (less altered) rocks	Older syn-volcanic
		Overprints an overlying bed	Younger than overlying bed
		Overprints intercalated intrusion	Younger than intrusion and beds that overlie the intrusion
3.	Relationship to diagenetic compaction, compaction fiamme	Protects primary texture from compaction	Pre-compaction
		Compaction of more clay/mica-altered parts	Pre- to syn-compaction
		Overprints compaction foliation	Syn- to post-compaction
4.	Relationship of hydrothermal assemblages to diagenetic ones	Overprinted by early diagenetic minerals	Pre- to early-diagenetic
		Overprinted by late but not early diagenetic minerals	Intermediate-diagenetic
		Overprints late diagenetic minerals	Post-diagenetic
5.	Overprinting relationships between all alteration assemblages		Provides paragenetic sequence of hydrothermal and/or diagenetic alteration
6.	Relationship to early bedding-parallel tectonic foliation (S1)	Overprinted by stylolitic S1	Pre-S1
		Overprints stylolitic S1	Post-S1
7.	Relationship to main tectonic foliation and lineation	As deformed as primary fabrics	Pre-cleavage
		Foliated but less deformed than primary fabrics or S1	Syn-cleavage
		Undeformed	Post-cleavage
8.	Relationship to metamorphic assemblages	Overprinted by metamorphic assemblage	Pre-metamorphic
		Overprints metamorphic assemblage	Post-metamorphic
9.	Large scale distribution	Regional distribution	Diagenetic or metamorphic
		Stratabound in originally permeable rocks	Pre- to syn-lithification
		Locus in fractured competent rocks	Post-lithification, post-fracturing
		Restricted to faults, shears	Syn- to post-faulting

assemblages on a small scale.
- Different alteration styles preserve, enhance or destroy primary and post depositional textures:
  - early sericite enhances
  - quartz-feldspar preserves
  - sericite-chlorite enhances early fracture patterns but also destroys pumice textures
  - chlorite-epidote can either enhance fracture patterns or pervasively destroy groundmass textures
  - chlorite±magnetite destroys pumice textures
- Primary feldspar crystals are usually well preserved or pseudomorphed by diagenetic alteration styles.
- The distribution of sericite-rich and chlorite-rich alteration assemblages appears to be strictly controlled by the primary composition of the volcanic unit and by the primary or syn-volcanic textures. Feldspar alteration is less obviously controlled by primary features, particularly in the pumice breccias.
- Diagenetically altered volcanics have relatively low AI and CCPI. Wholerock compositions plot close to or in the unaltered fields in the AI-CCPI boxplot, outlined as: Rhyolite AI 30–65, CCPI 20–45; Dacite AI 40–70, CCPI 20–60; Mafics AI 25–50, CCPI 65–80.
- Diagenetic alteration involves relatively minor mass transfers over a small scale. The principal mobile components are K, Na, Ca, Si, Mg, Fe, C, Rb, Ba and Sr. Nett mass gains and losses usually do not exceed ~10g/100g.
- Adjacent samples may show corresponding depletion and enrichment of the same elements, suggesting that the chemical exchanges due to diagenesis are of limited scale.

Diagnostic features of hydrothermal alteration

- Local distribution or discrete zones.
- Many hydrothermal alteration styles are pervasive and exist as broad, transgressive zones rather than different alteration assemblages in individual flow bands or clasts within an emplacement unit.
- The degree of textural modification is dependent on the intensity of alteration:
  - primary and syn depositional textures are preserved in zones of weak alteration
  - in medial facies of hydrothermal alteration the pre-existing groundmass textures are modified or obliterated but feldspar crystals are still recognisable
  - in proximal zones of intense hydrothermal alteration, typically containing assemblages of quartz+sericite±pyrite and chlorite±pyrite, the groundmass textures and feldspar crystals are usually obliterated.
- carbonate in medial to proximal zones may either preserve uncompacted pumice clasts or be totally texturally destructive.
- Distribution and textures of distal-medial hydrothermal alteration zones are more or less influenced by the primary or synvolcanic textures but intense alteration in proximal zones tends to be totally pervasive.
- The hydrothermal alteration assemblage generally does not reflect primary rock composition, as the systems usually involve high water/rock ratios.
- Wholerock compositions plot away from the least altered field on AI-CCPI box plots; the actual position dependent on the alteration assemblage.
- Mass gains and losses of chemically mobile components are at least an order of magnitude greater than those related to diagenetic alteration styles.
- Mass changes are consistent over greater volumes.

Diagenetic alteration styles in the Mount Read Volcanics

Muscovite or sericite

Muscovite (frequently referred to as sericite) is the most abundant and widespread alteration phase. It formed largely as a result of greenschist metamorphism of diagenetic clay minerals and, although pervasive, it generally exists as a thinly disseminated phase that rarely masks primary volcanic textures.

Sericite exists in felsic coherent rocks as fine disseminations throughout the recrystallised quartzo-feldspathic matrix and rims on feldspar phenocrysts, spherulites and micropoikolitic quartz. In volcaniclastics, fine dustings of sericite and clay coated the originally glassy walls of pumice fragments and

shards as thin films, ***before*** feldspar±quartz infilling of the vesicles. Feldspar crystals, in both volcaniclastic and coherent facies, are frequently dusted to partially or completely replaced by sericite.

Feldspar±quartz

The main diagenetic feldspar is albite dusted with hematite, however relict K-feldspar (of an earlier, lower temperature phase of diagenesis) is preserved in some less altered samples.

Feldspar alteration tends to be selective, or domainal in character, forming pink feldspar-rich zones. In both coherent and clastic rocks, it is commonly associated with chlorite+sericite or sericite alteration, producing distinctive pink and dark green polyphase alteration patterns.

The textural manifestations of feldspar alteration include:

- replacements and overgrowths on the margins of plagioclase crystals
- fracture fillings within plagioclase crystals, laths enclosed in micropoikolitic quartz scattered throughout the groundmass of coherent units
- selective replacement of more crystalline flow-bands and spherulites whereas glassy flow-bands are replaced by sericite-chlorite dominated assemblages
- vesicle fillings and replacement of the glassy walls of uncompacted pumice fragments and glass shards
- pink halos or rinds around lithic clasts contained in a green sericite-chlorite altered groundmass in volcaniclastics
- also a common vein assemblage.

Silica

Silica alteration is a widespread and pervasive low intensity alteration type that rarely obscures primary volcanic textures.

Sericite+chlorite (±carbonate±quartz±pyrite)

This style of alteration is typically inhomogenous producing dark green patches or lenses of chlorite + sericite in a paler feldspar-rich matrix. In volcaniclastics, dark sericite+chlorite alteration highlights fiamme representing compacted glassy pumice clasts, whereas in coherent in flow banded rhyolites the glassy bands tend to be preferentially altered.

Ferromagnesian phases in all volcanic facies are typically partly to completely pseudomorphed by chlorite.

Chlorite

There are several types of chlorite dominated alteration assemblages that include sericite, magnetite and pyrite which may be transitional, in places, to hydrothermal alteration styles.

Chlorite ± magnetite, however, is widespread and exists as patchy to pervasive, disseminated fine grained aggregates in the groundmass and interstitial to microspherulites, micropoikolitic quartz and glomeroporphyritic clusters of phenocrysts.

Chlorite alteration is most prominent in mafic volcanics.

In coherent volcanics, chlorite defines perlitic fractures and later hydraulic and tectonic fractures, pseudomorphs mafic phenocrysts, fills vesicles, exists as rims on feldspar phenocrysts and rarely replaces plagioclase. In pumiceous volcaniclastics it occurs in stylolites or dissolution seams parallel to the compaction foliation.

Chlorite alteration halos are also associated with mafic dykes and sills, and with brittle fractures and faults; these are respectively, local contact metamorphic or hydrothermal effects.

Chlorite + epidote ± feldspar

This assemblage is essentially restricted to mafic to intermediate volcanics where it defines perlitic fractures, forms fine grained irregular patches in the groundmass and partially replaces hornblende and plagioclase grains.

Sphene, commonly replaced by leucoxene, is a minor alteration phase of mafic volcanics existing as fine grained irregular patches concentrated along grain boundaries.

Carbonate

Carbonate alteration is generally of low intensity and not texturally destructive, occurring as disseminations, filling primary porosity such as vesicles, and replacing or rimming glass shards and feldspar phenocrysts, in advanced cases. However, more intense carbonate alteration masks primary volcanic textures resulting in a fine grained massive homogenous pale rock.

Carbonate more commonly occurs in veins associated with chlorite or quartz that appear to have been activated during the Devonian metamorphism.

Rosebery–Hercules area as a case example

Documentation of diagenetic alteration in the Rosebery–Hercules area, and the method of using overprinting relationships to backstrip through the layers of metamorphic, syn-tectonic, hydrothermal and diagenetic alteration were given in the previous report (Allen, 1997). It is not intended to repeat that discussion here. Instead, photographs (Plate 1; data sheets in Vol. 2, this report) and a summary model (Fig. 1) are presented; and Table 1 (in Vol. 2, this report) provides an update of the paragenetic timing relationships presented earlier.

Throughout the Rosebery–Hercules area, altered, rhyolitic to dacitic pumice and glass shards are the main constituents of the footwall, hangingwall, and host rocks to the massive sulphides. The pumice and shard textures are remarkably well preserved in hand specimen and thin section, despite the strong deformation and long history of alteration. The textures are well preserved due to widespread replacement by mechanically competent minerals such as feldspar, prior to deformation and metamorphism (Allen, 1990, 1991, 1994a, b; Allen & Cas, 1990). These feldspar-rich assemblages have replaced the pumiceous rocks on a regional scale, that is at least an order of magnitude more extensive than hydrothermal alteration spatially associated with the ore deposits. Consequently the feldspar alteration must be diagenetic or metamorphic in origin. The very early paragenesis of the earliest feldspar alteration (Table 1, Vol. 2: pre-S1 diagenetic compaction foliation) indicate that the feldspar is diagenetic. The recognition of these textures and overprinting/timing relationships have been the key to discriminating between hydrothermal, diagenetic and metamorphic alteration in the Rosebery–Hercules area. Allen (1997) proposed as a general rule that alteration assemblages that are regional in distribution and pre-date or are synchronous with a stylolitic S1 compaction foliation can be defined as diagenetic. Alterations that show similar timing relationships but which are only local in distribution are related to discrete local hydrothermal alteration systems, or the cooling of particular volcanic emplacement units.

Plate 1a, b provide typical examples of relics of the diagenetic feldspar alteration distal to ore. The diagenetic feldspar is best preserved around phenocrysts, where it forms irregular, pale-coloured, competent clots. The main regional cleavage anastomoses around these competent clots, and on a micro-scale deformation increases in intensity outward through the clots (Plate 1a), with the result that the relict diagenetic feldspar textures and primary textures become progressively more overprinted, recrystallised and sericitised by cleavage development away from the feldspar phenocrysts. Close to the phenocrysts, some primary and diagenetic textures are almost perfectly preserved. Plate 1b shows the overprinting relationship between two generations of feldspar alteration in the same feldspar clot as in Plate 1a. The central feldspar phenocryst (partly sericitised) has a thin rim of clean, optically continuous K-feldspar (pale rim), which changes outwards into mottled, twinned albite. Observation of different samples with varying stages of the feldspar replacement indicates that the albite replaces the K-feldspar. Consequently, K-feldspar was the first diagenetic feldspar alteration, and is only preserved locally.

Alteration assemblages that are strongly foliated by S2 and also overprint S1 are regarded as broadly syntectonic. Alteration assemblages unaffected or only very weakly affected by S2 foliation post date the main deformation. Plate 1c shows pyrite layers associated with strong hydrothermal quartz-sericite-pyrite alteration in footwall pumice breccia in the B-lens ore zone at Rosebery. The pyrite layers are folded, foliated, lineated and locally transposed by the main cleavage-lineation deformation (S2-L). However, a weak to moderate S1 foliation is parallel to the pyrite layers. Consequently the alteration and mineralisation are pre- or syn-S1 and therefore apparently pre-main deformation and pre-metamorphic.

Plate 1d, e, f provide examples of other overprinting relationships of alteration, mineralisation and volcanic facies at the Rosebery mine.

Combining all the data on overprinting relationships, the spatial distribution of alteration types, and

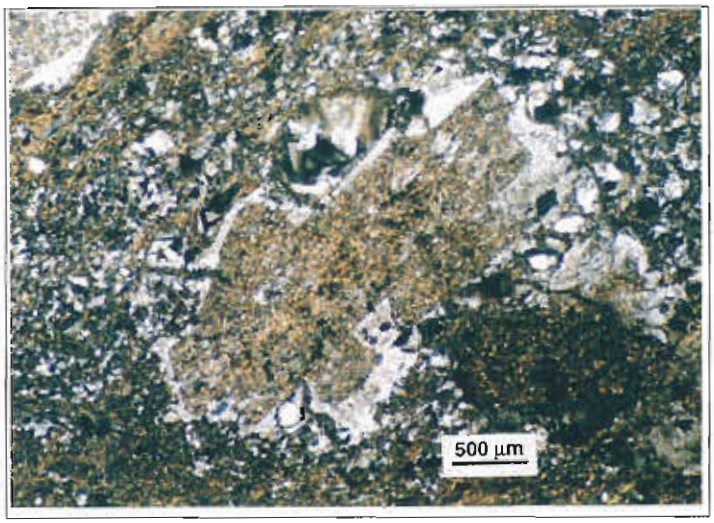

a) Photomicrograph (plane polarised light) of a diagenetic feldspar alteration spot enclosing feldspar phenocrysts in massive, feldspar-phyric, rhyolitic pumice breccia of the footwall volcanics. Frothy round-vesicle pumice texture is well preserved around the feldspar phenocrysts due to a thin film of sericite (dark yellow-green) that lines the inside walls of original vesicles. The remainder of the vesicle walls have been replaced, and the inside of the vesicles have been infilled by feldspar (pale domains). Sample 109R-726m; a hand specimen and other details of this sample are shown in Rosebery data sheet 1: 109R-726.

b) Photomicrograph (crossed nicols) of the same view as in photograph (a). The plagioclase feldspar phenocryst is partially replaced by sericite, and is rimmed by optically continuous K-feldspar (pale rim), which changes outward to mottled, twinned albite. Sample 109R-726m; a hand specimen and other details of this sample are shown in Rosebery data sheet 1: 109R-726.

c) Strong hydrothermal quartz-sericite-pyrite alteration replacing footwall pumice breccia in the B-lens ore zone. Pyrite layers are folded, foliated, lineated and locally transposed by the main cleavage-lineation deformation (S2-L). A weak to moderate S1 foliation is parallel to the pyrite layers. Consequently the alteration-mineralization is pre- or syn-S1 and clearly pre-dates the main S2 deformation. Sample R4452-73.3.

PLATE 1

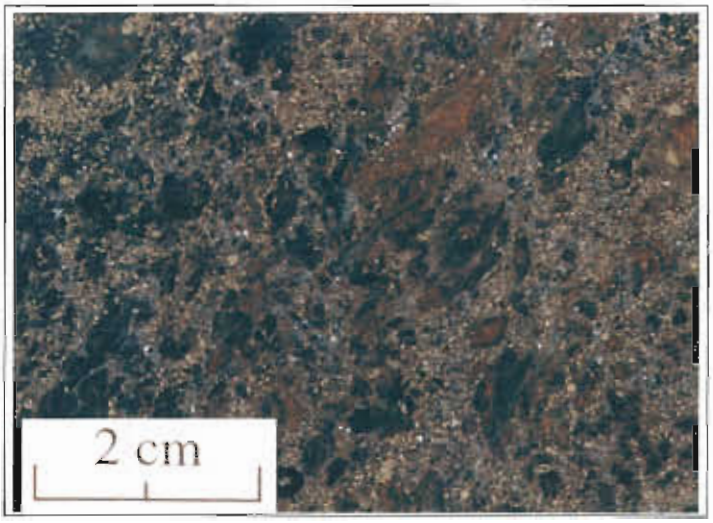

d) Semi-massive sphalerite-galena-minor pyrite ore at the upper margin of the K-lens massive sulphide. The sulphide is homogeneous, recrystallized and relatively undeformed, but encloses numerous strongly foliated and variably rotated wall rock clasts. This texture is attributed to mechanical remobilisation and intrusion of the margin of the massive sulphide lens into its wall rocks at a late stage of the main deformation (after strong alteration and foliation of the wall rocks). Sample 120R-1366.

e) Altered, foliated, intrusive hyaloclastite breccia (= peperite) at the top margin of the feldspar-quartz-biotite porphyritic dacite sill that overlies K-len. Pale domains are porphyry hyaloclastite clasts and the dark domain is siltstone with abundant fine grained pyrite. Both the porphyry clasts and matrix sediment have been strongly sericite-quartz-pyrite altered and then strongly foliated (S2). Sample 128-1136.8.

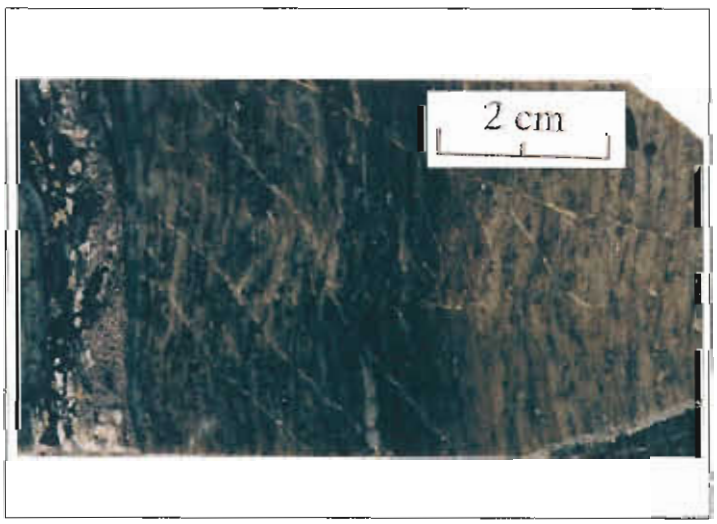

f) Very strongly foliated footwall pumice breccia, cut by an undeformed, post-S2 cleavage, cleavage-parallel, hydrothermal chlorite-carbonate-arsenopyrite-tourmaline vein (left side). The pumice breccia has moderate sericite-quartz-carbonate alteration that is overprinted by the S2 cleavage. The cleavage is in turn overprinted by dark chlorite-carbonate-sphene alteration probably related to the adjacent veins. Sample 120R-1436.2.

mineral transformations, allows construction of an evolutionary model for alteration in the Rosebery–Hercules area (Fig. 1).

The Rosebery–Hercules footwall pumice breccia was emplaced rapidly from a major caldera-forming pyroclastic eruption. The area developed rapidly into a high-grade diagenetic alteration system (Fig. 1, parts 1–2) that was zoned from smectite±opal alteration at the top, through a zeolite zone (probably clinoptilolite - mordenite), and a K-feldspar zone, to a lower albite-zeolite zone. Comparison with data from young basins indicates that the zeolite-free smectite zone represents diagenetic alteration from very low temperatures up to 40–50°C. The clinoptilolite-mordenite zone represents alteration from 40-50°C up to 130°C. The K-feldspar zone probably corresponds to temperatures up to around 150°C, whereas albite alteration occurred above 150°C and up to 250°C or more (see references in Allen, 1997). Directly after deposition of the pumice breccia, as the diagenetic system encroached up through the sequence and established itself, the geothermal gradient would have progressively increased, and consequently the thickness of the diagenetic zones would have decreased.

Overprinting relationships and the stratigraphic extent of the diagenetic assemblages, suggest that the diagenetic alteration system initially preceded ore formation. Local, hydrothermal, pre-ore spotty carbonate alteration overprinted smectite alteration near the seafloor, resulting in smectite-altered (now sericite) glass shards being enclosed and completely preserved inside the carbonate spots. The hydrothermal system prograded upwards and outwards forming a quartz-sericite zone, a chlorite zone and massive sulphide mineralisation, after initial development of the spotty carbonates (Fig. 1, part 2). The lower intensity of hydrothermal alteration within the base of the hangingwall sill or in the TSV, suggests that the peak intensity of the hydrothermal system and massive sulphide mineralisation probably occurred just before or just after emplacement of the hangingwall sill. Intrusive contact relationships indicate that the TSV and lower part of the hangingwall black shale were present when the hangingwall sill was emplaced.

As the hangingwall mass flow succession accumulated, isotherms and hence the diagenetic zones prograded up through the succession (Fig. 1 part 3). The local hydrothermal system that formed the Rosebery massive sulphides entered a long period of decline. Low grade hydrothermal alteration consisting of stratabound lenses of calcite impregnation and minor sericite-carbonate, formed an extensive diffuse plume above the high grade footwall and ore zone alteration.

Accumulation of hangingwall strata and progradation of the diagenetic system presumably continued well after the ore-related hydrothermal system had died, because relatively high temperature diagenetic feldspar-bearing assemblages occur throughout the hangingwall succession. Finally, during regional deformation and metamorphism, the diagenetic and hydrothermal alteration minerals were variably recrystallised and replaced by syn-tectonic, metamorphic greenschist facies albite-chlorite-sericite-epidote assemblages (Fig. 1 part 4). Hydrothermal and diagenetic smectite and illite were converted to sericite and chlorite, hydrothermal chlorite was recrystallised to metamorphic chlorite, diagenetic zeolites and feldspars were replaced by albite except for local relics of diagenetic K-feldspar, and deformation zones that experienced high fluid flow were sericitised.

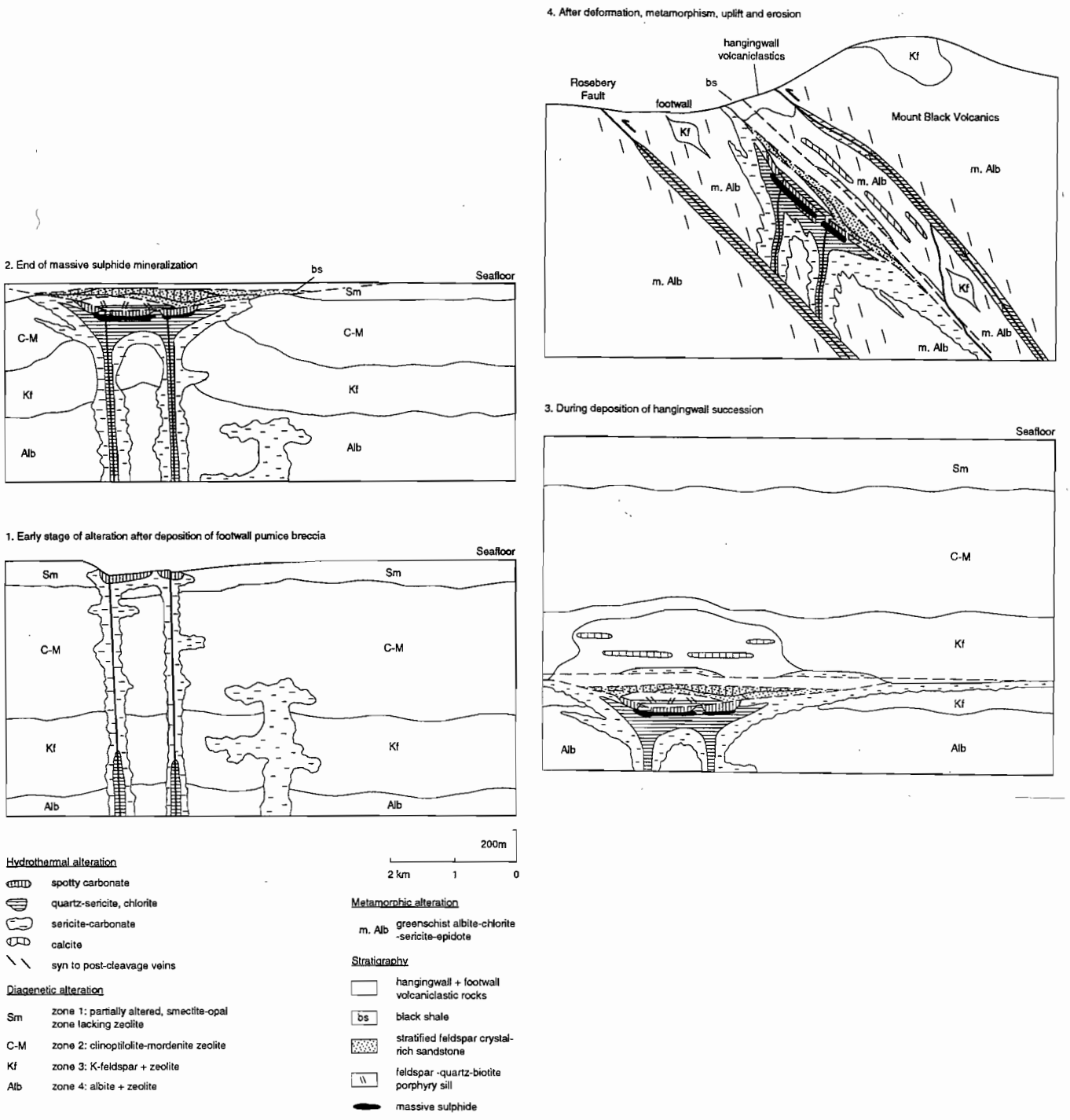

Figure 1: Model for the evolution of, and relation between, hydrothermal alteration, diagenetic alteration, metamorphism and deformation at the Rosebery massive sulphide deposit. Post-volcanic, late to post-deformation, Devonian granite-related alteration is omitted.

PART 2: Geochemistry

R. Large and W. Herrmann

An examination of the compositions of a large number unaltered volcanics from modern oceanic and continental margin arc settings by Stolz et al. (1996a) indicated that:

- Except for some unusual K_2O rich alkaline varieties, very few unaltered modern arc volcanics have <2% Na_2O; most have between 2 and 5% Na_2O, (Fig. 2a).
- Most unaltered volcanics have a restricted range of alteration index* (AI) between about 15 and 65, (Fig. 3a).
- They have rather coherent near linear trends in terms of SiO_2 vs. MgO and CaO, reflecting the limited range of compositions produced by upper mantle partial melting and crystal-liquid differentiation, (Fig.s 4a & 5).
- Modern arc volcanics contain upto about 100ppm Cu, 30ppm Pb and 150ppm Zn; Cu and Zn tend to decrease with increasing SiO_2 (differentiation) whereas Pb increases with SiO_2.

Rocks of the Mt Read Volcanics (MRV), by comparison, show greater ranges and variability reflecting the different styles and degrees of alteration:

- Na_2O ranges from 0 to 8% (Fig. 2b).
- AI spans the full range from 0 to 100, (Fig. 3b).
- Trends in SiO_2 vs MgO & CaO are fuzzier due to alteration changes, (Figs 4b & 5b).
- Cu, Pb and Zn range upto two orders of magnitude higher than in fresh modern volcanics but are not particularly correlated with AI.

These distributions led Large et al. (1996) to propose a threefold classification based on Na_2O contents as follows:

- hydrothermally altered volcanics: <1.5% Na_2O (subsequently revised to <2% Na_2O)
- unaltered volcanics: 1.5 - 5% Na_2O
- albitised volcanics: >5% Na_2O

Na_2O content and AI (alteration index) provide a fair indication of the degree of plagioclase destruction typical of VHMS footwall alteration zones, or in the last category, the degree of (probably diagenetic) albitisation of K feldspar.

However, the AI alteration index is deficient in discriminating sericite from chlorite alteration zones; it fails as an indicator of alteration intensity, where carbonates are part of the alteration assemblage. This is because the carbonates usually contain CaO, which is in the denominator of the AI formula and results in lowering of the index, even where plagioclase destruction may be complete.

Recognition of this problem inspired the development of the Chlorite–Carbonate–Pyrite Index** (CCPI), (Large et al., op. cit.) which, when plotted against AI, graphically distinguishes the main alteration minerals and serves as an indicator of alteration intensity.

On plots of CCPI vs AI, the compositions of most unaltered modern arc volcanics and the least altered Mt Read Volcanics, lie in a "box" between about 20–65 AI and 15–85 CCPI, roughly in the central left of the diagram (Fig. 6). Compositions of felsic rocks plot near the bottom of the unaltered box (15-40 CCPI) whereas mafic rocks plot near the top (65–85 CCPI), due to the differing proportions of felsic and mafic minerals in them.

The control of primary volcanic composition (ie. parent magma fractionation) on the CCPI is clearly shown in Fig. 7a, where CCPI increases systematically from values of 20 – 40 for rhyolites with Ti/Zr <10 to values of 70–90 for andesites and basalts with Ti/Zr >20. A similar pattern is not shown for the Ishikawa alteration index (AI) which is independent of magma fractionation (Fig. 7b).

The three alteration groupings defined above, based on Na_2O content, overlap significantly on the AI-CCPI box plot, but show different patterns related to alteration mineralogy (Fig. 8). Most of the least altered volcanics (2 <Na_2O <5 wt%) of the MRV data set plot in the "unaltered" box, however there are

* $AI = 100(MgO+K_2O)/(MgO+K_2O+CaO+Na_2O)$

** $CCPI = 100(MgO+FeO)/(MgO+FeO+Na_2O+K_2O)$; previously termed Chlorite Index.

about 15% of the samples outside the box indicating that Na_2O alone is not the best discriminator of alteration.

Albite altered volcanics with Na_2O >5 wt% trend diagonally across the diagram from the unaltered box toward the albite corner. This reflects diagenetic carbonate and chlorite alteration associated with albite development. Hydrothermally altered volcanics with Na_2O <2 wt%, that have suffered feldspar destruction, spread across the RHS of the diagram with the majority of samples plotting in the sericite-chlorite-carbonate triangle.

The various alteration trends evident from our studies on both the regional traverses and the mine-scale alteration are summarised below, in reference to the AI-CCPI box plot in Figure 8.

Hydrothermal alteration trends (Fig. 9)

Trend 1: Weak hydrothermal alteration at the margins of ore systems (deep footwall, hangingwall or lateral ore position) involves sericite alteration of feldspars and ground mass. This trend is typical at the margins of systems in felsic volcanics, (eg., Rosebery, Fig. 10)

Trend 2: Strong hydrothermal alteration adjacent to the sericite-chlorite±pyrite join typical of intense footwall alteration. This trend of increasing chlorite and pyrite is toward the centre of the hydrothermal system (eg., Western Tharsis, Fig. 11). Note this trend is also usually accompanied by increased hydrothermal quartz.

Trend 3: Strong chlorite-pyrite±sericite alteration typical of chlorite-rich footwall alteration (eg., Hellyer) or the halo to copper-rich systems (eg., Highway–Reward, Fig. 12).

Trend 4: Strong chlorite-carbonate alteration usually found lateral to the ore zone either in the immediate footwall or at the ore position. Examples are found at Thalanga (Fig. 13) and Hellyer.

Trend 5: Strong Fe-Mn carbonate-sericite ± chlorite alteration usually confined to the ore horizon or its lateral equivalents (eg., Hercules and Rosebery (Fig. 14), or forming a distal halo surrounding copper-gold systems (eg: Western Tharsis, Fig. 11).

Trend 6: Intense K-feldspar-chlorite ± sericite ± magnetite alteration found deep in the hydrothermal system adjacent to syn-volcanic granitoids (eg., Jukes Pty).

Diagenetic Alteration Trends (Fig. 9)

Trend 7: Diagenetic albite±chlorite; a regional alteration assemblage developed in porous volcanic units (eg., volcanic sandstones and volcaniclastics) usually unrelated to VHMS systems. However albite alteration is known in the hangingwall to ore at Hellyer and Henty where it may be related to hydrothermal alteration. Further work is needed to discriminate these types of albite alteration.

Trend 8: Albite-calcite±epidote alteration typically developed during metamorphism of mafic volcanics, and is unrelated to VHMS formation.

Trend 9: Diagenetic K-feldspar±albite alteration unrelated to VHMS systems, and developed very early during diagenesis (Allen, this volume).

Trend 10: Paragonitic sericite±albite alteration observed in the hangingwall volcanic sandstones at Rosebery. Most probably a diagenetic trend, but maybe related to albite alteration zones in the hangingwall at Hellyer and Henty.

In summary, it is apparent that the major hydrothermal alteration trends in Figure 9 are confined above the sericite-calcite tie line, and the diagenetic alteration trends are generally below this line. In addition, the hydrothermal VHMS related trends are generally texturally destructive (except Trend 1) while the diagenetic alteration trends preserve textures.

Conclusions

By combining textural, mineralogical and lithochemical observations as outlined above it is possible to easily discriminate the hydrothermal trends related to VHMS systems from the diagenetic trends, however the boundary or margins between the two can present problems. This is particularly the case for Trend 1, where increasing sericite content may either be related to hydrothermal activity at the margin of a system, or diagenesis followed by metamorphism. This means that it is critically important to collect and study a *suite of samples* so

that alteration trends can be established to assist the discrimination process.

A combination of textural studies with the alteration box plot and other vectors discussed by Large et al. (this volume) is the ultimate way to characterise a suite of altered volcanic samples.

References

Allen, R. L. 1990. Subaqueous welding, or alteration, diagenetic compaction and tectonic dissolution? IAVCEI International Volcanological Congress, Mainz, Germany, Abstracts volume.

Allen, R. L., 1991, Stratigraphy, structure, volcanology and ore genesis of the Rosebery – Hercules ZnPbCuAu massive sulphide district, Tasmania. Unpublished report to Pasminco Exploration, Melbourne Australia. 3 volumes.

Allen, R. L. 1994a. Volcanic facies analysis indicates large pyroclastic eruptions, sill complexes, synvolcanic grabens, and subtle thrusts in the Cambrian "Central Volcanic Complex" volcanic centre, western Tasmania. Contentious Issues in Tasmanian Geology Symposium, Geological Society Australia Tasmania Division, Hobart. Abstracts number 39, p. 31-3.

Allen, R. L. 1994b. Synvolcanic, subseafloor replacement model for Rosebery and other massive sulphide ores. Contentious Issues in Tasmanian Geology Symposium, Geological Society Australia Tasmania Division, Hobart. Abstracts number 39, p. 89–91.

Allen, R.L. 1997Rosebery alteration study and regional alteration studies in the Mount Read Volcanics: The record of diagenetic alteration in the strongly deformed felsic volcaniclastic succession enclosing the Rosebery and Hercules massive sulphide deposits. AMIRA/ARC Project P439, Report 5, Oct 1997, 135–145. CODES, University of Tasmania

Allen, R. L. and Cas, R. A. F. 1990. The Rosebery controversy: Distinguishing prospective submarine ignimbrite-like units from true subaerial ignimbrites in the Rosebery–Hercules ZnCuPb massive sulphide district, Tasmania. 10th Australian Geological Convention. Geological Society Australia, Abstracts 25, p. 31–32.

Doyle M.G. 1998. The Ordovician Highway–Reward sub-seafloor replacement deposit, Mount Windsor Subprovince, Queensland. AMIRA/ARC Project P439, Report 6, May 1998, (in prep.).

Huston, D. L. and Kamprad, J. 1998 Alteration zonation and geochemical dispersion at the Western Tharsis deposit, Mt Lyell, Tasmania: a summary. Unpub. CODES P439 AMIRA Report 6, (in prep.)

Large, R.R., Stolz, A.J. and Duhig, N. 1996 Preliminary assessment of MRV geochemical database in terms of possible vectors to ore. AMIRA/ARC Project P439, Report 2, May 1996, 197–209. CODES, University of Tasmania

Large, R.R., Allen, R.L., Blake, M. and Herrmann, W. 1998 Alteration halo model for the Rosebery VHMS deposit, western Tasmania. AMIRA/ARC Project P439, Report 6, May 1998, (in prep.).

Stolz, A.J., Large, R.R. and Duhig, N. 1996a Progress report on the utilisation of the Mount Read Volcanics database. AMIRA/ARC Project P439, Report 2, May 1996, 181-196. CODES, University of Tasmania

Stolz, A.J., Allen, R.L., Gifkins, C., Davidson, G.J., McPhie, J. and Blake, M. 1996b Petrographic and geochemical characteristics of alteration from the Hall Rivulet Canal – Mt Read – Red Hills – Anthony Dam traverses, Mt Read Volcanic Belt. AMIRA/ARC Project P439, Report 3, Oct 1996, 181–196. CODES, University of Tasmania.

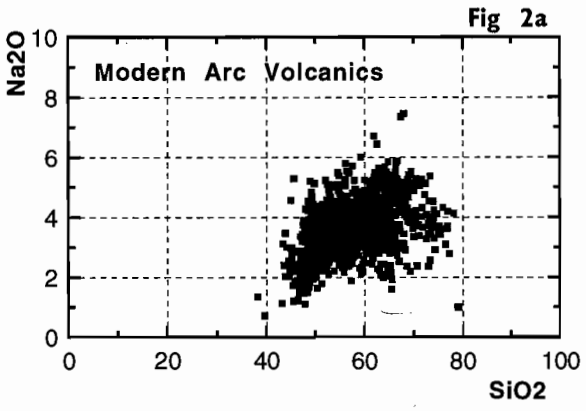

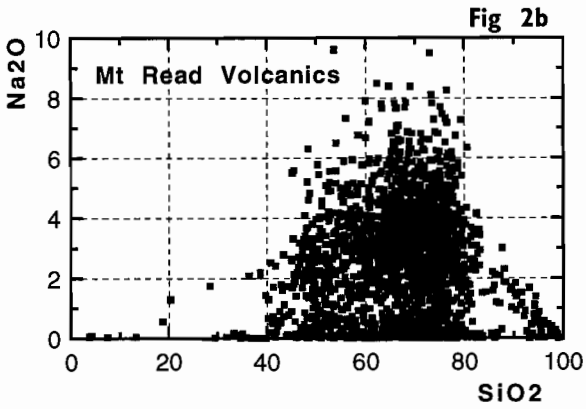

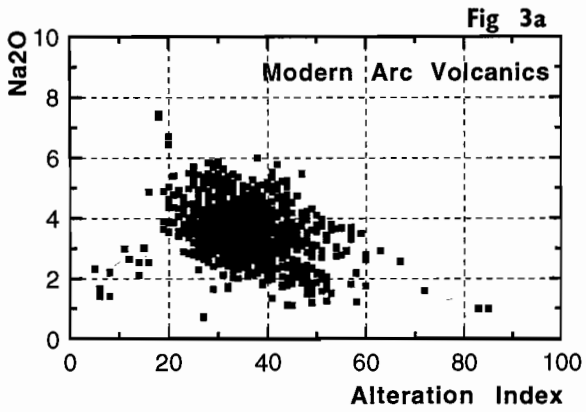

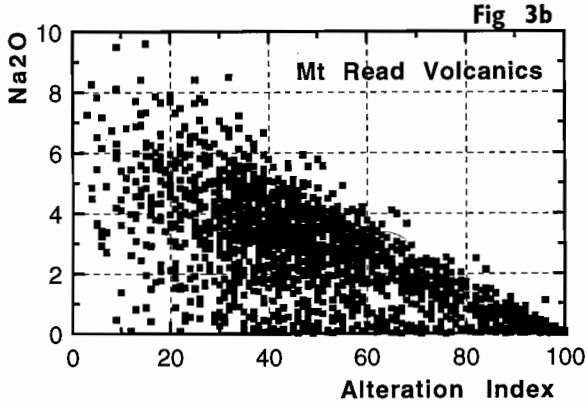

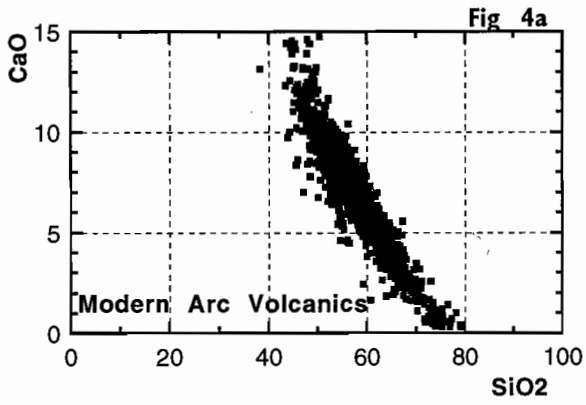

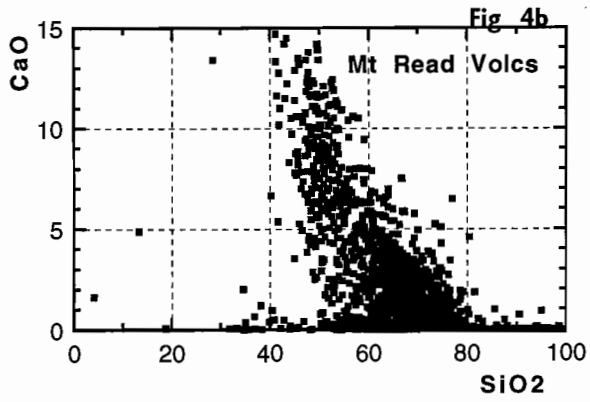

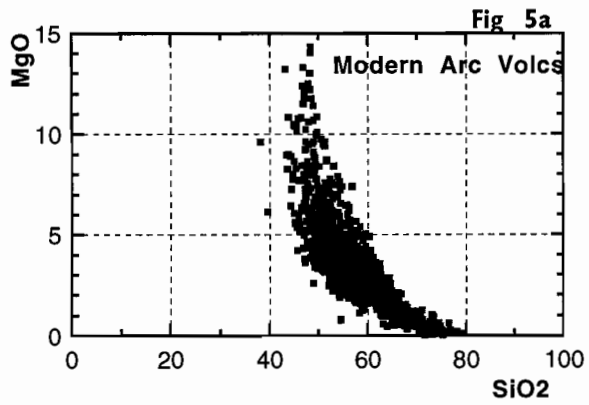

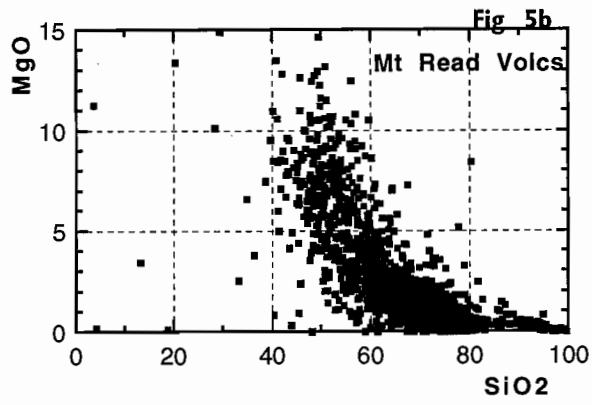

Figures 2 to 5 Scatterplots comparing variations in Na_2O, SiO_2, CaO, MgO and Alteration Index of fresh volcanics from the Aleutian, Scotia, Indonesian and Andes modern arcs with fresh and altered Mt Read Volcanics.

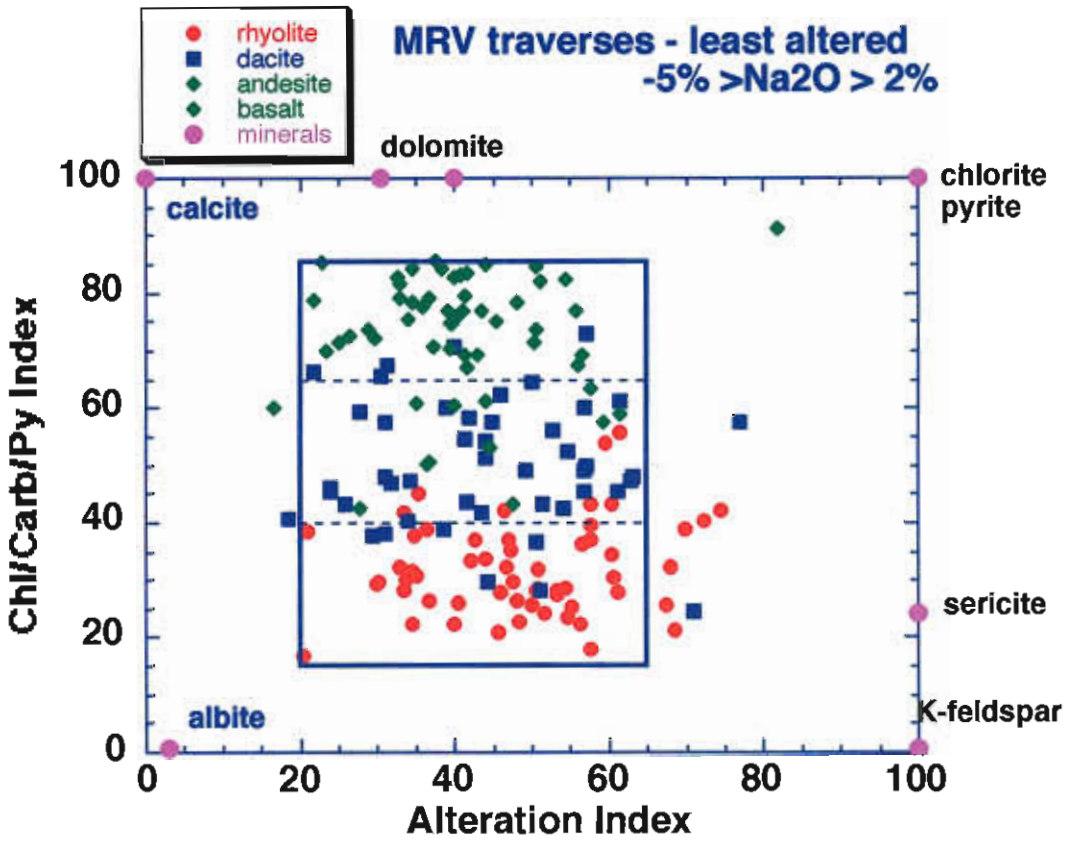

Figure 6. Alteration box plot for "least altered" volcanics from the MRV regional traverses. Samples plotted have 2 <Na_2O <5 wt%. The samples define the unaltered field bounded by AI = 20 to 65 and CCPI = 15 to 85. Note that rhyolitic volcanics (Ti/Zr <12) plot in the lower part of the unaltered box (CCPI 15 to 40) while the andesite and basalts (Ti/Zr >20) plot in the upper part with CCPI >65.

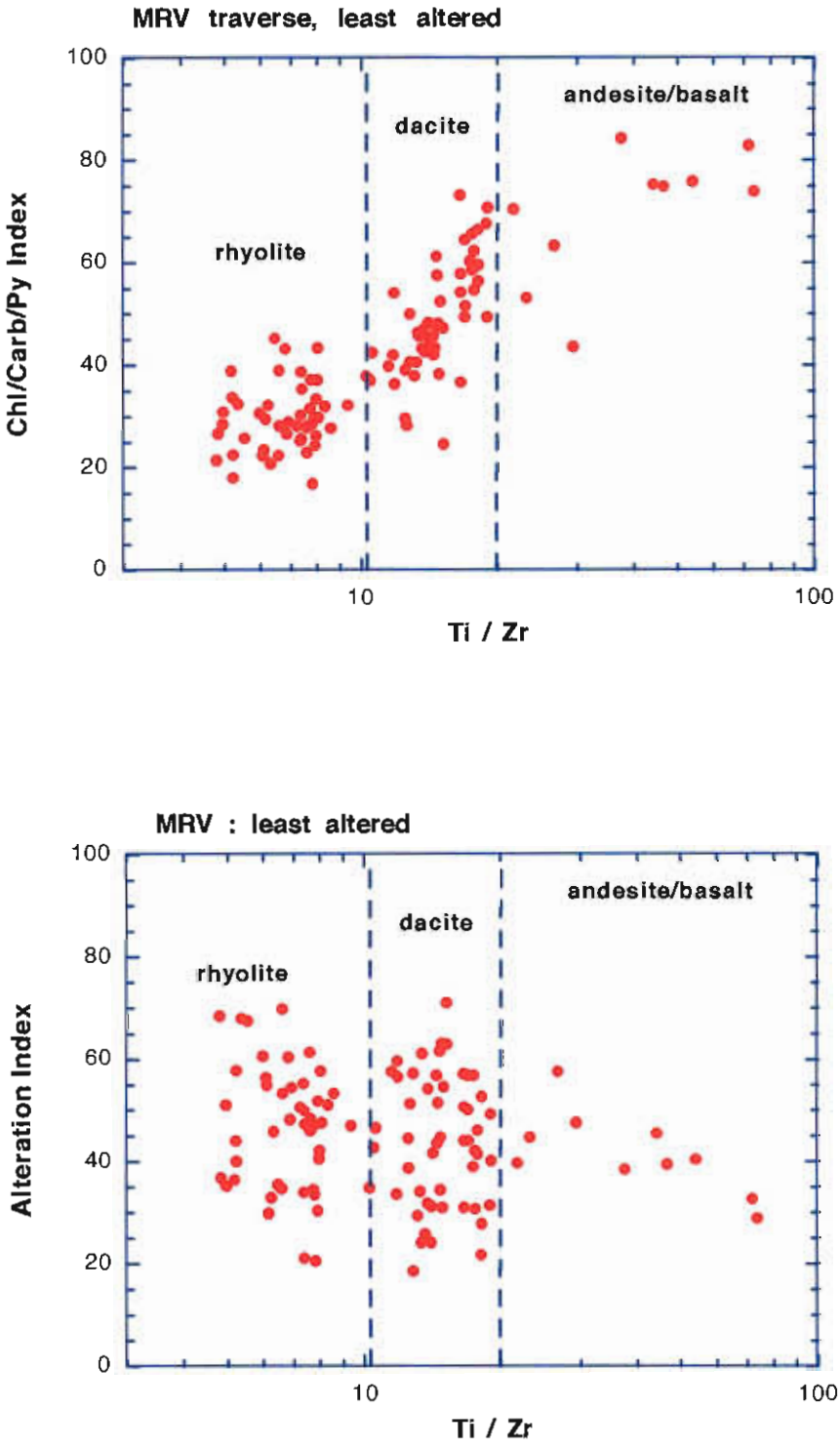

Figure 7. (a) Trend of increasing CCPI with Ti/Zr ratio for least altered volcanics from the MRV regional traverses
(b) By comparison the Ishikawa AI shows no trend related to volcanic composition (Ti/Zr).

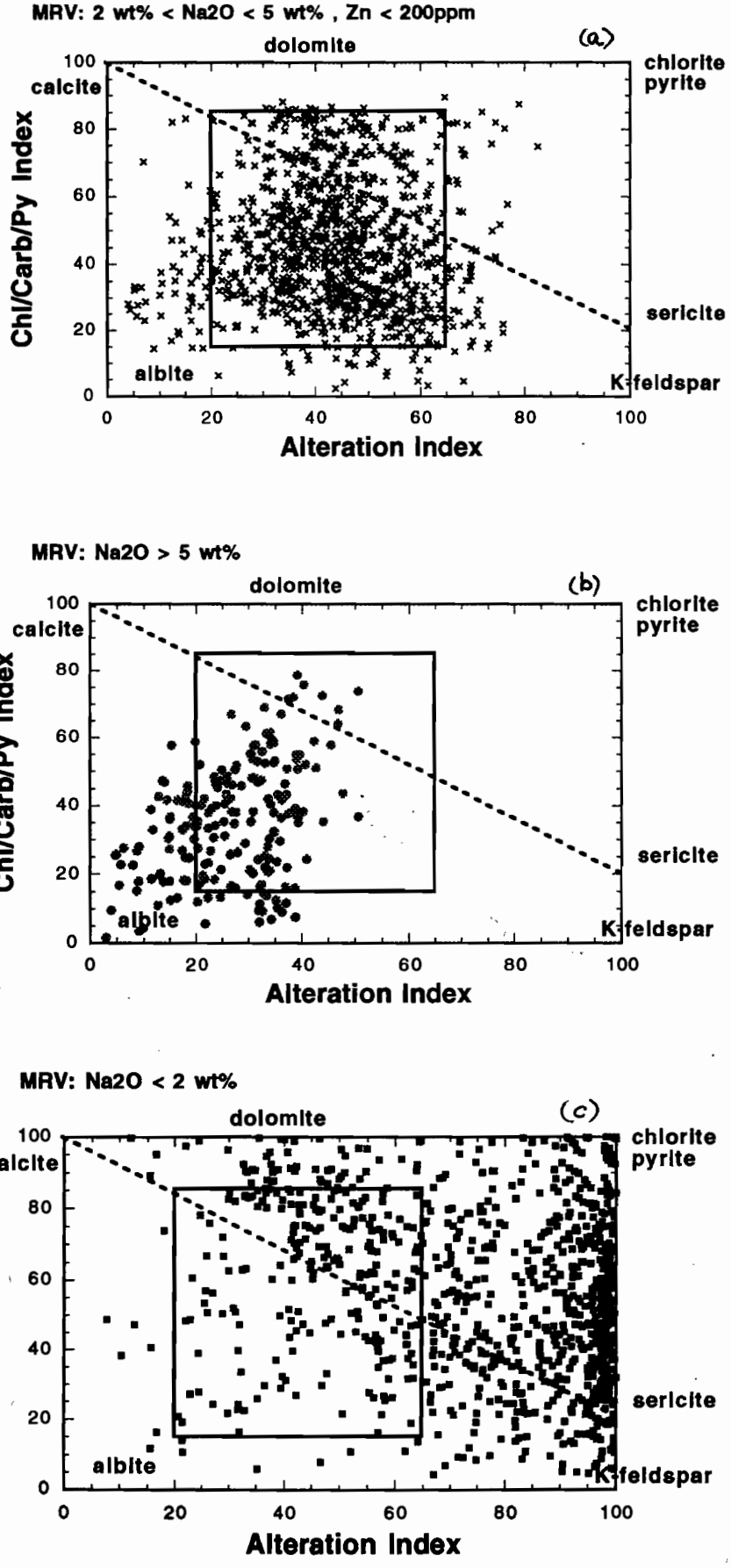

Figure 8. Alteration box plots for the total MRV data set.
(a) "unaltered volcanics" with $2 < Na_2O < 5$ wt%,
(b) albitised volcanics with $Na_2O > 5$ wt%,
(c) hydrothermally altered volcanics with $Na_2O < 2$ wt%.

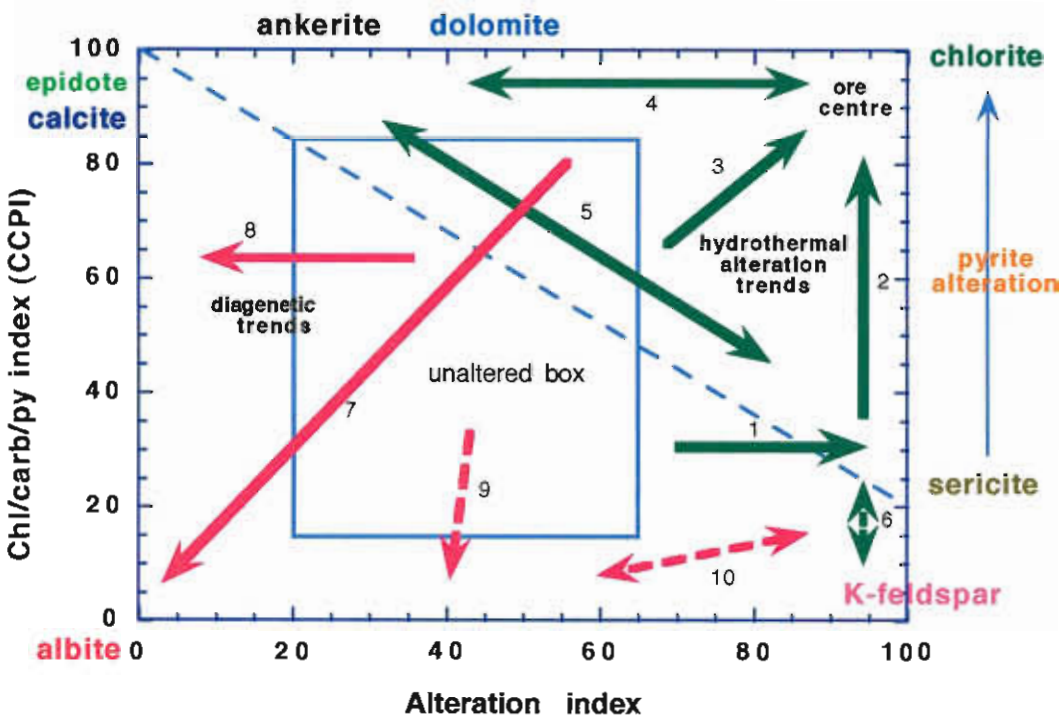

Figure 9. Alteration trends on the alteration box plot.
Hydrothermal trends: 1) sericite alteration at margins of system; 2) sericite-chlorite±pyrite; 3) chlorite±sericite±pyrite; 4) chlorite-carbonate; 5) Fe/Mn carbonate-sericite; 6) K-feldspar-chlorite±sericite.
Diagenetic trends: 7) albite±chlorite; 8) albite-calcite±epidote; 9) K-feldspar±albite; 10) paragonitic sericite±albite.

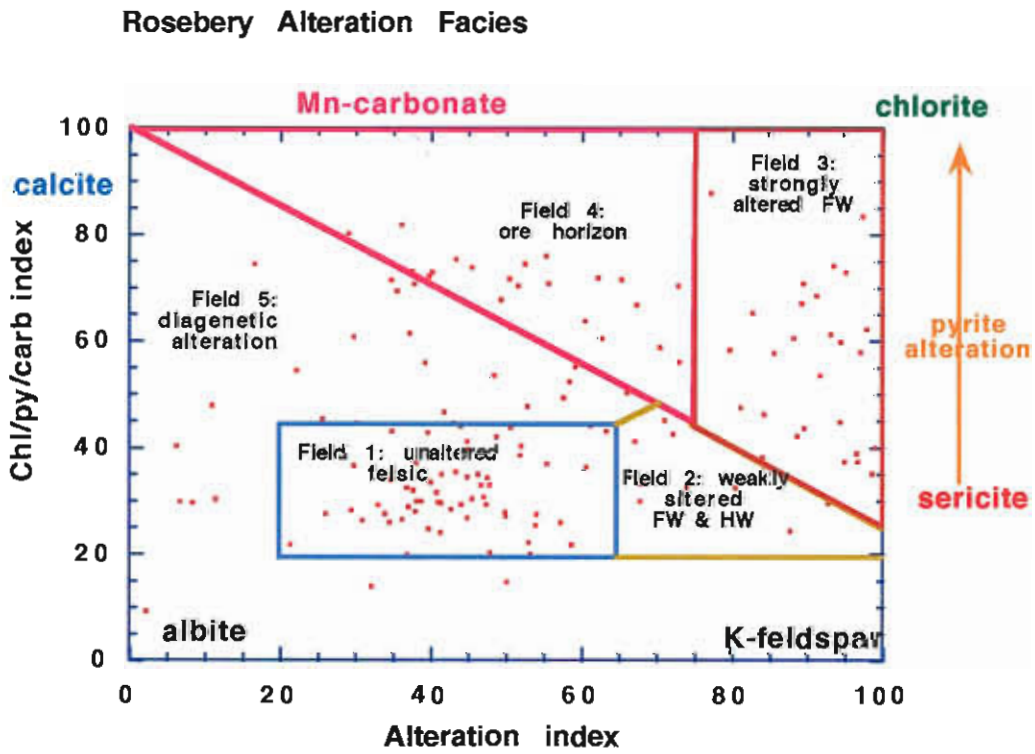

Figure 10. Rosebery alteration facies (Large et al., this volume) note that the weakly altered sericite zone (Trend 1, Fig. 8) related to marginal FW and proximal hangingwall alteration corresponds with Trend 1 in Figure 9.

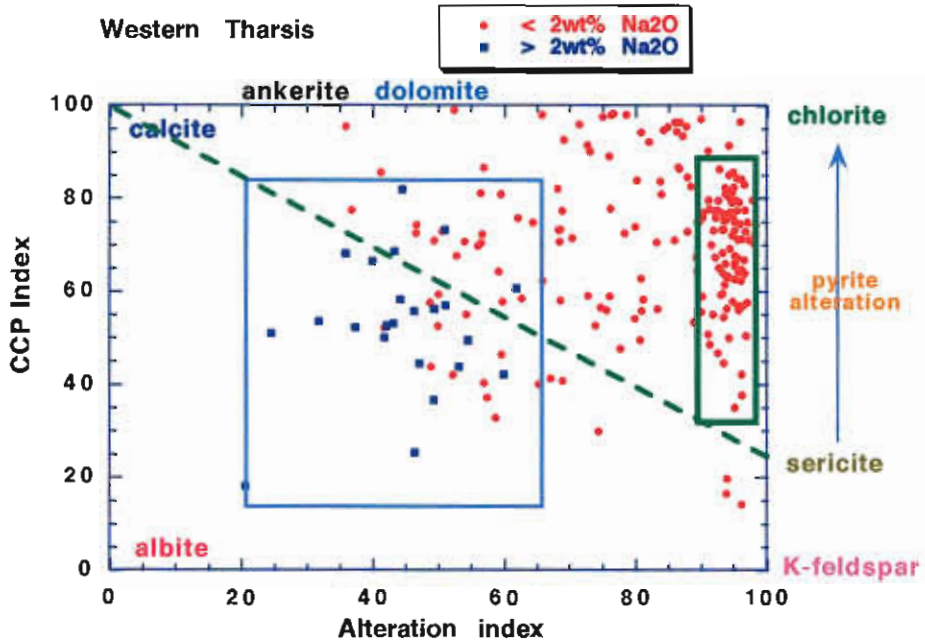

Figure 11. Western Tharsis alteration box plot (data from Huston and Kamprad, this volume) showing the dominant quartz + sericite ± chlorite ± pyrite (Trend 2) which forms the alteration halo within 200m of the ore zone.

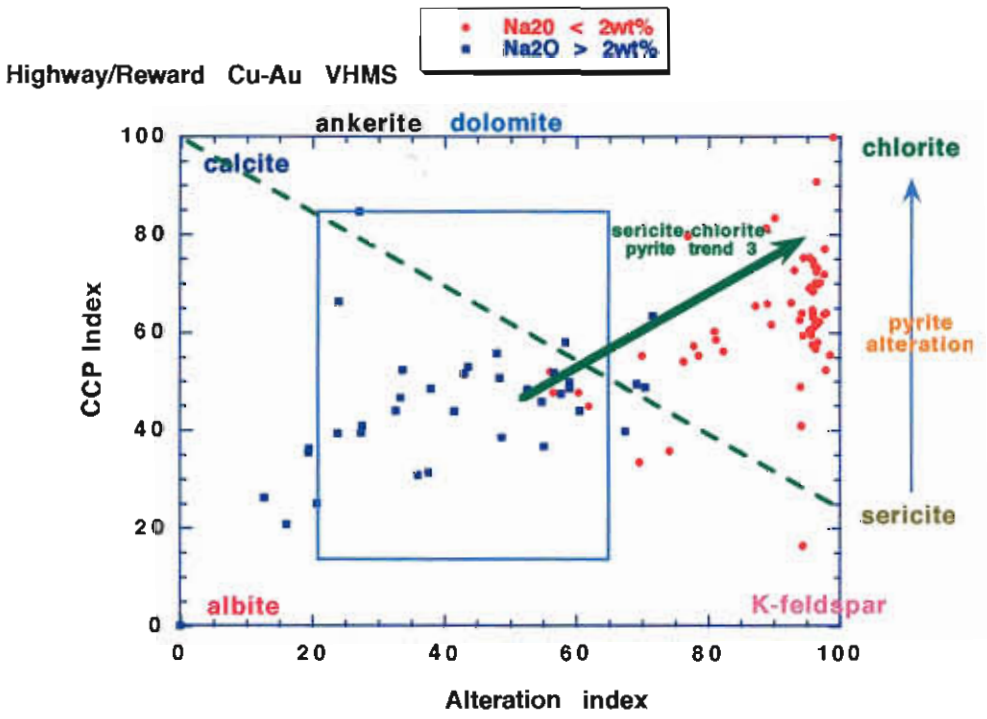

Figure 12. Highway-Reward alteration box plot showing a chlorite-sericite±pyrite alteration trend away from the unaltered field. This is an example of Trend 3 in Figure 9.

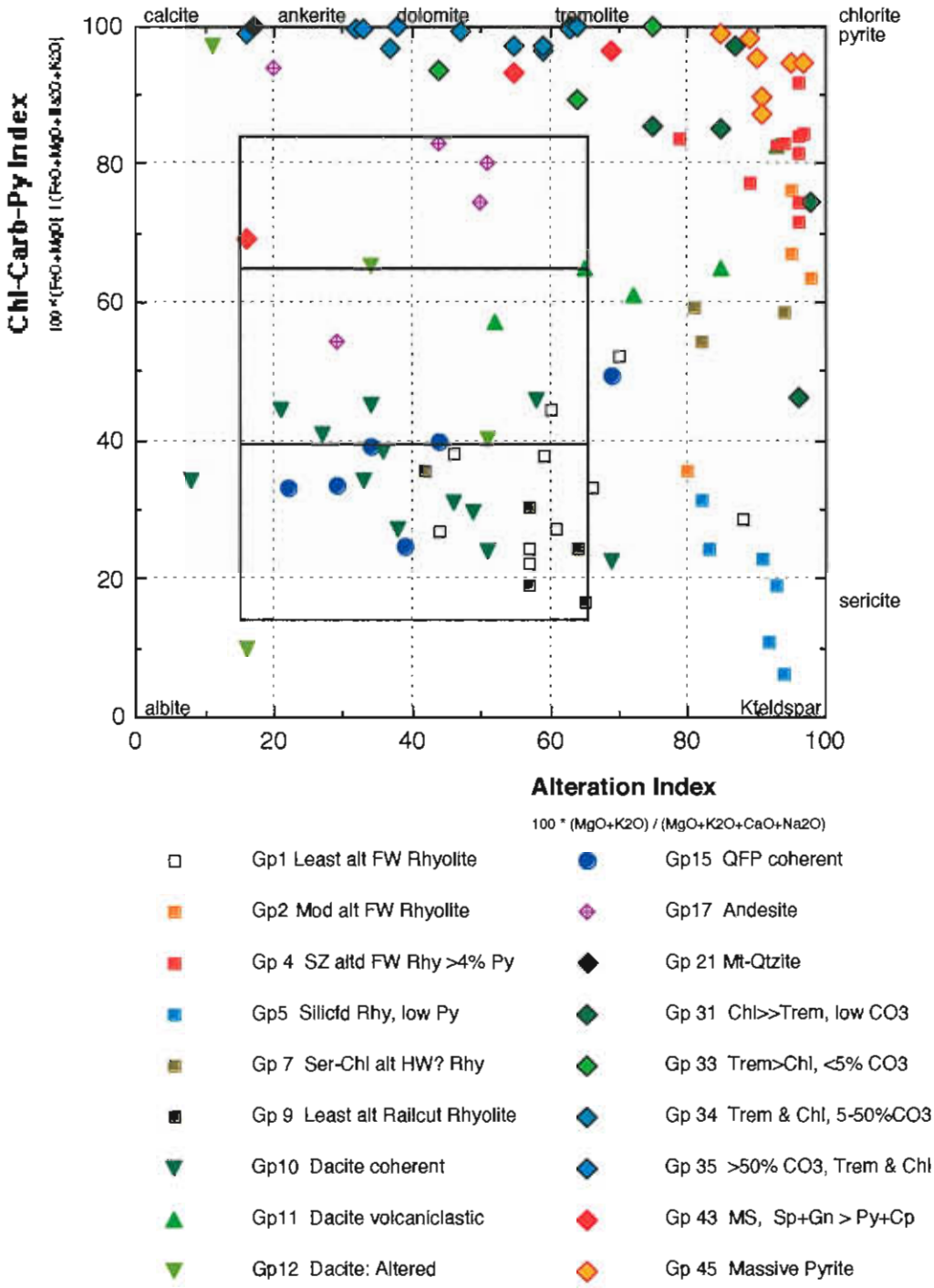

Figure 13. Thalanga alteration box plot showing the chlorite-carbonate (±tremolite) trend typical of a lateral ore zone position (Trend 4 in Fig. 9).

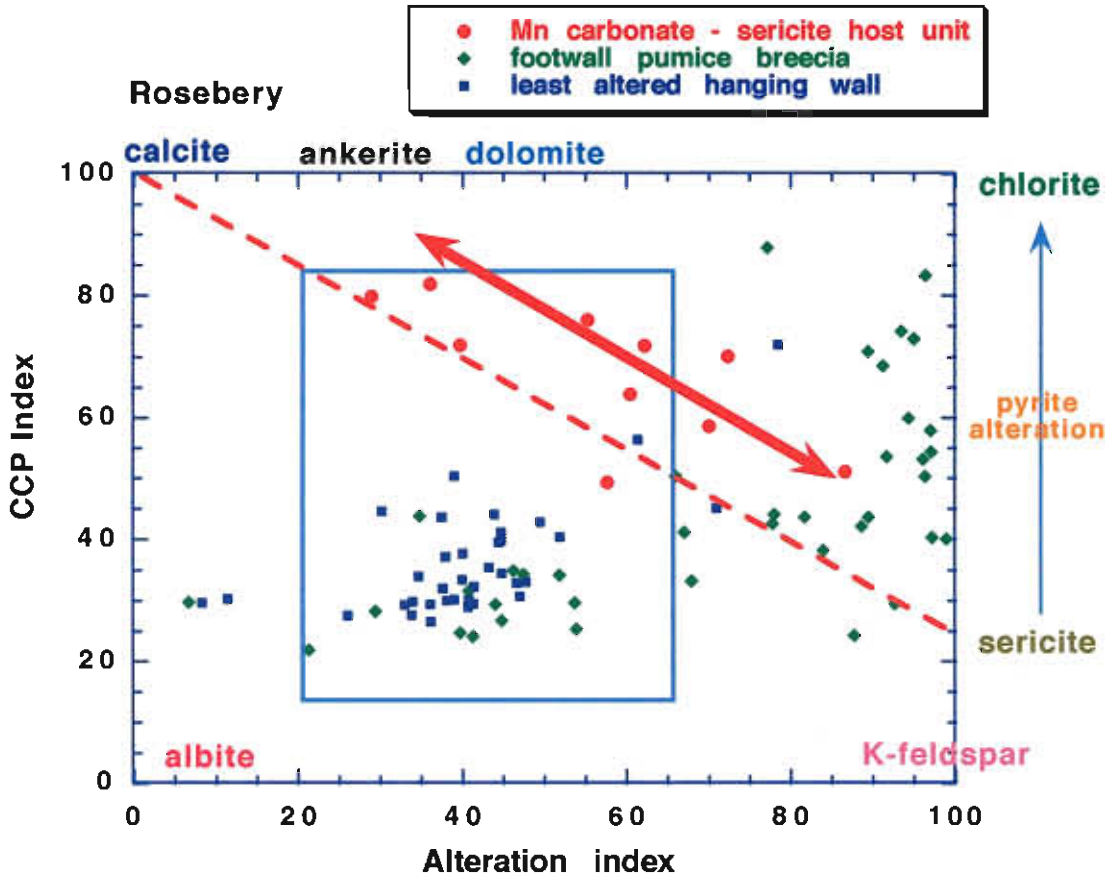

Figure 14. Trend of Mn carbonate-sericite alteration in the dacitic pumice breccia host horizon, Rosebery K lens (Trend 5 in Fig. 9).

Geochemical modelling of low temperature (5° to 150°C) seawater–andesite interaction: Implications for regional alteration assemblages in VHMS districts

Stephen B. Bodon and David R. Cooke
Centre for Ore Deposit Research

Summary

Our numerical simulations predict that diagenetic alteration occurs under oxidised conditions, within the hematite stability field. Results indicate that secondary K-feldspar will precipitate during seawater–andesite interaction from 5° to 75°C. K-feldspar precipitation causes the progressive decrease in ΣK^+ and increase in the Na^+/K^+ ratio in the evolving diagenetic pore water (modified seawater), coincident with decreasing pH. Low temperature K-metasomatism is predicted to result in enrichment of K and Mg, and depletion of Na, Ca and Si in the andesite.

From 75°C to limit of our heating simulations (150°C), Na-metasomatism occurs. Albite precipitation causes a progressive decrease in ΣNa^+ in the pore water coincident with decreasing pH and Na^+/K^+ ratios. Enrichment of Na and Mg, and depletion of Ca, Si and K are predicted to occur in the altered andesite. There is a narrow window at 75°C where K-feldspar and albite coexist in equilibrium. Overall, the whole-rock geochemistry predictions are close to actual variations measured in the felsic volcanics.

Increasing concentrations of Cu, Pb and Zn are predicted to occur in the pore waters throughout the simulation due to leaching of the andesite. This result indicates that Zn–Cu–(Pb)-bearing fluids can be produced by diagenetic alteration of andesites. Regional diagenetic alteration of the volcanic pile most likely contributes to the overall metal budget of mineralising solutions involved in the formation of massive sulphide deposits such as Hercules and Rosebery. In natural systems, metal concentrations and metal ratios in the mineralising solutions will depend on the initial metal contents of the host lithologies (i.e. the source rocks), and the ease by which each metal is stripped from them (ie. relative reactivity (kenetics) of pyroxenes versus feldspars, etc.).

Introduction

Water-rock interaction in submarine volcanic settings occurs under a wide range of conditions from low temperature (2°C) seafloor alteration to high temperature hydrothermal alteration ≥350°C (Muehlenbachs & Clayton, 1976; Seyfried & Bischoff, 1979; Guy et al., 1992). Much is known about the high temperature alteration processes, especially for basalt (Seyfried & Bischoff, 1981; Seyfried & Mottl, 1982; Campbell et al., 1988; Bowers, et al., 1988; and many others), yet a significant component of water-rock interaction occurs at lower temperatures from 2° to 150°C (Seyfried & Bischoff, 1979; Guy et al., 1992) under diagenetic conditions. Diagenetic alteration is intimately related to the prevailing regional geothermal gradient within the depositional basin, and ranges in temperature from ~0° to 5°C on the seafloor, to ~250°C at ~2–10 km depth (Allen, 1997). Due to this, diagenetic alteration patterns are typically characterised by flat-lying alteration zones comprised of particular mineral assemblages that formed within distinct temperature ranges. This temperature controlled mineral zonation pattern essentially defines a series of prograde diagenetic stages with depth.

Although resultant alteration minerals and their paragenetic relationships in volcanic rocks have been documented by many workers (e.g. Munhá et al., 1980; Henneberger & Browne, 1988; Ogihara, 1996;

Allen, 1997; Gifkins, 1997; and others), the processes of low temperature seawater-volcanic interaction have received little attention from a hydrothermal geochemical point of view. The experimental work of Seyfried & Bischoff (1979) on seawater-basalt interaction at 70°C and 150°C at low water–rock ratios (10), indicated that alteration produces minor loss of Mg, Na and K, and enrichment of Ca and $SiO_{2(aq)}$ in the seawater, with a concomitant gradual decrease in pH. Numerical modelling of seawater-basalt interaction at 25°C under variable water–rock ratios by Guy et al. (1992) also highlighted a decrease in Mg and Na, increase in Ca, and an initial decrease in pH followed by an increase to >9.0. The alteration paragenesis comprised early deposition of Mg-rich saponite (smectite), chlorite, gibbsite, geothite, pyrite and calcite, followed by Fe-enrichment of saponite and the deposition of phillipsite (K-rich zeolite). The compositional progression of the modified seawater and alteration minerals closely reflected those observed in the natural system they studied.

Observed diagenetic alteration sequences in felsic volcaniclastic rocks are generally consist of early smectite±opal alteration, followed by various stages of zeolite alteration that has been progressively replaced by adularia–quartz alteration, which in turn is replaced by albite at higher temperatures (Lagerblad & Gorbatschev, 1985; Henneberger & Browne, 1988; Ogihara, 1996; Allen, 1997). These alteration assemblages commonly form a vertical zonation pattern from early, shallow, low temperature smectite alteration assemblages to later, deeper, high temperature albite alteration assemblages with increasing depth. With regards to diagenetic alteration processes in the Cambrian Mount Read Volcanics, Tasmania, the typical observed overprinting relationships are early (low temperature?) smectite±opal alteration assemblages, followed by poorly preserved zeolite assemblages progressively replaced by K-feldspar alteration assemblages, which are overprinted by later (high temperature?) albite alteration assemblages (Allen, 1997). The conditions under which these alteration assemblages formed are not well understood, but are particularly important for gaining insights into the diagenetic processes that were occurring during and shortly after the accumulation of the volcanics.

Unlike previous low temperature studies of seawater-basalt interaction (Seyfried & Bischoff, 1979; Guy et al., 1992), this study aims to simulate the reaction progress of seawater-andesite interaction at variable water-rock ratios from 5° to 150°C, and determine at what stage K-feldspar alteration is replaced by albite as the major alkali-aluminosilicate alteration mineral. In addition, the capacity of seawater to leach metals from submarine volcanic rocks to form ore-forming fluids has been hypothesised and demonstrated experimentally at elevated temperatures ≥ 300°C (eg. Seyfried & Bischoff, 1981; Seyfried & Ding, 1995). However, the capacity of seawater to leach metals from seafloor volcanics during diagenesis has not been examined. Hence, this contribution also aims to examine to what degree seawater is capable of leaching metals from andesite and whether possible 'precursor' metal-bearing solutions are capable of forming during sub-seafloor diagenesis.

Method

Numerical modelling of seawater-andesite interaction was conducted using the computer codes SOLVEQ and CHILLER (Reed, 1982, Spycher & Reed, 1990). These programs can be used to calculate the distribution of aqueous species, heterogeneous reactions between solids and the aqueous phase, and changes in the temperature and bulk composition of a hydrothermal solution during water-rock interaction, heating and variety of other processes. SOLVEQ calculates the distribution of chemical species in an aqueous solution from the input of analytical data, and calculates the concentration (total molality) and activity of all ionic and molecular species for which thermodynamic data are available. Saturation indices for individual minerals are calculated to determine which phases are saturated, or undersaturated. Minerals and concentrations of aqueous species can be determined, suppressed, or constrained by forcing mineral equilibration with the fluid. Numerical simulations of transport and depositional processes are undertaken using CHILLER, which is capable of modelling several types of mass transfer scenarios (e.g. cooling, boiling, fluid mixing, water-rock interaction) via a series of incremental reaction path steps along the liquid-

vapour solidus, i.e. a reaction path that may be followed by an open, or closed system in equilibrium. Calculations in this study assumed an open system, such that precipitated minerals were removed from subsequent calculations as soon as they were precipitated. Such open system calculations are well-suited for modelling alteration assemblages produced by fluids percolating through a volcanic pile, because they accurately simulate natural systems.

Unfortunately, CHILLER and other similar computer codes are incapable of simultaneously modelling water-rock interaction and temperature changes (i.e. coupled heating and/or cooling, and water-rock interaction). To simulate coupled processes requires separate iterations of heating and water-rock interaction. Due to this limitation, results presented here involved a combination of step-wise heating (from 5° to 150°C), and water-rock interaction at predefined temperature increments. In practical terms, water-rock interaction was modelled by the addition of small predefined quantities (0.001–0.1 grams) of unaltered andesite into 1 kg of oxidised seawater at a starting temperature of 5°C. Calculations were conducted until a total of 1 gram of andesite had been added to the seawater. The resultant modified seawater was then heated from 5° to 25°C without any water-rock interaction. This 'heated' fluid was then used for the next water-rock simulation at a fixed temperature of 25°C. Step-wise heating and water-rock interaction simulations were repeated up to 150°C at increments of 25°C.

The components used in all calculations included:

- H^+ H_2O Cl^-
- HCO_3^- SO_4^{-2} $SiO_{2\,(aq)}$
- Al^{+3} Ca^{+2} Mg^{+2}
- Fe^{+2} Na^+ K^+
- Mn^{+2} Zn^{+2} Cu^+
- Pb^{+2} Ba^{+2} $O_{2\,(aq)}$ (oxidised fluid)

Initial compositions and thermodynamic data

As a prerequisite to the modelling, initial oxidised seawater and unaltered andesite compositions were selected. The composition of 'modern-day' oxidised seawater was taken from the published data of Drever (1982), and then equilibrated at 5°C and a pH of 8.1 to produce the final 'end-member' seawater composition used in the numerical simulations (Table 1). There are no 'pristine' Cambrian andesites preserved in the Mount Read Volcanics, Tasmania, due to pervasive post-depositional alteration, diagenesis and metamorphism. The composition of a least-altered andesite was taken from a single normalised whole-rock analysis obtained by Stolz & Large (1988; Table 2).

Guy et al. (1992) noted that alteration minerals produced during seawater–basalt interaction included phillipsite, mixed-layer chlorite and Fe-rich to Mg-rich saponite (tri-octahedral smectite). Allen (1997) also noted the existence of poorly preserved zeolites in felsic volcaniclastics hosting the Hercules and Rosebery massive sulphide deposits. To include these minerals in our calculations, the SOLTHERM thermodynamic database was modified to include thermodynamic data from 5° to 300°C for zeolites (phillipsite, stilbite) and smectites (beidellite, nontronite, saponite) from the Geochemist's Workbench software package (Bethke, 1994). Log K data at 25°C for montmorillonite was taken from Guy et al. (1992).

Results

Alteration minerals

Figure 1 illustrates the predicted sequence of mineral precipitation as log moles (mineral) versus reaction progress and temperature. Spikes in the data are artefacts of the method employed to simulate coupled heating and water-rock interaction. Our results predict that dolomite would be precipitated during the initial stages of seawater-andesite interaction at 5°C and up to a rock-water ratio (R:W) of 1.0 g/l (Fig. 1a). Calcite was precipitated over the full temperature interval (5°–150°C) and water-rock interaction (0.1–7.0 g/l R:W; Fig. 1a). K-feldspar was precipitated during the early stages of the simulation, and persisted up to 75°C and a R:W ratio of 4 g/l (Fig. 1b). Albite precipitated from 75° to 150°C, at R:W ratios between and 3.4 to 7 g/l. K-feldspar and albite precipitated together at 75°C, at R:W ratios between 3.4 to 4.0 g/l. Hematite and quartz were precipitated throughout the simulation (Fig. 1c). Witherite precipitated between 5° and 75°C, at R:W ratios of up to 4.0 g/l (Fig. 1d). At temperatures >75°C and at >4 g/l R:W, Ba^{+2} precipitated as barite.

Table 1. Modern-day oxidised seawater composition (after Drever, 1982), the final recalculated seawater composition at 5°C used for the water-rock simulations, and the final calculated seawater composition at 150°C after the simulations. All concentrations expressed as ppm with the exception of H_2O (kg).

	Oxidised seawater (5°C)	**Equilibrated seawater (5°C)**	**Final seawater composition (150°C)**
pH	8.1	8.1	7.96
$\log fO_2$	-2.69	-2.70	-22.90
H_2O	1 kg	1 kg	1kg
Cl^-	17383.4	20052.2	20052.2
SO_4^{-2}	2709.9	2808.7	2807.7
HCO_3^-	142.0	147.2	<u>7.3</u>
$SiO_{2(aq)}$	0.5	0.518	**231.29**
Al^{+3}	0.002	*0.0001*	**8.23**
Ca^{+2}	411.0	*163.5*	**276.03**
Mg^{+2}	1289.6	*7.9*	<u>1.9</u>
Fe^{+2}	0.002	*4.82 E-08*	**5.23**
K^+	399.0	413.3	<u>154.6</u>
Na^+	10760.0	13957.1	**13972.0**
Mn^{+2}	0.0002	0.0002	**6.56**
Zn^{+2}	0.002	0.002	**0.6089**
Cu^+	0.0005	0.0005	**0.0944**
Pb^{+2}	0.00003	0.00003	**0.05657**
Ba^{+2}	0.002	*0.002*	**0.207**
$O_{2(aq)}$	0.01	0.104	**0.748**

• Italicised text indicates total concentrations of component species that were calculated by forcing equilibration between the seawater and the following minerals: Al^{+3} – muscovite; Ca^{+2} – calcite; Mg^{+2} dolomite; Fe^{+2} – hematite; and Ba^{+2} – witherite. K^+ was 'indirectly' adjusted due to the forced equilibration of muscovite for Al^{+3}. Na^+ was adjusted to maintain charge balance in the equilibrated seawater.

• Bold text indicates increases in concentration for the final seawater composition in comparison to initial equilibrated seawater.

• Underlined text indicates decreases in concentration for the final seawater composition in comparison to initial equilibrated seawater.

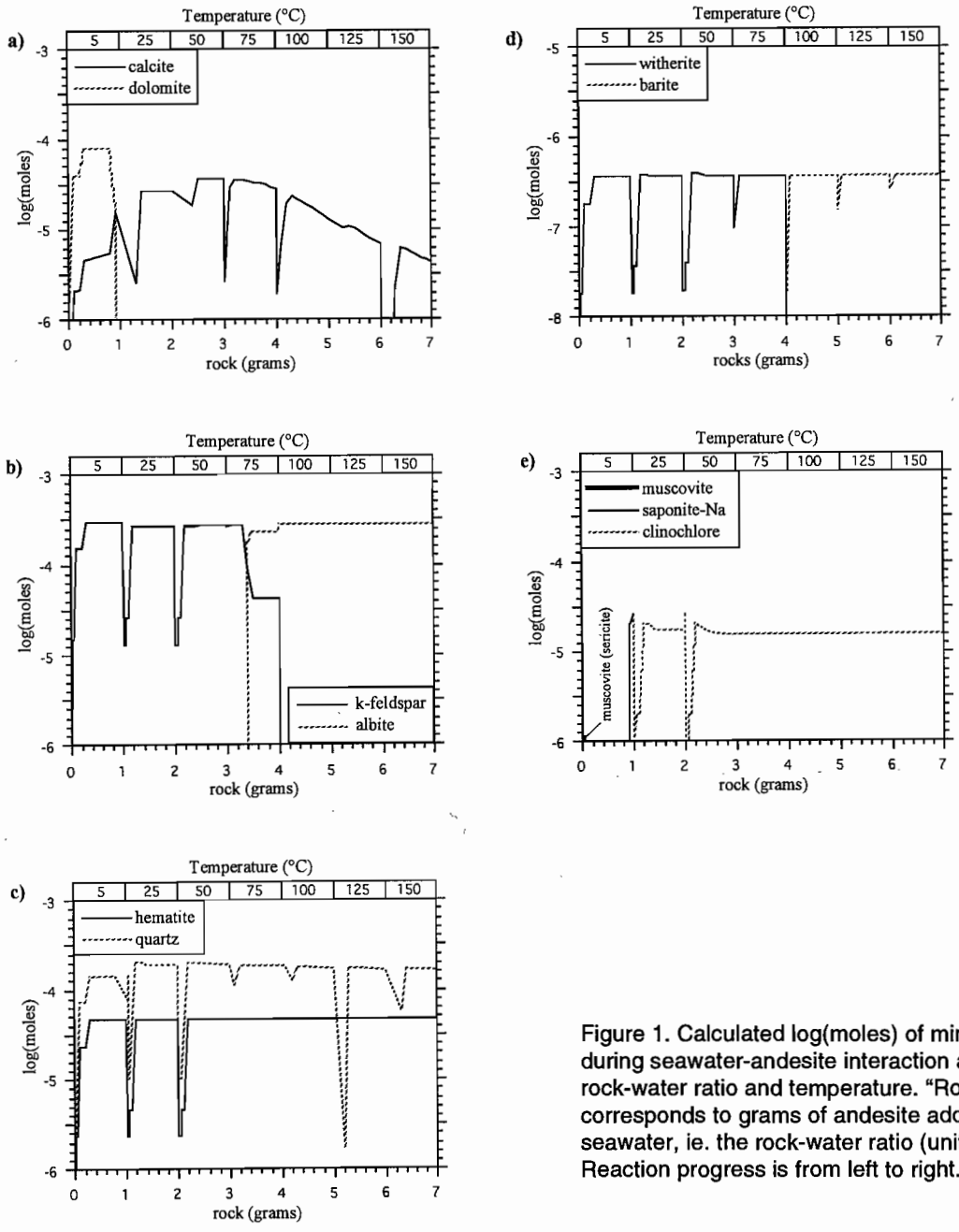

Figure 1. Calculated log(moles) of minerals precipitated during seawater-andesite interaction as a function of the rock-water ratio and temperature. "Rock (grams)" corresponds to grams of andesite added to 1 litre of seawater, ie. the rock-water ratio (units are grams/litre). Reaction progress is from left to right.

Muscovite precipitated in the very first stages of seawater-andesite interaction (5°C and up to 0.002 g/l R:W; Fig. 1e). Na-rich saponite precipitated at 5°C, between 0.9 to 1.0 g/l R:W, whereas clinochlore precipitated from 25°C to 150°C, corresponding to a R:W ratio of 1.0 to 7.0 g/l (Fig. 1e).

In general, the results indicate initial seafloor diagenetic alteration of andesite should be characterised by K-metasomatism, with early low temperature K-feldspar and quartz precipitated in conjunction with minor Na-rich saponite, dolomite, clinochlore, calcite, hematite, and trace muscovite (sericite) and witherite. At 75°C and 3.4 to 3.5 g/l R:W, there was an obvious 'switch-over' to Na-metasomatism manifested as albite-quartz and minor hematite, clinochlore, calcite and trace barite (Fig. 2). No zeolite minerals were precipitated during the calculations, possibly due to the low R:W ratios used, and the concentration of ΣHCO_3^- in the fluid (refer discussion).

Fluid composition

As the concentrations of elements are much higher in the andesite than seawater, the fluid chemistry provides a more accurate and sensitive measure of the evolving chemistry during metasomatism, whereas the rock typically records the combined effects of multiple metasomatic events. Hence, monitoring the progressive change in seawater composition during the simulation provides a means by which the metasomatic processes involved in seawater-andesite interaction can be fully appreciated.

Each modelled 1 g/l rock–water interaction at a fixed temperature, resulted in an ***increase*** in pH up to 0.4 log units (Fig. 3a). In contrast, the next 25°C heating step caused a ***decrease*** in pH of <0.6 log units. Obviously, the effects of water–rock interaction and heating compete with each other in terms of the

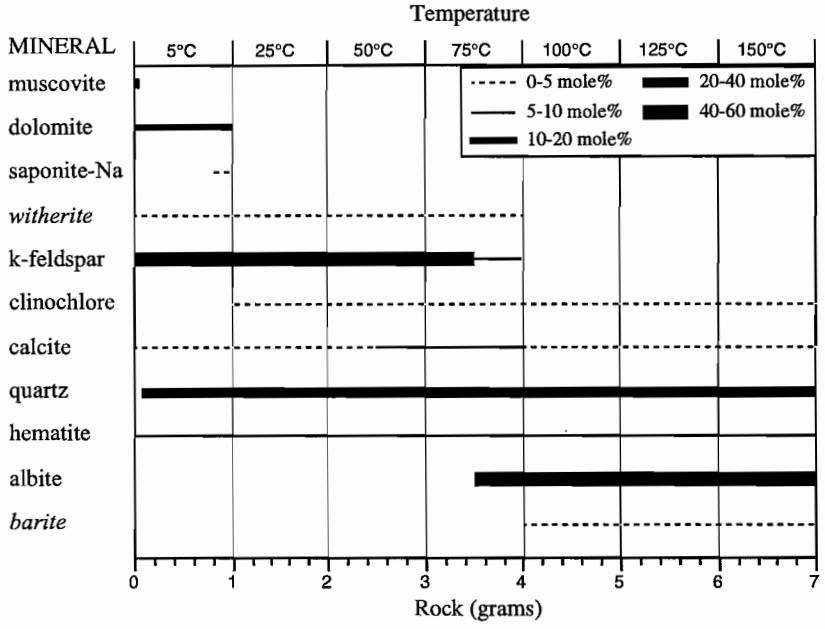

Figure 2. Summary of the calculated mineral paragenesis and mole% of minerals precipitated during seawater-andesite interaction as a function of the rock-water ratio and temperature. Minerals in *italicised* text constitute <1 mole%. "Rock (grams)" corresponds to grams of andesite added to 1 litre of seawater, ie. the rock-water ratio (units are grams/litre). Reaction progress is from left to right.

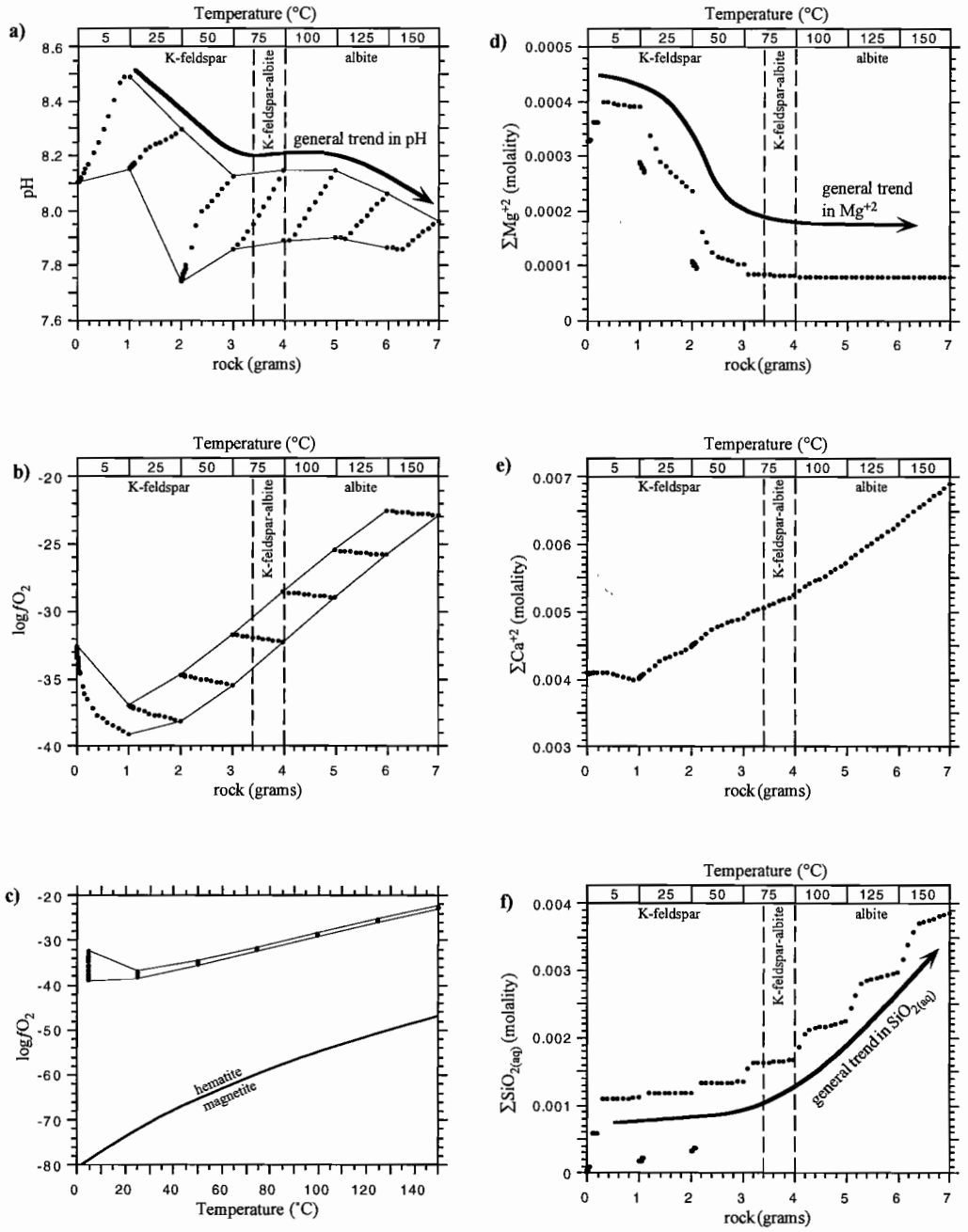

Figure 3. Evolution of the calculated pH, $\log fO_2$, oxidation state, and concentrations of total Mg^{+2}, Ca^{+2} and $SiO_{2(aq)}$ components in seawater during seawater–andesite interaction as a function of the reaction progress. K-feldspar, coexisting K-feldspar–albite, and albite precipitation regions have been superimposed on the plots except for c) that have the calculated stability fields of hematite (oxidised field) and magnetite (reduced field). "Rock (grams)" corresponds to grams of andesite added to 1 litre of seawater, ie. the rock-water ratio (units are grams/litre). Reaction progress is from left to right.

pH evolution of a water reacting with a submarine volcanic pile. For our simulation, plotting the ranges in pH for every water–rock interaction run as a function of overall reaction progress, highlights a general pH decrease from 5° to 50°C. This is followed by pH-buffering during the K-feldspar–albite transition, and finally by a second overall decrease in pH from 100° to 150°C (Fig. 3a). Taking the mid-point value for pH for each water-rock interaction step, the pH decreased from ~8.3 to ~7.9 from 5° to 150°C. It is worth emphasising that the gradient of the overall trend in pH values is controlled by the size of the heating steps versus the amount of water-rock interaction in each intervening step.

Figure 3c illustrates that the oxidation state of the fluid remained within hematite stability field throughout the simulation (i.e. an oxidised system), and explains why no sulphide precipitation occurred. Ranges in $\log fO_2$ for each water-rock interaction step highlights an overall steady increase with increasing temperature and R:W ratios from approximately –36 to –23 (Fig. 3b). At low R:W ratios in the 5°C step, initial reaction with the andesite produced a sharp decrease in $\log fO_2$ from –32.5 to –39 (Fig. 3c). Similar to the pH, the gradient of the overall trend in $\log fO_2$ is partly an artefact of the size of the heating steps versus the R:W ratio in each intervening step.

The ΣMg^{+2} component in the seawater decreases from ~0.0004 to ~0.0001 molal mostly between 5°C to 50°C and <3 g/l R:W due to the consumption of Mg from seawater to form dolomite, followed by later clinochlore (Fig. 3d). Between 75°C and 150°C (i.e. 3–7 g/l R:W) the concentration of ΣMg^{+2} remained steady at 0.000084 molal even though clinochlore continues to precipitate, and indicates rock buffering of the fluid with respect to the Mg concentration.

ΣCa^{+2} initially decreases during the 5°C iteration due to the co-precipitation of calcite and dolomite, but steadily increases to ~0.0069 molal after the cessation of dolomite formation at 5°C (Fig. 3e). This trend indicates that Ca is leached from the rock even though minor calcite precipitates, and that the concentration is controlled by the Ca budget within the andesite.

$\Sigma SiO_{2(aq)}$ component in the fluid has a similar increasing trend to ΣCa^{+2} (compare Fig. 3f to Fig. 3e). Consequently, the fluid progressively leaches SiO_2 from the andesite throughout the simulation, even though quartz is precipitated over the full temperature range of interest.

ΣHCO_3^- decreases sharply during the 5°C iteration due to the co-precipitation of calcite and dolomite, and then progressively decreases throughout the simulation once dolomite precipitation stops (Fig 4a). This trend indicates that dissolved CO_2 (i.e. the ΣHCO_3^- component) in the seawater is added to the andesite during precipitation of dolomite and calcite, and that amount of carbonate precipitation is controlled by the concentration of ΣHCO_3^- in the seawater. At higher rock-water ratios it likely that calcite precipitation will cease due to complete consumption of ΣHCO_3^- from seawater, and that once this stage is reached, the ΣHCO_3^- concentration in the seawater will subsequently be rock buffered.

ΣNa^+ in the modified seawater initially increases in concentration from 5°C to 100°C (up to 4.1 g/l R:W), followed by a steady decrease to the end of the simulation at 150°C (Fig. 4b). The initial increase is due to leaching of Na from the andesite, whereas the decreasing trend is due to the consumption of Na by the precipitation of albite. This contrasts with the initial decrease in ΣK^+ as K-feldspar is precipitated, followed by a steady increase in ΣK^+ after the K-feldspar–albite transition (Fig. 4c). The relationship between K-feldspar and albite is well illustrated by the Na^+/K^+ ratios in the fluid as a function of reaction progress and temperature (Fig. 4d). The early stages of seawater–andesite interaction are characterised by a steady increase in the Na^+/K^+ ratio due to loss of K^+ from the seawater during precipitation of K-feldspar. At 75°C and R:W ratios of 3.4 to 4.0 g/l, both K-feldspar and albite precipitation takes place and the Na^+/K^+ ratio reaches a maxima (225). From 100° to 150°C (i.e. R:W ratios of 4.0 to 7.0 g/l) the Na^+/K^+ ratio decreases as a response to albite precipitation. However, there was an overall net gain in ΣNa^+ (although minor) and loss in ΣK^+ concentrations in the final modified seawater composition (Table 2). These findings translate to an overall net loss in Na and gain in K for the altered andesite.

Figure 5 shows that the concentration of total dissolved metals in the fluid increases as a function of temperature and rock-water ratio. Steady leaching of metals from the andesite occurs throughout the simulation. ΣZn^{+2} attains a maximum concentration of 0.61 ppm in the fluid on completion of the

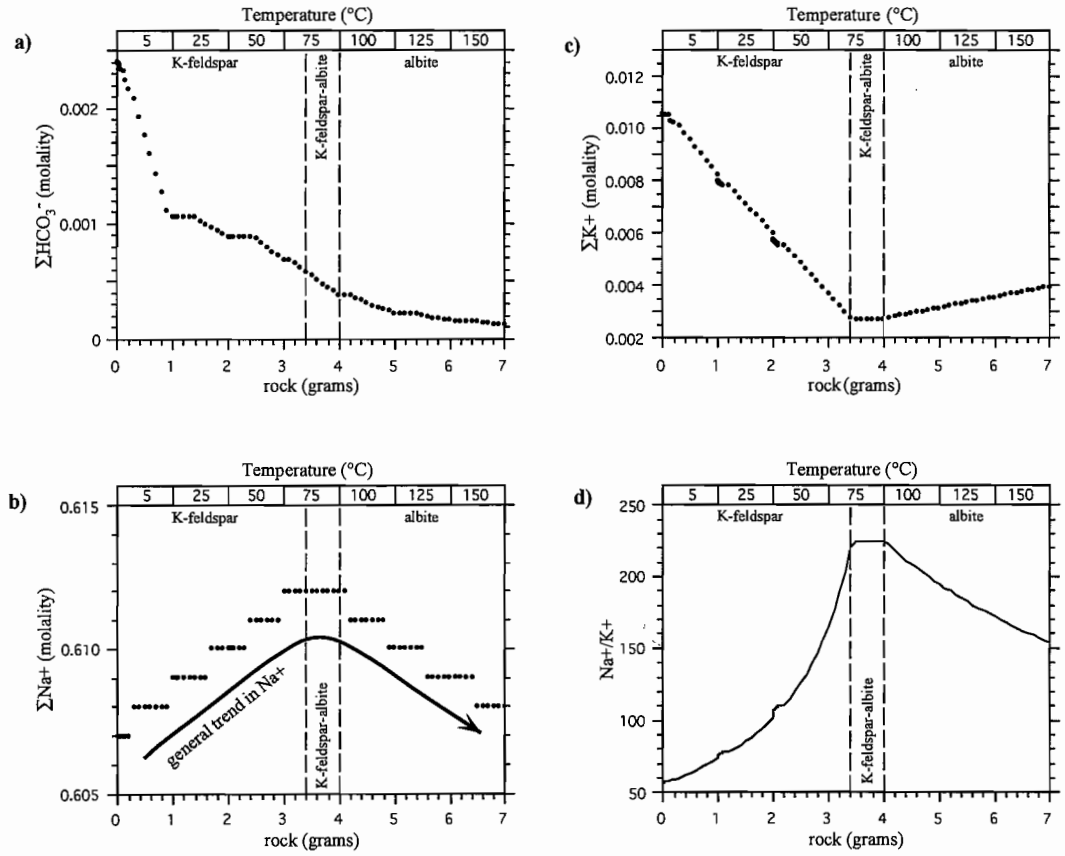

Figure 4. Evolution of the calculated concentrations of total HCO_3^-, Na^+ and K^+ components, and the evolution of the Na^+/K^+ ratio in the seawater during seawater–andesite interaction as a function of reaction progress. K-feldspar, coexisting K-feldspar–albite, and albite precipitation regions have been superimposed on the plots. "Rock (grams)" corresponds to grams of andesite added to 1 litre of seawater, ie. the rock-water ratio (units are grams/litre). Reaction progress is from left to right.

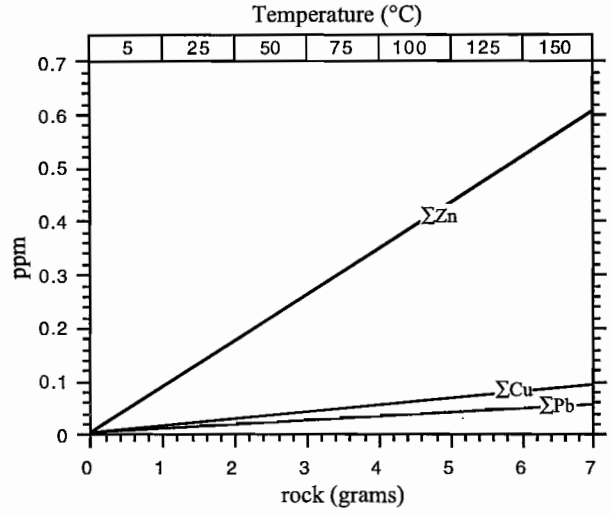

Figure 5. Evolution of the calculated concentrations of total Cu^+, Pb^{+2} and Zn^{+2} components in seawater during seawater–andesite interaction as a function of reaction progress. "Rock (grams)" corresponds to grams of andesite added to 1 litre of seawater, ie. the rock-water ratio (units are grams/litre). Reaction progress is from left to right.

Table 2. Normalised andesite composition from the Mount Read Volcanics adjacent to the Que River deposit (after Stolz & Large, 1988; sample no. QR1001/A). Trace element data (ppm) was converted to equivalent wt%. Other elements in the whole-rock analysis (e.g. TiO_2) were ignored and totals recalculated then normalised for the purpose of the water-rock interaction simulations. Ba was not analysed in the original whole-rock analysis, and a concentration of 500ppm was assumed on the basis of other whole-rock data from the Mount Read Volcanics.

	Andesite QR1001/A (wt%)	**Andesite QR1001/A normalised data (wt%)**
SiO_2	63.24	63.69
Al_2O_3	15.43	15.54
Fe_2O_3	7.41	7.46
MnO	0.12	0.12
MgO	3.09	3.11
CaO	3.53	3.56
Na_2O	4.49	4.52
K_2O	1.92	1.93
CuO	0.001502	0.001513
ZnO	0.01071	0.01079
PbO	0.000862	0.000868
BaO	0.05583	0.05622
TOTAL	**99.299**	**100.01**

calculations at 150°C. ΣPb^{+2} and ΣCu^{+} attain maximum concentrations of 0.057 ppm and 0.095 ppm respectively, due to their low concentrations in the andesite relative to zinc (Tables 1 and 2, and Fig. 5). Overall, base metal concentrations in the modified seawater are controlled by the initial composition of the andesite, and the amount of water-rock interaction that occurs (independent of temperature).

Other elements leached from the andesite (i.e. increased concentrations in the final modified seawater when compared to the initial equilibrated seawater composition) include Al, Fe, Mn and Ba (Table 2).

Discussion

Guy et al. (1992), defined an alteration paragenesis of early Mg-rich saponite (smectite), chlorite, gibbsite, geothite, pyrite and calcite, followed by Fe-enrichment of saponite and the deposition of phillipsite from numerical simulations of seawater-basalt interaction at 25°C under variable water–rock ratios. This was accompanied by a decrease in Mg and Na, increase in Ca, and an initial decrease in pH followed by an increase to >9.0 in the fluid phase. In contrast, the numerical simulations of seawater–andesite interaction presented here, predicts the formation of early K-feldspar alteration with minor quartz, hematite, chlorite, dolomite, calcite and Na-rich saponite, followed by albite alteration with minor quartz, hematite, chlorite and calcite. However, changes in the fluid chemistry with respect to Mg and Ca were similar to the results of Guy et al. (1992), but decreasing Na was observed only at temperatures ≥75°C, when Na-metasomatism occurred. Decreasing pH as a function of reaction progress was also predicted by the seawater-andesite interaction presented here, but an increase in pH during the latter stages of the reaction progress was not observed. These major differences in mineral assemblages and chemical evolution of the seawater are probably due to differences in the reaction paths assumed for each model. Hence, it is difficult to make meaningful comparisons between results presented here, and the work of Guy et al. (1992).

Diagenetic alteration in the felsic volcaniclastic succession (Mount Read Volcanics, Tasmania) hosting the Rosebery and Hercules massive sulphide deposits

is characterised by an initial alteration assemblage of smectite ± opal that was succeeded by various poorly preserved zeolite stages, a K-feldspar stage, and finally an albite stage (Allen, 1997). Our results do not predict an early smectite assemblage, with only minor smectite (Na-rich saponite) precipitated during K-metasomatism. Calcite, dolomite and trace witherite were predicted in the modelling, but do not comprise part of the diagenetic alteration assemblage observed by Allen (1997).

Furthermore, the modelling did not predict the precipitation of any zeolites. This feature essentially relates to the concentration of dissolved CO_2 in the seawater (ie. the ΣHCO_3^- component). As noted earlier, the ΣHCO_3^- decreases during our simulations presented here, due to carbonate (dominantly calcite) precipitation, and that once the ΣHCO_3^- has been consumed at higher rock–water ratios carbonate will cease to precipitate. At this stage, it possible that zeolite precipitation may occur due to the availability of Ca^{+2} in the fluid, i.e. Ca^{+2} from the fluid is available for the precipitation of zeolites when calcite precipitation ceases due lowering of the ΣHCO_3^- concentration in the fluid. Guy et al. (1992) noted that phillipsite did not precipitate until higher rock-water ratios >25 g/l had been attained when numerically modelling seawater-basalt interaction at 25°C. It is possible therefore, that greater rock–water ratios are required in the simulations to precipitate zeolites as alteration minerals. In addition, the temperature dependency on zeolites has not been fully explored in the modelling, and it possible that varying the temperature with respect to the rock-water ratio may promote zeolite precipitation, or possibly inhibit it. Such hypotheses remain speculative and require further detailed modelling by testing a diversity of scenarios to fully understand the physicochemical controls on the formation of zeolite assemblages.

The modelling predicted the occurrence of hematite and chlorite as sub-seafloor alteration products of andesite diagenesis. These minerals have been reported in association with diagenetic K-feldspar in felsic volcaniclastics of the Mount Black Volcanics (Gifkins, 1997).

Early K-feldspar and subsequent albite alteration stages defined by Allen (1997) were also successfully modelled. This feldspar transition is of particular importance because the presence or absence of one or the other, or even the coexistence of both alteration stages affects much of the whole-rock geochemistry. For example, K-metasomatism results in increased K, Al and depleted Na ± Ca ± Mg, whereas Na-metasomatism results in depleted K with a concomitant increase in Na (Allen, 1997; Gifkins, 1997). It is clear from the results of the modelling that the transition from K-feldspar to albite alteration assemblages is caused by K^+ and Na^+ exchange between rock and convecting seawater under oxidised conditions. K-feldspar alteration involves the exchange of K^+ in seawater for Na^+ in the rock to maintain charge balance within the seawater component. This exchange results in K enrichment and Na depletion in the rock and vice versa for the modified seawater. At higher temperatures (≥75°C), Na^+ from seawater is exchanged for K^+ in the rock resulting in late stage albite precipitation, and Na enrichment and K depletion in the rock and vice-versa for the modified seawater. However, the data suggest that at least some K enrichment could be preserved in albite altered rocks (Table 2; Fig. 4c). These relationships are illustrated by the evolution of the Na^+/K^+ ratio in the fluid as a function of reaction progress (Fig. 4d), as well as the whole-rock geochemistry. Lagerblad & Gorbatschev (1985) also attributed feldspar alteration to alkali exchange between glassy volcanic rocks and seawater convecting through the volcanic edifice, and considered that at greater depths in the volcanic pile exchange of K for Na in the rock to form albite alteration occurred at temperatures >150°C. Other studies estimated that K-metasomatism occurred up to 190°C, but typically below 150°C (Munhá et al., 1980; Henneberger & Browne, 1988), and that Na-metasomatism took place at temperatures >150°C (Munhá et al., 1980), and up to ≥250°C (Allen, 1997). Results from our modelling indicate that the K-feldspar–albite transition may occur at temperatures as low as 75°C.

The observed Ca depletion in K-feldspar altered rocks (Allen, 1997; Gifkins, 1997) was accurately predicted by the modelling, as Ca from the rock is continually leached by the fluid at temperatures ≥25°C, even though minor concurrent calcite precipitation took place. However, the observed depletion in Mg was not predicted by the water-rock

modelling; infact, Mg enrichment in the rock was predicted due to the precipitation of dolomite and clinochlore during K-metasomatism. The concentration of the ΣMg^{+2} component in the fluid phase remained constant during the Na-metasomatism, even though clinochlore was precipitated, indicating that elevated Mg concentrations in the rock remained constant. Overall, the modelling suggests that no Mg depletion should occur in K-feldspar and albite-altered rocks.

The concentration of total dissolved metals in the modified seawater increased as a function of reaction progress. These results confirm that diagenetic fluids (i.e. seawater) have the capacity to leach metals in sufficient concentrations to produce low temperature 'precursor' Zn–Cu–(Pb)-bearing hydrothermal fluids that may play a significant role in the overall metal budget during the formation of massive sulphide deposits. In reality, metal concentrations and metal ratios in the evolving seawater will depend on the initial metal contents of the host lithologies, and the ease by which each metal is stripped from the host rocks. This is partly a function of the relative reactivity (kinetics) of minerals that contain trace metals (e.g. pyroxenes vs feldspars, etc.), and partly a function of textures (porphyritic, fine grained vs. coarse-grained, fractured, etc.), which control access of fluids to the sites where metals reside within the rocks.

Conclusions

Alteration assemblages and mineral paragenesis predicted by numerical modelling of seawater-andesite interaction from 5° to 150°C and rock-water ratios up to 7.0 g/l, generally coincide with observed diagenetic assemblages and paragenetic sequences in felsic volcaniclastics hosting the Hercules and Rosebery massive sulphide deposits. Differences in the mineral assemblages are attributed to the assumed reaction pathway (i.e. temperature and water-rock ratio) used in the modelling, as well as the whole-rock geochemistry of the rock modelled (i.e. andesite versus rhyolite). Further simulations of various scenarios involving various rock types and reaction pathways (temperature rates, water-rock ratios, reaction rates, etc.) are required to fully assess the spectrum of possible diagenetic alteration assemblages and their paragenetic relationships, as well as the associated chemical evolution of seawater and rock.

From the numerical simulations, early K-metasomatism occurs up to 75°C and is produced by the exchange of K^+ in seawater for Na^+ in the rock under oxidised conditions and decreasing pH. Rocks that have undergone K-metasomatism should be enriched in K and Mg, and depleted in Na, Ca and Si. Na-metasomatism occurs at temperatures ≥75°C, and results from the exchange of Na^+ in seawater for K^+ in the rock under oxidised conditions and decreasing pH. The modelling predicts an enrichment in Na and Mg, and depletion in Ca, Si and K for albite-altered rocks. Overall, the whole-rock geochemistry predictions are close to actual variations measured in felsic rocks. However, the predicted enrichment in Mg differs from the reported Mg depletion in diagenetically altered felsic volcaniclastics.

The results confirm that low temperature Zn–Cu–Pb-bearing fluids can be produced by leaching of submarine volcanics during diagenesis. It is therefore likely that evolved seawater associated with regional diagenesis contributes to the metal budget of mineralising solutions involved in the formation of massive sulphide deposits such as Hercules and Rosebery.

References

Allen, R.L., 1997, Rosebery alteration study and regional alteration studies in the Mount Read Volcanics: the record of diagenetic alteration in the strongly defo'med, felsic volcaniclastic succession enclosing the Rosebery and Hercules massive sulphide deposits: Centre for Ore Deposit and Exploration Studies, University of Tasmania, AMIRA/ARC project P439, Report 5, p. 135-145.

Bethke, C.M., 1994, The Geochemist's Workbench — a users guide to Rxn, Act2, Tact, React and Gtplot: University of Illinios, Hydrogeology Program, 213 p.

Bowers, T.S., Campbell, A.C., Measures, C.I., Spivack, A.J., Khadem, M. and Edmond, J.M., 1988, Chemical controls on the composition of vent fluids at 13°-11°N and 21°N, East Pacific Rise: Journal of Geophysical Research, 93, p. 4522-4536.

Campbell, A.C., Bowers, T.S., Measures, C.I., Falkner, K.K., Khadem, M. and Edmond, J.M., 1988, A time series of vent fluid composition from 21°N East Pacific Rise (1979, 1981, 1985), and the Guyamas Basin, Gulf of California (1982, 1985): Journal of Geophysical Research, 93, p. 4537-4549.

Drever, J.I., 1982, The geochemistry of natural waters: Prentice-Hall, New Jersey, 234 p.

Gifkins, C., 1997, Background alteration in the Mount Black Volcanics: textures mineralogy and geochemistry: Centre for Ore Deposit and Exploration Studies, University of Tasmania, AMIRA/ARC project P439, Report 5, p. 85-127.

Guy, G., Schott, J., Destrigneville, C. and Chiappini, R., 1992, Low-temperature alteration of basalt by interstitial seawater, Mururoa, French Polynesia: Geochimica et Cosmochimica Acta, 56, p. 4169-4189.

Henneberger, R.C. and Browne, P.R.L., 1988, Hydrothermal alteration and evolution of the Ohakuri hydrothermal system, Taupo Volcanic Zone, New Zealand: Journal of Volcanology and Geothermal Research, 34, p. 211-231.

Lagerblad, B. and Gorbatschev, R., 1985, Hydrothermal alteration as a control of regional geochemistry and ore formation in the central Baltic Shield: Geologische Rundschau, 74, p. 33-49.

Ogihara, S., 1996, Diagenetic transformation of clinoptilolite to analcime in silicic tuffs of Hokkaido, Japan: Mineralium Deposita, 31, p.548-553.

Muehlenbachs, K and Clayton, R.N., 1976, Oxygen isotope composition of the oceanic crust and its bearing on seawater: Journal of Geophysical Research, 81, p. 4365-4369.

Munhá, J., Fyfe, W.S. and Kerrich, R., 1980, Adularia, the characteristic mineral of felsic spilites: Contributions to Mineralogy and Petrology, 75, p. 15-19.

Reed, M.H., 1982, Calculation of multicomponent chemical equilibria and reaction processes in systems involving minerals, gases and an aqueous phase: Geochimica et Cosmochimica Acta, 46, p. 513-528.

Seyfried, W.E., and Bischoff, J.L., 1979, Low temperature basalt alteration by seawater: and experimental study at 70°C and 150°C: Geochimica et Cosmochimica Acta, 43, p.1937-1947.

Seyfried, W.E., and Bischoff, J.L., 1981, Experimental basalt-seawater interaction at 300°C, 500 bars, chemical exchange, secondary mineral formation and implications for the transport of heavy metals: Geochimica et Cosmochimica Acta, 45, p. 135-149.

Seyfried, W.E. and Ding, K., 1995, Phase equilibria in subseafloor hydrothermal systems: a review of the role of redox, temperature, pH and dissolved Cl on the chemistry of hot spring fluids at mid-ocean ridges, in Humphris et al., eds., Seafloor Hydrothermal Systems, Physical, Chemical, Biological and Geological Interactions: Geophysical Monograph 91, American Geophysical Union, p. 248-272.

Seyfried, W.E. and Mottl, M.J., 1982, Hydrothermal alteration of basalt by seawater under seawater-dominated conditions: Geochimica et Cosmochimica Acta, 46, p. 985-1002.

Spycher, N.F. and Reed, M.H., 1990, Users guide for CHILLER: a program for computing water-rock reactions, boiling, mixing and other reaction processes in aqueous-mineral-gas systems: University of Oregon, unpublished.

Stolz, J. and Large, R.R., 1988, The source of the gold in the western Tasmanian VMS deposits: Geology Department, University of Tasmania, AMIRA Project 84/P210, Final Report, p. 71-135.

Application of ironstone geochemistry to exploration for VHMS deposits in the Mt Windsor Volcanic Belt

Garry Davidson
Centre for Ore Deposit Research

Summary

This study evaluated the exploration vector potential of some iron silica deposits in the Cambro-Ordovician Mount Windsor Volcanic Belt, Queensland, complementing a similar study in the Highway-Reward area (Doyle 1997). "Ironstones", jaspilites, ferruginous cherts, barite lenses, and other styles of chemical sedimentation are generally used in exploration as stratigraphic markers for hydrothermal activity, however, their geochemistry suggests they can be far more useful than this.

Near-ore and "barren" ironstones were geochemically and texturally compared. The near-ore samples came from 3 ironstone lenses near Thalanga, very close to recently discovered base metal mineralisation, and from the Magpie area SE of Charters Towers. Barren ironstones were obtained from the Britannia and Sunrise Spur areas at the Trooper Creek Fm-Rollston Range Fm contact. The approach was to build on previous reconnaissance work by Nathan Duhig and Joe Stolz (Duhig et al. 1992), by analysing members of these two ironstone groups in detail to determine their internal chemical variability. Numbers of samples varied from 3 to 19/lens, depending on the size of the body. Sample spacing was 5–20 m across the strike of each stratiform ironstone; 20 m was determined to be the optimum spacing.

In all ironstones examined, regardless of scale, the dominant textural characteristic is early massive to inhomogeneous iron-silica deposition, overprinted by several generations of veining, in most cases becoming more silicic and metal-rich with time. However, the later generations of veining do not extend across the entire early ironstone, but tend to be more focussed around one or more smaller areas, creating more confined geochemical anomalies within the ironstone. The vein networks forming the ironstones are commonly fine and difficult to observe on uncut surfaces. This has given rise to the premise that ironstones are geochemically massive because at first sight they are texturally massive, but this is not the case. Crucially, apparently barren ironstones may contain a smaller "near-ore" signature zone, requiring very careful screening of ironstone geochemistry.

The ironstones can be genetically divided into three stages, which are not all always present:

- *Stage 1* involved low temperature to microbial and inorganic precipitation of iron oxyhydroxides,and colloidal silica directly over zones of diffuse upflow.
- *Stage 2* involved selective overprinting of Stage 1 deposits by fine chert/quartz goethite networks. Geochemically these zones were more silica-rich than Stage 1 products, also containing higher base metals, As, Mo, Ba, Se, Cd and Bi. Hydrothermal REE patterns were similar to Stage 1, with LREE-enrichment and -Eu anomalies. Oxygen isotope measurements of quartz indicate that the temperature of deposition was between 85 and 190°C.
- *Stage 3* mainly characterised near-ore ironstones, and involved the formation of localised zones of barite-quartz veins, disseminated barite concentrations at % levels, elevated base-metals, and strong +Eu anomalies. The temperature of vein quartz deposition of this stage in the Thalanga and Magpie areas was between 127 and 277° C, on the basis of oxygen isotopes and an assumed broad range of potential initial water values. This unusual tendency of systems to "shrink" as they evolved to higher temperature may have reflected local heating cycles that were quickly exhausted, or

possibly was a symptom of the choking of general crustal permeability by mineral precipitation and its refocussing into one or more major channelways which formed massive sulfide deposits.

The following geochemical associations are correlated with increasing temperature in ironstones and are useful in separating near-ore from barren ironstones. Broadly this folows an evolution from Fe-Si, to Fe-Si-Ba, to Fe-Si-Ba-+Eu±base metals, to Si-Ba-±Eu-base metals±Fe:

Stage 1: $Fe_2O_3(T)/(Fe_2O_3(T) + SiO_2)$= 0.15–0.35, U >0.2 ppm, P_2O_5 < 0.03 wt. %, Cu+Pb+Zn <20 ppm (in weathered samples), Cu/Cu+Pb+Zn =0.2–0.5, Zn/Cu+Pb+Zn = 0.2–0.45, Ba may be up to 800 ppm but is mainly <250 ppm, Ba/Cu+Pb+Zn variable from <1 to >50 (because the stage includes Ba-rich but base-metal poor ironstones towards higher temperatures), As < 10ppm, Sb -4–6 ppm, Mo < 5 ppm, -Eu anomalies, strong -Ce anomalies.

Stage 2: $Fe_2O_3(T)/(Fe_2O_3(T) + SiO_2)$= 0.05–0.15 but locally massive hematite around veins or coalesced veins, U <0.2 ppm, P_2O_5 > 0.03 wt. %, Cu+Pb+Zn =20–200 ppm (in weathered samples), Cu/Cu+Pb+Zn =0.2–0.5, Zn/Cu+Pb+Zn = 0.2–0.45, Ba may be up to ~2000 ppm, , Ba/Cu+Pb+Zn >15, -Eu anomalies, -Ce anomalies, As =20–80 ppm, Sb up to 10 ppm, sporadic Mo up to 20 ppm; La_N/Sm_N is a highly variable 2.95–18.31; ΣREE of 20–60, with some samples up to 150 ppm; Na_2O/K_2O <1, $\delta^{18}O_{qutz\ vns}$>14‰.

Stage 3: $Fe_2O_3(T)/(Fe_2O_3(T) + SiO_2)$= <0.20, mainly <10; Se >1 ppm, Cu+Pb+Zn >100 ppm, Cu/Cu+Pb+Zn =0.0–0.9, Zn/Cu+Pb+Zn = 0.0–0.8, Ba >500 ppm, Ba/Cu+Pb+Zn <15 with the exception of barite lenses, MnO> As <30 ppm, Na_2O/K_2O <0.35–8.7, $\delta^{18}O_{qutz\ vns}$<14‰, La_N/Sm_N 2–7; ΣREE <20 ppm although exceptions occur (see Duhig et al. 1992), +Eu anomalies, P_2O_5>0.03 wt %, U>1 ppm, Mo <5 ppm.

In summarising this data, the key parameters for the recognition of populations of near-ore ironstones in the MWVB are (1) +Eu; (2) Ba >500 ppm; (3) Cu+Pb+Zn >100 ppm; (4) Se > 1ppm; (5) Ba/Cu+Pb+Zn < 15, (6) $Fe_2O_3(T)/(Fe_2O_3(T) + SiO_2)$= <0.20; (7) a trend of increasing Mn in a given population. In analysing ironstones, care should be taken to use an ICP technique with very high resolution, because some elements of interest occur at the 0.01–0.1 ppm level.

Contents

Background

In 1992 a broad study of the Mt Windsor silica iron deposits (Fig. 1a) documented their general geology, geochemistry, and probable means of accumulation (Duhig 1990, Duhig et al. 1992a, 1992b). In particular this study determined that (1) microbial organisms played an important role in iron deposition, and (2) much of the non-microbial fabrics were consistent with crystallisation of silica gels in open space, to produce silica spheroid fabrics. Some spheroids show evidence of infiltration by microbial organisms as they developed. Unlike many of the world's "exhalitive" horizons, the Mt Windsor examples represent near-pure chemical precipitation sites, characterised by very low levels of detrital elements such as Al, Ti and Zr. In this respect Duhig et al. (1992) found them to be most similar to oxidised Cretaceous cherts from the west Pacific (Adachi et al. 1986). They contrast sharply with well-known exhalite examples such as the Japanese Kuroko district Tetsusekiei, the Key Tuffite of the Canadian Matagami district, and the Main Contact Tuff, Millenbach Mine, Noranda, which are all characterised by very significant abundances of altered hostrock intimately intermixed with a chemical component (Kalogeropoulos & Scott 1983, Kalogeropoulos & Scott 1988, Liaghat & MacLean 1992), forming compact silicic lenses close to massive suphide ore (descriptions of the Handcuff chert, stratigraphically equivalent to base metal mineralisation at Handcuff in the MWVB, resemble these examples; Berry et al. 1992). During the term of the current project Doyle (1997) has found that silica-iron bodies in some areas of the Mt Windsor Volcanic Belt (e.g., Reward) also show evidence of significant hostrock assimilation or replacement, giving rise to a suite of distinctive textural characters in thin-section. In places these are consistent with sub-surface replacement of glassy coherent to pumiceous felsic volcanic precursors, and in others a component of growth in open-space is indicated. It seems probable that Mt Windsor iron silica bodies grew in a variety of surficial to sub-surface settings, both by open growth beneath an oxidised water column, and by replacement and infill of glassy rocks to as yet undetermined depths, with and without microbial assistance. This report only explores some geochemical aspects of this genetic diversity, with emphasis on those parameters that indicate the proximity of VHMS deposits.

Following the Duhig study, a detailed geochemical investigation of two barren ironstones in the MWVB was undertaken (Davidson et al. 1993), with the aim of determining the source components of such bodies. The "barren ironstone" database and interpretation used in the current study derives from this earlier work, and consequently does not fall within the confidentiality limits of this AMIRA project. The preliminary results of the 1993 investigation were reported to the AMIRA group at commencement of the project as the basis for further investigation, and it is very encouraging to observe that industry immediately saw the potential of the work, and in some ways out-distanced the research in its application of the concepts to iron silica bodies throughout the MWVB over the last three years. For instance, it seems that ironstone geochemistry was one of the tools which pinpointed a blind zone of mineralisation (referred to throughout as Thalanga west 45) ~1.8 km west ofthe Thalanga deposit. The most useful concept for exploration was the realisation in 1993 that near-ore iron silica bodies have a distinct rare earth element (REE) signature (the +Eu character identified by Duhig et al. 1992a for some Thalanga jaspilites) compared to "barren" systems in the MWVB. This was not detected in the earlier Duhig study because of high detection limits for REE using XRF methods. Subsequently Doyle (1997) also found that REE were useful near-ore indicators for replacement ironstones in the Reward area.

Following the exploration successes of earlier work, this study has aimed to refine the use of iron-silica deposit geochemistry as an exploration vector in the Mount Windsor Volcanic Belt. The scope of the study is comparitive analysis of near-ore ironstones at Thalanga and Magpie, to barren ironstones at Britannia and Sunrise Spur (Areas 1 and 2 in Fig. 1a).

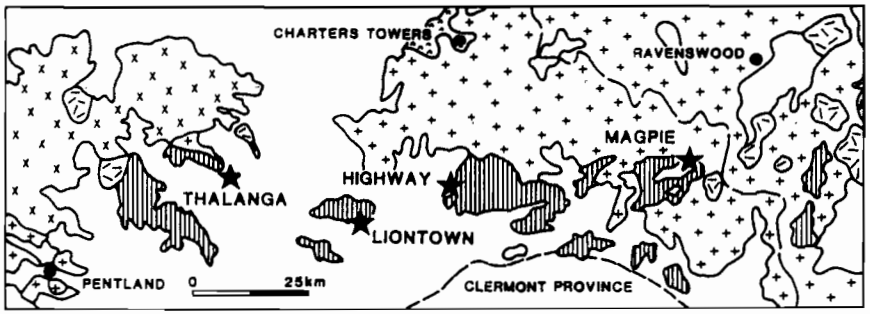

LEGEND

CAINOZOIC		Basalt, laterite and alluvial sediments
PERMO-CARBONIFEROUS		Acid intrusives and extrusives
SILURO-DEVONIAN		Granitoids
ORDOVICIAN		Granitoids
CAMBRIAN-ORDOVICIAN		Acid intermediate volcanics, volcaniclastics and marine strata (Seventy Mile Range Group)

TERTIARY–TRIASSIC

Younger cover rocks; sands, grits, gravels

DEVONIAN–ORDOVICIAN

Granitoids of the Lolworth–Ravenswood batholith

ORDOVICIAN–CAMBRIAN

Rollston Range Formation — siltstone, greywacke, minor volcaniclastics and dacitic volcanics

Trooper Creek Formation — Rhyolitic, dacitic and andesitic volcanics and volcaniclastics; psammitic, pelitic and calcareous rocks, minor doleritic intrusives

Mt Windsor Formation — Rhyolitic volcanics and volcaniclastics

CAMBRIAN

Puddler Creek Formation — Greywacke, siltstones, andesitic volcanics and intrusives

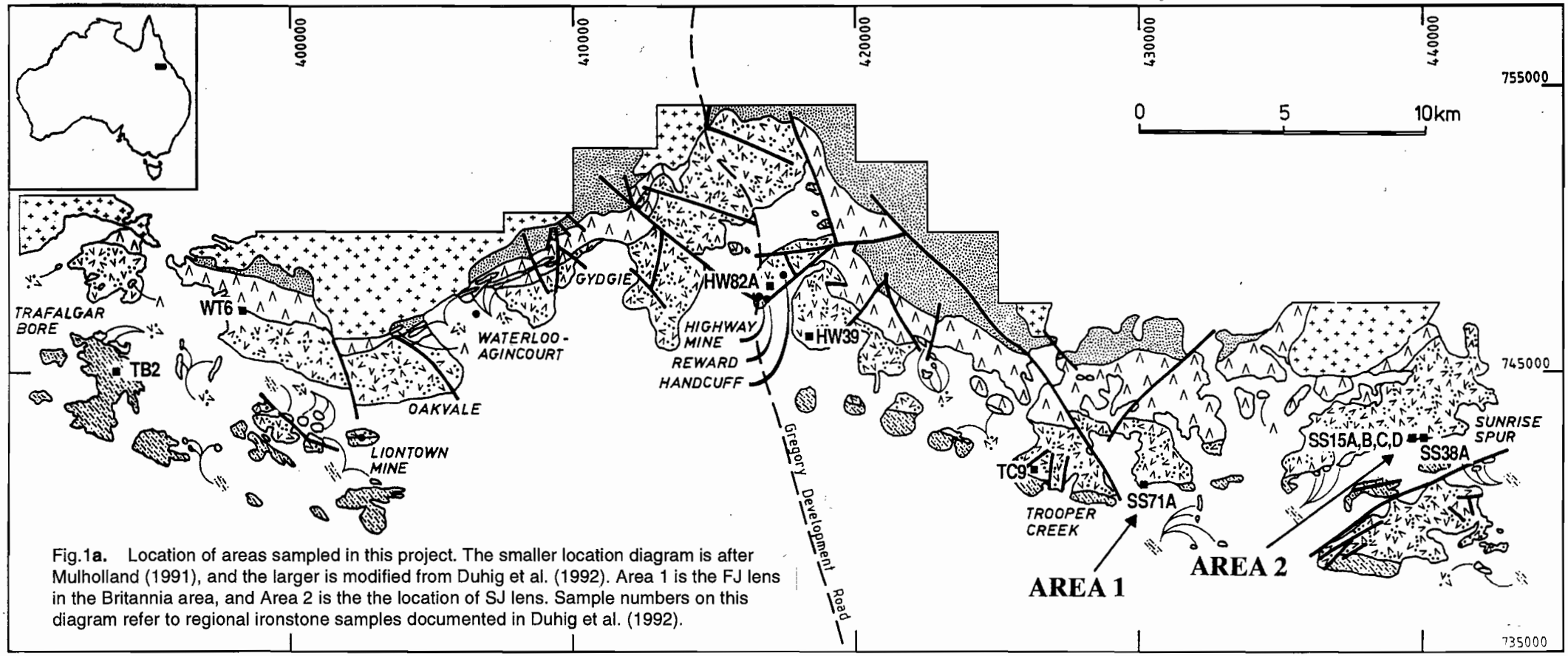

Fig.1**a.** Location of areas sampled in this project. The smaller location diagram is after Mulholland (1991), and the larger is modified from Duhig et al. (1992). Area 1 is the FJ lens in the Britannia area, and Area 2 is the the location of SJ lens. Sample numbers on this diagram refer to regional ironstone samples documented in Duhig et al. (1992).

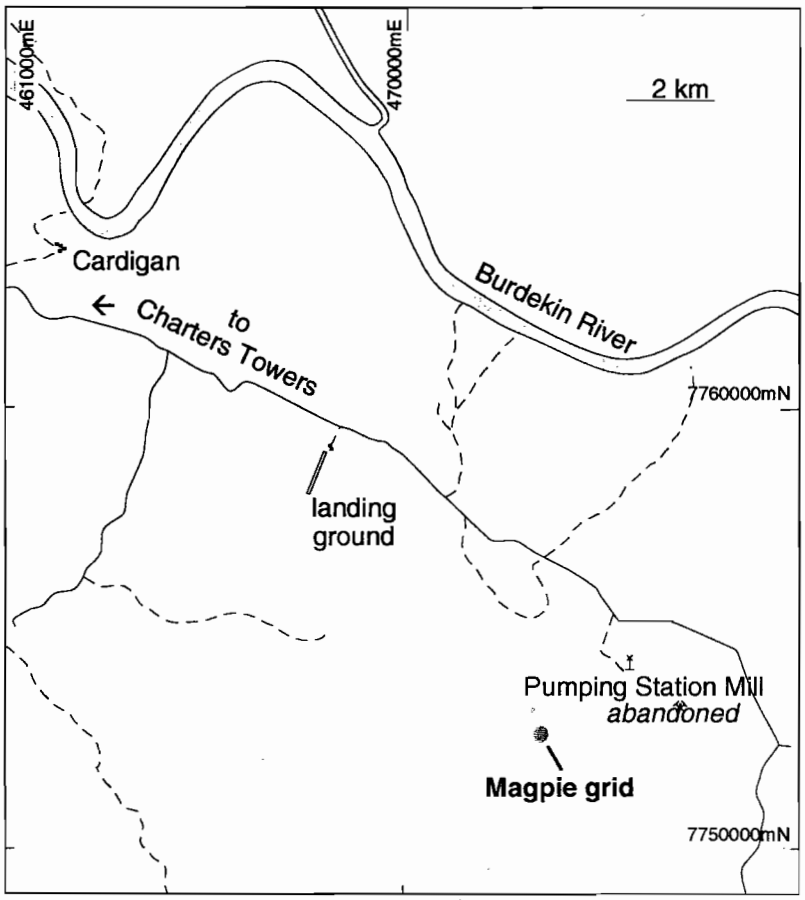

Fig. 1b. Location of the Magpie deposit, 70 km southeast of Charters Towers.

Aims

1. Obtain comparable representatitive data bases for both near-ore and "barren" iron silica deposits;
2. Determine the best sampling density for iron silica deposts that will ensure representability;
3. Extract the useful geochemical parameters for exploration vectors;
4. *If possible formulate a genetic model that assists in the understanding of the iron silica deposit geochemistry.*

Methods

All samples were from outcrop, and consisted of 1–2 kg of rock chips collected evenly across the width of ironstone bodies. Oxidised coatings on joints, and soil debris, were removed prior to sample crushing in a jaw crusher and tungsten and chrome mills. Polished thin-sections of all samples were prepared, and a representative chunk of each sample was retained for reference in the University of Tasmania collection.

For determination of the REE by ICP-MS, PAR but not TW samples were ignited and treated with HCl(2x) 3ml before normal HF/HNO_3 digestion as they were thought to contain magnetite.This dissolved the Fe-oxides, but barite was largely undissolved in both groups. The FJ and SJ samples were dissolved using a sequential leach of HF, $HClO_4$ and HNO_3.

PAR and TW REE were obtained using a Finnigan Element high resolution magnetic sector ICP-MS at University of Tasmania, whereas FJ and SJ REE and a large group of trace elements were obtained at the Research School of Earth Sciences using a VG Plasmoquad PQ2 ICP-MS in collaboration with Dr Stephen Eggins.

All major element analyses, and a range of trace elements for TW and PAR samples, were obtained by standard determinative XRF methods (Appendices 1, 2). Oxygen isotopes from quartz were obtained by laser ablation of powders at the University of Arizona under the direction of Dr Mark Barton and Jennifer Becke.

Terminology

Unless otherwise stated, the REE presented graphically have been normalised to the chondrite values of Taylor & Gorton (1977). The practice of normalisation to shales for chemical sediments is not seen as useful here because the volcanics are the dominant hostrock: chondrite normalisation permits a wider comparison with the literature. The term La_N/Yb_N, shortened in places to La/Yb etc, is the ratio of the chondrite-normalised abundances of these elements. Eu_N/Eu_N^* is a term which describes the extent of Eu depletion or enrichment relative to Sm and Gd, its nearest neighbours:

$$Eu_N/Eu_N^* = Eu_N/(Sm_N+Gd_N/2).$$

Values of Eu/Eu* less than 0.95 indicate europium depletion, and greater than 1.05, enrichment. In places this term is conversationally shortened to +Eu or -Eu anomaly, referring to whether the chondite normalised abundance of Eu lies below or above the general REE pattern. Other abbreviations used here are HREE, MREE, and LREE, which are acronyms for heavy, middle and light rare earth elements.

Geology and geochemistry of near-ore ironstones

Magpie South-Parakeet ironstones

Background

Magpie occurs 70 km southeast of Charters Towers (Fig. 1a, b), in an inlier of the Mount Windsor Volcanic Belt termed the 'Dreghorn block', and was discovered in 1982 by Ian Mulholland during exploration for Esso Minerals (Mulholland 1991). It consists of 250 000 tonnes grading 2% Cu, 2% Pb, 15% Zn, 30 g/t Ag, and 1 g/t Au, hosted within the locally defined "Middle Tuffaceous Member" of the Trooper Creek Formation. This is considered by Mulholland (1991) to be stratigraphically equivalent to the Thalanga ore position, all within the 0.6 km wide aureole of the Middle Ordovician Ravenswood Granodiorite Complex. However, Berry et al. (1992) describe Thalanga as occurring on the Mt Windsor-Trooper Creek Formation contact. The mineralised area contains three lenses, A, B and C, of which A is the largest (Fig. 2). The sulfide lenses occur at the contact between a steeply dipping and south-younging rhyodacitic tuff, and a series of rhyodacitic and rhyolitic pyroclastic units; a widespread contact with basalt occurs ~50 m into the footwall below lens A. Mulholland (1991) considered that a distinct hiatus in volcanism coincided with ore deposition, during which silicate dominated exhalitive products accumulated above and along strike from the massive sulfides; these originally consisted of chert and chlorite± pyrite beds. There is a distinct alteration envelope, consisting of a zone of semi-conformable Mg-Fe-K-Mn alteration in and around the mineralisation with a 500m strikelength, underlain by a "mushroom stalk" of discordant alteration extending to the north (Fig. 3). The hangingwall is also characterised by moderate Fe-Mg alteration up to 100m above the known ore lenses. Zr, Ti, Nb, Y and Al remained immobile through the alteration. The metamorphosism lead to the conversion of the alteration to cordierite-phlogopite schist, quartz-biotite-chlorite-sericite schist, and cordierite-anthophyllite-pyrite-magnetite schist close to the massive sulfides.

Two zones of chert are shown on the section provided by Mulholland (1991): a 10–15 m wide zone immediately overlying the zone A sulfides, and a second 5–15 m wide zone 50 m above this. However, these cherts do not outcrop, and although of considerable interest to this study, were not sampled. Commencing ~700 m to the west, Gregory (1984) documents a swarm of iron-silica lenses with a collective distribution that is approximately the same width and stratigraphic position as the ore package. This swarm continues to the west for ~3 km, and includes several zones of cordierite-pyrite-chlorite alteration that have been explored for base metals, including Magpie South, Parakeet, and Bowerbird

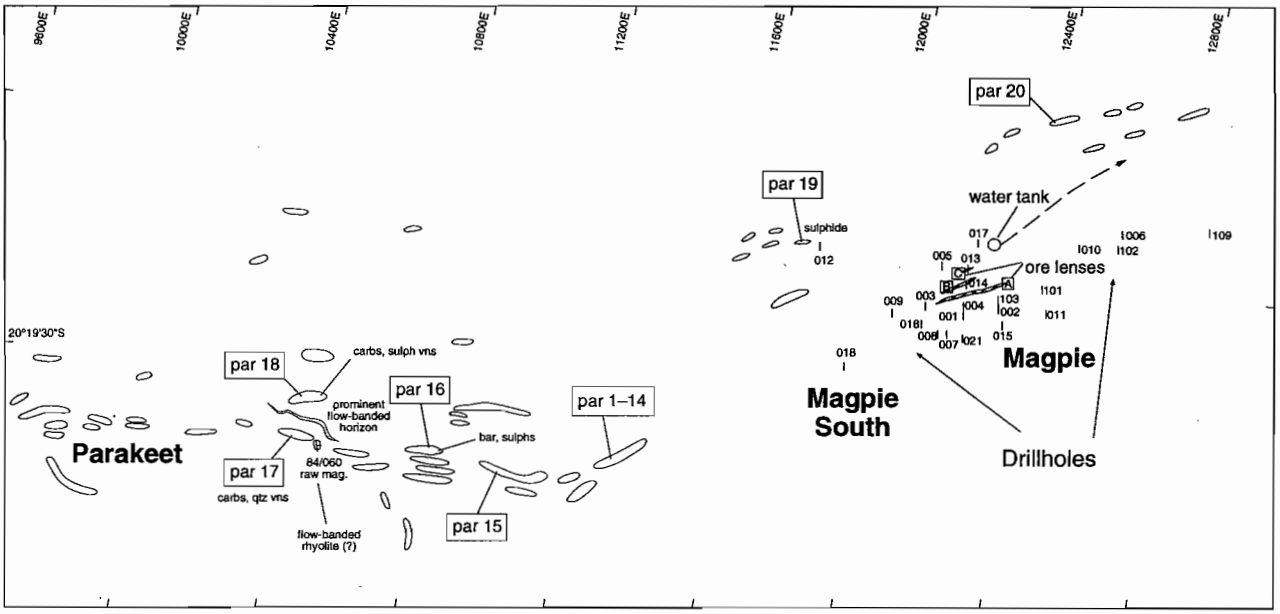

Fig. 2 Location of the Magpie South, and Parakeet prospects, with respect to ironstones mapped by Gregory (1984) and sampled in this project.

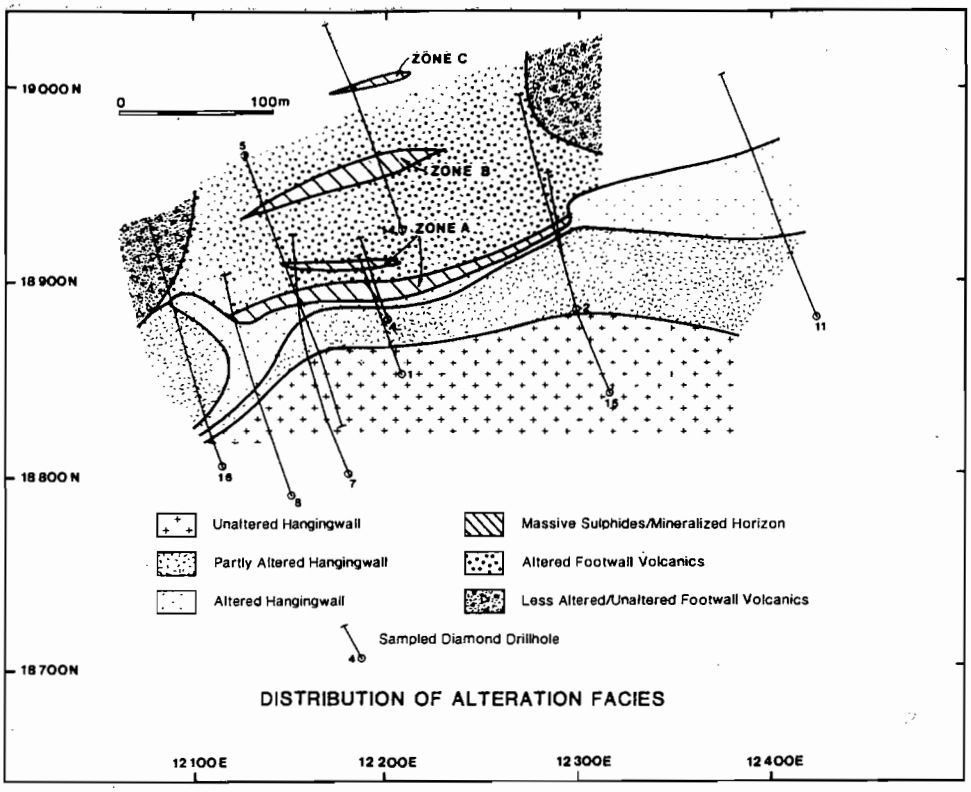

Fig. 3 Distribution of alteration facies and some drill holes at Magpie VHMS deposit, projected onto a dip-corrected hypothetical horizontal plane, after Mulholland (1991).

prospects. Ironstones average 50–100 m long x 3–10 m thick, but include small pods a few metres long, to major lenses 700 m long close to Bowerbird. The BHP compilation map, largely reliant on earlier Mulholland mapping, also suggests that the main mineralised zones in the area coincide with the tips of dacite-to-rhyolite wedges within a generally basaltic to andesitic sequence, but that the ironstone swarm (marking the ore horizon) extends for 2800 m between the felsic volcanic piles. A cluster of minor ironstones also occur ~300m into the footwall both west and north east of Magpie.

Work undertaken

Twenty samples were obtained in the Magpie-Parakeet area, consisting of 14 from iron-silica±barite lenses, and 6 hostrocks (Fig. 2). The most detailed sampling occurred at the nearest iron-silica lens along strike from mineralisation (~700 m west) (Fig. 4), where the ironstone was sampled at 20 m intervals. Ironstones were sampled up to 900 m further west along-strike, and consequently 1600 m from mineralisation, together with two ironstone samples 300 m into the Magpie footwall.

Results

The stratigraphy in this area is broadly similar to that at Magpie, with a distinct basalt-rhyodacite/rhyolite contact 50 m below the ironstone, and enclosure of most ironstones by variably altered flow banded felsic volcanics. Alteration at the Par 1–14 ironstone consists of strong hematite+sericite alteration of flow bands below and along strike from ironstone, and more pronounced silicification in the immediate hangingwall. Nodular fabrics ghosted by hematite-quartz assemblages near the margins of the ironstone are consistent with at least some replacement following devitrification, assuming the nodules correspond to deformed spherulites. The hostrock exhibits exceptional homogeneity in terms of its immobile element ratios (n=6; Table 1) despite potassic alteration (4.7–6.4% K_2O) and sodic depletion (Na_2O = 0.1–0.37 wt. %), and this is consistent with field evidence that it is a coherent lava. Only minor fractionation occurs across the physical area of interest (~50 m across stratigraphy). The rhyodacite overall is notably more fractionated (Zr averaging 527 ppm resulting in Ti/Zr of ~2.7) than any of the lithologies documented 700 m east around Magpie, where Ti/Zr = 8–30 (recalculated from Mulholland 1991).

Macroscopic textural evidence near the margins of the ironstone suggests partial replacement of the coherent rhyolite during ironstone formation. However, the majority of the ironstone is unlikely to have formed by replacement, on the basis of the immobile element concentrations. For instance, most of the ironstone samples possess Zr = 1–3 ppm, which for the primary adjacent hostrock averaging 527 ppm Zr, represents a dilution ratio of ~0.003. Such low dilution ratios could not be accounted for by replacement of coherent flow-banded rhyolite unless the 'immobile' elements were in fact mobile, and this seems unlikely given that severe alteration in the adjacent hostrock has produced no change in Ti/Zr ratio. Ironstone Ti/Zr values do not overlap at all with the hostrock range, which is evidence that the immobile compositions of the ironstone were not controlled by the immediate hostrock, but by an external detrital component that is more typical (in terms of its Ti/Zr) of the regional lithologies. The most likely interpretation on the basis of this evidence is that the ironstone formed mainly on the seafloor rather than by replacement. The XRF data for Ti and Zr in the ironstone samples is near to below detection, so that better quality geochemical data should be acquired to test these observations and conclusions.

The Par 1-14 ironstone consists of a red to dark purple-brown, massive, early quartz-hematite ± magnetite phase, which is variably transected by (1) anastomosing quartz± carbonate±sulfide veins up to 2 cm wide, in places with open growth cockade textures (Plate 1), and (2) manganiferous veins (mineralogy undetermined) identified by pyrolusite staining. The western end of the ironstone displays an increase in the density of veins (Fig.4). The ironstone has:

(1) $Fe_2O_{3(T)}/Fe_2O_{3(T)}+SiO_2$ =0.06–0.11, with $Fe_2O_{3(T)}$= 5.7–9.5 wt %, which are very low Fe contents compared to barren ironstones in the belt (see later);
(2) In areas of Mn-rich veining, the Mn contents of the ironstone (0.01–5.9 wt .% MnO_2) approaches the Fe content.
(3) low Ba contents (<0.01wt. %) with the exception of the most eastern sample Par 9 (0.45wt. %);

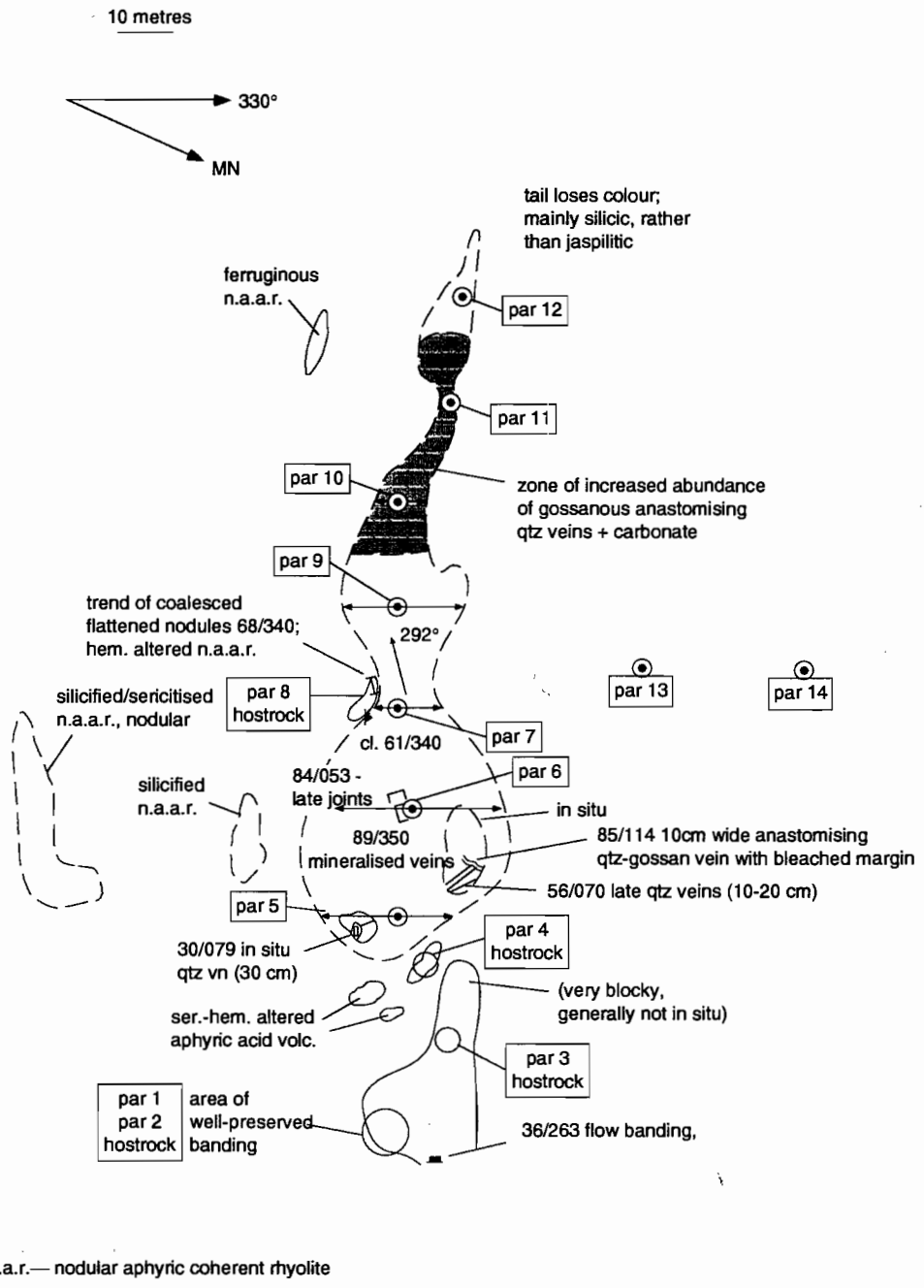

n.a.a.r.— nodular aphyric coherent rhyolite

Fig. 4 Geology and sample locations of ironstone Par 1–14 700 m west of Magpie base-metal mineralisation.

Table 1 Hostrock compositions at Par 1–14 ironstone (see Fig. 4 for locations).

	Par1	Par3	Par4	Par8	Par13	Par14
wt. %	35 m along strike	20m along strike	3m along strike	2 m above	~30 m below	~60 m below
SiO_2	63.39	65.92	64.81	61.53	73.03	68.68
TiO_2	0.24	0.22	0.25	0.25	0.21	0.25
Al_2O_3	19.3	16.7	18.2	18.53	14.46	16.38
Fe_2O_3	3.97	3.83	3.69	5.35	2.38	3.84
MnO	0.22	0.13	0.07	0.14	0.09	0.07
MgO	2.35	3.75	2.77	3.49	1.55	1.88
CaO	0.02	0.06	0.06	0.03	0.01	0.03
Na_2O	0.19	0.19	0.21	0.37	0.11	0.1
K_2O	5.96	5.62	5.93	6.4	4.72	5.31
P_2O_5	0.05	0.04	0.06	0.05	0.03	0.05
Loss	3.96	2.98	3.48	3.24	2.73	3.11
Total	99.65	99.44	99.53	99.38	99.32	99.7
S	<0.01	<0.01	<0.01	<0.01	<0.01	<0.01
Ba %	0.19	0.15	0.16	0.12	0.09	0.1
ppm						
Cu	4	2	4	4	3	2
Pb	9	6	6	7	6	4
Zn	67	137	111	107	59	104
Ni	4	6	9	8	3	4
U	<1	<1	<1	<1	4.1	2.5
Th	31.5	26.3	30.3	31.1	23.6	27
Se	<1	<1	<1	<1	<1	<1
Nb	56.3	50.4	58.7	56.4	39.8	47.4
Zr	546	485	539	548	485	563
Sr	26	26	40	24	12	13
Y	99	93	111	115	72	87
Rb	204	209	225	214	161	196
Ti/Zr	2.64	2.72	2.78	2.74	2.60	2.66
Y/Nb	1.76	1.85	1.89	2.04	1.81	1.84

(4) very low Cu, Pb and Zn contents (<20 ppm);

(5) Na_2O/K_2O = 0.67–8.2, which is exceptionally sodic compared to the hostrock values of 0.01–0.05. This suggests either that the alteration conditions for silicates differed significantly to those of the adjacent hostrock, at albite or paragonite stability, or perhaps that the silicate material that was incorporated detritally into the ironstone had been sodically altered prior to its arrival at the site.

(6) Rb/Sr of 0.03–1, compared to 5.6–15.1 in the hostrocks. This is a result that would be expected from the change in alkali element behaviour seen at point (5), however, it is exacerbated by partitioning of Sr into barite.

(7) Se values of 2.8–4.4 ppm, whereas the hostrocks contain <1ppm Se.

Ironstones farther west within the Magpie ironstone swarm possess similar geochemical characteristics to the Par 1–14 ironstone (Appendix 1), with the possible exception of lower Sr (av. 6.6 ppm versus 26 ppm in Par 1–14). This similarity suggests that the ironstones sampled to date at Magpie are generally of equal prospectivity and were formed under similar conditions. However, the REE evidence suggests some important differences, and highlights more prospective areas (see REE section below).

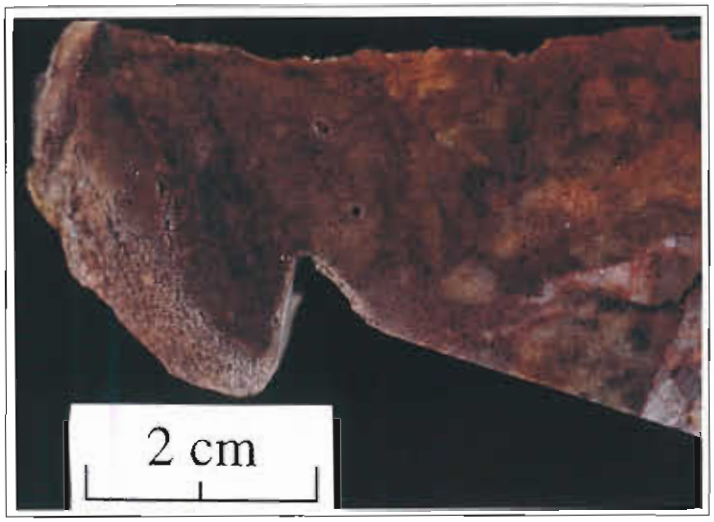

TW1 Near-ore ironstone from Thalanga; note barite at farbottom right.

TW6 Near-ore ironstone consisting mainly of quartz and barite with minor magnetite (Thalanga).

TW8 Near-ore siliceous ironstone (Thalanga) cut by sucrosic quartzveins (stage 3 veins)

Par5 Cockade quartz +- sulphide veins. Near ore ironstone (Magpie).

Par 7 Near-ore ironstone at Magpie, with quartz +- iron oxide veins cutting hematite ironstone

TW4 Sucrosic 'ironstone' near ore lens, Thalanga Range

Thalanga

Background

The detailed geology of Thalanga is described elsewhere in this volume and in Berry et al. (1992). Ironstone geology, microtextures and geochemistry are described in Duhig et al. (1992). Thalanga occurs at the contact between the Mt Windsor Formation and the Trooper Creek Formation. It possesses a poorly preserved thin cap of quartz-magnetite-barite rocks, and is also associated with a cluster of small quartz-magnetite±hematite±barite bodies at two main stratigraphic positions extending 2.3 km west of Thalanga: one on the ore position, and a second ~80m above this in the Trooper Creek Formation. Recent RGC drilling has determined that a small massive sulfide body (Thalanga west 45) occurs in the midst of these ironstones/Ba-quartzites ~1.8 km from the main outcropping Thalanga mineralisation and on the same horizon, so that they are far closer to massive sulfides than previously thought.

The ironstone pods in the Thalanga area are individually far smaller than those at Magpie, or most regional occurrences. The typical size range is 1–30 m long x 1–10 m thick in steeply dipping hostrocks; actual thickness and shape is difficult to determine in most instances because of the rubbly outcrop character.

Work undertaken

Duhig et al. (1992) sampled 19 separate ironstone bodies up to 5.5 km west of Thalanga for a wide range of major and trace elements, but only limited REE studies (Fig. 5, Appendix 3). In the current study two pods of iron-silica, TW1–7 and TW8–10, were analysed in detail to determine the uniformity of their chemical characteristics. Twelve samples were collected in all, and analysed for wholerock, trace and REE elements. Samples from these sites were also used for oxygen isotope studies on quartz. These samples are the closest jaspilites to the newly discovered massive sulfide mineralisation in the area, with TW11 occurring ~40 m updip of sulfides at the same stratigraphic horizon, whereas TW8–10 is 60 m west of TW11, and the TW1–7 ironstone is 250 m SE within the Trooper Creek Formation (Figs 6, 7). Ironstone samples were taken at 5 m intervals across strike.

Results

Geology—The immediate hostrocks to the TW1–7 ironstone ~80 m above the Thalanga horizon are not exposed (Fig. 8), with the nearest outcropping lithologies 60 m NW comprising pyritic chlorite schist, baritic sericite schist, and silicifed brecciated variably calcareous sediment. The ironstone consists of fine-grained red to grey chert, abundantly cross-cut by white to red sucrosic quartz veins with disseminated sulfide pitting, gossanous textures, and associated 1–3 cm wide irregular veins of barite (mainly at the east end). The textures are interpreted as mainly a vein complex overprinting ferruginous chert, with sulfides and barite mainly being emplaced during the vein stages.

The TW8–10 ironstone is hosted in the upper section of quartz phyric rhyolite, 5–10 m below its contact with feldspar phyric dacite. TW12 is a sericite-altered rhyolite representing the closest altered hostrock ~30 m west of the TW8-10 ironstone (within a shallow costean). The TW8-10 ironstone consists of massive reddish-purple jasper cut by numerous anastomosing medium-fine quartz±pyrite veins up to 2 cm wide, with surrounding silicification haloes. Hematite occurs in distinct patches with cuspate edges up to 10 cm long.

TW11 was taken from the jaspilitic portion of a small discontinuous barite-jasper zone ~3 m long, which is interpreted here as a likely updip equivalent to massive sulfides.

Geochemistry—

(1) At TW1–7, $Fe_2O_{3(T)}/Fe_2O_{3(T)}+SiO_2$ =0.01–0.5, with $Fe_2O_{3(T)}$= 1.6–4.7 wt %, which are low Fe contents compared to barren ironstones in the belt (Duhig et al. 1992, this study), but are similar to Magpie values; At TW8–10 two transects provided values of $Fe_2O_{3(T)}/Fe_2O_{3(T)}+SiO_2$ = 0.07–0.17, and $Fe_2O_{3(T)}$ = 7.0–16.7 wt. %, with one hematitic patch containing 52 wt. % (Appendix 1). The up-dip equivalent to sulfides, TW11, contained 17 wt. % $Fe_2O_{3(T)}$ more similar to TW8–10. Duhig et al. (1992) found an $Fe_2O_{3(T)}$ range from 1.41–50.92% in the Thalanga area, with most values ~10wt. % (Appendix 3). Fig. 13 shows a broad increase in $Fe_2O_{3(T)}/Fe_2O_{3(T)}+SiO_2$ toward Thalanga west 45 mineralisation.

(2) Mn contents are low in all ironstones: <0.01–0.12 wt. %, with higher values occurring in the iron-rich samples, which correlate broadly with the

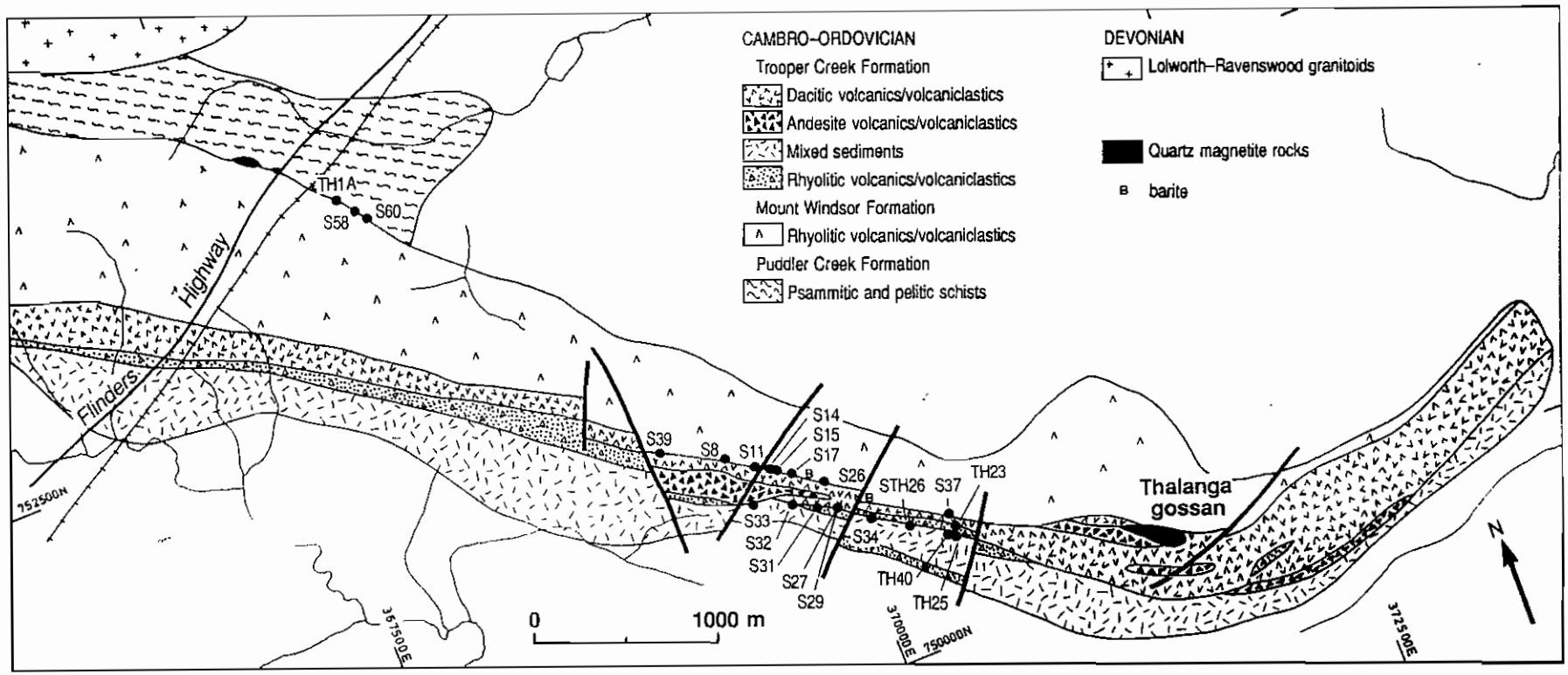

Fig. 5 A geological map of the area around Thalanga showing the locations of jaspilites sampled by Duhig et al. (1992). New sulphide mineralisation has been intersected by RGC Exploration in the S17–S26 area, and is referred to in this paper as Thalanga west 45.

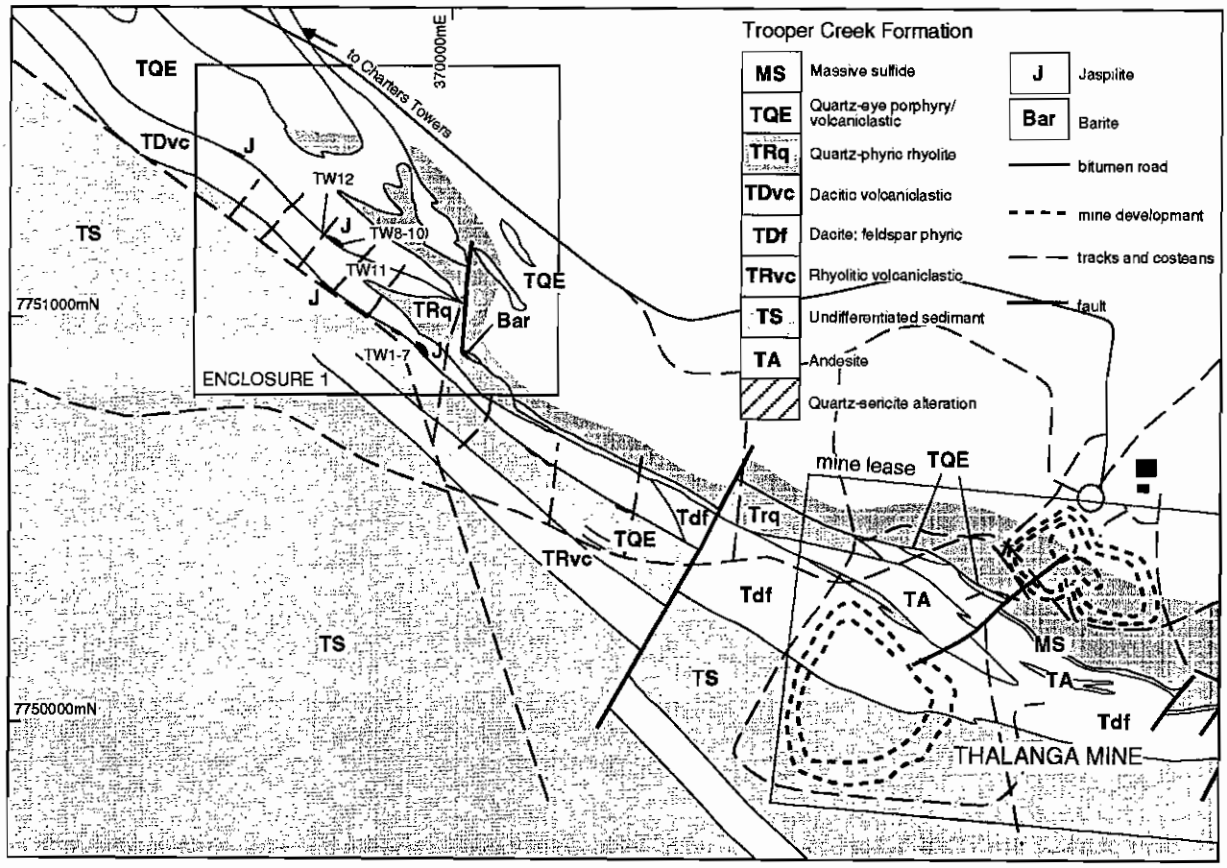

Fig. 6 A detailed geological and cultural map of the Thalanga mine area, supplied by RGC Exploration in 1996.

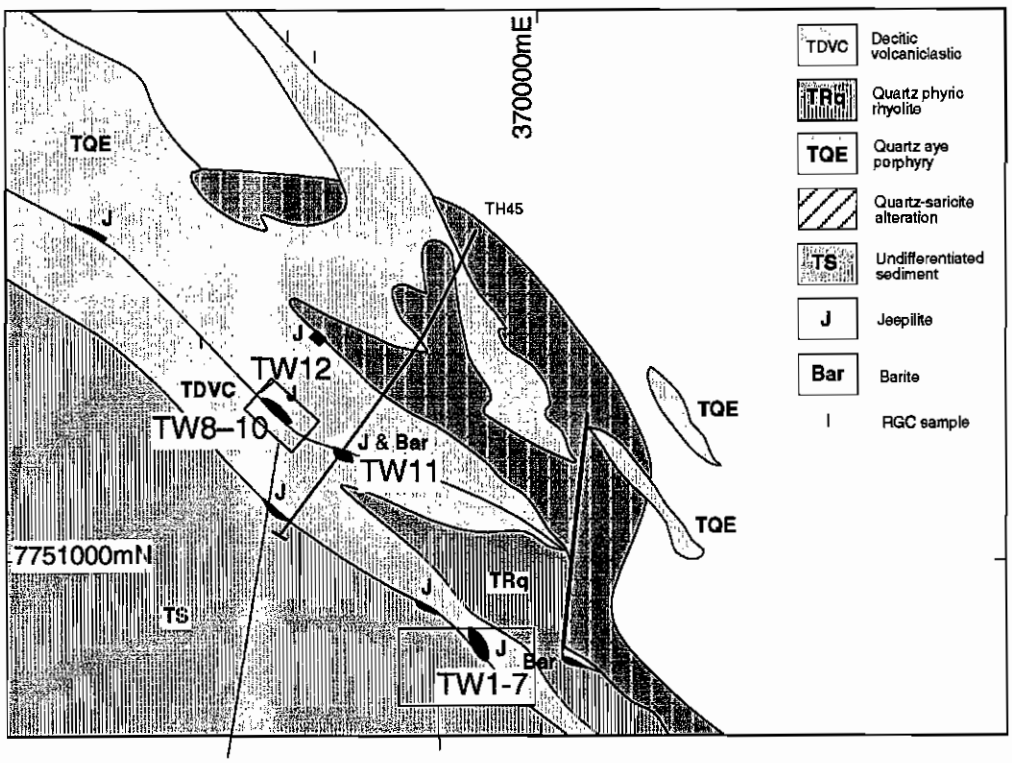

Fig. 7 Enclosı

Fig. 7 Enclosure 1 from Fig. 6, showing sample locations used in this study.

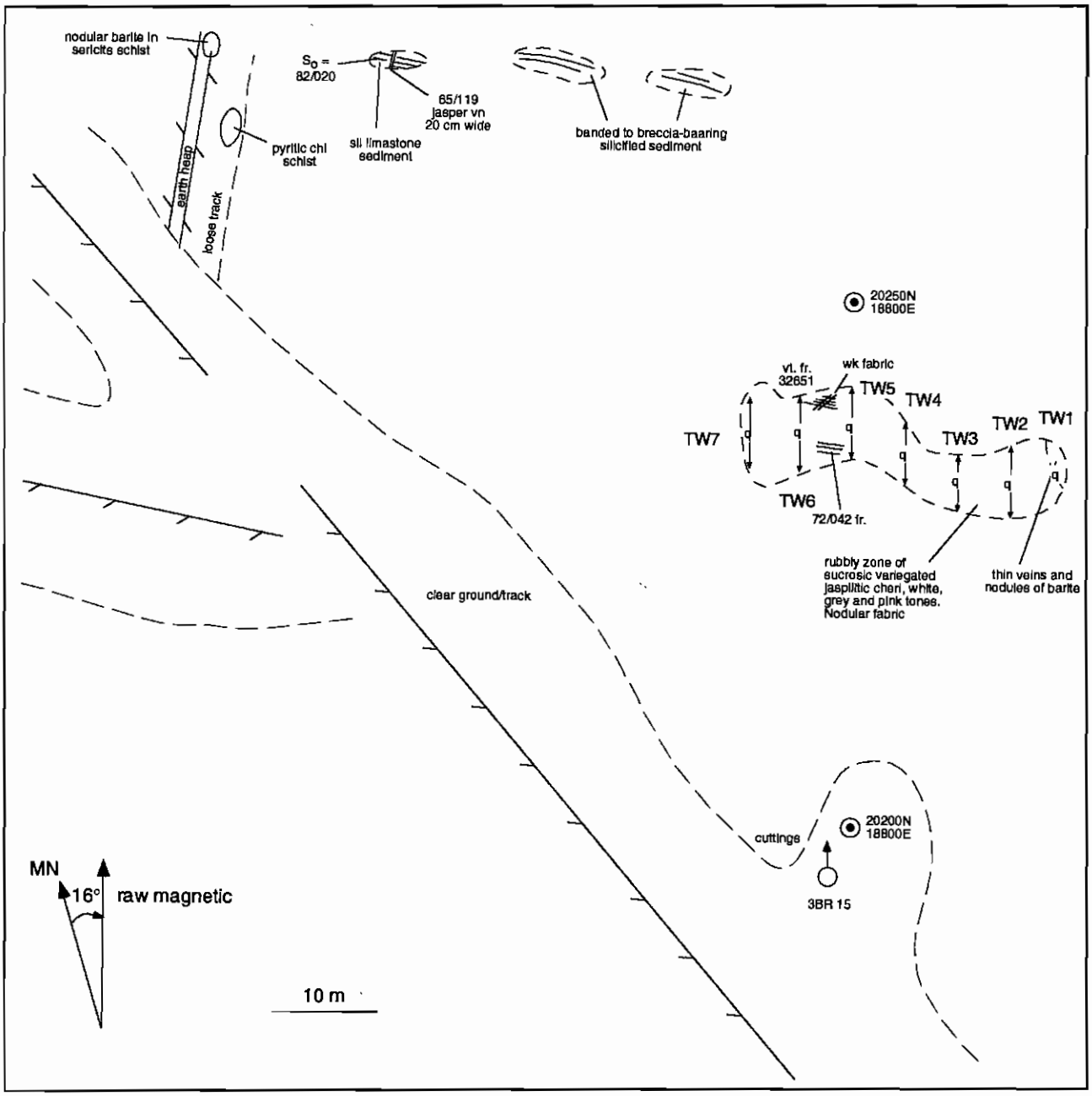

Fig. 8 Enclosure 2 from Fig. 7, showing the detailed geology of ironstone TW1–7.

position of Thalanga west 45 (Fig. 13). There is a hint of higher MnO (0.06 wt. %) and Fe at ~1100–1300 m from Thalanga that may represent a separate hydrothermal system (see also comments on REE values).

(3) Ba contents are very high in the TW1–7 lens, and drop from east to west (3.5 – <0.01 wt .%). However, in TW8–10, Ba is below detection, whereas ~900 ppm occurs in TW11 updip from mineralisation.Consideration of the Duhig et al. (1992) data for Ba, Cu, Pb and Zn for the area indicates that all of these elements approach highs 1500–2000 metres-from Thalanga, whereas ironstones closer to Thalanga display lower values (Fig. 11). This supports the view that the ironstones are reflecting the Thalanga west 45 hydrothermal centre in the TW11 area rather than the Thalanga system.

(4) Cu, Pb and Zn contents, although derived from weathered samples, vary systematically with the Ba content, and are anomalously high compared to "barren" ironstone populations. TW11 contains the highest values, with 86 ppm Cu, 220 ppm Pb and 210 ppm Zn, and the other two ironstones sampled in this study also contain elevated values. See also comments on trends with distance above, and Fig. 11. Considering all base metal data together, and separating the data into its two main horizons, it is apparent that with the exception of the TW1–7 lens, most of the more anomalous response derives from the Thalanga-equivalent horizon (Fig. 12); this would favour this level for further exploration.

(5) Na_2O/K_2O = 0.35–3.8, although Na and K values are near to below detection. Rhyolitic hostrock at TW12 is ~0.5. The Duhig data set supports this observation, with samples in which detectable Na and K occurred having Na_2O/K_2O = 2.8–42 (n=9), with most values in the range 3–7. As noted for Magpie, this suggests either that the alteration conditions for silicates in the ironstones differed significantly to those of the adjacent hostrock, or perhaps that the silicate material that was incorporated detritally into the ironstone had been sodically altered prior to its arrival at the ironstone site. However, further data on hostrock composition and mineralogy of Thalanga Range alteration is required to test this.

(6) Rb/Sr of 0.005–0.42, compared to 3.2 in hostrock sample TW12.

(7) Se values of 1.0–4.4 ppm, whereas the hostrock sample contains 1ppm Se. Unfortunately none of the Duhig data set was analysed for Se.

(8) Arsenic values mainly <3 ppm, with minor values as high as 9 ppm. Ironstones within Thalanga have As = 2–28 ppm. Sb in near-Thalanga ironstones is 0.2–8.5 ppm, and within Thalanga the range is similar (1.7–9.8 ppm; n=3; Duhig 1990).

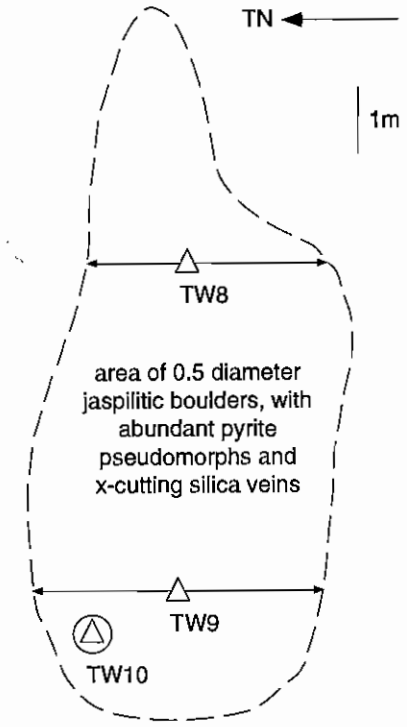

Fig. 9 Enclosure 3 from Fig. 7, showing the detailed geology of ironstone TW8–10.

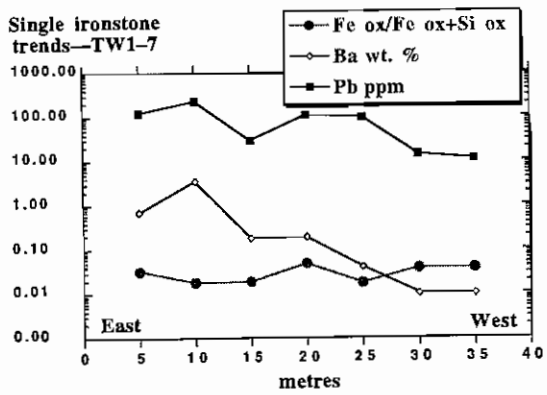

Fig. 10 Geochemical trends within the TW1–7 baritic jaspilite west of Thalanga.

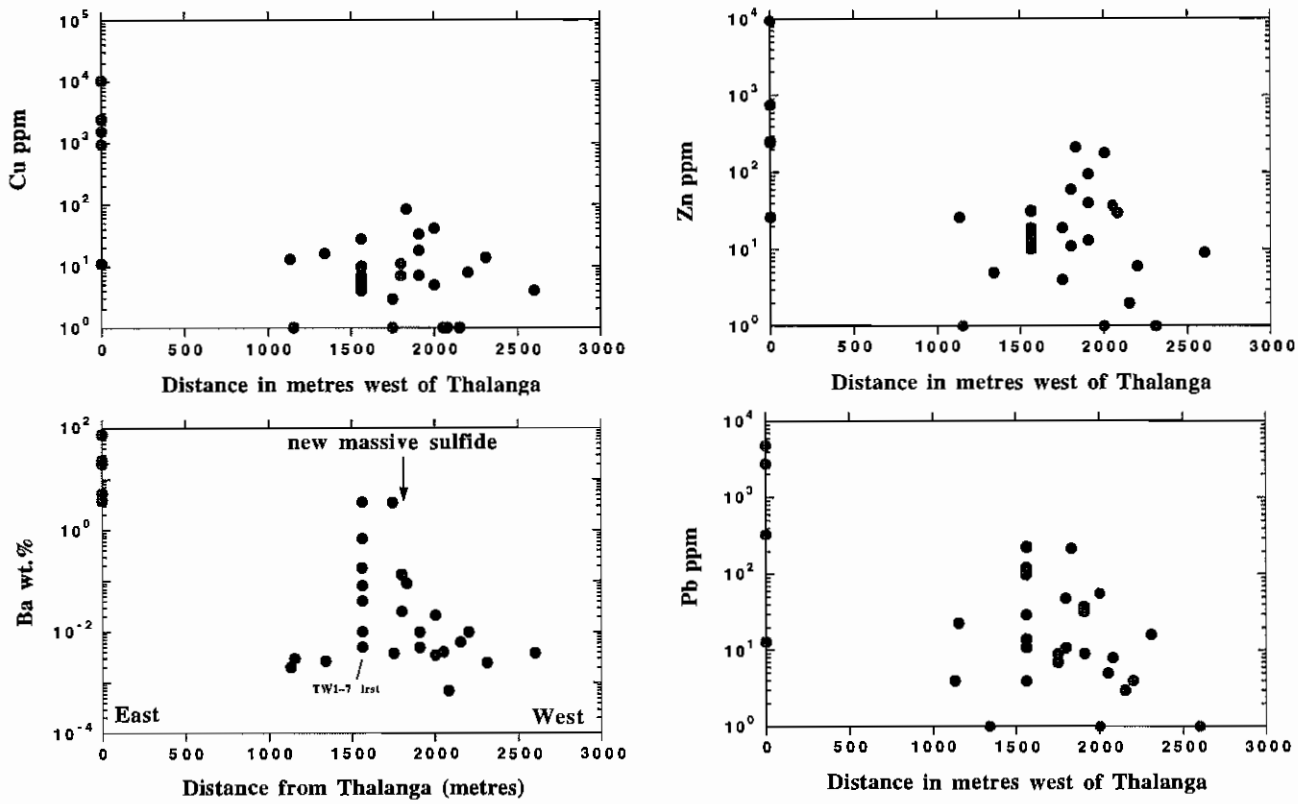

Fig. 11 Ba, Cu, Pb and Zn concentrations with distance from Thalanga, with data from this study and Duhig et al. (1992).

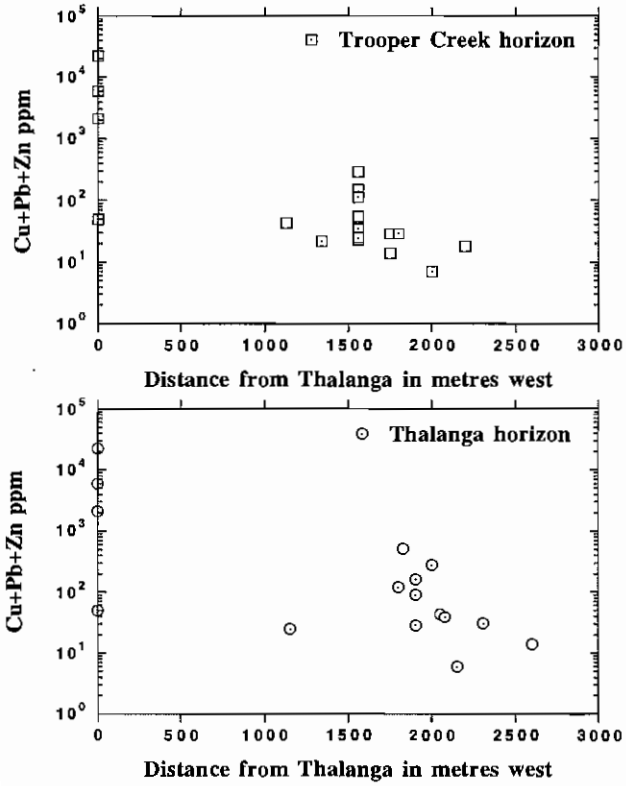

Fig. 12 Cu+Pb+Zn concentrations with distance from Thalanga, separated by horizon, with data from this study and Duhig et al. (1992).

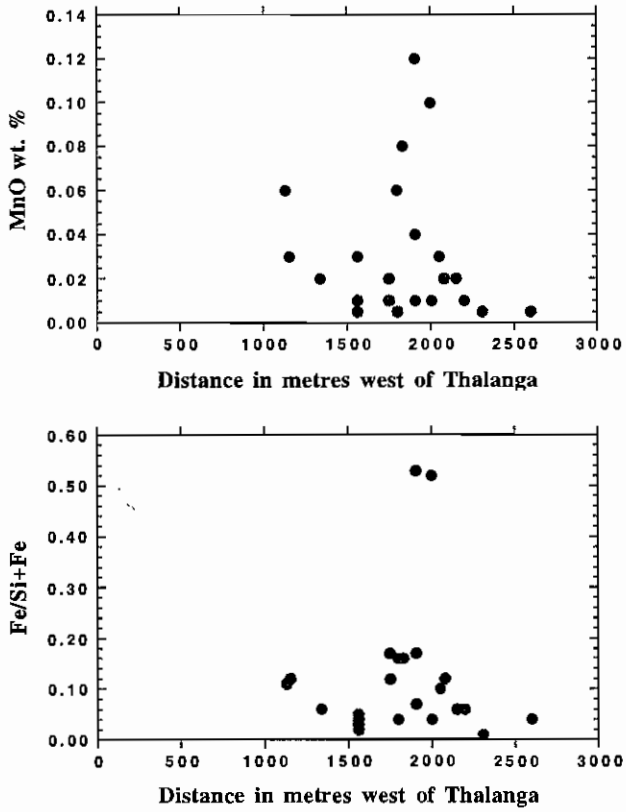

Fig. 13 $Fe_2O_{3(T)}/Fe_2O_{3(T)}+SiO_2$ and MnO contents increase towards the Thalanga west 45 ore position, with MnO contents particularly showing sharp increases close to sulfides at ~1800 m.

Geology and geochemistry of "barren" ironstones

FJ & SJ lenses

Background

The identification of a truly barren sample set was critical to the comparitive approach this vector study has taken. The areas were selected on the basis of:

(1) Results of the Duhig et al. (1992) study, which found both FJ and SJ lens contained excellent microbial textures, suggesting that they may have had a low temperature history, and that both contained low base metal contents;

(2) No known VHMS system within 3km of each study site;

(3) Subsequent REE analysis, which has confirmed that no high temperature hydrothermal component is present in either area.

FJ lens in the Britannia area was originally sampled by Joe Stolz as SS71A, and SJ lens as SS15A–D, in the Sunrise Spur area (Fig. 1a).

Work Undertaken

Sampling of the barren systems took place as part of a separate precursor study in 1992–93. This study mapped the ironstones and parts of their surrounding area (Fig.1a, Figs 14–16). Ironstones were sampled at 20 m intervals along strike; these were analysed for major and trace elements, as well as high precision REEs (see methods section). Significant hostrock chemistry was only obtained from the FJ lens area.

Results

Geology

Both FJ and SJ lenses occur at the contact between the Trooper Creek Formation and the overlying Rollston Range Fm, which is the stratigraphic position of the Liontown massive sulfide deposit to the west in the belt.

The FJ lens has ~400m strikelength. It overlies a thin veneer of poorly outcropping volcaniclastic breccias, which in turn overlies a substantial thickness of carbonate-chlorite-altered andesitic hyaloclastite.

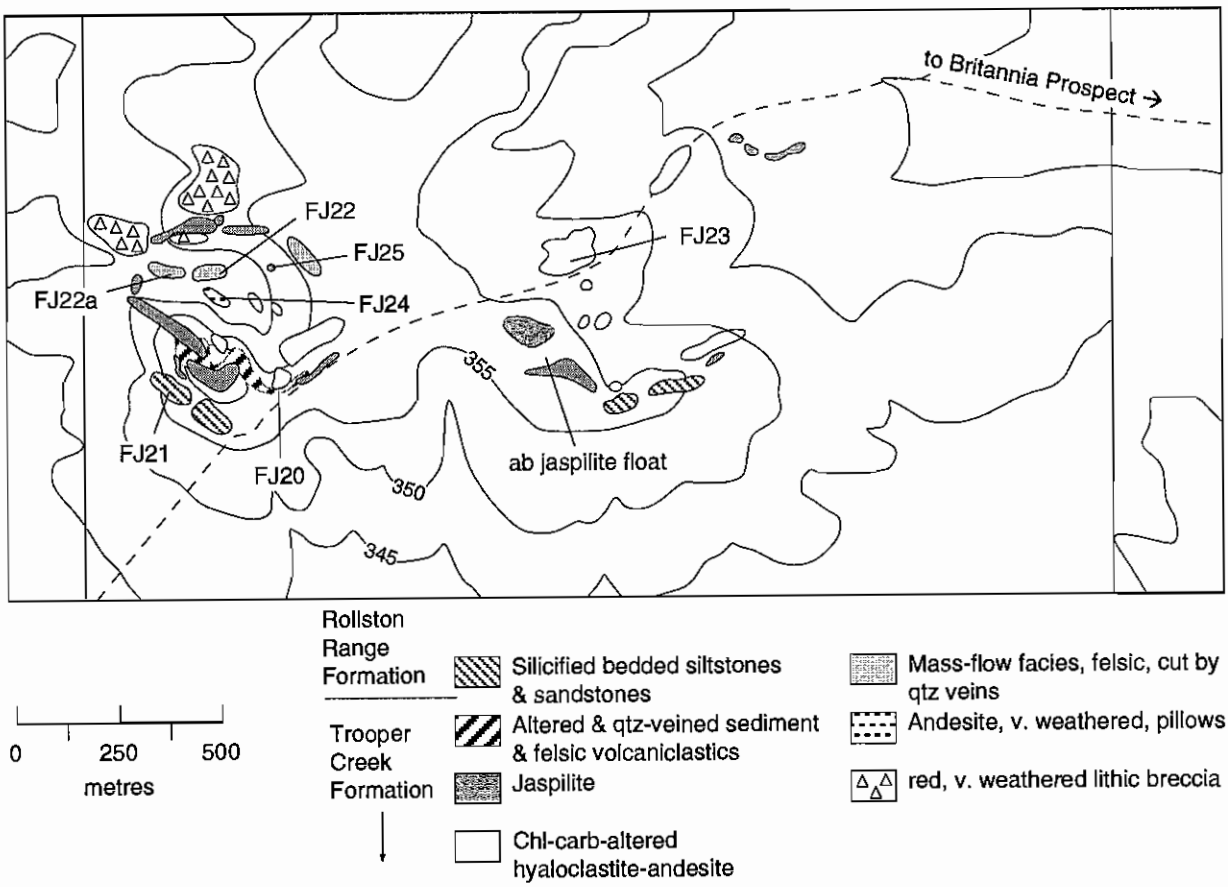

Fig. 14 Local geological setting of the FJ lens, with mapping from this study.

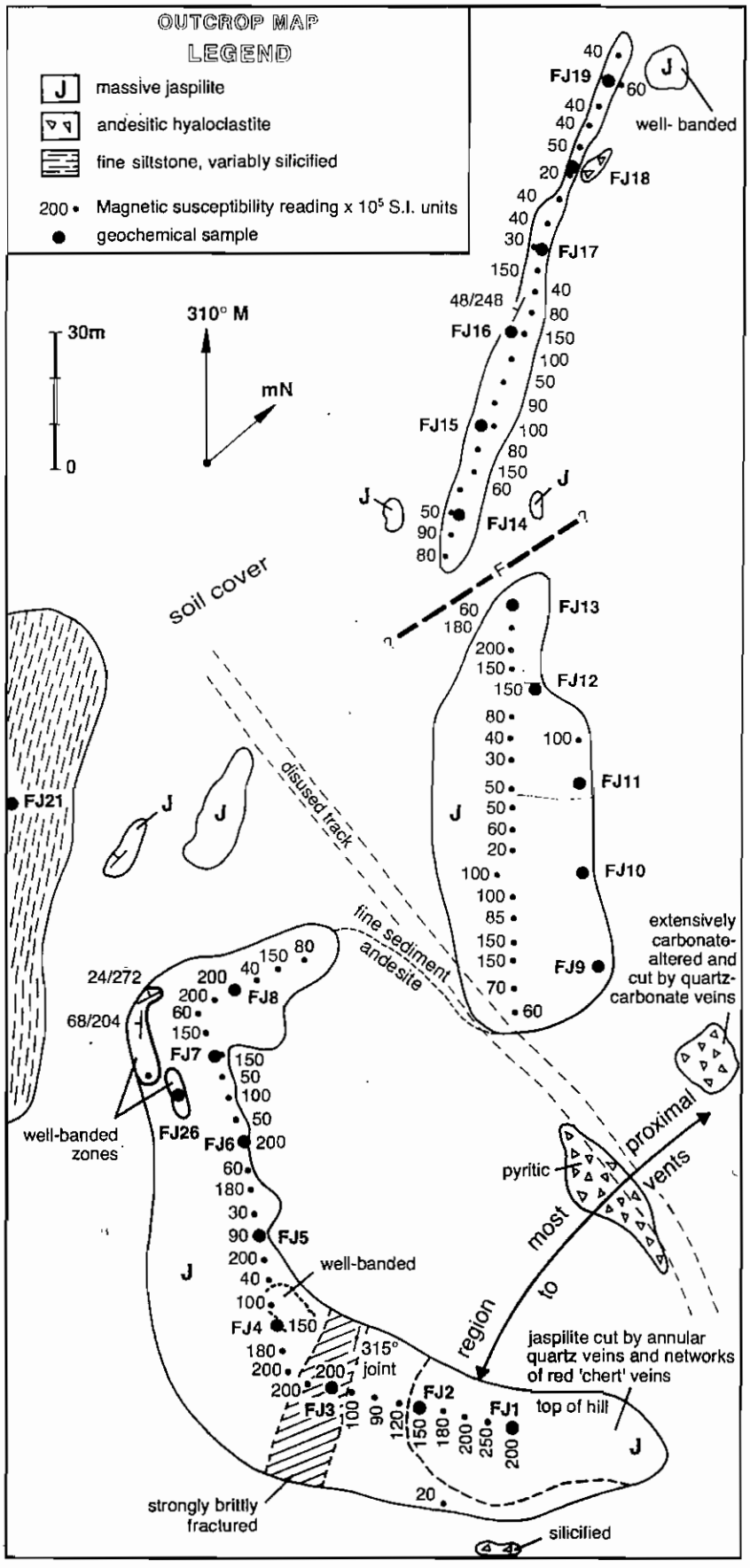

Fig. 15 Detailed geology, magnetic response, and sampling details for the FJ lens.

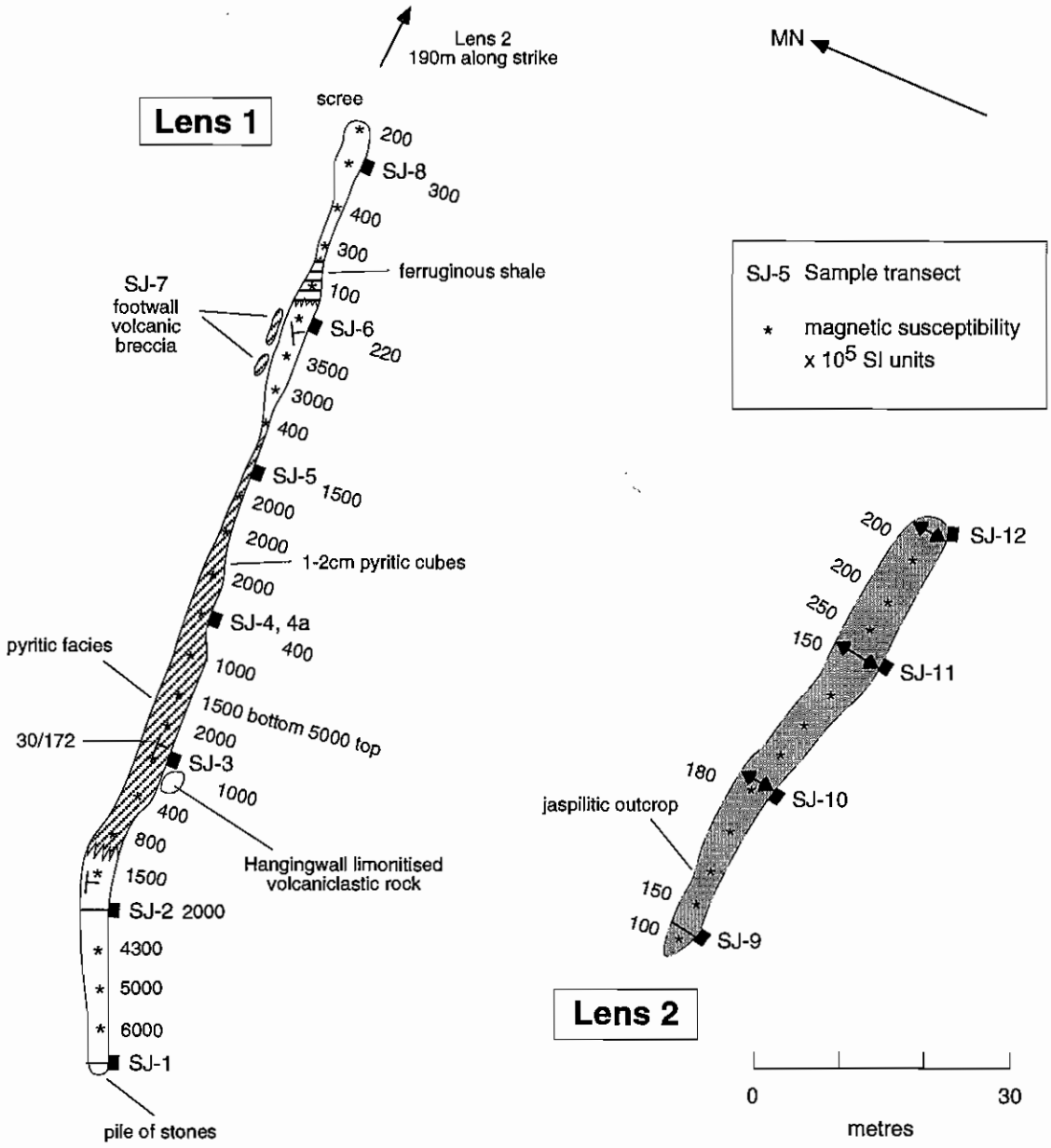

Fig. 16 Detailed geology, magnetic response and sampling details for the SJ lens (consisting of two sub-lenses).

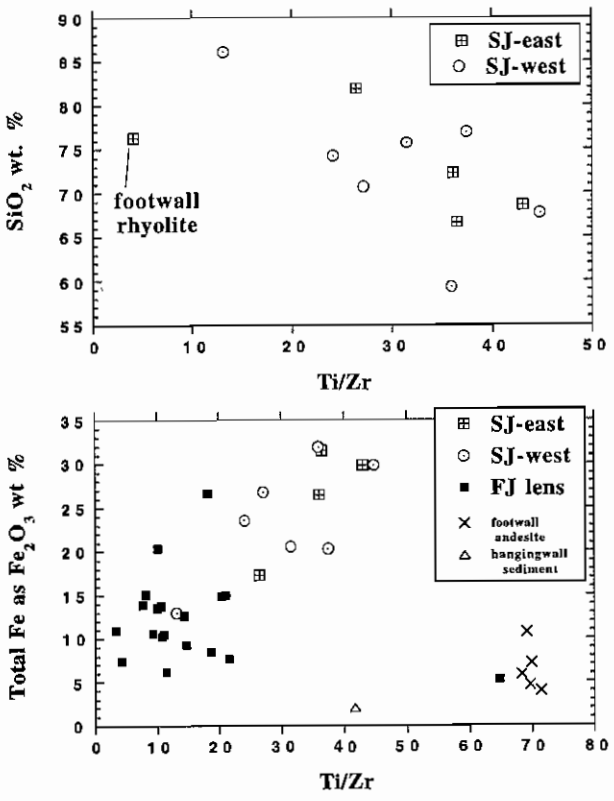

Fig. 17 Ti/Zr versus Fe content for all lithologies at FJ and SJ lens, illustrating that the ironstones do not share the geochemical provenance of the immediate hostrocks at FJ lens, and that they have a strongly mixed provenance at SJ lens.

The jaspilite is overlain by silicified Rollston Range sediments (sample FJ21 in Figs 14, 15). It is just one of several large examples that dip gently southward in this area; it is possible that the ironstone outcropping to the north of the east-west creek in Fig. 15 is a down-faulted extension of the sampled ironstone. A maximum thickness of 20 m is attained at the eastern end, but most of the body is 5–10 m thick. It is characteristically brick red and outwardly massive, with a hackly fracture pattern, although several thin, banded zones occur at the top of the body (Fig. 15). The most eastern portion contains unusual annular quartz veins ~10 cm in diameter that are interpreted as paleo-chimney infill structures (Plate 2). However, most samples in detail consist of fine cross-cutting veinlets of goethite, red hematite, black hematite, chert, and megaquartz, with minor sulfide pitting, and very minor barite veining— this textural characteristic indicates that the whole ironstone developed above a general area of fluid upflow, rather than from a single focussed discharge point, and there is very little material that is interpreted to have precipitated wholly from a modified or unmodified water column in the classic exhalite sense. The ironstone is characterised by magnetic susceptibilities of 20–250 x 10^{-5} SI units. The immediate footwall is only exposed at a few points at the eastern end of the body, where carbonate-chlorite alteration ±pyrite occurs, transected by sinuous 5 cm wide quartz-carbonate veins.

SJ lens (Fig. 16) is an east-west trending steeply dipping set of two lenses 200m apart, with an average thickness of <3 m, each ~100 m long. They are underlain by 2–10 m of tuffaceous siltstone, above coherent rhyolite (SJ13). The jaspilite has similar characteristics to the FJ lens material but appears more shaly in parts. The central section of the western sub-lens contains coarse pyrite cubes (weathered), and rare clasts of altered fine-grained intermediate volcanics. The western sub-lens is characterised by an order of magnitude higher magnetic susceptibilities (200–6000 x 10^{-5} SI units) than the western sub-lens (100–250 x 10^{-5} SI units).

Geochemistry—FJ lens

The trace element ICPMS data for both FJ and SJ lenses are far more comprehensive than the XRF trace element data from the near-ore systems, partly because the quartz-hematite mixtures dissolved very readily during sample preparation, but mainly because of the exceptionally low detection limits for the ICP-MS method. As will be seen, this has permitted the resolution of element relationships at very low element abundances, which is important for subtle source contributions. Plotting of elements along the strike-length of the ironstones has also been very useful for this purpose.

FJ lens fundamental features are $Fe_2O_{3(T)}/Fe_2O_{3(T)}+SiO_2$ =0.05–0.27, with $Fe_2O_{3(T)}$= 6–27 wt %, and $\sum Fe_2O_{3(T)}+SiO_2$ =97.3–100.0, ie very little other than iron and silica. Zr contents mainly between 0.5 and 9 ppm, and Al_2O_3 mainly in the range 0.15–0.75 wt. %, suggest that the hostrock component is low. The identity of the hostrock component is indicated by rhyolite to rhyodacitic Ti/Zr values of 3.2–21, which differs from the footwall andesite values of 65–72, and the hangingwall sediment value of ~40 (n=1; Fig. 17). Although rhyodacite does not occur in

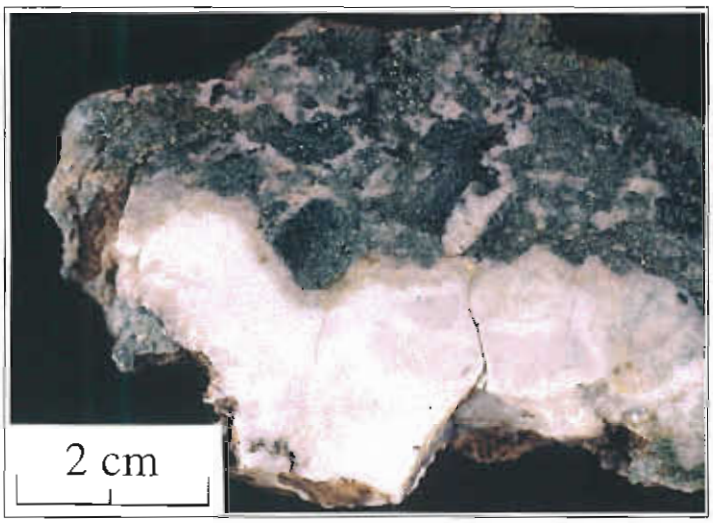

FJ24C Footwall quartz -calcite vein cutting andesitic chlorite altered hyaloclastite beneath barren ironstone.

FJ26 'bedded' ironstone at the top of a massive barren facies. The pale patches were sampled for oxygen isotopes, and consist of fine grained quartz.

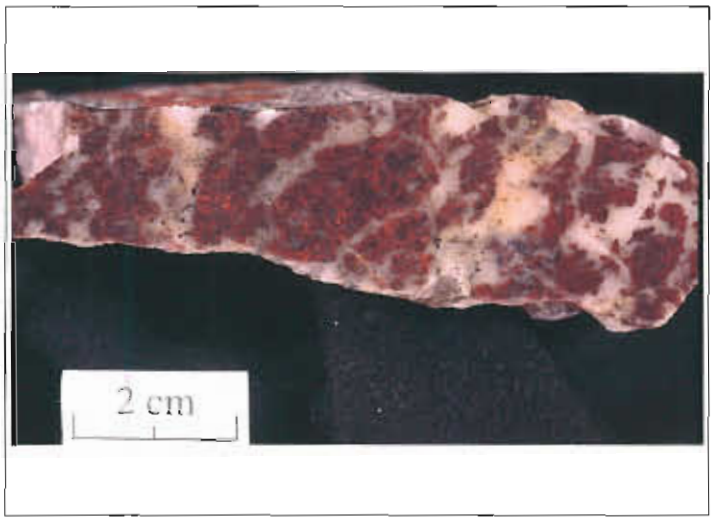

PAR 10 Near-ore ironstone, Magpie

FJ4A Barren ironstone in which hematite-goethite zone is transected by late specular hematite veins

FJ8 Barren ironstone, in which a stage 1 mega-quartz pocket is cross cut by stage 2 hematite-quartz zone

In place fossil fumarole zone FJ lens, consisting of circular vein structures, defined by quartz

the immediate footwall, felsic breccias were identified in the footwall along strike (Fig. 15). At FJ lens there is no consistent trend in the clastic indicators with distance along the body.

Plotting other parameters along the FJ strikelength (Fig. 18):

(1) a significant zone of increased Fe occurs in the centre of the body, imposed on a general dish pattern. U also follows this pattern closely;

(2) P also displays enrichment at both ends of the body, but its lowest values occur in the central zone. As, Cu, Pb and Zn, and Ba/Cu+Pb+Zn all follow this pattern. The As values (10–70 ppm) are the highest found in any ironstone in the Mt Windsor Volcanic Belt, even within the Thalanga deposit;

(3) Ba has a spike of 1600 ppm, but most data is 100–300 ppm, distributed randomly along strike;

(4) Co and Ni display striking increases from east to west that are independent of the variations in other chemical parameters;

(5) Mo displays a distinct anomaly 4–5 times the 3 ppm background at ~30–70 m from the east end—this anomaly does not correlate with any other parameter apart from the high Ba spike mentioned above;

(6) ΣREE elements remain at ~18 ppm for most of the strikelength with the exception of the western 60m, where a sharp increase to >100 ppm occurs. La_N/Lu_N ratios increase steadily from east to west, although the western end values are far more erratic than the eastern end. Ce/Ce* also displays regular patterns, indicating that -Ce anomalies are concentrated in the middle and western end of the body.

(7) Se values are very low compared to the near-ore systems (0.001–0.054 ppm).

(8) Na_2O/K_2O is < 0.5, with many samples <0.2, and Rb/Sr is 0.14–0.67.

Geochemistry—SJens

SJ lens shows sufficient similarities to FJ lens to combine them in the definition of a general barren systems model. One important difference as indicated above is mixed provenance for Ti/Zr for SJ lens, and an intriguing relationship between Fe, Si and Ti/Zr (Fig. 17). Mixed provenance of the detrital component is likely to cause complexity in the patterns of other elements. SJ lens-west contains higher Mn abundances than FJ lens, and SJ lens east, and this appears to have influenced other aspects of the geochemistry. Positive correlations are observed between Mn and Cu+Pb+Zn, ΣREE and Co-Ni. The transition elements do not display a strong relationship to Fe.

In terms of alkali element behaviour, like FJ lens, Na_2O/K_2O is low, with most samples in the range 0.5–1.5, and Rb/Sr of 0.06–0.2.

Plotting of element abundances versus position within the SJ lens system indicates that the SJ-east lens was not enriched in base metals, but does contain Ba-enrichment. It also contains far higher REE abundances than the SJ-western lens.

Discussion

The FJ lens geochemistry and textures indicate that several geochemical sources contributed to the composition of the body. While factor analysis of the data identifies groups of associated elements which might be assigned to each source, plotting the data spatially, and using ratios that are known to be sensitive to particular processes, are the most useful methods of untangling the different sources.

The uniformity of Ti/Zr values is evidence that only one clastic source is present for the FJ lens, whereas at SJ lens, two detrital sources are required to account for large variations and systematic trends in this ratio.

The textures of both lenses indicate that:

(1) early jaspilitic ironstones consisted of fine-grained specular hematite, chert, and megaquartz, with a patchy massive to mixed distribution;

(2) this phase was pervasively transected by fine-grained networks of chert and red goethite/hematite veins (internally forming common spherule textures) which were infilled by megaquartz in places. These veins define circular structures on some outcrops at the eastern end, and hence were part of exhalative vents in the developing body. This phase was texturally corrosive to the earlier hematite-quartz assemblages, but did not affect hematitic sediments emplaced at the surface of the developing body, which are crudely banded but unveined. It is most apparent in samples at the east end of the body, because the veins here are thickest. In places specular hematite selvages characterise the latest quartz veins;

(3) stages 1 and 2 above were in places transected by small barite veins.

This textural history suggests that the hydro-

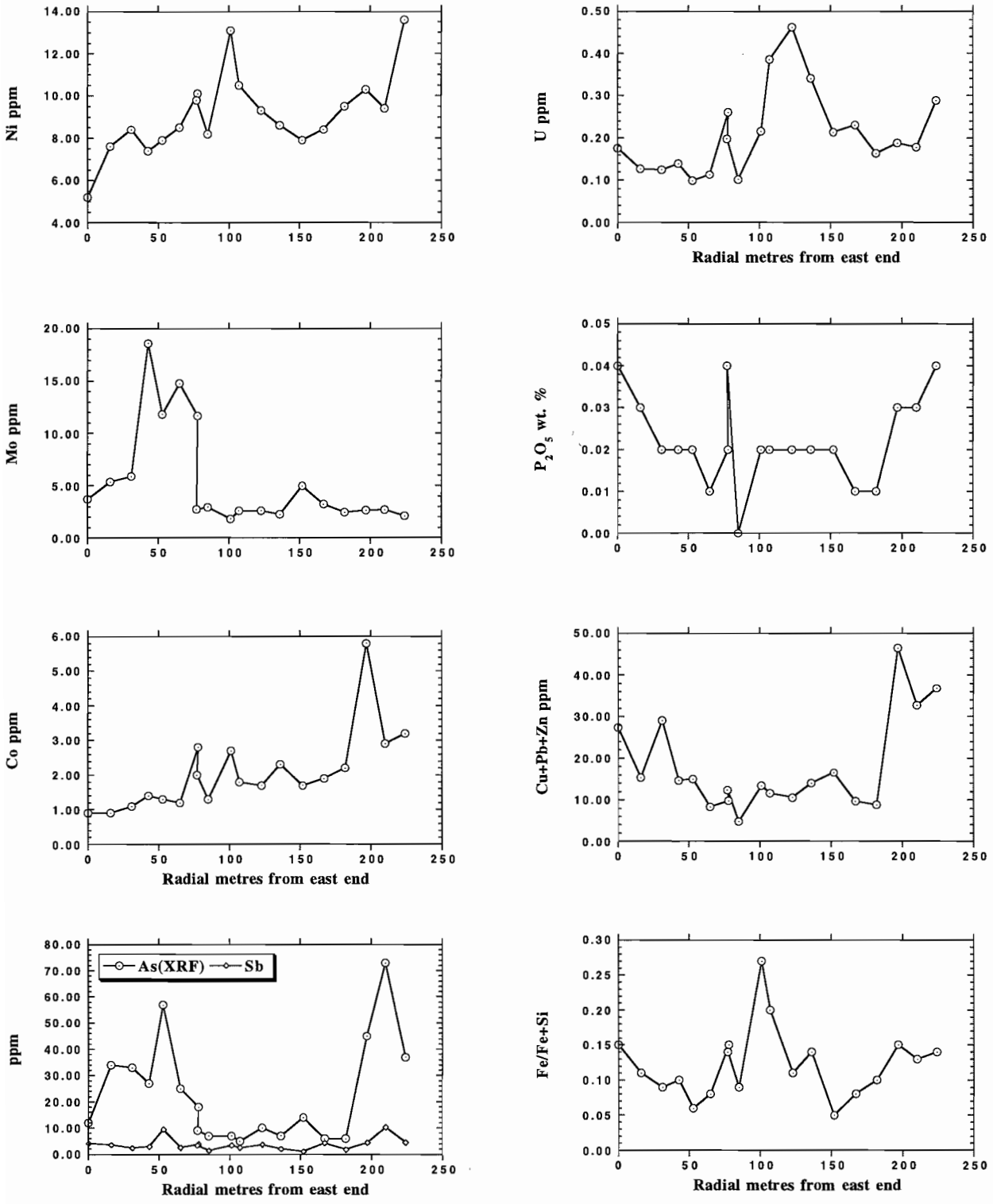

Fig. 18 Trends of selected elements along the FJ lens strikelength.

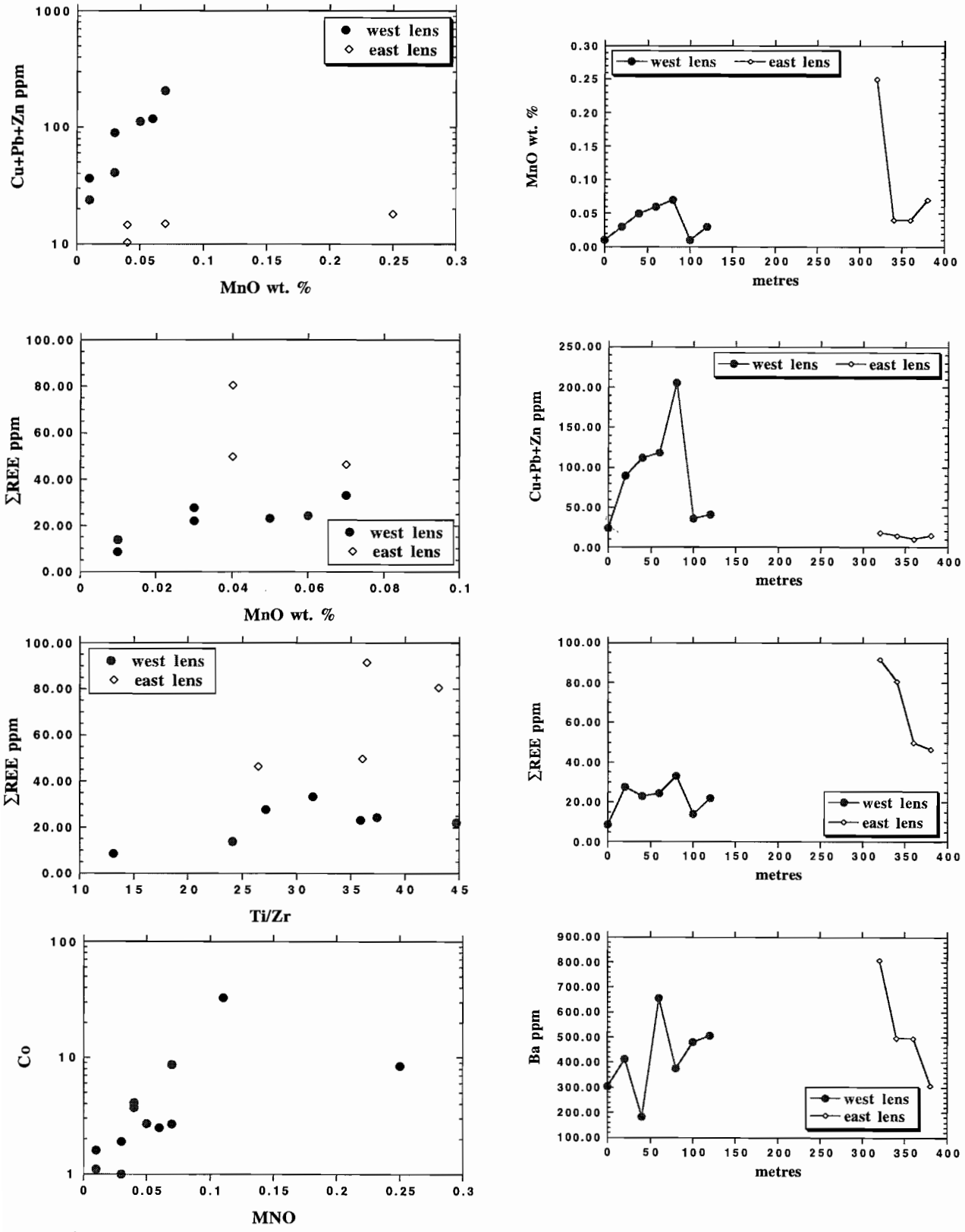

Fig. 19 Trends of selected elements along the SJ lenses, and relationships between Mn and Cu, Pb, Zn, Ba and ΣREE.

thermal development may have been characterised by more than one signature, a point that is considered in the following assignment of components to sources:

High Fe— the central iron-rich zone may represent an area of stage 1 ironstone that was not pervasively replaced by stage 2 silica-rich ironstone. Uranium was also concentrated during this phase, but was leached in Stage 2.

Low Fe(ie high silica)+high base metals + Ba + As + P + Mn— The coincidence of these parameters indicates that hotter hydrothermal fluids formed during stage 2 at the east and west ends of the FJ body. The positive correlations of Cu, Pb, Zn and ΣREE in SJ lens-west could either be accounted for by primary hydrothermal addition, with all components arriving in the same hydrothermal fluid, or by seawater adsorption of these elements on to hydrothermal Mn-oxides. However, given that the total abundance of adsorped elements would exceed the measured abundance of Mn, co-precipitation from a hydrothermal fluid was more likely. Consequently Mn enrichment is seen as mainly par of the overprint, rather than as part of the early ironstone.

Mo-Ba— Specific distinctive fluids during Stage 3 formed a localised zone of Mo-Ba near the east end of the body, possibly by late overprint, as is texturally observed for barite. There is a distinct Ba/Cu+Pb+Zn anomaly associated with this zone.

Co-Ni— Adsportion of transition elements from seawater occurs in proportion to the time of exposure of surfaces, and the amount of Mn and Fe on these surfaces. At FJ lens, hydrogenous adsorption of seawater transition elements does not show a clear relationship to Mn and Fe contents, but does vary very systematically spatially. At SJ lens-west, the abundance of Mn oxides was clearly important because there is a strong Mn-Co+Ni correlation.

Since little correlation is observed between Co-Ni values and Mn and Fe at FJ lens, the Co-Ni values here are interpreted to reflect the relative period of exposure of surfaces to seawater. Exposure must have been longest in the west of the lens compared to the east, which also correlates with the thickness of the iron silica body. It follows that construction of the deposit occurred fastest at the eastern end, resulting in a thickened zone in which individual Fe/Mn-oxides were exposed for less time to seawater. Applied more generally, Co and Ni concentrations are good potential indicators of the exposure history of MWVB ironstones to seawater.

Mixed processes— many other elements appear to have been influenced by more than one process, giving rise to mixed patterns which are difficult to interpret. For instance, the REE were added in proportion to the amount of detrital or relict replaced hostrock, but the -Ce anomalies were inherited from seawater, probably by convective mixing rather than Mn scavenging, because Ce is not depleted relative to other indicators of seawater scavenging, such as Co.

Rare earth element applications

Much emphasis is placed on the Eu anomaly and the shape of the REE pattern as a guide to mineralisation in the literature. However, the REE composition of iron-silica deposits includes potential contributions from:

(a) hydrothermal fluid;
(b) seawater REE incorporated by mixing at the moment of exhalation;
(c) detrital grains and replaced hostrock;
(d) hydrogenous adsorption/leaching by seawater; and possibly
(e) microbial additions.

The first four of these sources all make important contributions under particular circumstances, while the fifth is as yet poorly quantified. Some of these sources have very different REE compositions which makes them very recognisable from an exploration viewpoint. In particular, hydrothermal fluid is the only source that produces +Eu, with the exception of extremely plagioclase-rich detrital hostrocks. However, the explorationist needs to know whether the hydrothermal component is partly or completely obscured by the other source contributions. Consequently methods of subtracting the effects of the other sources are of interest. By way of example, Fig. 20 shows hypothetically how the addition of increasing abundances of silicate hostrock can 'swamp' the Eu anomaly in a hydrothermal ironstone; these examples model the addition of adjacent hostrock to ironstone sample Par 5 from Magpie, to

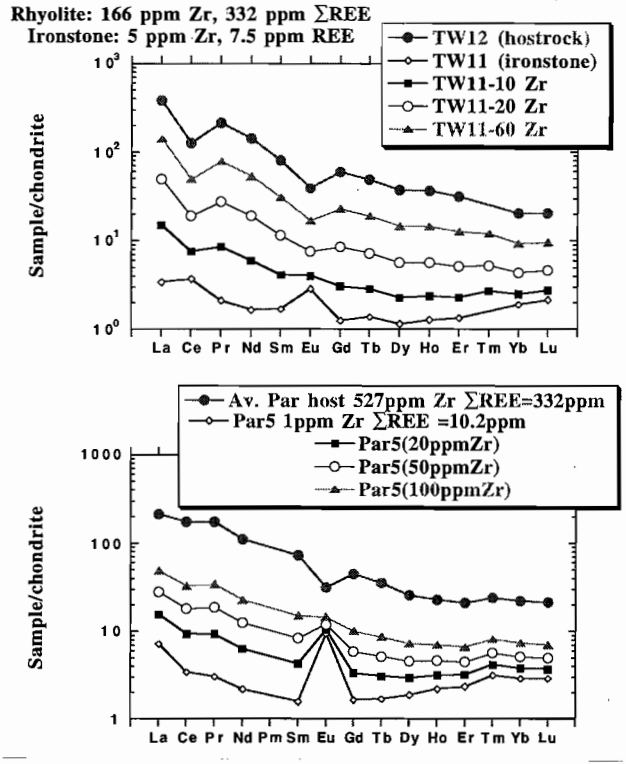

Fig. 20 **Upper.** Modelling of physical mixing of Thalanga TW11 ironstone with adjacent rhyolite (TW12—notably Ce depleted). **Lower.** Modelling of the hypothetical physical mixing of Magpie Par 5 ironstone with its immediate average hostrock. In both cases the aim is to determine at what added detrital Zr content(a proxy parameter modelling the amount of added hostrock) the Eu anomaly would be obscured. In reality the Ti/Zr values do not support such a mixing in this case.

show that the Eu signal is swamped at ~20% hostrock addition. For sample TW11 at Thalanga, the signal is obscured by a much smaller addition of 5 ppm Zr-equivalent hostrock. The difference between the two examples is the abundance of REE in the hostrock, and particularly the size of the +Eu anomaly.

A real example of submergence of the hydrothermal REE component by clastic REE is provided by the classic tetsukiei of the Japanese Kuroko belt. Here REE patterns in highly geochemically anomalous silica-iron rocks immediately overlying ore are LREE-enriched with flat to -Eu anomalies (Kalogeropolous & Scott 1983). This is a very surprising observation, given the metal enrichments involved. The likely solution to this is the very high clastic contents of tetsukiei, evidenced geochemically by Zr contents of 64–129 ppm— far higher than values in Mt Windsor ironstones, which imply that the Eu hydrothermal signal is swamped in this instance.

One aim of the following section is to review methods of subtracting the detrital component and quantifying the remaining pattern.

REE studies of high temperature >250° C VHMS systems on the modern seafloor have found that vent fluids and their sulfide precipitates have strongly LREE-enriched profiles with very strong +Eu anomalies (Mills & Elderfield 1995, and many previous papers), whereas metalliferous sediments that have formed tens of kilometres down-current from such systems by particulate settling, are characterised by seawater-like patterns (Ruhlin & Owen 1986). Seawater-like patterns also occur in some proximal vent precipitates (Fig. 21 ; Barrett et al. 1990). The seawater REE patterns in metalliferous sediments develop by adsorption of REE on to manganese oxide particles in the water column and on the sediment surface once settling has occurred. ΣREE and the seawater-like character are more pronounced with greater distance from the hydrothermal source. The -Ce anomalies and flat REE/chondrite patterns in some vent precipitates are probably produced by convective mixing of hydrothermal and marine waters at the time of exhalation (Barrett et al. 1990). Iron oxyhydroxides also adsorp REE at low temperatures, and seafloor sites where these materials are exposed to seawater for prolonged periods, such as low temperature Fe-Mn vent zones, and the oxidised zones of seafloor sulfides, may approach a seawater REE pattern, although in the latter case, residual high temperature barite retains its hydrothermal signature (Barrett et al. 1990).

LREE-enriched patterns with +Eu have been observed in ancient iron formations associated with various styles of massive sulfide deposit, and in all cases have been attributed to high temperature seafloor vent processes (e.g., Lottermoser 1989, Peter & Goodfellow 1996, Spry in press, and many others). In similar fashion, Duhig et al. (1992) attributed positive Eu anomalies from near-Thalanga ironstones to high temperature fluids. Where Lottermoser (1989) observed Fe-Mn-rich lithologies with negative Eu anomalies in the Broken Hill area, he suggested that they represented locations in which a high detrital component obscured the hydrothermal signature;

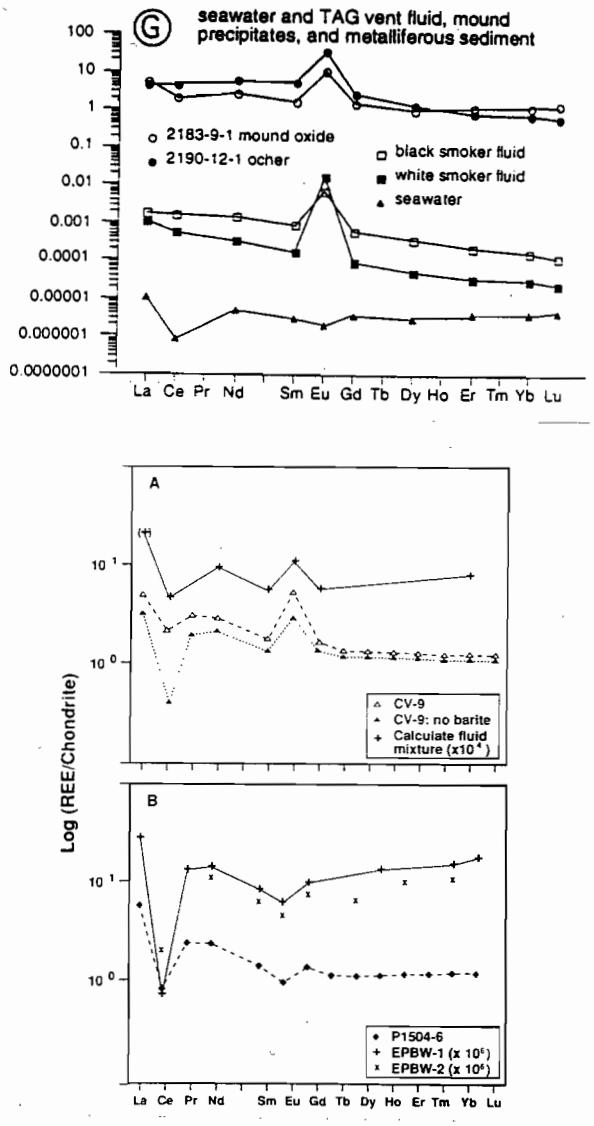

Fig.21a REE/chondrite compositions of seawater, metalliferous sediment on mounds, mound debris, and hydrothermal fluid compositions from the modern TAG seafloor sulfides (Mills & Elderfield 1995); 21b Illustration from a seafloor system that is characterised by "hybrid" hydrothermal-seawater REE patterns—the fluid mixture is calculated at 500 seawater: 1 hydrothermal fluid. CV9 — a barite-sulfide silica sample; P1504–6— composition of silica from the same area, interpreted to reflect non-hydrothermal silica deposition; EPBW— East Pacific Bottom Water (after Barrett et al. 1990).

Spry et al. (in press) suggest that >~30% detrital component will achieve this. As shown in the examples in Fig.20, the actual hostrock percentage needed to achieve this will depend on the strength of the primary hydrothermal Eu anomaly, the type of Eu anomaly in the hostrock, the REE abundances in both hostrock and the primary hydrothermal material, as well as the mixing ratio of each.

REE elements have excellent potential as exploration guides in ancient VHMS terrains. However, many questions remain to be answered. For instance, the distance from ore to particular types of REE response is not yet well-defined. The uniformity of REE response for a given ironstone is also yet to be established, although this question is addressed below.

Near-ore ironstones

Magpie area

For the Par 1–14 ironstone, the typical REE pattern is 'dish'-shaped, with distinct negative Ce anomalies, and smaller negative Eu anomalies. The extremely low Zr contents of these samples (mainly 1–3 ppm) is good evidence that the patterns dominantly reflect the non-detrital component. La_N/Sm_N, an index of the gradient of the LREE part of the pattern, is 2.6–8.5. A strong positive Eu anomaly is present in the most eastern sample of the Par 1–14 ironstone, which is the only barite-bearing sample. It is accompanied by a distinctly weaker negative Ce anomaly than in the other samples (Fig. 22).

A strong +Eu anomaly also occurs in a more distal ironstone at Par16 (Fig. 2), again associated with a very weak -Ce anomaly, and anomalous Ba (0.62 wt. %). Weak positive anomalies are also present in ironstones Par 18 and Par 20 in the deep Magpie footwall. Lower La/Sm ratios for these samples are consistent with some inheritance of the basalt REE signature of the hostrocks here, but this cannot account for the +Eu anomaly.

ΣREE for all Magpie ironstones varies from 2.6–57 ppm. The nearest ironstone to ore (=Par 1–14) contains subtly higher ΣREE values (lowest values ~7 ppm) than the lowest values of those farther away (~2–3 ppm),but more data is required to substantiate this, and given the variations observed in the detailed sampling of the SJ and FJ lenses, it is not considered significant.

Lastly, the hostrocks to the Par 1–14 ironstone are distinctly REE enriched (ΣREE = 245–434 ppm), but most notably possess similar negative Ce anomalies to the adjacent ironstones, an unusual feature for igneous rocks, in that it requires preferential removal of Ce.

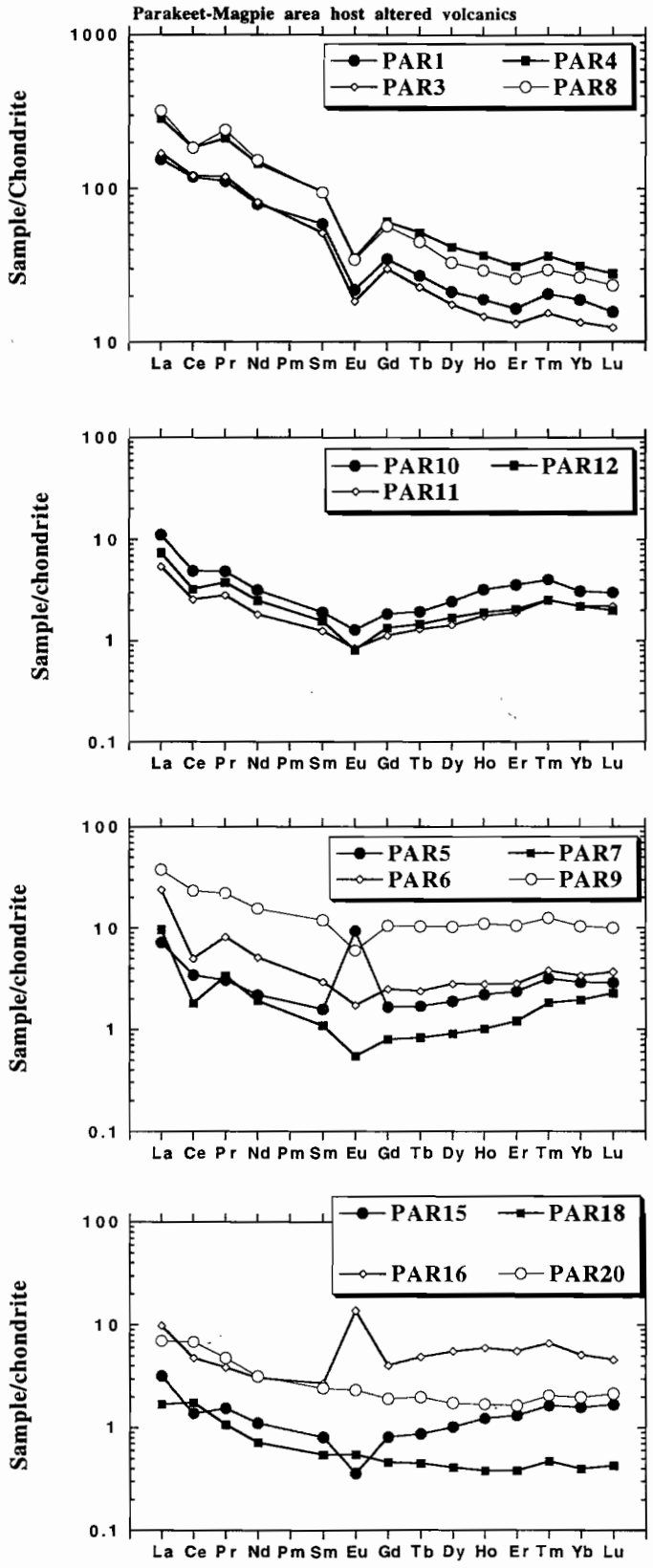

Fig.22 REE/chondrite compositions of hostrocks and ironstones from the Magpie area. Par 1–4, Par 8 host strongly fractionated rhyolite; Par 5–12— single ironstone 700 m from Magpie; Par 15–20 selected ironstones from the Magpie area (see Fig. 2 for locations).

On the basis of the previous discussion, great significance is attached to the samples with +Eu, especially as these mainly have very low Zr contents, suggesting that the detrital REE contribution is very small. The +Eu is probably also understated, given that most barite was not dissolved in the analysis of these rocks (see methods section). The following conclusions are drawn:

(1) ironstones up to 700 m from the Magpie VHMS mineralisation contain components that were originally leached by high temperature fluids;
(2) where the ironstone has a significant size, it should be sampled at at least 20m intervals. If this had not been done at Par 1–14, the +Eu sample at the site would probably have been missed, and the exploration significance of the site down-graded;
(3) Par 16 (Fig. 2) also contains a +Eu anomaly. Unfortunately, none of the nearby ironstones were sampled at the same density as Par 1–14, so it is not possible to determine whether the "influence" of the Magpie hydrothermal site extends at least as far as Par 16 (such that +Eu was missed in other ironstones because of inadequate sampling), or whether Par 16 represents a separate high temperature hydrothermal system. In any case, Par 16 would be an important sample to follow up in an exploration program.

Thalanga area

+Eu anomalies were discovered in the Thalanga area by Duhig et al. (1992), and confirmed by RGC exploration. In our minor follow-up sampling program, ironstones were sampled in more detail, at 5 m intervals.

Previous analyses in Duhig et al. (1992) had determined that +Eu anomalies characterised 3 ironstones to the west of Thalanga, raising the possiblity that all ironstones in the cluster may possess this feature. In the current study, TW1–7 ironstone uiformily possessed the +Eu anomaly, as did the TW11 sample up-dip from massive sulfide mineralisation, but the adjacent TW8–10 ironstone was characterised by flat to -Eu (Fig. 23). Samples with and without +Eu anomalies had similar La/Sm ratios of 2.0–7.0, indicating this parameter is not a useful discriminant from barren ironstones.

Variation within a single lens 35 m long at TW1–7 (Fig. 23) confirmed the observation that even at small scales, iron-silica bodies are not geochemically uniform, but the geochemical variation that is present is very systematic. At this site, the size of the Eu anomaly dropped from east to west from Eu_N/Eu_N^* = 8 to ~2, in concert with a ΣREE drop from 15 to 5 ppm, and orders of magnitude drops in base metals and Ba. Zr in the centre of the lens is 8–12 ppm, which is evidence that there is a significant detrital REE component in the ironstone that has not been subtracted out in Fig. 23.

In summary, (1) both "barren" and "near ore" signature ironstones may occur within 100 m of massive sulfide mineralisation; (2) individual ironstones exhibited a similar REE signature along their length, although the strength and shape of this signature varied systematically; and (3) ΣREE even in "fertile" ironstones is low, <15 ppm, raising the strong possibility that their signature could be obscured by a high detrital component.

"Barren" ironstones

SJ and FJ areas

Patterns at FJ and SJ lenses show strong similarities, summarised as LREE-enriched to 'dish" patterns (in which there is an increase in the HREE from ~Eu on), -Ce anomalies in some samples, and ubiquitous small -Eu anomalies (Fig. 24). In the FJ lens, there is a pronounced zone of -Ce in the middle of the deposit, coinciding with high Fe values (Fig.18), and a second zone at the western end. The western end also exhibits higher ΣREE, and an erratic increase in La/Lu (ie an increase in LREE to HREE ratio). La/Sm is highly variable, 2.95–18.31, with a mode at ~7. Hostrocks display highly variable patterns depending on the degree of alteration. Strong carbonate-chlorite alteration of andesite resulted in very LREE-enriched patterns with weak to strong -Ce, a feature of hostrocks that is repeated at both barren and near-ore sites (e.g., Par 1–4, TW12 too).It is not present in the high temperature alteration at Thalanga (Paulick, this volume). -Ce in footwall alteration is not a well documented feature, and may be a hallmark of shallow oxidised seawater alteration that requires further investigation.

At SJ lens, the eastern sub-lens has markedly

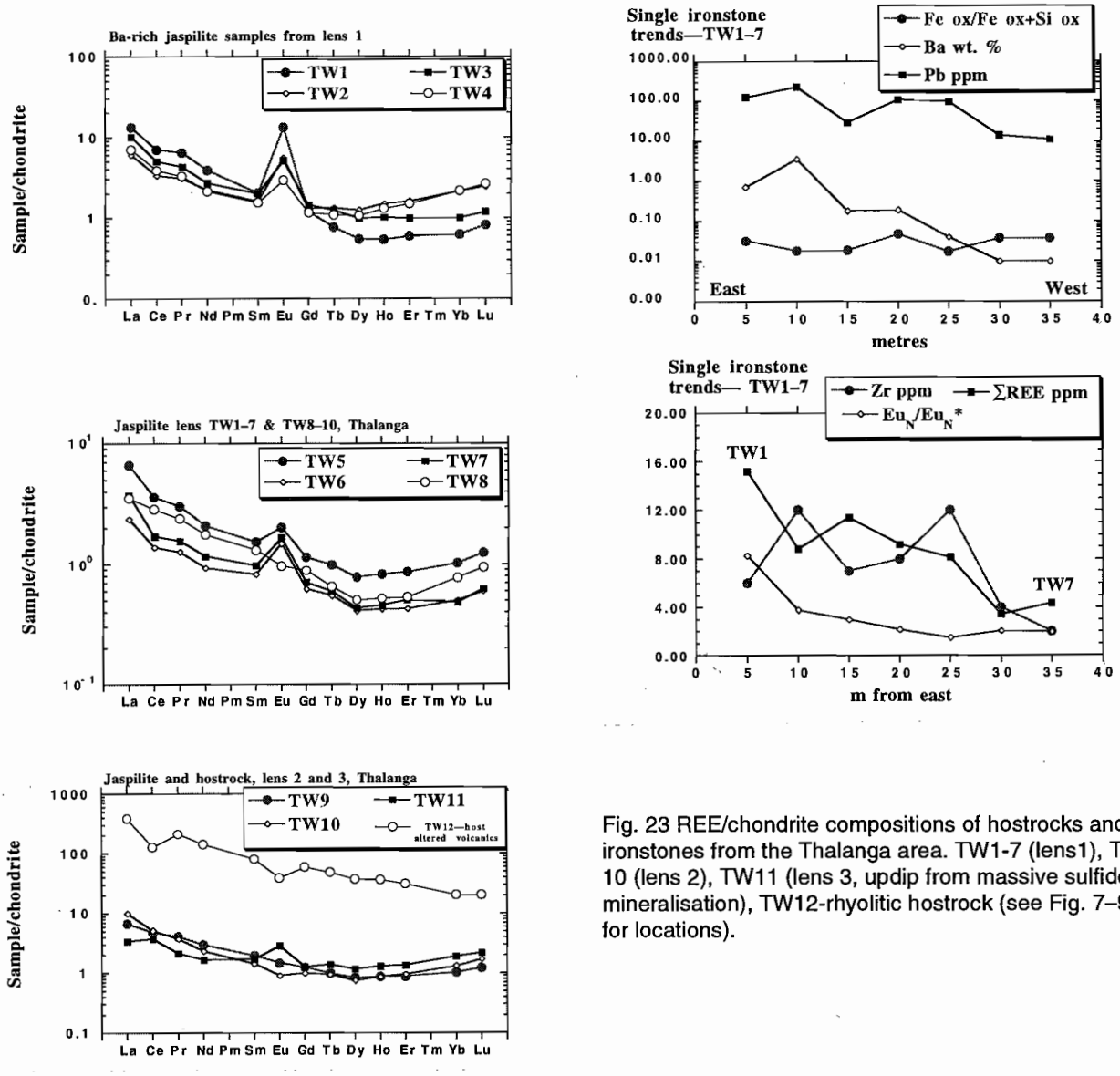

Fig. 23 REE/chondrite compositions of hostrocks and ironstones from the Thalanga area. TW1-7 (lens1), TW8–10 (lens 2), TW11 (lens 3, updip from massive sulfide mineralisation), TW12-rhyolitic hostrock (see Fig. 7–9) for locations).

higher REE than the western sub-lens. ΣREE at this site display a positive correlation with Mn and possibly Ti/Zr, illustrating the complexity caused by mixed provenance at SJ lens (Fig. 19).

In summary, the detailed analysis of these barren ironstones has shown that they possess generally similar REE patterns within and between lenses, although ΣREE is variable, from 6.5–150.8 (mode ~20) for FJ lens, and ΣREE of 8–91.6 ppm (modes at 24 and 50 ppm) for SJ lens. The typical features are small -Eu anomalies, variable -Ce anomalies, and moderate LREE enrichment.

Subtracting the detrital component

Low-immobile element ironstones

The simplest means of identifying the non-detrital component is to select samples with very low immobile element compositions, such as Zr <1 ppm. This is certainly possible in the MWVB, for instance at Magpie, and the FJ lens.

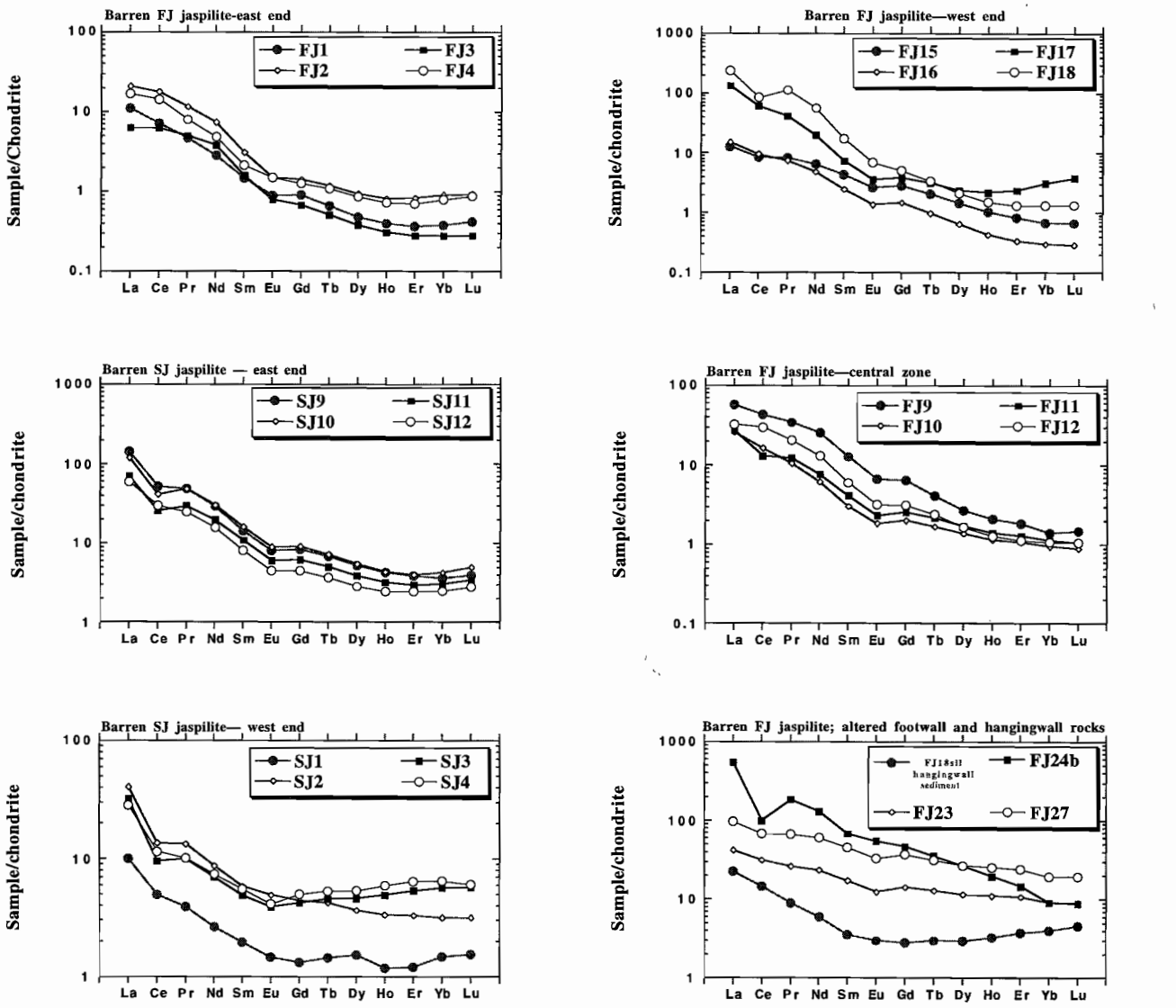

Fig. 24 REE/chondrite compositions of hostrocks and ironstones from the Brittania (FJ) and Sunrise Spur (SJ) areas. FJ1–18 (FJ lens ironstones, locations shown in Fig. 15), FJ18.sil–27 (hostrocks from the FJ lens area; locations in Fig. 14), SJ1–12 (SJ lens ironstones).

Ironstones— known detrital chemistry

Where there is strong evidence that an ironstone formed by replacement of hostrock (e.g., Doyle 1997), or the detrital material in the ironstone has been precisely quantified, an appropriate percentage of the REE composition of the hostrock can be subtracted from that of the ironstone to produce a non-detrital/non-hostrock REE ironstone composition. The assumptions of this method are:

(1) Elements such as Ti, Zr and Al remained immobile during ironstone formation;

(2) The hostrock REE values do not vary greatly in the vicinity of the ironstone, and so can be used as a reasonable estimate of the replaced material;

The advantage of the method is that the detrital component is removed from each sample, rather than from some average of the overall population. This is important because of sampling evidence presented above that only a part of some ironstones may contain a near-ore signature.

The detrital component is quantified by assuming that the % hostrock within an ironstone is indicated by the ratio: immobile elements in the ironstone/immobile elements in the unaltered hostrock, ie:

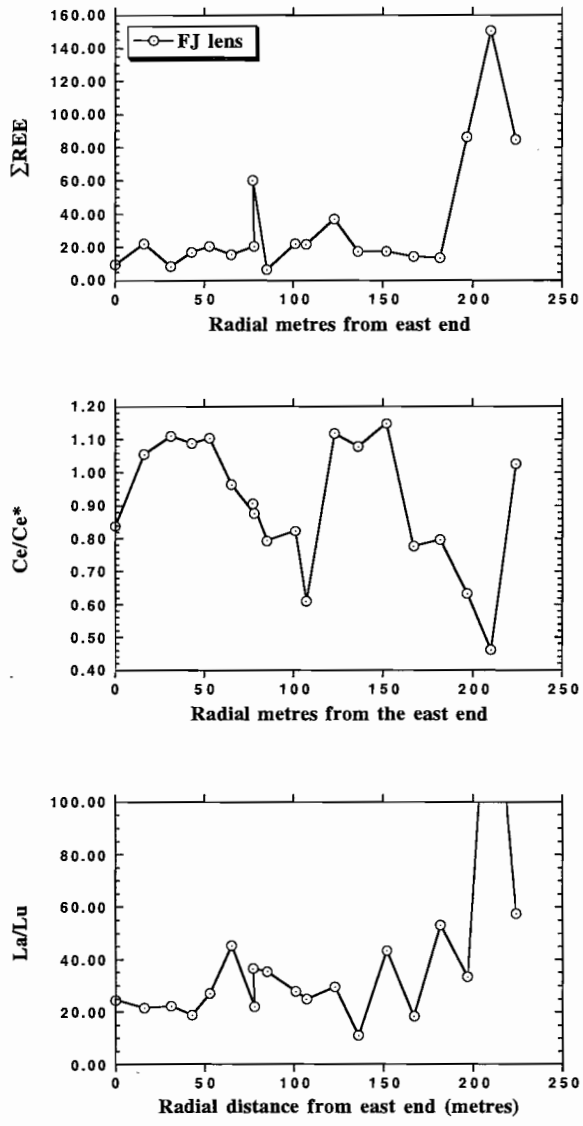

Fig. 25 REE behaviour with distance in the ironstone at the FJ lens.

(1) ppm REE_{irst} - [(ppm $Zr_{irst.}$/ ppm Zr_{host}) x ppm REE_{host}] = ppm non-detrital REE_{irst}

The resulting values are normalised to chondrite for plotting. The method does not take account of mass or volume changes, which may influence concentration.

No good example was found in the data base to apply this method by example.

Ironstones—unknown detrital chemistry

In most of the examples examined in this study, the Ti/Zr values indicate that the immediate hostrocks do not represent the detrital component in the ironstone. This may be because many ironstones were deposited at a stratigraphic break, with nearby volcanogenic sedimentation adding fine particulates to the growing deposit. This idea accounts for the generally larger range of Ti/Zr values found in ironstones compared to most MWVB rocks, if these elements are considered to be immobile. Liaghat & MacLean (1992) outline a method of determining the detrital or replaced precursor using the immobile elements in a chemical sediment to determine the position in a regional igneous fractionation sequence. However, this technique requires complete documentation of regional geochemistry, and the precision supplied may not be sensitive enough to subtract a detrital REE component.

An alternative method with a similar principle is illustrated at FJ lens, and is applicable where immobile elements and the REE are related by good linear correlations. The method is simple. It assumes regression of the linear correlations to Zr = 0 ppm for each element, and then normalising the new REE values to chondrite. A test of the reliability of the method is the smoothness of the resulting pattern, which should represent the average non-detrital component of the ironstone. The method requires excellent analytical data for the immobile elements and REE.

By example, Fig. 26 shows the regressions for FJ lens, and Fig. 27 shows the resulting average non-detrital composition, compared to low- and high-Zr samples. The smoothness of the pattern, as well as the statistically significant R values for the linear regressions, indicate that the conclusion is reliable. However, it is an averaged result, which does not inform us about variation within the ironstone due to other non-detrital processes. Some insight into these could be gained by comparing only low-Zr sample patterns.

The conclusion reached by the application of this method to the FJ ironstone is that for some samples, ~50% of the REE are detritally sourced, even though the maximum Zr value is only 13.8 ppm. The non-detrital signature indicates a LREE-enriched hydrothermal fluid with weak -Eu and -Ce anomalies,

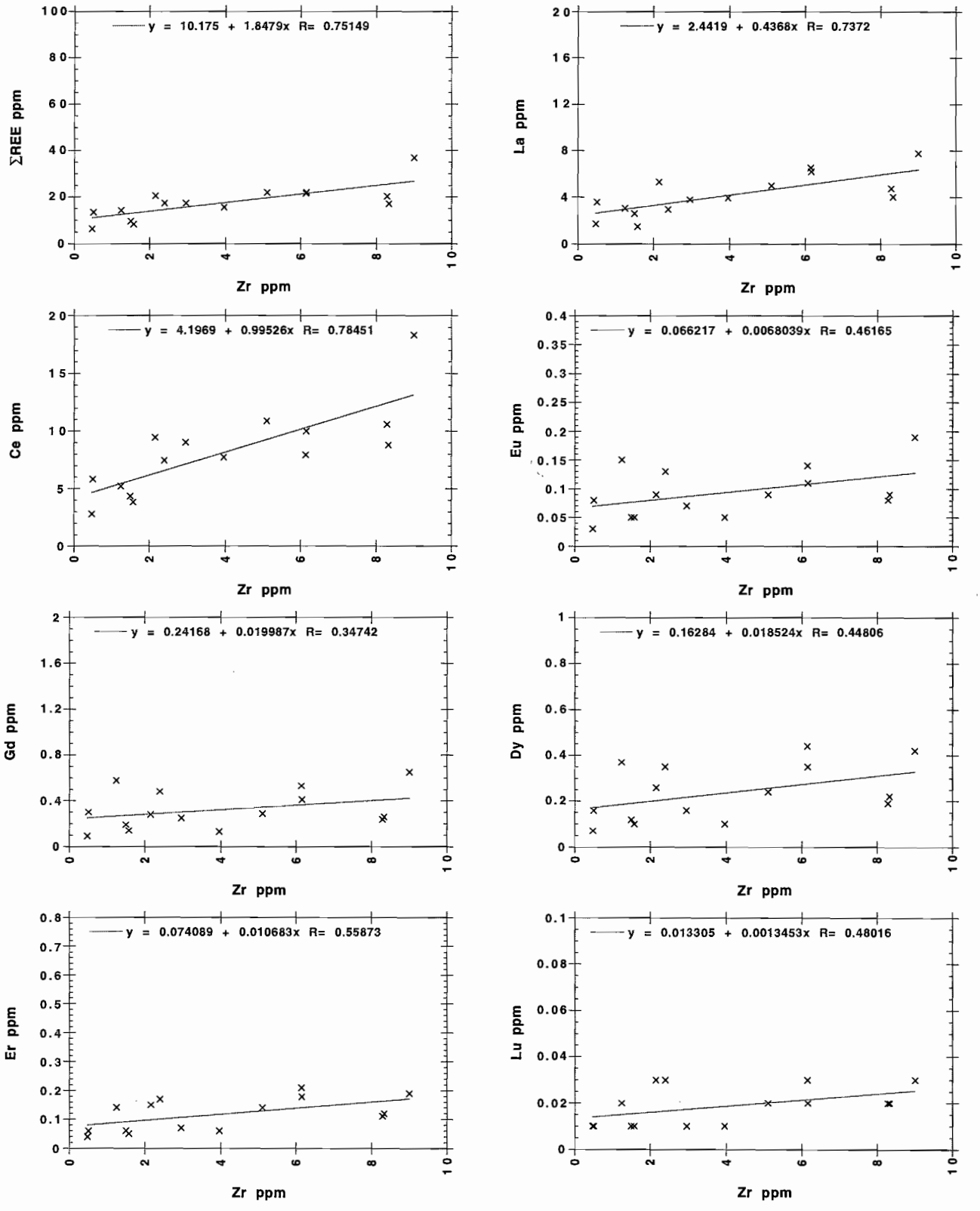

Fig. 26 REE-Zr correlations at FJ lens.

unlike that observed associated with high temperature VHMS fluids.

Normalising the data to hostrock

Normalising the chondritic ironstone values to associated hostrock of similar Ti/Zr values will highlight the relative enrichments and depletions of REE in the ironstone. However, care must be taken in using this method to identify +Eu anomalies because it highlights **relative** enrichments. Consequently a hostrock with strong -Eu, ratioed to an ironstone with a weaker -Eu anomaly, with give rise to a +Eu anomaly after normalisation, but this anomaly does not indicate that the ironstone itself had a chondritic +Eu anomaly, as shown in Fig. 28.

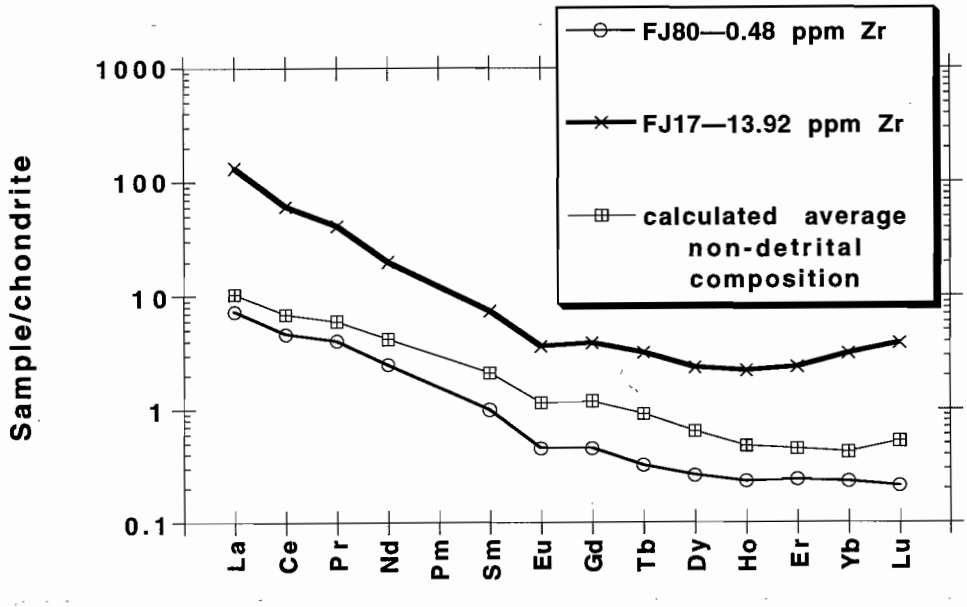

Fig. 27The calculated average non-detrital FJ ironstone composition, compared to ironstones with low and high Zr contents. Greater detrital component results in higher ΣREE, and LREE-enrichment.

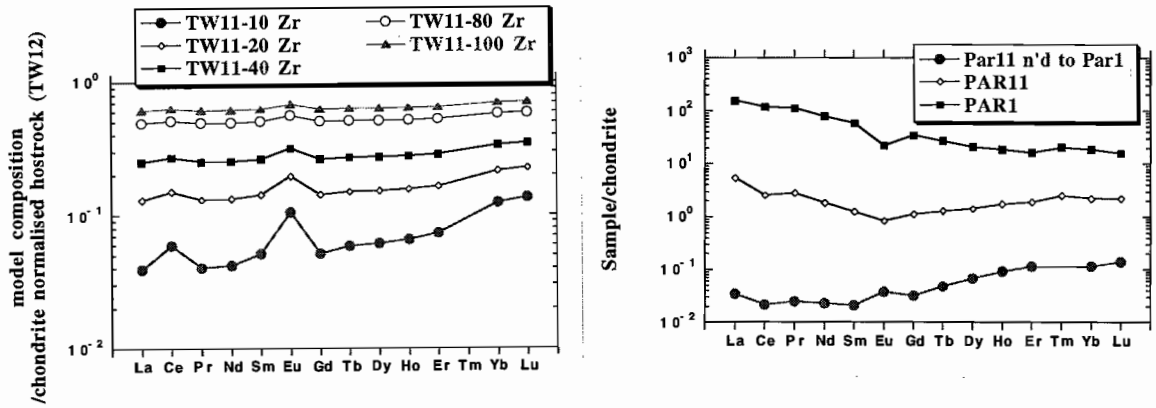

Fig. 28 Two examples of normalising ironstones to hostrock. In the top example, the model ironstone REE pattern that was formed by adding hostrock to TW11 (Fig. 20) is ratioed to hostrock TW12, and this process identified a geniune Eu enrichment in the ironstone. However, in the second example, normalising Par11 to adjacent hostrock Par1 produced a spurious +Eu anomaly.

Oxygen isotopes

Introduction and work undertaken

Oxygen isotopes are a useful exploration tool in some ore systems, particularly where only one mineral is sampled. Mineral oxygen isotopes display a strong fractionation with temperature, which permits the detection of heating or cooling gradients that accompanied mineral deposition. If the temperature of deposition is known from independent sources, the isotope data can also be used to determine the oxygen isotope composition of source waters. Generally, mixed aggregates of fine-grained iron oxide, chert and quartz are not useful for this purpose because iron oxide and quartz have fractionate oxygen in opposing directions with temperature. However, quartz veins ±sulfide, carbonate or barite are common in the late stage paragenesis of many ironstones, and these are coarse enough for drill-separation. Samples were obtained for a pilot study from Thalanga (TW4, 6, 8), Magpie (Par 5, 7, 10, 17), and FJ lens (FJ4a, FJ8, FJ24c, FJ26). Typical material is shown in Plates 1 and 2, to assist explorationists with sample selection. Care was taken to avoid post-ironstone quartz veins related to tectonism; these are generally planar or gash veins of milky quartz, whereas syn-ironstone veins are very irregular in thickness and vein-wall shape, and additionally may contain ironstone gangue minerals.

Results

Results are shown in Fig. 29 and Table 2. There is an excellent separation of near-ore ($d^{18}O$ = 9.1–13.8‰) and "barren" ironstones (14.1–19.5‰), which has strong potential application in exploration. If a seawater value of 0‰ is assumed for the formative fluids, then using the combined quartz-calcite and calcite-water curves of Sharp & Kirschner (1994) and O'Neil et al. 1969 (considered most appropriate for low temperature systems) a temperature range of 131–190° C is calculated for the barren FJ lens (a uniform 180° C for the footwall veins), whereas the near-ore systems are in the range 197–277.4 (most are below 235° C). However, the fluid value is an assumption only, and requires independent evidence to support it. For instance, Pisutha-Arnond & Ohmoto (1983) determined that lower temperature fluids in the Kuroko ore systems (<200° C) in the Kuroko

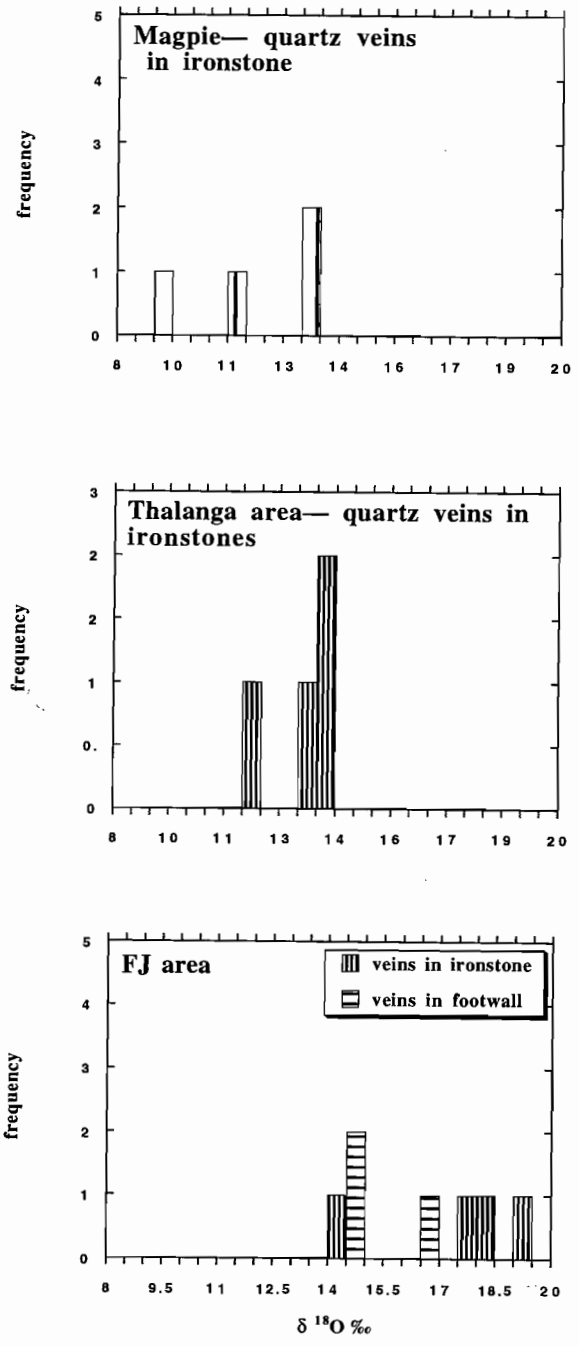

Fig. 29 Histograms of $\delta^{18}O_{quartz}$ from mineralised and barren ironstones.

Table 2 Oxygen isotope values of quartz veins and amoeboid megaquartz sections of ironstones.

	Sample	$d^{18}O$ ‰	Comment
FJ lens	FJ 1	18.212	quartz vein in ironstone
FJ lens	FJ 4a	17.519	quartz vein in ironstone
FJ lens	FJ 8	19.466	quartz vein in ironstone
FJ lens	FJ 26	14.120	quartz/chert in ironstone
FJ lens	FJ 24a	14.824	quartz vein in footwall
FJ lens	FJ 24c	14.857	quartz vein in footwall
FJ lens	77514	16.717	quartz vein in footwall
Thalanga area	TW2	13.583	quartz vein in ironstone
Thalanga area	TW4	13.813	quartz vein in ironstone
Thalanga area	TW6	13.390	quartz vein in ironstone
Thalanga area	TW8	11.560	quartz vein in ironstone
Magpie area	PAR 5	13.024	quartz vein in ironstone
Magpie area	PAR 7	13.343	quartz vein in ironstone
Magpie area	PAR10	11.194	quartz vein in ironstone
Magpie area	PAR 17	9.142	quartz vein in ironstone
Highway	HW 50	-0.237	barite vein
Highway	HW 75	1.77	barite vein
Sunrise Spur	SS71a	1.292	barite vein

systems had $d^{18}O$ as low as -6‰ (and higher temperature fluids had values of 0 to >0‰), which when employed here indicate temperatures of 85–176° C. This was supported at Fukazawa and Furotobe mines in the Kuroko district, where Tsutsumi & Ohmoto(1983) calculated fluid values of -9±5 and -3±5‰ respectively for the tetsuskiei phase.

Barites are also documented for comparison but are not discussed in the text. See Plates 1 and 2 for typical appearance of samples.

Discussion

For each of the sample populations, a maximum varation of 5‰ was found. Consequently, the sample sizes used in this pilot study are the minimum required per lens to statistically characterise the isotopic composition. Suitable quartz veins do not occur in all parts of ironstones, so that careful sampling is also required, particularly to ensure that the quartz formed as part of the ironstone. Oxygen isotope analysis from other ancient iron-silica deposits provided the following temperature estimates: Kuroko deposit tetsusekiei: 90±30° C and 110°±30° C° (Tsutsimi & Ohmoto 1983); Norwegian Caledonian Lokken and Hoydal deposit area: 150–220° C (Spry et al. in press); Iberian pyrite belt deposit Aljustrel: ~120° C (Spry et al. in press). It is encouraging that Mt Windsor ironstones formed in the same range, although the presence of abundant microbial fossils in these suggests, in agreement with Tsutsimi & Ohmoto (1983), that much of the earlier history occurred at lower temperatures. It is also encouraging that the oxygen isotope evidence supports the conclusion from the trace elements that the late phase of near-ore ironstones was on average at least ~50° C hotter than "barren" systems.

General model of seafloor ironstone formation

Although many explorers feel that genetic models do not help locate ore deposits, in this case a genetic model is useful in explaining the observed geochemistry of ironstones and helps us recognise fertile and barren systems.

In all ironstones examined, regardless of scale, the dominant textural characteristic is early massive to inhomogeneous iron-silica deposition, overprinted by several generations of veining, in most cases becoming more silicic and metal-rich with time. However, the later generations of veining do not extend across the entire early ironstone, but tend to become more focussed around one or more smaller areas, creating more confined geochemical anomalies within the ironstone. This unusual tendency of systems to "shrink" as they evolved to higher temperature may have reflected local heating cycles that were quickly exhausted, or possibly were a symptom of the choking of general crustal permeability by mineral precipitation and its refocussing into one or more major channelways which formed massive sulfide deposits. Whichever reason is correct, the MWVB ironstones represent unusual windows into the heating cycle of VHMS mineralisation, and will warrant further study.

The vein networks that make up ironstones are commonly fine and difficult to observe on uncut surfaces. This has given rise to the premise that ironstones are geochemically massive because at first sight they are texturally massive. This is not the case.

Stage 1—low temperature hematite-chert-quartz ±barite deposition

Although Doyle (1997) has presented excellent evidence that some ironstones in the Reward area formed by replacement of volcanic glass in the sub-surface, evidence of microbial fabrics, very low immobile element contents, immobile element ratios that do not correlate with hostrock, preserved vent structures, and bedded fabrics near the tops of some bodies, require that many others formed at least partly at the sediment surface. During this stage a range of processes discussed by Duhig et al. (1992) operated, including inorganic and microbially catalysed deposition of iron oxyhydroxides, and enclosure of these by colloidal silica which subsequently crystallised and formed a range of textures, including chert spherules and megaquartz nodules in vughs. The fabrics and sparse footwall exposures of widespread alteration and veining indicate that most chemical precipitates formed directly upon zones of diffuse outflow. There is evidence at FJ lens that minor U and elevated Ba was deposited during this phase (see below). A wider range of Ti/Zr than seen in MWVB hostrocks suggests that the clastic content may reflect particulate transport from more than one source during ironstone deposition.

Stage 2— low to moderate temperature veining (Ba and base-metals mobile)

As with VHMS deposits, these lower temperature sister systems evolved with time, but by a process of focussing zone refining (Fig.30). This may have occurred because the Stage 1 deposits choked the exhalation zone, and fluid flow retreated to zones of higher permeability. At FJ lens the second stage appears to have been corrosive, pervasively cutting through first stage products, and so providing its own renewed permeability. Geochemically these zones were more silica-rich than Stage 1, also containing higher base metals, Mn, As, Mo, Ba, Se, Cd and Bi. Hydrothermal REE patterns were similar to Stage 1, with LREE-enrichment and -Eu anomalies; -Ce anomalies were common, resulting either from Mn-Fe scavenging or from direct seawater precipitation by convective mixing. Co, Ni and other transition metals were deposited from cold seawater in proportion to the exposure time of surfaces, and their Mn-Fe contents. If oxygen isotope fluid values

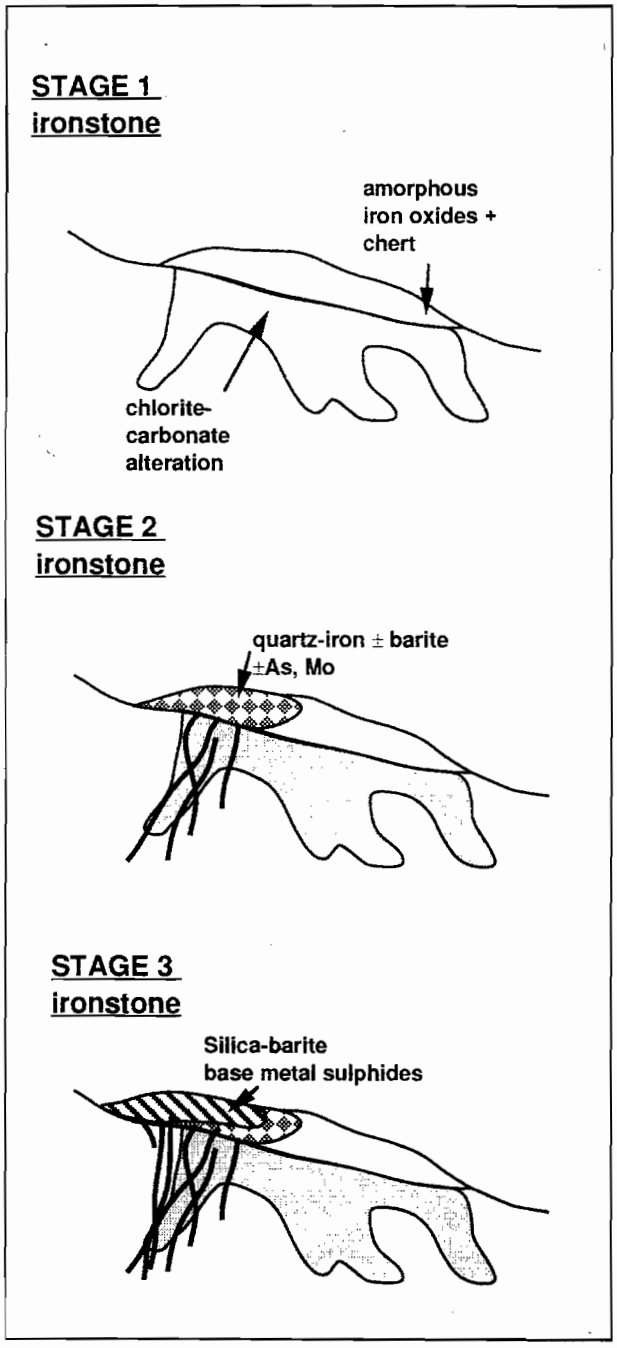

Fig.30 A schematic representation of the evolution of sediment surface ironstones.

of -6 to 0‰ are assumed, the temperature of quartz deposition of this stage at FJ lens was between 85 and 190° C.

Stage 3—moderate temperature veining (Ba, base metals and Eu)

If oxygen isotope fluid values of -6 to 0‰ are assumed, the temperature of vein quartz deposition of this stage in the Thalanga and Magpie areas was between 127 and 277° C.The evidence that low temperature systems evolved towards higher temperature systems, comes from ironstones such as Par1–14 at Magpie and TW8–10 at Thalanga. Here most of each ironstone is a uniform stage 1–2 deposit. However, localised zones contain barite-quartz veins, barite concentrations at % levels, elevated base-metals, and strong +Eu anomalies (with the latter feature marking the real difference between late Stage 2 and early Stage 3). This is interpreted as a continuing, focussed, moderate temperature over-print, that only occurred in ironstones in the vicinity of massive sulfide systems. At Par 1–14 the anomalous Stage 3 zone occurs near the edge of the Stage 1-2 ironstone, which may be evidence that fluid flow was forced to the margins by choking of permeability. The most extreme product of this process seen in this study was TW1–7, where within 35 m, one end of a ferruginous chert contains below detection Ba, and a small +Eu anomaly, grading to the other end, with 3.5% Ba, and strong +Eu, base-metals, and higher ΣREE, correlating with a visual increase in silica-barite vein density (Fig. 23).

Synthesis of exploration vectors provided by iron-silica deposits

Size of ironstone

Near-ore ironstones may be easily overlooked because in places they are very small (up to a few tens of metres long at Thalanga and Highway-Reward) poddy deposits, whereas many barren ironstones can be much larger. Near-ore ironstones are not always small, as illustrated at Magpie, but where they are large, the "stage 3" sections of them are about the same size as the Stage 3-only pods. The implications of this observation for the genetic model above are that the volume and duration of low

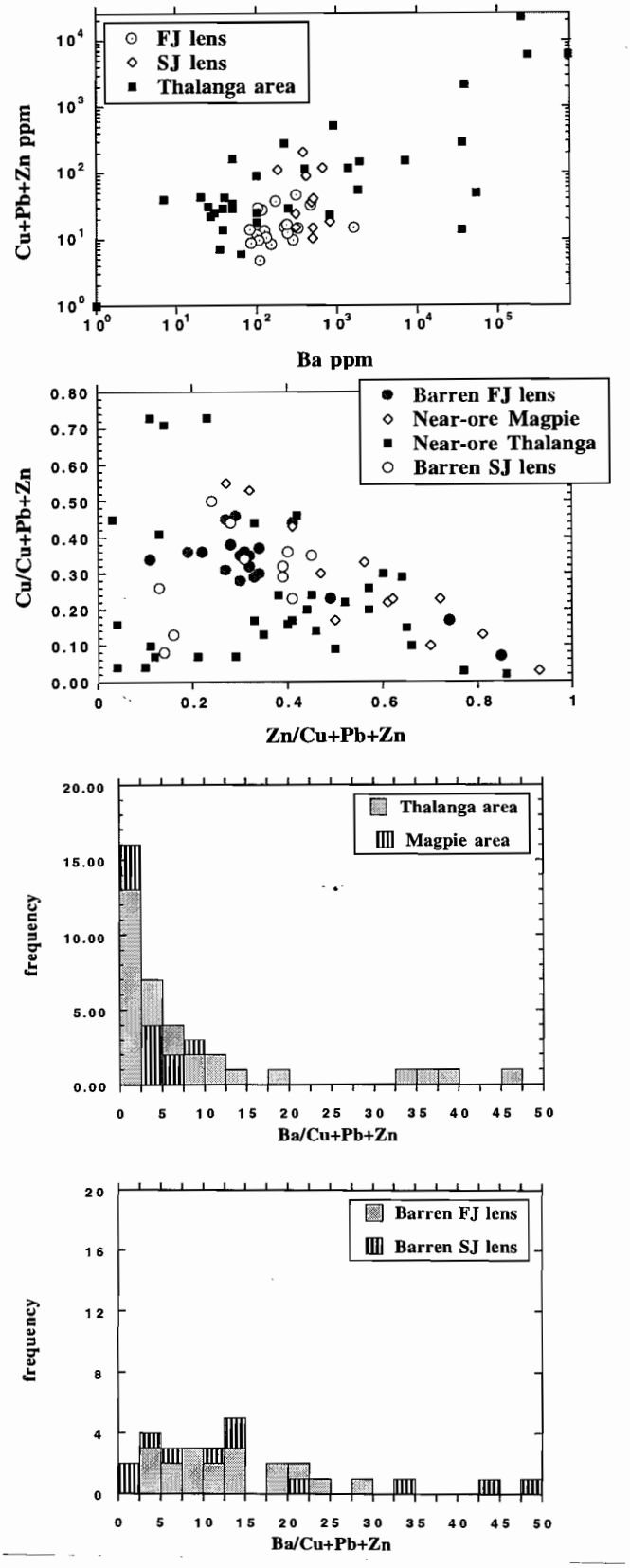

Fig.31 An overview of base-metal and Ba trends for near ore and barren ironstones

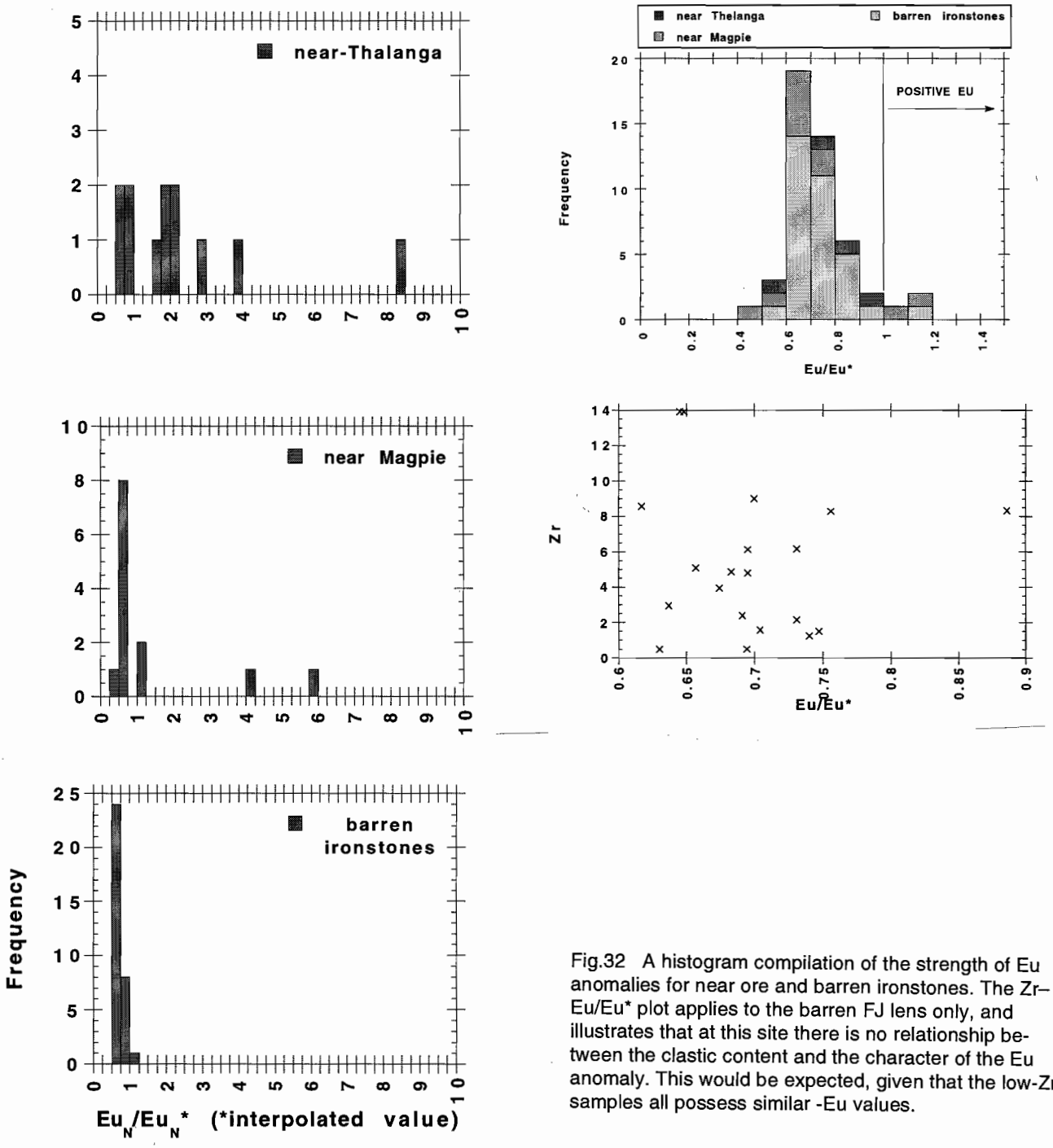

Fig.32 A histogram compilation of the strength of Eu anomalies for near ore and barren ironstones. The Zr–Eu/Eu* plot applies to the barren FJ lens only, and illustrates that at this site there is no relationship between the clastic content and the character of the Eu anomaly. This would be expected, given that the low-Zr samples all possess similar -Eu values.

temperature Stage 1-2 activity seems to vary from site to site, so for instance the TW1–7 lens is mainly a Stage 2-3 body, whereas Par1–14 has a large Stage 1-2 section and a small Stage 3 zone.

Position of sulfides relative to ironstones

There is only limited data relevant to this question, so the conclusions must be treated cautiously, and new discoveries could change the picture dramatically, as seen in the Thalanga west 45 area. Hill (1996) documented the variable replacement of magnetite-quartz ironstones within and on the margins of the Thalanga orebody, indicating that targeting of ironstones can potentially lead directly to buried VHMS mineralisation. The recent Thalanga west 45 discovery within 40m of ironstone is another direct indicator of this. Taken in overview however, the Thalanga hydrothermal products consist of a cluster of ironstones at two stratigraphic levels around a small massive sulfide body, ~1800 m west of a large massive sulfide body with few ironstone relicts. The two may represent two linked hydrothermal fields, so that exploration should target ironstone clusters directly as well as along-strike positions. This is extremely relevant to Magpie, which shows similarities to Thalanga, in that the known mineralisation occurs ~700 m along strike from a large region of ironstone bodies, but there is alteration (zones of cordierite+ elevated base metals; Gregory 1984) and geochemical evidence of localised high heat flow within the ironstone field. Here important heat flow/fluid flow factors may also be the edge of the felsic volcanic pile, which tapers into the ironstone cluster.

Field textures

Recognition of increasing vein complexity, increasing silicification, and abundant barite and pyrite/base-metal relicts all reflect hotter parts of ironstones, and are good exploration guides. Within silicification, an increase in hematite around late veins is a proximal feature. However, the textures of ironstones can be very fine-grained and complex, so that high quality geochemical data with sub-ppm detection limits is also required, and may be the only basis for recognising the hotter sections, as at FJ lens.

Sampling strategy

A 20m interval was the minimum effective spacing in this study. It is vital that ironstones are sampled systematically because important information can be missed if only one or two samples are considered representative of a typical ironstone (60-100 m long). This is because of the focussing of the ironstone fluids into smaller areas as the system evolves. This should be considered in drill intersections also— a single intercept of an ironstone with barren geochemistry in a drillhole does not downgrade the potential of the ironstone!

Geochemical zoning

The following geochemical associations seem to occur with increasing temperature in ironstones. Broadly this folows an evolution from Fe-Si, to Fe-Si-Ba, to Fe-Si-Ba±base metals, to Si-Ba-base metals±Fe. This can be used to evaluate prospectivity:

Stage 1: $Fe_2O_3(T)/(Fe_2O_3(T) + SiO_2)$= 0.15–0.35, U >0.2 ppm, P_2O_5 < 0.03 wt. %, Cu+Pb+Zn <20 ppm (in weathered samples), Cu/Cu+Pb+Zn =0.2–0.5, Zn/Cu+Pb+Zn = 0.2–0.45, Ba may be up to 800 ppm but is mainly <250 ppm, Ba/Cu+Pb+Zn variable from <1 to >50 (because the stage includes Ba-rich but base-metal poor ironstones towards higher temperatures), As < 10ppm, Sb -4–6 ppm, Mo < 5 ppm, -Eu anomalies, strong -Ce anomalies.

Stage 2: $Fe_2O_3(T)/(Fe_2O_3(T) + SiO_2)$= 0.05–0.15 but locally massive hematite around veins or coalesced veins, U <0.2 ppm, P_2O_5 > 0.03 wt. %, Cu+Pb+Zn =20–200 ppm (in weathered samples), Cu/Cu+Pb+Zn =0.2–0.5, Zn/Cu+Pb+Zn = 0.2–0.45, Ba may be up to ~2000 ppm, , Ba/Cu+Pb+Zn >15, -Eu anomalies, -Ce anomalies, As =20–80 ppm, Sb up to 10 ppm, sporadic Mo up to 20 ppm; La_N/Sm_N is a highly variable 2.95–18.31; ΣREE of 20–60, with some samples up to 150 ppm; Na_2O/K_2O <1, $\delta^{18}O_{qutz\ vns}$>14‰.

Stage 3: $Fe_2O_3(T)/(Fe_2O_3(T) + SiO_2)$= <0.20, mainly <10; Se >1 ppm, Cu+Pb+Zn >100 ppm, Cu/Cu+Pb+Zn =0.0–0.9, Zn/Cu+Pb+Zn = 0.0–0.8, Ba >500 ppm, Ba/Cu+Pb+Zn <15 with the exception of barite lenses, As <30 ppm, Na_2O/K_2O <0.35–8.7, $\delta^{18}O_{qutz\ vns}$<14‰, La_N/Sm_N 2–7; ΣREE <20 ppm although exceptions occur (see Duhig et al. 1992), +Eu anomalies, P_2O_5>0.03 wt %, U>1 ppm, Mo <5 ppm.

Base metal and Ba ratios

Elaborating on an aspect of the above zonation, a fundamental expected character of the increasing temperature of the ironstone overprint is an increase in alkali elements and base metal contents in the fluid (Fig. 31). Although the ironstones in the database are all weathered, there are still empirical trends in the base metal data that appear useful, and are consistent with the genetic model proposed. Very low temperature ironstones (Stage 1) contain low contents of base metals, Ba and Sr, but higher temperature examples may contain high Ba-Sr with low base metals (e.g., 300–800 ppm Ba in SJ lens east). With increasing temperature into stage 2 ironstone formation, base metals also increased, with the rate of Ba-Sr deposition accelerating, resulting in anomalous concentrations of all these components, accompanied by Ba/Cu+Pb+Zn > 15 (rising from values of ~5–10 in Ba-poor Stage 1 ironstones). Metal ratios in Stage 1 and 2 form a comparitively uniform population with Cu/Cu+Pb+Zn =0.2–0.5, Zn/Cu+Pb+Zn = 0.2–0.45. Where Stage 3 fluids were present, Ba and base metal contents continued to increase (Fig. 30) and deposited metal ratios became far more variable, perhaps in response to temperature gradients and interaction with metals from previous stages. This increase in metal contents resulted in a large proportion of the near-ore ironstones having Ba/Cu+Pb+Zn < 15 (see histograms in Fig. 31).

Eu anomalies

The presence/absence of +Eu anomalies is a fundamental prospectivity tool, primarily because (1) they are easy to recognise; (2) they are a reliable indicator of high temperature reduced fluids; and (3) no other mechanism for their formation is reasonable in the VHMS environment. This study and previous work (Davidson et al. 1993, Doyle 1997) has shown that Stage 1–2 ironstones do not contain this feature, which fundamentally may reflect a greater shallow seawater character in the low temperature fluids, or simply be evidence that temperatures at depth in the system

Table 3 A summary of the key geochemical features that have potential use as exploration vectors.

Vector	*Stage 1 ironstones*	*Stage 2 ironstones*	*Stage 3 ironstones*
Mineralogy	Hematite-chert-quartz	Vein zones of hematite,goethite and quartz, with minor barite	Vein zones of quartz±hematite-barite-sulfides
Key features			
Fe oxide/Fe+Si oxides	0.15–0.35	0.05–0.15	<0.20, but increasing toward mineralisation
Eu	negative (Eu/Eu*<1)	negative (Eu/Eu*<1)	positive (Eu/Eu*>1)
Cu+Pb+Zn	<20 ppm	20–200 ppm	>200 ppm
Cu/Cu+Pb+Zn	0.2–0.5	0.2–0.5	0–0.9
Ba/Cu+Pb+Zn	<1 to >50	>15	<15
Se	0.001–0.054ppm	0.001–0.054ppm	>1 ppm
As	<10 ppm	20–80 ppm	<30 ppm
ΣREE	20–60 ppm	20–60 ppm	<20ppm
U	>0.2 ppm	<0.2 ppm	
P	<0.03 wt .%	>0.03 wt .%	.0.03wt.%
δ^{18}O-qutz vns	>14‰	>14‰	<14‰
MnO	<0.02 wt. %	0.02–0.05 wt. %	>0.05 wt. %
Mo	<5 ppm	>5 ppm	>5 ppm

were insufficient to mobilise Eu (<250° C; Sverjensky 1984). +Eu anomalies may occur directly associated with mineralisation, or simply mark a general region of high temperature fluid activity, as far away as 1km from mineralisation (empirical conclusion on data to date). In most instances they are also associated with high Ba and base metal contents, but there is an important occurrence at TH40, 1130 m from Thalanga between Thalanga and Thalanga west 45 mineralisation (Fig.6), that contains low base metals and Ba, yet possesses +Eu. LikeThalanga west 45, this sample may occur close to as yet unlocated mineralisation, or it may be part of the larger Thalanga halo. Such a sample might be interpreted as a system in which base-metal+barite deposition occurred at depth but the Eu was not similarly removed from the fluid. Whatever the interpretation, empirically, +Eu-only ironstones may occur within 1 km of massive sulfide mineralisation.

As explored earlier, dilution by the detrital or replacement component of REE can obscure +Eu anomalies. Methods of subtraction of the detrital REE component can be employed, but these rely mainly on excellent characterisation of the immobile element concentrations in the ironstone, and characterisation of the REE and immobile element values in the hostrock and along-strike units if possible. This is very important because dilution is more of a problem in the near-ore environment, where ironstone ΣREE decreases to <15 ppm. Empirically, the dilution problem indicates that ironstones with higher Zr contents (>5ppm) and flat to slightly -Eu anomalies (Eu/Eu*>0.9; Fig. 32) should be evaluated carefully.

Transition elements Co and Ni

Inter-element correlations in the barren ironstones are evidence that Co and Ni, and perhaps some proportion of other elements, are deposited by scavenging by Mn and Fe oxyhydroxides. In some cases the quantitative effect of this was in proportion to Mn concentrations, and in others it was more likely that the period of exposure was important, and in this case at FJ lens, it appears that the eastern end of the lens must have accumulated 4X faster than the western end. Co and Ni are not enriched in near-ore or Thalanga ironstones. These elements are not direct ore indicators in the Mount Windsor Volcanic Belt, although their concentrations can provide information on the depositional rates of the host-sequence, and the duration of stratigraphic breaks. However, in some ironstone-bearing VHMS districts of the world, Co and Ni occur at much higher concentrations; for instance Noranda Main Tuff exhalites contain an average 50 ppm Co. The genetic importance of these occurrences is uncertain, compared to the MWVB.

Regional indicators—wonder elements?

Some elements appear to be reliable **regional** indicators of near-ore systems. Levels of these elements to date are unambiguously higher in the near-ore districts, even though the concentrations of the important indicator elements are low in many ironstones.

Se— In the barren systems sampled to date, Se values are universally in the range 0.001–0.054 ppm, whereas near-ore systems contain Se 1–4 ppm. Se is highly anomalous in the Japanese tetsusekiei, Bathurst near-ore iron formations, and Noranda exhalites (Kalogeropoulos & Scott 1983, Spry et al. in press).

Hg— Although it was not analysed in this study, Hg is highlighted by Spry et al. (in press) because it reliably provides haloes of 1–2 km around massive sulfide mineralisation in reduced carbonate-facies iron formation (Bathurst district, Canada). Values of >100–1000 ppb Hg are anomalous, versus background values <20 ppm Hg.

Acknowledgements

This study was funded by AMIRA project P439 and an Australian Research Council small grant, with salary for the last 1.5 years from an ARC Australian Post-doctoral Fellowship. Samples were obtained with the help and cooperation of RGC Exploration. Analytical data was produced with the assistance of Dr Steve Eggins, Phil Robinson, Nilar Hlaing, Katie McGoldrick and Ashley Townsend. Although they are not co-authors of this paper, the assistance and interpretation provided by Dr Stephen Eggins and Dr Joe Stolz will ensure their elevation to authorship when this work appears in the public domain. Nathan Duhig is thanked for introducing me to these

fascinating rocks during his honours investigations. Lastly, thanks are due to Mike Blake and June Pongratz for helping to metamorphose the manuscript into a half-decent report, and to my project colleagues for excellent and lively discussion of the topic over the last three years.

References

Adachi, M., Yamamoto, K., & Sugisaki, R., 1986. Hydrothermal chert and associated siliceous rocks from the Northern Pacific: their geological significance as indication of ocean ridge activity. Sedimentary Geol., 47: 125-148.

Barrett T.J., Jarvis I. & Jarvis K.E., 1990, Rare earth element geochemistry of massive sulfides-sulfates and gossans on the Southern Explorer Ridge. Geology, v. 18, p. 583–586.

Berry, R.F., Huston, D.L., Stolz, A.J., Hill, A.P., Beams, S.D. and Kuronen, U., 1992. The stratigraphy, structure and mineralization of the Mt Windsor Subprovince, North Queensland, Australia. *Econ. Geol.* 87, 739-763.

Davidson, G.J., Eggins, S.M. & McCulloch, M.T., 1993 Detailed rare earth element (REE) geochemical anatomy of an ancient ferruginous chert lens, northern Australia: a preliminary report. Third RIDGE Theoretical Institute, Physical, chemical, biological and geological interactions within seafloor hydrothermal systems, 28th August 1993, T10.

Doyle M., 1997 A Cambro-Ordovician volcanic succession hosting massive sulfide mineralisation: Mt Windsor Subprovince, Qld. Unpublished Ph.D thesis, University of Tasmania.

Duhig, N.C., 1991, The geology of East Waddy's Mill and the geochemical and textural aspects of ironstone near Thalanga, north Queensland. Unpublished honours thesis, University of Tasmania.

Duhig N.C., Davidson G.J. & Stolz J., 1992, Microbial involvement in the formation of Cambrian seafloor silica-iron oxide deposits, Australia. *Geology* 20: 511–514.

Duhig N.C., Stolz J., Davidson G.J. & Large R.R., 1992, Cambrian microbial and silica gel textures preserved in silica-iron exhalites of the Mt Windsor Volcanic Belt, Australia: their petrography, geochemistry, and origin. *Econ. Geol.* (special issue: Australian VMS deposits and their volcanic environment) 87: 764–784.

Gregory P. (1984) Authority to Prospect 3513M Dreghorn, Queensland. Report for the six months ended 9 December, 1984. unpublished BHP report 62663.

Hill A., 1996Structure, volcanic settting, hydrothermal alteration, and genesis of the Thalanga massive sulphide deposit. Unpublished Ph.D thesis, University of Tasmania, 404 p.

Kalogeropoulos S.I. & Scott S.D, 1989. Mineralogy and geochemistry of an Archean tuffaceous exhalite: the Main Contact Tuff, Millenbach mine area, Noranda, Quebec. Can. J. Earth Sci., 26: 88-105.

Kalogeropoulos S.I. & Scott S.D., 1983. Mineralogy and geochemistry of tuffaceous exhalites (tetsusekiei) of the Fukazawa mine, Hokuroku District, Japan. Econ. Geol. Mon., 5: 412-432.

Liaghat S. & MacLean W.H., 1992. The Key Tuffite, Matagami mining district: origin of the tuff components and mass changes. Exploration MIning Geology, v. 1, p 197–207.

Lottermoser B., 1989, Rare earth element study of exhalites withn the Willyama Supergroup, Broken Hill block, Australia, Mineralium Deposita, v. 24, 92–99.

Mills R.A. & Elderfield H, 1995, Rare earth element geochemistry of hydrothermal deposits from the active TAG mound, 26 degrees N Mid-Atlantic Ridge. Geochimica Cosmochimica Acta, v. 59, p. 3511–3524.

Mulholland I.R., 1991, The geology, petrology and alteration geochemistry of the Magpie volcanogenic massive sulfide prospect, north Queensland, Australia. Economic Geology, v. 86, p. 1387–1400.

O'Neil J.R., Clayton R.N. & Mayeda T.K., 1969 Oxygen isotope fractionation in divalent metal carbonates. Journal of Chemical Physics, v. 51, p. 5547–5558.

Peter J.M. & Goodfellow W.D., 1996, Mineralogy, bulk and rare earth element geochemistry of massive sulphide-associated hydrothermal sediments of the Brunswick horizon, Bathurst mining camp, New Brunswick. Canadian Journal of Earth Science, v. 33, p. 252–283.

Pisutha-Arnond V. & Ohmoto H., 1983 Thermal history, and chemical and isotopic compositions of the ore forming fluids responsible for the Kuroko massive sulfide deposits in the Hokuroko district of Japan. Economic Geology Monograph 5, p. 523–558.

Ruhlin D.E. & Owen R.M., 1986, The rare earth element geochemistry of hydrothermal sediments for the East Pacific Rise: Examination of a seawater scavenging mechanism. Geochimica Cosmochimica Acta, v. 50, p. 393–400.

Sharp, Z.D., and Kirschner, D.L., 1994, Quartz-calcite oxygen isotope thermometry: A calibration based on natural isotopic variations: Geochimica Cosmochimica Acta, v. 58, p. 4491–4501.

Spry, P.G., Peter, J.M. & Slack J.F., in press, Meta-exhalites as exploration guides to ore. Geological Survey of Canada Contribution #1997162 (Ore Geology reviews).

Sverjensky D.A., 1984, Europium redox equilibria in aqueous solution: Earth and Planetary Science Letters, v. 67, p. 70–78.

Taylor S.R. & Gorton M.P., 1977 Geochemical applications of spark-source mass spectrography, III. Element senstitivity, precision and accuracy. Geochimica Cosmochimica Acta, v. 41, p. 1375–1380.

Tsutsumi M. & Ohmoto H., 1983 A preliminary oxygen isotope study of Tetsusekiei ores associated with Kuroko deposits in the Hokuroku District, Japan. Economic Geology Monograph 5, p.433–438.

Appendix 1
Major and trace elements—ironstones and hostrocks.

Thalanga area ironstone geochemistry

Ident		m from east	SiO2	TiO2	Al2O3	Fe2O3	MnO	MgO	CaO	Na2O	K2O	P2O5	Loss	Total	Fe/Fe+Si ox	Na/K ox	S	Ba
TW-1	TW1–7 lens	5	95.96	0.01	0.2	3.21	0.01	0.02	0.01	0.19	0.05	0.04	0.72	100.42	0.03	3.80	0.18	0.7
TW-2		10	90.47	0.05	0.19	1.64	0.03	0.02	0.01	0.025	0.03	0.03	1.55	94.02(100.05*)	0.02	0.83	0.97	3.55
TW-3		15	97.95	0.01	0.27	1.87	0	0.02	<0.01	0.025	0.07	0.02	0.44	100.65	0.02	0.36	0.07	0.18
TW-4		20	94.92	0.01	0.24	4.77	0.01	0.04	0.01	0.025	0.03	0.03	0.61	100.67	0.05	0.83	0.05	0.19
TW-5		25	98.33	0.03	0.47	1.75	0	0.02	<0.01	0.2	0.14	0.02	0.38	101.34	0.02	1.43	0.02	0.04
TW-6		30	96.7	<0.01	0.29	3.75	0.01	0.02	<0.01	0.06	0.06	0.02	0.36	101.27	0.04	1.00	0.02	<0.01
TW-7		35	96.71	<0.01	0.12	3.75	0	<0.01	<0.01	0.025	0.02	0.02	0.38	101	0.04	1.25	0.01	0.01
TW-8	TW8–10 lens		93.03	<0.01	0.08	7.08	0.01	<0.01	<0.01	0.025	0.02	0.04	0.25	100.51	0.07	1.25	<0.01	<0.01
TW9			82.35	<0.01	0.16	16.78	0.04	0.02	<0.01	0.025	0.02	0.05	0.48	99.9	0.17	1.25	0.01	0.01
TW10			46.35	0.02	0.29	51.99	0.12	0.02	0.01	0.025	0.01	0.03	0.62	99.46	0.53	2.50	<0.01	<0.01
TW11	TW11 lens		82.54	<0.01	0.26	16	0.08	0.01	0.01	0.025	0.02	0.03	0.61	99.56	0.16	1.25	0.01	0.09

Thalanga area ironstone geochemistry

Ident	Cu	Pb	Zn	Cu/Cu+Pb+Zn	Ni	U	Th	Se	Nb	Zr	Sr	Y	Rb
TW-1	10	124	19	0.07	1	1.8	<1.5	2.3	<1	6	96	<1	0.5
TW-2	28	229	32	0.1	1	2	<1.5	2.5	<1	12	530	1	0.5
TW-3	7	29	19	0.13	<1	1.1	<1.5	3.9	<1	7	18	4	2
TW-4	10	107	31	0.07	<1	1.1	<1.5	4.4	<1	8	11	2	0.5
TW-5	5	98	11	0.04	1	<1	<1.5	3	<1	12	7	3	3
TW-6	5	14	16	0.14	1	<1	<1.5	3.4	<1	4	2	2	2
TW-7	4	11	10	0.16	<1	<1	<1.5	4.3	<1	2	3	1	0.5
TW-8	7	9	13	0.24	1	<1	<1.5	1.7	<1	<1	5	1	0.5
TW9	18	32	40	0.2	2	1.3	<1.5	3.2	<1	2	6	2	0.5
TW10	33	38	93	0.2	6	<1	<1.5	1	<1	8	2	5	0.5
TW11	86	220	210	0.17	2	1.9	<1.5	3.5	<1	5	14	3	0.5

Magpie ironstone geochemistry

	SiO2	TiO2	Al2O3	Fe2O3	MnO	MgO	CaO	Na2O	K2O	P2O5	Loss	Total	Fe/Fe+Si ox	Na/K ox	S	Ba	Cu	Pb
PAR5	92.06	0.01	0.08	7.45	0.01	<0.01	<0.01	<0.05	0.02	0.06	0.65	100.34	0.07		0.12	0.45	6	2
PAR6	91.83	0.005	0.22	7.15	1.03	0.04	0.03	0.04	0.06	0.03	0.33	100.76	0.07	0.67	<0.01	0.005	2	4
PAR7	91.88	0.005	0.21	7.49	0.04	0.03	0.02	0.74	0.09	0.01	0.26	100.77	0.08	8.22	<0.01	0.005	1	2
PAR9	79.33	0.06	2.98	9.45	5.19	0.13	2.6	0.03	0.04	0.03	0.89	100.73	0.11	0.75	<0.01	0.01	4	3
PAR10	89.21	0.01	0.27	5.7	3.44	0.04	0.31	0.24	0.12	0.06	0.8	100.2	0.06	2	<0.01	0.005	1	1.5
PAR11	92.46	0.005	0.13	7.09	0.39	0.01	0.06	0.32	0.05	0.05	0.26	100.82	0.07	6.4	<0.01	0.005	3	2
PAR12	93.76	0.01	0.09	6.55	0.02	<0.01	<0.01	0.03	0.03	0.01	0.29	100.79	0.07	1	0.02	0.005	6	2
PAR15	92.28	0.005	0.04	8.02	0.02	0.01	0.03	0.06	0.01	0.04	0.13	100.64	0.08	6	<0.01	0.005	5	1.5
PAR16	87.35	0.01	0.13	9.75	1.03	0.02	0.18	<0.05	0.01	0.12	0.96	99.56	0.1		0.14	0.62	7	1.5
PAR17	90.13	0.005	0.05	10.3	0.01	0.01	0.07	<0.05	<0.01	0.03	0.09	100.69	0.1		0.02	0.01		
PAR18	86.5	0.005	0.09	13.09	0.02	0.01	0.09	<0.05	<0.01	0.08	0.44	100.32	0.13		<0.01	0.005	20	7
PAR19	91.4	0.005	0.08	7.39	0.01	0.01	1.07	<0.05	0.01	0.05	0.33	100.35	0.07		0.01	0.005	6	3
PAR20	89.53	0.03	2.11	7.29	0.07	0.06	0.14	0.77	0.22	0.03	0.24	100.49	0.08	3.5	<0.01	0.01	9	7

Appendix 1 cont.
Major and trace elements—ironstones and hostrocks.

Magpie ironstone geochemistry

	Zn	Zn/Cu+Pb+Zn	Ba/Cu+Pb+Zn	Cu/Cu+Pb+Zn	Ni	U	Th	Se	%Ba	Nb	Zr	Sr	Y	Rb	Ti/Zr	Y/Nb
PAR5	10	0.56	250	0.33	5	<1	<1.5	3.6	0.45	1.1	1	69	5	<1	59.95	4.26
PAR6	14	0.7	2.5	0.1	4	<1	<1.5	3.4		1.5	2	16	4	2	14.99	3.01
PAR7	3	0.5	8.33	0.17	1	1.1	<1.5	4.4		2.3	1	2	2	2	29.98	0.91
PAR9	11	0.61	5.56	0.22	16	2.3	3	2.3		7.3	44	29	22	1	8.18	2.97
PAR10	34	0.93	1.37	0.03	6	<1	<1.5	4.4		1.3	7	55	9	2	8.56	7.26
PAR11	8	0.62	3.85	0.23	3	<1	<1.5	2.8		<1	1	9	3	<1	29.98	
PAR12	3	0.27	4.55	0.55	2	<1	<1.5	4		<1	3	4	4	<1	19.98	
PAR15	3	0.32	5.26	0.53	2	<1	<1.5	2.6		1.4	1	1	4	<1	29.98	2.65
PAR16	22	0.72	203.28	0.23	7	<1	<1.5	2.6	0.62	<1	2	72	10	<1	29.98	
PAR17										<1	1	1	2	<1	29.98	
PAR18	19	0.41	1.09	0.43	2	1.1	<1.5	3.1		<1	1	2	<1	<1	29.98	
PAR19	39	0.81	1.04	0.13	26	<1	<1.5	3.7		<1	<1	2	<1	<1		
PAR20	14	0.47	3.33	0.3	2	1.7	2.4	3.1		1.1	9	27	5	6	19.98	4.00

Magpie ironstone hostrock geochemistry

	SiO2	TiO2	Al2O3	Fe2O3	MnO	MgO	CaO	Na2O	K2O	P2O5	Loss	Total	Na/K ox	Rb/Sr	S	Ba	Cu	Pb	Zn	Ni
PAR1	63.39	0.24	19.3	3.97	0.22	2.35	0.02	0.19	5.96	0.05	3.96	99.65	0.0319	7.8462	<0.01	0.19	4	9	67	4
PAR3	65.92	0.22	16.7	3.83	0.13	3.75	0.06	0.19	5.62	0.04	2.98	99.44	0.0338	8.0385	<0.01	0.15	2	6	137	6
PAR4	64.81	0.25	18.2	3.69	0.07	2.77	0.06	0.21	5.93	0.06	3.48	99.53	0.0354	5.625	<0.01	0.16	4	6	111	9
PAR8	61.53	0.25	18.53	5.35	0.14	3.49	0.03	0.37	6.4	0.05	3.24	99.38	0.0578	8.9167	<0.01	0.12	4	7	107	8
PAR13	73.03	0.21	14.46	2.38	0.09	1.55	0.01	0.11	4.72	0.03	2.73	99.32	0.0233	13.417	<0.01	0.09	3	6	59	3
PAR14	68.68	0.25	16.38	3.84	0.07	1.88	0.03	0.1	5.31	0.05	3.11	99.7	0.0188	15.077	<0.01	0.1	2	4	104	4
All samples occur adajcent to the Par 1–14 ironstone, and consist of flow- banded, altered, sericite-rhyolite																				
	Relationship to Par 1-14 ironstone																			
PAR1	35 m along strike																			
PAR3	20 m along strike																			
PAR4	3 m along strike																			
PAR8	2 m above																			
PAR13	~30 m below																			
PAR14	~60 m below																			

Magpie ironstone hostrock geochemistry

	U	Th	Se	Nb	Zr	Sr	Y	Rb	Ti/Zr	Y/Nb
PAR1	<1	31.5	<1	56.3	546	26	99	204	2.6353	1.76
PAR3	<1	26.3	<1	50.4	485	26	93	209	2.72	1.85
PAR4	<1	30.3	<1	58.7	539	40	111	225	2.78	1.89
PAR8	<1	31.1	<1	56.4	548	24	115	214	2.74	2.04
PAR13	4.1	23.6	<1	39.8	485	12	72	161	2.6	1.81
PAR14	2.5	27	<1	47.4	563	13	87	196	2.66	1.84

Appendix 2
Rare earth elements— ironstones and hostrocks.

ppm	TW1	TW2	TW3	TW4	TW5	TW6	TW7	TW8	TW9	TW10	TW11	TW12
raw	ironstone	ironstone	ironstone	ironstone	ironstone	ironstone	ironstone	ironstone	ironstone	ironstone	ironstone	rhyolite host
La	4.20	1.90	3.18	2.21	2.08	0.74	1.17	1.11	2.10	3.12	1.07	120.84
Ce	5.71	2.70	4.06	3.13	2.92	1.12	1.38	2.33	3.88	4.17	3.01	103.31
Pr	0.74	0.36	0.50	0.38	0.35	0.15	0.18	0.28	0.47	0.43	0.25	24.57
Nd	2.34	1.31	1.61	1.26	1.24	0.56	0.70	1.05	1.77	1.38	0.99	85.63
Sm	0.39	0.31	0.38	0.30	0.29	0.16	0.19	0.25	0.37	0.27	0.33	15.51
Eu	0.96	0.40	0.37	0.21	0.14	0.11	0.12	0.07	0.11	0.07	0.21	2.80
Gd	0.31	0.34	0.37	0.30	0.30	0.16	0.18	0.23	0.32	0.26	0.33	15.53
Tb	0.04	0.06	0.06	0.05	0.05	0.03	0.03	0.03	0.05	0.05	0.07	2.39
Dy	0.18	0.40	0.32	0.35	0.25	0.13	0.14	0.16	0.27	0.24	0.38	12.18
Ho	0.04	0.11	0.07	0.10	0.06	0.03	0.03	0.04	0.06	0.06	0.09	2.68
Er	0.13	0.34	0.21	0.32	0.18	0.09	0.11	0.11	0.19	0.20	0.29	6.69
Tm	0.02	0.06	0.03	0.06	0.03	0.02	0.02	0.02	0.03	0.04	0.06	0.85
Yb	0.13	0.44	0.21	0.45	0.21	0.10	0.10	0.16	0.21	0.27	0.40	4.25
Lu	0.03	0.08	0.04	0.09	0.04	0.02	0.02	0.03	0.04	0.05	0.07	0.66
%Ba XRF	**0.70**	**3.55**	**0.18**	**0.19**								
TotalREE	**15.21**	**8.82**	**11.41**	**9.21**	**8.15**	**3.41**	**4.36**	**5.88**	**9.88**	**10.62**	**7.53**	**397.90**
chondrite normalised												
La	13.340	6.040	10.104	7.017	6.591	2.355	3.715	3.522	6.657	9.908	3.405	383.628
Ce	7.029	3.325	4.990	3.856	3.593	1.380	1.698	2.865	4.778	5.131	3.705	127.074
Pr	6.404	3.087	4.289	3.273	3.006	1.266	1.554	2.379	4.050	3.723	2.122	211.772
Nd	3.921	2.198	2.694	2.117	2.079	0.932	1.166	1.764	2.962	2.316	1.659	143.434
Pm												
Sm	2.009	1.596	1.988	1.546	1.522	0.825	0.975	1.310	1.946	1.415	1.694	80.807
Eu	13.271	5.490	5.109	2.938	2.008	1.485	1.660	0.969	1.471	0.904	2.867	38.816
Gd	1.204	1.297	1.440	1.157	1.139	0.621	0.706	0.887	1.251	1.002	1.260	59.974
Tb	0.763	1.320	1.248	1.094	0.990	0.548	0.597	0.652	0.992	0.944	1.385	48.679
Dy	0.546	1.244	0.977	1.071	0.777	0.411	0.430	0.504	0.838	0.751	1.155	37.488
Ho	0.535	1.483	1.011	1.303	0.822	0.424	0.454	0.519	0.876	0.867	1.285	36.649
Er	0.593	1.602	0.985	1.501	0.866	0.426	0.505	0.532	0.879	0.948	1.348	31.403
Tm												
Yb	0.626	2.116	0.999	2.146	1.020	0.497	0.483	0.775	1.008	1.310	1.903	20.443
Lu	0.822	2.458	1.189	2.643	1.247	0.595	0.624	0.946	1.208	1.690	2.158	20.523

Appendix 2 cont.
Rare earth elements— ironstones and hostrocks.

	PAR1	PAR3	PAR4	PAR5	PAR6	PAR7	PAR8	PAR9	PAR10	PAR11	PAR12	PAR13	PAR14	PAR15	PAR16	PAR17	PAR18	PAR19	PAR20	Normalising
	Flow-banded hostrock	Flow-banded hostrock	Flow-banded hostrock	Jaspilite	Jaspilite	Jaspilite	Haningwall felsic volcanic	hostrock	Jaspilite	Jaspilite	Jaspilite	hostrock	hostrock	Jaspilite	Jaspilite	Jaspilite	Jaspilite	Jaspilite	Jaspilite	factors
La	48.867	53.574	89.911	2.259	7.507	3.049	101.457	11.871	3.496	1.707	2.332	54.070	67.074	1.012	3.098	0.924	0.537	0.873	2.205	0.315
Ce	96.335	98.433	149.418	2.790	4.045	1.480	150.328	18.981	3.969	2.085	2.624	121.360	142.377	1.124	3.876	1.072	1.425	0.834	5.556	0.813
Pr	12.999	13.889	24.748	0.353	0.946	0.391	28.046	2.572	0.562	0.326	0.438	15.019	20.226	0.180	0.447	0.183	0.124	0.117	0.554	0.116
Nd	47.092	48.753	86.822	1.310	3.062	1.147	91.682	9.279	1.890	1.084	1.485	48.678	65.745	0.662	1.825	0.633	0.431	0.397	1.890	0.597
Pm																				
Sm	11.325	9.863	18.318	0.304	0.565	0.208	18.160	2.292	0.365	0.241	0.299	10.528	14.005	0.155	0.519	0.149	0.106	0.080	0.466	0.192
Eu	1.587	1.330	2.555	0.675	0.125	0.039	2.495	0.433	0.092	0.061	0.059	1.741	2.280	0.026	0.996	0.029	0.039	0.017	0.168	0.0722
Gd	9.008	7.783	15.733	0.429	0.645	0.207	14.711	2.724	0.477	0.290	0.346	10.129	11.616	0.209	1.043	0.170	0.120	0.071	0.494	0.259
Tb	1.329	1.117	2.539	0.083	0.117	0.041	2.206	0.509	0.095	0.064	0.071	1.881	1.737	0.042	0.239	0.037	0.022	0.015	0.097	0.049
Dy	6.891	5.704	13.495	0.611	0.911	0.295	10.702	3.348	0.793	0.464	0.550	10.485	8.386	0.327	1.795	0.254	0.134	0.096	0.561	0.325
Ho	1.383	1.073	2.685	0.161	0.204	0.074	2.141	0.807	0.233	0.128	0.139	2.260	1.677	0.090	0.435	0.061	0.028	0.020	0.123	0.073
Er	3.519	2.800	6.626	0.500	0.601	0.257	5.523	2.244	0.757	0.404	0.437	6.199	4.468	0.279	1.180	0.177	0.081	0.060	0.349	0.213
Tm	0.616	0.464	1.089	0.095	0.114	0.055	0.884	0.377	0.121	0.076	0.076	1.027	0.725	0.049	0.198	0.033	0.014	0.011	0.062	0.03
Yb	3.927	2.795	6.508	0.603	0.706	0.405	5.514	2.160	0.644	0.459	0.458	6.407	4.607	0.328	1.070	0.221	0.083	0.070	0.409	0.208
Lu	0.508	0.402	0.903	0.093	0.119	0.074	0.760	0.325	0.097	0.071	0.064	0.949	0.690	0.054	0.148	0.035	0.014	0.010	0.069	0.0323
XRF %Ba	0.19%	0.15%	0.16%	0.45%			0.12%					0.09%	0.10%		0.62%					
TotalREE	245.388	247.981	421.351	10.266	19.667	7.722	434.610	57.921	13.590	7.459	9.378	290.733	345.613	4.538	16.870	3.978	3.158	2.670	13.004	
chondrite	PAR1	PAR3	PAR4	PAR5	PAR6	PAR7	PAR8	PAR9	PAR10	PAR11	PAR12	PAR13	PAR14	PAR15	PAR16	PAR17	PAR18	PAR19	PAR20	
La	155.13	170.07	285.43	7.17	23.83	9.68	322.09	37.68	11.10	5.42	7.40	171.65	212.93	3.21	9.83	2.93	1.70	2.77	7.00	
Ce	118.49	121.07	183.79	3.43	4.98	1.82	184.91	23.35	4.88	2.56	3.23	149.27	175.13	1.38	4.77	1.32	1.75	1.03	6.83	
Pr	112.06	119.73	213.35	3.05	8.15	3.37	241.78	22.17	4.84	2.81	3.77	129.47	174.36	1.55	3.86	1.58	1.07	1.00	4.78	
Nd	78.88	81.66	145.43	2.19	5.13	1.92	153.57	15.54	3.17	1.82	2.49	81.54	110.13	1.11	3.06	1.06	0.72	0.66	3.17	
Pm																				
Sm	58.99	51.37	95.41	1.58	2.94	1.09	94.58	11.94	1.90	1.25	1.56	54.83	72.94	0.81	2.70	0.78	0.55	0.41	2.43	
Eu	21.98	18.43	35.39	9.35	1.73	0.55	34.56	6.00	1.28	0.84	0.81	24.12	31.58	0.36	13.79	0.40	0.55	0.24	2.33	
Gd	34.78	30.05	60.74	1.66	2.49	0.80	56.80	10.52	1.84	1.12	1.34	39.11	44.85	0.81	4.03	0.66	0.46	0.27	1.91	
Tb	27.12	22.81	51.81	1.69	2.38	0.83	45.02	10.38	1.93	1.30	1.46	38.38	35.45	0.87	4.88	0.75	0.45	0.32	1.97	
Dy	21.20	17.55	41.52	1.88	2.80	0.91	32.93	10.30	2.44	1.43	1.69	32.26	25.80	1.01	5.52	0.78	0.41	0.30	1.73	
Ho	18.95	14.70	36.78	2.20	2.79	1.01	29.33	11.05	3.19	1.75	1.91	30.96	22.98	1.23	5.96	0.83	0.38	0.27	1.69	
Er	16.52	13.15	31.11	2.35	2.82	1.21	25.93	10.54	3.55	1.90	2.05	29.10	20.98	1.31	5.54	0.83	0.38	0.28	1.64	
Tm	20.54	15.45	36.29	3.16	3.79	1.83	29.48	12.56	4.02	2.53	2.53	34.23	24.16	1.63	6.61	1.10	0.47	0.37	2.06	
Yb	18.88	13.44	31.29	2.90	3.39	1.95	26.51	10.38	3.10	2.21	2.20	30.80	22.15	1.58	5.14	1.06	0.40	0.33	1.97	
Lu	15.71	12.45	27.96	2.89	3.70	2.28	23.54	10.05	3.00	2.20	1.99	29.38	21.38	1.68	4.59	1.10	0.43	0.32	2.14	
LaN/SmN	2.63	3.31	2.99	4.53	8.10	8.92	3.41	3.16	5.84	4.32	4.76	3.13	2.92	3.97	3.64	3.77	3.08	6.68	2.88	

Appendix 2 cont.
Rare earth elements— ironstones and hostrocks.

	FJ1	FJ2	FJ3	FJ4	FJ5	FJ6	FJ7	FJ8	FJ9	FJ10	FJ11	FJ12	FJ13	FJ14	FJ15	FJ16	FJ17	FJ17-2	FJ18	FJ18ftwl	FJ19
Raw	Jaspilite	Jaspilite	Jaspilite	Jaspilite	Jaspilite	Jaspilite	Jaspilite	Jaspilite	Jaspilite	Jaspilite	Jaspilite	Jaspilite	Jaspilite	Jaspilite	Jaspilite	Jaspilite	Jaspilite	Jaspilite	Jaspilite	Andesitic	Jaspilite
	veined	veined	veined	veined	veined	veined	veined	veined	veined	veined	veined	veined	veined	veined	veined	veined	veined	veined(repeat	veined	footwall	veined
La	2.62	4.99	1.51	4.01	4.73	3.95	5.32	1.72	13.49	6.20	6.53	7.75	2.98	3.79	3.04	3.60	31.40	32.30	56.71	5.31	16.14
Ce	4.36	10.91	3.85	8.78	10.61	7.74	9.46	2.81	26.38	10.03	7.97	18.33	7.51	9.02	5.22	5.85	37.54	38.22	51.49	8.85	37.42
Pr	0.45	1.11	0.48	0.77	0.92	0.81	1.07	0.39	3.30	1.02	1.18	1.98	1.04	0.91	0.80	0.72	3.97	3.96	10.81	0.86	4.49
Nd	1.33	3.46	1.79	2.26	2.88	2.41	3.19	1.15	11.94	2.89	3.59	6.12	3.81	2.65	3.04	2.25	9.33	9.29	26.25	2.80	17.90
Sm	0.23	0.48	0.24	0.33	0.38	0.26	0.41	0.15	1.95	0.46	0.63	0.92	0.61	0.41	0.66	0.38	1.12	1.14	2.66	0.54	3.38
Eu	0.052	0.086	0.046	0.088	0.080	0.046	0.087	0.026	0.388	0.107	0.136	0.186	0.127	0.071	0.154	0.079	0.209	0.214	0.401	0.173	0.671
Gd	0.186	0.292	0.140	0.261	0.240	0.128	0.283	0.092	1.327	0.414	0.530	0.648	0.484	0.249	0.578	0.302	0.789	0.813	1.035	0.578	2.418
Tb	0.025	0.044	0.019	0.041	0.035	0.018	0.045	0.012	0.154	0.063	0.082	0.090	0.066	0.033	0.078	0.037	0.119	0.119	0.127	0.112	0.311
Dy	0.122	0.238	0.096	0.218	0.192	0.099	0.258	0.065	0.689	0.352	0.436	0.421	0.352	0.159	0.370	0.164	0.593	0.623	0.540	0.754	1.335
Ho	0.023	0.046	0.017	0.042	0.036	0.019	0.050	0.013	0.118	0.066	0.080	0.072	0.064	0.027	0.059	0.024	0.124	0.131	0.086	0.186	0.191
Er	0.062	0.138	0.047	0.117	0.105	0.056	0.146	0.039	0.304	0.179	0.214	0.188	0.172	0.071	0.136	0.056	0.391	0.408	0.218	0.618	0.368
Yb	0.064	0.155	0.047	0.136	0.115	0.061	0.166	0.039	0.238	0.161	0.190	0.182	0.177	0.059	0.116	0.051	0.526	0.543	0.224	0.674	0.224
Lu	0.011	0.024	0.007	0.022	0.018	0.009	0.025	0.005	0.038	0.023	0.027	0.027	0.028	0.009	0.017	0.007	0.097	0.098	0.034	0.116	0.029
Total	9.531	21.973	8.283	17.069	20.343	15.596	20.509	6.515	60.320	21.959	21.596	36.910	17.425	17.442	14.270	13.518	86.206	87.858	150.583	21.584	84.884
Chondrite normalised																					
	FJ1	**FJ2**	**FJ3**	**FJ4**	**FJ5**	**FJ6**	**FJ7**	**FJ8**	**FJ9**	**FJ10**	**FJ11**	**FJ12**	**FJ13**	**FJ14**	**FJ15**	**FJ16**	**FJ17**	**FJ17-2**	**FJ18**	**FJ18sil**	**FJ19**
La	11.06	21.08	6.36	16.90	19.95	16.65	22.43	7.26	56.94	26.16	27.57	32.72	12.59	15.98	12.81	15.20	132.50	136.27	239.27	22.41	68.12
Ce	7.13	17.82	6.29	14.35	17.34	12.64	15.46	4.60	43.10	16.39	13.02	29.94	12.28	14.74	8.53	9.56	61.33	62.45	84.13	14.47	61.15
Pr	4.68	11.57	5.01	7.98	9.59	8.40	11.11	4.02	34.36	10.58	12.29	20.63	10.84	9.44	8.33	7.48	41.31	41.24	112.62	8.97	46.74
Nd	2.84	7.41	3.83	4.84	6.16	5.16	6.84	2.47	25.57	6.18	7.68	13.10	8.15	5.66	6.51	4.81	19.97	19.90	56.22	6.00	38.33
Sm	1.48	3.11	1.59	2.14	2.49	1.71	2.71	0.99	12.77	3.03	4.15	6.00	3.99	2.65	4.34	2.47	7.35	7.44	17.37	3.56	22.10
Eu	0.89	1.49	0.80	1.51	1.38	0.79	1.49	0.45	6.68	1.85	2.34	3.20	2.19	1.23	2.65	1.37	3.61	3.69	6.91	2.98	11.57
Gd	0.91	1.42	0.68	1.27	1.17	0.62	1.38	0.45	6.46	2.02	2.58	3.15	2.35	1.21	2.81	1.47	3.84	3.96	5.03	2.81	11.77
Tb	0.66	1.18	0.51	1.09	0.92	0.49	1.21	0.32	4.12	1.69	2.19	2.41	1.75	0.88	2.08	0.98	3.16	3.17	3.39	2.98	8.29
Dy	0.48	0.94	0.38	0.86	0.75	0.39	1.01	0.26	2.71	1.38	1.72	1.66	1.39	0.63	1.46	0.65	2.34	2.45	2.12	2.97	5.26
Ho	0.40	0.82	0.31	0.73	0.63	0.33	0.88	0.23	2.09	1.16	1.40	1.28	1.13	0.48	1.03	0.43	2.19	2.31	1.51	3.28	3.37
Er	0.37	0.83	0.28	0.71	0.63	0.34	0.88	0.24	1.84	1.08	1.29	1.13	1.04	0.43	0.82	0.34	2.36	2.46	1.31	3.73	2.22
Yb	0.38	0.91	0.28	0.80	0.68	0.36	0.98	0.23	1.40	0.95	1.12	1.07	1.04	0.35	0.68	0.30	3.10	3.20	1.32	3.97	1.32
Lu	0.42	0.93	0.28	0.88	0.72	0.35	0.99	0.21	1.48	0.89	1.06	1.06	1.11	0.34	0.67	0.29	3.83	3.86	1.34	4.55	1.15

Appendix 2 cont.
Rare earth elements— ironstones and hostrocks.

	FJ20	FJ21	FJ23	FJ24a	FJ24b	FJ24c	FJ24d	FJ27	SJ1	SJ2	SJ3	SJ4	SJ4a	SJ5	SJ6	SJ8	SJ9	SJ10	SJ11	SJ12
	footwall	h'wall	carb-altered	F'wall	F'wall	F'wall	F'wall	F'wall	Jaspilite	Jaspilite	Jaspilite	Jaspilite	Jaspilite	Jaspilite	Jaspilite	Jaspilite	Jaspilite	Jaspilite	Jaspilite	Jaspilite
	volcanoclastic	sediment	footwall	carb-altered	carb-altered	carb-altered	carb-altered	carb-altered	veined	veined	veined	veined	veined	veined	veined	with host bx	, veined	, veined	, veined	, veined
La	3.04	8.11	9.93	8.84	129.40	8.15	7.61	22.83	2.37	9.58	7.56	6.69	6.99	7.33	3.91	7.05	34.03	28.36	16.40	14.14
Ce	5.69	20.60	19.19	17.15	60.85	15.87	15.98	41.71	3.01	8.26	5.81	7.01	13.98	12.14	5.53	7.97	31.80	25.35	15.76	18.39
Pr	0.74	2.49	2.52	2.15	17.64	2.01	2.54	6.46	0.38	1.28	0.96	0.97	1.87	1.39	0.61	1.01	4.66	4.65	2.83	2.38
Nd	2.98	9.95	10.94	8.73	60.66	8.19	11.28	28.20	1.23	4.05	3.27	3.45	7.57	5.15	1.94	3.07	13.64	14.11	9.24	7.35
Sm	0.75	1.92	2.64	1.99	10.37	1.93	2.87	6.95	0.30	0.89	0.74	0.84	2.87	1.14	0.39	0.60	2.17	2.47	1.67	1.23
Eu	0.168	0.420	0.718	0.642	3.186	0.623	0.901	1.906	0.085	0.285	0.225	0.239	0.723	0.340	0.151	0.154	0.467	0.520	0.349	0.260
Gd	0.751	1.490	2.942	2.019	9.631	2.043	3.176	7.649	0.271	0.899	0.866	1.029	5.157	1.304	0.372	0.549	1.717	1.871	1.278	0.928
Tb	0.138	0.200	0.484	0.337	1.328	0.352	0.523	1.176	0.054	0.159	0.170	0.199	1.197	0.230	0.060	0.092	0.255	0.271	0.188	0.138
Dy	0.904	1.180	2.937	2.047	6.720	2.156	3.130	6.804	0.390	0.926	1.166	1.351	8.829	1.511	0.349	0.542	1.337	1.382	0.985	0.718
Ho	0.239		0.626	0.449	1.108	0.475	0.665	1.444	0.067	0.190	0.279	0.335	2.033	0.337	0.068	0.111	0.242	0.245	0.181	0.139
Er	0.797	0.710	1.778	1.320	2.430	1.382	1.905	3.962	0.200	0.544	0.884	1.060	6.283	1.056	0.196	0.340	0.640	0.664	0.490	0.403
Yb	0.867	0.670	1.542	1.250	1.537	1.313	1.803	3.294	0.250	0.538	0.958	1.094	6.528	1.156	0.266	0.450	0.619	0.725	0.518	0.422
Lu	0.150		0.228	0.189	0.224	0.198	0.272	0.495	0.039	0.080	0.145	0.154	0.997	0.181	0.049	0.076	0.100	0.126	0.087	0.071
Total	17.209	47.740	56.485	47.105	305.086	44.694	52.648	132.880	8.632	27.673	23.042	24.427	65.023	33.268	13.896	22.020	91.677	80.738	49.982	46.580
Chondrite normalised																				
	FJ20	**FJ21**	**FJ23**	**FJ24a**	**FJ24b**	**FJ24c**	**FJ24d**	**FJ27**	**SJ1**	**SJ2**	**SJ3**	**SJ4**	**SJ4a**	**SJ5**	**SJ6**	**SJ8**	**SJ9**	**SJ10**	**SJ11**	**SJ12**
La	12.81	#REF!	41.89	37.30	545.98	34.40	32.09	96.33	10.00	40.41	31.92	28.23	29.49	30.93	16.50	29.76	143.57	119.68	69.21	59.67
Ce	9.29	#REF!	31.36	28.03	99.43	25.94	26.11	68.16	4.91	13.49	9.50	11.45	22.84	19.84	9.04	13.03	51.96	41.42	25.75	30.05
Pr	7.73	#REF!	26.28	22.35	183.70	20.93	26.47	67.30	3.91	13.29	9.97	10.10	19.52	14.46	6.32	10.49	48.58	48.39	29.51	24.83
Nd	6.38	#REF!	23.43	18.69	129.90	17.54	24.15	60.39	2.63	8.68	7.01	7.39	16.20	11.03	4.16	6.58	29.21	30.21	19.79	15.75
Sm	4.88	#REF!	17.27	12.98	67.79	12.60	18.78	45.41	1.95	5.81	4.86	5.52	18.77	7.48	2.57	3.91	14.17	16.13	10.93	8.04
Eu	2.90	#REF!	12.39	11.07	54.93	10.74	15.53	32.86	1.46	4.91	3.88	4.13	12.47	5.87	2.60	2.66	8.05	8.97	6.02	4.48
Gd	3.66	#REF!	14.32	9.82	46.87	9.94	15.46	37.22	1.32	4.38	4.21	5.01	25.10	6.35	1.81	2.67	8.35	9.10	6.22	4.51
Tb	3.69	#REF!	12.91	8.99	35.42	9.38	13.95	31.35	1.44	4.24	4.53	5.30	31.92	6.13	1.61	2.44	6.80	7.22	5.01	3.68
Dy	3.56	#REF!	11.56	8.06	26.46	8.49	12.32	26.79	1.53	3.64	4.59	5.32	34.76	5.95	1.37	2.14	5.26	5.44	3.88	2.83
Ho	4.22		11.04	7.92	19.54	8.37	11.73	25.47	1.18	3.34	4.91	5.90	35.85	5.95	1.20	1.96	4.27	4.33	3.20	2.45
Er	4.81	#REF!	10.74	7.98	14.68	8.35	11.51	23.94	1.21	3.29	5.34	6.41	37.96	6.38	1.18	2.06	3.87	4.01	2.96	2.44
Yb	5.10	#REF!	9.07	7.35	9.04	7.72	10.61	19.37	1.47	3.16	5.63	6.43	38.40	6.80	1.57	2.65	3.64	4.26	3.05	2.48
Lu	5.91		8.99	7.45	8.83	7.78	10.71	19.47	1.54	3.16	5.70	6.05	39.23	7.13	1.93	3.01	3.93	4.98	3.42	2.80

Appendix 3

Major and trace element contents of ironstones from Duhig et al. (1992) and Duhig (1990) in the Thalanga area.

	Mineralised Samples					Regional Samples											
	UG-1	TH47	TH096	TH5/12	TH5/13	WM41	TH1A	S58	S60	TH26	TB2	WT6	HW39	TC9	SS15A	SS15C	SS15D
SiO2	89.98	27.62	74.39	92.15	18.38	95.52	85.58	82.13	95.39	92.43	86.03	95.62	86.32	89.87	70.60	60.24	93.89
TiO2	0.03	0.23	0.14	0.03	0.29	0.05	0.01	<0.01	0.02	<0.01	<0.01	<0.01	<0.01	<0.01	0.02	0.19	0.06
Al2O3	0.10	8.84	0.60	1.47	1.23	0.37	0.18	0.16	0.19	0.12	0.13	0.16	0.05	0.09	0.77	2.45	0.80
Fe2O3#	5.61	30.03	0.94	0.18	0.97	3.88	14.11	17.21	4.24	7.29	13.78	4.08	13.55	9.65	28.49	37.01	5.12
MnO	0.01	0.38	0.01	<0.01	<0.01	<0.01	0.01	0.02	0.01	0.02	0.02	0.01	0.03	0.33	0.03	0.03	0.01
MgO	0.08	7.29	0.03	0.21	0.40	<0.05	<0.05	<0.05	<0.05	<0.05	<0.05	<0.05	<0.05	<0.05	<0.05	<0.05	<0.05
CaO	0.23	5.06	0.06	0.09	1.10	<0.01	0.04	0.04	0.01	0.04	0.04	0.08	<0.01	0.02	0.03	0.03	0.03
Na2O	<0.2	0.40	<0.2	<0.2	0.67	<0.2	<0.2	0.32	<0.2	<0.2	<0.2	<0.2	<0.2	<0.2	<0.2	<0.2	<0.2
K2O	0.01	0.22	0.04	0.40	0.23	0.17	0.04	0.04	0.05	0.05	<0.01	0.05	0.01	0.03	0.01	0.04	0.05
P2O5	0.09	0.17	0.11	0.04	0.86	<0.02	0.03	0.08	0.02	0.05	<0.02	<0.02	0.04	<0.02	0.04	<0.02	0.03
BaSO4	3.84	19.77	23.67	5.31	75.86												
Total *	100.00	100.00	100.00	100.00	100.00	100.00	100.00	100.00	100.00	100.00	100.00	100.00	100.00	100.00	100.00	100.00	100.00
LOI	1.06	6.69	5.32	1.48	1.52	0.95	0.29	0.16	0.12	0.20	0.65	0.29	0.20	0.41	1.29	1.96	1.02
Sc						<1	<1			<1	<1	<1	<1	<1	<1	2.7	1.3
V						5.7	14	15	6	18	13	7	7	12	33	54	15
Cr	5	27	3			1.9	3	3	2	3	1.5	<2	2	4	4	4	5
Ni	2	11	5	9	91	1.7	8	9	1	7	7	2	7	5	12	11	3
Cu	1557	10425	2450	11	958	11	157	<2	6	2	53	7	2	12	14	<2	17
Zn	242	9400	751	26	254	<1	5	<2	<2	6	3	<1	1.4	5	10	4	8
Pb	332	2786	2776	13	4806	7.6	14			5	<3	3	6.2	4	36	29	97
Rb	1.6	17		12	30	2.1	<1			<1	<1	1.8	<1	<1	1.5	<1	<1
Sr	462	2265		654	7542	<2	3.6			<2	<2	<2	2.5	15	24	15	26
Y	2	61		5.5		5	4			<2	<2	4	3	4	4	6	26
Zr	1	99		15		11.1	4.5			1.8	2	2.2	2	1	5	19	11
Nb	<1	8		2		2.1	<1			<1	<1	<1	<1	<1	<1	1.5	<1
Ba	34000	160000	200000	37656			69	9	21	68	110	55	153	69	339	342	1703
Th				2.2		<2	<2			<2	<2	<2	<2	<2	<2	<2	<2
Au (ppb)	146	374	526								0.01	<0.005	<0.005	<0.005	<0.005	<0.005	0.01
As	2	28	24					<3	<3								
Ag	10	10	12							0.5	0.5	1	0.5	0.5	1	0.5	0.5
Bi	1.4	69	29	<3		<3	<3			0.1	<0.1	<0.1	<0.1	<0.1	0.2	0.2	0.4
Cd	1.5	26	55							<0.1	<0.1	<0.1	<0.1	<0.1	<0.1	<0.1	<0.1
Mo	17	6.1	1.8							1.2	0.8	0.6	2.9	0.7	0.6	1	0.4
Sb	1.7	9.8	1.5							0.1	0.2	1.1	4	0.4	0.9	3.7	1

 # Total Fe as Fe2O3; * Analyses recalculated and normalised to 100% anhydrous
Au by Fire Assay; Ag, Bi, Cd, Mo, Sb by ICP-MS; Others by XRF

Volcanic facies and alteration

J. McPhie
Centre for Ore Deposit Research

Introduction

Studies of alteration related to volcanic-hosted massive sulfide (VHMS) mineralisation undertaken for AMIRA/ARC Project P439 have focussed on the Cambrian Mount Read Volcanics in western Tasmania and the Cambro-Ordovician Mount Windsor Volcanics in Queensland. Both host successions comprise complex assemblages of texturally and compositionally diverse volcanic facies that have in addition, been variably deformed, altered and metamorphosed. In order to correctly define and apply vectors to VHMS mineralisation based on alteration mineralogy and alteration geochemistry, an understanding of the original character of the host volcanic facies and any subsequent textural evolution is imperative. Thus, one of the principal aims of the volcanic facies module was:

- to provide a geological framework, based on regional- and deposit-scale volcanic facies analysis, for companion geochemical and mineralogical research on alteration related to VHMS mineralisation.

Many studies of submarine volcanic successions have shown the abundance of volcanic facies that are initially glassy or partly glassy (e.g. Pichler, 1963; Yamagishi, 1987; Cas, 1992; McPhie & Allen, 1992). Volcanic glass is almost invariably converted to crystals through a variety of processes that may begin with first cooling (high temperature crystallisation, above the glass transition) and proceed though stages of diagenetic alteration, hydrothermal alteration and metamorphism. Each of these processes of devitrification may be accompanied by substantial textural, mineralogical and compositional changes. In addition, in many cases the glass is porous and burial leads to compaction. Compaction can occur prior to, during or after conversion of the glass to new mineral assemblages. In order to identify mineralogical, textural and compositional vectors to VHMS mineralisation, each of the stages in textural evolution must be defined. Thus, a second principal aim of the volcanic facies module was:

- to establish the textural, mineralogical and compositional changes that accompany cooling, hydration, devitrification, compaction and lithification of glassy volcanic rocks emplaced in submarine environments, especially glassy or partly glassy lavas, intrusions and pumice-rich deposits.

In an effort to achieve these aims, volcanic facies mapping, facies analysis and textural studies have been undertaken on both regional and ore deposit scales in the Mount Read Volcanics, and mainly on ore deposit scale in the Mount Windsor Volcanics. In particular, the Mount Read Volcanics were systematically mapped and sampled east-west along three main regional traverses and one shorter "step-out" traverse. The traverses provided important new data on the structure, stratigraphy and volcanic facies architecture of the Mount Read Volcanics, and have allowed discrimination of the characteristics of regional versus local alteration styles. In addition, samples from the traverses have provided very high quality data for the lithogeochemical and mineral chemistry databases. Detailed volcanic facies analyses have been undertaken at Rosebery and Hercules (Allen, Report 5, this report; Gifkins, Report 3,

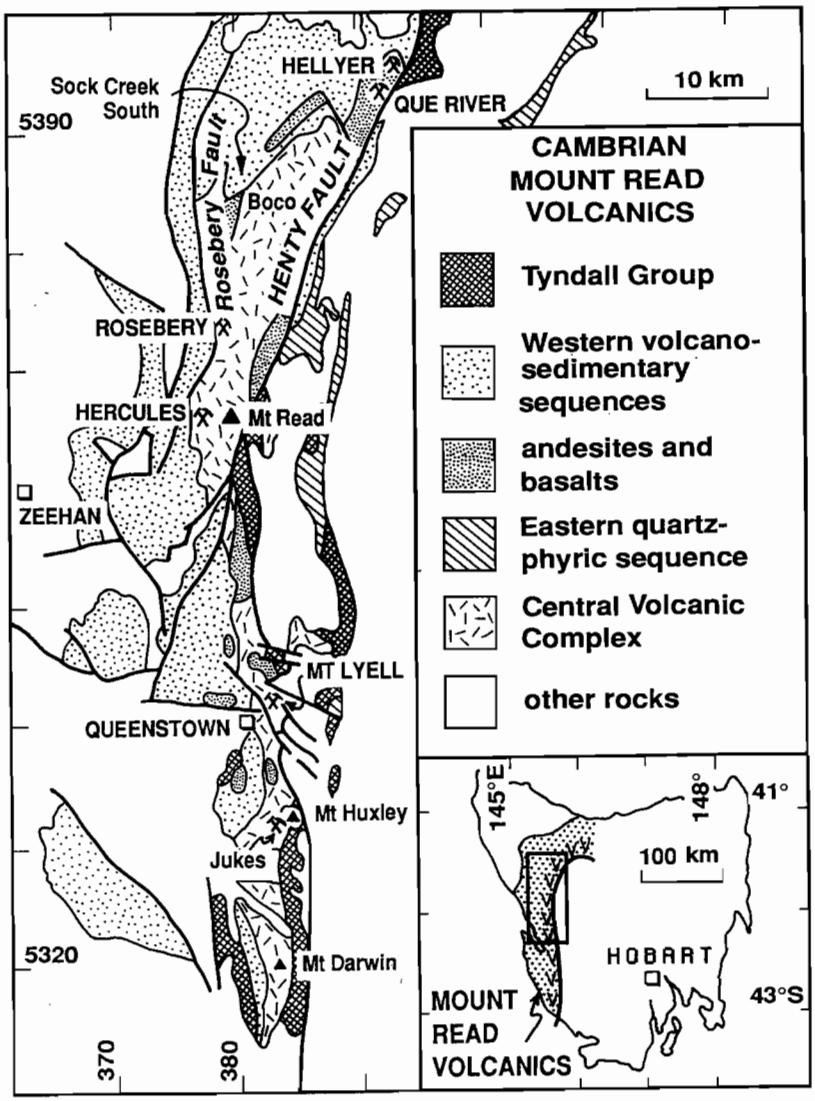

Figure 1: Distribution of the principal lithostratigraphic formations and major massive sulfide deposits in the Cambrian Mount Read Volcanics of western Tasmania. Modified from Corbett (1992).

Report 5, this report), Jukes (Wyman, Report 3) and Henty (Callaghan, Report 5).

In the Mount Windsor Volcanics, the host volcanic successions to the Thalanga and Highway-Reward massive sulfide deposits have been studied in detail (Hill, Report 1, Report 2; Paulick, Report 2, Report 4, this report; Doyle, Report 1, Report 4, Report 5, this report). However, while the regional lithostratigraphy has been established (Henderson, 1986; Berry et al., 1992), the regional volcanic facies architecture remains poorly understood.

Following is a summary of the results from facies architecture studies in the Mount Read Volcanics and the Mount Windsor Volcanics, giving cross references to the relevant report volumes. In addition, the significance of this research and important implications for defining vectors to VHMS mineralisation are reviewed.

Lithostratigraphy and volcanic facies architecture of the Mount Read Volcanics

The regionally mappable lithostratigraphic units within the Mount Read Volcanics (Corbett, 1992; Fig. 1) each comprise a varied assemblage of volcanic facies types, in some cases together with non-volcanic, principally sedimentary facies. The principal lithostratigraphic units and facies types are summarised below.

Central Volcanic Complex

The Central Volcanic Complex dominates the central portion of the Mount Read volcanics both north and south of the Henty Fault. It includes the Mount Black Volcanics and the host sequence to the Rosebery and Hercules massive sulfide ore bodies. The principal facies are:

- Dacitic and rhyolitic lavas, domes, and syn-volcanic intrusions (cryptodomes, sills), comprising both coherent and autoclastic facies. The autoclastic facies include autobreccia, hyaloclastite, resedimented hyaloclastite and intrusive hyaloclastite. Margins of the extrusions and intrusions are typically brecciated and glassy and in some cases, pumiceous; formerly glassy domains are commonly perlitic. Interiors are typically microcrystalline, spherulitic or micropoikilitic.
- Rhyolitic pumice breccia in very thick (tens of metres), massive to graded beds composed mainly of juvenile, feldspar-phyric tube pumice clasts together with minor lithic clasts and free crystals (feldspar). Uppermost parts of emplacement units are stratified and consist of pumiceous or crystal-rich sand and silt. When first deposited, this facies was substantially glassy and also highly porous and permeable.
- Very thick, graded beds of pumiceous and variably crystal- or lithic-rich breccia-sandstone. Units of this facies are quartz- and feldspar-phyric, and significant proportions of the components (pumice, matrix shards, some volcanic clasts) would have originally been glassy.
- Pale, massive or laminated tuffaceous mudstone, largely composed of originally glassy shards together with minor crystal fragments (feldspar, quartz).
- Black, pyritic laminated mudstone in relatively thin intervals.

Eastern quartz-phyric sequence (Murchison Volcanics)

This lithostratigraphic unit is widespread on the eastern side of the Mount Read Volcanics and may interfinger with the Central Volcanic Complex.

- Quartz-and feldspar-phyric rhyolitic lavas and syn-volcanic sills. The lavas are dominantly massive with only minor autoclastic facies (principally hyaloclastite). The sills range from finely to coarsely porphyritic, with moderate to high phenocryst abundances. The margins of some lavas are perlitised and were originally glassy.
- Feldspar-phyric dacitic sills with distinctive microspherulitic groundmass textures.
- Variably crystal-rich (quartz and feldspar) and pumiceous volcaniclastic sandstone to breccia. This facies contains significant proportions of components (pumice, shards) that would have originally been glassy.

Western volcano-sedimentary sequences

This lithostratigraphic unit includes three regionally defined subdivisions: the Yolande River sequence

south of the Henty Fault; the Dundas Group extending north from the Henty Fault to the Pinnacles area; the Mount Charter Group north of the Pinnacles area to beyond Hellyer. Similar associations of volcanic and non-volcanic lithofacies are present in each area. The White Spur Formation at the base of the Dundas Group and the Southwell Subgroup near the top of the Mount Charter Group have been distinguished on the basis of the abundance of thick, quartz-rich, pumiceous, mass-flow emplaced sandstone and breccia units.

- Volcanolithic sandstone and pebbly sandstone, micaceous mudstone and black pyritic mudstone. Sandstone beds are tabular, medium to thick, graded and show the facies sequences typical of turbidites (sharp bases overlain by massive, thick, lower intervals grading to finer, stratified and cross-laminated upper intervals). Mudstone beds are massive, graded or laminated, reflecting deposition from turbidity currents and from suspension. These facies have a mixed provenance comprising a dominant metamorphic basement source and a felsic volcanic source.
- Very thick, massive to graded units of pumiceous and variably crystal- or lithic-rich breccia-sandstone. Pumice and volcanic clasts in this facies are quartz- and feldspar-phyric, and originally would have had glassy groundmasses. These units may include significant amounts of non-volcanic mud as matrix components and as intraclasts derived from the underlying unconsolidated mud substrate.
- Pale, massive or laminated tuffaceous mudstone, largely composed of originally glassy shards together with minor crystal fragments (feldspar, quartz).
- Massive, quartz- and feldspar-phyric rhyolitic intrusions, most of which appear to be sub-conformable sills. Contacts range from passive and unmixed to peperitic. Only the margins of the sills were originally glassy, much of the interiors being finely crystalline.

Andesitic and basaltic volcanic sequences

Intermediate to mafic volcanics are locally important within the major lithostratigraphic units of the Mount Read Volcanics but are not laterally extensive. The most significant occurrences are the Que-Hellyer Volcanics in the Mount Charter Group (Waters & Wallace, 1992), the Hollway Andesite near the top of the Central Volcanic Complex, the Sterling Valley Volcanics conformably overlain by the Mount Black Volcanics, and the Lynch Creek basalts and the Anthony Road Andesite, both of which occur close to the boundary between the Yolande River sequence and the Tyndall Group.

- Feldspar- and pyroxene-phyric basaltic lava and sills, including pillow lava and pillowed sills, together with associated autoclastic breccia (pillow breccia, hyaloclastite) and peperite.
- Feldspar- and hornblende-phyric andesitic and basaltic andesite lava and sills, together with associated autoclastic breccia (mainly hyaloclastite) and peperite.
- Medium to very thick, graded beds of dacitic to basaltic sandstone and breccia. The principal components are porphyritic (feldspar, hornblende, pyroxene) lava clasts and both monomictic and polymictic clast assemblages occur. The clasts range in vesicularity from highly vesicular scoria to non-vesicular dense clasts. The groundmass in the clasts are typically microlitic although a significant proportion had formerly glassy (now perlitic) groundmass.

Tyndall Group

The Tyndall Group is the youngest lithostratigraphic unit of the Mount Read Volcanics and overlies the Central Volcanic Complex, the Eastern quartz-phyric sequence and Cambrian granites. Facies within it are diverse and include welded ignimbrite, coarse volcanic conglomerate and fossiliferous limestone that collectively suggest a shallower submarine setting than for the rest of the Mount Read Volcanics (White & McPhie, 1996, 1997).

- Very thick, crystal-rich sandstone units that vary from quartz-rich to quartz-poor. Both types are feldspar-rich and the quartz-poor variety contains significant amounts of ferromagnesian phases (principally clinopyroxene, very minor hornblende). Basal portions of very thick beds commonly include quartz- and feldspar-phyric volcanic clasts and relic pumice clasts are also present. Apart from abundant crystals, the matrix of this facies was composed of glass shards. Pumice and some volcanic clasts were also originally glassy.

- Coarsely quartz- and feldspar-phyric rhyolitic lava and associated autoclastic breccia. Flow banded and massive varieties occur. The flow banding originally consisted of glassy versus crystalline bands. The massive rhyolite may also have been originally glassy or partly glassy. The autoclastic facies principally comprises hyaloclastite and co-genetic resedimented hyaloclastite, both of which would have been composed of glassy clasts.
- Welded rhyolitic ignimbrite composed of quartz and feldspar crystals with well preserved eutaxitic texture defined by flattened relic pumice and matrix shards. The matrix is commonly perlitic, indicating that this facies was substantially glassy when first deposited.
- Massive to graded beds of polymictic volcanic conglomerate and sandstone. The clast population is diverse, dominantly comprising quartz- and feldspar-phyric volcanic clasts, with minor sedimentary intraclasts, metamorphic basement-derived quartzite, granite, feldspar- and ferro-magnesian-phyric (intermediate) clasts and other altered volcanic clasts. The clasts are dominantly subrounded to well-rounded, indicating reworking prior to deposition. The matrix is medium to very coarse sand largely comprising quartz crystals and lithic fragments.
- Massive, carbonate units up to several metres thick mainly near the base of the Tyndall Group. These units are composed of recrystallised calcite but locally contain a rich fossil assemblage (Jago et al., 1972).
- Laminated black mudstone, graded sandstone and pebble conglomerate, all of which represent a largely non-volcanic, metamorphic basement provenance.

Regional traverses in the Mount Read Volcanics: lithostratigraphy

In this section, the regional traverses undertaken in the Mount Read Volcanics are listed, giving the lithostratigrphic units sampled and cross-references to relevant sections in P439 Reports. The traverses are roughly oriented west–east, with Mount Black to Mackintosh Dam being the northernmost and the Jukes Road traverse being the southernmost.

(1) Mount Black-Murchison Highway-Anthony Road-Murchison Gorge-Mackintosh Dam: Central Volcanic Complex including the Mount Black Volcanics and Sterling Valley Volcanics, Farrell Slates (part of the Western volcano-sedimentary sequences), Murchison Volcanics (part of the Eastern quartz-phyric sequence), Murchison Granite, Owen Conglomerate. (Gifkins et al., Report 2; Gifkins, Report 3; Stolz et al., Report 4; Gifkins, Report 5).

(2) Hall Rivulet Canal-Hercules-Mount Read-Red Hills-Anthony Dam: Dundas Group and White Spur Formation, Central Volcanic Complex including the Hercules host sequence and Mount Black Volcanics, Tyndall Group. (McPhie et al., Report 2; Stolz et al., Report 3; Large, Report 3).

(3) Dobson Creek-White Spur "step-out" traverse: Central Volcanic Complex, White Spur Formation. (Allen et al., Report 4; Herrmann et al., Report 5).

(4) Jukes Road:Yolande River sequence, Eastern quartz-phyric sequence, Tyndall Group. (Wyman et al., Report 2; Wyman, Report 3).

Lithostratigraphy and volcanic facies architecture of the Mount Windsor Volcanics

The regional lithostratigraphy of the Mount Windsor Volcanics was described by Henderson (1986) and refined by Berry et al. (1992). There are four formations: the Puddler Creek Formation at the base, the Mount Windsor Formation, the Trooper Creek Formation, and the Rollston Range Formation at the top (Fig. 2). The middle two formations (Mount Windsor Formation and Trooper Creek Formation) are dominated by volcanic facies whereas the lowest and topmost formations are dominated by sedimentary facies. The Mount Windsor Formation is composed of quartz-phyric rhyolitic lavas and intrusions, together with minor felsic volcaniclastic facies. The Trooper Creek Formation is more varied in the volcanic facies types present (lavas, sills and cryptodomes and a wide variety of volcaniclastic

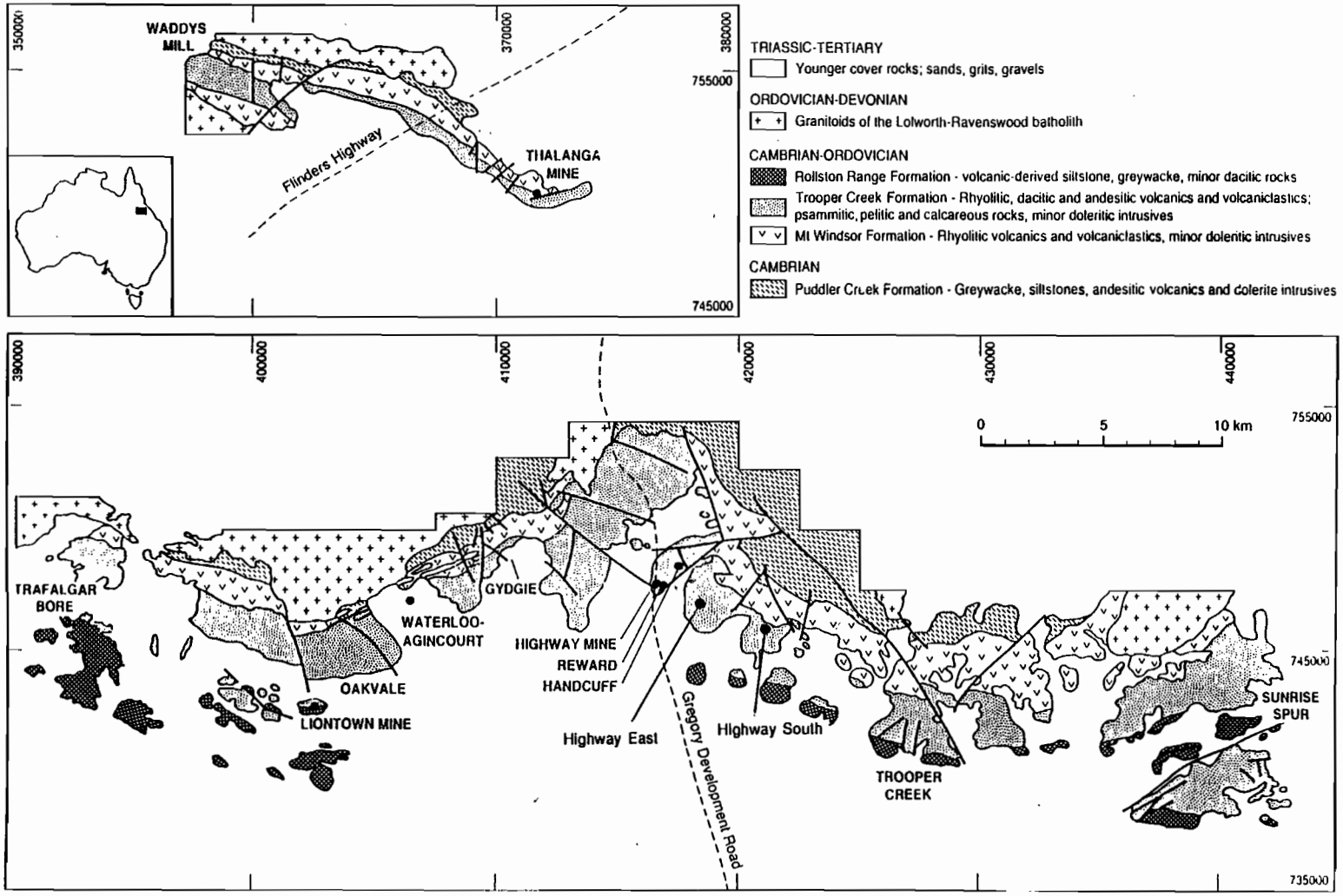

Figure 2 Distribution of the principal formations and major massive sulfide deposits in the Cambro-Ordovician Mount Windsor Volcanics of northern Queensland. Modified from Berry et al. (1992).

facies), and in the compositions (basalt through to rhyolite). Studies of the volcanic facies in the Mount Windsor Volcanics are limited to detailed research at the Thalanga and Highway-Reward massive sulfide ore bodies.

Thalanga

The Thalanga massive sulfide mineralisation occurs at the contact between the Mount Windsor Formation and the Trooper Creek Formation. The footwall succession is dominated by strongly quartz- and feldspar-phyric rhyolitic lavas, including both coherent and autoclastic facies (hyaloclastite, resedimented hya;loclastite, autobreccia). Despite strong alteration, diverse original textures (including perlite, spherulites, micropoikilitic texture, flow banding) and separate units have been identified (Hill, Report 1, Report 2; Paulick, Report 2, Report 4). The mineralisation occurs in a complex succession of quartz- and feldspar-bearing, crystal-rich sandstone and breccia, quartz- and feldspar-phyric rhyolitic lavas and syn-volcanic sills, and peperite. The hangingwall succession is dominated by feldspar-phyric dacitic lavas and associated autoclastic facies (hyaloclastite, resedimented hyaloclastite), polymictic felsic volcanic breccia, feldspar crystal-rich sandstone, feldspar- and pyroxene-phyric andesitic sills and non-volcanic mudstone and sandstone. Importantly, quartz-rich sandstone and quartz-phyric rhyolite previously thought to be restricted to the ore horizon are now known to occur in the hangingwall succession as well (Paulick, Report 2).

Highway-Reward

The Highway-Reward massive sulfide mineralisation occurs in a part of the Trooper Creek Formation that is dominated by a complex association of small, porphyritic, rhyolitic, rhyodacitic and dacitic, syn-volcanic intrusions (Doyle, Report 1, Report 4). The felsic intrusions have the form of cryptodomes and sills and were emplaced into wet, poorly consolidated sand and mud resulting in extensive development of peperite along intrusive contacts. The margins of the intrusions were quench-fragmented and originally dominantly glassy. Other important facies in the host succession are widespread pumice breccia units, andesitic lavas, andesitic volcanic breccia and polymictic volcanic breccia intercalated with siltstone and sandstone turbidites of mixed provenance. The highway and Reward massive sulfide ore bodies are pipe-like and constrained by the glassy, fractured margins of cryptodomes. The mineralisation and alteration have been interpreted as subseafloor replacement style, with hydrothermal system being focussed by the proximal, intrusion-dominated felsic volcanic association.

The influence of volcanic facies on alteration textures and alteration mineralogy

The facies architecture of submarine volcanic successions that host VHMS deposits is complicated, comprising compositionally and texturally diverse facies that have complex spatial and temporal relationships and unusual geometries (Fig. 3). In addition, stratigraphic and structural complexities are introduced by the prevalence of synvolcanic intrusions, facies that have high aspect ratios (very thick but not laterally extensive) and abrupt contacts, and syn-volcanic faults. Sites of ore deposition in VHMS host successions such as the Mount Read Volcanics and Mount Windsor Volcanics are highly variable. Footwall facies include thick lava and autoclastic breccia successions (e.g. Hellyer, Thalanga), syn-volcanic intrusions (e.g. Highway, Reward) and volcaniclastic mass-flow units (e.g. Hercules). Ore bodies may have formed in shallow subseafloor settings where they are replacements of mass-flow units or syn-volcanic intrusions, or else formed at the seafloor. In both settings, syn-volcanic faults could have controledl or influenced the sites of ore deposition.

Even though submarine volcanic successions are potentially immensely complex, their response to alteration, whether diagenetic, hydrothermal or metamorphic, is at least in part, predictable. Factors that appear to strongly control textural and compositional responses of volcanic facies to alteration include the presence of volcanic glass, the porosity and permeability, the composition and external conditions such as depth, pressure, temperature and water/rock ratio. Studies undertaken in the Volcanic Facies Module (e.g. Gifkins, this report; Allen, Report 5; Doyle, Report 4, this

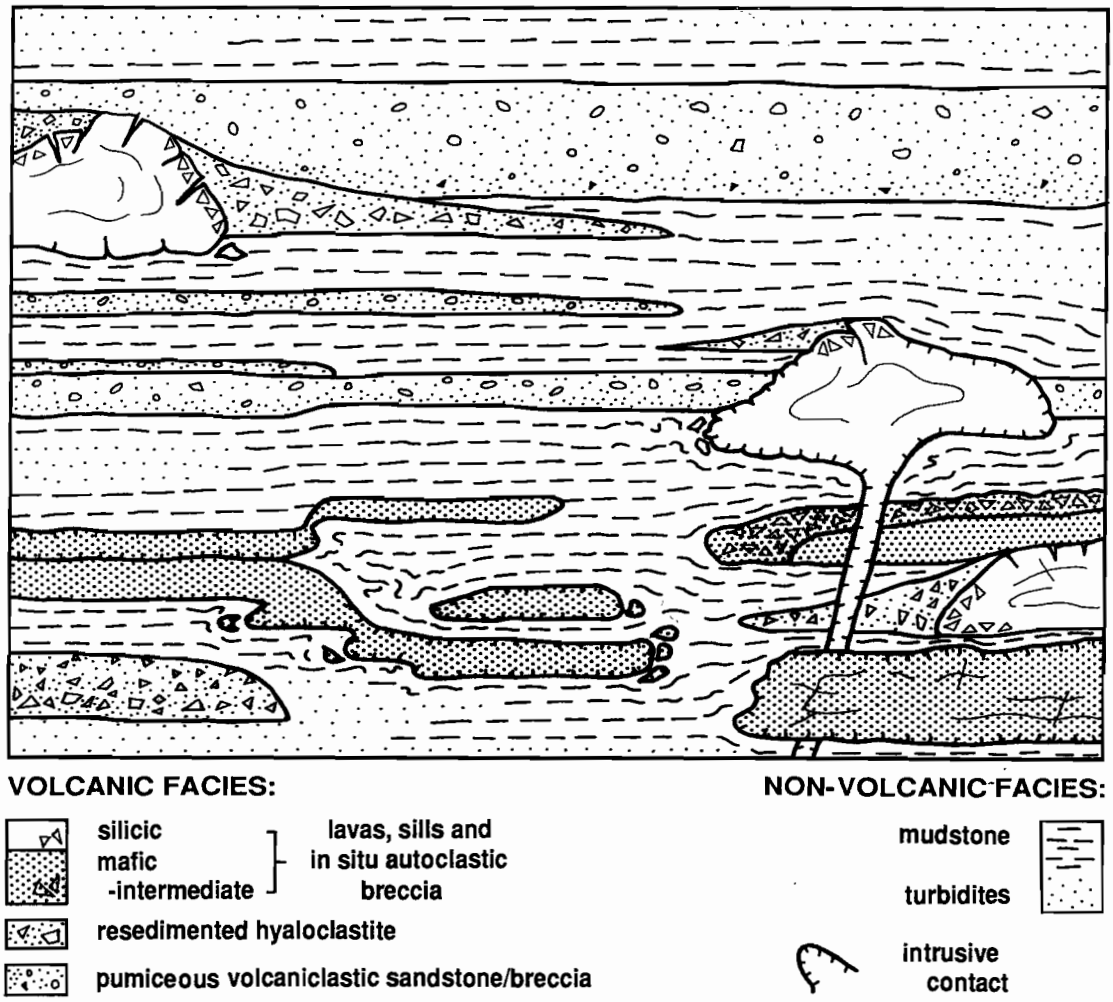

Figure 3 Schematic facies architecture of submarine volcanic sequences, such as the Mount Read Volcanics. Typically there are considerable regional variations in relative proportions of lavas, sills and volcaniclastic facies, and in volcanic versus non-volcanic facies. Modified from McPhie and Allen (1992).

report) have highlighted the particular importance of the presence of glass, and the porosity and permeability characteristics of the host facies.

(1) The proportion and distribution of glassy versus crystalline domains

Submarine lavas, high level intrusions and some volcaniclastic facies are commonly initially glassy or at least partly glassy (Fig. 4). Once formed, both the texture and composition of volcanic glass may be partially or completely modified by a variety of processes, such as hydration, devitrification (crystallisation below the glass transition temperature), diagenetic alteration and compaction. The rate at which these modifications proceed is in general accelerated by the presence of water and by elevated temperature. In contrast, crystalline components of volcanic facies are generally unaffected by hydration and compaction, and may remain largely stable during diagenetic alteration. Thus glassy domains will undergo longer and more complex textural evolution, and exhibit greater compositional changes than crystalline domains in the same facies. This generalisation holds on scales ranging from millimetres, such as in the case of delicate, glassy versus crystalline flow bands in lavas, to metres, such as in the case of glassy margins versus the crystalline interiors of lavas and syn-volcanic intrusions.

(2) The porosity and permeability of the volcanic facies

The creation of submarine volcanic facies takes place in the presence of seawater. The extent of physical and chemical interaction of the volcanic facies with seawater, diagenetic fluids and/or hydrothermal fluids depends on the porosity and permeability. These properties vary enormously among different volcanic facies types, spatially within some volcanic facies, and also temporally, from the time of emplacement through compaction and diagenetic alteration. However, in simplest terms, coherent and clastic volcanic facies show fundamentally different styles of porosity and permeability (Fig. 5).

Coherent volcanic facies are dominated by fracture-controlled porosity and permeability. This style varies in scale from very large (metres) where the fractures are quench fractures or cooling joints, to very small (millimetres), where perlitic fractures are present. The former will prevail in the coherent parts of lavas and syn-volcanic intrusions (commonly the interior). The latter will prevail in the glassy parts of lavas and syn-volcanic intrusions (commonly the margins), and within glassy clasts derived from them.

In **clastic** volcanic facies, the interparticle and intraparticle pores control porosity and permeabilty, so grain type (pumice or scoria versus dense), grain size and sorting are all important. Well sorted pumice breccia, such as that forming the footwall to the Rosebery and Hercules massive sulfide deposits, at least initially have uniformly high porosity and permeability. Poorly sorted mixtures of shards, crystals and dense volcanic clasts (for example, resedimented autoclastic facies) have lower and more heterogeneous porosity and permeability. The matrix character and abundance are particularly important in poorly sorted aggregates.

The abundance of glass and the porosity and permeability characteristics are not independent properties but are instead, are closely interrrelated. The conversion of fresh glass to relict glass results in profound changes in porosity and permeability, composition, texture and mineralogy, and simultaneously affects both the chemistry and circulation of pore fluids. In some cases, the primary porosity is increased by dissolution of the glass, introducing the possibility of compaction and marked changes in volume synchronous with diagenesis. In others, volcanic facies with high primary porosity may be rapidly sealed by growth of new diagenetic minerals in pores, greatly reducing the porosity and permeability, and minimising the effects of compaction.

The textural and compositional responses of different volcanic facies to diagenetic or other alteration (hydrothermal, metamorphic) within one succession can thus be highly variable. Glass-rich facies and more porous and permeable facies in submarine volcanic successions are the most easily affected. Moreover, early textural and compositional modifications that occur during diagenesis and/or compaction, are commonly accentuated by later alteration episodes, such those specifically related to VHMS ore-forming hydrothermal activity. The textural and compositional contrasts that initially

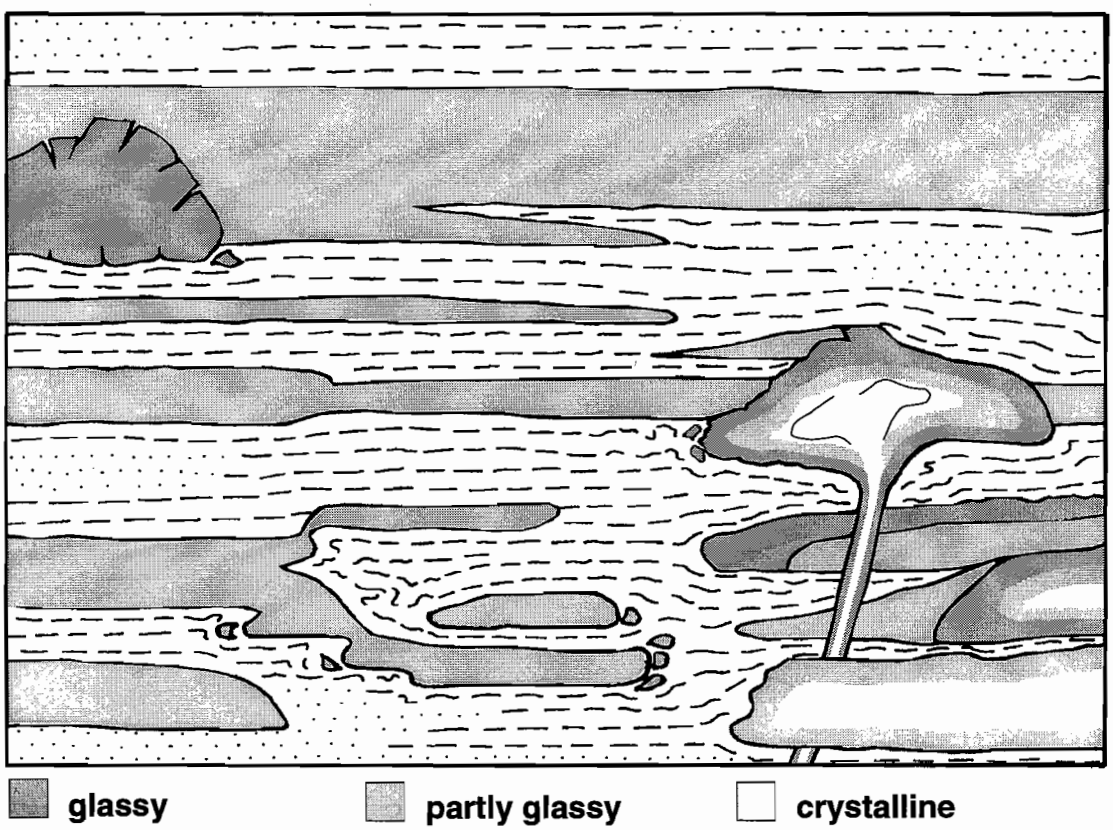

Figure 4. Abundance and distribution of glassy, partly glassy and crystalline domains within the principal volcanic facies types found in submarine volcanic successions. Outlines of volcanic facies types correspond to those shown in Figure 3.

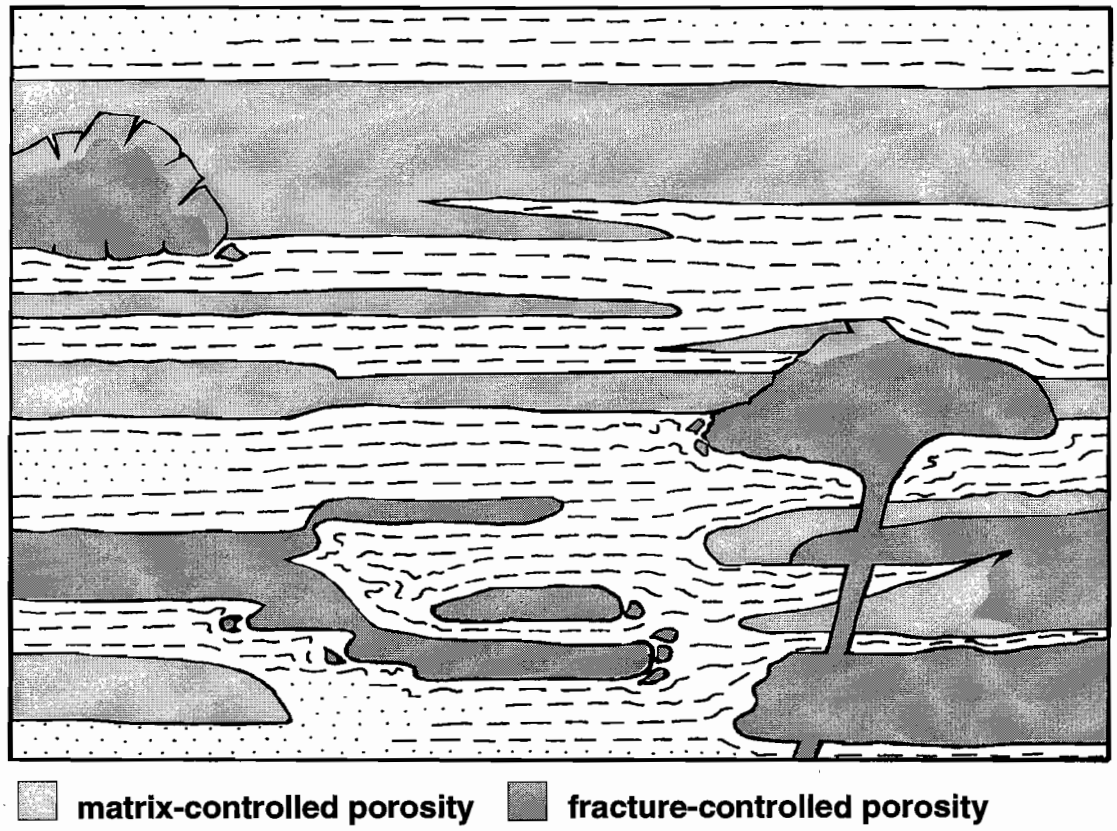

Figure 5 . Distribution of fracture-controlled versus matrix-controlled porosity in the principal volcanic facies types found in submarine volcanic successions. Outlines of volcanic facies types correspond to those shown in Figure 3. The coherent parts of lavas and intrusions have fracture-controlled porosity whereas the porosity of volcaniclastic facies is matrix-controlled.

exist between glassy and crystalline domains will persist during, and influence, later alteration. Exchange between glass and pore fluid can alter the glass composition (especially alkalis, Ca, Mg and silica) substantially. Thus, the mineralogy of the first-formed crystalline phases replacing the glassy domains may differ significantly from that of the initially crystalline domains. Early fracture-controlled alteration inherited from fracture-controlled porosity and permeability will influence later alteration styles. In the same way, early matrix-controlled alteration that reflects primary, matrix-versus-clast heterogeneity in porosity and permeability will affect later alteration styles.

Distinguishing diagenetic and hydrothermal alteration in VHMS successions

In host succesions to VHMS deposits, superimposed on the inherent complexity of the original volcanic facies and volcanic textures are regional textural and compositional changes related to burial and diagenesis, and more local textural and compositional changes related to hydrothermal alteration. Distinguishing textures and mineralogies specifically related to hydrothermal alteration is critical for successful exploration for VHMS mineralisation. However, the distinction of diagenetic from hydrothermal alteration may be very difficult because the two processes may overlap temporally, spatially and in physical conditions such as temperature, pressure and fluid/rock ratios.

In addition, the alteration mineralogies are strongly controlled by the primary rock composition and generalisations that hold for one composition are not necessarily correct for another.

One important result from the regional traverses in the Mount Read Volcanics has been recognition of the characteristics of early (largely diagenetic) versus hydrothermal alteration styles. Although some mineral assemblages are distinctive and can be confidently linked to hydrothermal alteration in the field, some are not. Alteration assemblages involving sericite, carbonate, secondary feldspar and quartz are common in the host facies to massive sulfides in the Mount Read Volcanics but are also ubiquitous elsewhere. At least in the field, textural criteria can be useful in making the distinction.

- Hydrothermal alteration is spatially restricted (metres to tens of metres) and more focussed, whereas the assemblages regarded as regional diagenetic and/or regional metamorphic in origin are widespread (hundreds of metres to kilometres). Although widespread, regional diagenetic assemblages are not necessarily uniform in the assemblage or relative abundances of the diagenetic mineral phases present (Gifkins, this report). Instead, there is commonly a zonation that reflects variations in physical conditions (temperature, pressure) and rates of burial.
- Diagenetic alteration commonly accentuates and enhances primary textures, especially in cases involving fracture-controlled alteration. Primary textures in hydothermally altered facies may be strongly enhanced but in most cases, are destroyed and converted to apparent clastic textures, especially apparent matrix-supported breccia textures and apparent eutaxitic textures (Allen, 1988, 1992; McPhie et al., 1993).
- In some glassy and pumice-rich volcanic facies, early compaction resulted in development of a stylolitic, bedding parallel foliation (S1). The earliest diagenetic alteration assemblages were affected by this foliation whereas later hydrothermal alteration overprints the foliation (Gifkins, this report; Allen, Report 5).
- Two-phase or polyphase, patchy or banded alteration styles are commonly, but not exclusively, diagenetic. Perhaps the clearest cases are those involving patchy alteration of a particular stratigraphic unit that is widespread. For example, the quartz crystal-rich volcanic sandstone facies that dominates part of the Tyndall Group (Mount Julia Member) is characterised by pink, albite-rich patches or bands versus green chlorite-rich bands throughout its extent (White & McPhie, 1996). The regional extent and facies-bound nature of the alteration suggest a diagenetic origin. The current mineralogy may not be the original diagenetic mineralogy one but instead reflect the regional metamorphic overprint. The diagenetic alteration has principally affected originally glassy components in the matrix of the sandstone and may have been controlled by subtle grain size and porosity variations.

Significance of volcanic facies studies in VHMS alteration research

An understanding of volcanic facies architecture is critical for the correct interpretation of the stratigraphic, structural and temporal relationships of VHMS deposits, and hence also for the correct interpretation of alteration and mineralisation processes. Submarine volcanic successions are inherently complex and within one succession, there may be enormous variety in the geometry and character of the volcanic facies and hence, in potential VHMS-ore forming environments.

Submarine volcanic facies are commonly glass-rich and porous and especially susceptible to hydration, compaction and devitrification during diagenesis. These process profoundly alter the porosity, permeability, texture, mineralogy and composition, and may precede or accompany VHMS-related hydrothermal alteration. An appreciation of the early stages in textural modification of glassy volcanic rocks is thus critical in correct evaluation of the exploration significance of particular alteration textures and assemblages.

References

Allen RL 1988 False pyroclastic textures in altered silicic lavas, with implications for volcanic-associated mineralization. Econ Geol 83: 1424-1446.

Allen RL 1992 Reconstruction of the tectonic, volcanic and sedimentary setting of strongly deformed Zn–Cu massive sulfide deposits at Benambra, Victoria. Econ Geol 87: 825–854.

Berry RF, Huston DL, Stolz AJ, Hill AP, Beams SD, Kuronen U, Taube A 1992 Stratigraphy, structure and volcanic-hosted mineralisation of the Mount Windsor subprovince, North Queensland, Australia. Econ Geol 87: 739-763.

Corbett KD 1992 Stratigraphic-volcanic setting of massive sulfide deposits in the Cambrian Mount Read Volcanics, Tasmania. Econ Geol 87: 564–586.

Henderson RA 1986 Geology of the Mount Windsor subprovince - a lower Paleozoic volcano-sedimentary terrane in the northern Tasman orogenic zone. Aust J Earth Science 33: 343-364.

Jago JB, Reid KO, Quilty PG, Green GR, Daily B 1972 Fossiliferous Cambrian limestone from within the Mt Read Volcanics, Mount Lyell mine area, Tasmania. J Geol Soc Aust 19: 379–382.

McPhie J, Allen RL 1992 Facies architecture of mineralised submarine volcanic sequences: Cambrian Mount Read Volcanics, western Tasmania. Econ Geol 87: 587–596.

McPhie J, Dole M, Allen R 1993 Volcanic textures. A guide to the interpretation of textures in volcanic rocks. Centre for Ore Deposit and Exploration Studies, , Unversity of Tasmania, Hobart, 198 p.

Pichler H 1965 Acid hyaloclastites. Bull Volcanol 28: 293–310.

Waters JC, Wallace DB 1992 Volcanology and sedimentology of the host succession to the Hellyer and Que River volcanic-hosted massive sulfide deposits, northwestern Tasmania. Econ Geol 87: 650–666.

White MJ, McPhie J 1996 Stratigraphy and palaeovolcanology of the Cambrian Tyndall Group, Mount Read Volcanics, western Tasmania. Australian Journal of Earth Sciences. 43: 147-159.

White M, McPhie J 1997 A submarine welded ignimbrite-crystal-rich sandstone facies association in the CambrianTyndall Group, western Tasmania, Australia. J Volcanol Geotherm Res 76: 277-295.

Yamagishi H 1987 Studies on the Neogene subaqueous lavas and hyaloclastites in southwest Hokkaido. Geol Surv Hokkaido, Rept 59: 55–117.

Alteration in different glassy volcanics with emphasis on early diagenetic alteration; a case study from the Mount Black Volcanics

Cathryn C Gifkins
Centre for Ore Deposit Research

Summary

An integrated approach of facies analysis, petrography and geochemistry in the Mount Black Volcanics has resulted in the recognition of regional diagenetic alteration phases that have been active in different glassy volcanic facies. These diagenetic phases involve significant mineralogical and textural changes but only minor changes to the geochemical signature. The distribution of the diagenetic alteration phases generally reflects the complex and discontinuous nature of an originally glassy volcanic pile. In contrast local hydrothermal alteration stages form discrete pervasive zones where the geochemistry deviates more significantly from the least altered geochemical signature.

The Mount Black Volcanics were originally a complex package of dominantly glassy coherent silicic volcanics with lesser volcaniclastic material. The coherent units are typically discontinuous domes, lavas and or shallow intrusives. Although the original porosity was low, post depositional processes such as hydration leading to intense perlitic fracturing considerably increased the porosity. The highly unstable nature of glass and the perlitic margins of the coherent units therefore became highly permeable zones that have undergone subsequent alteration. The result is that coherent units particularly at the margins are not necessarily less intensely altered than the volcaniclastic units.

Introduction

Textural changes in glassy volcanic rocks begin immediately after eruption from the magma chamber. Emplacement or depositional processes may produce distinctive textures such as flow-banding and autobrecciation in coherent deposits and grading, bedding or welding in clastic deposits. These primary and secondary volcanic textures may be accentuated or obscured by later changes. The later post-depositional processes commonly affect not only the texture but the mineralogy and chemistry. Devitrification, hydration, hydrothermal and diagenetic alteration, burial and compaction, tectonic deformation and metamorphism have all acted to modify the primary facies.

The aim of this paper is to investigate early regional scale alteration that may be attributed to diagenetic alteration. Previous reports (Allen, 1997; Gifkins 1997; Stolz et al., 1997) have attempted to define the regional background alteration styles. Rocks in the Mount Black and Sterling Valley Volcanics have been variably modified by the combined effects of several alteration styles. The most common alteration assemblages are, silicification, feldspar ± quartz, sericite, sericite-chlorite ± carbonate ± quartz, carbonate, chlorite, chlorite-epidote ± carbonate and sphene. The wide distribution of many of these alteration styles and the remote location from known mineralisation suggests that these alteration assemblages are the product of regional processes rather than focussed hydrothermal events associated with mineralisation. Although the distribution is widespread the background alteration is not a blanket style alteration. Instead regional processes produce a complex pattern of overlapping alteration styles and intensities. This study intends to determine some of the controls on the alteration textures and distribution and changes in whole rock chemistry related to the diagenetic alteration.

Previous AMIRA P439 reports

- Gifkins, C.C., 1997. Background alteration in the Mount Black Volcanics: textures, mineralogy and geochemistry. AMIRA Report 5, project P439, 85–134.

- Gifkins, C.C., 1996. Mount Black Volcanics: Preliminary volcanic facies and alteration, petrography and geochemistry. AMIRA Report 3, project P439, 321–349.

- Gifkins, C.C., Allen, R.L., Stolz, A.J. and Duhig, N., 1996. Mount Black to Murchison Gorge: Preliminary volcanic facies analysis and alteration styles. AMIRA Report 2, project P439, 1–18.

- Gifkins, C.C., 1995. Subaqueous silicic volcanism in the Mount Black Volcanics, western Tasmania. AMIRA Report 1, project P439, 19–26.

Introduction to alteration of volcanic glass

Volcanic glass is a super-cooled silicate liquid with a poorly ordered internal structure consisting of loosely linked SiO_4 tetrahedra with considerable intermolecular space (Fisher and Schminke, 1984). The poor order of the crystal lattice results in volcanic glass being thermodynamically unstable and more readily decomposed than most mineral phases (Friedman and Long, 1984). Hence, rocks that are composed dominantly of volcanic glass are susceptible to alteration to more stable assemblages under changing temperature, pressure or chemical conditions. The conversion of fresh glass to a mineral assemblage may result in profound changes in porosity and permeability, composition, texture and mineralogy, and simultaneously affect both the chemistry and circulation of pore fluids within the volcanic pile. Pumice is highly vesicular volcanic glass (McPhie, Doyle and Allen, 1993; Fisher and Schminke, 1984; Dimroth and Yamagishi, 1987) and as a result is particularly susceptible to post depositional modification. It is porous and so readily allows the passage of circulating fluids; it is glassy and metastable, so readily alters or is replaced; and it is mechanically weak, so may take up significant strain during burial compaction or deformation or both.

The texture and/or composition of volcanic rocks which were originally glassy changes due to cooling and crystallisation, hydration, diagenetic alteration, burial compaction, hydrothermal alteration, metamorphism and deformation. Each process is influenced by the existing deposit texture and mineralogy but also modifies and overprints this. Thus the texture, mineralogy and geochemistry of volcanic rocks evolves by a series of steps, however the steps are not necessarily discrete and many overlap making the recognition of individual phases complicated. The result of this series of alteration processes operating is often a complex pattern of two or more phase alteration assemblages that may enhance or destroy pre-existing textures in the volcanic rock. There have been few previous studies of the textural and mineralogical evolution accompanying these stages. The concept of textural evolution in glassy volcanic rocks is unique. Characteristics of unmodified lavas and their subsequent textural evolution have been studied in some detail (Allen 1988; Yamagishi 1987; Kano et al., 1991; Gifkins, 1997), however, work on pumice and pumice-rich deposits, especially submarine examples is very limited (Allen, 1997; Torres et al., 1995; Tazaki and Fyfe, 1992; Gifkins, 1997).

Those processes that modify the texture and/or composition of volcanic glass and are contemporaneous with emplacement include devitrification, hydration and hydrothermal alteration (Cas and Wright, 1987).

Devitrification is the conversion of glass to crystalline mineral. Devitrification of thermodynamically unstable glasses involves the nucleation and growth of fibrous crystals of quartz and both Na-rich and K-rich alkali feldspar. Lofgren (1970), Lipman (1965) and Noble (1967) found that not only does the texture alter dramatically but the bulk rock chemistry changes accompanying hydration and devitrification, variations of up to 2% occur in SiO_2, H_2O, Fe_2O_3/FeO ratio, Na_2O and K_2O. It may be difficult to distinguish the effects of devitrification on the geochemistry from true hydrothermal silicification.

Hydration is the breakdown of glass as the result

of chemical interaction between solid glass and the interstitial pore fluid (Fisher and Schminke, 1984). Hydration reactions results in the transfer of H_2O from the fluid phase into the structure of a mineral phase or the glass increasing the salinity of the pore fluid (Torres et al., 1995). The fluid phase is commonly pore fluid although seawater or atmospheric water may also be absorbed. Rhyolite glass when erupted is undersaturated (H_2O) relative to water vapour and will absorb water on to its surface. This absorbed water will diffuse into the glass simultaneous with the diffusion of Na^+, Ca^{2+} and Mg^+ out of the rhyolite glass (Friedman and Long, 1984).

Hydrothermal alteration results from the reaction of hot water, steam or gas with pre-existing solid phases due to changing thermal and chemical conditions (Bates and Jackson, 1987 and Henley and Ellis, 1983). The process of hydrothermal alteration involves ion-exchange reactions, mineral phase transformations, mineral dissolution and new mineral growth. The main influences on the alteration mineralogy are permeability, T and fluid composition although the primary rock composition also has some effect. The result of hydrothermal alteration is significant changes in the primary whole rock geochemistry, particularly the mobile elements Na^+, K^+, Ca^{2+}, C^{4+}, Mg^+ and Fe^{3+} and changes to the texture and mineralogy.

Volcanic facies may also be significantly influenced by processes that post-date emplacement; diagenesis, prolonged hydrothermal alteration, metamorphism and deformation.

The transition between diagenesis and metamorphism has not been rigorously defined (Pettijohn et al., 1972, Bates and Jackson, 1987, Fisher and Schminke, 1984 and Morrow and McIlreath, 1990). Diagenesis involves minor changes in the rock components and crystallisation of cement minerals in the pore space whereas metamorphism occurs where the coarse crystal grains are also extensively involved in the reaction that the rock becomes substantially recrystallised (Morrow and McIlreath, 1990). No absolute ranges in pressure and temperature conditions have been defined for subsurface diagenetic environments, generally diagenesis is characterised by pressures of 0.1 MPa to 10 MPa (1 bar to 1 kb) and temperatures ranging from 0–300°C and depths of upto 10–15 km (Morrow and McIlreath, 1990).

Diagenesis is the process that occurs between surficial weathering and metamorphism and encompasses all chemical, physical and biological changes in a sediment/ rock after deposition, during lithification. It is the mineral changes that occur in response to the regional geothermal gradient in the depositional basin. Each basin records unique conditions of diagenesis (Torres et al., 1995). During diagenesis significant textural and mineralogical changes can be produced by dissolution of original components, precipitation of and replacement by new mineral phases, compaction, bacterial reactions and the growth of concretions (Bates and Jackson, 1987).

During the modification of primary textural features by diagenetic overprints, even minor variations in primary composition and pore space can cause significant changes. Primary textures can be enhanced, modified or obliterated. Commonly found types of diagenetic overprints in calcareous rocks can produce a wide variety of textures from the same primary texture (Einsele et al., 1991) and this study suggests that textures developed during diagenesis of glassy volcanics can preserve, enhance, modify or destroy the same primary volcanic texture. Although the textural modification that occurs during diagenesis can be significant the variations in the whole rock chemistry associated with these changes are subtle. In many cases diagenesis in glassy volcanics involves the formation of a new mineral by the rearrangement of mineral phases or glass rather than additions or depletions of ions. In fact many diagenetic mineral reactions are interrelated with ions released by one reaction being consumed by another.

The most important diagenetic processes are; mechanical compaction, cementation, and replacement of glass, dissolution and pressure dissolution. These processes selectively affect individual components or facies; thus one specific process operates at certain sites, while other processes occur simultaneously elsewhere in the volcanic pile.

Metamorphism involves pervasive mineralogical, chemical and textural changes as a result of changes in the physical and chemical conditions. Metamorphism may be isochemical where the composition of the rock remains the same except for removal or

addition of volatile species. This involves the parent mineral assemblage adjusting to new thermodynamic conditions while metasomatism also involves chemical exchange.

Deformation is a general term for structural changes in rocks including faulting, folding, shearing, compression and extension. Although deformation modifies the textures and fabric of most rocks, chemical changes that accompany deformation are the result of either metamorphism or prolonged hydrothermal alteration.

Regional geology and stratigraphy

The rocks of the Mount Black and Sterling Valley Volcanics compose a significant part of the northern Central Volcanic Complex (CVC), in the Mount Read Volcanic Belt. They unconformably overlie the Rosebery–Hercules sequence to the west and are truncated by the Henty Fault zone to the east. Regionally the Mount Black Volcanics represent a large open syncline. The western or upper most part of the Mount Black Volcanics and the Rosebery–Hercules sequence form the eastern limb of the adjacent anticline to the west. This NNE trending regional anticline extends for 20 km from Hercules in the south to Pinnacles in the north. The Sterling Valley Volcanics occur in the core and on the western limb of a regional anticline that extends from the north of Mount Block and is truncated to the south by the Henty Fault.

The local stratigraphy to the Hercules and Rosebery mineralisation has been divided from base to top by Allen (1991, 1993, 1994) (Fig. 1a) into (i) footwall pyroclastics which are dominated by thick feldspar-phyric, pumice-rich, mass flow units with minor massive dacite and autoclastic breccias, (ii) "host rock" or transitional stratified volcaniclastics that are composed of bedded siltstones, crystal-rich and tuffaceous sandstones, (iii) black mudstone and (iv) hangingwall volcaniclastics which are massive thick-bedded quartz and feldspar, crystal-, lithic-, and pumice-rich volcaniclastic sandstones and breccias. Interbedded in the hangingwall sequence are a number of thin black mudstone beds.

The original stratigraphic relationship between the Mount Black Volcanics and the Rosebery–Hercules hangingwall is uncertain. The contact between the feldspar-phyric Mount Black Volcanics and the quartz-phyric volcaniclastic mass-flow units of the Rosebery–Hercules Hangingwall is a brittle thrust fault, the Mount Black Fault. A 2–10 m zone of intense ductile shearing and silicification exists either side of the brittle fault suggesting that the fault was reactivated. The significance of the Mount Back Fault is unclear, its narrow width contrasts with the sharp change in lithofacies. Basaltic dykes of the Henty dyke suite that intruded into the Mount Black Volcanics are truncated by the Mount Black Fault and are absent in the Rosebery–Hercules sequence.

The Mount Black Volcanics have previously been considered to be younger than the Rosebery–Hercules sequence, however their similarity to the Rosebery–Hercules footwall sequence is quite marked. The main difference is that the Mount Black Volcanics contain more lava and intrusives than massflow units while the footwall is predominantly composed of pumiceous massflow deposits. Based on this observation Allen (1994) suggested that the Mount Black Volcanics are a fault repetition of the Rosebery footwall and that there may be potential for the Rosebery and Hercules ore horizons to be repeated to the east of the Mount Black Fault.

Comparison of pumice breccias from the Rosebery footwall and the Mount Black Volcanics (Table 1) shows the similar facies characteristics and ranges in immobile elements. A more detailed comparison of the whole rock geochemistry is presented in Appendix 1. The pumice breccias from both the Rosebery footwall and the Mount Black Volcanics plot in a tight cluster on a Winchester and Floyd (1977) discrimination diagram as rhyolites to rhyodacites (Fig. 2). The tight cluster of points suggests that they represent homogenous monomictic volcaniclastic units of similar composition. The interpretation that the rhyolitic pumice breccias of both the Rosebery Footwall and Mount Black Volcanics and the lavas and syn-sedimentary sills of the Mount Black Volcanics represent explosive and effusive products of the single volcanic centre is also supported by the compositional similarities. Furthermore mafic clasts taken from pumice breccias in the Rosebery Footwall have compositions that are typical of the dacites and basalts in the Sterling Valley Volcanics (Fig. 2) suggesting that they were derived

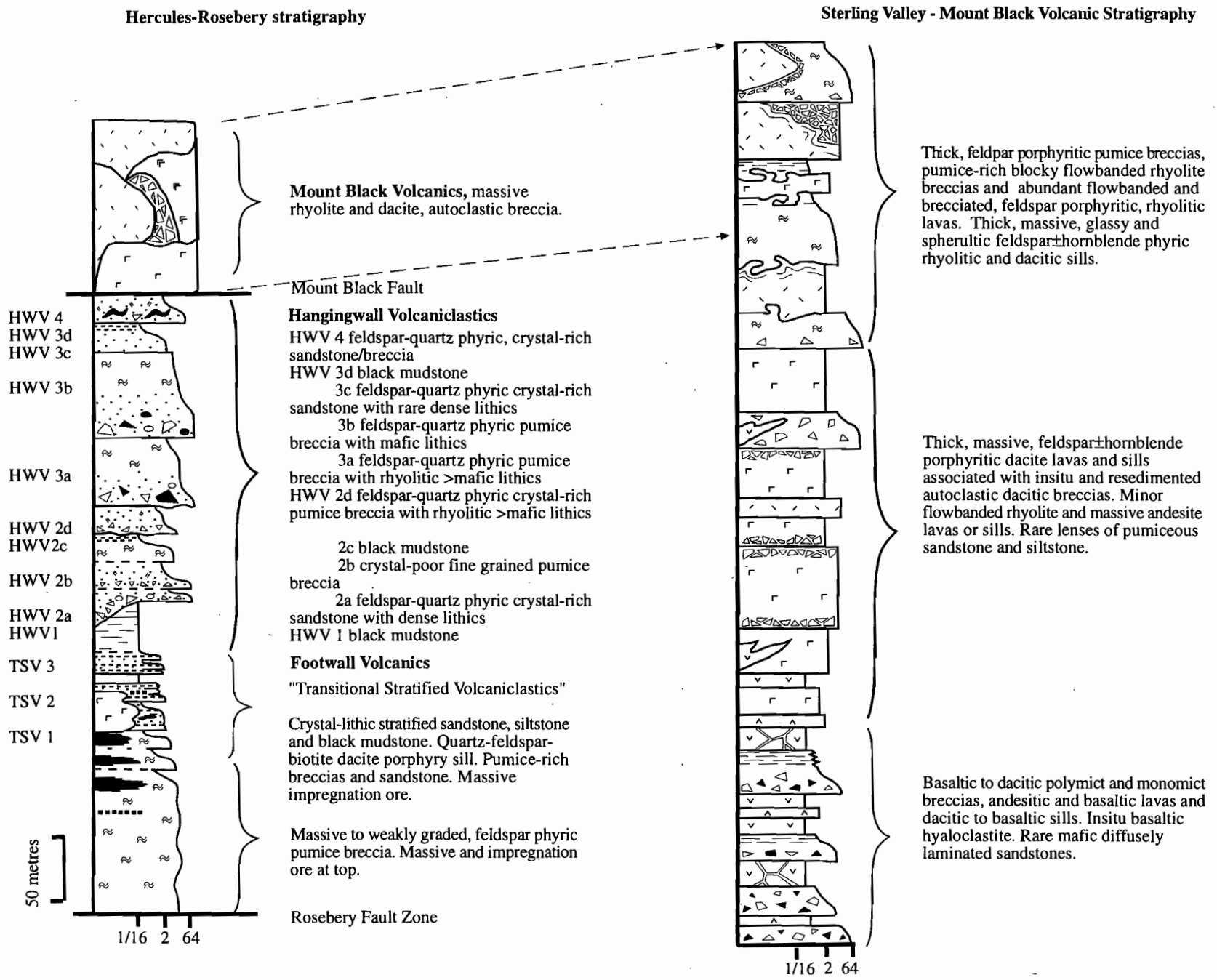

Figure 1: a) Simplified graphic log of the host volcanic sequence to the Rosebery-Hercules massive sulfide mineralisation from Allen (1994). The total illustrated thickness of the section is ~ 2000 m. b) Simplified graphic log of the Sterling Valley and Mount Black Volcanics. The total illustrated thickness is ~5000+ m.

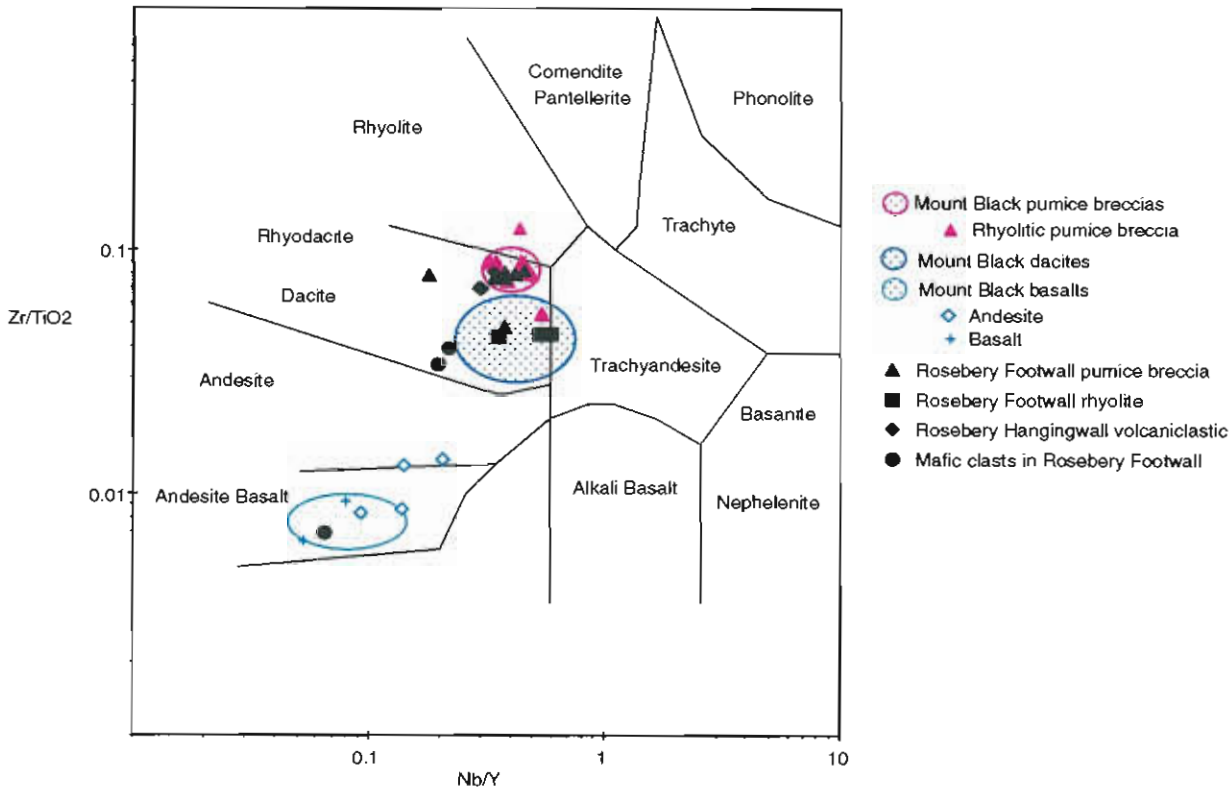

Figure 2: Discrimination diagram of Nb/Y versus Zr/TiO_2 for rocks from the Mount Black Volcanics and the Rosebery Footwall (after Winchester and Floyd, 1977). This depicts identical immobile element fields for the pumice breccias. It also illustrates the similarity between the mafic clasts in the lithic-rich base of the Rosebery Footwall pumice breccias and the basaltic lavas and sills of the Sterling Valley Volcanics.

Table 1: Comparison of characteristics of pumice breccias from the Rosebery Footwall and the Mount Black Volcanics. Rosebery Footwall pumice breccia lithofacies characteristics from Allen (1991, 1993 and 1994).

	Rosebery Footwall pumice breccias	*Mount Black Volcanics pumice breccias*
Lithofacies characteristics	thick, normally graded deposits with sandy stratified tops, lithic-rich bases, fiamme, increasingly crystal-rich towards top	thick normally graded deposits with sandy and silty stratified and cross-bedded tops, lithic-rich bases, fiamme
Components	tube pumice, feldspar crystal fragments, glass shards, dense dacitic and mafic lithics, mudstone rip-up clasts	tube pumice, feldspar crystal fragments, glass shards, dense rhyolite and dacitic lithics, mudstone rip-up clasts
Ti/Zr	7-9	6.75-8
Nb/Y	0.2-0.45	0.3-0.5
SiO_2	38-75%	55-74%
Al_2O_3	8-15.5%	13-20%
Ba	500-1520 ppm	700-1640 ppm
Rb	52-250 ppm	84-280 ppm
Sr	8-250 ppm	84-270 ppm
Th	14-25 ppm	16-27 ppm

from the Sterling Valley. This primary geochemical evidence supports the possibility that the Mount Black Volcanics are an up faulted block equivalent to the Rosebery Footwall, however the interpretation of the Mount Black Fault is still inconclusive.

Local geology and stratigraphy of the Mount Black and Sterling Valley Volcanics

The Mount Black Volcanics are a several kilometre thick package of feldspar-phyric massive, flow-banded and flow-brecciated lavas and sills of generally rhyolitic to dacitic composition with minor andesite. Variable proportions of lithic and/or pumice-rich volcaniclastic breccias, shard-rich sandstones and siltstones, and crystal-rich sandstones are interbedded with, or intruded by the more coherent units. The facies distribution and contact relationships are quite complex reflecting the large volume of laterally discontinuous high relief lava domes and the high proportion of lava-like intrusive bodies. These intrusions are interpreted to be shallow sills that were coeval with the continuing volcaniclastic activity and extrusion of lavas. The lavas and intrusions have similar mineralogy, geochemistry and primary volcanic textures and are best differentiated based on their contact relationships. Table 2 summarises the distinctive characteristics of the dominant lithofacies in the Mount Black and Sterling Valley Volcanics. Accompanying Plates 1–6 show many of the textural and alteration features described within this report. For more detailed descriptions of the facies refer to Gifkins (1997) in AMIRA report 5.

Stratigraphically at the top of the Mount Black Volcanics the facies are dominated by flow-banded and brecciated rhyolite lavas and pumice-rich rhyolitic breccias intruded by thick feldspar phyric dacitic sills (Fig. 1b). Below this the volcanics are dominated by massive red-brown to grey feldspar ± hornblende phyric dacitic, andesitic and less commonly rhyolitic lavas, sills and thick piles of autoclastic debris.

Conformably underlying the Mount Black Volcanics to the east is a package of basaltic to dacitic volcanics, locally known as the "Sterling Valley Volcanics" (Fig. 1b). These are composed of numerous monomictic and polymictic basaltic to andesitic mass-flow breccias, basaltic to dacitic lavas and sills, laminated basaltic sandstones and rare tuffaceous siltstones. The Sterling Valley Volcanics and Mount Black Volcanics are in stratigraphic contact and appear to be petrographically and chemically related.

Volcanic architecture

The schematic volcanic architecture is a method of graphically displaying the generalised stratigraphy and the relationship between facies within the volcanic pile. The volcanic architecture of the Mount Black Volcanics highlights the discontinuous nature of the facies and their complex internal textures (Fig. 3). A single unit with a consistent Ti/Zr ratio may display a wide variety of primary volcanic and post-depositional textures, it may also be extrusive, intrusive or both. The volcanic architecture also depicts lava-like intrusions scattered throughout the volcanic pile like raisins in a pudding. Most of the intrusions were emplaced into water-saturated unconsolidated sediment probably only a few metres to a kilometre below the seafloor and typically have peperitic contacts. The presence of spherulites and micropoikolitic textures in the lavas and sills are the product of high temperature devitrification indicating that the rhyolites were originally coherent volcanic glass (Lofgren, 1971 and McPhie et al., 1993). Associated with coherent facies are thick piles of insitu and resedimented hyaloclastite or an abundance of flow-banded autobrecciated debris. Flow breccias and hyaloclastite are syn-eruptive volcaniclastic deposits formed by non-explosive fragmentation processes, flow-brecciation and quench fragmentation respectively. Fragmentation occurs at the margins of moving lavas, domes and sills and less commonly may form bands within individual coherent unit. Deposits of hyaloclastite are recognised on the basis of curviplanar clast margins which are typical of quench brecciation (Pichler, 1965).

Less prominent are a variety of juvenile volcaniclastic deposits. Two main types of subaqueous volcaniclastic deposits occur. The first are rhyolitic to dacitic pumice-lithic breccias composed of dense originally glassy fragments, that now contain perlitic

Table 2: Distinctive characteristics of the main lithologies in the Mount Black and Sterling Valley Volcanics. Where fsp= feldspar, qtz= quartz, hbl= hornblende, px= pyroxene, ser= sericite, chl= chlorite, CO3 = carbonate, ep= epidote and mag= magnetite.

UNIT	LITHOFACIES CHARACTERISTICS	MINERALOGY/ COMPONENTS	TEXTURES	ASSOCIATED FACIES	ALTERATION STYLES
COHERENT FACIES					
Feldspar phyric rhyolite lavas and sills (Plate 1)	massive, flowbanded	0-10% fsp	amygdaloidal, pumiceous, perlitic, spherulitic or micropoikolitic, glomeroporphyritic	flow-brecciated or quench brecciated volcaniclastic debris	fsp-qtz, ser-qtz, ser-chl, chl, CO3, silica
Feldspar-quartz phyric rhyolite sills	massive, rarely flow-banded, peperitic contacts	5-10% fsp> qtz	densely microspherultic or micropoikolitic		fsp-qtz, ser-qtz
Feldspar phyric dacite lavas and sills (Plate 4)	massive	0-25% fsp	densely microspherulitic or micropoikolitic, vesicular or perlitic, glomeroporphyritic	flow-brecciated or quench brecciated volcaniclastic debris	fsp-qtz, ser-qtz, ser-chl, chl, chl-ep, ser
Feldspar-hornblende phyric dacite lavas and sills (Plate 5)	massive, flow aligned phenocrysts	10-30% fsp>hbl	densely microspherultic or micropoikolitic, rarely perlitic or vesicular	rarely with pumiceous quench brecciated fsp-hbl porphyritic debris	fsp-qtz, ser-qtz, chl-mag, chl-ep, ser
Aphyric andesite (Plate 6)	massive, fine grained		felt textured		chl-ep, ser
Feldspar-hornblende phyric andesite (Plate 6)	massive	5-20% fsp±hbl		quench fragmented breccias	chl-ep, ser
Basaltic lavas and sills (Plate 6)	massive, insitu quench fragmented, fine grained glassy margins, peperitic	0-10% px, fsp, hbl, px		quench fragmented breccias	chl-ep, ser
Basaltic dykes (Henty dyke suite) (Plate 5)	massive, fine grained chilled margins	0-3% fsp±px	commonly weakly vesicular, felt textured		chl-ep, CO3, chl-mag
VOLCANICLASTIC FACIES					
Rhyolitic-dacitic pumice breccias (Plate 3)	massive to normally graded	0-30% fsp crystal fragments, tube pumice, shards and rare dense lithics	fiamme or compaction foliation, S_0 parallel styolites	pumiceous and shard-rich sandstones and siltstones	fsp-qtz, ser-qtz, ser-chl, chl-mag, ser, CO3
Rhyolitic-dacitic pumice-lithic breccias (Plate 2)	massive and normally graded	0-15% fsp crystal fragments, tube pumice and dense rhyolitic-dacitic lithic clasts	fiamme, perlitic, spherulitic or vesicular dense clasts	sometimes with an adjacent flow-banded and pumiceous rhyolite	fsp-qtz, ser-qtz, ser-chl, chl, CO3, ser
Volcaniclastic sand and siltstones (Plate 3)	laminated, graded and cross bedded	juvenile volcanic material (shards, pumice, crystals and lithics)	wispy lenses of compacted pumice clasts	occurs as reworked top of a graded volcaniclastic breccia	fsp-qtz, ser-qtz, chl
Mafic volcaniclastic breccia (Plate 6)	massive to graded with diffusely laminated tops	5-10% fsp± hbl± px crystals, clasts of andesite, dacite, basalt and scoria	clasts have glassy rinds and commonly perlitic	related to dacitic to basaltic quenched lavas	fsp-qtz, chl-ep, ser, chl-mag

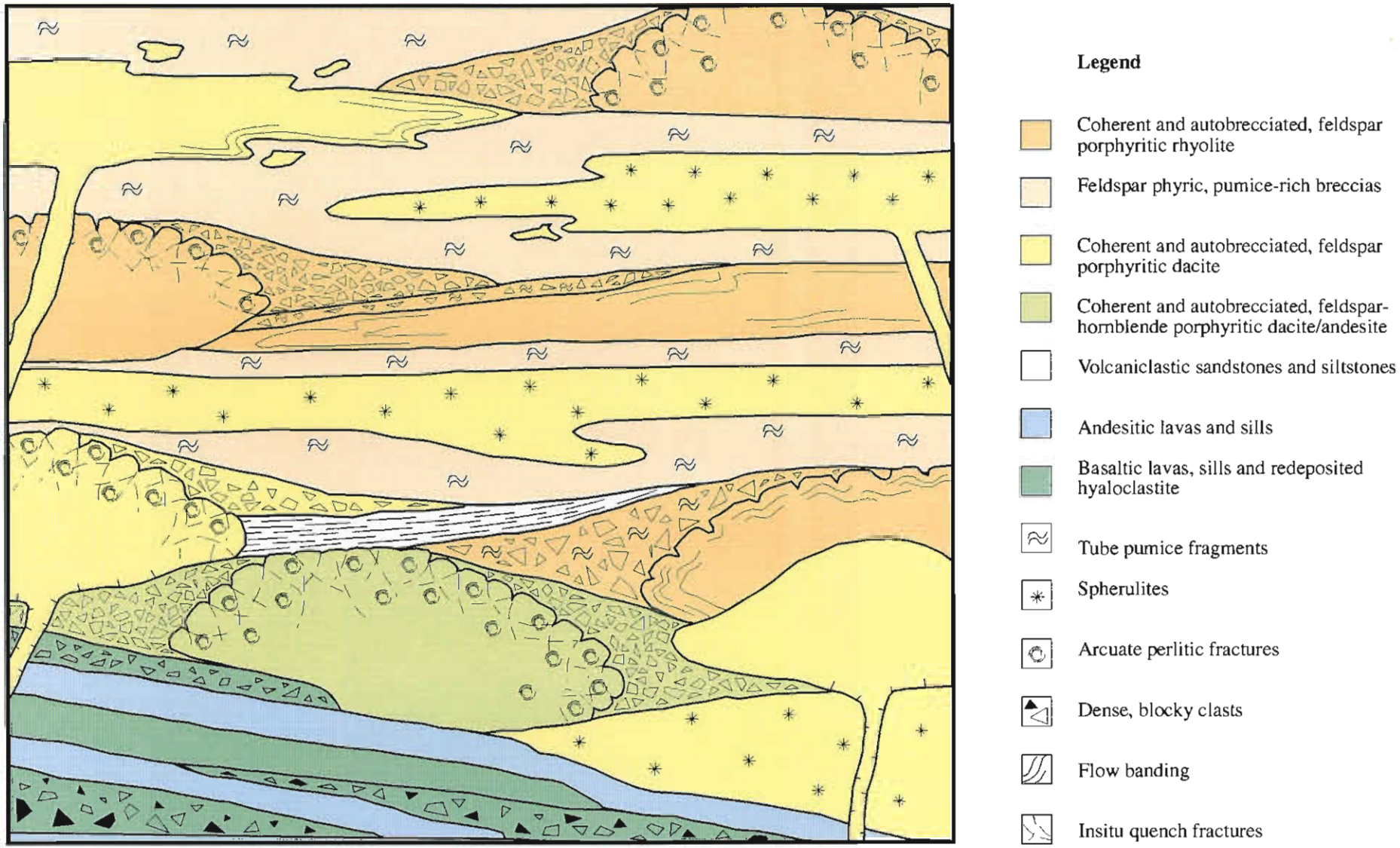

Figure 3: Schematic facies architecture of the submarine Mount Black Volcanic succession. Showing the relationships between the main lithofacies and variations in the internal texture of many of these units.

fractures, spherulites or vesicles (Plates 2a, b, d, e, f) and a range of fine banded clasts that vary from pumiceous to flow-banded. The variation in vesiculation and the association with vesicular coherent facies suggests that many of the pumiceous clasts were not derived from a large explosive eruption but are the product of autoclastic fragmentation of more vesicular or pumiceous margins of a flow or sill (Fink and Manley, 1987, Gifkins et al., 1996b). However, not all the pumice lithic breccias can be attributed to effusive volcanism. The second variety of volcaniclastic lithofacies are rhyolitic pumice-only breccias interpreted to be the product of large volume explosive eruption/s.

Sedimentary facies such as black mudstone are very limited indicating that ongoing volcanic activity probably swamped any background sedimentation.

From the stratigraphic base of the succession the Sterling Valley Volcanics are a thick succession of mass-flow deposits, extrusive lavas and intrusive shallow sills which record the eruptive history and erosional events of one or more mafic volcanic centres. The volcanic centre was predominantly basaltic but also produced more fractionated magmas that were extruded into the submarine environment. Quenching of the hot lava during extrusion brecciated the andesitic to basaltic magma and this debris was redeposited down slope by mass-flow events. The quenched lava clasts indicate that part of the source volcano was subaqueous or that lava flowed into the sea from a summit that emerged above sea level. The base of the volcano has been removed by displacement along the Henty Fault. The regional significance of the Sterling Valley Volcanics is that they are the structural relic of the medial facies association of a large marine mafic volcano that was active early in the eruptive history of the CVC.

The emplacement of the basal succession of the Mount Black Volcanics, a thick pile of intermediate lavas and sills followed the mafic to intermediate activity of the Sterling Valley Volcanics. These feldspar±hornblende phyric dacites, pre-dated the more felsic lavas and pumiceous debris, may represent a period of intermediate lava dome or cryptodome formation. The margins of the lavas are commonly autobrecciated, but little redeposition of this autoclastic material has occurred.

Following this was a period of complex extrusion and shallow intrusion of coherent felsic lavas and sills coeval with the deposition of felsic pumiceous mass-flow units. The felsic lavas and intrusions were commonly autobrecciated during emplacement and quench fragmented as they came into contact with seawater or wet unconsolidated sediment. Clastic debris derived from the coherent lavas remained in-situ, was deposited on the flanks of the moving flow or redeposited by mass-flow forming poorly sorted, normally graded breccias. Evidence for the environment of emplacement of the Mount Black Volcanics and Sterling Valley Volcanics is the abundance of quench fragmented debris and the presence of facies and sedimentary structures typical of a subaqueous setting. Finely laminated and cross-bedded tuffaceous siltstones have been deposited by turbidites in below wave base conditions. Rare mudstones also indicate that background conditions to the volcanic activity were relatively quiet marine. During this phase densely spherulitic, massive to faintly flow-banded, feldspar±hornblende phyric dacite sills swarmed throughout the felsic and intermediate Mount Black succession and into the upper part of the Sterling Valley Volcanics.

The final volcanic event recorded in the Mount Black Volcanics and Sterling Valley Volcanics is the intrusion of a series of mafic dykes that are correlated with the Henty Dyke Swarm.

Primary geochemistry

Major and trace element analyses for 164 samples from the Mount Black and Sterling Valley Volcanics and 4 samples of the Rosebery Hangingwall are available in AMIRA project P439 database. The chemical composition of these samples varies widely indicating that most elements have been mobile during alteration and the regional Greenschist facies metamorphism (McNeill and Corbett, 1989). However immobile elements Ti, Zr and Nb and relatively immobile Y can be used to discriminate the primary volcanic compositions. Previous studies (Large et al., 1989) have been used as a guide to divide the Mount Black and Sterling Valley Volcanics into compositional suites based on Ti/Zr ratios. Large

et al.. (1989) defined the following categories fro the CVC coherent volcanics;

	Ti/Zr
Rhyolite	4 to 12
Dacite	12 to 20
Andesite	20 to 60
Basaltic	60 to 120+

The Winchester and Floyd (1977) style discrimination diagram plot of Zr/TiO_2 versus Nb/Y (Fig. 4), indicates that the Mount Black–Sterling Valley Volcanic package spans a broad range of compositions from basalt to rhyolite, while the Henty Dyke Suite is composed only of basalts. The primary chemical variations in the Mount Black Volcanics and Sterling Valley Volcanics are consistent with magmatic fractionation of a single parent magma. The TiO_2 versus Zr plot (Fig. 5) shows four linear trends or suites can be defined. The rhyolite lavas, sills and pumice-breccias all belong to a single linear trend. Two suites of dacite are evident. The Sterling Valley basalt lavas and sills and the Henty Dyke Suite basaltic dykes plot together in the andesite-basalt field of Winchester and Floyd discrimination diagram but are separated by the TiO_2 versus Zr diagram.

Based on the immobile geochemistry of least altered samples (Appendix 2), petrography and facies characteristics the Mount Black–Sterling Valley volcanic package have been divided into five broad suites.

Suite 1 encompasses rhyolitic sills, lavas and volcaniclastics of the Mount Black Volcanics. Least altered samples (Plate 1a) contain 3–30% plagioclase phenocrysts. The rhyolites and rhyodacites are typified by very low (<0.3%) TiO_2, low Ti/Zr ratios of 5–8, low Al_2O_3 (12–15%), P_2O_5 <0.06% and high silica (typically >70% SiO_2). The silica percentage is not a good guide to composition as it is clearly mobile during the post-depositional changes. The Ishikawa et al.. (1976) Alteration Index for Suite 1 rocks covers a wide range from 16–99. The rhyolites and rhyodacites of the Mount Black package show affinities with the Suite I of Crawford et al. (1992).

Suite 2 feldspar-hornblende phyric dacites and feldspar phyric dacites (Plate 4a) are characterised by moderate TiO_2 values (0.4–0.7%), moderate Ti/Zr ratios of 10–18, low to moderate Al_2O_3 (14–16%), moderate P_2O_5 (0.07–0.13%) and high silica 62–70% SiO_2. Alteration Indices vary from 24–63. These rocks share affinities with Suite I and Suite II rocks of Crawford et al.. (1992).

Suite 3 feldspar porphyritic only dacites typical have moderate TiO_2 values of (0.5–0.7%), high Ti/Zr ratios (14–19), Al_2O_3 values of 14–16%, P_2O_5 values of 0.08–0.16% and lower SiO_2 values of (63–68%). Alteration Indices vary from 22–87. This group of feldspar phyric dacites are equivalent to Suite I of Crawford et al.. (1992).

The geochemistry of Suite 4 andesites (Plate 6d, g) overlaps with Suite 5 basaltic lavas and sills from the Sterling Valley Volcanics. They have a wide range of TiO_2 values (0.59–0.96%), variable Ti/Zr ratios from 20–53, Al_2O_3 16–18%, P_2O_5 0.06–0.18% and silica values of 44–69%. Low Nb <7 ppm is also characteristic of these more mafic suites. Alteration Indices vary from 29–45.

Suite 5 basalts includes both the Henty Dyke Suite samples and samples of basaltic lavas and sills from the Sterling Valley Volcanics. This basaltic suite is characterised by generally high TiO_2 values greater than 0.6%, Ti/Zr 64–135, low Nb < 3 ppm and low SiO_2 45–50%. Alteration Indices for the basaltic lavas and sills range from 23–42 while the Henty dyke samples range from 40–82. These are Suite IV rocks of Crawford et al.. (1992) and are considered to be similar to subduction zone basalts erupted during the early stages of arc splitting and back-arc basin development.

Alteration styles, petrology and geochemistry

A number of different alteration styles have been distinguished in the Mount Black Volcanics according to mineralogy, texture, timing and geochemistry (Table 3). The current mineral assemblages reflect the regional processes of diagenetic alteration, compaction, metamorphism and local small-scale hydrothermal alteration systems. Alteration assemblages that are regional in distribution and pre-date or are synchronous with the styolitic S1 foliation are interpreted to be diagenetic. Alteration styles that are only local in distribution are interpreted to be

Plate 1: Feldspar phyric rhyolites.

a) Sample 039799 from DDH 120R. This is a sample of least altered, massive, 15% feldspar phyric rhyolite. Weak pervasive feldspar alteration of the groundmass and weak selective sericite alteration of the feldspar phenocrysts is evident in handspecimen.

b) Sample R17 from Mount Black summit, is a finely flow-banded, 15% feldspar porphyritic rhyolite. Individual flow-bands are feldspar-quartz altered or sericite-chlorite altered. Some of the sericite-chlorite altered bands were originally highly vesicular or pumiceous and have been compacted.

c) Sample PR9 from the Pieman Rd, is a massive, densely microspherulitic, 5% feldspar porphyritic rhyolite. A fine sandy texture in handspecimen suggests that the groundmass might be either densely microspherulitic or micropoikolitic. Pervasive, moderate pink, feldspar-quartz alteration is evident in the photograph.

d) Sample 039789 from DDH 120R, is a massive, perlitic, 2% feldspar porphyritic, rhyolitic insitu hyaloclastite. Intense, pink, feldspar alteration destroys the primary volcanic textures, however in areas of chlorite alteration the perlitic texture can still be recognised.

e) Sample 039749 from DDH 128R is a massive, 8% feldspar porphyritic, perlitic, rhyolite. Patchy pink feldspar-quartz alteration and green-grey sericite-chlorite alteration are partly controlled by perlitic fractures.

f) Sample 039715 from DDH 128R. This 5% feldspar phyric, rhyolitic, autoclastic breccia contains angular blocky clasts of feldspar porphyritic and aphyric rhyolite and wispy pumice clasts in a finer grained matrix. The matrix is altered to patchy feldspar-sericite. Feldspar alteration haloes exist around the blocky rhyolite clasts. The pumice and dense glassy rhyolite clasts are selectively chlorite or feldspar-chlorite altered.

g) Sample 039704 from DDH 128R is a 5% feldspar phyric, blocky, rhyolitic, peperite. Intense carbonate alteration of the sediment component of the peperite advanced outwards into the dark coherent feldspar phyric rhyolite. The feldspar crystals are replaced by carbonate dusted with pale green sericite.

h) Sample 039725 from DDH 128R is a massive, 20% feldspar phyric rhyolite. Pervasive moderate sericite-chlorite alteration in this sample has destroyed many of the primary volcanic textures, however the porphyritic nature is still evident. The feldspar phenocrysts altered to a pink secondary feldspar.

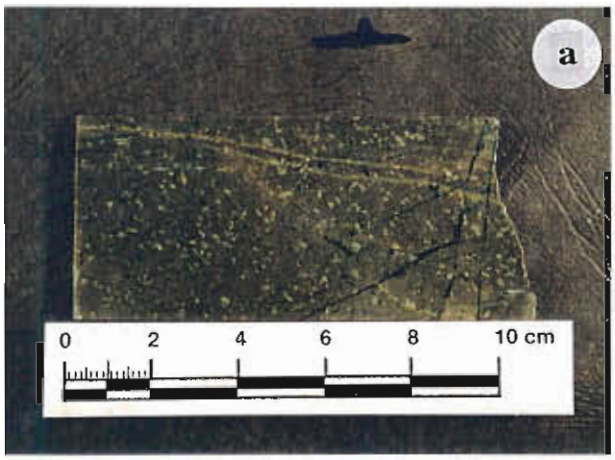
a
0 2 4 6 8 10 cm


b
0 2 4 6 8 10 cm


c
0 2 4 6 8 10 cm


d
0 2 4 6 8 10 cm

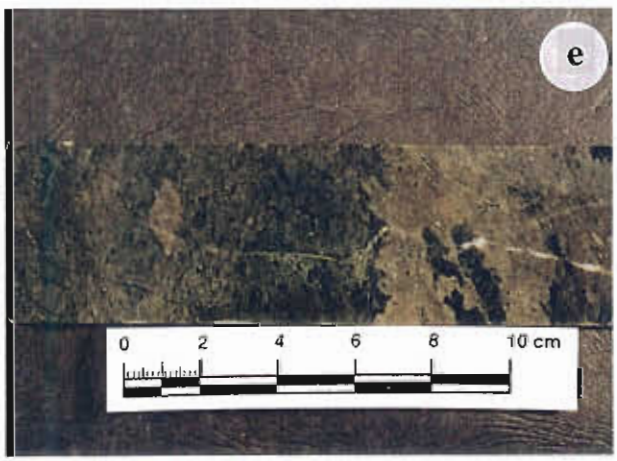
e
0 2 4 6 8 10 cm


f
0 2 4 6 8 10 cm


g
0 2 4 6 8 10 cm


h
0 2 4 6 8 10 cm

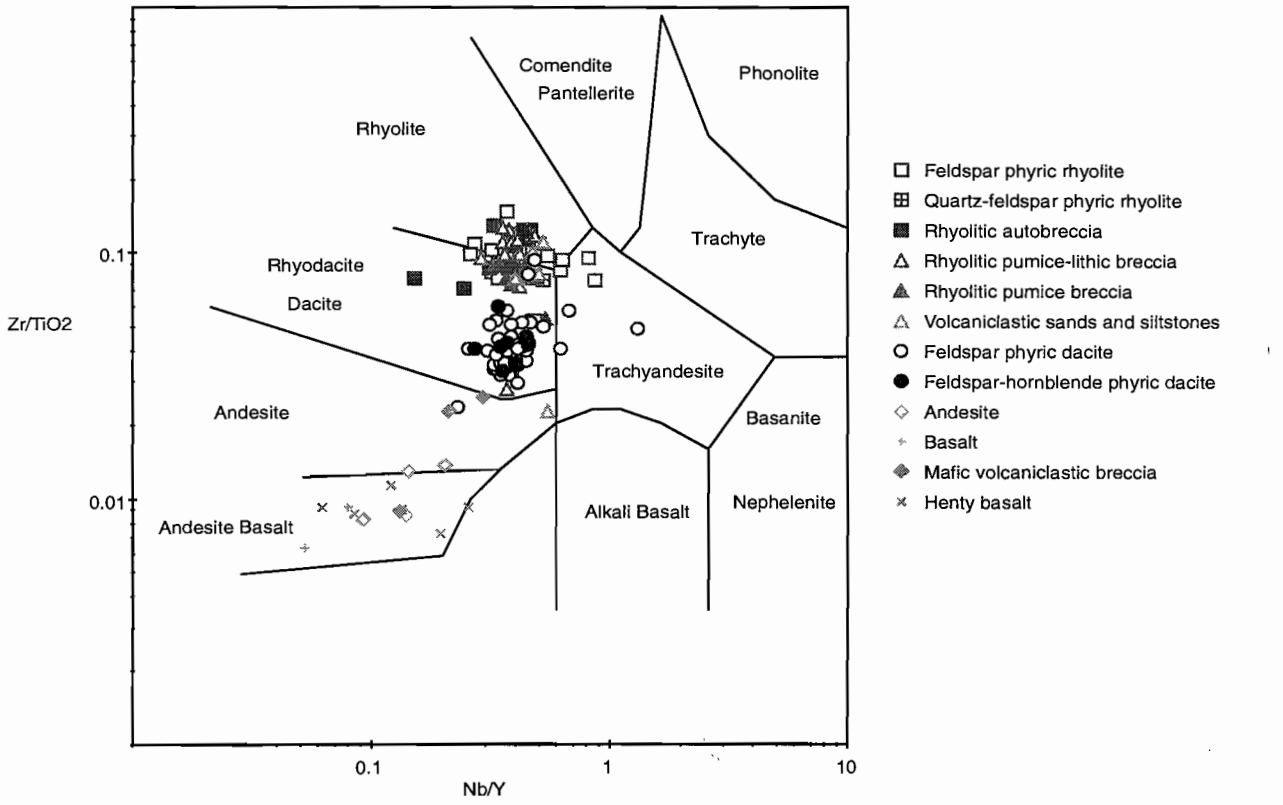

Figure 4: Discrimination diagram of Nb/Y versus Zr/TiO_2 for rocks from the Mount Black Volcanics and the Sterling Valley Volcanics (after Winchester and Floyd, 1977). This depicts the variation in immobile ratios from rhyolitic to basaltic, reflecting primary geochemical variations of the main lithofacies.

related to discrete hydrothermal cells or cooling of coherent sills.

Feldspar-quartz, sericite, sericite-chlorite, carbonate and chlorite-epidote alteration styles are related to early diagenetic alteration processes. Silicification although commonly widespread and related to diagenetic reactions also forms as distinctive alteration haloes around some of the more significant fault systems. A more pervasive style of sericite alteration is probably largely the result of the regional Greenschist facies metamorphism, while intense chlorite and carbonate alteration forms in discrete areas and is the product of localised hydrothermal activity.

The major and trace element data has been assessed with the aim of determining chemical changes associated with the main alteration styles and the difference in the intensity and styles of alteration in volcaniclastic versus coherent units. The Mount Black and Sterling Valley Volcanics display a wide range of Na_2O, K_2O, Rb, Sr, Ba and Ishikawa Alteration Index (Ishikawa et al., 1976) values which partly reflects the variation in primary geochemistry, and partly the different alteration types.

The Ishikawa et al. (1976) Alteration Index (AI) = $(100(K_2O+MgO)/ (K_2O+MgO+Na_2O+CaO)$ for the majority of the samples falls in a narrow window of 25–70. Unaltered arc-related rocks are assigned a window of 20–50 (Stolz et al., 1996) which suggests that the bulk of the Mount Black Volcanics are only weakly altered. This alteration index does not account for carbonate alteration and hence strongly carbonate altered rocks will plot in the unaltered window. To overcome this problem the Chlorite/carbonate/pyrite Index of Large (1996) was introduced. Chlorite/pyrite/carbonate Index (CCPI) = $(100(MgO+FeO) /(MgO+FeO+Na_2O+K_2O)$. Figure 6, shows a plot of Ishikawa Alteration Index against Chlorite/carbonate/pyrite Index. Using samples that represent least altered equivalents of the main lithological types in the Mount Black and Sterling Valley Volcanics (data in Appendix 2) least altered fields were determined for the AI versus CCPI box plot (Fig. 6). By comparing the position of data points on the box plot with the least altered box the degree of chemical alteration can be estimated. Data points

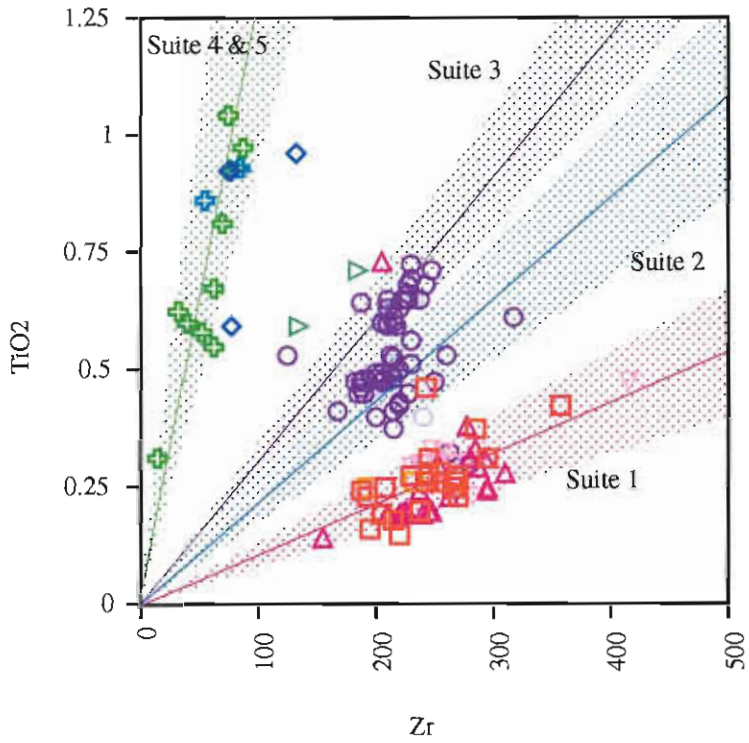

Feldspar phyric rhyolite

Quartz-feldspar phyric rhyolite

Rhyolitic pumice-lithic breccia

Rhyolitic pumice breccia

Feldspar phyric dacite

Feldspar-hornblende phyric dacite

Andesite

Basalt

Mafic volcaniclastic breccia

Henty Basalt

Figure 5: Plot of TiO_2 versus Zr. The shaded fields depict the five mineralogical and geochemical suites. Suite 1 is composed of rhyolite lavas, sills, pumice and lithic breccias. Suite 2 and suite 3 are dacites while suite 4 and 5 are composed of andesitic and basaltic rocks of the Sterling Valley Volcanics and the Henty dyke swarm.

Table 3; Characteristics of the main post-depositional processes in the Mount Black and Sterling Valley Volcanics. Geochemical changes during devitrification are from Lofgren (1970) and during hydration from Friedman and Long (1984).

Alteration style	*Mineralogy*	*Texture*	*Timing*	*Geochemistry*	*AI*
DEVITRIFICATION	qtz, Na- & K-fsp	spherulites, lithophysae	pre-dates ser	minor variations in SiO2, OH-, Na+, K+	unchanged
HYDRATION	ser	highlights fractures and glass surfaces	pre S1	gain OH- loss Na+, Ca2+, Mg	unchanged
DIAGENESIS					
sericite	muscovite	dusts glass surfaces, partially replaces plag rims spherulites	pre S1	gain K+, Mg+, Rb loss Na+, Al3+	relatively unchanged
feldspar-quartz	qtz, Na- or K-fsp	overgowths on plag, replaces plag, fills fractures and vesicles, replaces glass	pre S1, post ser	respective Na+/K+exchange, gain SiO2, loss Ca2+, Al3+	30-60, Na-mod low 30-45, K- mod high 35-60
sericite-chlorite	ser, chl, ±py ±CO3 ±qtz	patchy, alteration of compacted pumice (fiamme), pseudomorphs hbl and px	post fsp, pre to syn S1	gain SiO2, K+ loss Ca2+, Na+, Rb	45-50 mod high
chlorite-epidote	chl, ep ±fsp	disseminated patches, replaces hornblende, partially replaces plag	post fsp, pre S2	gain Al3+, Fe3+, Mg+, K+, Rb, Ba loss Ca2+, Na+, Sr, SiO2	mod ~45
chlorite-magnetite	chl ±mag	patchy or pervasive, interstitial in glomerocrysts, rims plag, styolites	syn compaction (S1)		
silicification	qtz	pervasive	? possibly syn fsp	gain SiO2	high >50
carbonate	calcite	replaces glass shards, pumice and fills vesicles	post ser, pre S1	gain Ca2+, C4+	mod low 35-45
HYDROTHERMAL					
sericite	ser, qtz	pervasive, disseminated, replaces fsp	pre S2, S1?	gain K+, Rb, SiO2 loss Na+	high >80
silicification	qtz, py	haloes around fractures, veins and shear zones	post S1, syn to post S2	gain SiO2	high >90
chlorite	chl ±py	intense pervasive zones, fractures, hydraulic breccia fill	post S1, also post S2	loss K+	high >70
carbonate	calcite	pervasive	pre S1	gain Ca2+	low <25
METAMORPHISM					
sericite	muscovite	weak disseminated, defines S2	syn S2		
chlorite	chl	disseminated in mafics, interstitial to glomerocrysts in felsics	post diagenetic chl, late to post S2		

Plate 2: Feldspar phyric, rhyolitic, pumice bearing lithic breccias.

a) This photograph of a finely flow-banded rhyolitic autobreccia outcrop comes from the eastern flank of Mount Read. The breccia is massive, poorly sorted and clast supported. The blocky angular, flow-banded clasts can be seen at high angles to one another on the weathered surface of the outcrop.

b) Sample PR26 is a massive, glassy rhyolitic breccia from the Pieman Rd. It is composed of abundant originally glassy rhyolite clasts that have classical and ladder perlite fractures. Many of the clasts are vesicular to pumiceous. All the clasts in this sample are interpreted to be the products of quench fragmentation of a rhyolitic dome that was extruded onto the seafloor. The massive, poorly sorted and clast supported nature of the outcrop is consistent with the clasts having been redeposited only a short distance down slope. Sericite ± chlorite alteration is pervasive, while patchy and selective white to pale-pink feldspar-quartz alteration highlights many of the larger clasts. This two-phase alteration assemblage gives the sample the appearance of being a matrix supported polymictic breccia.

c) From left to right samples 039783-039782-039790-039792 from DDH 120R are variably altered rhyolitic, pumice lithic breccia. These samples represent part of a thick, normally graded mass flow deposit. Pervasive sericite and lesser white feldspar alteration dominate alteration in 039783. The other samples show increasing pink feldspar alteration and decreasing sericite from left to right. Rare dark chlorite-rich lenses or fiamme are also evident.

d) This sample, from DDH 78R at 174.3m is a 7% feldspar phyric, rhyolitic, pumice-rich lithic breccia. Strong domainal pink feldspar and chlorite-sericite alteration are prominent. The darker chlorite-sericite altered clasts or domains are clearly feldspar porphyritic, while the feldspar alteration has destroyed the porphyritic texture.

e) Sample R112 (x2.5 PPL). This is a photomicrograph of rhyolitic pumice-rich lithic breccia from the southern side of Mount Black. In the photomicrograph number of angular perlitic clasts, feldspar crystal fragments and chlorite-sericite altered vesicular fragments can be recognised. The finer grained clasts, which compose the matrix, are dominantly pervasively sericite ± feldspar altered while the large dense originally glassy fragments are feldspar-quartz altered.

f) Sample 039711 from DDH 128R is a 10% feldspar phyric, finely flow-banded autoclastic rhyolite breccia. The dense blocky rhyolite clasts are massive porphyritic and flow-banded. Domainal feldspar-quartz and sericite-chlorite alteration highlights the crystalline and glassy bands in the clasts. Massive clasts are generally feldspar-quartz altered and the finer grained matrix is strongly sericite-chlorite altered. The feldspar phyric nature of the matrix is easily recognised in the sericite domains.

g) Sample R30 is from the Mount Black summit area (x1.5, PPL). This photomicrograph captures the insitu flow-brecciation of a finely flow-banded, weakly feldspar phyric rhyolite. Individual bands are preserved by feldspar alteration versus a fine mosaic of sericite, feldspar and quartz.

h) Sample 039783 is from DDH 120R (x2.5, PPL). The photomicrograph of variably vesicular clasts is from a sample of rhyolitic pumice-rich lithic breccia. At the base of the photograph is a dense perlitic rhyolite clast. Above this are moderately vesicular and highly vesicular rhyolite clasts. A fine dusting of sericite or opaques defines the vesicle walls. The dense clasts and glassy vesicle walls are feldspar-quartz altered, although some of the more pumiceous clasts show patchy phyllosilicate alteration.


a


b
PR26
0 2 4 6 8 10 cm


c
0 2 4 6 8 10 cm


d
0 2 4 6 8 10 cm

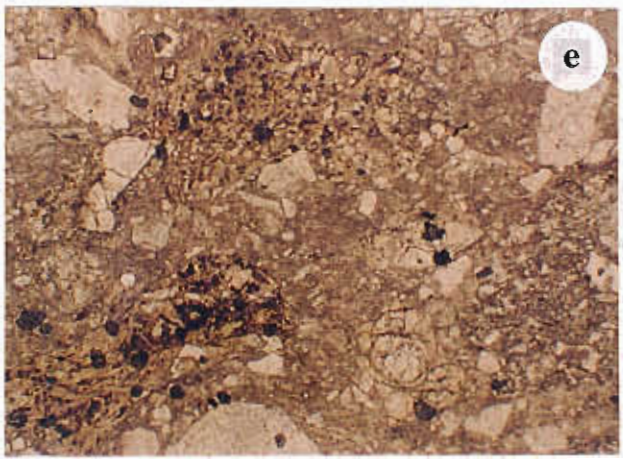
e


f
0 2 4 6 8 10 cm


g

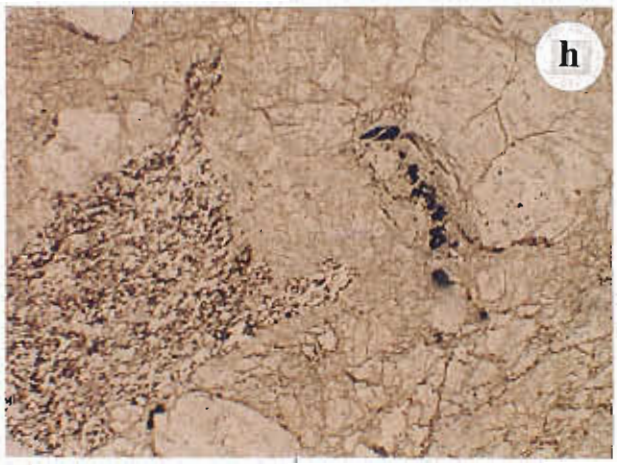
h

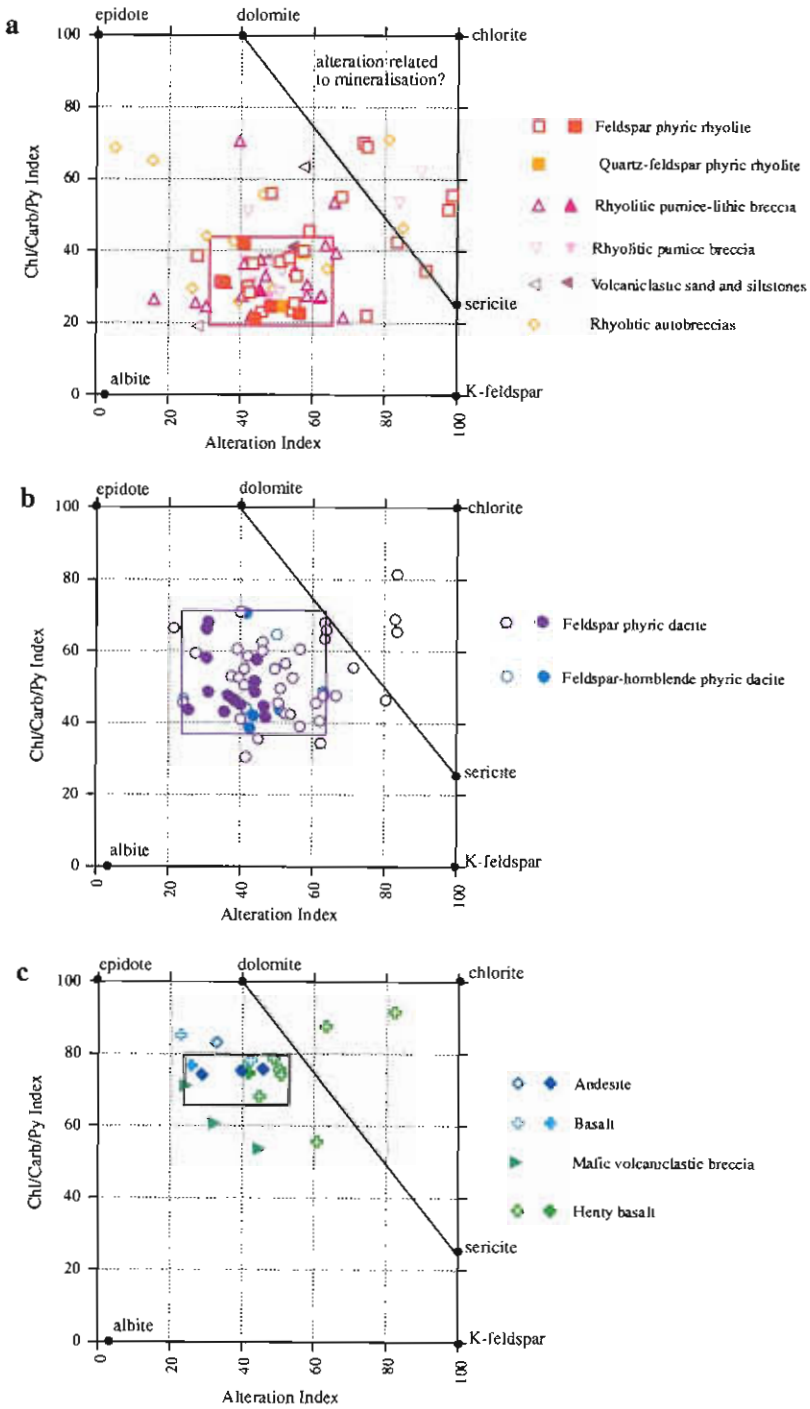

Figure 6: Alteration box plots: Alteration Index (Ishikawa et al, 1976) versus Chlorite/carbonate/pyrite Index (Large et al, 1996) for the Mount Black and Sterling Valley Volcanics. Closed symbols represent samples that are least or only weakly altered, while open symbols represent noticeably altered samples. The degree of alteration has been determined using petrography and handspecimen analysis. The majority of samples plot in or near the least altered boxes. However, altered samples that plot in the dolomite-chlorite-sericite triangle are interpreted as hydrothermally altered samples. a) Represents least altered to strongly altered suite 1 (rhyolites) rocks. The least altered field is drawn in red. b) Depicts the variation in alteration indices for the dacites (suite 2 and 3). The least altered field is drawn in purple. c) Depicts the andesitic and basaltic rocks of suites 4 and 5. Least altered field is drawn in black.

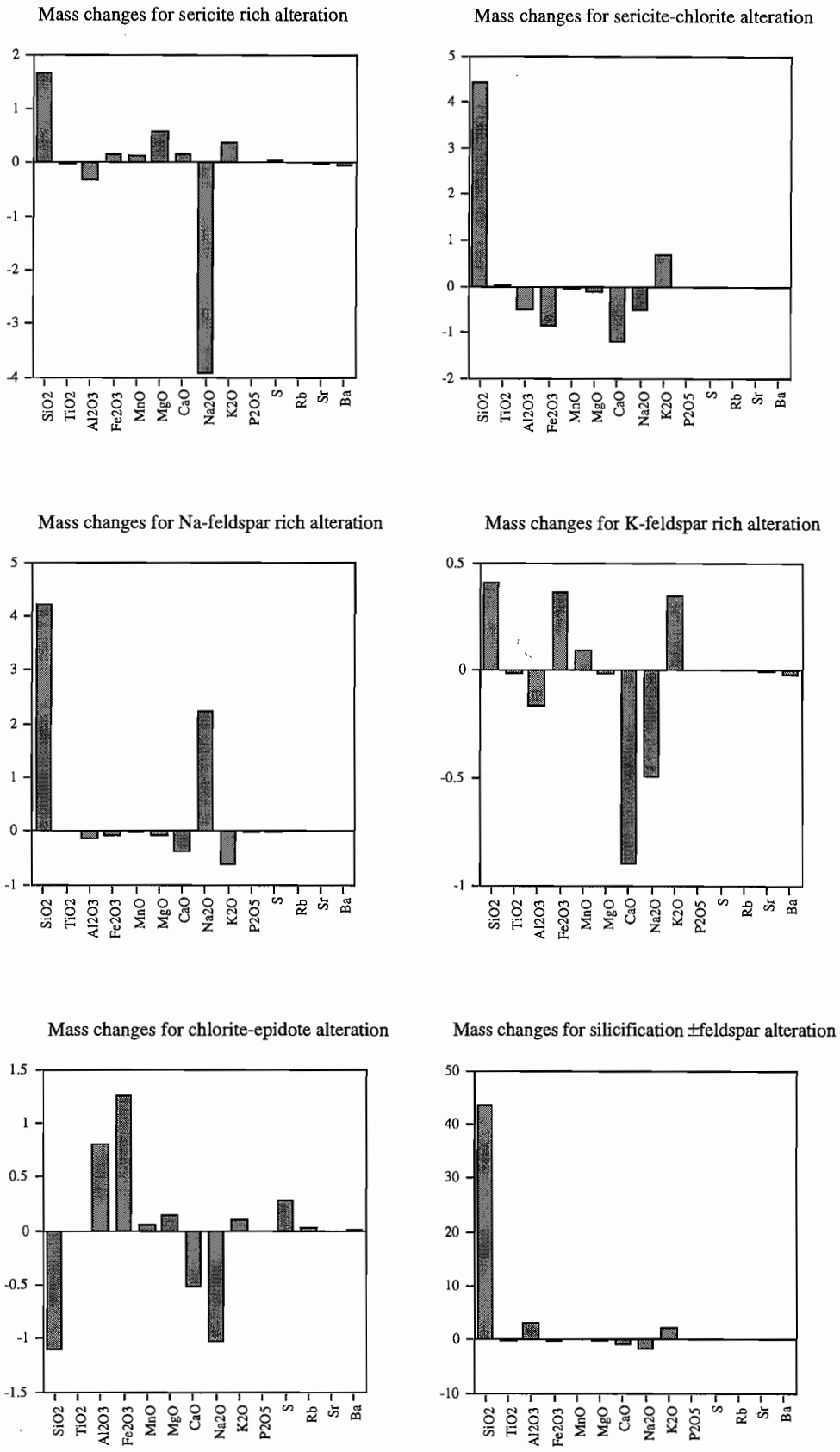

Figure 7: Major element mass changes calculated using Barrett and Maclean (1994) are plotted in g/100g for the main alteration assemblages. Actual calculated values are presented in appendix 3. This illustrates that mass changes during hydrothermal silicification are an order of magnitude higher than mass changes associated with the diagenetic alteration styles.

that plot well away from the position of the least altered box have undergone significant chemical exchange, while points adjacent to the unaltered box generally represent samples that have not. However, the polyphase nature of the alteration in a large portion of the Mount Black Volcanics, has the effect of moving the position of the altered data points back and forth across the box plot. For example, a perlitic dacite with Na-feldspar alteration will plot with low AI and CCPI value towards albite but subsequent sericite-chlorite alteration overprinting the feldspar alteration will increase the AI and CCPI values. The sample finally plots towards the middle of the box plot near the least altered fields.

Barrett and Maclean (1994) style mass change calculations have been applied to a carefully selected groups of samples to determine relative losses and gains in oxides and elements during the dominant diagenetic alteration styles. Various altered samples have been compared to a least altered or weakly altered sample from the same unit with identical Ti/Zr. The results of these calculations are presented in Appendix 3 and illustrated in Figure 7. The general geochemical trends for different alteration styles are summarised in Table 3.

Regional diagenetic alteration

The imprint of early diagenesis is preserved because of the large porosity reduction and lithification that occurs during the initial episode of burial diagenesis. This severely limits the subsequent mineral precipitation, unless secondary porosity is developed allowing further precipitation. Commonly, sediments undergo multiple stages of diagenesis in the subsurface reflecting successive episodes of cementation, dissolution and recrystallisation (Morrow and McIlreath, 1990). These episodes are part of the diagenetic cycle involving departures from the fluid-rock equilibrium. These departures are followed by interaction between the pore fluid and the rock. With increasing depth of burial the pressure temperature conditions continue to change and the thermodynamics of the system continue to evolve.

Within the Mount Black Volcanics early alteration assemblages are overprinted by later diagenetic alteration phases reflecting the evolution of the diagenetic system. However, in this study no distinct regional zonation of the diagenetic alteration has been observed. This suggests that the geothermal gradient was high or that accumulation of volcanics was too rapid, not allowing sufficient time for diagenetic reactions or the development of pore water gradients to occur at depth (Marsaglia and Tazaki, 1992). Thermal pulses brought about by the intrusion of volcanic sills could also have raised the geothermal gradient and accelerated diagenesis.

One of the earliest alteration phases recorded in the Mount Black Volcanics is fine-grained **muscovite or sericite.** Sericite is one of the most common minerals in these rocks and is probably the result largely of the Greenschist facies metamorphism of clay minerals rather than hydrothermal alteration. Although sericite is widespread it is a pervasive weak disseminated phase that it is rarely strong enough to mask primary volcanic textures. More intense, pervasive, and texturally destructive sericite alteration is associated with significant variations in the chemistry, most notably gains in K_2O. This more intense alteration is interpreted to be the product of hydrothermal alteration.

Within the pumice breccias and pumice-lithic breccias all the originally glassy surfaces of the glass shards and vesicle walls are coated with thin films of sericite dust (Plate 3d). This thin film of sericite dust pre-dates the infilling vesicles and compaction. In some samples much of the originally glassy shards or vesicle walls have been replaced by sericite. This is identical to the first stage of diagenetic alteration of felsic pumice and glass shards in both marine and subaerial environments where thin films of smectic clay and opal develop on all glass surfaces (Iijima, 1974). The alteration phase represented by the early sericite may be the metamorphosed equivalent of early clay alteration that pre-dates sealing of the porosity and compaction.

Sericite is also scattered as disseminated grains throughout the recrystallised quartz-felspathic groundmass of many of the coherent units, giving a green-grey colouration to the Mount Black dacites (Plate 4d). Commonly fine grained muscovite dusts or partially to completely replaces the primary plagioclase crystals. It also rims feldspar phenocrysts, spherulites and micropoikolitic quartz.

The next diagenetic alteration phase is represented

Plate 3: Feldspar phyric, rhyolitic, pumice-rich breccias.

a) Sample PR6 from the Pieman Rd is a feldspar phyric tube pumice breccia. Strong pink feldspar alteration and patchy chlorite-sericite alteration dominate the sample. Pumice in the feldspar-rich domains are uncompacted, while pumice in the chlorite-sericite altered domains have undergone compaction and are crenulated by the later regional cleavage. The orientation of the chlorite-sericite rich lenses or fiamme can be used to determine the bedding parallel compaction foliation (S1).

b) Sample 039717 from DDH 128R. This rhyolitic pumice breccia has strong domainal feldspar and sericite-chlorite alteration more typical of the pumice breccias. The dark phyllosilicate-rich lenses or fiamme are clearly feldspar phyric and define a foliation at low angle to the core.

c) Sample EHP319 538.6m is from a very thick pumice-breccia to the east of South Hercules. This rhyolitic pumice breccia has large uncompacted pink-white fibrous tube pumices. The pink feldspar alteration is associated with disseminated magnetite and dark chlorite-rich fiamme and is similar to many of the pumice breccias observed away from the ore environment in the Rosebery and Hercules footwall.

d) Sample EHP319 538.6m (x1.5, PPL). This photomicrograph shows well-preserved feldspar altered tube pumices at high angles to one another. The tubes are defined by fine sericite, while the glassy walls are composed of fine granophyric feldspar and quartz. The primary plagioclase crystals are pseudomorphed by chlorite.

e) Sample 039720 from DDH 128R is an example of the fine-grained stratified top of a thick normally graded rhyolitic pumice breccia. The laminations are discontinuous, have uneven thicknesses and are typically variably altered.

f) Sample 039796 from DDH 120R. This is a handspecimen of fine-grained laminated shard-rich siltstone. Shards are well preserved in the feldspar-quartz altered domains, however only the feldspar phyric nature of the deposit can be recognised in the more sericite-chlorite rich domains.

g) Sample 039796 from DDH 120R (x5, PPL). This photomicrograph is from the feldspar-quartz altered domain in the top right-hand corner of the previous photograph. It shows well preserved feldspar altered, angular shards in fine-grained mosaic of feldspar-quartz-sericite.

h) Sample PR11 from the Pieman Rd (x5, PPL). In this photomicrograph patchy chlorite and carbonate rhombs are replacing the originally feldspar altered shards in the groundmass of a pumice breccia. The feldspar-quartz altered shards are hosted within a fine grained matrix of feldspar, quartz and sericite.


a
0
2
4
6
8
10

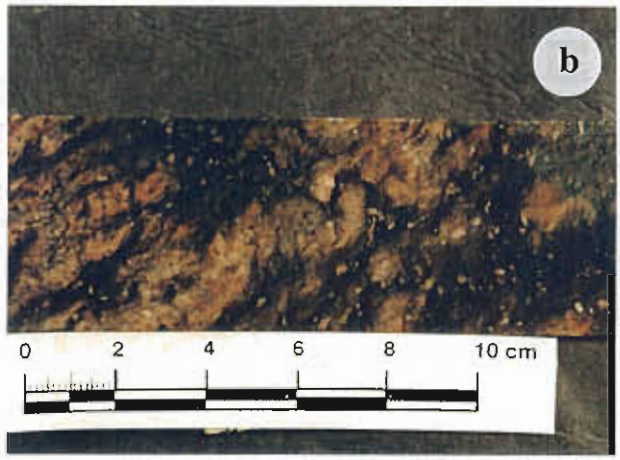
b
0
2
4
6
8
10 cm


c
0
2
4
6
8
10 cm


d


e
0
2
4
6
8
10 cm

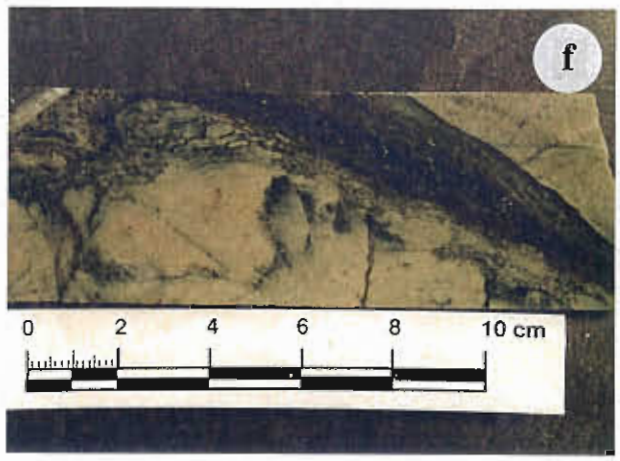
f
0
2
4
6
8
10 cm

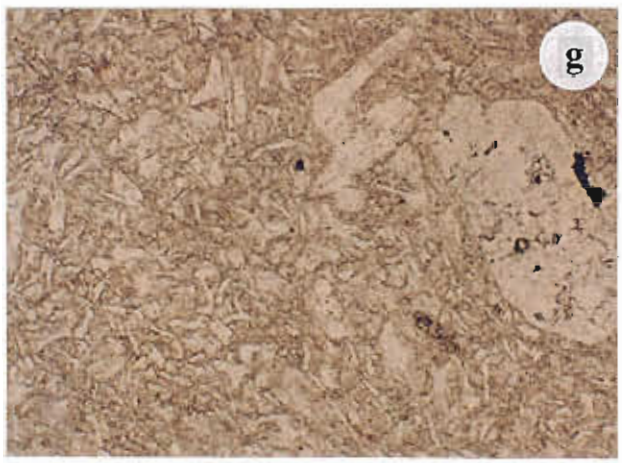
g


h

by **feldspar±quartz** alteration. In handspecimen feldspar alteration is characterised by a pink colouration which varies in intensity and texture. The secondary feldspar is mainly albite dusted with hematite, however relict K-feldspar is preserved in less altered samples. This suggests that there were at least two stages of feldspar alteration, K-feldspar pre-dating Na-feldspar (albite). Marsaglia and Tazaki (1992) found that hydrothermal experiments on rhyolitic glass indicated that at high temperatures (200°C), rhyolitic glass does not recrystallise but acts as Na-K ion exchanger. Quenched glass fixes potassium whereas slowly cooled glass fixes sodium. Therefore variations in the cooling history of individual fragments might explain why some originally glassy pumiceous or dense rhyolitic fragments alter more readily to different minerals.

Feldspar alteration may be selective, or domainal in character, forming pink feldspar-rich zones. In rhyolitic pumice-rich breccias feldspar alteration is commonly domainal, enclosing dark phyllosilicate-rich lenses (Plates 2a, b and c). These lenses or fiamme are bedding parallel and comprise of compacted pumice clasts that have been flattened during diagenesis and lithification (Branney and Sparks 1990). The quartz-feldspar domains contain relic uncompacted tube pumice. The pumice tubes are defined a thin films of sericite, while secondary feldspar or a mosaic of feldspar-quartz -sericite replaces the originally glassy walls and fills vesicles (Plates 2g, 2h and 3d). The uncompacted nature of these pumices indicates that the deposits were originally non-welded and that the feldspar alteration occurred prior to compaction. The feldspar alteration was either early diagenetic or feldspar replaces an early diagenetic mineral phase. Allen (1997) suggested that fan-shaped fibrous textures locally preserved by K-feldspar or albite in the Rosebery Footwall pumice breccias may be the product of feldspar alteration of a common diagenetic mineral with a radiating fibrous texture, namely zeolites. Similar radiating textures have been observed infilling vesicles within the Mount Black pumice breccias. A number of authors working on diagenetically altered volcaniclastic sediments in the Izu-Bonin arc (Torres et al., 1995 and Tazaki and Fyfe, 1992) have recorded early clay alteration followed by the formation of zeolite cements and zeolite alteration of volcanic glass. The alteration products appeared first on the outside of shards and grew inwards. Thin clay films were followed by the production of smectite and zeolites in fractures, forming cement and progressively replacing the glass shards. With progressing diagenesis dissolution of the zeolite cements occurred and carbonate and K-feldspar cements precipitated (Marsagalia and Tazaki, 1992).

Feldspar alteration also occurs as overgrowths on the margins of plagioclase crystals, fills fractures within the plagioclase crystals and may partially replace primary plagioclase phenocrysts (Plate 1h). Fine-grained feldspar also occurs as laths enclosed in micropoikolitic quartz scattered throughout the groundmass of coherent units. It is commonly associated in both coherent and clastic rocks with chlorite-sericite or sericite alteration producing a distinctive pink and green polyphase alteration patterns.

In massive, coherent facies patchy pink-green alteration forms a contrasting green and pink mottled pattern on a scale of 2–20 cm. In the flow-banded units the pink and green alteration is confined to individual bands where sericite-chlorite defines the originally glassy flow-bands and feldspar-quartz the spherulitic flow-bands (Plate 1d, e and b). False clastic and polymictic textures are often developed in the coherent flow-banded units by this polyphase alteration and primary clastic textures in the volcaniclastic units are enhanced. In many of the autobreccias and hyaloclastite feldspar-quartz alteration forms pink halos or rinds around lithic clasts set in a green sericite-chlorite groundmass (Plate 1f).

Silicification is widespread and pervasive occurring most notably within the high-level dacitic sills. Silicification is a common diagenetic product and ranging in extent (Hesse, 1990). The process of silicification may occur at elevated temperatures and fall on the borderline between diagenesis and metasomatic metamorphism.

Sericite–chlorite±carbonate±quartz±pyrite alteration occurs in coherent flow-banded lavas and sills, autobreccias, hyaloclastite and pumiceous breccias (Plates 1b, 1e, 1f, 2d, 2f, 3b, 4e, 4g and 5c). Pale green, variably silicified and chloritised, it is often non-homogenous alteration producing patches or lenses of dark green chlorite-sericite in a paler feldspar-rich

composition. These dark lenses typically form in pumiceous debris with carbonate-sericite altered feldspar phenocrysts but they can also form in individual flow-bands of a coherent unit or the flow-banded clasts of autoclastic deposits. This is common in the Mount Black rhyolites where weak pervasive sericite-quartz-chlorite alteration overprints an earlier feldspar-chlorite ± epidote phase. In the pumice-rich breccias dark sericite-chlorite altered lenticular patches are set in quartz-feldspar rich domains. Within the chlorite-sericite rich domains the phenocrysts are preserved but other primary volcanic textures are largely destroyed. These lenses or fiamme comprise pumice clasts that have been compacted during burial. The resulting foliated fabric that resembles eutaxitic texture is the S1 fabric indicating that the sericite-chlorite alteration is pre to syn S1.

The felsic rocks of the Mount Black volcanics display only limited chlorite>sericite alteration while the more mafic units of the Sterling Valley Volcanics and Henty Dyke Suite contain substantially more chlorite-CO_3 ± sericite alteration.

Diagenetic **carbonate** alteration is poorly preserved in the Mount Black Volcanics, it occurs infilling primary porosity such as vesicles in the pumice breccias and less commonly as replacement of volcanic glass. Carbonate cement is a common product of diagenetic alteration. Albitisation takes place as sediment is buried (Boles, 1982) and provides a source of calcium for the production of carbonate cements. Many diagenetic mineral reactions are interrelated like this. Diagenetic carbonate is much more abundant and better preserved in the Rosebery–Hercules sequence (Allen, 1997).

A number of phases of **chlorite** dominated alteration are evident. The earliest chlorite alteration is associated with sericite (see diagenetic sericite-chlorite) overprinting this is a darker blue-green chlorite associated with magnetite. The chlorite ± magnetite alteration is very widespread occurring in almost all units in a number of different forms. Most commonly as patchy to pervasive disseminated fine grained aggregates in the groundmass of the coherent rocks throughout the volcanic package. It also occurs commonly as fibrous and fine-grained material interstitial to the crystals in glomeroporphyritic clusters and between microspherulites and micro-poikolitic quartz in the groundmass. It can rim individual feldspar phenocrysts in many of the coherent units (Plate 5b). In the hornblende porphyritic rocks chlorite ± magnetite commonly pseudomorphs the hornblende crystals.

Chlorite±magnetite occurs in the pumice-rich volcaniclastics as styolitic textures parallel to the compaction foliation (Plate 3f). The magnetite associated with this alteration phase occurs as blebs concentrated along the styolites. The presence of a spaced chlorite-magnetite styolitic dissolution foliation supports early leaching and dissolution of glassy clasts. The chlorite alteration post dates dissolution and is synchronous or post compaction (S1).

Chlorite–epidote±feldspar alteration is largely associated with the more basic rocks of the Sterling Valley Volcanics. It completely replaces hornblende and partially alters primary plagioclase (Plate 5f). It also occurs as weak fine-grained irregular patches in the groundmass of many of the coherent dacites, andesites and basalts. Chlorite-epidote alteration was synchronous with sericite-chlorite alteration and pre dates some of the feldspar±quartz alteration as is indicated by the polyphase alteration of perlitic fractures in many of the coherent originally glassy units. The arcuate perlitic fractures (Plate 4h) are commonly defined by dark chlorite±epidote alteration while the perlite cores are feldspar±quartz altered.

Hydrothermal alteration

Hydrothermal phases are recognised based on their local distribution and more significant variations in chemistry and Alteration Indices. The common hydrothermal products recognised in the Mount Black Volcanics are chlorite, carbonate, silicification and pervasive sericite alteration.

Hydrothermal **chlorite** alteration is pervasive, intense and texturally destructive. Chlorite is commonly associated with fine-grained disseminated pyrite and carbonate and forms in discrete zones. The distribution of less intense chlorite alteration is controlled by porosity with chlorite commonly highlighting both early syn-volcanic fractures, ie, perlitic fractures (Plate 4g and 5c), and later hydraulic and tectonic fractures. The timing of the hydrothermal

chlorite alteration may vary with some of these zones related to brittle fracturing, faults or shearing while other chlorite alteration halos are also associated with mafic dykes and sills throughout the region.

Narrow bands of pervasive moderate to intense **silicification** are associated with major faults and shear zones throughout the sequence.

Hydrothermal **carbonate** alteration is fine grained, either disseminated, replacing or rimming feldspar phenocrysts. Carbonate alteration is generally weak, however more intense carbonate alteration masks primary volcanic textures resulting in a fine grained massive homogenous pale rock. In zones of weak carbonate alteration carbonate rhombs have been observed to replace the shard-rich matrix of some of the pumice breccias and pumiceous sandstones (Plate 3h). Carbonate also occurs in late veins associated with chlorite or quartz that appear to have been activated during the Devonian metamorphism.

Controls on the distribution of diagenetic alteration styles

The diagenetic alteration facies have a patchy distribution and vary considerably in intensity throughout the Mount Black and Sterling Valley Volcanics. The distribution and intensity of the alteration styles in part can be related to the texture and geochemical signature of the volcanics. However this is not necessarily the primary volcanic texture and chemistry, as the present alteration assemblages reflect the combined effects of different post-depositional processes on the primary mineralogy and textures. Thus the composition and texture of the volcanic facies has evolved. Despite this complex evolution, the original composition of the volcanic units has exerted a strong control on the less intense alteration assemblage influencing the distribution and textures formed. It appears that at low temperatures the composition of the glass is probably the most important factor in determining the type of alteration, however permeability and competency contrast also influence the alteration. With increasing intensity of alteration the permeability and competency contrasts have less control on the alteration.

The alteration assemblages, which dominate in felsic rocks versus mafic rocks, are partly controlled by the primary volcanic composition. The silicic volcanics are dominated by feldspar-quartz, sericite-chlorite and carbonate alteration assemblages while more mafic rocks are typically dominated by chlorite, epidote and carbonate assemblages.

Within the more felsic rhyolites, rhyodacites and dacites the primary volcanic, devitrification and hydration textures are varied, discontinuous and often complexly related. Subsequent alteration textures observed within the felsic rocks appear complex and patchy due to these primary and secondary variations in texture. The alteration of the more mafic units is typically more uniformly pervasive, reflecting the more massive style of volcanic deposits.

Many of the diagenetic alteration styles in felsic rocks are texturally enhancing. In a pile of glassy volcanic rocks the texture and hence porosity can vary considerably over a short distance due to both the primary volcanic textures and the post-depositional modification of these textures. The patterns of permeability and competence contrasts in the felsic rocks have a marked effect on the alteration patterns. Alteration is strongly controlled by fluid pathways, in the coherent facies it is controlled by the fractures that are generally produced by quenching, flow and hydration and by the distribution of more crystalline versus glassy textures, such as spherulites and flow-banding. In the massive lavas and sills, alteration has progressed as fronts moving outward from the primary fractures, perlitic fractures and chilled margins towards the unaltered domains. Alteration in clastic facies is controlled by the distribution of porous matrix to less porous clasts. Early phases of alteration in clastic facies, although commonly patchy, are more pervasive and less focussed than similar alteration in the coherent facies.

As the diagenetic alteration evolved, early alteration phases have sealed some of the more porous or permeable pathways thus affecting the subsequent porosity. The early feldspar-quartz alteration although not clearly controlled by the permeability has significantly affected the subsequent alteration textures. It forms competent irregular patches or domains in both the volcaniclastic and coherent rocks. In contrast phyllosilicate dominated alteration assemblages (sericite-chlorite, chlorite-

Plate 4: Feldspar phyric, dacite lavas and sills.

a) Sample M67 from the Murchison Highway is an example of the most voluminous lithofacies in the Mount Black Volcanics. This massive feldspar phyric dacite is considered to be one of the least altered rocks in the Mount Black Volcanics. Pervasive very weak feldspar alteration of the groundmass is overprinted by weak fracture controlled chlorite alteration.

b) Sample PR17 from the Pieman Rd is a typical massive weakly feldspar porphyritic sill of the Mount Black Volcanics. This sample has a fine-grained micropoikolitic textured groundmass and is weakly altered by red-brown pervasive feldspar.

c) These samples from DDH 112R at 358.9m and 363.1m respectively are from the base of a dacitic lava flow. The upper sample in the photograph is finely brecciated. The clasts have fine grained chilled margins and curviplanar edges typical of quench fragmentation. The sample has been interpreted as insitu hyaloclastite at the base of a lava flow that was extruded into the water. The second sample is a peperitic mixture, of dacite lava clasts and pumiceous sandstone, at the very base of the flow. Clasts of the underlying pumiceous sediments have been incorporated into the base of the flow as it travelled along the wet unconsolidated sediments on the seafloor.

d) Sample M90 from the Murchison Highway south of Mount Black, is a typical crystal-rich feldspar porphyritic dacite of the Mount Black Volcanics. is moderately pervasively chlorite altered. The feldspar phenocrysts are largely pristine.

e) Sample PR51 from the Pieman Rd is an example of the more variable alteration that occurs in some of the coherent originally glassy dacites. Fine perlitic fractures in the groundmass of this sample have acted as permeable pathways for fluid during sericite-feldspar and sericite-chlorite alteration.

f) These four samples of a massive sandy dacite are from DDH 80R between 351 m and 394 m. This photograph illustrates the variety of alteration assemblages that commonly pervasively alter the massive dacites. From left to right the alteration styles are; weak feldspar-sericite, moderate feldspar-quartz, mottled pink feldspar and chlorite and moderate sericite accompanied by chlorite-magnetite replacement of the feldspar phenocrysts.

g) Sample PR56 from the Pieman Rd is an example of strong domainal two-phase alteration in a coherent perlitic dacite. This dacite has fine perlitic fractures throughout the groundmass and abundant curviplanar fractures, which define blocky clasts. The deposit is interpreted to be an insitu quench breccia. The distribution of the two phases of alteration; red feldspar-quartz and dark green epidote-chlorite; has been controlled by the quench fracture pattern.

h) The photomicrograph of PR1 (x2.5, PPL) is dominated by fine arcuate overlapping perlitic fractures, that are highlighted by fine-grained sericite. The perlite cores are feldspar-quartz altered.


a
0 2 4 6 8 10 cm


b
0 2 4 6 8 10 cm


c
0 2 4 6 8 10 cm

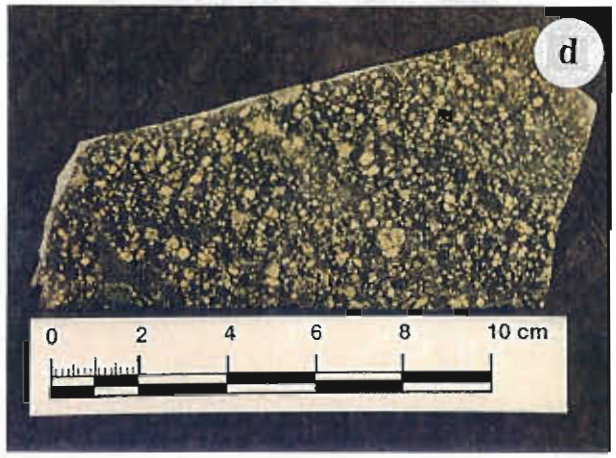
d
0 2 4 6 8 10 cm


e
0 2 4 6 8 10 cm

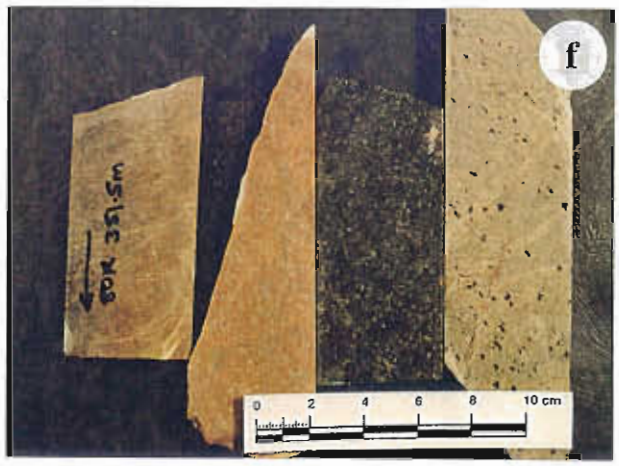
f
BOR 351.5m
0 2 4 6 8 10 cm


g
PRS6
0 2 4 6 8 10 cm


h

epidote etc) appear to be strongly controlled by fluid pathways, except in areas of intense alteration. As a result the later phyllosilicate-rich alteration phases occur in the next most porous or reactive portion. The result is polyphase alteration.

Within the pumice-rich breccias feldspar alteration nucleated on feldspar phenocrysts and spread outwards filling pore space and replacing the glassy bubble walls. The feldspar alteration is often incomplete and may leave diffuse to well defined less altered patches, which are subsequently altered to more phyllosilicate rich patches.

Similarly within flow-banded and spherulitic lavas and sills the quartz-feldspar-rich bands, nodules and devitrification textures (spherulites) have been recrystallised and replaced during the early feldspar-quartz alteration. In contrast the glassy domains have been replaced by phyllosilicate assemblages dominated by sericite and chlorite. The phenocrysts are more prominent in these darker phyllosilicate-rich bands and give the false impression that the darker domains are more phenocryst-rich than the paler quartz-feldspar domains (Plate 1b). The alternating pink and green flow-bands can resemble folded, thinly bedded, volcaniclastic rocks with apparent crystal-rich phyllosilicate layers and crystal-poor siliceous layers.

Polyphase alteration of perlitic glass is another good example of successive alteration styles developing in the most permeable zone. Perlitic fractures in many of the originally glassy lavas, sills and piles of autoclastic material, have been highlighted by sericite-chlorite alteration and the enclosed core has been altered by paler quartz-feldspar±sericite. The alteration has enhanced the fractures creating a contrast in composition and colour between the fractures and the areas that they enclose, resulting in a pseudoclastic texture (Plate 4e, 4g, 4h, 5c and 5d). The more advanced the prominent fracture controlled alteration the more matrix supported the resulting alteration texture.

Pseudoclastic textures are common particularly in the more felsic units and can develop an apparently polymictic appearance. The apparent polymictic character can be due to a number of features; phenocrysts in the dark phyllosilicate domains can appear more prominent than those in the quartz-feldspar altered domains; differences in the intensity of alteration and hence colour within individual units; and overprinting alteration assemblages in the same unit.

In summary it appears that the alteration in glassy coherent lavas and sills evolves towards a texture resembling matrix supported monomictic and polymictic textures typical of volcaniclastic mass flow deposits. With increasing alteration the false clastic textures converge to produce textures similar to those of welded pyroclastic deposits (Allen, 1988). In volcaniclastic deposits alteration is also commonly polyphase and the preservation of pre-existing textures is controlled by the intensity of the alteration phases. In weak to moderately altered deposits the primary clastic texture is enhanced by the alteration stages and this often imparts a polymictic appearance (Plate 1f). The alteration is matrix and fracture controlled in a similar manner to the fracture controlled alteration in coherent lavas and sills. In more intensely altered units the primary nature of the unit becomes obscured.

Discriminating diagenesis from hydrothermal alteration

Distinguishing between the products of diagenesis and hydrothermal alteration is difficult due to similar mineralogies, variable intensities and complex timing relationships. Hydrothermal and diagenetic alteration may occur simultaneously with the addition of circulating hydrothermal fluid intensifying diagenetic reactions. However alteration assemblages that are regional in distribution and pre-date or are synchronous with the styolitic S1 compaction foliation are interpreted to be diagenetic. Alteration styles that are only local in distribution are interpreted to be related to discrete hydrothermal cells or cooling of coherent sills. Hydrothermal alteration can be distinguished from contact metamorphic effects based on significant variations in the geochemistry and the Alteration Index (Ishikawa et al., 1976).

Regional diagenetic alteration generally involves only weak to moderate intensities of alteration and subtle deviations in the chemical signature. Alteration intensity is reflected in the degree of replacement of the volcanic groundmass and the degree of replacement of phenocrysts. Least altered volcanics

have well-preserved groundmass or matrix textures and pristine feldspar phenocrysts. It appears that the glassy groundmass alters before the plagioclase phenocrysts. With increasing intensity of alteration the groundmass textures are initially enhanced by many of the alteration styles and then progressively destroyed or obscured by pervasive alteration. With moderate intensity of alteration feldspar phenocrysts are partially replaced. During strong or intense hydrothermal alteration all primary volcanic textures including the feldspar phenocrysts are destroyed. Table 4 summarises regional diagenetic alteration textures and chemistry in the Mount Black Volcanics and compares these with medial hydrothermal alteration in the Rosebery footwall. Different diagenetic alteration styles are initially preserving or enhancing primary volcanic textures. Sericite alteration enhances perlitic fractures, shard and pumice shapes; feldspar-quartz alteration preserves uncompacted shards and pumice fragments. Chlorite-rich assemblages are texturally more destructive, preserving only the porphyritic nature of pumice in the chlorite-sericite-rich fiamme. The feldspar phenocrysts remain relatively pristine either being dusted with fine-grained sericite or replaced by secondary feldspar.

Mass gains and losses during diagenetic alteration are significantly smaller than changes related to medial facies hydrothermal alteration. Total mass changes during diagenetic alteration are generally between 1–15g/100g (Fig. 7) while medial facies hydrothermal alteration varies from 10–50g/100g. Hydrothermal silicification in the Mount Black Volcanics is characterised by SiO_2 enrichment an order of magnitude greater than the mass changes associated with the diagenetic alteration styles (Fig. 7). Diagenetic alteration also appears to be more complicated with different alteration facies enriched or depleted in SiO_2, Na_2O, CaO, K_2O, Fe_2O_3, MgO, MnO, Rb, Sr and Ba over small distances. Dissolution and precipitation of material has probably been occurring simultaneously within the volcanic pile. Mobile elements were removed from one site while concurrent deposition of the same elements occurred at a more favourable site. For example, sodium leached during the early sericite alteration may have contributed to the formation of Na-feldspar during the secondary feldspar alteration. Hydrothermal alteration in the Rosebery Footwall however shows more consistent enrichments in SiO_2, K_2O, Rb and dilutions in CaO, Na_2O, P_2O_5, Sr, Ba, Tl (Aung Pwa et al., 1992). Changes in MgO, MnO and Fe_2O_3 concentrations appear more dependent on the alteration minerals in the individual sample.

Proximal facies hydrothermal alteration in the Rosebery Footwall pumice breccias is generally intense and totally texturally destructive. Less intense medial facies alteration however only partially obscures the primary textures. Groundmass textures are modified and/or destroyed by sericite-carbonate, sericite-quartz and sericite-chlorite alteration. Weak sericite alteration forms disseminated grains in the groundmass while carbonate alteration forms spots in which the pumice and shards textures are well preserved. The feldspar phenocrysts and crystal fragments are significantly more altered by hydrothermal alteration than diagenetic alteration. Alteration of the feldspars varies from dusting with sericite, preservation by chlorite, sericite or sericite-carbonate pseudomorphs, to total destruction.

References

Allen, R.L., 1997. Rosebery alteration study and regional alteration studies in the Mount Read Volcanics: The record of diagenetic alteration in the strongly deformed, felsic volcaniclastic succession enclosing the Rosebery and Hercules massive sulphide deposits. AMIRA Project P439, Report 5, Oct. 1997. Unpubl.

Allen, R.L., 1994. Syn-volcanic, sub-seafloor replacement model for Rosebery and other massive sulphide ores. Contentious issues in Tasmanian geology. Ed by Cooke, D.R. and Kitto, P.A. in Geol Soc of Aust Abstracts 39, 31–34.

Allen, R.L., 1993. Geological cross-section and interpretation, 1320mN Rosebery mine north end. Unpubl. Report to Pasminco Exploration, Tasmania.

Allen, R.L., 1991. Structure, stratigraphy and volcanology of the Rosebery-Hercules Zn, Pb, Cu, Au Massive Sulphide District Tasmania: Results 1988–1990. Unpubl. report to Pasminco Exploration, Tasmania.

Allen, R.L., 1988. False pyroclastic textures in altered silicic lavas, with implications for volcanic-associated mineralisation. Econ. Geol. 83: 1424–1446.

Aung Pwa, Naschwitz, W., Hotchkis, M. and VanMoort, J.C., 1992. Exploration rock geochemistry in the Rosebery Mine area, western Tasmania. In; Tasmania- an island of potential. Bull. Geol. Surv. Tasm. 70, no.7, p. 7–16.

Barrett, T. and Maclean, W.H., 1994. Mass changes in hydrothermal alteration zones associated with VMS deposits of the Noanda area. Explor. Mining Geol. 3, No. 2, p. 131–160.

Bates, R.L. and Jackson, J.A., 1987. Glossary of geology. Third edition. American Geological Institute. p788.

Boles J.R., 1982. Active albitization of plagioclase, Gulf Coast Tertiary. American Journal of Science, V.282, p. 165–180.

Branney M.J. and Sparks R.S.J., 1990. Fiamme formed by diagenesis and burial compaction in soils and subaqueous sediments. Journal of the Geological Society of London. 147: 919–922.

Cas, R.A.F. and Wright, J.V., 1987. Volcanic successions: modern and ancient: a geological approach to processes, products and successions. Allen and Unwin. p487.

Crawford, A.J., Corbett, K.D. and Everard, J.L., 1992. Geochemistry of the Cambrian volcanic-hosted massive sulfide-rich Mount Read Volcanics, Tasmania, and some tectonic implications. Econ Geol v.87, 597–619.

Dimroth, E. and Yamagishi, H., 1987. Criteria for the recognition of ancient subaqueous pyroclastic rocks. Report of the Geological Survey of Hokkaido. v.58, p.55–88

Fink, J. and Manley, C., 1987. Origin of pumiceous glassy textures in rhyolitic flows and domes. Geol. Soc. Am Spec. Pap. 212, 77–88.

Fisher, R.V. and Schminke, H.-U., 1984. Pyroclastic rocks. New York. Springer-Verlag.

Friedman I. and Long W., 1984. Volcanic Glasses; Their Origins and Alteration Processes. Journal of Non-Crystalline Solids 67: 127–133.

Einsele, G., Ricken, W. and Seilacher, A., 1991. Cycles and Events in Stratigraphy-Basic Concepts and Terms. In Einsele, G., Ricken, W. and Seilacher, A. (Eds.), 1991. Cycles and Events in Stratigraphy. Springer-Verlag, Berlin Heidelberg. p955.

Gifkins, C.C., 1997. Background alteration in the Mount Black Volcanics: textures, mineralogy and geochemistry. AMIRA Report 5, project P439, 85–134. Unpubl.

Gifkins, C.C., Allen, R.A., Stolz, A.J. and Duhig, N., 1996a. Mount Black to Murchison Gorge: Preliminary volcanic facies analysis and alteration styles. AMIRA Project P439 Report 2, May 1996. Unpubl.

Gifkins, C.C., Allen, R.A. and McPhie, J., 1996b. Fiamme associated with silicic lavas and intrusions. EOS, Transactions, AGU, v.77, No. 22, p W125.

Gifkins, C.C., 1996. Mount Black Volcanics: Preliminary volcanic facies and alteration, petrography and geochemistry. AMIRA Project P439, Report 3, Oct. 1996. 321–349. Unpubl.

Gifkins, C.C., 1995. Subaqueous silicic volcanism in the Mount Black Volcanics, western Tasmania. AMIRA Report 1, project P439, 19–26. Unpubl.

Iijima, A., 1974. Clay and zeolitic alteration zones surrounding Kuroko deposits in the Hokuroku District, Northern Akita, as submarine hydrothermal-diagenetic alteration products. Mining Geology Special Issue, no. 6, p 267–289.

Ishikawa, Y., Sawaguchi, T., Iwaya, S. and Horiuchi, M., 1976. Delineation of prospecting targets for Kuroko deposits based on modes of volcanism of underlying dacite and alteration haloes. Mining Geology, 26, 105–117 (in Japanese with English abstract).

Henley, H.R. and Ellis, A.J., 1983. Geothermal systems ancient and modern; a geochemical review. Earth Science Reviews. 19, no. 2, p. 1–50.

Hesse R, 1990. Silica Diagenesis: Origin of inorganic and replacement cherts. In McIlreath I.A. and Morrow D.W. (Eds) Diagenesis. Geoscience Canada reprint series; 4 p. 253–275.

Kano, K., Takeuchi, K., Yamamoto, T. and Hoshizumi, H., 1991. Subaqueous rhyolite block lavas in the Miocene Ushikiri Formation, Shimane Peninsula, SW Japan. Journal of Volcanology and Geothermal Research. v.46, p. 241–253.

Large, R.R., 1996. The Hercules-Mt Read traverse: Relationships between volcanic mineralogy, alteration and geochemistry. AMIRA Project P439, October 1996: 153–233.

Large, R.R., Crawford, A.J. and Duhig, N., 1989. Primary alteration chemistry of the Mount Read Volcanics. AMIRA Project P210, November 1989: 38–45.

Lipman, P.W., 1965. Chemical comparison of glassy and crystalline volcanic rocks. US Geol Surv. Bull., no. 1201-D.

Lofgren, G., 1971. Experimentally produced devitrification textures in natural rhyolitic glass. Geol Soc Am Bull. v. 82:111–124.

Lofgren, G., 1970. Experimental devitrification rates of rhyolitic glass. Geol. Soc. Am. Bull. 81, p. 553–60.

McNeill, A.W. and Corbett, K.D., 1989. Geology of the Tullah-Mt Block area. Mt Read Volcanics Project Geological Report 2.

McPhie, J., Doyle, M. and Allen, R.L., 1993. Volcanic Textures: a guide to the interpretation of textures in volcanic rocks. p198.

Marsaglia K.M. and Tazaki K., 1992. Diagenetic trends in Leg 126 sandstones. In Taylor B., Fujioka, K. et al.. (eds) Proc. ODP, Sci. Results 126: College Station. TX (Ocean Drilling Program). p. 125–138.

Morrow D.W. and McIlreath I.A., 1990. Diagenesis general introduction. In McIlreath I.A. and Morrow D.W. (Eds) Diagenesis. Geoscience Canada reprint series; 4 p.

Noble, D.C., 1967. Sodium, potassium and ferrous iron contents of secondarily hydrated natural silicic glasses. Am. Mineral. 52, 230–85.

Pettijohn, F.J., Potter, P.E. and Siever, R, 1972. Sand and sandstones. New York: Springer.

Pichler, H., 1965. Acid Hyaloclastites. Bull. Volc. 28, 293–310.

Stolz, J., Allen, R., Gifkins, C., McPhie, J. and Blake, M., 1997. Petrographic and geochemical characteristics of alteration from the Macintosh Dam–Anthony Road–Mt Black traverse, Mt Read Volcanic Belt.

Stolz, A.J., Large, R. and Duhig, N., 1996. Progress report on the utilisation of the Mount Read Volcanics database. AMIRA Project P439 Report 2, May 1996. Unpubl.

Tazaki K. and Fyfe W.S., 1992. Diagenetic and hydrothermal mineral alteration observed in Izu–Bonin deep-sea sediments, Leg 126. In Taylor B., Fujioka, K. et al.. (eds) Proc. ODP, Sci. Results 126: College Station. TX (Ocean Drilling Program). p. 101–112.

Torres, M.E., Marsaglia, K.M., Martin, J.B. and Murray, R.W., 1995. Sediment Diagenesis in Western Pacific Basins. In Taylor, B. and Natland, J. (eds) Active margins and marginal basins of the western Pacific. Geophysical monograph :88 p. 241–258.

Winchester, J.A. and Floyd, P.A., 1977. Geochemical discrimination of different magma series and their differentiation products using immobile elements. Chemical Geology, v. 20, p. 325–344.

Yamagishi, H., 1987. Studies on the Neogene subaqueous lavas and hyaloclastites in South-west Hokkaido. Geological Survey of Hokkaido. v.59

Plate 5: Feldspar-hornblende phyric dacites and basaltic dykes of the Henty Dyke Swarm.

a) Sample PR58 from the Pieman Rd is an example of coherent, massive, feldspar-hornblende porphyritic dacite of the Mount Black Volcanics. The groundmass is weakly feldspar altered and the hornblende phenocrysts are replaced by chlorite-epidote.

b) This photomicrograph of a densely spherulitic groundmass is from massive dacite sample 040612. Radiating fibres of feldspar and quartz exhibit radial extinction patterns. The spherulites are partly recrystallised and are dusted with fine-grained sericite. (x2.5, crossed polars)

c) Sample PR57 from the Pieman Rd is a massive, perlitic, feldspar-hornblende porphyritic dacite with fracture controlled polyphase alteration. The two dominant alteration facies are; red feldspar-quartz and dark green chlorite-epidote. The alteration is controlled by fine perlitic fractures in the groundmass.

d) The photomicrograph of sample PR57 covers both a feldspar-quartz rich domain on the left side of the photograph and a chlorite-epidote rich domain on the right side. No textures are evident in the strongly feldspar altered domain, however perlitic fractures are recognisable near the middle of the photograph in the chlorite-epidote domain. Chlorite and epidote forming along the crystal cleavage is progressively replacing the feldspar phenocrysts.

e) Sample 039712 is a fine grained, weakly vesicular basaltic dyke of the Henty Dyke Suite. The right hand side of the photograph shows a fine-grained sheared intrusive contact. The white spots are carbonate filled amygdales. The basaltic dyke is strongly chlorite-epidote-carbonate altered.

f) Photomicrograph of M39, a basaltic dyke similar to 039712, on the Murchison Highway near Sterling Saddle. It is fine-grained, weakly feldspar porphyritic basalt. The feldspar phenocrysts are zoned and altered to chlorite-epidote. The groundmass is a mass of fine interlocking needles of feldspar, pyroxene, chlorite and epidote. The brown-green chlorite patches in the top of the photomicrograph are elongated chlorite filled amygdales. (x5, PPL).

g) Sample 040631 is of one of the coarser grained basaltic dykes of the Henty Dyke Suite. The white patches are feldspar phenocrysts and the dark blebs are round chlorite filled amygdales. The groundmass is pervasively chlorite-epidote altered and this is overprinted by pink feldspar bearing veins.

h) Photomicrograph of sample M42, a coarse grained basaltic dykes shows a groundmass of fine interlocking needles of feldspar, pyroxene, chlorite and epidote. (x5, PPL).


a
0 2 4 6 8 10 cm


b


c
0 2 4 6 8 10 cm

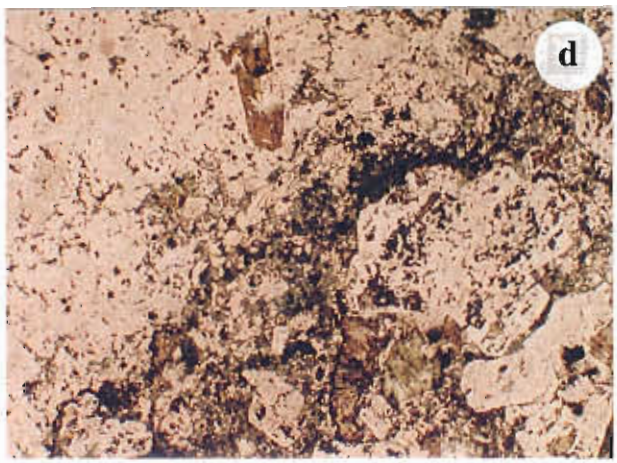
d


e


f

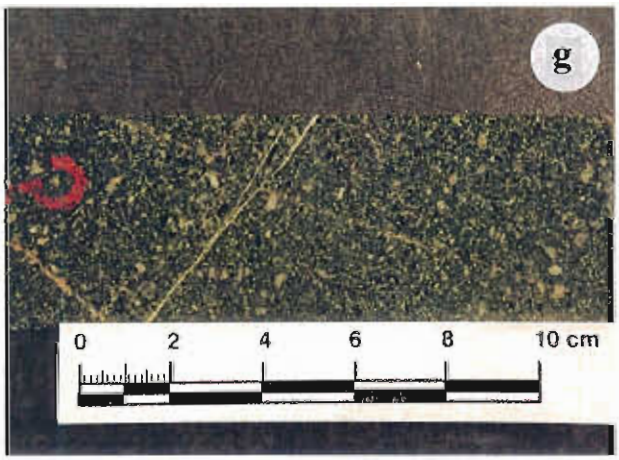
g
0 2 4 6 8 10 cm


h

Plate 6: Mafic breccias, andesitic and basaltic lavas and sills of the Sterling Valley Volcanics.

a) This sample from DDH STP218 at 85.5 m in the Sterling Valley is typical of the polymictic mafic breccias. It is from a poorly sorted, clast supported normally graded unit. The sample is composed of blocky, angular, feldspar porphyritic dacitic to basaltic clasts that have curviplanar margins typical of the products of quench fragmentation. The alteration style is characterised by pervasive chlorite-sericite-epidote.

b) Photomicrograph of the same mafic breccia ("as above") is from STP218 at 113.6 m. In thin section a number of trachytic basalt clasts, fine massive andesite clasts, perlitic glassy dacite fragments and feldspar crystals can be recognised. (x1.5, PPL).

c) This sample from DDH STP 218 at 127 m is medium-grained, poorly stratified mafic sandstone.

d) Sample M9, from the Murchison Highway, is typical of the feldspar-hornblende phyric andesites of the Mount Black and Sterling Valley Volcanics. It is coarse grained massive and pervasively chlorite-sericite-epidote altered.

e) Photomicrograph of massive feldspar-hornblende phyric andesite from DDH STP 218 at 16.5 m in the Sterling Valley Volcanics. (x1.5, PPL).

f) Sample M6, from the Murchison Highway near the Henty Fault Zone, is an example of a massive, fine-grained, aphyric andesite. The alteration is pervasive chlorite-epidote.

g) Sample M7, from the Murchison Highway, is a typical Sterling Valley lava, a medium grained feldspar porphyritic basalt. The margin in the upper left of the sample is fine grained and perlitic. The groundmass is strongly chlorite altered.

h) This sample of a fine grained basalt in DDH STP 234 at 129.4 m is massive and strongly chlorite-epidote altered giving it a similar appearance to the Henty dyke basalts however reworking and quench fragmentation at the top of the deposit indicate the extrusive origin of this basaltic lava.


a
0 2 4 6 8 10 cm


b


c
0 2 4 6 8 10 cm

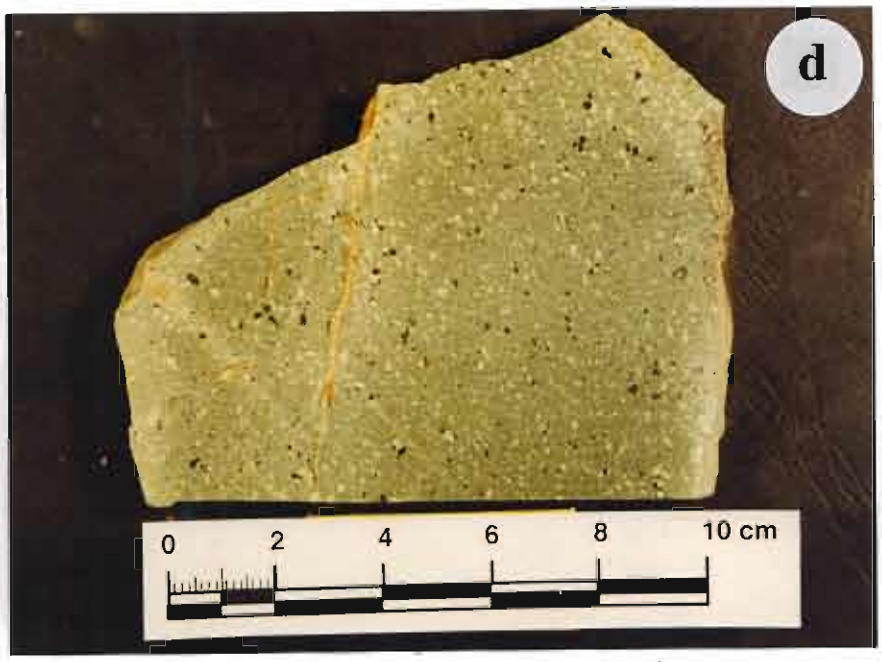
d
0 2 4 6 8 10 cm


e


f
0 2 4 6 8 10 cm


g
0 2 4 6 8 10 cm


h
0 2 4 6 8 10 cm

Appendix 1. Pumice breccias.

Sample	Alteration	Ti/Zr	Nb/Y	SiO2	TiO2	Al2O3	Fe2O3	MnO	MgO	CaO	Na2O	K2O	P2O5	S	Total	Sc	V	Cr	Ni
Mount Black Volcanics pumice breccia																			
39717	CO3+ser	7.54	0.38	71.37	0.29	13.23	2.74	0.07	0.69	2.00	4.43	2.21	0.06	0.01	97.09	4.70	9.89	2.54	1.00
39719	ser+qtz	7.98	0.39	70.18	0.33	13.46	2.74	0.08	0.82	2.74	2.70	2.99	0.07	0.02	96.11	6.00	11.53	3.35	<1
39793	ser>chl	6.80	0.35	54.93	0.47	20.37	7.17	0.06	2.60	0.69	1.10	6.83	0.08	2.08	94.30	8.90	14.89	7.61	3.40
MB96-40	fsp>ser	4.90	0.44	74.24	0.23	13.93	2.15	0.01	0.49	0.04	3.21	2.88	0.02	0.02	99.91	4.60	2.90	2.60	1.70
MB96-41	fsp>ser±chl	6.76	0.32	74.03	0.30	13.74	2.38	0.01	0.46	0.04	3.95	3.24	0.05	<0.01	99.99	3.60	12.30	2.60	1.10
MB96-46	ser+qtz	7.55	0.48	71.55	0.30	13.87	5.74	0.12	1.06	0.02	0.48	3.40	0.04	0.01	99.52	4.10	17.50	4.10	1.10
PR11	fsp>ser+chl	7.40	0.46	70.91	0.31	14.08	2.78	0.07	0.77	1.66	2.68	3.16	0.07	0.01	96.49	5.60	20.20	4.00	2.00
EHP319-245.2	fsp+ser>chl	11.11	0.53	63.26	0.46	15.12	5.59	0.32	1.37	2.44	3.42	2.85	0.11	0.08	94.94	9.10	60.70	14.80	10.50
EHP319-538.6	fsp>>ser±bt	7.48	0.42	73.69	0.32	13.96	2.27	0.05	0.69	1.28	3.37	2.83	0.06	0.04	98.52	4.10	12.00	1.80	1.30
118R-515	fsp>ser	6.78	0.45	70.07	0.30	14.92	2.87	0.09	0.86	1.23	3.00	3.62	0.06	0.04	97.02	4.60	11.60	2.00	2.80
Rosebery Footwall pumice breccia																			
109R-638	silica	7.60	0.42	71.55	0.36	15.15	2.01	0.03	0.71	0.71	3.89	3.03	0.05	0.02		5.80	10.10	1.50	3.30
109R-670	silica	7.35	0.45	74.09	0.30	13.28	1.73	0.04	0.56	0.85	3.91	2.58	0.04	0.03		4.10	8.30	1.40	2.20
109R-707	least altered	7.57	0.41	74.20	0.30	12.88	2.24	0.09	0.94	1.15	2.94	2.59	0.04	0.03		4.10	7.10	1.30	2.00
109R-709	CO3 + ser	7.55	0.18	38.70	0.18	7.95	21.10	8.71	1.40	1.15	0.08	2.76	0.03	0.06		2.20	6.30	1.30	3.10
120R-1378	q + chl	7.90	0.34	75.76	0.27	11.26	4.37	0.28	0.90	0.06	0.07	3.47	0.04	0.89	99.22	3.70	7.20	1.00	2.50
120R-1386	q +chl	7.97	0.38	75.46	0.22	9.79	6.50	0.38	1.29	0.11	0.09	2.58	0.04	1.09	99.42	3.10	6.70	1.00	2.30
120R-1440	q + chl	7.48	0.38	73.84	0.30	12.70	1.44	0.10	0.63	1.69	5.58	1.35	0.05	0.01	99.87	5.40	6.40	1.00	1.90
Transitional Stratified Zone pumice breccia																			
120R-1356	CO3 + ser	12.81		17.98	0.35	9.31	12.91	9.96	2.44	14.33	0.05	3.46	0.10	8.06	91.49	9.80	31.80	2.00	1.80
120R-1361AB	CO3 + ser	12.33	0.38	25.60	0.59	15.57	5.70	20.02	2.48	3.22	0.05	5.31	0.08	1.85	98.15	13.20	41.10	1.00	1.00

Appendix 1. cont.

Sample	Cu	Zn	Rb	Sr	Y	Zr	Nb	Ba	La	Ce	Nd	Pb	Th (XRF)
Mount Black V													
39717	2.40	22.90	84.30	166.50	36.50	230.45	13.70	698.20	49.80	106.40	45.80	4.00	15.70
39719	2.60	36.50	119.40	103.50	35.70	247.96	14.00	725.50	21.10	50.60	22.70	2.70	14.80
39793	4.80	73.70	282.50	50.90	60.70	414.21	21.30	1639.40	73.80	155.90	69.50	4.50	27.00
MB96-40	2.50	23.20	120.60	77.60	37.80	281.50	16.80	787.10	46.60	81.60	42.30	8.20	22.13
MB96-41	3.40	20.70	112.20	111.60	41.40	266.10	13.40	942.30	54.40	107.40	44.20	6.50	21.76
MB96-46	13.70	70.10	153.90	8.40	24.30	238.10	11.60	703.20	41.20	81.60	31.90	6.50	17.40
PR11	3.70	47.90	124.10	87.00	27.70	251.00	12.80	786.00	37.90	81.00	32.10	2.47	18.40
EHP319-245.2	4.30	111.70	101.00	100.40	26.20	248.30	13.90	901.10	37.70	80.20	36.00	2.60	20.20
EHP319-538.6	4.00	46.50	125.80	270.10	31.40	256.50	13.30	1002.10	30.90	76.30	33.10	3.22	20.10
118R-515	5.90	35.20	254.10	103.70	35.90	265.40	16.20	917.80	39.60	91.40	38.20	6.11	19.80
Rosebery Footv													
109R-638	2.50	34.00	133.80	238.30	37.00	284.10	15.60	1253.70	46.80	102.80	43.90	6.60	24.70
109R-670	2.20	24.50	99.60	278.60	31.30	244.70	14.20	1520.10	46.40	100.40	38.80	4.60	20.30
109R-707	1.90	30.30	137.10	188.20	31.40	237.70	12.90	772.10	42.30	89.40	37.00	4.70	20.00
109R-709	87.40	51.00	217.70	13.50	37.10	143.00	6.70	515.00	27.60	53.00	22.00	158.60	14.30
120R-1378	11.00	92.00	177.00	9.80	37.00	204.80	12.60	879.70	30.90	71.40	28.80	8.00	17.90
120R-1386	344.00	398.00	133.00	8.40	24.00	165.40	9.00	548.60	34.20	75.00	29.30	31.00	15.30
120R-1440	2.00	22.00	52.00	195.40	32.00	240.60	12.20	506.20	56.60	108.90	45.40	4.00	17.80
Transitional St													
120R-1356	668.00	10900.00	150.00	243.70	0.00	163.80	5.90	3392.00	65.00	157.00	59.00	13800.00	11.80
120R-1361AB	13.00	314.00	247.00	53.80	41.00	286.90	15.50	5285.00	3.10	0.00		213.00	21.00

Appendix 2. Unaltered samples.

Sample	Ti/Zr	Nb/Y	AI	SiO2	TiO2	Al2O3	Fe2O3	MnO	MgO	CaO	Na2O	K2O	P2O5
Feldspar phyric rhyolite													
39745	6.82	0.37	35.49	70.45	0.28	13.43	2.4	0.13	0.66	2.8	3.49	2.8	0.05
39764	5.81	0.32	48.69	71.96	0.26	13.66	2.42	0.03	0.45	0.94	3.96	4.2	0.04
39770	5.74	0.43	43.96	71.69	0.26	14.23	1.89	0.02	0.43	1.23	4.2	3.83	0.04
109R1	6.43	0.65	41.15	73.89	0.26	12.6	3.37	0.12	0.83	1.27	3.15	2.26	0.05
MB96-35	6.00	0.42	56.26	74.58	0.27	13.85	2.08	0.01	0.38	0.13	3.54	4.34	0.03
Quartz-feldspar phyric rhyolite													
39728	6.69	0.44	57.46	71.64	0.26	12.8	3.22	0.43	0.7	1.96	1.52	4	0.06
M78	7.80	0.52	51.72	74.18	0.25	13.65	2.12	0.02	0.5	0.4	3.66	3.85	0.04
Rhyolitic pumice breccia													
39719	7.98	0.39	41.19	70.18	0.33	13.46	2.74	0.08	0.82	2.74	2.7	2.99	0.07
MB96-41	6.76	0.32	48.11	74.03	0.3	13.74	2.38	0.01	0.46	0.04	3.95	3.24	0.05
EHP319-538.6	7.48	0.42	43.08	73.69	0.32	13.96	2.27	0.05	0.69	1.28	3.37	2.83	0.06
Rhyolitic pumice-lithic breccia													
PR26	6.04	0.37	45.60	73.43	0.24	12.38	2.23	0.06	0.51	1.96	2.74	3.43	0.05
Volcaniclastic sand and siltstones													
MB96-44	7.65	0.40	46.98	71.51	0.36	15	3.15	0.02	0.89	0.06	3.8	2.53	0.05
BY1-46.2	5.92	0.47	54.28	72.98	0.21	13.27	2.82	0.17	1.09	1.08	2.34	2.97	0.04
Feldspar phyric dacite													
40621	14.41	0.36	46.92	67.53	0.52	14.51	4.37	0.06	1.3	2.38	3.56	3.95	0.13
40635	13.65	0.37	39.96	68.01	0.47	13.96	4.57	0.09	1.44	1.68	4.27	2.52	0.12
DP310-91.2	15.49	0.34	36.86	63.2	0.47	14.58	4.49	0.16	1.4	4.19	3.16	2.89	0.14
80R-388.5	15.05	0.45	35.38	63.58	0.48	14.04	3.74	0.13	1.31	4.72	3.19	3.02	0.14
80R-358.2	14.37	0.42	46.80	66.02	0.48	14.14	4.15	0.21	1.2	2.23	2.92	3.33	0.14
80R-351.5	14.65	0.40	44.20	64.15	0.45	13.55	4.59	0.29	1.29	3.45	2.42	3.36	0.13
BY2-53.5	14.22	0.39	38.08	65.39	0.45	13.61	4.22	0.19	1.28	3.02	3.29	2.6	0.13
BY2-98.3	14.65	0.40	38.72	63.67	0.46	13.55	4.03	0.23	1.36	4.03	2.87	3	0.16
M120	17.37	0.37	30.57	63.11	0.66	14.95	6.12	0.1	2.43	6.29	2.66	1.51	0.09
M86	18.66	0.34	31.30	62.81	0.65	15.34	6.33	0.09	3.03	4.92	3.42	0.77	0.11
M84	14.52	0.43	44.71	66.77	0.56	14.83	5.32	0.07	2.56	2.02	3.52	1.92	0.08
M77	13.42	0.34	25.71	66.65	0.48	16.41	4.15	0.03	2.03	0.24	7.07	0.5	0.12
M63	16.39	0.46	30.87	64.92	0.65	15.5	5.64	0.09	3.12	1.3	5.91	0.1	0.1
M67	13.92	0.44	30.99	67.73	0.48	15.14	4.95	0.1	1.58	1.59	5.09	1.42	0.12
M29B	16.77	0.39	43.93	68.15	0.59	14.09	4.66	0.11	1.66	3.03	2.7	2.83	0.08
Feldspar-hornblende phyric dacite													
39799	10.01	0.34	42.69	69.01	0.4	13.75	3.21	0.24	0.84	2.56	2.85	3.19	0.07
M4	18.12	0.35	41.80	62.51	0.68	15.66	6.54	0.1	2.74	4.61	1.78	1.85	0.1
M10	14.19	0.34	51.33	65.89	0.51	15.70	4.70	0.08	1.35	0.77	3.81	3.49	0.13
M24	14.25	0.46	43.44	66.52	0.49	15.3	4.36	0.06	1.22	2.17	3.78	3.35	0.12
MB96-43	14.66	0.27	62.96	69.5	0.51	14.95	4.6	0.14	1.42	0.21	2.62	3.39	0.13
Andesite													
M6	45.70	0.14	39.27	53.86	0.59	16.34	7.79	0.13	6.02	8.73	2.9	1.5	0.06
M7	72.38	0.09	28.74	50.66	0.92	18.32	10	0.19	4.38	8.64	4.03	0.73	0.1
M9	43.63	0.21	45.39	50.49	0.96	18.39	10.36	0.16	4.73	6.46	2.19	2.46	0.11
STP218-103.7	65.75	0.09	25.70	48.38	0.93	18.33	9.16	0.15	3.35	10.45	2.5	1.13	0.18
Mafic volcaniclastic breccia													
MBE96-8	22.91	0.29	44.56	62.71	0.71	15.01	5.96	0.1	2.62	4.29	3.46	3.61	0.11
STP218-67.2	26.16	0.21	32.19	64.3	0.59	12.1	4.56	0.09	2.1	6.87	2	2.11	0.1
Basalt													
STP218-113.6	67.58	0.11	24.17	51.52	0.93	15.48	9.32	0.19	3.76	8.69	4.52	0.45	0.15
Henty basalt													
40626	88.71	0.03	41.51	45.08	0.6	16.33	9.34	0.34	6.09	9.45	2.57	2.44	0.14

Appendix 2. cont.

Sample	Total	S	Sc	V	Cr	Ni	Cu	Zn	As	Rb	Sr	Y	Zr	Nb	Ba	La	Ce
Feldspar phyric rh									(ICP)								
39745	96.49	0.01	5	7	2	1	16	22	11	107	111	42	246	15.7	611.5	43	93
39764	97.92	<0.01	5	4	2	1	2	13	18	143	132	52	268	16.6	937.6	52	109
39770	97.82	<0.01	5	4	2	1	2	13	17	120	136	38	271	16.6	858.8	41	92
109R1	97.80	0.02	4	17	3	2	2	32	1	93	107	25	242	16	737.2	147	308
MB96-35	100.32	<0.01	4	4	2	1	2	17	<	136	96	41	270	17	988	57	102
Quartz-feldspar pl																	
39728	96.59	0.07	5	7	2	1	5	84	14	184	95	33	233	14.6	875.2	25	59
M78	99.97	<0.01	4	13	5	2	4	32	<	118	121	20	192	10.5	942	23	50
Rhyolitic pumice b																	
39719	96.11	0.02	6	12	3	<1	3	37	8	119	104	36	248	14	725.5	21	51
MB96-41	99.99	<0.01	4	12	3	1	3	21	1	112	112	41	266	13.4	942	54	107
EHP319-538.6	98.52	0.04	4	12	2	1	4	47	<4	126	270	31	257	13	1002	31	76
Rhyolitic pumice-l																	
PR26	97.03	0.35	5	5	2	1	3	42	8	102	141	36	238	13	1116	35	76
Volcaniclastic sand																	
MB96-44	99.60	0.02	6	12	3	1	6	38	<	103	98	40	282	16	606	41	74
BY1-46.2	96.97	0.01	3	12	4	3	2	46	<4	127	65	36	213	17	555	38	81
Feldspar phyric da																	
40621	98.31	0.01	10	70	6	1	4	51	22	102	242	34	216	12.2	958.1	46	89
40635	97.13	0.01	10	66	6	2	2	45	22	72	129	32	206	11.7	697.3	41	87
DP310-91.2	94.68	<0.01	10	63	3	3	4	52	<4	152	191	30	182	10	790	26	57
80R-388.5	94.35	<0.01	11	68	7	4	3	36	<4	111	233	18	191	8	783	27	58
80R-358.2	94.82	0.03	10	75	6	3	2	24	<4	155	152	26	200	11	606	35	76
80R-351.5	93.68	<0.01	10	72	7	2	3	29	<4	162	128	27	184	11	555	32	64
BY2-53.5	94.18	0.05	11	67	6	2	5	50	<4	115	202	27	190	11	763	37	81
BY2-98.3	93.36	0.02	11	74	12	3	2	32	<4	118	160	28	188	11	674	34	78
M120	100.32	<0.01	18	126	47	8	5	64	8	39	352	33	228	12.0	515	31	70
M86	99.83	<0.01	15	132	40	8	5	92	6	36	283	32	209	11.0	223	29	62
M84	100.15	<0.01	12	109	29	6	5	71	6	76	188	29	231	12.2	499	23	58
M77	99.63	<0.01	10	63	5	2	2	68	<	20	94	39	214	13.3	91	53	110
M63	99.84	<0.01	18	136	49	10	3	108	2	4	160	27	238	12.1	42	27	56
M67	100.07	<0.01	8	61	4	2	4	75	2	46	253	28	207	12.2	362	28	63
M29B	99.95	0.02	15	114	46	7	17	67	3	88	233	28	211	11.0	813	26	63
Feldspar-hornblen																	
39799	96.12	0.01	9	23	2	1	4	75	16	118	190	34	240	11.6	877.6	42	84
M4	99.96	<0.01	17	129	43	9	11	104	5	84	263	34	225	12.0	429	40	81
M10	99.33	0.06	9	65	4	2	4	63	1	97	134	36	213	12.4	968	46	81
M24	99.27	0.11	8	60	5	2	5	47	<	90	214	26	206	11.8	755	30	63
MB96-43	99.89	0.02	11	81	7	3	7	40	<	129	78	41	209	11.1	711	49	101
Andesite																	
M6	100.39	<0.01	33	176	67	34	73	81	2	69	268	24	77	3.4	410	15	33
M7	100.58	0.04	35	292	83	54	163	82	10	28	385	24	76	2.2	285	9	19
M9	100.01	0.09	29	271	61	31	112	118	1	84	267	26	132	5.3	1017	15	33
STP218-103.7	94.56	0.26	26	232	93	46	143	102	5	108	335	25	85	2	325	8	31
Mafic volcaniclasti																	
MBE96-8	100.35	0.13	22	157	31	8	37	47	1	115	205	33	186	9.7	809	27	62
STP218-67.2	94.82	0.04	17	146	55	7	22	39	<4	96	209	33	135	7	651	18	46
Basalt																	
STP218-113.6	95.01	0.04	27	250	29	20	101	102	5	23	216	23	83	3	153	11	26
Henty basalt																	
40626	92.38	0.05	34	244	53	53	198	164	22	116	279	19	41	<1	620	13	33

Appendix 2. cont.

Sample	Nd	Pb	Bi	Th	U
Feldspar phyric rh			(ICP)	(ICP)	(ICP)
39745	40	3	0.1	13.9	4.19
39764	46	5	0.4	15	4.32
39770	39	3	0.2	13.7	3.34
109R1	113	2	0.2	19.3	6.99
MB96-35	45	3	<	22	5.4
Quartz-feldspar pl					
39728	26	170	0.2	17.2	3.86
M78	16	11	<	19.3	3.84
Rhyolitic pumice b					
39719	23	3	0.2	15.7	3.32
MB96-41	44	7	0.1	22.3	5.73
EHP319-538.6	33	3			
Rhyolitic pumice-l					
PR26	34	14			
Volcaniclastic sand					
MB96-44	37	3	0.3	20.6	4.98
BY1-46.2	33	<1.5			
Feldspar phyric da					
40621	37	4	0.1	15.1	4.9
40635	37	4	<	12.3	4.3
DP310-91.2	27	3			
80R-388.5	27	5			
80R-358.2	32	7			
80R-351.5	28	9			
BY2-53.5	34	8			
BY2-98.3	38	2			
M120	32	22	<	13.9	3.41
M86	30	18	<	13.5	3.31
M84	25	16	0.1	15.3	3.89
M77	47	8	<0.1	16	2.41
M63	26	9	<0.1	14.5	3.49
M67	26	11	0.1	16	3.25
M29B	26	10	0.1	12.6	3.04
Feldspar-hornblen					
39799	36	3	<	14.5	3.87
M4	35	147	0.1	13.4	3.24
M10	38	4	0.3	16	3.54
M24	29	13	<	15.3	3.56
MB96-43	45	2	<	19.3	4.66
Andesite					
M6	13	10	<	4.39	1.07
M7	10	16	<	3.37	1.18
M9	15	20	<	6.81	1.86
STP218-103.7	19	29			
Mafic volcaniclasti					
MBE96-8	28	20	<	10.3	2.64
STP218-67.2	21	5			
Basalt					
STP218-113.6	18	14			
Henty basalt					
40626	19	48	0.1	9.17	1.2

Appendix 3. Mass change.

Sample	Ti/Zr	Alteration	SiO2	TiO2	Al2O3	Fe2O3	MnO
39725	6.43	ser±qtz,chl>fs	68.02	0.3	15	2.71	0.1
39726	6.48	fsp>ser+chl	72.28	0.27	13.07	2.8	0.11
39726	mass change	(g/100g)	12.85	0	-0.38	0.42	0.02
39764	5.81	fsp>ser+chl	71.96	0.26	13.66	2.42	0.03
39770	5.74	fsp>ser>>CO3	71.69	0.26	14.23	1.89	0.02
39771	5.66	fsp	72.57	0.25	13.63	2.21	0.02
39775	5.58	ser+qtz>>fsp	73.76	0.25	13.37	2.57	0.16
39770	mass change	(g/100g)	-1.15	0	0.4	-0.55	-0.01
39771	mass change	(g/100g)	1.49	-0.01	0.14	-0.18	-0.01
39775	mass change	(g/100g)	1.66	-0.01	-0.32	0.15	0.13
39780	4.81	fsp+ser>CO3	71.81	0.2	14.1	1.8	0.13
39779	4.81	fsp>CO3>ser	74.94	0.19	12.05	1.48	0.13
39781	4.91	fsp>ser>>CO3	70.6	0.2	14.13	2.1	0.25
39782	5.2	fsp>ser>>CO3	74.05	0.19	12.12	1.79	0.07
39783	5.11	fsp>ser+qtz>s	74.4	0.19	12.05	1.85	0.07
39784	5	fsp>ser±chl	76.5	0.19	12.09	1.76	0.02
39779	mass change	(g/100g)	7.06	0	-1.42	-0.24	0.01
39781	mass change	(g/100g)	0.25	0	0.32	0.34	0.13
39782	mass change	(g/100g)	12.44	0.02	-0.31	0.24	-0.05
39783	mass change	(g/100g)	11.48	0.01	-0.61	0.27	-0.05
39784	mass change	(g/100g)	11.95	0.01	-0.86	0.13	-0.11
109R1	6.43	fsp>ser>bt	73.89	0.26	12.6	3.37	0.12
109R3	6.3	fsp	70.82	0.31	15.64	2.52	0.05
109R3	mass change	(g/100g)	-15.75	-0.01	0.24	-1.3	-0.08
109R5	7.8	fsp>ser+chl	65.01	0.37	15.43	6.97	0.1
109R11	7.14	fsp	73.64	0.23	12.56	4.6	0.11
109R11	mass change	(g/100g)	43.56	-0.03	3.09	-0.19	0.06
STP218-16.5	16.94	ser+ep>chl>fs	62.83	0.61	14.53	5.61	0.13
STP218-39.2	16.79	chl+ep>fsp	61.24	0.6	15.21	6.81	0.19
STP218-39.2	mass change	(g/100g)	-1.1	-0.01	0.8	1.25	0.06
EHP319-245.2	11.11	fsp+ser>chl	63.26	0.46	15.12	5.59	0.32
EHP319-296.6	11.31	ser+chl=fsp	70.32	0.47	14.35	3.3	0.07
EHP319-296.6	mass change	(g/100g)	6.83	0.01	-0.82	-2.3	-0.25
BY2-53.5	14.22	ser	65.39	0.45	13.61	4.22	0.19
BY2-98.3	14.65	fsp	63.67	0.46	13.55	4.03	0.23
BY2-98.3	mass change	(g/100g)	-1.21	0.01	0.05	-0.16	0.04
80R-388.5	15.05	fsp>bt	63.58	0.48	14.04	3.74	0.13
80R-394.2	15.08	ser>chl	64.14	0.47	13.58	4.26	0.25
80R-358.2	14.37	fsp>>ser	66.02	0.48	14.14	4.15	0.21
80R-351.5	14.65	fsp>>ser	64.15	0.45	13.55	4.59	0.29
80R-394.2	mass change	(g/100g)	2.04	0	-0.15	0.62	0.13
80R-358.2			-0.56	-0.02	-0.54	0.22	0.07
80R-351.5			3.01	-0.01	0.02	1.02	0.17

Sample	MgO	CaO	Na2O	K2O	P2O5	S	Total	Sc
39725	0.83	1.7	1.6	4.68	0.06	0		5.4
39726	0.62	1.56	4.47	2.05	0.04	0.01		3.9
39726	-0.14	0.05	3.4	-2.39	-0.02	0.01	13.84	-1.04
39764	0.45	0.94	3.96	4.2	0.04	0		4.7
39770	0.43	1.23	4.2	3.83	0.04	0		4.6
39771	0.4	1.17	4.04	4	0.04	0		4.2
39775	1.04	1.09	0.03	4.59	0.04	0.03		4.7
39770	-0.03	0.27	0.19	-0.42	0	0	-1.3	-0.16
39771	-0.05	0.24	0.13	-0.15	0	0	1.61	-0.45
39775	0.59	0.15	-3.93	0.38	0	0.03	-1.17	-0.01
39780	0.59	2.6	0.05	4.12	0.03	0.02		5.3
39779	0.44	2.2	2.53	2.62	0.03	0.01		4.2
39781	0.55	1.82	1.65	5.07	0.03	0.01		4.8
39782	0.54	2.35	2.82	2.97	0.03	0		3.2
39783	0.34	2.3	3.88	2.39	0.03	0.01		4.6
39784	0.43	0.59	4.11	3.11	0.02	0.01		3.2
39779	-0.13	-0.28	2.61	-1.36	0	-0.01	6.24	-0.88
39781	-0.03	-0.74	1.63	1.05	0	-0.01	2.95	-0.4
39782	0.02	0.07	3.16	-0.74	0	-0.02	14.84	-1.66
39783	-0.21	-0.03	4.29	-1.44	0	-0.01	13.71	-0.15
39784	-0.12	-1.95	4.45	-0.71	-0.01	-0.01	12.76	-1.8
109R1	0.83	1.27	3.15	2.26	0.05	0.02		3.9
109R3	0.78	0.33	4.46	2.69	0.05	0.01		3.8
109R3	-0.19	-1	0.51	-0.05	-0.01	-0.01	-17.65	-0.78
109R5	1.09	0.86	1.73	4.38	0.06	0.01		4.8
109R11	0.66	0.07	0.07	4.53	0.04	0.11		2.9
109R11	-0.12	-0.76	-1.63	2.3	0	0.15	46.43	-0.52
STP218-16.5	2.44	4.09	3.94	2.86	0.12	0.09		15.3
STP218-39.2	2.57	3.55	2.9	2.94	0.12	0.37		16.6
STP218-39.2	0.15	-0.51	-1.02	0.1	0	0.28	0.02	1.43
EHP319-245.2	1.37	2.44	3.42	2.85	0.11	0.08		9.1
EHP319-296.6	0.93	1.04	4.02	3.2	0.11	0.01		10.2
EHP319-296.6	-0.44	-1.4	0.59	0.34	0	-0.07	2.49	1.07
BY2-53.5	1.28	3.02	3.29	2.6	0.13	0.05		10.8
BY2-98.3	1.36	4.03	2.87	3	0.16	0.02		10.8
BY2-98.3	0.09	1.04	-0.4	0.42	0.03	-0.03	-0.11	0.09
80R-388.5	1.31	4.72	3.19	3.02	0.14	0		10.8
80R-394.2	1.5	3.6	1.54	3.92	0.14	0.05		10.2
80R-358.2	1.2	2.23	2.92	3.33	0.14	0.03		9.9
80R-351.5	1.29	3.45	2.42	3.36	0.13	0		9.7
80R-394.2	0.22	-1.04	-1.61	0.99	0	0.05	1.25	-0.37
80R-358.2	-0.16	-2.59	-0.4	0.16	-0.01	0.03	-3.81	-1.35
80R-351.5	0.03	-1.14	-0.68	0.47	-0.01	0	2.89	-0.73

Appendix 3. cont.

Sample	V	Cr	Ni	Cu	Zn	Rb	Sr	Y
39725	8.36	2.54	1.6	2.8	33.9	182.6	83.8	37.8
39726	7.34	2.23	1.2	2	40.5	75.8	107.6	38.8
39726	-0.15	-0.04	-0.26	-0.56	11.41	-97.8	36.58	5.61
39764	3.98	2.03	0.8	1.6	12.5	142.5	132	51.8
39770	3.77	2.03	1.4	1.9	13.4	119.8	136.2	38.3
39771	4.59	1.83	1.1	4.1	18.2	111.6	155.4	39
39775	6.63	1.83	4.6	2.5	59.5	371.3	24.2	30.6
39770	-0.25	-0.02	0.58	0.28	0.74	-24.16	2.54	-13.97
39771	0.67	-0.18	0.31	2.55	5.92	-29.54	25.29	-12.33
39775	2.64	-0.21	3.79	0.9	46.89	228.09	-107.85	-21.26
39780	1	1.52	1.2	30.4	35.6	186.9	40.9	35.5
39779	2.14	1.52	0.7	3.6	17.8	127.4	68.8	32.6
39781	1	1.62	1.3	23.8	50.7	185.2	67.5	39
39782	1	2.03	0.9	3.2	13.9	116.8	92.8	37.7
39783	1.63	2.13	1.2	3.7	24.1	94.5	107.6	34.1
39784	1	1.52	0.9	2.1	17.9	81.8	93	36.1
39779	1.25	0.08	-0.46	-26.61	-16.87	-52.82	31.51	-1.19
39781	0.02	0.14	0.13	-6.11	16.15	2.13	28	4.31
39782	0.14	0.79	-0.18	-26.76	-19.78	-54	64.69	7.4
39783	0.83	0.86	0.14	-26.26	-8.62	-81.11	79.56	2.68
39784	0.09	0.14	-0.21	-28.1	-16	-97.34	60.93	4.03
109R1	17.14	2.54	2.3	1.9	31.6	92.9	106.8	24.6
109R3	12.44	2.44	1.4	1.5	25.5	113.3	127.4	24.1
109R3	-6.92	-0.54	-1.15	-0.67	-10.67	0.11	-2.21	-4.82
109R5	21.93	4.06	2.5	3.4	24.4	178.8	52.7	19.6
109R11	2.24	1.62	1.8	9.3	23.9	175.4	5.7	42.1
109R11	-18.62	-1.67	0.15	10.31	10.83	79.79	-44.3	42.47
STP218-16.5	122.1	42.3	8	21.9	174.8	139.5	178.3	31.7
STP218-39.2	128.7	49.8	8.2	38.7	120.3	432.2	149.1	33.2
STP218-39.2	7.62	7.9	0.27	17.11	-53.55	296.13	-28.02	1.76
EHP319-245.2	60.7	14.8	10.5	4.3	111.7	101	100.4	26.2
EHP319-296.6	32.2	2.1	1.3	2.6	48.3	94.2	154.5	38.5
EHP319-296.6	-28.6	-12.71	-9.2	-1.71	-63.56	-7.1	53.6	12.18
BY2-53.5	67.2	6.2	1.9	5.4	49.9	115	201.9	26.7
BY2-98.3	73.6	12	2.9	2.4	32.4	117.5	159.8	27.9
BY2-98.3	6.99	5.9	1.02	-2.98	-17.24	3.44	-40.83	1.42
80R-388.5	68.4	6.7	3.5	3.2	36.1	111.3	232.7	17.9
80R-394.2	72.4	5.7	2.5	2.6	24.4	164.4	72.7	27.4
80R-358.2	74.5	6.3	2.9	2.1	23.5	155.4	151.8	25.9
80R-351.5	71.9	6.8	2.3	3	28.8	162.1	127.6	26.5
80R-394.2	5.67	-0.87	-0.94	-0.54	-11.14	56.88	-158.33	10.13
80R-358.2	2.72	-0.69	-0.73	-1.2	-13.67	37.04	-87.8	6.82
80R-351.5	6.23	0.36	-1.11	-0.09	-6.21	56.96	-100.25	9.61

Appendix 3. cont.

Sample	Zr	Nb	Ba	La	Ce	Nd	Tl(ICP)	Pb
39725	279.55	18.3	1105.1	37	93.1	38.7	0	1.9
39726	249.87	15.1	440.2	18.9	44.2	19.4	0	3
39726	0	-1.41	-612.6	-15.85	-43.65	-17	0	1.46
39764	268.16	16.6	937.6	51.5	109.2	45.6	0.5	4.5
39770	271.47	16.6	858.8	40.9	92.1	39.3	0	2.5
39771	264.94	15.8	986.2	46.4	106.6	43.1	0	4.6
39775	268.67	15.7	380.9	34.1	75.3	31.7	1.5	3.5
39770	0	-0.2	-89.29	-11.1	-18.23	-6.78	-0.5	-2.03
39771	0	-0.61	60.59	-4.54	-1.3	-1.98	-0.5	0.16
39775	0	-0.93	-557.43	-17.47	-34.04	-13.96	1	-1.01
39780	249.31	15.8	692.9	44.7	102.4	43.5	0.7	10.7
39779	236.89	15.4	430.5	5.5	13.2	5.7	0.5	5.6
39781	244.26	16	1378.7	35.6	83.4	35.2	0.7	19.4
39782	219.12	14.6	730.3	41.3	89.1	36.9	0	2.9
39783	222.7	15.1	652.6	18.5	43.7	18.7	0	3.6
39784	227.7	14.9	1162.9	36	82	34.3	0	1.7
39779	0	0.41	-239.81	-38.91	-88.51	-37.5	-0.17	-4.81
39781	0	0.53	714.31	-8.36	-17.28	-7.57	0.01	9.1
39782	0	0.81	138.04	2.29	-1.02	-1.52	-0.7	-7.4
39783	0	1.1	37.7	-23.99	-53.48	-22.57	-0.7	-6.67
39784	0	0.51	580.37	-5.28	-12.62	-5.94	-0.7	-8.84
109R1	242.3	16	737.2	146.9	307.9	112.5	0	2.4
109R3	295.14	19.4	697.5	38.6	81.7	29.4	0	2.7
109R3	0	-0.07	-164.59	-115.21	-240.83	-88.36	0	-0.18
109R5	284.52	17.2	1119.1	9	22.6	9.2	0.6	3.2
109R11	192.99	13.4	1160.3	49.3	116.8	45.6	0.6	4
109R11	0	2.56	591.49	63.68	149.59	58.03	0.28	2.7
STP218-16.5	215.9	11.2	680.2	27	60	29.5		50.68
STP218-39.2	214.2	11.6	756.5	31.4	65.9	29		14.59
STP218-39.2	0	0.49	82.3	4.65	6.42	-0.27	0	-35.97
EHP319-245.2	248.3	13.9	901.1	37.7	80.2	36		2.6
EHP319-296.6	249.1	13.3	1078	39.2	90.2	41.8		5.92
EHP319-296.6	0	-0.64	173.44	1.37	9.71	5.67	0	3.3
BY2-53.5	189.7	10.5	762.7	37	80.8	34		7.78
BY2-98.3	188.2	11.1	674.3	34	78.4	37.9		1.87
BY2-98.3	0	0.69	-83.03	-2.73	-1.78	4.2	0	-5.9
80R-388.5	191.2	8	783.3	26.5	57.7	26.5		4.59
80R-394.2	186.9	10.3	643.9	37	70.1	30.1		2.88
80R-358.2	200.3	10.9	605.7	35.2	75.6	31.9		6.86
80R-351.5	184.2	10.6	555.2	31.8	63.9	27.7		8.97
80R-394.2	0	2.54	-124.59	11.35	14.01	4.29	0	-1.64
80R-358.2	0	2.4	-205.12	7.1	14.47	3.95	0	1.96
80R-351.5	0	3	-207	6.51	8.63	2.25	0	4.72

Appendix 3. cont.

Sample	Bi (ICP)	Th (XRF)
39725	0.1	20.2
39726	0	19.4
39726	-0.1	1.5
39764	0.4	19.8
39770	0.2	22
39771	0.1	20
39775	0	18.4
39770	-0.2	1.93
39771	-0.3	0.44
39775	-0.4	-1.44
39780	0	20.6
39779	0.1	18.9
39781	0	22.7
39782	0	18.6
39783	0	18.1
39784	0	19.1
39779	0.11	-0.71
39781	0	2.57
39782	0	0.56
39783	0	-0.34
39784	0	0.31
109R1	0.2	22.3
109R3	0	22.2
109R3	-0.2	-4.07
109R5	0	20.2
109R11	0.2	15.5
109R11	0.29	2.65
STP218-16.5		13.6
STP218-39.2		11
STP218-39.2	0	-2.51
EHP319-245.2		20.2
EHP319-296.6		20.3
EHP319-296.6	0	0.03
BY2-53.5		16.4
BY2-98.3		16.6
BY2-98.3	0	0.33
80R-388.5		15.9
80R-394.2		15.5
80R-358.2		16.5
80R-351.5		15.8
80R-394.2	0	-0.04
80R-358.2	0	-0.15
80R-351.5	0	0.5

Influence of volcanic facies on hydrothermal and diagenetic alteration: Evidence from the Highway–Reward deposit, Mount Windsor Subprovince, Queensland

Mark G. Doyle
Centre for Ore Deposit Research

Introduction

Highway-Reward is a sub-seafloor Cu-Au pipe-style volcanic-hosted massive sulfide (VHMS) deposit located in the Cambro-Ordovician Mount Windsor Subprovince of northern Queensland. A detailed study of the Highway-Reward deposit has provided insights into the role of volcanic facies and textures in influencing the distribution, form and mineralogy of massive sulfide mineralisation and associated hydrothermal and diagenetic alteration. In this section, the results of preceding reports (Doyle, 1995, 1996, 1997a,b,c) are combined into a synthesis addressing the various elements controlling hydrothermal alteration and mineralisation at Highway-Reward. The results of the research have application to other parts of the Mount Windsor Subprovince and comparable volcanic successions (e.g. Mount Read Volcanics).

Interpreting timing relationships of alteration in volcanic rocks

Alteration is defined as a change in the mineralogy or texture of a rock facilitated by the action of hot or cold aqueous solutions or gases. All volcanic facies in the host succession to the Highway-Reward deposit have been altered. These include mineralogical and textural changes resulting from emplacement (hydration, devitrification), diagenetic alteration and compaction, metamorphism and hydrothermal alteration. Each represents an *alteration stage* although the time between each stage may be very short or even overlap and several stages may be unimportant or not affect all parts of a volcanic deposit/rock. Several *steps*, each recorded by a characteristic mineral assemblage, are often involved in forming the alteration texture which characterises each stage.

Determination of the relative roles, timing and significance of each alteration stage in modifying a volcanic rock or facies is dependant on: (1) establishing the regional extent of mineral assemblages; (2) interpreting overprinting relationships of alteration minerals to primary volcanic textures, volcanic facies and intrusive units; (3) relation of alteration minerals and assemblages to tectonic, diagenetic and stylolitic foliations; (4) overprinting relationship between different alteration mineral assemblages; (5) consideration of mineral stability fields; and (6) knowledge of alteration assemblages in comparable modern volcanic successions (e.g. Green Tuff Belt, Japan; Table 1).

Graphic log technique

Detailed drill core logging of alteration and volcanic facies allow for investigation of the interplay between primary volcanic texture, the texture and mineralogy of each alteration stage, and mineralisation (Fig. 1). Textural relationships between each alteration stage and the pre-alteration texture, mineral abundances and associations, and chronology have been recorded using a code system which is outlined in Figure 2. Graphic lithological logs incorporating alteration codes are an effective means of establishing spatial and temporal relationships between volcanic textures, facies and alteration assemblages as the information is visible at a glance (Fig. 1; Doyle, 1995, 1997b). This approach has been successfully used to investigate alteration in lava- and intrusion-dominated volcanic centres (e.g. Highway-Reward; Doyle, 1995, 1997a,b) and in pumice-dominated host successions to massive

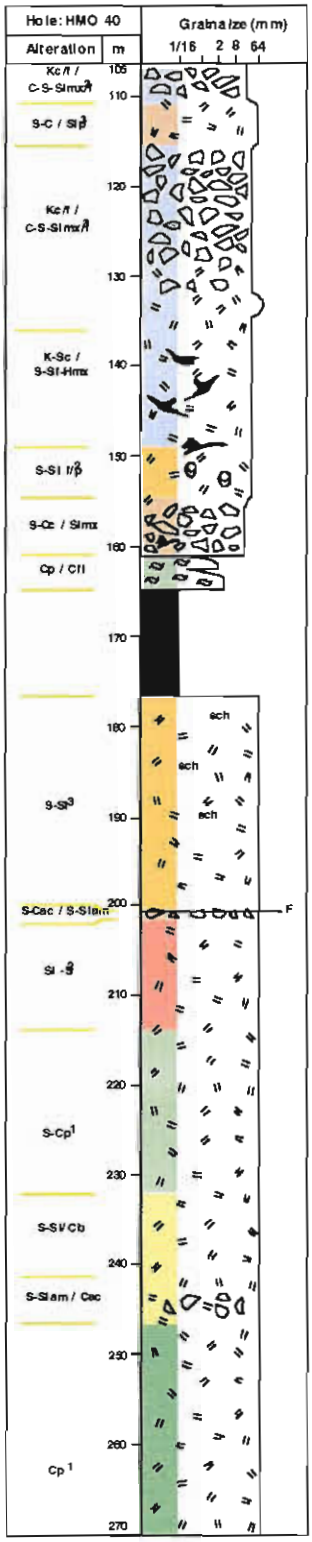

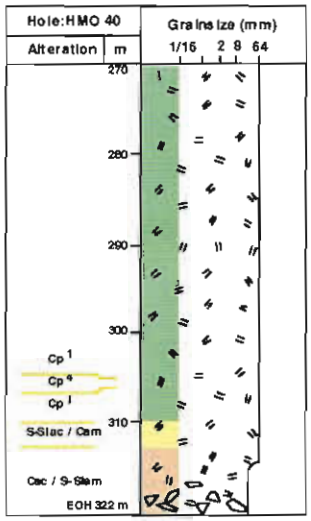

Lithology

- Rhyolite
- Perlite
- Non-stratified monomictic breccia (hyaloclastite)
- Siltstone-matrix-poor breccia (peperite)
- Siltstone seams in coherent facies
- Massive pyrite-chalcopyrite±sphalerite
- Pumice breccia
- F — Fault

Alteration

- Sericite-quartz
- Quartz-sericite
- Sericite-quartz-chlorite
- Sericite-chlorite
- Chlorite
- Chlorite-sericite-quartz
- Albite/K-feldspar-sericite-quartz-chlorite

Figure 1. Graphic log for diamond drill hole HMO 40. Alteration codes as outlined in Figure 2.

Figure 2: Facies codes for alteration in volcanic rocks (Doyle, 1995)

(a) Phase(s)

• mineralogical and textural changes accompany hydrothermal alteration. Each alteration mineral can be referred to as a phase.
• each alteration domain comprises an area of rock that is characterised by a particular alteration mineral assemblage or by different proportions of similar minerals (phases) in similar mineral assemblages.

C	- chlorite	S	- sericite
SI	- quartz	K	- albite/K-feldspar
H	- hematite	CB	- carbonate
PY	- pyrite		

e.g. SI-S quartz-sericite (alteration domain comprising quartz and sericite)

(b) Relative abundance (phases - domains)

• the least abundant mineral within an alteration domain is presented on the right hand side (RHS) and the most abundant mineral on the left hand side (LHS).

e.g. S-SI (sericite-quartz) dominant phase - subordinate phase

• in a rock comprising two or more alteration domains, the phase(s) comprising the dominant domain are presented on the LHS and those of the remaining domains on the RHS in order of relative abundance

e.g. C / S-SI (chlorite & sericite-quartz domains) dominant - subordinate

(c) Intensity

• allocation of a number to describe the intensity of alteration within each domain

Weak (1-2) Moderate (3-4) Strong to intense (5-6)

• e.g. C^5 (strong chlorite alteration)
$S\text{-}SI^3$ (moderate sericite-quartz alteration)

(d) Controls/textures

The distribution of alteration minerals and domains can be controlled by the pre-alteration texture or superimposed structures. Alternatively, the alteration phases/ domains can generate a range of new textures and patterns in the rock.

x	- crystal	am	- apparent matrix	pt	- patchy
mx	- matrix	ac	- apparent clast	s	- spotty
c	- clasts	mo	- mottled	sh	- shear
fr	- fracture (perlite, quench)	w	- wash	v	- vein
hf	- hydraulic fracture	fi	- fiamme	d	- disseminated
fb	- flow banding	k	- fleck		

• e.g. Cp^5 (strong pervasive chlorite alteration)

• e.g. Cp^5 / $SIfr^3$ (strong pervasive chlorite alteration and moderate, fracture-controlled quartz alteration)

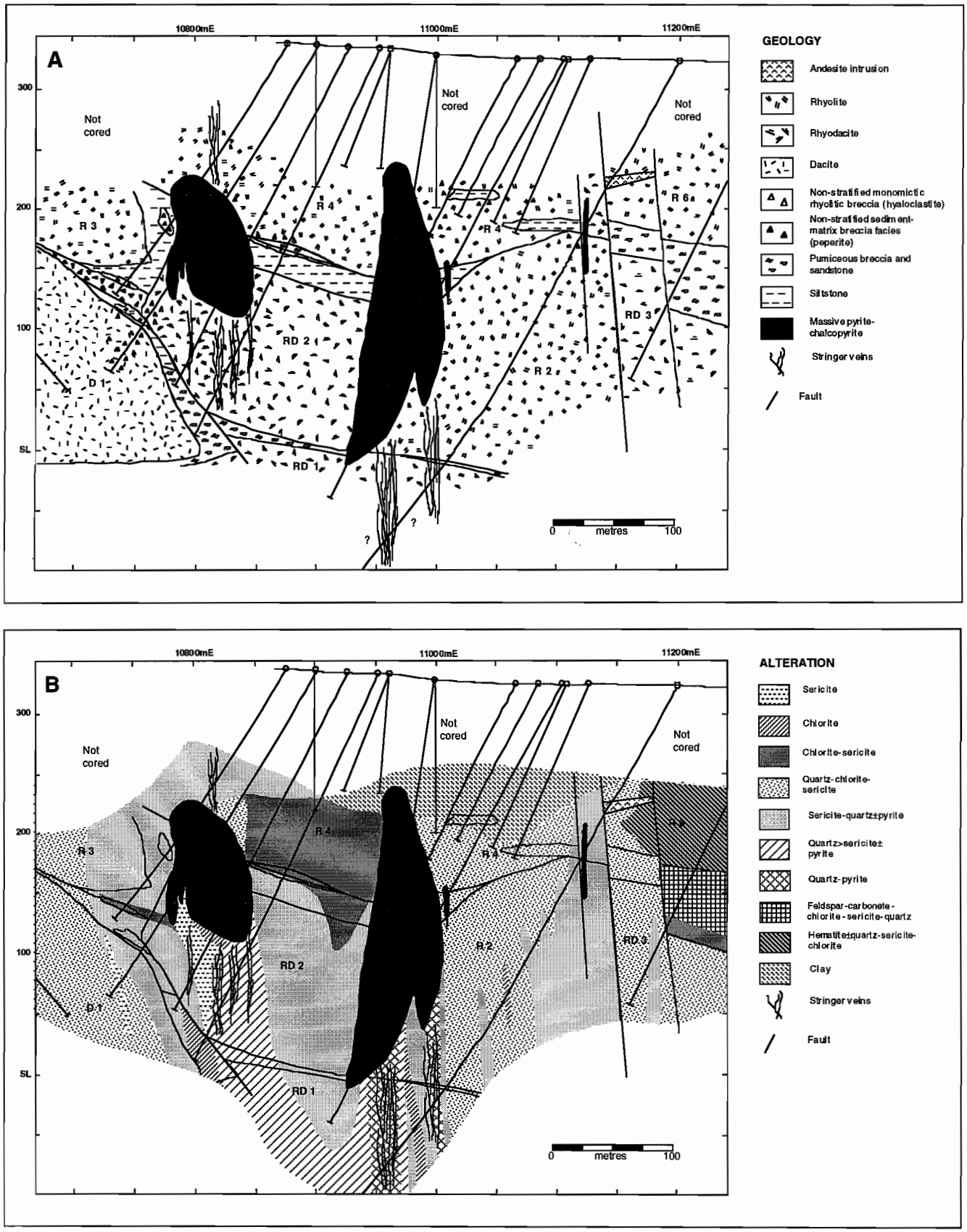

Figure 3. Simplified geological cross section showing the distribution of (A) lithofacies and (B) alteration at 10150N. The position of the massive sulfide bodies is also shown. Dacite D1, rhyodacites RD1-RD3 and rhyolites R2-R4 and R6 are exposed on section 10150mN (after Doyle, 1997b).

Table 1. Timing relationships of alteration in volcanic rocks (after Allen and Large, 1996)

Relationship	Interpretation
(1) Relationship of alteration to primary volcanic texture	
Alteration truncated by clast margins	Pre-fragmentation
Clasts of different alteration types in same rock	Pre-deposition
Infills primary porosity ± rims clast margins	Pre-lithification
Rock has relict high-temperature devitrification textures	Post-devitrification
(2) Relation to successive volcanic units/intrusions	
Alteration assemblage cut by younger (less altered) units	Older syn-volcanic/intrusive
Overprints younger rocks	Syn- to post-younger facies
(3) Relation to diagenetic compaction	
Protects primary texture from compaction	Pre-compaction
Overprinted by early diagenetic minerals	Early diagenetic
Overprints late diagenetic minerals	Post diagenesis
(4) Relationship of hydrothermal alteration assemblages	
Overprinted by hydrothermal assemblages	Pre-hydrothermal alteration
Overprinted by early hydrothermal assemblages	Early hydrothermal
(5) Relationship to early stylolitic dissolution foliation	
Overprinted by stylolitic foliation	Pre-dissolution
Overprints stylolitic foliation	Post-dissolution
(6) Relation to tectonic foliations and lineations	
Cut by tectonic foliation	Pre-cleavage
Less deformed than tectonic foliation	Pre- to syn-cleavage
Undeformed	Post-cleavage
(7) Relationship to metamorphic assemblages	
Overprinted by metamorphic assemblage	Pre-metamorphic
Overprints metamorphic assemblage	Post-metamorphic
(8) Regional distribution	
Regionally distributed	Diagenetic or metamorphic
Stratabound in formerly permeable facies	Pre- to syn-lithification
Locus in fractured domain of coherent facies	Post-lithification & fracture
Restricted to faults or shears	Syn- to post-faulting

sulfide mineralisation (e.g. Liontown and Snake Oil; Doyle 1998a, Doyle, unpub. data).

Alteration mineralogy and textures

In the study area, felsic volcanic rocks have altered to various assemblages of sericite, muscovite, chlorite, quartz, feldspar (albite, K-feldspar), hematite, carbonate, rutile, talc, phrenite, pumpelyite, fuchsite, anhydrite, topaz and pyrophyllite. Mafic volcanic rocks have altered to assemblages of chlorite, epidote, sericite, quartz, feldspar, calcite, epidote and hematite.

Interpretation of alteration assemblages

Timing relationships suggest that 5 principal alteration styles are identifiable: (a) regional diagenetic alteration of formerly glassy volcanic facies; (b) "barren" alteration associated with local, "low temperature" hydrothermal systems; (c) syn-volcanic hydrothermal alteration concurrent with mineralisation; (d) regional metamorphic assemblages; and (e) quartz-topaz-pyrophyllite alteration. Summary descriptions and interpretations of each alteration style are presented in the following section. The exception is the quartz-topaz-pyrophyllite alteration, which is regarded as epigenetic and of a syn- to post-D4 (Siluro-Devonian) age.

Hydrothermal alteration

The Highway-Reward massive sulfide deposit is enclosed within a well-developed alteration pipe. The alteration pipe is discordant to local bedding and records the upward path of hydrothermal fluids that deposited sub-seafloor massive sulfide mineralisation. Three principal alteration zones have been identified (Fig. 3; Doyle, 1995; 1997a,b; Doyle 1998b): (1) an inner zone of sericite-quartz±pyrite alteration (Fig. 4A) is centred beneath the pyrite pipes and extends at least 60 m above the Highway orebody; (2) zones chlorite±anhydrite alteration (Fig. 4B-C) occur at the margins of the pyrite pipes within the sericite-quartz±pyrite zone; and (3) a sericite-chlorite±quartz alteration shell (Fig. 4D). The outer most alteration zone passes into background sericite-chlorite±feldspar±hematite±quartz alteration (Fig. 4E-H) interpreted as the greenschist facies metamorphic equivalent of early diagenetic and hydrothermal assemblages (below). In addition, sericite occurs through out the alteration envelope, but mostly within shear zones and as the gangue in massive sulfide.

The most intense hydrothermal alteration occurs within the sericite-quartz ± pyrite and chlorite ± anhydrite zones. Within these zones, alteration is pervasive or patchy and often masks or destroys original volcanic textures, creating apparent clastic textures. Relic quartz phenocrysts are often the only indication of the primary lithofacies character. Less intense alteration, as indicated by variable preservation of feldspar phenocrysts and delicate volcanic textures (e.g. perlite, uncompacted pumice) occurs within the sericite-chlorite±quartz zone and outside the hydrothermal alteration envelope.

A syn-volcanic hydrothermal origin for the alteration at Highway-Reward is indicated by: (1) the localised spatial association with the massive sulfide mineralisation; (2) the mineral assemblages are overprinted by the main S4 cleavage and shear zones; (3) the alteration envelope overprints earlier diagenetic alteration assemblages; and (4) similarities between the alteration zonation at Highway-Reward and other Australian VHMS deposits with well developed alteration pipes.

Regional diagenetic alteration

In the Trooper Creek Formation, regional diagenetic alteration is recorded by various assemblages of feldspar, carbonate, chlorite, sericite and quartz. The assemblages are regionally distributed and selectively replace the glassy parts of lavas and intrusions, pumiceous units and crystal-vitric breccia and sandstone beds. In pumiceous and shard-rich deposits, pyroclasts have altered to domains of feldspar±quartz and sericite-chlorite±hematite. The extent to which each alteration domain encloses, or is enclosed by, the other varies considerably. In feldspar±quartz altered domains, secondary feldspar or carbonate fills vesicles and has replaced formerly glassy vesicle walls. The alteration is nodular or coalescing nodules form pervasive and patchy feldspar±quartz±sericite±chlorite-alteration (Fig. 4E). Many pumice fragment margins and vesicles are outlined by sericite, chlorite or hematite (e.g. Doyle, 1996). In some samples, fine-grained mosaics of albite

and quartz replace optically continuous K-feldspar filling vesicles and replacing vesicle walls. The feldspar±quartz alteration often encloses phyllosilicate-altered domains which are typically strongly elongate and define a bedding-parallel diagenetic compaction (or early tectonic) foliation (Fig. 4F; cf. Allen and Cas, 1990). Other pumice beds have entirely altered to sericite-chlorite±hematite. In these beds, most pumice fragments are compacted generating an evenly porphyritic texture more typical of coherent lavas and intrusions.

In the glassy parts of lavas and intrusions, early feldspar-carbonate-chlorite alteration is typically pervasive or fracture controlled. More advanced phyllosilicate-dominated alteration generally spread outward from fractures or the matrix, overprinting earlier feldspar alteration (Fig. 4G).

The regional distribution of the feldspar-carbonate-chlorite-sericite-quartz alteration assemblages is consistent with an early diagenetic or regional metamorphic origin. The feldspar alteration protected some pumice clasts from diagenetic compaction, suggesting alteration occurred prior to, or during, diagenesis. The diagenetic compaction foliation is crenulated by the regional cleavage indicating that the alteration was complete prior to regional deformation. Sericite, chlorite and hematite which outlines pumice fragments and vesicles formed prior to infilling of vesicles and is interpreted as the greenschist facies equivalent of early diagenetic clay minerals (cf. Tazaki and Fyfe, 1992; Marsaglia and Tazaki, 1992).

The domainal feldspar-carbonate-chlorite-sericite-quartz alteration is similar to that documented by Allen and Cas (1990) in pumiceous breccia units at Rosebery and Hercules, in western Tasmania. It is considered likely that chlorite, sericite, albite and K-feldspar replaced earlier diagenetic minerals such as zeolites and smectite, which are the first formed minerals in comparable young volcanic rocks (e.g. Tazaki and Fyfe, 1992; Marsaglia and Tazaki, 1992).

Andesitic and basaltic andesite facies have altered to assemblages that are also interpreted as the greenschist grade equivalent of early diagenetic minerals. Lavas comprise euhedral pyroxene and feldspar phenocrysts and a groundmass of feldspar laths and interstitial chlorite (probably after glass). In scoriaceous deposits, former glassy scoria walls are now chlorite, sericite and calcite. A thin (10μ) rind of recrystallised quartz bounds many fragments. Quartz, chlorite, calcite alteration of clast margins generates smoother, rounder and more bulbous outlines, generating a more extensive apparent matrix domain. Vesicles are filled with calcite, chlorite, sericite, hematite or zones of quartz-chlorite or hematite-chlorite. Sericite, epidote and quartz often occur in the groundmass. Many scoria fragments have delicate margins and uncompacted vesicles suggesting that the calcite, quartz and hematite alteration occurred prior to significant compaction. Vesicles are lined by phyllosilicate minerals or hematite, recording an early alteration stage.

"Barren" hydrothermal alteration

A second common alteration style in the Trooper Creek Formation comprises hematite ± quartz ± sericite ± chlorite ± albite assemblages (e.g. Doyle, 1996, 1997b). The alteration is pervasive or domains of hematite, chlorite-sericite and chlorite-carbonate alteration generate patchy, mottled or pseudoclastic textures (Fig 4H). Both mafic and felsic coherent and volcaniclastic rocks have been overprinted by this alteration style. Formerly glassy, porous and permeable facies (e.g. pumice breccia beds, andesitic scoria breccia and fractured glassy lava) are particularly susceptible to hematite-rich alteration. In other cases, hematite overprints lamination and bedding within siltstone and crystal-vitric sandstone. The alteration is generally restricted to a single depositional unit or only a few beds.

Hematite-rich alteration is regionally distributed but forms discrete alteration domains ranging from a few metres wide to around 500 m across. The most widespread domains of hematite alteration are associated with quartz-hematite±sericite±chlorite lenses ("ironstone"). The best-exposed and most continuous example crops out at Trooper Creek prospect. At this locality, intense pervasive hematite alteration occurs beneath, sometimes above and as a lateral equivalent of stratabound ironstone lenses replacing dacitic pumice breccia (Doyle, 1996, 1997b). There are gradations from massive ironstone into tuffaceous ironstone with relic pumice, crystals, shards and microbialites into pervasively sericite-hematite±quartz-altered pumice breccia. In the ironstone lenses, formerly glassy pyroclasts are now

Figure 4

Examples of typical alteration features at Highway-Reward.

(A) Quartz-sericite ± pyrite zone. Drill core showing quartz-sericite ± pyrite alteration in lithofacies from the footwall (1) and hanging wall (2) of the Reward and Highway orebodies. REW 807, 434.7 m; REM 137, 168.9 m.

(B) Chlorite±anhydrite zone. Intensely chlorite-altered volcanic rock containing abundant euhedral anhydrite crystals (a). Core is 5 cm wide. HMO 41, 283.6 m; Reward.

(C) Chlorite±anhydrite zone. The foliation (arrow) wraps around the anhydrite (a) suggesting a pre- or syn-kinematic timing for anhydrite. Plane polarised light. HMO 41, 283.6 m; Reward.

(D) Quartz-chlorite-sericite zone. This breccia is strictly monomictic, comprising blocky and cuneiform dacite clasts (c) that form jigsaw-fit aggregates. Brecciation was probably caused by quench fracturing of a formerly glassy cryptodome, producing in situ hyaloclastite. Quartz-sericite alteration (q) along and adjacent to the matrix overprints earlier, pervasive chlorite-sericite alteration. Core is 5 cm wide. REM 560, 305 m; Highway.

(E) These three drill core samples come from a pumiceous, subaqueous mass-flow deposit. Cores 1 and 2 contain nodular domains (n) of albite alteration, separated by sericite-chlorite-altered pumice clasts (arrow). Alignment of compacted pumice clasts defines a bedding-parallel compaction foliation (S1). In core 3, nodules merge and form patches within the pumice breccia. Core is 5 cm wide. REW 805 (277.9-278.4 m).

(F) Samples of pumice breccia are composed of variably compacted pumice clasts and are non-welded. Sericite-chlorite-altered pumice clasts (c) are compacted around the more competent albite-altered pumice clasts (p) and define a diagenetic compaction foliation. The albite-altered pumice clasts have uncompacted tube vesicles (bar). Plane polarised light. REW 578, 203.7 m.

(G) The formerly glassy groundmass of this rhyolite contains relic classical perlitic fractures. The fractures are delineated by chlorite and sericite (c). The remainder of the glass has been replaced by albite (a) and quartz (q). Plane polarised light. REW 802, 183.1 m.

(H) These four samples are from a rhyolitic intrusion. In situ hyaloclastite (core 1) passes gradationally down into peperite comprising rhyolite clasts and a pumiceous matrix (core 2, 3). Clasts and the matrix in the breccia have been silicified, sericitised and hematite-altered (core 3). Pumice breccia away from the contact (core 4) is sericite-quartz-altered. Core is 5 cm wide. HMO 52, 146-160 m, Highway-Reward.

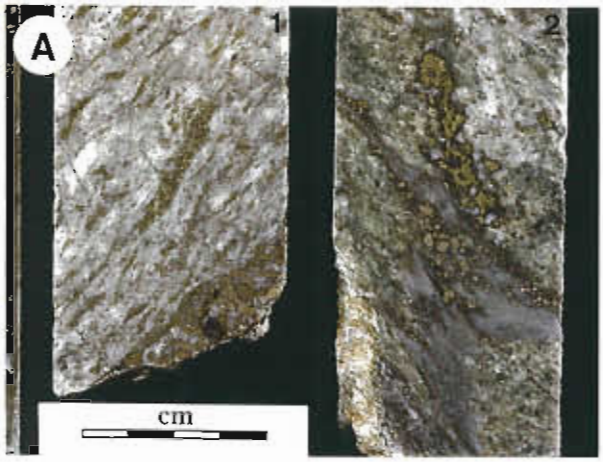
A
1
2
cm


B
a

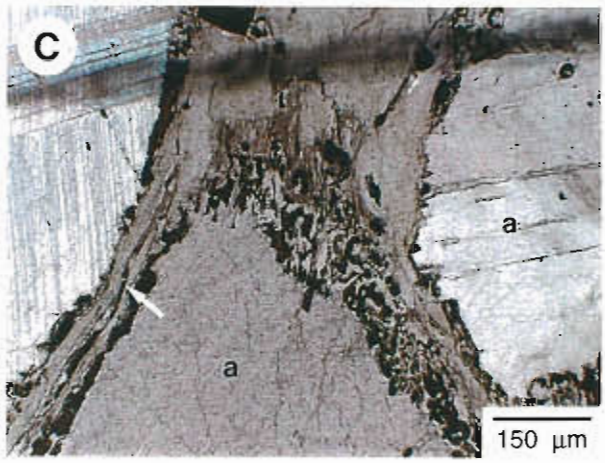
C
a
a
150 µm


D
q
c

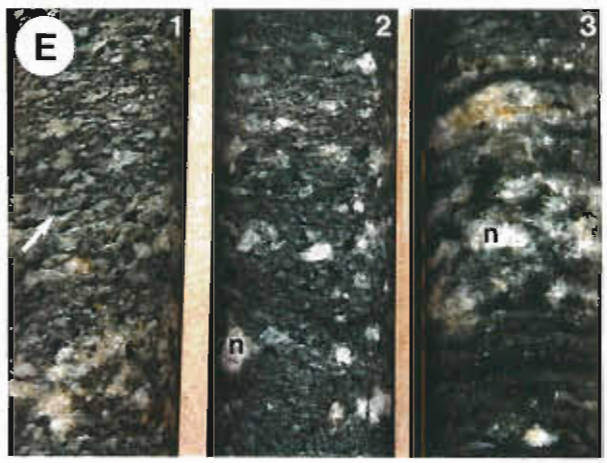
E
1
2
3
n
n

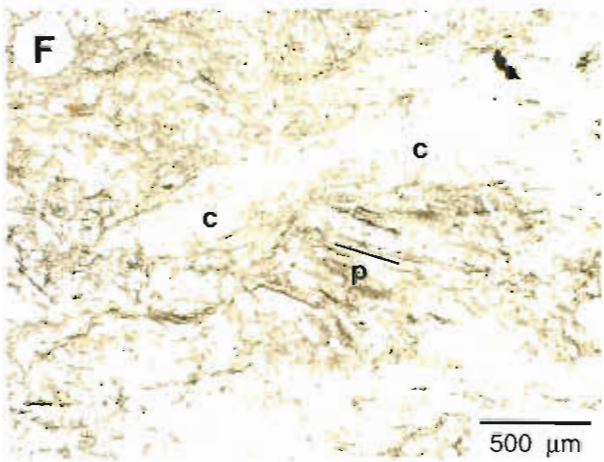
F
c
c
p
500 µm

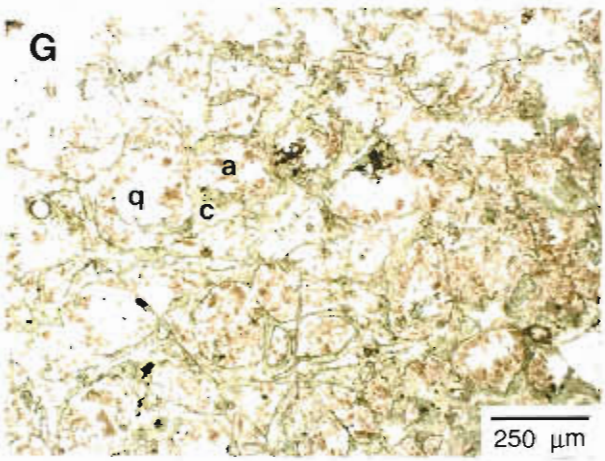
G
a
q
c
250 µm

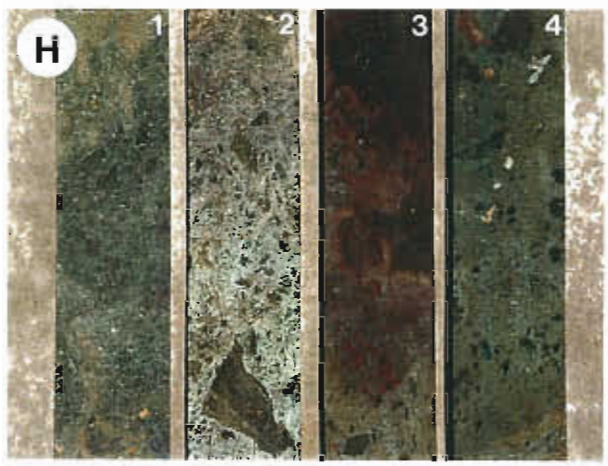
H
1
2
3
4

composed of hematite±quartz and vesicles and pyroclast margins are outlined by hematite. In areas of strong sericite-hematite alteration, the pumice fragments and vesicles within them are delineated by fine hematite. Many phyllosilicate-altered pumice fragments are compacted and deformed around feldspar crystals and occasional quartz-hematite-altered pumice and nodules. The compacted pumice define a bedding parallel foliation (S1) interpreted as an early diagenetic compaction foliation.

In the Trooper Creek ironstones, preservation of uncompacted pumice fragments and shards implies replacement by quartz and hematite prior to significant compaction. Hematite outlines many vesicle walls, pyroclast margins and microbialite structures. As pyroclasts and vesicle walls are now quartz or sericite, an early phase of hematite alteration is recorded. Cuspate patches of hematite between quartz-altered pyroclasts probably deposited later. The ironstone lenses are interpreted to mark the seawater-mixing zone, whereas the hematite-sericite alteration may mark diffuse feeder zones within the sub-seafloor strata.

Trace and rare earth element patterns for many of the ironstones (Type 2 ironstones, Doyle, 1997b), including those at Trooper Creek prospect, suggest that they are distinct from ironstones which are spatially and genetically associated with massive sulfide mineralisation at Thalanga (Type 1 ironstones, Doyle, 1996, 1997b; cf. Duhig et al., 1992; Davidson et al., 1996). Type 2 ironstones and associated hematite-rich alteration deposited from oxidised, alkaline/neutral, "low" temperature hydrothermal fluids passing through the volcanic pile. In lava- and intrusion-dominated volcanic centres, type 2 ironstones and hematite alteration are interpreted to have formed from low temperature fluids circulating within lavas and intrusions (cf. Einsele et al., 1980; Einsele, 1986; Boulter, 1993a,b). The convecting pore water leached Fe, Si, and other elements from the glassy volcanic rocks and reprecipitated the iron and silica by conductive cooling and mixing with seawater in the enclosing volcanic package (cf. Sigurdsson, 1977). The same hydrothermal systems may have been important in contributing elements for regional diagenetic feldspar alteration.

Regional metamorphic assemblages

Regional mapping and petrographic studies suggest that the Seventy Mile Range Group has been affected by low to medium grade regional metamorphism (Hutton et al., 1993; Henderson, 1986; Berry et al., 1992). There is a gradation in metamorphic grade from prehnite-pumpellyite facies around Trooper Creek prospect in the east, to greenschist facies in the central part of the subprovince near Highway-Reward (Berry et al., 1992; Doyle, 1997b). To the west around Trafalgar Bore and Thalanga, metamorphic grade increases through actinolite, hornblende, biotite and andalusite isograds to amphibolite facies at Waddys Mill. The regional metamorphic assemblage is correlated with deformation event D3 and regional S3 cleavage development (Berry, 1991; Berry et al., 1992).

Alteration geochemistry

A detailed analysis of trace and major element variations of the principal alteration styles is presented by Doyle 1998b (this volume). The research demonstrates that the hydrothermal alteration envelope surrounding the Highway-Reward deposit is geochemically anomalous relative to the "background" alteration types. The Ishikawa Alteration Index, Chlorite-carbonate-pyrite index (CCPI) and box plots are an effective means of distinguishing the different alteration types. Also useful are plots of CaO, Na_2O, MgO and K_2O and ratios of Rb/Sr, S/Na_2O and Sr/Ba. Furthermore, AlOH wavelength values for the Highway-Reward alteration envelope are anomalously low (2202 to 2222) in comparison with feldspar-sericite-chlorite and hematite-rich samples (2195 to 2212).

Alteration of coherent lavas and intrusions

In zones of weak to moderate alteration, textural evidence suggests that primary volcanic textures and facies strongly influenced the passage of diagenetic and hydrothermal fluids and the subsequent distribution of alteration minerals. In the following section, the textural effects of diagenetic and

hydrothermal alteration on lavas and intrusions are briefly discussed and summarised in Figures 5 to 7. A diverse range of mineralogical and textural permutations are present and the following summary dose not aim to document all those identified during the study. Furthermore, is likely that some of the present mineral assemblages are the greenschist grade metamorphic equivalent of earlier minerals which may have included clay, zeolites, mica, feldspars, quartz and carbonate (e.g. McPhie et al., 1993; above).

Primary texture and zonation

Petrographic studies of lavas and syn-sedimentary intrusions from Highway-Reward indicate that prior to diagenetic and hydrothermal alteration, the rhyolites to dacites comprised glassy margins. The margins are often peperitic or comprise coherent and hyaloclastite facies. The originally glassy margins pass inward to cores characterised by zones of glass, glass with coalescing spherulites and/or crystalline domains characterised by spherulitic, micropoikilitic and granophyric textures. The distribution of these facies has strongly influenced the texture and distribution of diagenetic and hydrothermal alteration assemblages (cf. McPhie et al., 1993).

Glassy margins and zones

The originally glassy margins display a complex history of successive alteration stages. Fracture and matrix permeability strongly influenced the final distribution of alteration minerals. The glassy domains originally comprised coherent volcanic glass (Fig. 5.1A), in situ quench fractured glass (Fig. 5.1B) and variably matrix-rich autoclastic (hyaloclastite, autobreccia) breccia facies (Fig. 5.1C). After emplacement and late in the cooling history of glass, or following cooling to surface temperatures, perlitic cracks sometimes developed in response to hydration of the glass. Circulating fluids moved out from fractures (perlitic, quench) and the matrix progressively altering the glass in several stages. The initial alteration was either pervasive (Fig. 5.3.2) or ceased before completely affecting the whole rock, leaving domains of glass that were altered during a second alteration step or stage (Fig. 5.4.1).

Outside the Highway-Reward hydrothermal alteration envelope, perlite kernels and clasts in autoclastic breccia have often completely altered to feldspar (albite) during initial diagenetic alteration. Later sericite, chlorite or quartz alteration often commenced along fractures and moved out from these into the albite-altered domains (Fig. 4G). Elsewhere, initial chlorite alteration extended out from fractures into all the glassy parts. Subsequent generations of sericite and/or quartz alteration overprinted earlier phyllosilicate alteration and were also fracture controlled. In some samples, feldspar alteration has been partially replaced by quartz±feldspar. The result in hand specimen and thin section, is abundant cuspate shaped domains which resemble shards in pyroclast-rich rocks (cf. Allen, 1988; McPhie et al., 1993).

A similar style of alteration characterises glassy facies within the Highway-Reward hydrothermal alteration envelope. Hyaloclastite clasts often pervasively sericite-chlotite-altered and feldspar phenocryst are variably sericite, chlorite and/or carbonate-altered. Subsequent quartz-sericite alteration commenced along fractures and the matrix of autoclastic breccia (Fig. 4D; Fig. 5.4.2). In other cases, perlitic fractures and the matrix between clasts have altered to sericite, whereas perlite kernels have altered to fine quartzo-feldspathic mosaics (HMO 40, 158.5m). More advanced alteration rarely extends far from the fractures or matrix, possibly due to the reduction in porosity accompanying initial alteration stages.

Mixed glassy and devitrified domains

Prior to alteration, mixed glassy and devitrified domains comprised devitrification structures (spherulites, lithophysae) scattered in glass (Fig. 6.1A), coalescing spherulites enclosing cuspate patches of residual glass (Fig. 6.1B), and flow bands of glass alternating with devitrified bands (Fig. 6.1C). Hydrothermal and diagenetic alteration of the glassy domains has progressed along a similar path to the glassy margins (Fig. 6.3). Most often the glass has altered to assemblages of sericite, chlorite, feldspar and sometimes carbonate or micropoikilitic quartz, whereas phenocrysts are now sericite, albite or chlorite. In contrast, crystalline and devitrified domains are silicified or have recrystallised to quartzo-feldspathic mosaics (Fig. 6.4). Relic radial fibrous textures are preserved in some spherulites. The original bulbous outline of the bands is generally

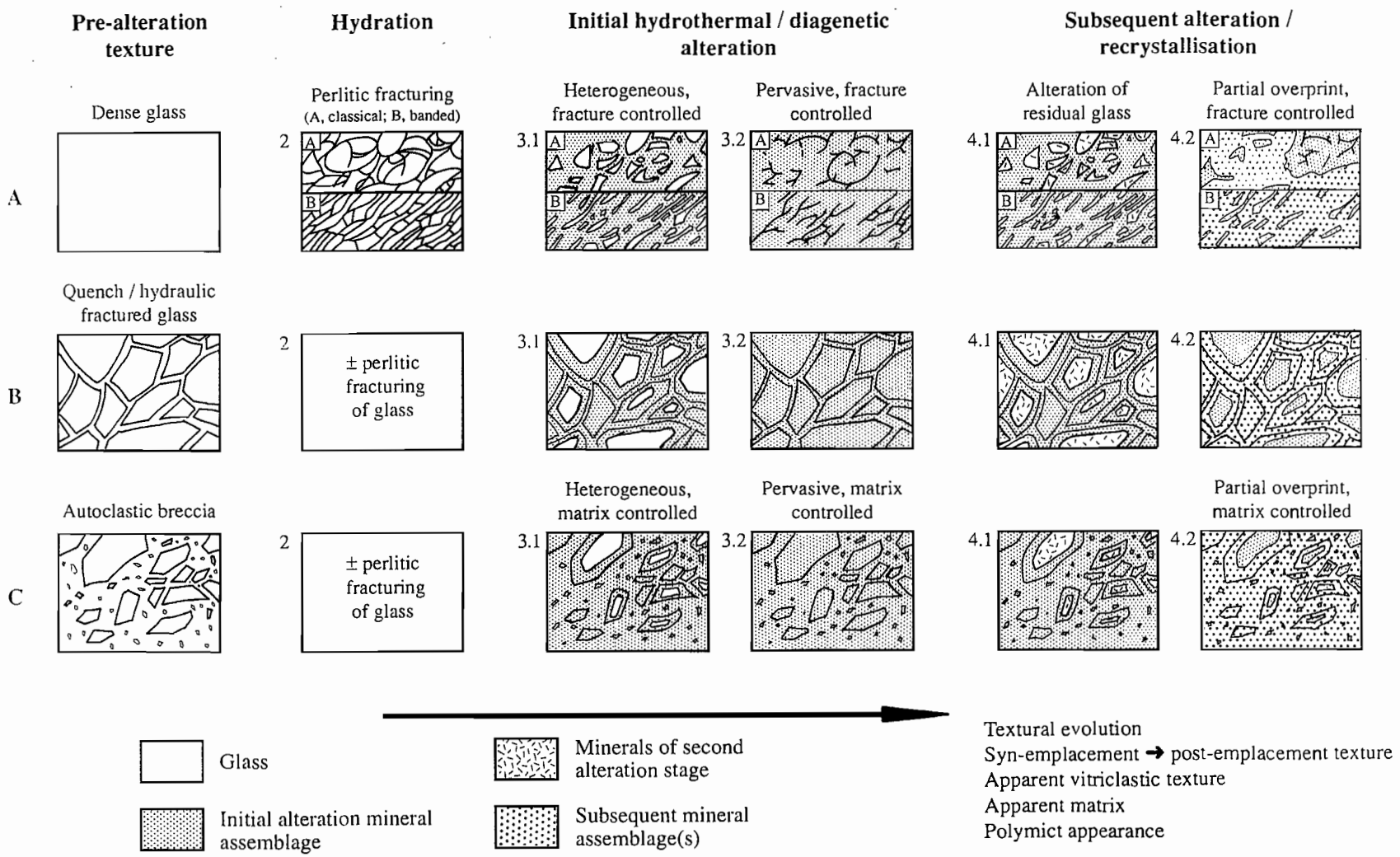

Figure 5. Stages in the textural evolution of the glassy margins of lavas and syn-sedimentary intrusions. 1— Prior to the onset of alteration the glassy margins comprised: (1A) dense glass; (1B) quench fragmented glass; and/or (1C) autoclastic breccia. 2— After emplacement and late in the cooling history of glass, or following cooling to surface temperatures, perlitic cracks sometimes developed in response to hydration of the glass. The cracks can be arcuate and concentrically arranged (classical perlite) or form rectilinear networks (banded perlite). 3— Initial hydrothermal or diagenetic alteration can proceed by a combination of fracture and/or matrix-controlled alteration or pervasive alteration. Two cases arose: (3.1) Alteration minerals progressively replaced glass out from perlitic fractures (3.1A), quench fractures (3.1B) or the matrix in autoclastic breccia (3.1C). However, the alteration was incomplete, leaving isolated kernels or domains of glass. (3.2) Alteration commenced along fractures and progressed right through the glass generating a pervasive alteration style. 4— Subsequent alteration and recrystallisation. In cases where the first alteration stage was incomplete, residual glassy cores were replaced during the second alteration stage(4.1). Subsequent alteration was also mainly localised along fractures or the matrix of autoclastic breccia or overprinted alteration domains of similar mineralogy (4.2).

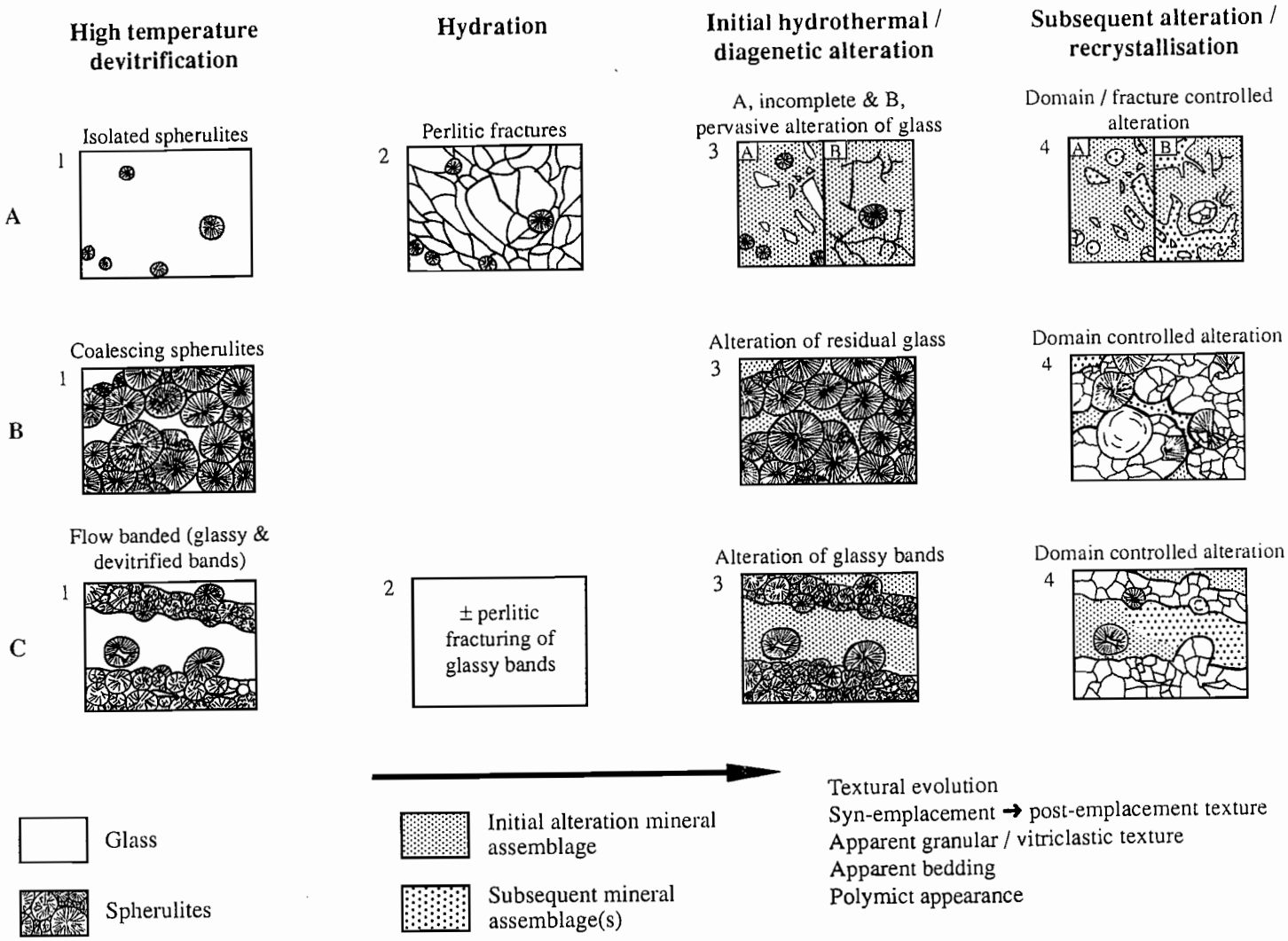

Figure 6. Stages in the textural evolution of the mixed glassy and devitrified domains in lavas and syn-sedimentary intrusions. 1— Prior to the onset of alteration the mixed glassy and spherulitic zones comprised: (1A) glass with scattered spherulites; (1B) coalescing spherulites with cuspate areas of glass; and/or (1C) devitrified bands alternating with glassy bands. 2— After emplacement perlitic cracks sometimes developed in glassy bands. 3— Initial hydrothermal or diagenetic alteration of the glassy domains was similar to alteration in the glassy margins. Alteration was fracture controlled or pervasive and trended towards sericite- or chlorite-rich assemblages (6.3). 4— Subsequent alteration of the glassy domains was also mainly localised along fractures or overprinted alteration domains of similar mineralogy (6.4). In contrast, single spherulites and bands or nodules of devitrification structures were recrystallised, silicified or replaced by feldspar during alteration (6.4).

preserved, even when radial fibrous textures are completely recrystallised. The exception is in zones of intense hydrothermal alteration, where patchy and mottled textures are common.

In autobreccia facies, clasts are often flow banded and show a similar alteration history. Apparent polymictic breccia textures sometimes develop as alteration mineralogy varies between clasts in response to different degrees of devitrification and overprinting alteration. Phenocrysts are often obscured in quartzo-feldspathic bands and accentuated in formerly glassy phyllosilicate domains. This sometimes results in apparent variation in phenocryst abundance between domains or clasts, and so apparent polymictic textures.

Crystalline domains

Large parts of some lavas and intrusions have a groundmass comprising spherulites, micropoikilitic texture or granophyric texture. In many samples, hydrothermal alteration and metamorphism have recrystallised original fibrous devitrification textures to pale quartzo-feldspathic mosaics with interstitial sericite±hematite±pyrite (Fig. 7.3-7.5). Other spherulites are now monocrystalline quartz or comprise a few subgrains (e.g. REW 600, 245.5m). Outside the hydrothermal alteration envelope, devitrification textures are better preserved and comprise feldspar and quartz with interstitial sericite and chlorite. The result in hand specimen is a granular texture (e.g. HMO 86, 169.3m).

Moderate to strong hydrothermal alteration generates mottled and patchy domains of different mineral assemblages. Feldspar phenocrysts are variably altered to sericite, chlorite, pyrite, quartz and carbonate. This alteration style often generates apparent clastic and polymictic textures.

Implications

The final texture and mineralogy of volcanic facies evolves as diagenetic alteration, hydrothermal alteration and metamorphism act on the primary texture. The textural progression is often preserved and can be traced by careful hand specimen and thin section studies. The influence of each process in modifying the primary texture varies between localities so that different parts of the volcanic succession or single unit (e.g. a lava or syn-sedimentary intrusion) can vary markedly in texture, mineralogy and appearance. In lavas and syn-sedimentary intrusions, vesiculation, crystallisation, devitrification and hydration combine to generate a complex textural zonation, which strongly influences subsequent mineralogical and textural changes during diagenetic and hydrothermal alteration and metamorphism. The polyphase alteration often generates apparent clastic textures which can resemble those of pyroclastic rocks (cf. Allen, 1988; McPhie et al., 1993; Doyle et al., 1993).

Controls on the localisation of hydrothermal alteration

Hydrothermal alteration involves dissolution, replacement, infilling of pore space, and precipitation of minerals along fluid pathways. Consequently, the shapes, dimensions and distribution of hydrothermal circulation (and therefore alteration and mineralisation) are closely related to the initial patterns of permeability and compositional contrasts in the volcanic host rock. In the context of VHMS deposits, principal pathways for hydrothermal fluids may include syn-volcanic faults, porous and permeable volcaniclastic facies and the glassy margins of lavas or syn-sedimentary intrusions (Doyle, 1997a,b).

Influence of lithofacies associations

Many massive sulfide deposits are hosted by rapidly emplaced units, particularly pumiceous facies (e.g. Khin Zaw and Large, 1992; Allen, 1994; Allen et al., 1996). The originally highly porous, permeable, water saturated and glassy nature of these lithofacies make them favorable host rocks for the formation of sub-seafloor replacement massive sulfide mineralisation (Fig. 8; Rosebery, Hercules (Allen, 1994), Liontown (Miller, 1996; Doyle, unpub. data). Ascending hydrothermal fluids will be poorly focussed and permate through the substrate to produce wide-spread strata-bound alteration and lens- or sheet-style massive sulfide mineralisation (cf. Large, 1992). Sulfide deposition is interpreted to commences at the interface between the ascending hydrothermal fluid and overlying cold, seawater-saturated strata (e.g. Khin Zaw and Large, 1992; Allen et al., 1996) or at the seafloor (e.g. Large, 1992).

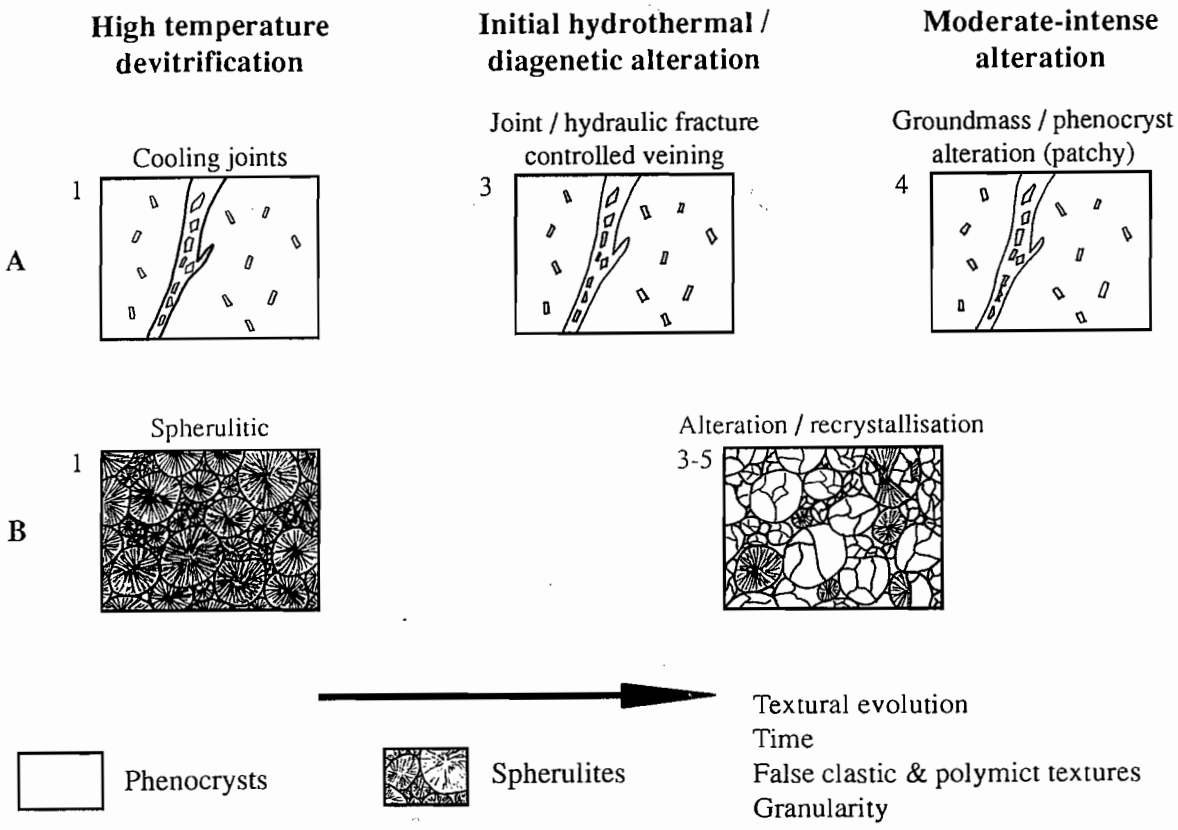

Figure 7. Stages in the alteration of the crystalline and devitrified domains in lavas and syn-sedimentary intrusions. 1— These domains have a groundmass of closely packed spherulites, microlites or micropoikilitic quartz. Joints are sometimes present. 3— Diagenetic and hydrothermal alteration often commence along joints or hydraulic fractures. 4— Subsequent alteration attacked phenocrysts (e.g. feldspar) and generated patchy and mottled textures. 5— Recrystallisation and silicification of spherulites during hydrothermal alteration and metamorphism destroys fibrous devitrification structures generating a quartzo-feldspathic mosaic.

Within less permeable, syn-sedimentary intrusion- and lava-dominated volcanic piles fluids are likely to be focussed along faults, local autoclastic breccia intervals, or within the fractured glassy margins of lavas and/or intrusions (cf. Large, 1992). Under these circumstances, well focussed fluid flow gives rise to lens- or pipe-shaped massive sulfide deposits and well developed, zone alteration pipes (Fig. 8; Highway-Reward; Doyle, 1997a,b). Massive sulfide deposition probably commences beneath a relatively impermeable barrier (e.g. massive crystalline/devitrified lava) and grows downward by mixing with seawater convecting through the fractured, glassy, porous and permeable parts of lavas and shallow intrusions and volcaniclastic deposits. In the absence of a barrier, ascending hydrothermal fluids are more likely to reach the seafloor, and may well form a seafloor massive sulfide deposit.

In VHMS host successions comprising mixtures of relatively poorly porous rocks (e.g. lavas and shallow intrusions) and incompetent, very porous deposits (e.g. pumiceous units), a variety of mineralisation types and alteration styles may develop in close proximity. Figure 8 summaries the main attributes of some types of massive sulfide deposits and alteration styles. It does not aim to present a comprehensive account of all possible scenarios for VHMS mineralisation, but simply to highlight the spectrum of deposit style and alteration halos which may form and their relationship to the enclosing strata.

Influence of syn-volcanic intrusions

The dominance of syn-sedimentary intrusions in the Trooper Creek Formation between Highway-Reward and Highway South prospect probably significantly modified the physical environment and pore-fluid properties in these parts of the basin. Deformation, disruption, dewatering, resedimentation and low-grade metamorphism of the enclosing sediment probably accompanied emplacement of the intrusions (cf. Einsele et al., 1980; Delaney, 1982; Kokelaar, 1982; Duffield et al., 1986; Hanson, 1991; McPhie, 1993; Davis and Becker, 1994; Brooks, 1995). Quenching of the cryptodomes generated abundant glassy, perlitic, fractured coherent and breccia facies, and slumping at the margins of some partly extrusive cryptodomes introduced small volumes of glassy detritus into flanking environments. These porous and permeable facies may have acted as conduits for connate and hydrothermal fluids circulating beneath the seafloor.

In the Trooper Creek Formation, emplacement of syn-sedimentary intrusions locally deformed bedding in the enclosing volcano-sedimentary sequence (cf. Pollard et al., 1975; Lorenz, 1984; Duffield et al., 1986; Krynauw et al., 1988) and updoming of sediment above the intrusions sometimes generated seafloor topography (cf. Yamamoto et al., 1991; Davis and Villinger, 1992). Young submarine sediment mounds associated with high level syn-sedimentary intrusions and massive sulfide mineralisation have been mapped in the Middle Valley rift of the northern Juan de Fuca Ridge using seismic reflection, SeaBeam bathymetry and SeaMARC side-scan imagery (Davis and Villinger, 1992; Goodfellow and Franklin, 1993). Faults generated during updoming of sediment above syn-sedimentary intrusions not only localise the sediment deformation but focus convecting hydrothermal fluids (and so the hydrothermal alteration; e.g. Denlinger and Holmes, 1994). At Highway-Reward, the density of syn-sedimentary intrusions suggests that this was probably important.

The peperitic margins of the syn-sedimentary intrusions suggest that the earliest response of intrusion was fluidisation of wet sediment in the interfacial zone. Fluidisation implies a change in the temperature, pressure and density of pore water at the contact (Kokelaar, 1982). Heat released from syn-sedimentary intrusions may have also modified pre-existing circulation patterns (cf. Einsele et al., 1980; Delaney, 1982; McPhie, 1993; Boulter, 1993b). Delaney (1982) demonstrated experimentally that transfer of heat from the magma affects pore-fluid flow in two stages. The early stage response is thermal expansion and pressurisation of pore fluids at the contact. This drives fluid flow to cooler regions. Hours to weeks after initiation of heat transfer, the second stage begins when hydrothermal convection driven by buoyancy contrasts becomes dominant (Delaney, 1982). The late history of this phase is marked by seawater convection through the hot fractured intrusion as it cools to ambient temperatures (Denlinger and Holmes, 1994). The circulating pore fluids may hydrothermally alter the cooling intrusion (e.g. Wilshire and Hobbs, 1962; Brooks et al., 1982; Pike, 1983; Hanson and Wilson, 1993) and leach Fe, Si and

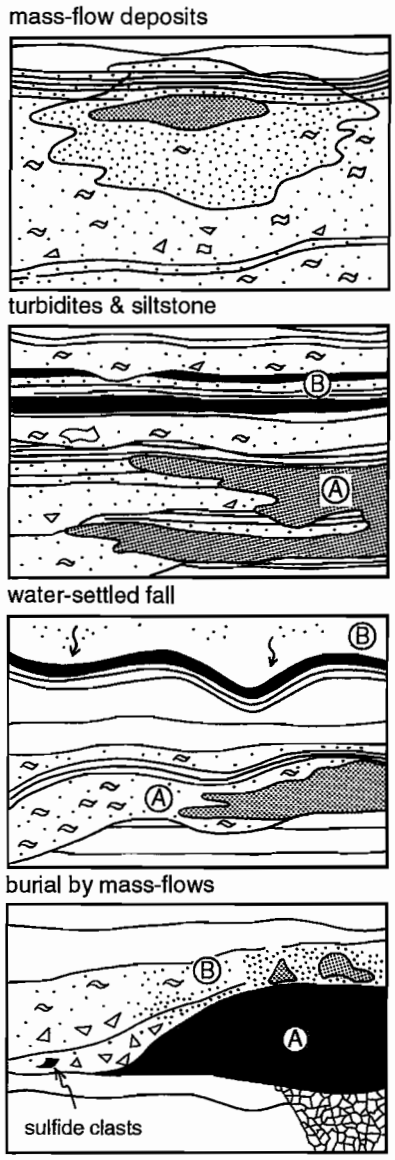

- Sub-seafloor replacement of rapidly emplaced mass-flow deposits(s)
- Host commonly syn-eruptive & pumiceous

(e.g. Rosebery, Allen, 1994; South Hercules, Khin Zaw & Large, 1995; Liontown, Miller, 1996; Långdal & Långsete, Allen et al.,1997b)

Ⓐ Sub-seafloor sulfide replacement front within rapidly emplaced units

Ⓐ + Ⓑ Synchronous sedimentation & sulfide precipitation both above & below the seafloor

(e.g. Currawong, Bodon & Valenta, 1995; Ansil, Galley et al., 1995)

Ⓐ Sub-seafloor replacement of a single rapidly emplaced unit
(e.g. Renström, Allen et al., 1997b)

Ⓐ + Ⓑ Synchronous sedimentation & massive sulfide deposition by replacement, infiltration & exhalation

Ⓐ Seafloor massive sulfide

Ⓐ + Ⓑ Burial; replacement of volcaniclastic deposits during ongoing hydrothermal activity
(e.g. Que River, Large et al., 1988)

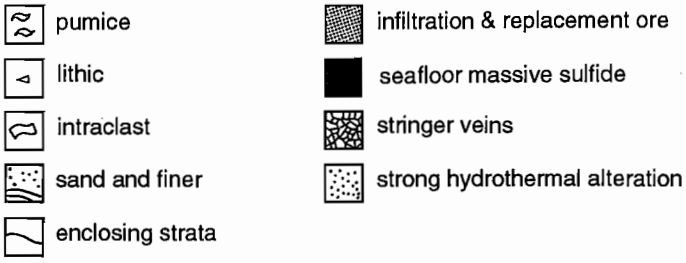

Figure 8. Schematic representation of various scenarios in which massive sulfide deposits may form and the morphology of the alteration halo associate with each. (Doyle, 1997a,b).

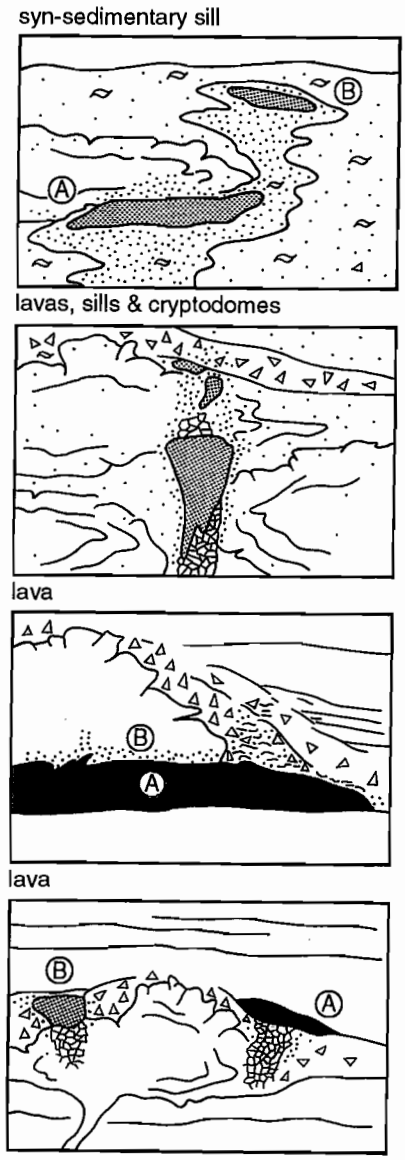

Ⓐ Ponding of hydrothermal fluids beneath a syn-sedimentary sill. Sub-seafloor replacement of the sill margin & host

Ⓑ Ascending fluids form a stacked system

(e.g. Rosebery, Allen, 1994)

- Sub-seafloor replacement within a discordant alteration envelope
- Stacked massive sulfide pipes & stratiform lenses

(e.g. Highway-Reward)

Ⓐ Seafloor massive sulfide mineralisation

Ⓑ Burial by lavas. Hanging wall alteration develops during continued hydrothermal activity. May form a stacked system

(e.g. Fukazawa, Sato et al., 1979)

Ⓐ Seafloor massive sulfide

Ⓑ Replacement of in situ & resedimented autoclastic breccia units

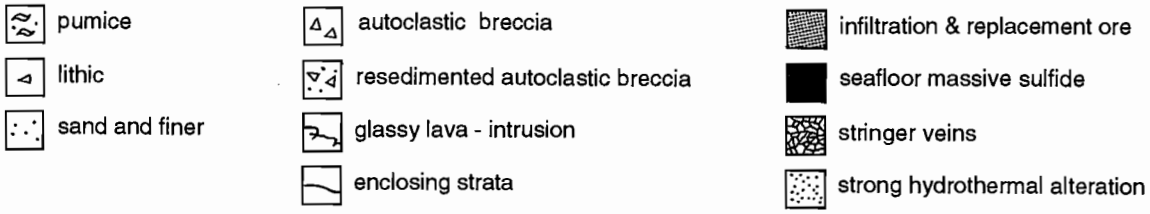

Figure 8 continued. Cartoon showing the various circumstances under which massive sulfide mineralisation may develop and the alteration halo associated with each. In these examples the host succession also includes lavas and intrusions.

other elements from glassy parts of the succession (cf. Sigurdsson, 1977). In the Trooper Creek Formation, widespread hematite alteration and discontinuous ironstone lenses are interpreted to have deposited from similar fluids circulating around lavas and intrusions (cf. Einsele et al., 1980; Einsele, 1986; Boulter, 1993a).

Stable isotope studies of hydrothermal vent fluids at the Escanaba Trough have suggested that the magma may also contribute to the hydrothermal fluid (Böhlke and Shanks, 1994). In the Escanaba Trough, the hydrothermal fluids ascend growth faults above the intrusion and deposit massive sulfides at the seafloor (e.g. Davis and Becker, 1994). Considering the case of a hydraulically open intrusion, Delaney (1982) demonstrated that if magmatic pressure is high, magmatic fluids will flow out into the host rock and displace connate water around the intrusion. If the magmatic pressure is low, connate water will flow into the intrusion.

In the Trooper Creek Formation, sediments at the margins of many intrusions display evidence of induration and dewatering which is consistent with observations from other volcanic successions (e.g. Kokelaar, 1982; Einsele, 1986; Kano, 1989; Hanson, 1991). Einsele (1986) noted that sediment within several tens of metres of syn-sedimentary sills in the Guaymas Basin, Gulf of California, were indurated, metamorphosed to low grades, and less porous than the enclosing strata. The reduction in porosity accompanying intrusion is a mechanism for creating sufficient space for the magma without uplifting the host sequence. In areas of long-lived magmatism, progressive dewatering and induration of sediments by early intrusions may favour the emplacement of subsequent magma at even shallower levels in the sequence where sediments remain poorly consolidated (e.g. Einsele et al., 1980). Eruption of lavas and domes may result as interactions between magma and sediment are minimised and magma ascends through discrete conduits in intrusions and sedimentary rock.

By acting as a relatively impermeable barrier (cf. McPhie, 1993), the indurated sediment may have inhibited the development of broad convection cells during syn-genetic hydrothermal discharge. Circulating connate fluids and ascending hydrothermal fluids may have been focussed through more porous and permeable units, including the fractured glassy margins of lavas and intrusions, pumice breccia beds, resedimented hyaloclastite units and fractures and faults within the host sequence. An increase in the strength of the host sediment may have also enhanced the ability of fractures to form and remain open. The resulting hydrological configuration probably promoted very efficient, focused, hydrothermal fluid discharge. At Highway-Reward, this was important in localising sulfide accumulation and promoted the formation of the pipe-like sub-seafloor massive sulfide deposits and discordant hydrothermal alteration envelope (Doyle, 1997b).

Conclusions

The mineralogy and distribution of alteration in volcanic rocks is complexly dependent on factors including, characteristics (mineralogy, distribution and morphology) of preceding alteration stages, porosity and permeability, primary rock composition and texture, and fluid chemistry and conditions. Successive alteration stages acting on the primary volcanic texture can be traced by examining the interrelationships between alteration and the nature and position of contacts, volcanic textures and facies, foliations (diagenetic and metamorphic) and mineralisation.

References

Allen R.L., 1988. False pyroclastic textures in altered silicic lavas, with implications for volcanic-associated mineralization. Econ. Geol., 83: 1424-1446.

Allen R.L., 1992. Reconstruction of the tectonic, volcanic and sedimentary setting of strongly deformed Zn-Cu massive sulfide deposits at Benambra, Victoria. Econ. Geol., 87: 825-854.

Allen R.L., 1994. Syn-volcanic, subseafloor replacement model for Rosebery and other massive sulfide ores. In: Cooke D.R. and Kitto P.A., Contentious issues in Tasmania Geology, Geol. Soc. Aust. Abstracts, 39: 107-108.

Allen R.L. and Large R.R., 1996. Rosebery alteration study. AMIRA - P439, Studies of VHMS-related alteration: geochemical and mineralogical vectors to ore. Report 3: 143-152.

Allen R.L. and Cas R.A.F., 1990. The Rosebery controversy: distinguishing prospective submarine ignimbrite-like units from true subaerial ignimbrites in the Rosebery-Hercules ZnCuPb massive sulphide district, Tasmania. Geological Society of Australia, Abstracts, 25: 31-32.

Allen R.L., Weihed P. and Svenson S.Å., 1996b. Setting of Zn-Cu-Au-Ag massive sulfide deposits in the evolution and facies architecture of a 1.9 Ga Marine Volcanic Arc, Skellefte District, Sweden. Econ. Geol., 91: 1022-1053.

Berry R.F., 1991 Structure of the Mount Windsor Sub-Province. In: Pongratz, J. and Large, R. (eds.) Geological controls on VMS mineralisation in the Mt Windsor Volcanic Belt. [unpub.] CODES, University of Tasmania, Australia: 1-22.

Berry R.F., Huston D.L., Stolz A.J., Hill A.P., Beams S.D., Kuronen U. and Taube A., 1992. Stratigraphy, structure, and volcanic-hosted mineralisation of the Mount Windsor Subprovince, north Queensland, Australia. Econ. Geol., 87: 739-763.

Böhlke J.K. and Shanks III W.C., 1994. Stable isotope study of hydrothermal vents at Escanaba Trough: observed and calculated effects of sediment-seawater interaction. In: Morton, J., Zierenberg, R. and Reiss, C. A. (eds.) Geologic, hydrothermal and biological studies at Escanaba Trough, Gorda Ridge, offshore California. US Geol. Surv. Bull., 2022: 223-239.

Boulter C.A., 1993a. High-level peperitic sills at Rio Tinto, Spain: implications for stratigraphy and mineralization. Trans. Instn. Min. Metall., 102: B30-B38.

Boulter C.A., 1993b. Comparison of Rio Tinto, Spain, and Guaymus Basin, Gulf of California: An explanation of a supergiant massive sulfide deposit in an ancient sill-sediment complex. Geology, 21: 801-804.

Brooks E.R., 1995. Palaeozoic fluidisation, folding, and peperite formation, northern Sierra Nevada, California. Can. J. Earth Sci., 32: 314-324.

Brooks E.R., Wood M.M. and Garbutt P.L., 1982. Origin and metamorphism of peperite and associated rocks in the Devonian Elwell Formation, northern Sierra Nevada, California. Geol. Soc. Am. Bull., 93: 1208-1231.

Davis E.E. and Villinger H., 1992. Tectonic and thermal structure of the Middle Valley sedimented rift, Northern Juan De Fuca Ridge. Proc ODP, Initial Reports, 139: 9-41.

Davis E.E. and Becker K., 1994. Thermal and tectonic structure of the Escanaba Trough: new heat-flow measurements and seismic reflection profiles. In: Morton, J., Zierenberg, R. and Reiss, C. A. (eds.) Geologic, hydrothermal and biological studies at Escanaba Trough, Gorda Ridge, offshore California. US Geol. Surv. Bull., 2022: 45-64.

Davidson G., Stolz A.J. and Eggins S.M., 1996. Exhalite geochemistry: A preliminary geochemical documentation of two barren ferruginous chert bodies in the Mount Windsor Volcanics. AMIRA - P439, Studies of VHMS-related alteration: geochemical and mineralogical vectors to ore. Report 2: 231-257.

Delany P.T., 1982. Rapid intrusion of magma into wet rock: groundwater flow due to pore pressure increases. J. Geophys. Res., 87: 7739-7756.

Denlinger R.P. and Holmes M.L., 1994. A thermal and mechanical model for sediment hills and associated sulfide deposits along the Escanaba Trough. In: Morton, J. L., Zierenberg, R. and Reiss, C. A. (eds.) Geologic hydrothermal and biological studies at Escanaba Trough, Gorda Ridge, offshore California. US Geol. Surv. Bull., 2022: 65-75.

Doyle M.G., 1995. Preliminary investigation of alteration at the Highway and Reward deposits, Mount Windsor Volcanics, Queensland. [unpub.] Report 1, AMIRA - P439, 149-160.

Doyle M.G., 1996. Volcanic influences in the formation of iron oxide-silica deposits in a volcanogenic-massive sulfide terrain, Mount Windsor Volcanic belt, Queensland. Australian Mineral Industries Research Association Limited - P439. Report 3: 87-142.

Doyle MG, 1997a. Alteration associated with sub-seafloor replacement style massive sulfide deposits: evidence from the Cambro-Ordovician Highway-Reward deposit, Mount Windsor Subprovince. AMIRA - P439, Studies of VHMS-related alteration: geochemical and mineralogical vectors to ore. Report 4: 231-257.

Doyle MG, 1997b. A Cambro-Ordovician volcanic succession hosting massive sulfide mineralisation: Mount Windsor Subprovince, Queensland. [unpub. Ph.D thesis]. University of Tasmania, 264 pp.

Doyle MG, 1997c. Alteration geochemistry of the sub-seafloor replacement style Highway-Reward deposit, Mount Windsor Subprovince. AMIRA - P439, Studies of VHMS-related alteration: geochemical and mineralogical vectors to ore. Report 5: 201-219.

Doyle MG 1998a. Snake Oil prospect: a brief description of the volcanic facies and mineralisation. CODES-SRC, University of Tasmania, 16pp.

Doyle MG 1998b. The Ordovician Highway-Reward sub-seafloor replacement deposit, Mount Windsor Subprovince, Queensland. AMIRA - P439, Studies of VHMS-related alteration: geochemical and mineralogical vectors to ore. Report 6.

Doyle M.G., Allen R.L. and McPhie J., 1993. Textural effects of devitrification and hydrothermal alteration in silicic lavas and shallow intrusions, Mount Read Volcanics (MRV), Cambrian, Tasmania. IAVCEI General Assembly, Ancient Volcanism and Modern Analogues, Abstracts, Canberra, 51.

Duffield W.A., Bacon C.R. and Delaney P.T., 1986. Deformation of poorly consolidated sediment during shallow emplacement of a basalt sill, Coso Range, California. Bull. Volc., 48: 97-107.

Duhig N.C., Stolz J.S., Davidson G.J. and Large R.R., 1992b. Cambrian microbial and silica gel textures in silica iron exhalites from the Mount Windsor Volcanic Belt, Australia: Their petrography, chemistry, and origin. Econ. Geol., 87: 764-784.

Einsele G., 1986. Interaction between sediments and basalt injections in young Gulf of California-type spreading centres. Geol. Rund., 75: 197-208.

Einsele G., Gieskes J.M., Curray J.R., Moore D.M., Aguayo E., Aubry M.P., Fornari D., Guerrero J., Kastner M., Kelts K., Lyle M., Matoba Y., Molina-Cruz A., Niemitz J., Rueda J., Saunders A., Schrader H., Simoneit B. and Vacquier V., 1980. Intrusion of basaltic sills into highly porous sediments and resulting hydrothermal activity. Nature, 283: 441-445.

Goodfellow W.D. and Franklin J.M., 1993. Geology, mineralogy, and chemistry of sediment-hosted clastic massive sulfides in shallow cores, Middle Valley, Northern Juan de Fuca Ridge. Econ. Geol., 88: 2037-2068.

Hanson R.E., 1991. Quenching and hydroclastic disruption of andesitic to rhyolitic intrusions in an submarine island-arc sequence, northern Sierra Nevada, California. Geol. Soc. Am. Bull., 103: 804-816.

Hanson R.E. and Wilson T.J., 1993. Large-scale rhyolite peperites (Jurassic, southern Chile). J. Volcanol. Geotherm. Res., 54: 247-264.

Henderson R.A., 1986. Geology of the Mt Windsor Subprovince-a Lower Proterozoic volcano-sedimentary terrane in the northern Tasman Orogenic Zone. Aust. J. Earth Sci., 33: 343-364.

Hutton L.J., Hartley J.S. and Riekins I.P., 1993. Geology of the Charters Towers region. In: Henderson, R. A. (ed.) Guide to the economic geology of the Charters Towers region, northeastern Queensland. Geol. Soc. Aust., Queensland division, 1-12.

Kano K.I., 1989. Interactions between andesitic magma and poorly consolidated sediments: examples in the Neogene Shirahama Group, South Izu, Japan. J. Volcanol. Geotherm. Res., 37: 59-75.

Khin Zaw and Large R.R., 1992. The precious metal-rich South Hercules mineralisation, western Tasmania: A possible subsea-floor replacement volcanic-hosted massive sulfide deposit. Econ. Geol., 87: 931-952.

Kokelaar B.P., 1982. Fluidization of wet sediments during emplacement and cooling of various igneous bodies. J. Geol. Soc. London, 139: 21-33.

Krynauw J.R., Hunter D.R. and Wilson A.H., 1988. Emplacement of sills into wet sediments at Grunehogna, western Dronning Maud Land, Antarctica. J. Geol. Soc. London, 145: 1019-1032.

Large R.R., 1992. Australian volcanic-hosted massive sulfide deposits: features, styles, and genetic models. Econ. Geol., 87: 471-510.

Lorenz B.E., 1984. Mud-magma interactions in the Dunnage Mélange, Newfoundland. In: Kokelaar, B. P. and Howells, M. F. (ed.) Marginal Basin geology - volcanic and associated sedimentary and tectonic processes in modern and ancient marginal basins. Geol. Soc. Lond. Spec. Pub., 16: 271-277 pp.

Marsaglia K.M. and Tazaki K., 1992. Diagenetic trends in leg 126 sandstones. Leg 126. Proc. ODP, Sci. Results, 126: 125-138.

McPhie J., 1993. The Tennant Creek porphyry revisited: a syn-sedimentary sill with peperite margins, early Proterozoic, Northern Territory. Aust. J. Earth Sci., 40: 545-558.

McPhie J. and Allen R.L., 1992. Facies architecture of mineralised submarine volcanic sequences: Cambrian Mount Read Volcanics, western Tasmania. Econ. Geol., 87: 587-596.

Miller C.R., 1996. Geological and geochemical aspects of the Liontown VHMS deposit, NE Queensland [M. Econ. Geol.]. University of Tasmania, 90 pp.

Pike J.E.N., 1983. Composition of Tertiary volcanic rocks, Mohave Mountains, Arizona. Geol. Soc. Am. Abst. with Programs, 15(5), 304.

Pollard D.D., Mullar O.H. and Dockstader D.R., 1975. The form and growth of fingered sheet intrusions. Geol. Soc. Am. Bull., 86: 351-363.

Sigurdsson H., 1977. Chemistry of the crater lake during the 1971-72 Soufriére eruption. J. Volcanol. Geotherm. Res., 2: 165-186.

Tazaki K and Fyfe W.S., 1992. Diagenetic and hydrothermal mineral alteration observed in Izu-Bonin deep-sea sediments. Leg 126. Proc. ODP, Sci. Results, 126: 101-112.

Wilshire H.G. and Hobbs B.E., 1962. Structure, sedimentary inclusions, and hydrothermal alteration of a latite intrusion. J. Geol., 70: 328-341.

Yamamoto T., Soya T., Suto S., Uto K., Takada A., Sakaguchi K. and Ono K., 1991. The 1989 submarine eruption off eastern Izu Peninsula, Japan: ejecta and eruption mechanisms. Bull. Volc., 53: 301-308.

Divergence indices — an experiment in geochemical alteration vectors

Garry J. Davidson
Centre for Ore Deposit Research

Summary

A geochemical method is documented for quantifying the amount of chemical change in a hydrothermal system within previously geochemically uniform rocks. The method presented here uses the wholerock analysis of alteration ratioed with that of an average unaltered precursor. The power of the method is its employment of the entire major element analysis of an altered rock to determine chemical change, whereas many other methods use selected elements that are considered to be sensitive to alteration processes. The method has applications to some VHMS systems, and also to many other ore deposit styles, such as porphyry mineralisation. It may be a particularly useful technique to apply to very large alteration systems, where it may be difficult to identify paths to ore. An example from Que River illustrates that the method may also have the "halo power" of wholerock oxygen isotopes, such that it extends well beyond visually recognisable alteration, and also beyond the halos of other single elements such as Cu, Pb, Zn, Au, K_2O enrichment and Na_2O depletion.

Introduction

Geochemical alteration vectors towards hydrothermal centres currently use either:

(1) True abundances of single elements or isotopes; or

(2) Ratios of enriched over depleted elements, in which the abundance of individual elements are scaled to render the "weight" of each relatively uniform within the index.

An example of the latter is the Alteration Index of Ishikawa et al. (1976) for VHMS deposits, which has subsequently been adapted for carbonate-rich shale-hosted Zn-Pb deposits by Large & McGoldrick (1993).

Alteration indices aim to (1) amplify a geochemical signal until it is unique and distinguishable from the background, and (2) provide a signature that changes characteristically towards ore. In the following approach, a method is proposed that uses the variation of geochemistry away from a known composition as a tool for mineral exploration, although the method can also be regarded as a general tool for quantifying geochemical change due to many different processes, such as for instance, the degree of chemical weathering of a soil, or the degree of fractionation of an igneous composition away from its primary melt.

Method

The method has several prerequisites:

(1) Knowledge of the unaltered geochemical composition, or a least altered composition which will be used as the standard for comparison. However, any composition can be used as a reference in the system. For example, if there is widespread background alteration imposed on a uniform rock, then an average of this material would be an appropriate starting composition;

(2) Wholerock data in a standard format. In this paper this is taken to include Fe expressed as Fe_2O_3, and volatile elements expressed as a loss on ignition (LOI).

The simple principle of the technique is to use as large a number of elements as possible from a rock composition, and to sum the changes in these elements to provide an index of divergence from the original composition.

The advantage of this is that, for instance, the full range of a geochemical composition can be brought to bear, unlike ratios of enriched over depleted elements, which use only some components of a composition, and also artificially and in part arbitrarily alter the concentrations of those elements within the index.

STEP 1 Recalculate the major element analyses to 100 wt. %. Express each element oxide as a ratio of altered wt. %/unaltered wt % = x. x is the factor decrease or increase. Where x = 1, the concentration has not changed; if x > 1, the altered concentration has increased over that in the unaltered rock, and if x < 1, the altered concentration has decreased. Use only geochemical data for which all elements in the index are available, to provide a valid comparison between samples.

STEP 2 Take the inverse of any value of x that is <1. This now provides a set of x's in which the fraction of change is expressed as a number that is greater than 1. In this way decreases and increases are now all expressed similarly in a parameter of change, and they can be dealt with together.

STEP 3 Add the values of x together. Subtract **n**, the number of elements, to produce a quantified index of chemical change that is independent of the number of elements used.

In summary, this becomes:

$$DI = (\Sigma(x)\{\text{for values of } x>1\}) + (\Sigma(1/x)\{\text{for values of } x<1\}) - n$$

where $x = (C_a/C_o)_i$
C_a = altered concentration of element **i**
C_o = unaltered concentration of element **i**
n = number of elements

Advantages

(1) This method is similar to a Gresens Analysis in that it relies on a comparison between altered and unaltered compositions to determine the degree of change of a given element, but it differs in **not requiring immobility of high field strength elements** as the basis of the comparison. It provides an empirically determined number for the degree of chemical change in any given sample that is caused by real metasomatism, mass change or volume change, all of which may occur as a natural part of alteration. In its present form it does not distinguish between any of these different means of achieving chemical change;

(2) The method is applicable to many different alteration styles without change to the index, unlike element-specific indices, such as the alteration index of Ishikawa. In VHMS terrains, one hydrothermal system may produce alkali enrichment in the footwall, and alkali depletion in the hangingwall, providing conflicting vectors if the one index is applied to both situations. Unfortunately, the identity of hangingwall and footwall are not always known;

(3) Greater sensitivity, because of the large number of elements that contribute to the final index of change. At present this index is intended only for major element analyses, but it may be possible to extend it to trace element concentrations too. The main thing is that the same trace elements are always used, to provide a meaningful index of comparison;

(4) The method minimises the influence of elements which make up most of the analysis, such as silica, by measuring their amount of change, rather than their absolute concentration;

(5) The method may provide a guide towards more intense alteration in areas of widespread alteration, where mineralogy is not changing, as for instance, in widespread sericite-quartz-pyrite alteration.

Disadvantages

(1) The requirement of an unaltered equivalent precursor limits the technique to homogeneous units; this contrasts with Ishikara-like indices, which are tethered to a particular alteration style, because they are defined specifically by the enrichments and depletions of that style;

(2) The method does not automatically take account of subtle chemical changes in original compositions that are due to (1) standard errors in the chemical analysis; (2) variation due to igenous or sedimentary fractionation of an apparently homogeneous lithology. However, it is possible to determine the standard deviation of the primary unaltered composition for a given lithology, and employ this to define the background of interest for altered samples.

Example

Que River

Que River was selected because of excellent previous geological and geochemical control, and because of the previous use of drillhole QR97 by Stolz & Large (1992) for experimenting with alteration parameters. All geochemical data employed in this example are shown in the accompanying table. Stolz & Large (1992) illustrated that the Que River alteration zone has extremely distinct high K_2O values, accompanied by highly anomalous Au, Cu, Pb, Zn values, and very low Na_2O values, giving rise to anomalous AI numbers. None of these parameters extend beyond the obvious alteration. They also demonstrated that $d^{18}O$ is the only parameter that does extend beyond the obvious alteration, which is an excellent advertisement for stable isotopes.

In this example the unaltered comparison analyses were obtained from the Que-Hellyer sequence data base that was analysed for low-gold by Stolz & Large (1992). These were averaged. Variation of these analyses away from the averaged analysis provided a divergence index range of 1.4–3.5, which roughly sets the background threshold at this site. A greater number of averaged samples would provide a more accurate estimate of the background threshold value.

Application of the DI or Divergence Index to the samples from QR97 showed that DI values were anomalous well beyond the obvious alteration zone, providing a halo at least as large as wholerock oxygen isotopes. Values varied from 3.3 to 524 (Fig. 1).

Conclusions

These results are extremely encouraging, and suggest that the combination of the variation of elements away from an unaltered average may be a powerful technique that can be applied to routinely collected data. However, the technique must be trialed at a wide range of sites to determine its power and its shortcomings. It is clearly applicable beyond the VHMS environment. The method was conceived near the end of the current AMIRA project, and consequently this example, and even the present form of the index, are at a pilot study stage. For instance, no attempt has been made to take account of mass or volume changes, although if this was done, it would require more sophisticated Gresens analysis, etc. Such an extension of the analysis might be useful for discriminating false (ie primary unaltered variations) from true (hydrothermally generated) anomalies, but taking it to the next level of sophistication also reduces its appeal to average exploration geologists. The application of the method to the Que River alteration zone illustrates the potential of the method to enlarge the chemical target in VHMS exploration.

References

Ishikawa, Y., Sawaguchi, T., Iwaya, S. & Horiuchi, M., 1976. Delineation of prospecting targets for Kuroko deposits based on modes of volcanism of underlying dacite and alteration halos. Mining Geology, v. 26, p. 105–117 (in Japanese with English abstract!).

Large R.R. & McGoldrick P.J. 1993. Primary geochemical halos related to Proterozoic sediment hosted Pb-Zn deposits and applications to exploration. Centre for Ore Deposit and Exploration Studies, AMIRA/ARC Project P.384 Report 3, 63–126 (unpubl.).

Stolz, A.J. and Large, R.R., 1992. Evaluation of the source-rock control on precious metal grades in VHMS deposits from western Tasmania. *Econ. Geol.* 87, 720-738.

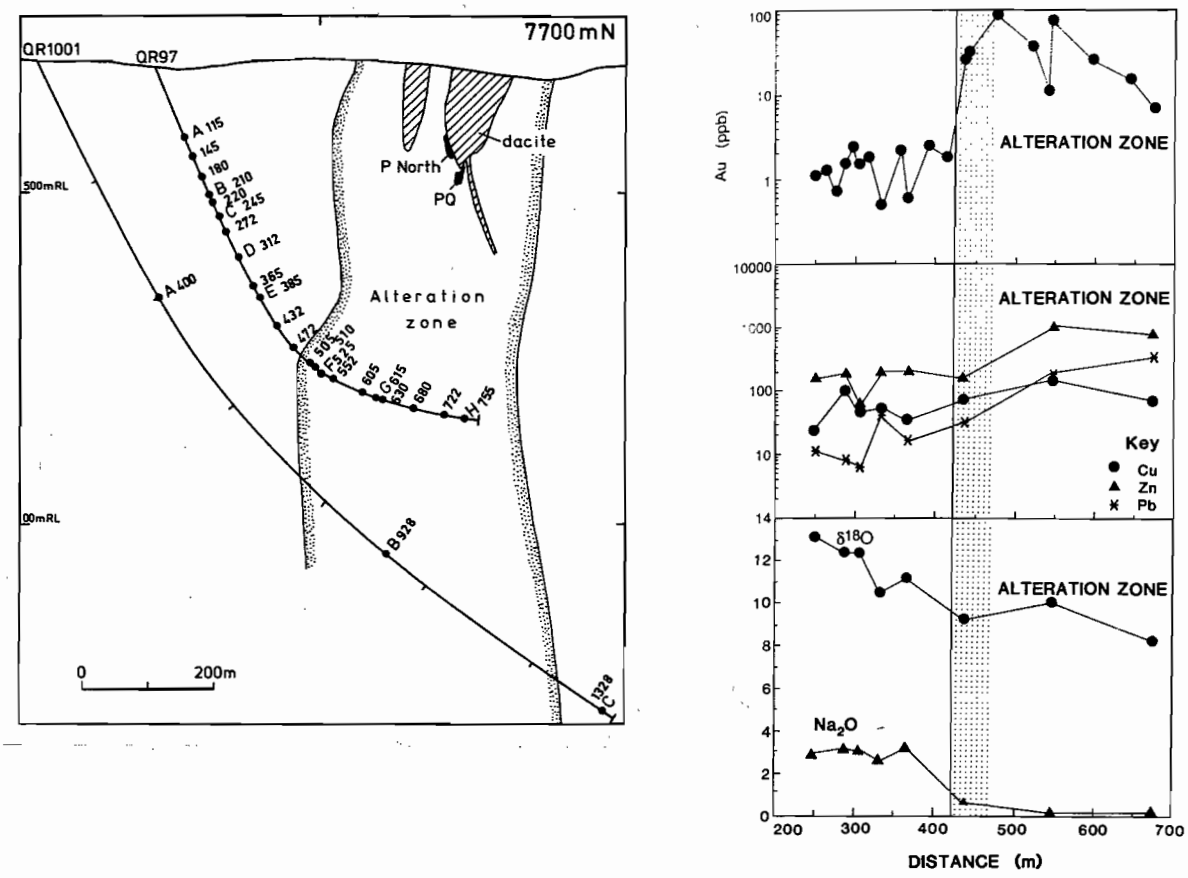

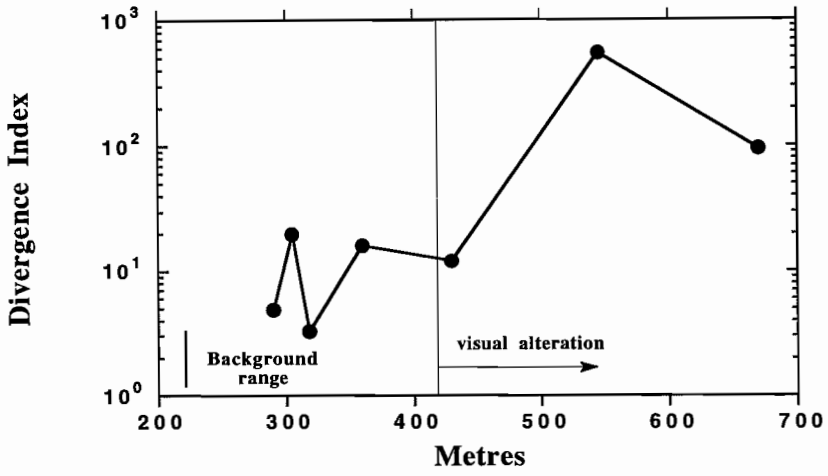

Figure 1. A compilation of results through the Que River alteration zone for DDH QR97, after Stolz & Large (1992), with a third graph added illustrating the divergence index halo. Note the DI halo extends as far away from visual alteration as the halo attributed to wholerock oxygen isotopes.

Table 1 A spreadsheet illustrating the steps taken in the analysis of the QR97 samples for the Divergence Index.

	SiO2%	TiO2%	Al2O3%	Fe2O3%	MnO	MgO	CaO	Na2O%	K2O%	P2O5%	LOI%	Total	X.VALUES	SiO2%	TiO2%	Al2O3%	Fe2O3%
Unaltered comparisons																	
MAC10/C	62.91	0.41	12.97	6.36	0.16	5.63	6.21	3.92	1.24	0.19	4.44	104.44		0.98358171	0.7628592	0.86322019	0.94057591
														1.01669235	1.3108579	1.15845298	1.06317841
MAC10/D	63.37	0.6	15.33	7.27	0.15	3.16	2.95	5.05	1.94	0.18	3.7	103.7		0.99746165	1.12391514	1.02717753	1.08241273
														1.00254481	1.12391514	1.02717753	1.08241273
HL30/A	64.15	0.59	16.43	6.5	0.09	2.8	2.32	6.12	0.88	0.1	2.66	102.66		1.019571	1.1159445	1.11160178	0.97719255
														1.019571	1.1159445	1.11160178	1.02333977
AV. UNALT	63.47	0.5333	14.91	6.71	0.133	3.8633	3.8267	5.03	1.3533	0.1567	3.6	103.59					
AV.Unalt'd100%	**61.26**	**0.515**	**14.39**	**6.477**	**0.129**	**3.729**	**3.694**	**4.855**	**1.306**	**0.151**	**3.475**	**99.99**					
Samples																	
QR97/B	66.01	0.51	14.3	5.88	0.12	1.53	6.13	3.36	2.02	0.14	7.74	107.74					
normalising	61.291	0.4735	13.278	5.4596	0.111	1.4206	5.6917	3.1198	1.8756	0.13	7.1866	100.04	*Alt/unalt'd—*	1.00042673	0.9198468	0.92257662	0.84294426
to 100%													*Take inverse if*	1.000426	1.08713756	1.08392081	1.18631806
QR/97/C	65.92	0.52	14.49	6.24	0.12	1.4	6.01	3.16	1.84	0.15	5.99	105.84	*<1*				
	62.306	0.4915	13.696	5.8979	0.113	1.3233	5.6805	2.9868	1.7391	0.1418	5.6616	100.04		1.0170043	0.9547259	0.95162278	0.91061785
														2.03400859	2.09484209	2.1016731	2.19631101
QR97/D	58.65	0.61	14.9	9.17	0.17	5.68	6.16	2.67	1.24	0.15	4.79	104.19					
	56.286	0.5854	14.299	8.8004	0.163	5.4511	5.9117	2.5624	1.19	0.144	4.5969	99.99		0.91873774	1.13716411	0.99357501	1.35874779
														1.0884499	1.13716411	1.00646653	1.35874779
QR97/E	73.67	0.32	13.85	2.36	0.04	0.44	3.54	3.27	2.42	0.08	5.43	105.42					
	69.896	0.3036	13.14	2.2391	0.038	0.4175	3.3586	3.1025	2.296	0.0759	5.1518	100.02		1.14088354	0.58975332	0.91304309	0.34570736
														1.14088354	1.6956242	1.09523856	2.89261992
QR97/F	63.04	0.67	17.68	7.49	0.17	3.98	1.98	0.58	4.25	0.16	4.95	104.95					
	60.038	0.6381	16.838	7.1333	0.162	3.7905	1.8857	0.5524	4.0476	0.1524	4.7143	99.952		0.97998214	1.2395	1.16997094	1.10136115
														1.02042676	1.2395	1.16997094	1.10136115
QR97/G	63.96	0.61	15.33	7.96	0.51	5.97	1.35	0.01	4.13	0.17	10.11	110.11					
	58.093	0.554	13.924	7.2298	0.463	5.4223	1.2262	0.0091	3.7511	0.1544	9.1826	100.01		0.94822717	1.07622616	0.96746875	1.11625389
														1.05459961	1.07622616	1.03362511	1.11625389
QR97/H	60.59	0.75	15.88	8.58	0.47	6.13	3.95	0.06	3.41	0.18	9.37	109.37					
	55.384	0.6856	14.516	7.8428	0.43	5.6033	3.6106	0.0548	3.117	0.1645	8.5649	99.973		0.90401344	1.33169561	1.00859146	1.21089699
														1.10617824	1.33169561	1.00859146	1.21089699

Table 1 cont.

	MnO	MgO	CaO	Na2O%	K2O%	P2O5%	LOI%	*index*	
Unaltered comparisons								The 1st 3 indicate the	
MAC10/C	1.1908046	1.44612379	1.61038688	0.77335222	0.90923504	1.20347273	1.2238825	und the unaltered average	
	1.1908046	1.44612379	1.61038688	1.29307186	1.09982563	1.20347273	1.2238825	2.62	
MAC10/D	1.12391514	0.81715774	0.77016252	1.00300799	1.43211519	1.14782823	1.02678667		
	1.12391514	1.22375393	1.29842724	1.00300799	1.43211519	1.14782823	1.02678667	1.49	
HL30/A	0.68091529	0.7311141	0.61158477	1.22736221	0.65594467	0.64389152	0.74536406		
	1.46861147	1.36777556	1.6350963	1.22736221	1.52451884	1.55305663	1.34162627	3.39	
AV. UNALT									
AV.Unalt'd100%									
Samples									
QR97/B									
	0.86573816	0.38095467	1.54093349	0.64256245	1.43578907	0.85959817	2.06815227		
	1.15508366	2.62498423	1.54093	1.55626896	1.4357	1.16333425	2.06815	4.90	
QR/97/C									
	0.88128544	0.35484602	1.5378994	0.61516722	1.33133433	0.93753771	1.62929007		
	2.26941227	5.63624747	3.07579879	3.25114853	2.66266867	2.13324753	3.25858013	19.71	
QR97/D									
	1.26765835	1.46176713	1.60048687	0.52775859	0.91098021	0.95193368	1.32289401		
	1.26765835	1.46176713	1.60048687	1.89480572	1.09771869	1.05049335	1.32289401	3.29	
QR97/E									
	0.29487666	0.11194627	0.90928866	0.63899714	1.75763921	0.50191772	1.48257432		
	3.39124839	8.93285656	1.09976078	1.56495224	1.75763921	1.99235843	1.48257432	16.05	
QR97/F									
	1.258	1.01646247	0.51052265	0.11377071	3.09852217	1.00765957	1.35666667		
	1.258	1.01646247	1.95877696	8.78960857	3.09852217	1.00765957	1.35666667	12.02	
QR97/G									
	3.59918256	1.45406756	0.33195986	0.0018707	2.87155877	1.0210447	2.64253709		
	3.59918256	1.45406756	3.01241241	534.55888	2.87155877	1.0210447	2.64253709	542.44	
QR97/H									
	3.338117	1.5025908	0.97750479	0.01129603	2.38611864	1.08802365	2.46478773		
	3.338117	1.5025908	1.02301289	88.5267053	2.38611864	1.08802365	2.46478773	93.99	